N. Ise
I. S. Sogami

Structure Formation in Solution

Ionic Polymers and Colloidal Particles

Springer

Norio Ise
Ikuo S. Sogami

Structure Formation in Solution

Ionic Polymers and Colloidal Particles

Springer

Norio Ise
Professor Emeritus
Kyoto University
Kyoto, Japan

Ikuo S. Sogami
Kyoto Sangyo University
Kyoto, Japan

DOI 10.1007/b83993
ISBN-10 3-540-25271-1 Springer Berlin Heidelberg New York
ISBN-13 978-3-540-25271-9 Springer Berlin Heidelberg New York
e-ISBN 3-540-27715-3

Library of Congress Control Number: 2005921903

Springer is a part of Springer Science+Business Media
springeronline.com

Printed in Germany

Typesetting: By the Authors
Production: LE-TEX, Jelonek, Schmidt & Vöckler GbR, Leipzig
Coverdesign: design&production, Heidelberg

Printed on acid-free paper 2/YL – 5 4 3 2 1 0

Contents

1

Introduction

1.1 Macroionic Systems and the Scope of the Book

In the present monograph, we will discuss ionic polymer solutions and colloidal dispersions. When these substances are dissolved into a solvent, they produce ionic species having large molecular weights and their counterions. We know a variety of naturally occurring ionic polymers and chemically synthesized compounds. Examples of the former are nucleic acids and some proteins, which play an important role in biological systems. Examples of synthetic ionic polymers are polyacrylic acid (PAA), polystyrenesulfonic acid (PSS) and polyallylamine (PAAm).

PAA is a high polymer, in which m acrylic acid molecules $CH_2{=}CH(COOH)$ are linearly polymerized by *covalent bonds*. The number m is called the degree of polymerization and is usually of the order of 10^3. When PAA is dissolved in a dissociating solvent like water, anionic macroions and counterions are produced. In the following scheme, the counterions are protons but they may be metal cations such as Na^+:

$$\left[\begin{array}{l} -CH_2-CH- \\ \qquad\quad | \\ \qquad\quad COOH \end{array}\right]_m \rightarrow \left[\begin{array}{l} -CH_2-CH- \\ \qquad\quad | \\ \qquad\quad COO^- \end{array}\right]_m + \; m\,H^+$$

PAA PAA anion Counterions .

PAAm is a cationic polymer and dissociates into PAAm cations and anionic counterions as shown below:

$$\left[\begin{array}{l} -CH_2-CH- \\ \qquad\quad | \\ \qquad\quad CH_2-NH_2 \end{array}\right]_m + m\,HCl \rightarrow \left[\begin{array}{l} -CH_2-CH- \\ \qquad\quad | \\ \qquad\quad CH_2-NH_3^+ \end{array}\right]_m + m\,Cl^-$$

PAAm PAAm cation Counterions .

In the case of NaCl, it dissociates into Na^+ and Cl^-, which both have low molecular weights. On the other hand, PAA anions and PAAm cations have high molecular weights. If m is 10^3, one polymer ion (macroion) has an analytical charge number Z_a of 10^3, which is exceedingly larger than 1 for Na^+. Since the interionic interaction is proportional to the square of the charge number, the physical properties of macroionic solutions are largely different from those of simple salt solutions. Furthermore, the macroionic solutions behave in ways considerably different from non-ionic polymer solutions. This basic point was correctly realized by Trommsdorf and Staudinger [1]. They noticed in 1931 that the viscosity of aqueous solutions of metal salts of PAA was much higher than that of non-ionic polymers, attributed it to a kind of structure formation by electrostatic interaction and made the following statement:

> *Like in NaCl solutions ···, PAA ions are surrounded by Na^+ in solutions of sodium salt of polyacrylic acid, and Na^+ interacts with PAA anions. As the consequence, the relative position of PAA anions is fixed. This is a kind of structure formation. This structure is distorted in flow, so that the solution viscosity is increased.*

These molecules are flexible in solution because of the free rotation around C-C bonds in the main chain. They cannot assume a definite conformation or shape. Even if they are stretched out into rods, the end-to-end distance is about 100 nm, so that their shapes and the distribution in solution cannot be directly observed.

In order to confirm the properties indirectly inferred, we avail ourselves of colloidal particles, which are so large that they can be "seen" by microscope. We study the dynamics and distribution of particles in their dispersions. The colloid field was called "*Die Welt der Vernachlässigten Dimensionen*" [2] and was one of the fields which could not be studied smoothly. Recent technical developments, however, have made it possible to control the particle diameter, its distribution, and the charge number. As a result, it is now possible to study the behavior of well-defined particles in dispersions in real time. The microscopic information thus obtained is expected to provide support to the indirectly derived conclusion on the behavior of "invisible"}, flexible ionic polymers in solution.

In this monograph our discussion will be limited to a recent topic, namely structure formation in dilute solutions or dispersions. We imply by the structure formation that solute ions or colloidal particles form a more or less three-dimensionally regular distribution, though not in the solid state. Such a structure was anticipated in an early stage of the investigation of ionic systems. For example, in the case of simple electrolyte solutions, Ghosh assumed lattice-like ionic arrangements to calculate the osmotic coefficient (the activity coefficient of the solvent) [3]. With such an assumption, the interionic distance is inversely proportional to the cube-root of the concentration. On the other hand, physico-chemical properties at low concentrations are experimentally found to show square-root relationships. This concentration de-

pendence could be accounted for by the Debye-Hückel (DH) theory of strong electrolytes [4]. When the concentration is raised, however, the cube-root dependence is found experimentally [5]. For ionic polymer solutions, a cube-root law is also experimentally observed [6]. In early theoretical treatments of ionic polymer solutions, some sorts of lattice-like distribution of rodlike macroions were explicitly or implicitly assumed [7–11].

Regardless of whether the geometrical model of infinitely long rods is realistic or not, we need to mention that, like in the case of Ghosh, *space-filling* ordered arrangements were assumed in these theories. In other words, the entire solution was assumed to be uniformly covered by the regular arrangement. This is what we call the one-state structure in the present monograph. Such a structure can be easily accepted by invoking repulsive interaction between similarly charged macroions which are confined by closed container walls.

What we wish to emphasize in the present monograph is not such a uniform distribution of macroions, however. Instead, we pay attention to *localized, ordered structures* of ionic polymers or particles, or *self-sustaining structures* without the help of walls. As a result of the existence of such structures, the systems are microscopically inhomogeneous. Although the existence of this inhomogeneity is surprising in condensed systems, it has been inferred for flexible ionic polymer solutions by scattering experiments (Chap. 3) and "visualized" for colloidal dispersions (Chap. 4). These experimental observations are difficult to explain when we admit the existence of repulsion only or if we assume no interaction between macroions [11]. The observations led the present authors to accept an attraction between macroions albeit similarly charged. In the present monograph, we wish to describe and understand the microscopic inhomogeneity in macroionic systems from experimental and theoretical points of view, while we try not to be redundant with some recent publications [12–15].

1.2 Principles for Structure Analysis on Macroionic Systems

The structure of a macroionic system means the average configuration of macroionic solutes in the dispersion. Analysis of such structures is made by using diffraction and scattering methods with visible light, X-rays and neutrons. The macroionic solutes forming an ordered configuration give rise to coherent contributions to diffraction and scattering amplitudes. By contrast, contributions from the solvent molecules associated always with random phases due to thermal motion are cancelled out on average.

Electromagnetic waves of visible light and X-rays being incident into solutions are scattered by charged constituents of atoms and molecules, viz, electrons and atomic nuclei. As shown below, the scattering effect of electromagnetic waves by charged particles is proportional to the inverse-square of

the mass of the particle (See (1.10) and (1.13)). Accordingly the scattering effects from atomic nuclei are negligibly small. The scattering effect of a proton (the lightest atomic nucleus) is smaller than that of an electron by a factor 4.0×10^6, since the ratio of masses of the proton and electron is about 2.0×10^3. Therefore, the structure analysis of macroionic solution by electromagnetic waves observes electron distributions in macromolecules in the solution.

To investigate colloidal dispersions, in which the size of the particles is approximately of the order of visible light, the optical microscope is useful in addition to laser diffraction analysis. In particular, the method of optical microscopy can be used to observe both random motion and ordering formation of colloidal particles.

If the macroions do not include atoms with magnetic moments, neutrons can penetrate a cloud of electrons and interact directly with atomic nuclei through the strong nuclear force. Accordingly, by observing scattering cross sections of neutrons, it is possible to obtain information concerning the distribution of atomic nuclei of solutes. To make structural analysis of macroionic systems by neutron scattering and diffraction, we must use a facility where cold neutrons and an apparatus with a long camera length are available.

In this section, we explain basic concepts and theories that are necessary to understand scattering and diffraction of electromagnetic waves using a simple model. States of electrons bound in macromolecules and their interactions with electromagnetic waves must be described, respectively, by quantum mechanics and quantum field theory [16–18] in principle. However, it is well known that a simple oscillator model for bound electrons, i.e., the *Thomson model*, is effective for the structure analysis of matter. In this section we use the Thomson model with modification to explain the scattering of electromagnetic waves by bound electrons.

In the Thomson model, the electron is assumed to be bound around an equilibrium position and make a simple harmonic oscillation with a proper frequency. The electron which is accelerated by external electromagnetic waves executes a forced oscillation and emits electromagnetic waves. The motion of the electron is described by Newton's equations of motion. We formulate the scattering theory of electromagnetic waves by bound electrons in the classical Thomson model by using minimum information on the quantum distributions of electrons inside atoms and molecules.

1.2.1 Electromagnetic Waves Emitted by Accelerated Electrons

Suppose that one electron around the equilibrium point E in a solute molecule is accelerated by electromagnetic waves. We observe expanding electromagnetic waves emitted by the electron at the point P on a spherical surface which has its origin at E and a sufficiently large radius R.

Note that the electromagnetic wave emitted at the time $\tau = t - R/c$ from the point E is observed at the time t at the point P where c is the speed of

light. The observed electric and magnetic fields, $\boldsymbol{E}$ and $\boldsymbol{B}$, are calculated to be

$$\boldsymbol{E} = -\frac{e}{c^2}\frac{1}{R}\boldsymbol{n} \times [\boldsymbol{n} \times \boldsymbol{a}(\tau)] \tag{1.1}$$

and

$$\boldsymbol{B} = \boldsymbol{n} \times \boldsymbol{E} \tag{1.2}$$

where $\boldsymbol{a}(\tau)$ is the acceleration of the electron at τ and $\boldsymbol{n}$ is the unit vector for the direction from E to P. Derivation of these equations is explained in standard textbooks on electromagnetism [19]. The *Poynting vector* which represents the energy flux carried by the electromagnetic field per unit time is given by

$$\boldsymbol{S} = \frac{c}{4\pi}\boldsymbol{E} \times \boldsymbol{B} = \frac{c}{4\pi}\boldsymbol{E}^2\boldsymbol{n} = \frac{e^2}{4\pi c^3}\frac{1}{R^2} \mid \boldsymbol{n} \times \boldsymbol{a}(\tau) \mid^2 \boldsymbol{n}. \tag{1.3}$$

Then, the electromagnetic energy $\mathrm{d}P$ passing through the solid angle $\mathrm{d}\Omega$ in unit time is given by the *Larmor formula* [19]

$$\mathrm{d}P = (\boldsymbol{n} \cdot \boldsymbol{S})R^2\mathrm{d}\Omega = \frac{e^2}{4\pi c^3} \mid \boldsymbol{n} \times \boldsymbol{a}(\tau) \mid^2 \mathrm{d}\Omega \, . \tag{1.4}$$

1.2.2 The Modified Thomson Model

Let us assume that an electron with mass m executes a harmonic oscillation with proper frequency ω_0 around an equilibrium position. The forced oscillation of the electron by an external electric field is described by Newton's equation of motion.

Suppose that a monochromatic electromagnetic wave being incident into a macroionic dispersion has a wavelength λ inside the dispersion, a frequency ν and a unit vector $\boldsymbol{n}_0$ representing the direction of propagation. Choosing an origin O inside the dispersion, we express the equilibrium position E by a vector $\boldsymbol{r}$ and a displacement from E by $\boldsymbol{\eta}$. In the complex number representation, the incident electric field at the time t at E is expressed by

$$\boldsymbol{E}_0(\boldsymbol{r}, t) = \boldsymbol{E}_0 \, \mathrm{e}^{\mathrm{i}\boldsymbol{k}_0 \cdot \boldsymbol{r} - \mathrm{i}\omega t} = \boldsymbol{\epsilon}_0 E_0 \, \mathrm{e}^{\mathrm{i}\boldsymbol{k}_0 \cdot \boldsymbol{r} - \mathrm{i}\omega t} \tag{1.5}$$

where $\boldsymbol{k}_0 = (2\pi/\lambda)\boldsymbol{n}_0$ is the wave vector and $\omega = 2\pi\nu$ is the angular frequency. Here the electric field is decomposed as $\boldsymbol{E}_0 = E_0\boldsymbol{\epsilon}_0$ with E_0 the strength of the electric field and $\boldsymbol{\epsilon}_0$ the polarization vector. As is well known, observed quantities must be calculated by taking real parts in the complex number representation.

The electron around the equilibrium position E is driven by the external electric field $\boldsymbol{E}_0(\boldsymbol{r}, t)$ in (1.5) to make a forced oscillation described by the equation

$$m\frac{\mathrm{d}^2\boldsymbol{\eta}}{\mathrm{d}t^2} = -m\omega_0^2\boldsymbol{\eta} - m\gamma\frac{\mathrm{d}\boldsymbol{\eta}}{\mathrm{d}t} - eE_0\boldsymbol{\epsilon}_0 \, \mathrm{e}^{\mathrm{i}\boldsymbol{k}_0 \cdot \boldsymbol{r} - \mathrm{i}\omega t} \, . \tag{1.6}$$

Here, the velocity of the electron is assumed to be so small compared with the speed of light that effects of the magnetic component of the Lorentz force are negligible. On the right-hand side of this equation, the first and second terms represent, respectively, the elastic force with spring constant $m\omega_0^2$ and the damping factor associated with emission of radiation. The third term expresses the external force by the incident wave, and its phase factor $e^{\mathrm{i}\boldsymbol{k}_0\cdot\boldsymbol{r}}$ plays a crucial role in analyzing interference and diffraction of the scattered electromagnetic field.

It is crucial to recognize that the space part $\boldsymbol{k}_0 \cdot \boldsymbol{r}$ of the phase factor in (1.6) is independent of the time variable. Namely, the displacement vector $\boldsymbol{r}$ of the equilibrium point E is assumed not to depend on t. Otherwise (1.6) becomes a highly nonlinear differential equation with respect to t, which is hard to solve. As a matter of fact, the existence of the static equilibrium position E is a basic prerequisite for the Thomson model of the atom in which electrons are assumed to execute oscillatory motion around such equilibrium positions inside a sphere with positive charges. However, this basic postulate was disproved by the *Earnshaw theorem* insisting that "*A charged particle cannot have an equilibrium point in a static electric field*" [20].

The Earnshaw theorem is readily proved by the following argument. Suppose that a charged particle takes an equilibrium position in a static electric field. Then, such a position must be on the top (at the bottom) of the electric potential, and accordingly the second derivative of the electric potential takes positive (negative) values in an infinitesimal region surrounding the position. This implies that the divergence of the electric field strength which is the gradient of the electric potential is non-vanishing at the position. Consequently, owing to the Gauss theorem in (2.2) in Sect. 2.2, the equilibrium position for the particle must already be occupied by another charge. This is a contradiction.

Rutherford who had discovered atomic nuclei proposed a dynamical model of the atom, in place of the Thomson model, where electrons revolve around the nucleus. This model is free from criticism by the Earnshaw theorem. However, the new dynamical model was also doomed to suffer difficulty. As described in Sect. 1.2.1, the acceleration causes the charged particle to emit electromagnetic radiation. Accordingly the revolving electrons inside the atom have to fall into the nucleus in 10^{-11} second by losing their energy by radiation. This difficulty of the Rutherford model could be resolved only by the theory of quantum mechanics in which the stationary states of electrons are described by the new concept of quantum probabilistic distribution.

The advent of quantum mechanics has partially and effectively revived the once-denied Thomson model of the oscillating electron for electromagnetic radiation. In the *modified Thomson model*, the acceleration mechanism of the electron around the equilibrium position E is described by the Newtonian equation (1.6) provided that quantum mechanics is allowed to describe the position E by a probabilistic distribution inside an atom. Namely, we calculate first the electromagnetic waves emitted by the accelerated electron by solving

(1.6). Then we take the integral of observed quantities with respect to the displacement vector $\boldsymbol{r}$ by using a distribution function which is calculated from the electron wave function in quantum mechanics.

It is practically important to note that, as will be shown below, detailed information on the electron wave functions is not necessary at all for actual structure analyses of macroionic dispersions.

1.2.3 Electromagnetic Radiation in the Modified Thomson Model

By assuming $\boldsymbol{\eta}(t) \propto \boldsymbol{\epsilon}_0 \mathrm{e}^{-\mathrm{i}\omega t}$, we obtain a particular solution of the inhomogeneous equation (1.6) in the form

$$\boldsymbol{\eta}(t) = \frac{e}{m} \frac{1}{\omega^2 - \omega_0^2 + \mathrm{i}\gamma\omega} \boldsymbol{E}_0 \, \mathrm{e}^{\mathrm{i}\boldsymbol{k}_0 \cdot \boldsymbol{r} - \mathrm{i}\omega t} \tag{1.7}$$

which enables us to calculate the acceleration $\boldsymbol{a}(t)$ as [1]

$$\boldsymbol{a}(t) = \frac{\mathrm{d}^2 \boldsymbol{\eta}}{\mathrm{d}t^2} = -\frac{e}{m} \frac{\omega^2}{\omega^2 - \omega_0^2 + \mathrm{i}\gamma\omega} \boldsymbol{E}_0 \, \mathrm{e}^{\mathrm{i}\boldsymbol{k}_0 \cdot \boldsymbol{r} - \mathrm{i}\omega t} \, . \tag{1.8}$$

Substituting the acceleration of the electron at $\tau = t - R/c$ into (1.1), we obtain the electric field observed at P at the time t as

$$\boldsymbol{E} = r_\mathrm{c} \, g \, E_0 \, \boldsymbol{n} \times (\boldsymbol{n} \times \boldsymbol{\epsilon}_0) \frac{1}{R} \, \mathrm{e}^{-\mathrm{i}\omega(t - \frac{R}{c}) + \mathrm{i}\boldsymbol{k}_0 \cdot \boldsymbol{r}} \tag{1.9}$$

where r_c is a quantity with the dimension of length defined by

$$r_\mathrm{c} = \frac{e^2}{mc^2} = 2.81794 \times 10^{-13} \mathrm{cm} \tag{1.10}$$

and called the *classical electron radius* which characterizes the scattering of electromagnetic waves by electrons. The factor g is the function

[1] The homogeneous equation

$$m \frac{\mathrm{d}^2 \boldsymbol{\eta}}{\mathrm{d}t^2} = -m\omega_0^2 \boldsymbol{\eta} - m\gamma \frac{\mathrm{d}\boldsymbol{\eta}}{\mathrm{d}t}$$

associated with (1.6) has independent solutions

$$\exp\left(-\frac{1}{2}\gamma t \pm \mathrm{i}t \sqrt{\omega_0^2 - \frac{1}{4}\gamma^2} \right)$$

which describe damped oscillations. General solutions of the equation of motion (1.6) are given by linear combinations of these solutions and the particular solution of (1.7). However, it is possible and relevant to ignore the damped solutions and use the contribution of the forced oscillation only, because we need the response of the bound electron to the incident electromagnetic waves.

$$g(\omega, \omega_0, \gamma) = \frac{\omega^2}{\omega^2 - \omega_0^2 + \mathrm{i}\gamma\omega} \tag{1.11}$$

which describes the dependence of the emitted electromagnetic wave on the frequency of the incident wave and proper frequency of the bound electron. Evidently, the electric field in (1.9) represents a spherical wave expanding from the equilibrium position of the electron.

The magnitude of the Poynting vector $\boldsymbol{S}(t)$ expresses the energy passing through a unit cross section perpendicular to the direction of propagation of the scattered electromagnetic wave per unit time. Note that the time T which is necessary for the observation of the electromagnetic wave is sufficiently larger than the time scales characteristic of the propagation of the electromagnetic wave and the motion of the electron. Namely, there hold the relations ωT, $\omega_0 T \gg 1$. Therefore, it is natural to estimate the observed value of a physical quantity $Q(t)$ by the average

$$\overline{Q} = \lim_{T\to\infty} \frac{1}{2T} \int_{-T}^{T} Q(t)\,\mathrm{d}t\ . \tag{1.12}$$

Substituting the real part of (1.9) into the formula (1.3) for the Poynting vector and taking the average, we obtain the average strength of electromagnetic energy I_e observed at P as follows:

$$I_\mathrm{e} \equiv \overline{\boldsymbol{n}\cdot\boldsymbol{S}} = I_0\, r_\mathrm{c}^2\, |g|^2 \frac{P}{R^2} \tag{1.13}$$

where I_0 is the average strength of the incident electromagnetic wave defined by

$$I_0 \equiv \frac{c}{4\pi}\overline{\boldsymbol{E}_0(0,t)^2} = \frac{c}{8\pi}|E_0|^2 \tag{1.14}$$

and P is the *polarization factor* given by

$$P = |\ \boldsymbol{n}\times\boldsymbol{\epsilon}_0\ |^2 \tag{1.15}$$

which characterizes the correlation between the directions of the incident and scattered waves. The distribution of the magnitude of the emitted electromagnetic wave has a minimum in the plane perpendicular to the direction of the incident wave.

For description of the scattering processes of electromagnetic waves, it is convenient to use the concept of the *differential cross section* defined by

$$\mathrm{d}\sigma = \frac{I_\mathrm{e}\, R^2 \mathrm{d}\Omega}{I_0} \tag{1.16}$$

where $\mathrm{d}\Omega$ is the solid angle. From (1.13), we obtain the formula

$$\mathrm{d}\sigma = r_\mathrm{c}^2\, |g|^2\, P\, \mathrm{d}\Omega \tag{1.17}$$

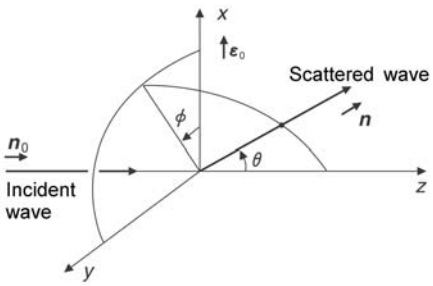

Fig. 1.1. Relation between incident wave and scattered wave. The unit vector $\boldsymbol{n}_0$ ($\boldsymbol{n}$) shows the direction of incident (scattered) wave and $\boldsymbol{\epsilon}_0$ is the unit vector for the incident electric field. The angle θ between the two vectors $\boldsymbol{n}_0$ and $\boldsymbol{n}$ is called the scattering angle. The z and x axes are chosen, respectively, in the direction $\boldsymbol{n}_0$ and $\boldsymbol{\epsilon}_0$. ϕ is the angle between the projection of $\boldsymbol{n}$ onto the x-y plane and the x axis

for the differential cross section of the electromagnetic wave for electrons.

In Fig. 1.1, the z and x axes are chosen in the directions of propagation $\boldsymbol{n}_0$ and polarization vector $\boldsymbol{\epsilon}_0$ of the incident plane wave. The scattered wave emitted from the electron at the origin of the Cartesian coordinates propagates along the direction $\boldsymbol{n}$ toward the observation point P. These three unit vectors have the following representations as

$$\boldsymbol{n}_0 = \begin{pmatrix} 0 \\ 0 \\ 1 \end{pmatrix}, \quad \boldsymbol{\epsilon}_0 = \begin{pmatrix} 1 \\ 0 \\ 0 \end{pmatrix}, \quad \boldsymbol{n} = \begin{pmatrix} \sin\theta\cos\phi \\ \sin\theta\sin\phi \\ \cos\theta \end{pmatrix} \tag{1.18}$$

where θ is the scattering angle defined by $\cos\theta = \boldsymbol{n} \cdot \boldsymbol{n}_0$. The polarization factor is expressed by

$$P = (\boldsymbol{n} \times \boldsymbol{\epsilon}_0)^2 = \sin^2\phi + \cos^2\theta\cos^2\phi\,. \tag{1.19}$$

If the incident electromagnetic wave is not polarized, the average strength $\langle I_\mathrm{e} \rangle$ is calculated by integrating (1.13) over the angle ϕ as

$$\langle I_\mathrm{e} \rangle = \frac{1}{2\pi}\int_0^{2\pi} I_\mathrm{e}\,\mathrm{d}\phi = I_0\, r_\mathrm{c}^2\,|g|^2 \frac{1}{R^2}\,\frac{1+\cos^2\theta}{2} \tag{1.20}$$

and the differential cross section is given by

$$\mathrm{d}\sigma = r_\mathrm{c}^2\,|g|^2\,\frac{1+\cos^2\theta}{2}\mathrm{d}\Omega \tag{1.21}$$

where $\mathrm{d}\Omega = \sin\theta\,\mathrm{d}\theta\,\mathrm{d}\phi$.

If the angular frequency ω of the incident electromagnetic wave is much larger than the proper frequency ω_0 of the bound electron as $\omega^2 \gg \omega_0^2$, the

function g in (1.11) reduces to 1. For large energy the total cross section σ of the electromagnetic wave is given by

$$\sigma = \int \mathrm{d}\sigma = \frac{8\pi}{3} r_{\mathrm{c}}^2 \ . \tag{1.22}$$

This result was first derived by Thomson who investigated the scattering of electromagnetic waves by free electrons. Such processes which are almost independent of ω and ω_0 are called *Thomson scattering*. The X-ray experiments for the structure analysis of macroionic dispersions are Thomson scattering.

If the condition $\omega^2 \ll \omega_0^2$ holds, we find $g \simeq (\omega/\omega_0)^2$ in (1.11) and obtain the total cross section as

$$\sigma = \frac{8\pi}{3} \left(\frac{\omega}{\omega_0} \right)^4 r_{\mathrm{c}}^2 \ . \tag{1.23}$$

In this case, the strength of the scattered wave is proportional to the fourth power of its frequency. Such a process is called *Rayleigh scattering*. Both the Thomson and Rayleigh scatterings are elastic scattering where the energies of the incident and scattered waves are subjected to no change. This elastic scattering is used for the structure analysis of matter.

If the angular frequency ω is close to the proper frequency ω_0, the factor g in (1.11) takes a large value leading to strong resonant scattering. In such a region of frequency, there occur inelastic processes with absorption and emission of photons which must be described by quantum mechanics and quantum field theory. However, electromagnetic waves in such a region of frequency are seldom used for the structure analysis of macroioinic dispersions. In this book the inelastic scattering is not considered.

1.2.4 Scattering of Electromagnetic Waves by Macromolecules

Let us consider the scattering of an electromagnetic wave by one macromolecule M whose center has the displacement vector $\boldsymbol{r}_M$ from the origin O. We notice one electron α in M and express its equilibrium position E by

$$\boldsymbol{r}_\alpha = \boldsymbol{r}_M + \boldsymbol{\xi}_\alpha \ . \tag{1.24}$$

As shown in Fig. 1.2, $\boldsymbol{\xi}_\alpha$ is the relative displacement vector of the electron α from the center of M to the equilibrium position E.

An incident electromagnetic wave with wavelength λ induces the electric field

$$\boldsymbol{E}_0(\boldsymbol{r}_\alpha, t) = \boldsymbol{E}_0 \, \mathrm{e}^{\mathrm{i}\boldsymbol{k}_0 \cdot \boldsymbol{r}_\alpha - \mathrm{i}\omega t} \tag{1.25}$$

at the equilibrium position E of the electron α at the time t. As in the previous subsection, the electron α is assumed to execute the harmonic oscillation with frequency ω_α around E. The electromagnetic field in (1.25) causes the forced

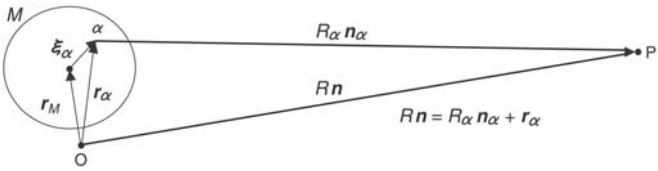

Fig. 1.2. A displacement vector $R_\alpha \boldsymbol{n}_\alpha$ from an equilibrium position E of an electron α in a macromolecule M to the point of observation P and a vector $R\,\boldsymbol{n}$ from the origin O to P. The distance $|\boldsymbol{r}_\alpha|$ between O and E is sufficiently smaller than the distances R and R_α

oscillation of α. From (1.9), we readily obtain the electric field which is created by α and observed at the point P at the time t as follows:

$$\boldsymbol{E}_\alpha = r_c g_\alpha E_0\, \boldsymbol{n}_\alpha \times (\boldsymbol{n}_\alpha \times \boldsymbol{\epsilon}_0)\, \frac{1}{R_\alpha}\, \mathrm{e}^{-\mathrm{i}\omega(t-\frac{R_\alpha}{c})+\mathrm{i}\boldsymbol{k}_0\cdot\boldsymbol{r}_\alpha} \tag{1.26}$$

where R_α is the distance from the equilibrium position E of α to the point of observation P and $\boldsymbol{n}_\alpha$ is the unit vector for its direction. The factor g_α is defined from the function g in (1.11) as

$$g_\alpha = g(\omega, \omega_\alpha, \gamma_\alpha) = \frac{\omega^2}{\omega^2 - \omega_\alpha^2 + \mathrm{i}\gamma_\alpha\omega}\ . \tag{1.27}$$

Suppose that $\boldsymbol{n}_\alpha$ and R_α ($\boldsymbol{n}$ and R) are, respectively, the unit vector and the distance from the equilibrium position E (the origin O) to the point of observation P. The two vectors $R\,\boldsymbol{n}$ and $R_\alpha \boldsymbol{n}_\alpha$ are related by

$$R\,\boldsymbol{n} = R_\alpha \boldsymbol{n}_\alpha + \boldsymbol{r}_\alpha \tag{1.28}$$

where $\boldsymbol{r}_\alpha$ is the relative displacement vector from O to E. In order to observe the macromolecule M in the dispersion, it is necessary for the electromagnetic wave to receive *coherent scattering* in which phases of scattered waves from electrons at various position in M take nearly the same value. As seen from Fig. 1.2, R and R_α can be taken to be sufficiently larger than the scale $|\boldsymbol{r}_\alpha|$ of the region of the source for coherent scattering by taking O and P appropriately. In such a situation, there hold the relations

$$\begin{cases} \boldsymbol{n}_\alpha \simeq \boldsymbol{n} \\ R_\alpha \simeq R - \boldsymbol{n}\cdot\boldsymbol{r}_\alpha \\ \dfrac{1}{R_\alpha} \simeq \dfrac{1}{R} \end{cases} \tag{1.29}$$

to a good approximation. These relations allow us to rewrite (1.26) as

$$\boldsymbol{E}_\alpha = r_c g_\alpha E_0\, \boldsymbol{n} \times (\boldsymbol{n} \times \boldsymbol{\epsilon}_0)\, \frac{1}{R}\, \mathrm{e}^{-\mathrm{i}\omega(t-\frac{R}{c})-\mathrm{i}\boldsymbol{K}\cdot\boldsymbol{r}_\alpha} \tag{1.30}$$

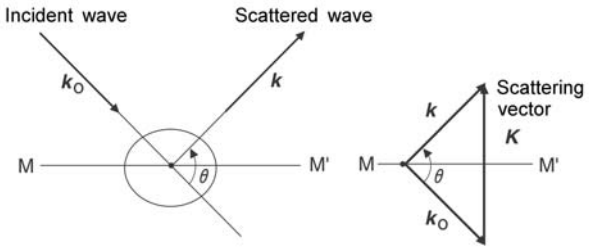

Fig. 1.3. The scattering vector $\boldsymbol{K} = \boldsymbol{k} - \boldsymbol{k}_0 = k(\boldsymbol{n} - \boldsymbol{n}_0)$ and the mirror plane MM′. $\boldsymbol{K}$ is normal to the mirror plane which bisects the directions of the incident and scattered waves

where $\boldsymbol{K}$ is the *scattering vector* $\boldsymbol{K}$ defined by

$$\boldsymbol{K} = \boldsymbol{k} - \boldsymbol{k}_0 \tag{1.31}$$

in terms of the wave vector of the scattered wave $\boldsymbol{k} = k\boldsymbol{n} = (2\pi/\lambda)\boldsymbol{n}$ and that of the incident wave $\boldsymbol{k}_0 = k\boldsymbol{n}_0 = (2\pi/\lambda)\boldsymbol{n}_0$. As a function of the variable R, (1.30) represents a spherical wave expanding from the origin O. The amplitude of the spherical wave carries information on the scattered electromagnetic field and the state of electron α.

The scattering vector $\boldsymbol{K}$ is normal to the plane which bisects the directions of the incident and scattered waves. This plane is called the mirror plane. As shown in Fig. 1.3, the mirror plane reflects the incident vector $\boldsymbol{k}_0$ into the scattered vector $\boldsymbol{k}$. Note that, for arbitrary points α and β on the mirror plane which have displacement vectors $\boldsymbol{r}_\alpha$ and $\boldsymbol{r}_\beta$, respectively, there holds the relation $\boldsymbol{K}\cdot(\boldsymbol{r}_\alpha - \boldsymbol{r}_\beta) = 0$. Therefore, scattered waves produced at arbitrary points on the mirror plane have no phase difference.

Let us investigate here the scattering by one isolated macromolecule M. For its purpose, we set $\boldsymbol{r}_M = 0$ by choosing the origin O at the center of M. In this case, $\boldsymbol{r}_\alpha = \boldsymbol{\xi}_\alpha$ and R is the distance from the center of M to the observation point P. To obtain the electric field $\boldsymbol{E}_M$ produced by M, we must superpose contributions from all electrons belonging to M. Equation (1.30) results in

$$\boldsymbol{E}_M = r_\mathrm{c} E_0 \left[\sum_{\alpha \in M} g_\alpha \mathrm{e}^{-\mathrm{i}\boldsymbol{K}\cdot\boldsymbol{\xi}_\alpha} \right]_M \boldsymbol{n} \times (\boldsymbol{n} \times \boldsymbol{\epsilon}_0) \frac{1}{R} \mathrm{e}^{-\mathrm{i}\omega(t - \frac{R}{c})} \tag{1.32}$$

where $\sum_{\alpha \in M}$ means to sum up all contributions from electrons which execute forced oscillations in M. Evidently, (1.32) is a spherical wave expanding from the center O of M. The information on the atomic structure and electron distribution of the molecule M is contained in the bracket $[\cdots]_M$ in the amplitude of the spherical wave.

It is quantum mechanics that determines the atomic and electronic states in the molecule M. The energy eigenvalue $\hbar\omega_\alpha$ and associated eigenfunction

from which the electron distribution function is determined are obtained by solving the Schrödinger equation for stationary states. Accordingly, we introduce here a *probability distribution function* $\rho_\alpha(\boldsymbol{r})$ for the electron α in M and replace the sum over α in the bracket $[\cdots]_M$ in (1.32) by the following integral as

$$[\cdots]_M \;\rightarrow\; f_M(\boldsymbol{K}) = \sum_{\alpha\,\in\,M} g_\alpha \int \mathrm{d}\boldsymbol{r}\rho_a(\boldsymbol{r})\mathrm{e}^{-\mathrm{i}\,\boldsymbol{K}\cdot\boldsymbol{r}} \,. \tag{1.33}$$

The function $f_M(\boldsymbol{K})$ is called the *form factor* of the molecule M. Then the electric field $\boldsymbol{E}_\alpha$ in the scattered wave is expressed by

$$\boldsymbol{E}_M = r_\mathrm{c} E_0\, f_M(\boldsymbol{K})\, \boldsymbol{n} \times (\boldsymbol{n} \times \boldsymbol{\epsilon}_0)\frac{1}{R}\,\mathrm{e}^{-\mathrm{i}\,\omega(t-\frac{R}{c})} \tag{1.34}$$

in terms of the form factor. In this way, the average strength and the differential cross section of the scattered electromagnetic wave from the isolated macromolecule M are calculated to be

$$I_M = I_0 r_\mathrm{c}^2 |f_M(\boldsymbol{K})|^2\, \frac{P}{R^2} \tag{1.35}$$

and

$$\frac{\mathrm{d}\sigma_M}{\mathrm{d}\Omega} = r_\mathrm{c}^2 |f_M(\boldsymbol{K})|^2\, P \tag{1.36}$$

respectively. With these formulas, scattering experiments with X-rays and laser beams enable us to obtain information on the structure of the macromolecule.

1.2.5 Scattering of Electromagnetic Waves by Macroionic Dispersions

As a basic assumption for investigation of the scattering of electromagnetic waves by macroionic dispersions, we postulate that the incident electromagnetic wave interacts coherently with electrons in sufficiently many macromolecules in the dispersion. Namely, the electromagnetic wave is regarded as interacting with many macromolecules through scattering by electrons without disturbances with random phases. This assumption corresponds to using a plane wave with infinite wave front for the incident electromagnetic wave as in (1.25). However, it is necessary to note that, in actual scattering experiments, we observe accumulated phenomena of such coherent elementary processes averaged over by thermal motion of the solute and solvent molecules.

The electric field $\boldsymbol{E}$ of the scattered wave resulting from interactions of the incident wave with an assembly of macromolecules in the dispersion is a superposition of the electric fields $\boldsymbol{E}_M$ over molecules multiplied by the phase factors depending on the position $\boldsymbol{r}_M$ of the molecules. From (1.34), we obtain

$$\boldsymbol{E} = \sum_M \boldsymbol{E}_M \, \mathrm{e}^{-\mathrm{i}\boldsymbol{K}\cdot\boldsymbol{r}_M} = r_\mathrm{c} E_0 F(\boldsymbol{K}) \boldsymbol{n} \times (\boldsymbol{n} \times \boldsymbol{\epsilon}_0) \frac{1}{R} \, \mathrm{e}^{-\mathrm{i}\omega(t-\frac{R}{c})} \tag{1.37}$$

where

$$F(\boldsymbol{K}) = \sum_M \mathrm{e}^{-\mathrm{i}\boldsymbol{K}\cdot\boldsymbol{r}_M} f_M(\boldsymbol{K}) \tag{1.38}$$

is the function related to the configuration of the macromolecules and called the *structure factor* of the dispersion. The average strength and the differential cross section of the electromagnetic wave scattered by the macroionic dispersion are derived, respectively, as follows:

$$I_\mathrm{sol} = I_0 r_\mathrm{c}^2 |F(\boldsymbol{K})|^2 \frac{P}{R^2} \tag{1.39}$$

and

$$\frac{\mathrm{d}\sigma_\mathrm{sol}}{\mathrm{d}\Omega} = r_\mathrm{c}^2 |F(\boldsymbol{K})|^2 \, P. \tag{1.40}$$

If the form factors of the macromolecules are known, the structure factor provides information on the average configuration of the solute molecules in the dispersion.

In X-ray experiments, the electrons in relatively inner shells of an atom also make contributions to the Thomson scattering. Note that the scattering is insensitive to the electronic energy levels and determined mostly by the probabilistic distribution of electrons. In optical laser experiments [21–24], the electrons in the outer shells of an atom with low energies make large contributions to the scattering.

To investigate distributions of macromolecules in dispersions, it is necessary to analyze the dependence of the structure function $F(\boldsymbol{K})$ in (1.38) on the configuration of molecules $\{\boldsymbol{r}_M\}$. However, it is generally difficult to determine the form factor $f_M(\boldsymbol{K})$ of a molecule in dispersions. In particular, studies on the form factors of linear macroions in solutions are not yet well established at the present stage neither in theory nor in experiment. Here we consider only *monodisperse dispersions* which consist of spherical macroions with uniform properties such as radius and surface charge number.

To make arguments clear, we investigate the structure factor $F(\boldsymbol{K})$ separately in two cases: (1) the *liquid state* where macromolecules are distributed uniformly without definite symmetry of translation and (2) the *solid state* which has a definite translational symmetry.

(1) Liquid State

Suppose the dispersion has N spherical macromolecules with the form factor f_M. The absolute square of (1.38) is written as

$$|\, F(\boldsymbol{K}) \,|^2 = \left| \sum_a f_M \, \mathrm{e}^{-\mathrm{i}\boldsymbol{K}\cdot\boldsymbol{r}_a} \right|^2 = |f_M|^2 \left| N + \sum_{a\neq b} \sum \mathrm{e}^{\mathrm{i}\boldsymbol{K}\cdot(\boldsymbol{r}_a - \boldsymbol{r}_b)} \right| . \tag{1.41}$$

Denoting the average density of the macromolecule by ρ_0, we express the average number of the molecules in a spherical shell sandwiched by the radii from r to $r + \mathrm{d}r$ by $\rho_0 g(r)(4\pi r^2\,\mathrm{d}r)$. The function $g(r)$ in this definition is called the *radial distribution function*. In the liquid state, the solute macroions are considered to take an isotropic distribution.

Let us consider the radial distribution function and the structure factor. To calculate the double sum of the second term in (1.41), we fix arbitrarily one molecule, say c, and take the sum over other molecules. Then we obtain the estimation

$$\sum_{a}\sum_{a\neq b} \mathrm{e}^{\mathrm{i}\boldsymbol{K}\cdot(\boldsymbol{r}_a-\boldsymbol{r}_b)} = N\sum_{b}{}' \mathrm{e}^{\mathrm{i}\boldsymbol{K}\cdot\boldsymbol{r}_b} = N\sum_{b}{}'\langle \mathrm{e}^{\mathrm{i}\boldsymbol{K}\cdot\boldsymbol{r}_b}\rangle \tag{1.42}$$

to a good approximation. Here the prime $'$ in the symbol $\sum_b{}'$ implies that molecules are excluded from the vicinity of c due to the existence of the molecule c. In a sufficiently large system, it is possible to regard that the molecule c is situated at the coordinate origin chosen arbitrarily. Further, the symbol $\langle\cdots\rangle$ in the last expression means to take an average over the distribution of molecules with respect to direction. This average can be estimated by the following angular integration

$$\langle \mathrm{e}^{\mathrm{i}\boldsymbol{K}\cdot\boldsymbol{r}}\rangle = \frac{1}{4\pi}\int_0^{\pi}\int_0^{2\pi} \mathrm{e}^{\mathrm{i}Kr\cos\theta}\sin\theta\,\mathrm{d}\theta\,\mathrm{d}\phi = \frac{\sin Kr}{Kr}\,. \tag{1.43}$$

The structure of the radial distribution function $g(r)$ depends on interactions between molecules and states in the dispersion. Since the distribution of molecules becomes uniform at the point far from the origin, $g(r) \to 1$ in the limit $r \to \infty$. With the radial distribution function, it is possible to estimate the double sum in (1.42) by the integral

$$4\pi N\rho_0 \int_0^{R_{\max}} g(r) r^2 \frac{\sin Kr}{Kr}\,\mathrm{d}r \tag{1.44}$$

where $R_{\max}$ is the size of the region illuminated by the coherent electromagnetic wave. Estimation of the integral in (1.44) is difficult, since it increases rapidly for large values of $R_{\max}$. To avoid this difficulty, we divide (1.44) into two parts as

$$4\pi N\rho_0 \left\{ \int_0^{R_{\max}} r^2[g(r)-1]\frac{\sin Kr}{Kr}\mathrm{d}r + \int_0^{R_{\max}} r^2\frac{\sin Kr}{Kr}\mathrm{d}r \right\}\,. \tag{1.45}$$

If $R_{\max}$ is sufficiently larger than the wavelength of the electromagnetic waves, the second integral of this equation becomes negligibly small except for the forward scattering [2] owing to cancellation of the oscillations of sinusoidal

[2] In order to investigate cluster structures in macroionic dispersions, it is necessary to analyze data of forward X-rays scattering at ultra-small-angles. In such a case, a careful estimation of the second term in (1.45) must be done.

functions. The upper bound $R_{\max}$ in the first integral of (1.45) can be set to ∞, since $g(r) - 1 \to 0$ in the limit $r \to \infty$. Consequently, we obtain the structure factor

$$| F_{\text{liq}}(\boldsymbol{K}) |^2 = N | f_M |^2 \left\{ 1 + 4\pi\rho_0 \int_0^\infty r^2 [g(r) - 1] \frac{\sin Kr}{Kr} \, \mathrm{d}r \right\} \tag{1.46}$$

for macroions in the liquid state in a dispersion. This equation plays a crucial role in relating the average strength of the electromagnetic wave to the radial distribution function in a macroionic dispersion. The structure function $| F_{\text{liq}}(\boldsymbol{K}) |$ observed in scattering experiments determines

$$J(K) = \frac{4\pi}{K} \int_0^\infty [g(r) - 1] r \sin Kr \, \mathrm{d}r = \frac{1}{\rho_0} \left[\frac{| F_{\text{liq}}(\boldsymbol{K}) |^2}{N | f_M |^2} - 1 \right] . \tag{1.47}$$

Then the inverse transformation of this relation

$$g(r) - 1 = \frac{1}{2\pi^2 r} \int_0^\infty K J(K) \sin Kr \, \mathrm{d}K \tag{1.48}$$

enables us to obtain the radial distribution function $g(r)$.

Even in dispersions of spherical molecules of one kind, the solute molecules must be highly monodisperse for the radial distribution to have sharp maxima of higher orders. In the case of the linear polymer solutions, high levels of conformation changes smear out the form of an individual molecule and make its form factor indefinite. Scattering experiments can determine only an averaged radial distribution function over possible conformation changes. How to analyze such averaged distribution functions is an important problem to be solved.

(2) Solid State

Crystals consist of *unit cells* regularly distributed on a lattice spanned by the *primitive translation vectors* $\boldsymbol{a}$, $\boldsymbol{b}$ and $\boldsymbol{c}$. The lengths a, b and c and mutual angles of the primitive translation vectors are called lattice parameters. The unit cells of crystals in macroionic dispersions include single and plural numbers of macroions.

Choosing one molecule in the unit cell, we form the linear combination of the displacement vector $\boldsymbol{r}$ of the molecule and the primitive translation vectors as

$$\boldsymbol{r}_M = p\boldsymbol{a} + q\boldsymbol{b} + r\boldsymbol{c} + \boldsymbol{r} . \tag{1.49}$$

The crystal has a periodic property in the sense that the molecules at the positions with the vectors $\boldsymbol{r}$ and $\boldsymbol{r}_M$ are equivalent if the coefficients p, q, r are integral numbers. Substituting (1.49) into (1.38) and taking the periodic property into account, we obtain the expression

$$F(\boldsymbol{K}) = \sum_{p=0}^{N_a - 1} e^{-ip\boldsymbol{K} \cdot \boldsymbol{a}} \sum_{q=0}^{N_b - 1} e^{-iq\boldsymbol{K} \cdot \boldsymbol{b}} \sum_{r=0}^{N_c - 1} e^{-ir\boldsymbol{K} \cdot \boldsymbol{c}} F_{\text{cell}}(\boldsymbol{K}) \tag{1.50}$$

for the *structure factor* of the crystal of macroions. Here, N_a, N_b and N_c are numbers of the unit cells repeated along the axes $\boldsymbol{a}$, $\boldsymbol{b}$ and $\boldsymbol{c}$, and $F_{\rm cell}$ is the structure factor of the unit cell defined by

$$F_{\rm cell}(\boldsymbol{K}) = \sum_{M \in \text{ unit cell}} e^{-i\boldsymbol{K}\cdot\boldsymbol{r}_M} f_M(\boldsymbol{K}) \,. \tag{1.51}$$

In terms of the *Laue function*

$$L(\boldsymbol{K}) = \frac{\sin^2(\frac{1}{2}N_a\boldsymbol{K}\cdot\boldsymbol{a})}{\sin^2(\frac{1}{2}\boldsymbol{K}\cdot\boldsymbol{a})} \frac{\sin^2(\frac{1}{2}N_b\boldsymbol{K}\cdot\boldsymbol{b})}{\sin^2(\frac{1}{2}\boldsymbol{K}\cdot\boldsymbol{b})} \frac{\sin^2(\frac{1}{2}N_c\boldsymbol{K}\cdot\boldsymbol{c})}{\sin^2(\frac{1}{2}\boldsymbol{K}\cdot\boldsymbol{c})}, \tag{1.52}$$

the absolute square of the structure factor is expressed as

$$|F(\boldsymbol{K})|^2 = L(\boldsymbol{K})|F_{\rm cell}|^2 \,. \tag{1.53}$$

When the scattering vector $\boldsymbol{K}$ satisfies the condition

$$\boldsymbol{K}\cdot\boldsymbol{a} = 2\pi h, \quad \boldsymbol{K}\cdot\boldsymbol{b} = 2\pi k, \quad \boldsymbol{K}\cdot\boldsymbol{c} = 2\pi l \tag{1.54}$$

where l, m and n are integers, the Laue function takes a maximum

$$\mathrm{Max}\, L(\boldsymbol{K}) = N^2 = (N_a N_b N_c)^2 \tag{1.55}$$

which dominates at large values of $N = N_a N_b N_c$. This result is confirmed by using the formula

$$\lim_{x\to 2\pi h} \frac{\sin(\frac{1}{2}N_a x)}{\sin(\frac{1}{2}x)} = \lim_{x\to 2\pi h} \frac{\dfrac{\mathrm{d}\sin(\frac{1}{2}N_a x)}{\mathrm{d}x}}{\dfrac{\mathrm{d}\sin(\frac{1}{2}x)}{\mathrm{d}x}} = N_a \,. \tag{1.56}$$

The half-width of this function is $2\pi/N_a$ and it is almost zero outside of the width. The condition in (1.54) is called the *Laue equation*. This is a necessary condition for diffraction to take place, but it is not a sufficient condition. Even when the Laue equation is satisfied, no diffraction is observed if the structure factor of the unit cell vanishes.

Reciprocal Vector Space

Let us find the solution of the Laue equation. Taking the vector products of the primitive translation vectors $\boldsymbol{a}$, $\boldsymbol{b}$ and $\boldsymbol{c}$, we introduce the following set of new vectors [25] as [3]

$$\boldsymbol{a}^* = \frac{2\pi}{V_c}\boldsymbol{b}\times\boldsymbol{c}, \quad \boldsymbol{b}^* = \frac{2\pi}{V_c}\boldsymbol{c}\times\boldsymbol{a}, \quad \boldsymbol{c}^* = \frac{2\pi}{V_c}\boldsymbol{a}\times\boldsymbol{b} \tag{1.57}$$

[3] This definition is adopted in textbooks on solid state physics [25]. It is traditional to omit the numerical factor 2π in (1.57) in crystallography [26].

where $V_c = \boldsymbol{a} \cdot (\boldsymbol{b} \times \boldsymbol{c}) = \boldsymbol{b} \cdot (\boldsymbol{c} \times \boldsymbol{a}) = \boldsymbol{c} \cdot (\boldsymbol{a} \times \boldsymbol{b})$ is the volume of the unit cell. These new vectors $\boldsymbol{a}^*$, $\boldsymbol{b}^*$ and $\boldsymbol{c}^*$ are called the *reciprocal lattice vectors*. The new vector space spanned by the reciprocal lattice vectors is convenient for representing solutions of the Laue equation. We call it reciprocal lattice space.

The fundamental vectors in the real lattice space and the reciprocal lattice space satisfy the relations

$$\begin{aligned} &\boldsymbol{a}^* \cdot \boldsymbol{a} = 2\pi, \ \boldsymbol{a}^* \cdot \boldsymbol{b} = 0, \quad \boldsymbol{a}^* \cdot \boldsymbol{c} = 0, \\ &\boldsymbol{b}^* \cdot \boldsymbol{a} = 0, \quad \boldsymbol{b}^* \cdot \boldsymbol{b} = 2\pi, \ \boldsymbol{b}^* \cdot \boldsymbol{c} = 0, \\ &\boldsymbol{c}^* \cdot \boldsymbol{a} = 0, \quad \boldsymbol{c}^* \cdot \boldsymbol{b} = 0, \quad \boldsymbol{c}^* \cdot \boldsymbol{c} = 2\pi \ . \end{aligned} \tag{1.58}$$

In the cubic and tetragonal crystal systems where the fundamental vectors are mutually orthgonal, $\boldsymbol{a}^*$, $\boldsymbol{b}^*$ and $\boldsymbol{c}^*$ are, respectively, parallel to $\boldsymbol{a}$, $\boldsymbol{b}$ and $\boldsymbol{c}$ and their magnitudes are inversely proportional to each other.

The *simple cubic structure* (sc) in real lattice space has the simple cubic structure in reciprocal lattice space. The *face-centered cubic structure* (fcc) and the *body-centered cubic structure* (bcc) in real lattice space have, respectively, the body-centered cubic structure and the face-centered cubic structure in reciprocal lattice space.

Taking the linear combination of the reciprocal lattice vectors with the three integers h, k and l as coefficients, we define the vector

$$\boldsymbol{G} = h\boldsymbol{a}^* + k\boldsymbol{b}^* + l\boldsymbol{c}^* \tag{1.59}$$

in the reciprocal lattice space. It is readily shown that the scattering vector $\boldsymbol{K}$ which coincides with such a reciprocal vector $\boldsymbol{G}$, i.e.,

$$\boldsymbol{K} = \boldsymbol{G}, \tag{1.60}$$

is a solution of the Laue equation.

A family of parallel lattice planes on which lattice points are regularly situated are specified by a set of three integers (hkl) called the *Miller indices*. As seen from Fig. 1.4, the Miller indices (hkl) are assigned to the family of parallel lattice planes when such a plane of the family that is closest to the origin touches the points of the vectors $\boldsymbol{a}/h$, $\boldsymbol{b}/k$ and $\boldsymbol{c}/l$.

The reciprocal lattice vector $\boldsymbol{G}$ is orthogonal to the planes with the Miller indices (hkl) and its length $|\boldsymbol{G}|$ is inversely proportional to the spacing d_{hkl} of the (hkl) planes. Namely, $\boldsymbol{G}$ has the following properties as

$$\boxed{\boldsymbol{G} \perp \text{ the } (hkl) \text{ lattice planes and } |\ \boldsymbol{G}\ | = \frac{2\pi}{d_{hkl}}} \tag{1.61}$$

In Fig. 1.4, the normal vector to the lattice plane with (hkl) is parallel to the vector product of two vectors $\overrightarrow{\mathrm{AB}}$ and $\overrightarrow{\mathrm{AC}}$. Namely

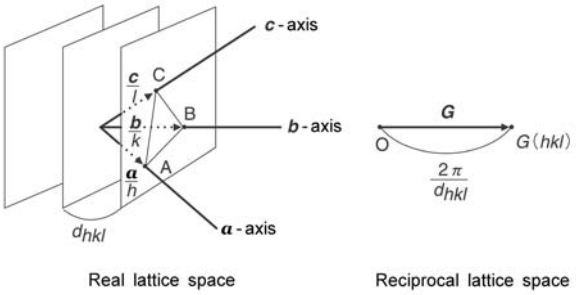

Fig. 1.4. Lattice planes with the Miller indicies (hkl). The $\boldsymbol{a}$, $\boldsymbol{b}$ and $\boldsymbol{c}$ axes intersect the closest lattice plane to the origin at the points A, B and C where $\overline{\mathrm{OA}} = a/h$, $\overline{\mathrm{OB}} = b/k$ and $\overline{\mathrm{OC}} = c/l$. To the plane with (hkl) in the real lattice space, there corresponds the reciprocal vector $\boldsymbol{G} = h\boldsymbol{a}^* + k\boldsymbol{b}^* + l\boldsymbol{c}^*$ in the reciprocal lattice space. The spacing d_{hkl} between parallel lattice planes normal to the direction $\boldsymbol{G}$ is $d_{hkl} = 2\pi/|\boldsymbol{G}|$

$$\overrightarrow{\mathrm{AB}} \times \overrightarrow{\mathrm{AC}} = \left(\overrightarrow{\mathrm{OB}} - \overrightarrow{\mathrm{OA}}\right) \times \left(\overrightarrow{\mathrm{OC}} - \overrightarrow{\mathrm{OA}}\right) = \frac{\boldsymbol{b}\times\boldsymbol{c}}{kl} + \frac{\boldsymbol{c}\times\boldsymbol{a}}{lh} + \frac{\boldsymbol{a}\times\boldsymbol{b}}{hk} \tag{1.62}$$

which is identical with the reciprocal vector $\boldsymbol{G}$ in (1.57) divided by the factor $2\pi hkl/V_c$. The spacing d_{hkl} between the lattice planes with (hkl) is obtained by taking the projection of the vectors $\overrightarrow{\mathrm{OA}}, \overrightarrow{\mathrm{OB}}$ and $\overrightarrow{\mathrm{OC}}$ to the normal $\hat{\boldsymbol{G}} = \boldsymbol{G}/|\boldsymbol{G}|$ as

$$d_{hkl} = \overrightarrow{\mathrm{OA}} \cdot \hat{\boldsymbol{G}} = \overrightarrow{\mathrm{OB}} \cdot \hat{\boldsymbol{G}} = \overrightarrow{\mathrm{OC}} \cdot \hat{\boldsymbol{G}} = \frac{2\pi}{|\boldsymbol{G}|} \,. \tag{1.63}$$

In this way the relations in (1.61) are proved.

Corresponding to a crystal system, the spacing d_{hkl} is given as a function of the lattice constants (a, b, c) and the Miller indices (hkl). The spacings d_{hkl} of typical examples of crystal structures are obtained as follows:

$$\begin{cases} \text{Orthorhombic system} & d_{hkl} = \dfrac{1}{\sqrt{\left(\frac{h}{a}\right)^2 + \left(\frac{k}{b}\right)^2 + \left(\frac{l}{c}\right)^2}}, \\ \text{Tetragonal system} & d_{hkl} = \dfrac{a}{\sqrt{h^2 + k^2 + \left(\frac{a}{c}\right)^2 l^2}}, \\ \text{Cubic system} & d_{hkl} = \dfrac{a}{\sqrt{h^2 + k^2 + l^2}}. \end{cases} \tag{1.64}$$

Ewald Sphere : Pictorial Representation of Diffraction Conditions
Figure 1.5 shows the method of construction for the diffraction maxima proposed by Ewald to analyze the diffraction of electromagnetic waves. The array of points in the right figure is the reciprocal lattice points with definite Miller indices. The condition for diffraction in real space is represented in reciprocal

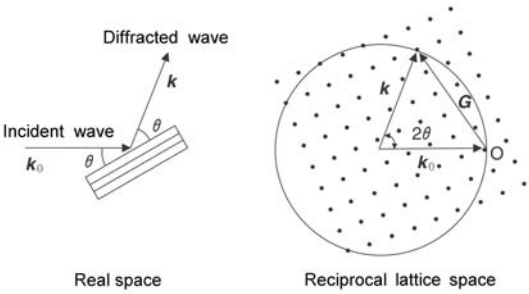

Fig. 1.5. Ewald's construction for the diffraction maxima. The condition for diffraction is drawn in the reciprocal lattice space correspondingly to the real lattice space. In the reciprocal vector space, the vector $\boldsymbol{k}_0$ is drawn in the direction of incidence so that the head of the vector coincides with one of the reciprocal lattice points, and the sphere with radius $2\pi/\lambda$ is drawn with the origin at its starting point. The condition for diffraction is satisfied on other reciprocal lattice points that are situated on the surface of the sphere (*Ewald's sphere*) and the diffracted wave emerges in the direction of $\boldsymbol{k} = \boldsymbol{k}_0 + \boldsymbol{G}$

lattice space. The incident wave vector $\boldsymbol{k}_0$ is put in the reciprocal vector space so that its end point coincides with one of the reciprocal lattice points. We draw a sphere with radius $2\pi/\lambda$ and origin at the starting point of the vector $\boldsymbol{k}_0$. Then the condition for diffraction is satisfied on other reciprocal lattice points that are situated on the surface of the sphere (*Ewald's sphere*) and the diffracted wave emerges in the direction of $\boldsymbol{k} = \boldsymbol{k}_0 + \boldsymbol{G}$.

In elastic scattering, the wave vectors are subject to the relation $\boldsymbol{k}^2 = \boldsymbol{k}_0^2$, since the energy of the electromagnetic wave does not change. With the condition $\boldsymbol{k} = \boldsymbol{k}_0 + \boldsymbol{G}$, we obtain the relation

$$2\boldsymbol{k}_0 \cdot \boldsymbol{G} + \boldsymbol{G}^2 = 0 \tag{1.65}$$

which results in $2 \times (2\pi/\lambda) \times \sin\theta = 2\pi/d_{hkl}$. If the Miller indices (hkl) have the greatest common divisor n as $h = nh'$, $k = nk'$ and $l = nl'$, there hold the relations $d_{hkl} = d_{(nh')(nk')(nl')} = d_{h'k'l'}/n$. Therefore, the condition of diffraction agrees with the *Bragg condition for diffraction* as

$$2d_{h'k'l'} \sin\theta = n\lambda \,. \tag{1.66}$$

So far, the reciprocal lattice points have been considered to be the points without extent. This is realized only in an idealistic situation with an infinite crystal. Owing to thermal vibrations and distortions in a crystal grain with a finite size, the reciprocal lattice points have finite extent in a real crystal. In the crystals of macromolecules, conformation changes and polydispersities are extra causes for the reciprocal lattice points to have extent. It is possible to explain these phenomena by using characteristics of the Laue function.

Suppose that the size of a crystal grain is small in the direction of the $\boldsymbol{a}$ axis and the number N_a is not large. Then the half-width $2\pi/N_a$ of the Laue function becomes large. This means that the diffraction peak becomes broad and low. Consequently the condition for diffraction is softened. In diffraction theory, this phenomenon is described by saying that the reciprocal lattice point elongates (or broadens).

An important difference between ordinary atomic crystals and crystals of spherical macromolecules in dispersions is the length scale. As shown in Chaps. 4 and 5, the lattice constants of the latter are a thousand or so times larger than those of the former. This implies that the elastic constants of crystals of macromolecules are smaller than those of atomic crystals by $10^9 \sim 10^{10}$, since the elastic constant of matter is essentially proportional to its density. Therefore, the crystals of macromolecules are so soft that defects and distortions occur readily and, as a result, the reciprocal lattice points tend to broaden. The defects have additional effects on the diffraction of laser beams by the crystals. Namely, the incident laser beams scattered by such a defect produce spherical waves which create a characteristic pattern of diffraction called the Kikuchi-Kossel diffraction image [4] [27, 28]. We shall employ the Kikuchi-Kossel diffraction method of optical lasers extensively for the structure analysis of crystals of macromolecules [29–31] in Chap. 5.

Extinction Rules

For the diffraction to take place, the scattering vector must coincide with a reciprocal lattice vector as in (1.60). Provided that (1.60) holds, let us investigate the structure factor of the unit cell for the bcc and fcc crystal systems.

Since two macromolecules are at $\boldsymbol{r}_M = 0$ and $\frac{1}{2}(\boldsymbol{a}+\boldsymbol{b}+\boldsymbol{c})$ in the unit cell of the bcc crystal, the structure factor in (1.51) takes the form

$$\begin{aligned} F_{\mathrm{bcc}} &= f_M[1 + \mathrm{e}^{-\mathrm{i}\pi(h+k+l)}] \\ &= \begin{cases} 0 & : \ h+k+l = \text{odd}, \\ 2f_M & : \ h+k+l = \text{even}. \end{cases} \end{aligned} \tag{1.67}$$

In the fcc crystal, four macromolecules exist at $\boldsymbol{r}_M = 0$, $\frac{1}{2}(\boldsymbol{a}+\boldsymbol{b})$, $\frac{1}{2}(\boldsymbol{b}+\boldsymbol{c})$ and $\frac{1}{2}(\boldsymbol{c}+\boldsymbol{a})$ in the unit cell, and the structure factor is calculated to be

$$\begin{aligned} F_{\mathrm{fcc}} &= f_M[1 + \mathrm{e}^{-\mathrm{i}\pi(h+k)} + \mathrm{e}^{-\mathrm{i}\pi(k+l)} + \mathrm{e}^{-\mathrm{i}\pi(l+h)}] \\ &= \begin{cases} 0 & : \ \text{even and odd numbers exist in } h, k \text{ and } l, \\ 4f_M & : \ \text{all of } h, k \text{ and } l \text{ are either even or odd}. \end{cases} \end{aligned} \tag{1.68}$$

[4] The diffraction pattern of spherical expanding waves had been observed first by Kikuchi [27] in 1928 in electron diffraction experiments. Seven years later, Kossel and Voges [28] observed similar images in X-ray diffraction. Except for the generic name *Kikuchi-Kossel diffraction image*, however, we use technical terms such as Kossel line, Kossel ring and so on which are already established and widely accepted.

The diffraction signal becomes extinct in the cases where the sum of the Miller indices is odd in the bcc crystal and the Miller indices include both even and odd numbers in the fcc crystal. These rules which are called the *extinction rules* give us important clues in determining crystal structures.

1.3 Forces between Molecules

It is now established that there exist four fundamental interactions [32–34], i.e., the strong interaction, electromagnetism, weak interaction and gravity, in nature which rule the structures and properties of all kinds of matter. The strong interactions describe the structures and reactions of hadrons and nuclei. With the weak interactions we are able to explain the decay and rare reaction phenomena of hadrons and leptons. Accordingly, it is almost unnecessary to take these two kinds of interaction into account for the description of phenomena of matter which is at a higher level of existence than atoms. In other words, electromagnetism is considered to be responsible for governing the structures and changes of macroscopic and mesoscopic matter around us, which can exist in one of the three states of gas, liquid and solid. In those states, gravity plays only a restricted role in describing phenomena such as sedimentation of aggregated solutes in dispersions.

1.3.1 Cohesive Forces of Solids

A variety of phenomena of solids can be explained almost totally from electromagnetism. All of the cohesive forces stabilizing solids which are classified as (a) the *van der Waals attraction*, (b) *ionic interactions*, (c) *metallic interactions* and (d) *covalent bonds* are effectively induced from the basic electromagnetic interaction via many-body effects described by quantum mechanics and statistical mechanics [25]. As a diversity of such cohesive forces shows, the basic electromagnetic interaction manifests itself in different forms in a various spectrum of matter.

To derive an equation of state of a real gas, van der Waals [35] made modifications to the equation of state for an ideal gas by taking into account an excluded volume effect of the gas molecules and an attraction proportional to the inverse square of the gas volume. Later, London [36] proved that this van der Waals attraction (a) originates from interactions between electric dipoles induced by quantum fluctuation in neutral molecules. The short distance effect of the excluded volume of molecules is interpreted as the result of electric replusions of electron's orbits and quantum mechanical repulsions caused by the Pauli exclusion principle. It is widely accepted to use the so-called Lennard-Jones potential [25, 37]

$$U(r) = 4\epsilon \left[\left(\frac{\sigma}{r} \right)^{12} - \left(\frac{\sigma}{r} \right)^{6} \right] \tag{1.69}$$

to describe effectively the repulsion and attraction between neutral molecules such as He, Ne and Ar of the inert gas type.

It is a remarkable fact that van der Waals had discerned in the 1870's the existence of repulsive and attractive components of molecular forces through investigation of an equation of state for a macroscopic system of gas. Accordingly, it is natural to regard that the history of research on forces between molecules had its origin in the work of van der Waals. The van der Waals attraction (a) plays an important role in dispersions of macromolecules. Following London, we explain the derivation of the van der Waals attraction in Chap. 2.

Three other types of cohesive forces (b), (c) and (d) stated above do not take part directly in the description of macroionic dispersions. However, we make a brief consideration of them, since they have useful implications in analyzing effective forces between macroions in dispersion. The ionic bond (b) results from the electric interaction of oppositely charged ions. This interaction works so as to shield mutually the opposite charges of ions. We may think of a metallic crystal as an array of positive ions embedded in a sea of electrons. The positive ions exert shielded Coulomb repulsions with each other when they approach closer and receive attractions mediated through the intermediary of electrons in between them when they separate farther apart. Consequently, the positive ions take the regular array of a crystal lattice. It is not possible to reduce the metallic interactions (c) to a sum of pairwise potentials between ions. Generally speaking, properties of metals are determined from band structures of electrons in periodic electrostatic potentials and the Pauli exclusion principle. The covalent bond (d) for neutral atoms is an anisotropic interaction characterized by the overlapping of charge distributions of electrons with antiparallel spins. The overlapping of electron wave functions binds their associated ions by electrostatic attraction. The simplest system with a covalent bond is the hydrogen molecule H_2. Heitler and London founded the quantum theory of molecules by calculating the binding energy of H_2 [38].

Under certain conditions, the hydrogen atom is attracted by two atoms and works to form what is called (e) a *hydrogen bond* between them. The hydrogen bond binds two atoms such as F, O and N which tend to be negatively charged through the intermediary of an ion H^+ and is important in understanding binding mechanisms of organic materials such as proteins and nucleic acids. In macroionic dispersions also, the ion H^+ plays an important role as described in Chaps. 2 and 6.

1.3.2 Properties of Ionic Solutions

The Earnshaw theorem applied to an ionic solution tells us that any static distribution of ionic solutes cannot be at an equilibrium in the solution. However, stable ionic solutions do exist as the *strong electrolyte* in nature. Therefore, it is evident that the dynamical behavior of ionic species plays a decisive role

in stabilizing ionic solutions. Namely, both the effects of "thermal fluctuation of molecules" and "electric interactions" are indispensable for the stability of ionic systems. Henceforth, we describe ionic solutions as isothermal systems with temperature T and calculate their Helmholtz and Gibbs free energies. In addition to a passive role as a uniform dielectric medium, the *solvent* has an active role as a thermal bath which works to lower the free energies of the system by producing entropies of mixing with *solute* molecules.

The entropies of mixing of the solute and solvent molecules produce the *osmotic pressure* which causes the solute molecules to diffuse inside the solution. Consequently, the solute molecules behave as an ideal gas in a dilute solution of neutral molecules. This is the *van't Hoff law* explained in Sect. 2.3.1. Effects of electric interaction are imposed on solutions with ionic solute molecules. Debye and Hückel [4, 39] calculated the free energies of a strong electrolyte in which all solutes dissociate into ions and discovered that the positive and negative ions shielding each other form clusters called *ionic atmospheres*. The formation of ionic atmospheres weakens the electric field, turns the long-range Coulomb interaction into a short-range interaction and decreases the electric energy and the osmotic pressure inside the solution.

As in solids, it is the electric interaction which creates a variety of phenomena in ionic solutions and is partially responsible for their stability. Note that the role of the electrons in solids, which are governed by the laws of quantum mechanics, is played by the solute ions in ionic solutions which are described by the laws of classical mechanics and statistical mechanics. The formation of ionic atmospheres in strong electrolytes shows that a net electric interaction of whole ionic species surpasses thermal effects of diffusion. The clustering mechanism of oppositely charged solutes resembles ionic interactions and metallic bonding in solids. The van der Waals force which can be ignored in the Debye-Hückel theory of strong electrolyte is important in explaining the instability of macroionic dispersions as shown in Sects. 2.4.3 and 6.2.8.

1.3.3 Effective Interactions between Macroions in Dispersion

Let us consider a dispersion consisting of macroions with uniform radius and surface charge. Such a system is called *monodisperse*. It is relevant to use the monodisperse system in order to investigate effective interactions between macroions.

To clarify the major characteristics of macroionic dispersions, let us inquire into the following questions:

1. What is responsible for dispersing macroionic molecules and keeping them stably in solution?
2. What kind of a mechanism actuates ordering processes such as the formation of *colloidal crystals* in dispersions?

The main causes stabilizing macroions in solution are Coulomb repulsions, effects of excluded volumes and the random thermal motion of molecules. In solution, the charges of macroions are shielded by *counterions* which have opposite charges to those of the macroions and the electric potential takes the form of Debye-Hückel type as

$$\frac{z^2e^2}{r} \rightarrow \frac{z^2e^2}{r}\,\mathrm{e}^{-\kappa r}. \tag{1.70}$$

Even though the screening effects reduce the strength of the Coulomb interaction, the strong repulsion works between two approaching macroions so as to maintain the state of dispersion. This mechanism of stabilization by electrostatic repulsion is much stronger than the stabilization effect by excluded volumes in macroionic dispersions.

The osmotic pressure of small ions which works to push macroions apart is an important factor for the stabilization of macroionic systems. In particular its effect is dominant in the suspended system of plate macroions. As will be shown in Sect. 6.4, this effect is described by the free energies of the macroionic dispersion as a whole. By contrast, the macroions are naturally assumed not to increase the entropy of mixing with solvent molecules and not to make contributions to the osmotic pressure except for indirect effects due to the excluded volumes. The unique effect of macroions is the *Brownian motion* which occurs through collisions with solvent molecules and solute molecules. The Brownian motion is also one of the causes of diffusion of macroions in the dispersions.

The question 1 is asking also what makes the dispersed states of macroions unstable in dispersions. What is the cause of the *coagulation* of macroions in dispersions? In the standard theory of macroionic dispersions, the van der Waals attraction is considered to be its main cause. An increase in the concentration of small ions decreases the strength of electrostatic repulsions by screening the surface charges of the macroions. When the electrostatic repulsion becomes weaker than the van der Waals attraction, the macroions start to coagulate with each other and the dispersion becomes unstable. The coagulation effect is known to be proportional to the sixth power of the valency of the counterion in the added salt. This empirical fact called the *Schulze-Hardy rule* had been explained by the screening mechanism of the electrostatic interaction in the *DLVO theory* for *lyophobic colloids* [40, 41] which is based on the screened electrostatic repulsion and the van der Waals attraction. We shall examine this mechanism in Sects. 2.4.3 and 6.2.8. Historically the success of the DLVO theory granted it the position of the standard theory of colloidal dispersions. Then, is it possible for the DLVO theory to explain all characteristics of macroionic dispersions?

Now we must examine the question 2. When small impurity ions are removed from a monodisperse colloidal dispersion, the particles start to take regular arrays of configurations and colloidal crystals grow in the dispersion. The DLVO theory tried to explain the mechanism of this crystallization from

the profile change of the *DLVO potential* consisting of the van der Waals attraction and the screened Coulomb repulsion. Note that, while the concentration of small ions causes almost no change in the attractive part of the potential, it changes drastically the repulsive part. Accordingly, it is not unnatural to consider that the DLVO potential has a so-called *secondary minimum* at an appropriate concentration of small ions. The crystallization starts when the colloidal particles fall into a secondary minimum with a depth larger than the thermal energy. Until the early stage of the 1970's, the formation of colloidal crystals had been considered as an additional proof of the validity of the DLVO theory.

To verify the DLVO explanation for the formation of colloidal crystals, we investigate its inverse process, viz, the melting of colloidal crystal. In 1973, Hachisu [42] succeeded in drawing the phase diagram depicting the relation between the added salt concentration and the degree of crystallization and found that an increase of the salt concentration results in melting of colloidal crystals. In the DLVO theory, however, an increase of salt concentration leads necessarily to deepening of the secondary minimum of the DLVO potential and stabilizes the colloidal crystal. A detailed description of this mechanism is explained in Sect. 2.4.4.

In this way, although the DLVO theory succeeded in describing the irreversible process of coagulation of colloidal particles, it failed to make a quantitative explanation of the *salt-induced-melting* of colloidal crystals. Where does this defect of the DLVO theory stem from? It seems indispensable to assume the existence of the van der Waals attraction in describing the short-range irreversible process of the coagulation. On the other hand, *flocculation* and the formation of colloidal crystals are medium- and long-range reversible phenomena. It is natural to regard that the short-range strong attraction of van der Waals does not take an essential part in these medium- and long-range phenomena.

One compromise method [43] to make up for the shortcoming of the DLVO scheme is to resort to the Alder-Wainwright mechanism [44] for the ordering formation of medium-range in colloidal dispersions. This mechanism has its basis on the observation by computer simulation that groups of rigid balls exerting mutually pure repulsive forces in a box tend to form crystalline orderings when the volume fraction of the balls exceeds 55%. This simple mechanism, however, seem to be insufficient to explain a variety of medium- and long-range phenomena such as void formation and multi-stage phase transitions in crystallization described in Chaps. 4 and 5.

In order to describe various phenomena of macroionic dispersions on the medium- and long-range scales in a unified way, it is necessary to investigate possible ways of manifestation of electric interactions in macroionic dispersions. In the DLVO theory, it is conclusively assumed to manifest itself as the screened Coulomb repulsion. As pointed out in Sect. 1.3.1, the electric interaction appears in diversified forms such as the metallic interaction and covalent bond in solids. In metals, for example, the basic electric interaction

works on the positive ion cores as the screened strong short-range repulsion and as the weak cohesive long-range force through the intermediary of electron clouds. If this picture is applied to macroionic dispersions, the macroions are described as forming ordered arrays by exerting the screened repulsion in the medium-range and a weak long-range cohesive force through the intermediary of counterions. Of course it is necessary to make quantitative estimation of the free energies of the system in order to decide what kind of manifestation mechanism of electric interaction gives a correct picture for the description of macroionic dispersions.

In the DLVO theory, the *Helmholtz free energy* F of a dispersion is calculated, provided that the colloidal particles take a quasi-static configuration in the dispersion. The free energy F determined as a function of the configuration of the particles leads to an adiabatic pair potential of screened Coulomb type for colloidal particles. We shall discuss this pure repulsive potential which is called simply the DLVO potential in Sect. 2.4 and Sect. 6.2. It is crucially important to recognize that the *Gibbs free energy* G is not dealt with in the DLVO theory.

In the DH theory of strong electrolytes, both of the Helmholtz and Gibbs free energies, F and G, were calculated and the electric interaction was proved to decrease the osmotic pressure derived from the difference of them. In a strong electrolyte, it is the Gibbs free energy that governs the thermodynamic state of the system in which small ions have the most dominant thermodynamic degrees of freedom. In the macroionic dispersion too, the thermodynamic state of the system is largely influenced by the osmotic behavior of small ions. Therefore, the thermodynamic state of the macroionic dispersion must be described in terms of the Gibbs free energy.

In Sect. 2.3, we present the derivation of the Helmholtz and Gibbs free energies of a strong electrolyte in the DH theory. In Sect. 6.2, we shall examine carefully characteristic features of the macroionic dispersions and applicabilities of the concepts of thermodynamic functions to the macroionic systems. In particular, it is shown that the macroionic dispersions, which are intrinsically inhomogeneous, requires a unique way in defining the "Gibbs free energy" for the systems. Then we shallderive the Helmholtz and Gibbs free energies of the macroionic dispersion under similar assumptions to those in the DLVO theory. While the Helmholtz free energy gives rise to an adiabatic pair potential with purely repulsive nature for effective interactions, the Gibbs free energy is proved to result in an adiabatic pair potential which is strongly repulsive at short distances and weakly attractive at long distances.

References

1. Trommsdorf E (1931) Thesis. In: Staudinger H (1960) Die Hochmolekularen Organischen Verbindungen-Kautschuk und Cellulose, Springer, Berlin, Heidelberg, New York, pp.333-377
2. Ostwald Wo (1921) Die Welt der Vernachlässigten Dimensionen, 4th edn. Steinkopf, Dresden
3. Ghosh JC (1918) J Chem Soc 113:449,627,707,790; (1921) Z phys Chem 98:211
4. Debye P, Hückel E (1923) Physik Z 24:185, 305; Debye P (1924) Physik Z 25:97
5. Robinson RA, Stokes RH (1959) Electrolyte solutions. Butterworth Scientific Publications, London
6. Ise N, Okubo T (1966) J Phys Chem 70:1936
7. Fuoss RM, Katchalsky A, Lifson S (1951) Proc Natl Acad Sci USA 37,:579
8. Alfrey T, Berg PW, Morawetz H(1951) J Polym Sci 7:543
9. Lifson S, Katchalsky A (1954) J Polym Sci 13:43
10. Alexandrowicz Z, Katchalsky A (1963) J Polym Sci A1:3231
11. Manning GS (1969) J Chem Phys 51:924
12. Hirzel CS, Rajagopalan R (1985) Colloidal phenomena, Advanced topics. Noyes Publications, Park Ridge, NJ
13. Schmitz KS (1993) Macroions in solution and colloidal suspension. VCH Publishers, New York
14. Arora AK, Tata BVR (1996) Ordering and phase transitions in charged colloids. VCH Publishers, New York
15. Fitch RM (1997) Polymer colloids: A comprehensive introduction. Academic Press, San Diego
16. Kramers HA, Heisenberg W (1925) Z Physik 31:681
17. Heitler W (1954) Quantum theory of radiation. Clarendon Press, Oxford
18. Sakurai JJ (1973) Advanced quantum mechanics. Addison-Wesley, Reading
19. Jackson JD (1999) Classical electrodynamics. Wiley, New York
20. Panofsky WKH, Phillips M (1974) Classical electricity and magnetism. Addison-Wesley Publishing Company, New York
21. Bern BJ, Pecora R (1976) Dynamic light scattering. Wiley, New York
22. Schmitz KS (1990) An Introduction to dynamic light scatterting by macromolecules. Academic Press, New York
23. Chu B (1991) Laser light scattering: Basic principles and practice. Academic Press, Boston

24. Johnson CS, Gabriel DA (1994) Laser light scattering. Dover Publications, New York
25. Kittel C (1976) Introduction to solid state physics. John Wiley & Sons, New York
26. James RW (1967) The optical principles of the diffraction of x-rays. G. Bell and Sons LTD, New York
27. Kikuchi S (1928) Jpn J Phys 5:83
28. Kossel W, Voges H (1935) Ann Phys (Leipzig) 23:677
29. Yoshiyama T, Sogami IS, Ise N (1984) Phys Rev Lett 53:2153
30. Yoshiyama T, Sogami IS (1986) Phys Rev Lett 56:1609
31. Yoshiyama T, Sogami IS (1996) In Arora AK, Tata BVR (eds), Ordering and phase transitions in charged colloids. VCH, New York, p. 41
32. Cheng T-P, Li L-F (1988) Gauge theory of elementary particles, 2nd edn. Clarendon Press, Oxford
33. Aitchison JJR, Hey AJG (1989) Gauge theory in particle physics, 2nd edn. Adam Hilger, Bristol
34. Ryder L (1996) Quantum field theory, 2nd edn. Cambridge University Press, Cambridge
35. van der Waals JD (1873) Dissertation (Univ Leiden); English transl by van der Waals JD (1890) Physical Memoirs, Physical Society of London, Taylor and Francis, Milton Road, vol 1, Part 3
36. London F (1930) Z Physik 63:245; (1937) Trans Faraday Soc 33:8; (1930) Z Phys Chem B11:222
37. Hirschfelder JO, Curtiss CF, Bird RB (1954) Molecular theory of gases and liquids, John Wiley and Sons, New York
38. Heitler W, London F (1927) Z Physik 44:455
39. Chu B (1969) Molecular forces (Based on the Baker lectures of Peter J. W. Debye). John Wiley & Sons, New York
40. Derjaguin BV, Landau L (1941) Acta Physicochim URSS 14:633; (1941) J Exptl Theoret Phys URSS 11:802
41. Verwey EJW, Overbeek JThG (1948) Theory of the stability of lyophobic colloids. Elsevier, Amsterdam
42. Hachisu S, Kobayashi Y, Kose A (1973) J Coll Interface Sci 42:342
43. Wadati M, Toda M (1972) J Phys Soc Jpn 32:1147
44. Alder BJ, Wainwright TE (1957) J Chem Phys 27:1208; (1959) J Chem Phys 31:459

2

Effective Interactions between Macroions 1

2.1 Introductory Remarks

The history of the theory of ionic solutions started with the Debye-Hückel (DH) theory of electrolytes [1, 2]. In this classical theory, which is a prototype mean field description, the solvent is treated as a continuous dielectric medium, the solute ions are considered to be a dilute gas, and the free energies of the system are derived from the average electric potential calculated by the linear approximation. The framework of this linearized theory was applied to describe colloidal dispersions. However, Levine and Dube, who calculated the internal energy of the system, could not make a proper estimation of the entropy effects in their incipient attempts [3, 4]. As a result, they found an interaction between colloidal particles that had a medium-range strong repulsion as well as a long-range strong attraction, and failed to describe the stability and instability of colloidal dispersions.

The defect of the Levine-Dube theory for colloidal systems was corrected in the early 1940's by Derjaguin and Landau [5] and independently by Verwey and Overbeek [6]. Calculating the Helmholtz free energy from the internal electric energy with *Debye's charging-up method*, they found that entropy effects just cancel out the attractive part of the interaction in the Levine-Dube theory and there remained a screened pure repulsive potential. The *stability of colloidal dispersions* is explained by this repulsive potential. With this repulsion and the van der Waals attraction [7], they formulated the classical standard theory of colloidal dispersions which described successfully the irreversible process of coagulation of colloidal particles.

We formulate the *mean field theory* of ionic solutions and dispersions in an intuitive way in Sect. 2.2 and examine the DH theory in detail as a successful example of a linearized theory in the mean field description in Sect. 2.3. Then, the classical standard theory in colloid chemistry, i.e., the DLVO theory [6] is explained in Sect. 2.4. In particular, the effective thermo-electric interaction between charged plates and the London-van der Waals attraction between spherical macroions are derived from basic physical laws. After describing its

successful aspects such as the derivation of the Schulze-Hardy rule, we discuss the shortcomings of the DLVO theory.

2.2 Mean Field Description

In the mean field description of ionic solutions and dispersions, the solvent is considered first as a continuous medium with dielectric constant ϵ and the electric flux $\boldsymbol{D}(\boldsymbol{r}, t)$ and the electric field strength $\boldsymbol{E}(\boldsymbol{r}, t)$ are assumed to satisfy the relation

$$\boldsymbol{D}(\boldsymbol{r}, t) = \epsilon \boldsymbol{E}(\boldsymbol{r}, t) \; . \tag{2.1}$$

It is crucial to recognize that, in addition to this passive role, the solvent is assumed to play the active role of a discrete ensemble of molecules. Namely, at the stage of derivation of the Gibbs free energy, the particle nature of the solvent is postulated to take effect through the relation $V = Nv$ between the volume of the system V and the number of the solvent molecules N. Here, v is the *molecular volume*, viz, the volume occupied by one molecule of the solvent.

It is generally relevant to ignore the effect of the magnetic field in ionic solutions and dispersions, since the speeds of the ions are far smaller than that of light. Therefore, the *Maxwell equations* are reduced to the following set of equations for the electric field as

$$\mathrm{div}\, \boldsymbol{D}(\boldsymbol{r}, t) = 4\pi \sum_j z_j e f_j(\boldsymbol{r}, t) \tag{2.2}$$

and

$$\mathrm{rot}\, \boldsymbol{E}(\boldsymbol{r}, t) = 0 \tag{2.3}$$

where $f_j(\boldsymbol{r}, t)$ is the distribution function of j-species of small ions. Equation (2.2) represents the *Gauss law*.

In the description of macroionic dispersions, there are two methods for dealing with the surface charges of the macroions: one is to include the contributions from the surface charges in the distribution function $f_j(\boldsymbol{r}, t)$ in (2.2) and the other is to dispose of them by the boundary conditions at the surface of macroions (2.2). Here we use the latter method.

Owing to the condition (2.3) for integrability, the field strength $\boldsymbol{E}(\boldsymbol{r}, t)$ can be expressed by the electric potential $\Psi(\boldsymbol{r}, t)$ as

$$\boldsymbol{E}(\boldsymbol{r}, t) = -\nabla \Psi(\boldsymbol{r}, t) \; . \tag{2.4}$$

Substitution of this relation into (2.2) leads to the Poisson equation

$$\epsilon \nabla^2 \Psi(\boldsymbol{r}, \, t) = -4\pi \sum_j z_j e f_j(\boldsymbol{r}, t) \tag{2.5}$$

for the electric potential $\Psi(\boldsymbol{r}, t)$. By solving this equation, we obtain the electric energy of the system at a time t as follows:

$$E(t) = \frac{1}{8\pi} \int \boldsymbol{D}(\boldsymbol{r}, t) \cdot \boldsymbol{E}(\boldsymbol{r}, t) \mathrm{d}\boldsymbol{r} = \frac{\epsilon}{8\pi} \int [\nabla \Psi(\boldsymbol{r}, t)]^2 \mathrm{d}\boldsymbol{r} \,. \tag{2.6}$$

Therefore, as a result of the motions of the ions, the electric potential and the electric energy of the system have fluctuations depending on t.

On the other hand, the motions of the ions are considered to be described by Newton's equations. An ion receives an electric force proportional to the field strength $\boldsymbol{E}(\boldsymbol{r}, t)$ and a resistance proportional to its velocity. In addition to these, there exists a many body effect among the ions. To take such an effect into account, we pay attention to the concept of the *chemical potential* which measures the tendency for transfer of ions from one phase to another. Hereafter, the solution is assumed to be so dilute that the concentration of the j-th solute satisfies the condition $c_j \simeq N_j/N \ll 1$ where N is the number of molecules of the solvent and N_j is the number of j-th solute molecules.

In the case of a neutral solution in thermal equilibrium at the absolute temperature T, the chemical potential of the j-th solute μ_j is defined as a function of the concentration c_j by [8]

$$\mu_j = \mu_j^* + k_\mathrm{B} T \ln c_j \tag{2.7}$$

where k_B ($= 1.38062 \times 10^{-23}\,\mathrm{J\,K^{-1}}$) is the Boltzmann constant and μ_j^* is an increment of the Gibbs free energy by addition of one molecule of the j-th solute (See equation (2.22)). This equation holds in each phase of the solution. Here we enlarge the physical interpretation of this concept of chemical potential so as to apply it to fluctuated regions with slight differences in solute concentrations. For this purpose, we replace the concentration c_j by a distribution function $n_j(\boldsymbol{r})$ for the j-th solute in (2.7) and define the chemical potential function locally by

$$\mu_j(\boldsymbol{r}) = \mu_j^* + k_\mathrm{B} T \ln n_j(\boldsymbol{r}) \tag{2.8}$$

at the position $\boldsymbol{r}$ in the solution. The chemical potential function $\mu_j(\boldsymbol{r})$ should be interpreted as meaning that molecules of the j-th solute tend to move from a region with large $\mu_j(\boldsymbol{r})$ to a region with small $\mu_j(\boldsymbol{r})$. Accordingly, the molecules tend to diffuse in the direction where the chemical potential function decreases. This means that the molecules receive a diffusion force proportional to $-\nabla\mu_j(\boldsymbol{r})$. This thermal *diffusion force* works on both neutral and charged molecules. Consequently, a molecule with mass m_j on which the driving electric force, the resistance from the solvent and this diffusion force act is subject to the equation of motion

$$m_j \frac{\mathrm{d}\boldsymbol{v}_j}{\mathrm{d}t} = -z_j e \nabla \Psi(\boldsymbol{r}, t) - \xi_j \boldsymbol{v}_j - k_\mathrm{B} T \nabla \ln n_j(\boldsymbol{r}) \tag{2.9}$$

where the resistance force is assumed to be proportional to the velocity $\boldsymbol{v}_j(t)$ with a coefficient ξ_j.

The acceleration on the left-hand side of (2.9) vanishes when the ions are at *mechanical equilibrium*. Further, when *thermal equilibrium* is reached, the time average of the velocity of an ion over a certain time interval also vanishes as

$$\overline{\boldsymbol{v}_j} = 0 \tag{2.10}$$

where $\overline{\cdots}$ represents the time average. Applying the time averaging procedure to the electric potential $\Psi(\boldsymbol{r}, t)$, we define the *mean electric potential* by

$$\psi(\boldsymbol{r}) \equiv \overline{\Psi(\boldsymbol{r}, t)} \, . \tag{2.11}$$

Likewise, we take the time average of the distribution function $f_j(\boldsymbol{r}, t)$ and identify it with the distribution function $n_j(\boldsymbol{r})$ used in (2.8). Namely, the time averaging procedure is assumed to smear out the fluctuations, leading to the relation

$$n_j(\boldsymbol{r}) \equiv \overline{f_j(\boldsymbol{r}, t)} \tag{2.12}$$

at thermal equilibrium.

In this way, the time average simplifies (2.9) as

$$0 = -z_j e \nabla \, \psi(\boldsymbol{r}) - k_{\mathrm{B}} T \nabla \ln \, n_j(\boldsymbol{r}) \tag{2.13}$$

which results directly in the *Boltzmann distribution*

$$n_j(\boldsymbol{r}) = n_{j0} \exp \left[-\frac{z_j e}{k_{\mathrm{B}} T} \psi(\boldsymbol{r}) \right] \tag{2.14}$$

for the j-th solute. Here, the value of the distribution function at the point where the mean electric potential vanishes is specified by

$$n_{j0} = n_j(\boldsymbol{r}) \Big|_{\psi=0} \, . \tag{2.15}$$

The number of j-th ions N_j is related to the distribution function through the integral

$$N_j = \int_V n_j(\boldsymbol{r}) \mathrm{d}\boldsymbol{r} \tag{2.16}$$

over the volume of the solution V.

The time average of the Poisson equation (2.5) gives rise to the equation for the mean electric potential as follows:

$$\epsilon \nabla^2 \psi(\boldsymbol{r}) = -4\pi e \sum_j z_j n_j(\boldsymbol{r}) \, . \tag{2.17}$$

This is the *Poisson-Boltzmann equation* (PB equation) which plays the leading role in the mean field description. The mean electric potential $\psi(\boldsymbol{r})$ and the distribution function $n_j(\boldsymbol{r})$ in the ionic solution are determined by solving this

non-linear differential equation in a self-consistent way. Taking an arbitrary region with volume V and integrating the PB equation over the volume, we obtain the *condition for electric neutrality* as

$$\sum_j z_j N_j + \sum_n Z_n = 0 \tag{2.18}$$

where the sums are taken over all ions contained in the region. The first term is the contribution of the small ions of j-th species with valency z_j and the second term is that of the macroions with charge number Z_n. In this derivation, we used the boundary condition

$$\epsilon \boldsymbol{\nu}_n \cdot \nabla\psi(\boldsymbol{r}) = -4\pi e Z_n \sigma_n(\boldsymbol{r}) \tag{2.19}$$

where $\boldsymbol{\nu}_n$ is the unit vector normal to the surface of the n-th macroion and $\sigma_n(\boldsymbol{r})$ is the normalized density of surface charge.

The time average of (2.6) leads to the *mean electric energy* of the solution, viz,

$$E = \overline{E(t)} = \frac{\epsilon}{8\pi} \int \overline{[\nabla\Psi(\boldsymbol{r},t)]^2} \mathrm{d}\boldsymbol{r} = \frac{\epsilon}{8\pi} \int [\nabla\psi(\boldsymbol{r})]^2 \mathrm{d}\boldsymbol{r} \ . \tag{2.20}$$

In the mean field theory, this energy E is interpreted to be the electric part of the internal energy of the system, $U^{\mathrm{el}} = E$. As shown in Sect. 6.3, this part of the internal energy E and the electric part of the Helmholtz free energy of the system F^{el} are related by

$$e^2 \left(\frac{\partial F^{\mathrm{el}}}{\partial e^2} \right)_{T,V,N} = E \tag{2.21}$$

where e is the magnitude of the charge of the electron. Therefore, F^{el} is obtained through a parameter integral of E with respect to e^2. This is Debye's charging-up method.

2.3 Debye-Hückel Theory of Strong Electrolytes

The DH theory [1, 2, 9, 10] is one of the basic theories of physico-chemistry which describes the characteristics of dilute solutions of strong electrolytes. In this theory, the thermodynamic energies are calculated from the mean electric potential which is derived by solving the linearized PB equation. The positive and negative ions form *ionic atmospheres* mutually by surrounding ions with opposite charge. Formation of the ionic atmosphere, which decreases the strength of electric field on average, is considered to support the validity of the linear approximation of the PB equation.

2.3.1 Osmotic Pressure and van't Hoff Law

Let us consider first dilute solutions of neutral solute molecules. In terms of the total number N and the chemical potential μ_0 of solvent molecules and the number N_j and the chemical potential μ_j^* of j-th solute molecules, the Gibbs free energy is given by [8]

$$G^0 = N\mu_0 + \sum_j N_j \mu_j^* + k_{\mathrm{B}} T \sum_j N_j \ln \frac{N_j}{\mathrm{e}N} \,. \tag{2.22}$$

Note that N and the volume V of the solution are related by $N = V/v$ with the molecular volume v. The last term of (2.22) represents the *entropy of mixing*.

Origin of the Mixing Entropy

The increase of entropy by mixing of molecules is an important effect in the theory of solutions. The entropy is defined by the logarithm of "the number of microscopic states" multiplied by the Boltzmann constant k_{B}. In the isothermal and isobaric states, the mixing of two kinds of molecules with numbers ν_1 and ν_2 increases the entropy by an amount

$$k_{\mathrm{B}} \left[\ln(\nu_1 + \nu_2)! - \ln \nu_1! - \ln \nu_2!\right] \simeq k_{\mathrm{B}} \left[\nu_1 \ln \frac{\nu_1 + \nu_2}{\nu_1} + \nu_2 \ln \frac{\nu_1 + \nu_2}{\nu_2}\right] \tag{2.23}$$

in which the formula [1]

$$\ln \nu! \simeq \nu \ln(\nu/\mathrm{e}) \quad (\nu \gg 1) \tag{2.24}$$

is used provided that ν_1 and ν_2 are sufficiently large.

Substituting $\nu_1 = N$ and $\nu_2 = N_j$ in (2.23) and taking into account the relation $N \gg N_j$, the increase of the entropy S_j by the mixing of solute molecules j with the solvent molecules is estimated to be

$$S_j = k_{\mathrm{B}} N_j \ln \frac{\mathrm{e}N}{N_j} \,. \tag{2.25}$$

Consequently, the entropy of mixing of various solute molecules with the solvent molecules decreases the Gibbs free energy by an amount $T \sum_j S_j$. This is the effect included in the third term of (2.22).

It is possible to derive the entropy of mixing from the viewpoint that the solute molecules form an ideal gas with a volume V. This derivation is

[1] For a sufficiently large ν, we obtain the following approximate relation

$$\ln \nu! = \sum_{n=1}^{\nu} \ln n \simeq \int_0^{\nu} \ln x \mathrm{d}x = \nu \ln \frac{\nu}{\mathrm{e}} \quad (\nu \gg 1)$$

by replacing the sum by the integral.

instructive in understanding the relation between diffusion and an increase in the entropy of mixing and for recognizing the necessity of the replacement $V = Nv$ in the Gibbs free energy. Since a solute molecule occupies an arbitrary point in V with an equal probability, the number of "microscopic states" is proportional to V. In a system with mutually independent numbers of identical molecules N_j, the number of microscopic states is proportional to $V^{N_j}/N_j!$ where the factor $N_j!$ is necessary because the microscopic states of identical molecules should not be influenced by mutual replacements of the molecules. Accordingly, the entropy of the j-th species of solute is estimated to be $k_{\mathrm{B}} \ln(V^{N_j}/N_j!)$ up to an unknown constant. The value of this constant, whose existence shows the limitations of classical physics, can be fixed by introducing the quantum volume element in phase space.

At this stage, by interpreting that a solvent consisting of N molecules with molecular volume v occupies the volume $V = Nv$, we can estimate the entropy by

$$S_j = k_{\mathrm{B}} \ln \frac{(Nv)^{N_j}}{N_j!} \simeq k_{\mathrm{B}} N_j \ln \frac{N\mathrm{e}}{N_j} + k_{\mathrm{B}} N_j \ln v \ . \tag{2.26}$$

In this expression, there appears an additional term proportional to the number N_j of solute molecules. Note that such a term is included in the term of the chemical potential μ_j^* in (2.22).

Law of van't Hoff

From (2.22), the chemical potentials of the solvent and solute molecules are calculated, respectively, to be

$$\mu = \frac{\partial G^0}{\partial N} = \mu_0 - k_{\mathrm{B}} T \frac{1}{N} \sum_j N_j \tag{2.27}$$

and

$$\mu_j = \frac{\partial G^0}{\partial N_j} = \mu_j^* + k_{\mathrm{B}} T \ln \frac{N_j}{N} \ . \tag{2.28}$$

The pressure of the solution is a sum of the pressure P_0 of pure solvent and an *osmotic pressure* P. Consider a vessel divided into two compartments I and II by a semipermeable membrane as illustrated in Fig. 2.1. The osmotic pressure of the solution which is at equilibrium with the pure solvent is determined by measuring the difference in levels of the solutions.

The chemical potentials of the pure solvent and the solution which are, respectively, in the compartments I and II must be equal at equilibrium. Using (2.27), this condition is expressed by

$$\mu_0(T, P_0) = \mu(T, P_0 + P) = \mu_0(T, P_0 + P) - k_{\mathrm{B}} T \frac{1}{N} \sum_j N_j \ . \tag{2.29}$$

Provided that $P \ll P_0$, the term $\mu_0(T, P_0 + P)$ can be expanded with respect to P. Using the thermodynamic relation

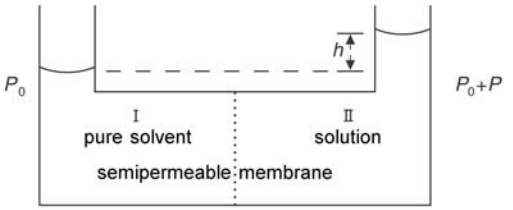

Fig. 2.1. The solution fills compartment II, separated by a semipermeable membrane from compartment I which is filled with the pure solvent. The pressure in I is P_0 (atmospheric pressure) and that in II is $P_0 + P$. The difference h in levels of the solution and the pure solvent leads to an osmotic pressure $P = \rho g h$ where ρ is the density of the solution and g is the acceleration due to gravity

$$\left(\frac{\partial G^0}{\partial P}\right)_{N,T} = N\left(\frac{\partial \mu_0}{\partial P}\right)_{N,T} = V \tag{2.30}$$

and noting that $(\partial \mu_0/\partial P)_T$ is the molecular volume $v = V/N$ of the solvent molecule, we obtain the compact relation

$$P = \frac{k_{\mathrm{B}}T}{V}\sum_j N_j \ . \tag{2.31}$$

This is the *van't Hoff law of osmotic pressure*. This famous law states that, in dilute solutions of neutral molecules, an equation of state identical to that of an ideal gas holds for the osmotic pressure. As the procedure of this derivation of the law shows, the osmotic pressure is deeply related with the entropy of mixing of solvent and solute molecules.

2.3.2 Debye-Hückel Theory: Point-Like Ions

For a solution which includes small ions with valency z_j to be neutral as a whole, the condition

$$\sum_j z_j N_j = 0 \tag{2.32}$$

must hold. The highly non-linear PB equation can be solved analytically only in the case of the one dimensional problem. For this reason, a linear approximation is adopted in general. Namely, assuming that the mean electric energy is lower than the thermal energy $k_{\mathrm{B}}T$, the Boltzmann distribution function in (2.14) is approximated by

$$n_j(\boldsymbol{r}) = n_{j0}\left[1 - \frac{z_j e}{k_{\mathrm{B}}T}\psi(\boldsymbol{r})\right] \ . \tag{2.33}$$

Accordingly, the PB equation is linearized as follows:

$$\nabla^2\psi(\boldsymbol{r}) = \kappa^2\psi(\boldsymbol{r}) \tag{2.34}$$

where κ is the *Debye screening factor* defined by

$$\kappa^2 = \frac{4\pi e^2}{\epsilon k_{\mathrm{B}} TV} \sum_j z_j^2 N_j \ . \tag{2.35}$$

The condition of neutrality (2.32) is used in the derivation.

Let us choose arbitrarily an ion in the solution and calculate the mean electric potential around it. Since the solution is homogeneous and isotropic at thermal equilibrium, the mean electric potential is assumed to be spherically symmetric, i.e., $\psi(\boldsymbol{r}) = \psi(r)$. Therefore, the linearized PB equation is simplified as

$$\frac{1}{r}\frac{\mathrm{d}^2}{\mathrm{d}r^2} r\psi(r) = \kappa^2\psi(r) \tag{2.36}$$

around the ion, which has the general solution

$$\psi(r) = A\frac{\mathrm{e}^{-\kappa r}}{r} + B\frac{\mathrm{e}^{\kappa r}}{r} \tag{2.37}$$

in which the integration constants A and B are fixed from the boundary conditions. It is natural to require that $\psi(r) \to 0$ at infinity ($r \to \infty$) and $\psi(r) \to z_j e/\epsilon r$ near an ion with charge $z_j e$ ($r \to 0$). The mean electric potential satisfying these conditions is the shielded Coulomb potential

$$\psi(r) = \frac{z_j e}{\epsilon r}\mathrm{e}^{-\kappa r} \tag{2.38}$$

specified by the Debye screening factor κ. This mean electric potential $\psi(r)$ around a point-like ion enables us to calculate thermodynamic quantities in a strong electrolyte.

Electric Energy E

Expansion of the exponential function in (2.38) leads to

$$\psi(r) = \frac{z_j e}{\epsilon r} - \frac{z_j e\kappa}{\epsilon} + \cdots \ . \tag{2.39}$$

The first term is the electric potential of the ion with charge $z_j e$ and the second term is the electric potential difference $\delta\psi$ which is produced by the ionic atmosphere at the position of the ion. Accordingly, the ion with the electric potential difference $\delta\psi$ has the electric energy $z_j e\delta\psi = -z_j^2 e^2\kappa/\epsilon$. Applying this argument to all ions, we obtain the total electric energy of all ions in the solution as follows:

$$E = -\frac{1}{2}\frac{e^2\kappa}{\epsilon}\sum_j z_j^2 N_j = -\frac{1}{8\pi} k_{\mathrm{B}} TV\,\kappa^3 \tag{2.40}$$

where the factor $1/2$ is necessary to avoid double counting.

Helmholtz Free Energy F

The Helmholtz free energy F is calculated by integrating either the charging-up formula (2.21) or the thermodynamic relation

$$\frac{\partial}{\partial T}\left(\frac{F}{T}\right)_{V,\,N} = -\frac{E}{T^2}\ . \tag{2.41}$$

Both of these methods lead us to the same result

$$F = F^0 + F^{\rm el} = F^0 - \frac{1}{12\pi} k_{\rm B} T V \kappa^3 \tag{2.42}$$

where F^0 is the Helmholtz free energy provided that there is no electric interaction. Taking the derivative of this F with respect to V results in the osmotic pressure

$$P = k_{\rm B} T \left(\frac{1}{V} \sum_j N_j - \frac{\kappa^3}{24\pi} \right)\ . \tag{2.43}$$

Comparison of this result with the van't Hoff law reveals that *the electric interaction decreases the osmotic pressure in a strong electrolyte*. It is reasonable to interpret this as meaning that the electric interactions among all of the ions induce a net attraction in a strong electrolyte.

Gibbs Free Energy G

There are two routes also which enable us to derive the Gibbs free energy G from the Helmholtz free energy F. One is to use the thermodynamic relation

$$G = F - V\left(\frac{\partial F}{\partial V}\right)_T\ . \tag{2.44}$$

We separate G into the sum of the neutral part G^0 in (2.22) and an electric part $G^{\rm el}$ as

$$G = G^0 + G^{\rm el} \tag{2.45}$$

where G^0 is related to F^0 by

$$G^0 = F^0 - V\left(\frac{\partial F^0}{\partial V}\right)_T\ . \tag{2.46}$$

In statistical mechanics it is standard to derive G from F which is calculated beforehand. However, we use the general form of G^0 in (2.22) for dilute solutions and construct F^0 by subtracting the (pressure $\times$ volume) term as follows:

$$F^0 = G^0 - (P_0 V + k_{\rm B} T \sum_j N_j)\ . \tag{2.47}$$

From (2.44) and (2.46), the electric part of the Gibbs free energy $G^{\rm el}$ is calculated as

$$G^{\rm el} = \left[F^{\rm el} - V \left(\frac{\partial F^{\rm el}}{\partial V} \right)_T \right]_{V=Nv} = -\frac{1}{8\pi} k_{\rm B} T N v \left[\kappa(T, N, N_j) \right]^3 \ . \qquad (2.48)$$

In the final expression for $G^{\rm el}$, the Debye factor κ must be interpreted as a function of N through $V = Nv$.

The other method to derive $G^{\rm el}$ is to use the *additivity* of the Gibbs free energy. Namely, $G^{\rm el}$ is identified with the sum of the chemical potentials of all molecules which are calculated from $F^{\rm el}$ as

$$\begin{aligned} G^{\rm el} &= \left[\left(N \frac{\partial F^{\rm el}}{\partial N} + \sum_j N_j \frac{\partial F^{\rm el}}{\partial N_j} \right)_{T,V} \right]_{V=Nv} \\ &= -\left[\frac{1}{12\pi} k_{\rm B} T V \sum_j N_j \left(\frac{\partial \kappa^3}{\partial N_j} \right)_{T,V} \right]_{V=Nv} \\ &= -\frac{1}{8\pi} k_{\rm B} T N v \left[\kappa(T, N, N_j) \right]^3 \ . \end{aligned} \qquad (2.49)$$

This is identical with (2.48). In the first stage of this derivation, there exists no contribution from the solvent molecules to $G^{\rm el}$, since $\partial F^{\rm el}(T, V, N_j)/\partial N = 0$ prior to the replacement $V = Nv$.

What does happen if the replacement $V = Nv$ is made in the first stage of the calculation in (2.49)? The replacement makes the factor κ^2 a homogeneous function of order -1 and 1 with respect to the variables N and N_j, viz,

$$N \frac{\partial}{\partial N} \left([\kappa^2]_{V=Nv} \right) = -\kappa^2, \quad \sum_j N_j \frac{\partial}{\partial N_j} \left([\kappa^2]_{V=Nv} \right) = \kappa^2 \ . \qquad (2.50)$$

Accordingly, contributions from the solvent and solute molecules via κ cancel with each other in (2.49). Consequently, the difference between the electric parts of the two free energies disappears [2] and the equation of state (2.43) for the osmotic pressure returns to the van't Hoff law (2.31).

Thus the two methods of derivation of G from F are equivalent with each other in the theory of strong electrolytes consisting of small ions only. This is a natural consequence of the fact that a strong electrolyte is a thermodynamically homogeneous system and that every ion with an ionic atmosphere remains as an ion maintaining the additivity. As a direct reflection of the homogeneity and additivity, the *Gibbs-Duhem relation*

$$N \mathrm{d}\mu + \sum_j N_j \mathrm{d}\mu_j = 0 \qquad (2.51)$$

[2] Overbeek made this replacement before the differentiation with respect to the number of molecules in an article [11] where he intended to criticize the theory on macroion interactions to be described in Chap. 6. Faithful application of his assertion to the DH theory results in the unreasonable relation $G^{\rm el} = F^{\rm el}$.

holds in a strong electrolyte under isothermal and isobaric conditions. The chemical potentials in (2.27) and (2.28) for neutral molecules are readily verified to satisfy this relation. The electric parts of the chemical potentials of the solvent and solute molecules are calculated from $G^{\rm el}$, respectively, as follows:

$$\mu^{\rm el} = \frac{\partial G^{\rm el}}{\partial N} = \frac{1}{16\pi} k_{\rm B} T v \kappa^3 \tag{2.52}$$

and

$$\mu_j^{\rm el} = \frac{\partial G^{\rm el}}{\partial N_j} = -\frac{3e^2}{4\epsilon} \kappa z_j^2 \ . \tag{2.53}$$

It is straightforward to prove that these parts of the chemical potentials also satisfy the Gibbs-Duhem relation.

Owing to its consistency proved above, the DH theory became established as a foundation of the thermodynamic theory of ionic solutions. In particular, the equivalence of the two routes of derivation of the Gibbs free energies and the Gibbs-Duhem relation are remarkable results of the DH theory of strong electrolytes. Unfortunately, however, this result does not hold as it stands in macroionic dispersions which are intrinsically inhomogeneous. Difficulties of this kind were pointed out by Hill [12] in his book on *Thermodynamics of small systems*. Thermodynamic fluctuations necessarily violate the homogeneity of a small system. As a matter of course, a system in an inhomogeneous external environment such as a gas of small ions in an array of macroions in a dispersion violates the homogeneousness and additivity which are necessary prerequisite for the ordinary thermodynamics. Using the framework of the ordinary thermodynamics in a restricted way under the assumption that effects of inhomogeneousness and non-additivity are small, we formulate a thermodynamic theory of macroionic dispersions in Chap 6.

Differentials of Neutrality Condition by Number of Molecules

We close this section by examining the condition for neutrality in (2.32) and its differential with respect to number of molecules. The numbers N_j of ions which are related by (2.32) cannot change independently. Accordingly, it is necessary to prove the consistency of the differentials in (2.49). Choosing ions of the k-th species, we consider that their number N_k depends on the numbers of the other ions via the neutrality condition. Since the condition is a homogeneous function of order 1 with respect to the numbers N_j $(j \neq k)$, there holds the relation

$$\sum_{j \neq k} N_j \frac{\partial N_k}{\partial N_j} = N_k \ . \tag{2.54}$$

Using this relation, let us differentiate a function f of independent variables N_j $(j \neq k)$ under the neutrality condition (2.32) as

$$\left(\sum_{j\neq k} N_j \frac{\partial f}{\partial N_j}\right)_{\text{neutrality cond.}} = \left(\sum_{j\neq k} N_j \frac{\partial N_k}{\partial N_j}\right)\frac{\partial f}{\partial N_k} + \sum_{j\neq k} N_j \frac{\partial f}{\partial N_j} = \sum_j N_j \frac{\partial f}{\partial N_j} \,. \tag{2.55}$$

Note that all variables are regarded as independent in the last line of this calculation. This is why we could take the derivatives in (2.49) as if all the variables were independent. This analysis has an important meaning in the investigation of macroionic dispersions in Chap. 6.

2.3.3 Debye-Hückel Theory: Ions with a Finite Radius

So far, the ions have been regarded as point-like particles. Here we investigate a solution consisting of ions with finite extent [1,2,10]. For simplicity, all ions are assumed to be spheres with the same radius a which are filled with a dielectric medium (dielectric constant ϵ) and have an electric charge $z_j e$ at the center.

From (2.37), we find the solution of the PB equation $\psi(r)$ which vanishes at infinity and $\psi(r) \to \psi_a$ at the surface of the ion $r \to a$ as follows:

$$\psi(r) = \psi_a \frac{a}{r} \mathrm{e}^{-\kappa(r-a)} \,. \tag{2.56}$$

The continuity of the electric field $\boldsymbol{E}$ is used to fix the surface potential ψ_a. Requiring that the gradients of the potentials outside and inside of the sphere, $\psi(r)$ and $z_j e/\epsilon r$, coincide with each other at the surface $r = a$, we obtain

$$\psi_a = \frac{z_j e}{\epsilon a(1+\kappa a)} \tag{2.57}$$

for the surface potential. As a result, the electric potential around a spherical ion is determined to be

$$\psi(r) = \frac{z_j e}{\epsilon r}\frac{\mathrm{e}^{-\kappa(r-a)}}{1+\kappa a} = \frac{z_j e}{\epsilon r}\mathrm{e}^{-\kappa(r-a)}\left(1 - \frac{\kappa a}{1+\kappa a}\right) \,. \tag{2.58}$$

Electric Energy E

The difference $\delta\psi$ between the potentials at the surface and center of the spherical ion with charge $z_j e$ is estimated to be

$$\delta\psi = \psi_a - \frac{z_j e}{\epsilon a} = -\frac{z_j e \kappa}{\epsilon(1+\kappa a)} \,. \tag{2.59}$$

Accordingly, the spherical ion has the electric energy $z_j e \delta\psi = (-z_j^2 e^2 \kappa)/\epsilon(1+\kappa a)$. Therefore, the electric energy of all ions in the solution is obtained as

$$E = -\frac{1}{2}\frac{e^2\kappa}{\epsilon}\frac{1}{1+\kappa a}\sum_j z_j^2 N_j = -\frac{1}{2}k_{\rm B}TV\frac{1}{4\pi}\frac{\kappa^3}{1+\kappa a}\ . \tag{2.60}$$

Helmholtz Free Energy F

The mean electric potentials around the point-like particle and the spherical particle with radius a are given in (2.38) and (2.58). Comparison of the electric energies in (2.40) and (2.60) shows that the effect of the extent of the ions influences the electric energy through the factor $1/(1+\kappa a)$. Taking this factor into account, we are able to calculate the electric part of the Helmholtz free energy $F^{\rm el}$. With the charging-up method, we obtain the Helmholtz free energy as

$$F = F^0 + F^{\rm el} = F^0 - \frac{1}{12\pi}k_{\rm B}TV\kappa^3\tau(\kappa a) \tag{2.61}$$

where the influence of the extent of the ion is expressed by the function

$$\tau(\kappa a) = \frac{3}{(\kappa a)^3}\int_0^{\kappa a}\frac{t^2}{1+t}{\rm d}t = \frac{3}{(\kappa a)^3}\left\{\ln(1+\kappa a) - \kappa a + \frac{1}{2}(\kappa a)^2\right\} \tag{2.62}$$

which can be expanded into a power series as

$$\tau(\kappa a) \simeq 1 - \frac{3}{4}\kappa a + \frac{3}{5}(\kappa a)^2 + \cdots \tag{2.63}$$

for small values of κa.

Gibbs Free Energy G

Derivatives of the Helmholtz free energy $F(T, V, N_j, \cdots)$ with respect to the numbers of solute and solvent molecules are calculated as

$$\left(\frac{\partial F^{\rm el}}{\partial N_j}\right)_{T,V} = -\frac{\kappa e^2}{2\epsilon(1+\kappa a)}z_j^2, \quad \left(\frac{\partial F^{\rm el}}{\partial N}\right)_{T,V} = 0\ . \tag{2.64}$$

Multiplying by the numbers of the respective molecules and summing up, the Gibbs free energy is determined as follows:

$$G = G^0 - \frac{1}{8\pi}k_{\rm B}TNv\frac{\kappa^3}{1+\kappa a}\ . \tag{2.65}$$

The Gibbs free energy obtained in this way must be considered to be a function of the number of solvent molecules through the screening factor $\kappa(T, Nv, \cdots)$. Noting this fact, we calculate the electric parts of the chemical potentials as

$$\mu^{\rm el} = \left(\frac{\partial G^{\rm el}}{\partial N_j}\right)_{T,N_j} = \frac{1}{16\pi}k_{\rm B}Tv\frac{\kappa^3}{(1+\kappa a)^2} \tag{2.66}$$

and

$$\mu_j^{\rm el} = \left(\frac{\partial G^{\rm el}}{\partial N_j}\right)_{T,N} = -\frac{e^2}{4\epsilon}\frac{\kappa(3+2\kappa a)}{(1+\kappa a)^2}z_j^2, \tag{2.67}$$

respectively, for the solvent and solute molecules. It is straightforward to verify that the Gibbs-Duhem relation in (2.51) holds for them.

The difference between the two free energies G and F gives rise to an osmotic pressure of the small ion gas as follows:

$$P = k_{\mathrm{B}}T \left[\frac{1}{V} \sum_j N_j - \frac{\kappa^3}{24\pi} \sigma(\kappa a) \right] \tag{2.68}$$

where $\sigma(\kappa a)$ is the function defined by

$$\sigma(\kappa a) = \frac{3}{(\kappa a)^3} \left[1 + \kappa a - \frac{1}{1+\kappa a} - 2\ln(1+\kappa a) \right] \tag{2.69}$$

which has the power series expansion

$$\sigma(\kappa a) \simeq 1 - \frac{3}{2}\kappa a + \frac{9}{5}(\kappa a)^2 + \cdots \tag{2.70}$$

for small values of κa. It is easily proved that the function $\sigma(\kappa a)$ has the integral representation

$$\sigma(\kappa a) = \frac{3}{(\kappa a)^3} \int_0^{\kappa a} \left(\frac{t}{t+1} \right)^2 \mathrm{d}t \tag{2.71}$$

which shows that $\sigma(\kappa a) \geq 0$ for an arbitrary value of κa. Consequently, the electric interaction acts to decrease the osmotic pressure in the solution regardless of the extent of the ions.

In this way the DH theory concludes that the attraction between ions with unlike charges and the repulsion between ions with like charges in total decreases the osmotic pressure in a strong electrolyte. Is this phenomenon characteristic of a solution with small ions only? Noting that the decrease of osmotic pressure occurs in both solutions of ions with finite extent and those of point-like ions, Langmuir [13] inferred that similar phenomena should take place in macroionic dispersions. Although this is an ingenious idea, he used the original framework of the DH theory to describe macroionic dispersions.

2.4 DLVO Theory

The DLVO theory is an effective framework for describing the structure and stability of colloidal dispersions with a linear combination of a screened repulsive Coulomb potential and the van der Waals potential. This theory has also been applied to more general systems with spherical macroions. Henceforth we call the spherical macroions described by DLVO theory the particles.

In contrast to the DH theory where anions and cations are dealt with symmetrically, macroions and small ions are handled in a completely asymmetric manner in the DLVO theory. Macroions with large masses and surface

charge numbers are considered to form a stationary environment in which a gas of small ions is assumed to take rapidly thermodynamic equilibrium. In the DLVO theory, the mean electric potential is derived first by solving the PB equation for the system of two charged plates immersed in an electrolyte. Then, with the electric potential, the densities of the small ions are calculated and the osmotic pressure is obtained through the van't Hoff law. Finally, the potential generating the osmotic pressure is derived and interpreted as a repulsive potential for charged plates. These results are generalized to spherical macroions.

In addition to the repulsive force originating from electric interactions, an attractive force is indispensable to describe instability of macroionic dispersion. The DLVO theory naturally identifies the van der Waals force as such an attraction.

In this section, we solve the PB equation for the systems with one and two charged plates and obtain a repulsive potential of screened Coulomb type. The results are generalized and applied to systems of spherical particles with large radius. Explaining the origin of the van der Waals attraction using an oscillator model, an attractive potential between two spherical molecules is derived. Then the Schulze-Hardy rule is proved in the DLVO theory.

2.4.1 Screened Coulomb Potential

To understand views and concepts in colloid chemistry, we examine first a single charged plate immersed in an electrolyte. Then we investigate the interactions between two parallel charged plates and between two charged spherical macroions.

Gouy-Chapman's Electric Double Layer [14, 15]

Suppose that one charged plate is immersed in an electrolyte with valences $\pm z$ (a z-z electrolyte). Taking the x axis normal to the plate, the PB equation for the mean electric potential is written as

$$\epsilon \frac{\mathrm{d}^2\psi}{\mathrm{d}x^2} = 8\pi z e n_0 \sinh(\beta z e \psi) \tag{2.72}$$

where $\beta = 1/k_{\mathrm{B}}T$. For brevity's sake, we introduce the non-dimensional electric potential $\Phi(x)$ by

$$\Phi(x) = ze\beta\psi(x) \ .$$

Then, (2.72) takes the simplified form

$$\frac{\mathrm{d}^2\Phi}{\mathrm{d}x^2} = \kappa^2 \sinh\Phi \tag{2.73}$$

where κ is the screening parameter $\kappa = \sqrt{8\pi n_0 z^2 e^2 \beta/\epsilon}$. Multiplication by the factor $d\Phi/dx$ makes this equation integrable. Choosing the origin $x = 0$ at the

plate surface and imposing the boundary conditions $\Phi = 0$ and $\mathrm{d}\Phi/\mathrm{d}x = 0$ at infinity ($x \to \infty$), we obtain the first order differential equation

$$\left(\frac{\mathrm{d}\Phi}{\mathrm{d}x}\right)^2 - 2\kappa^2 \cosh\Phi = -2\kappa^2 \tag{2.74}$$

which is factorized as follows:

$$\left(\frac{\mathrm{d}\Phi}{\mathrm{d}x} + 2\kappa \sinh\frac{1}{2}\Phi\right)\left(\frac{\mathrm{d}\Phi}{\mathrm{d}x} - 2\kappa \sinh\frac{1}{2}\Phi\right) = 0\ . \tag{2.75}$$

Since the boundary conditions require that $\mathrm{d}\Phi/\mathrm{d}x < 0$ ($\mathrm{d}\Phi/\mathrm{d}x > 0$) for $\Phi > 0$ ($\Phi < 0$), (2.75) is reduced to

$$\frac{\mathrm{d}\Phi}{\mathrm{d}x} + 2\kappa \sinh\frac{1}{2}\Phi = 0\ . \tag{2.76}$$

Consequently, we find the solution

$$\Phi(x) = 2\ln\frac{1 + \gamma\exp(-\kappa x)}{1 - \gamma\exp(-\kappa x)} \tag{2.77}$$

where γ is a constant defined by

$$\gamma = \frac{\exp[\Phi(0)/2] - 1}{\exp[\Phi(0)/2] + 1} = \frac{\exp(ze\beta\psi_0/2) - 1}{\exp(ze\beta\psi_0/2) + 1} \tag{2.78}$$

in terms of the surface potential $\Phi(0) = ze\beta\psi_0$.

In order to take the size of the counterions into account, Stern proposed using the potential value on the boundary surface which is separated from the plate surface by the radius of an ion. The region sandwiched between such a surface and the plate surface is called the *Stern layer*. It is not essential to distinguish between these two surfaces in our study of effective interactions in macroionic dispersions.

The mean electric potential in (2.77) decreases as an exponential function of the distance from the plate surface. The rate of decrease is inversely proportional to the screening factor κ. In the Gouy-Chapman theory, the distribution of ions governed by the potential (2.77) is called the *electric double layer*. The thickness of the electric double layer is characterized by the factor $1/\kappa$.

Repulsion due to Overlapping of Electric Double Layers

Let us calculate the electric force acting on two parallel plates with the same charges immersed in an electrolyte as illustrated in Fig. 2.2. The x axis is normal to the plates and the origin $x = 0$ is at the midpoint of parallel plates situated at $x = -l$ and $x = l$. We express the mean electric potential in this system by $\tilde{\Phi}(x) = ze\beta\tilde{\psi}(x)$ in order to distinguish it from $\Phi(x)$ in the one plate system. In the limiting case where $l \to \infty$, the density of the z-z electrolyte

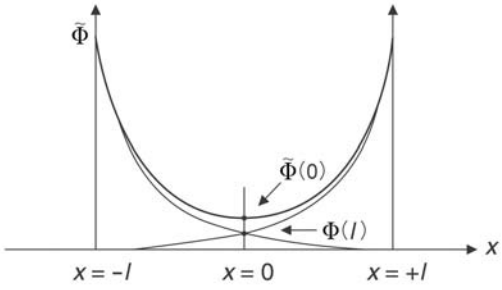

Fig. 2.2. The mean electric potential $\tilde{\Phi}(x)$ between parallel charged plates immersed in an electrolyte. The x axis is normal to the plates and the origin $x = 0$ is at the midpoint of parallel plates at $x = -l$ and $x = l$. While $\tilde{\Phi}$ is the mean electric potential at $x = 0$ when the two plates exist, $\Phi(l)$ is the potential when one plate exists

can be regarded as taking a constant value, e.g., n_0. The densities of the small ions at the midpoint $x = 0$ of the region $R = [-l, l]$ are given by

$$n_{\pm} = n_0 \exp[\mp\tilde{\Phi}(0)] \tag{2.79}$$

in terms of $\tilde{\Phi}(0) = ze\beta\tilde{\psi}(0)$. The increment of the small ion density at the midpoint compared with the value at $l = \infty$ is estimated by

$$\Delta n = (n_+ - n_0) + (n_- - n_0) = 2n_0[\cosh\tilde{\Phi}(0) - 1] \,. \tag{2.80}$$

With the van't Hoff law in (2.31), this increment brings about the increase

$$P(l) = k_{\mathrm{B}}T\Delta n = 2n_0k_{\mathrm{B}}T[\cosh\tilde{\Phi}(0) - 1] \tag{2.81}$$

$$\simeq n_0k_{\mathrm{B}}T\tilde{\Phi}(0)^2 \qquad (\tilde{\Phi}(0)^2 \ll 1) \tag{2.82}$$

in the osmotic pressure P. Note that the osmotic pressure depends on the interplate distance $2l$ and the surface potential through the mean electric potential $\tilde{\Phi}(0)$ at the midpoint of the plates.

The essential of the DLVO theory is to regard the osmotic pressure of this kind as all of the thermal and electric interactions exerted for the charged plates. The potential $U_{\mathrm{R}}(l)$ responsible for the osmotic pressure is obtained by calculating the work which is necessary to bring the two plates together against the pressure from $\pm\infty$ to $\pm l$ as

$$U_{\mathrm{R}}(l) = -2\int_{\infty}^{l} P(l)\mathrm{d}l \,. \tag{2.83}$$

The first integral of the PB equation is also readily obtained in the region R sandwiched between the two plates. Namely, noting that $\mathrm{d}\tilde{\Phi}/\mathrm{d}x = 0$ at the midpoint $x = 0$, we find

$$\left(\frac{\mathrm{d}\tilde{\Phi}}{\mathrm{d}x}\right)^2 - 2\kappa^2\cosh\tilde{\Phi} = -2\kappa^2\cosh\tilde{\Phi}(0) \tag{2.84}$$

in place of (2.74) for the Gouy-Chapman problem. Factorization of this equation leads to the first order differential equation

$$\frac{\mathrm{d}\tilde{\Phi}}{\mathrm{d}x} = +\kappa\sqrt{2\cosh\tilde{\Phi} - 2\cosh\tilde{\Phi}(0)} \tag{2.85}$$

for the interval $[0, 1]$, where the plus sign is required to adjust the gradient of the potential $\tilde{\Phi}(x)$ in Fig. 2.2. Integration of this equation over the interval $[0, l]$ brings about

$$\kappa l = \int_0^l \kappa \mathrm{d}x = \int_{\tilde{\Phi}(0)}^{\tilde{\Phi}(l)} \frac{\mathrm{d}\tilde{\Phi}}{\sqrt{2\cosh\tilde{\Phi} - 2\cosh\tilde{\Phi}(0)}} \,. \tag{2.86}$$

To proceed with the integral requires knowledge of elliptic functions. Leaving general investigation of this problem to Sect. 6.4, we restrict our consideration here to the situation where the magnitude of the potential is so small as to satisfy the relation $2\cosh\tilde{\Phi} \approx 2 + \tilde{\Phi}^2$. Then, the integration can be made in terms of elementary functions as

$$\kappa l = \int_{\tilde{\Phi}(0)}^{\tilde{\Phi}(l)} \frac{\mathrm{d}\tilde{\Phi}}{\sqrt{\tilde{\Phi}^2 - \tilde{\Phi}(0)^2}} = \ln\frac{\tilde{\Phi}(l) + \sqrt{\tilde{\Phi}(l)^2 - \tilde{\Phi}(0)^2}}{\tilde{\Phi}(0)} \tag{2.87}$$

which provides the formula

$$\tilde{\Phi}(l) = \tilde{\Phi}(0)\cosh\kappa l \tag{2.88}$$

relating the surface potential $\tilde{\Phi}(l)$ to $\tilde{\Phi}(0)$. This formula enables us to find the dependence of $\tilde{\Phi}(0)$ on l provided that the surface potential $\tilde{\Phi}(l)$ takes a definite value specific to the plate surface. It is generally accepted as a natural assumption to put $\tilde{\Phi}(l) = \Phi(0)$, since the surface potential hardly changes in the solutions with one plate and two plates.

In consequence, the osmotic pressure acting on a unit area of the plates was found to be

$$P(l) = n_0 k_\mathrm{B} T \Phi(0)^2 \frac{1}{\cosh^2\kappa l} \tag{2.89}$$

and the potential of repulsion working on the plates was derived as

$$U_\mathrm{R}(l) = 2n_0 k_\mathrm{B} T \Phi(0)^2 \int_l^\infty \frac{\mathrm{d}l}{\cosh^2\kappa l} = \frac{2n_0 k_\mathrm{B} T}{\kappa}\Phi(0)^2(1 - \tanh\kappa l) \tag{2.90}$$

from the integral in (2.83).

Here we take up an intuitive approximation used often in the DLVO theory. It approximates the electric double layer in the region R sandwiched between

two plates by the sum of those of each plate. The electric potential $\Phi(l)$ of one plate at the distance l from the surface which was given in (2.77) takes the form

$$\Phi(l) = 2\ln\frac{1+\gamma\exp(-\kappa l)}{1-\gamma\exp(-\kappa l)} \simeq 4\gamma\exp(-\kappa l) \tag{2.91}$$

provided that $\kappa l \gg 1$. Then, the electric potential $\tilde{\Phi}(0)$ at the midpoint of R is assumed to be given by the sum of the independent contributions from two plates as $\tilde{\Phi}(0) \approx 2\Phi(l)$ (Fig. 2.2). Substitution of this relation into (2.82) estimates the osmotic pressure on a unit area of the plates as

$$P(l) = 64 n_0 k_{\mathrm{B}} T \gamma^2 \exp(-2\kappa l)\ . \tag{2.92}$$

Subsequently, carrying out the integration in (2.83), we obtain the repulsive potential produced by the *overlapping of electric double layers* as follows:

$$U_{\mathrm{R}}(l) = 64 n_0 k_{\mathrm{B}} T \kappa^{-1} \gamma^2 \exp(-2\kappa l)\ . \tag{2.93}$$

When the interplate distance increases, the potential $U_{\mathrm{R}}(l)$ decreases exponentially. The rate of this decrease depends sensitively on the concentration of electrolyte through the screening factor κ. Equation (2.78) relates the coefficient γ to the surface potential $\Phi(0) = ze\beta\psi_0$. Therefore, if the electric interaction is weak, γ is proportional to ψ_0 and the repulsive potential $U_{\mathrm{R}}(l)$ is proportional to ψ_0^2.

In colloid chemistry, the expression "repulsion induced by overlapping of electric double layers" is often used. This is an ingenious phrase to express a characteristic of macroionic interactions. This phrase, however, tacitly ignores an important physical implication of the actual situation that *the counterions around the midpoint between the plates are shared by two plates.* In fact, as shown in Chap. 6, a cloud of counterions shared by two plates (or two spherical particles) has the effect of inducing a weak long-range attraction between them.

Osmotic Repulsion for Spherical Colloids

So far we have considered the interaction between charged plates only. It is not simple to investigate analytically interactions for spherical particles. Here, we calculate the interaction energy of two spheres with sufficiently large radius a under the condition $1/\kappa \ll a$. The distances between the centers O_1 and O_2 of the two spheres and the closest distance between their surfaces are, respectively, expressed by R and $S = R - 2a$.

Derjaguin [16] observed that the lines of the forces which act most dominantly for two spheres are parallel to the line $\overline{\mathrm{O_1O_2}}$ connecting the centers of the spheres. Let us choose arbitrarily a point P on the surface of one of the spheres and then draw two line segments, $\overline{\mathrm{PP'}}$ which is parallel to $\overline{\mathrm{O_1O_2}}$ with the point P′ on the surface of the other sphere and $\overline{\mathrm{PQ}}$ which is orthogonal to the line $\overline{\mathrm{O_1O_2}}$ at the point Q. As shown in Fig. 2.3, h and s are, respectively, the lengths of the segments $\overline{\mathrm{PQ}}$ and $\overline{\mathrm{PP'}}$.

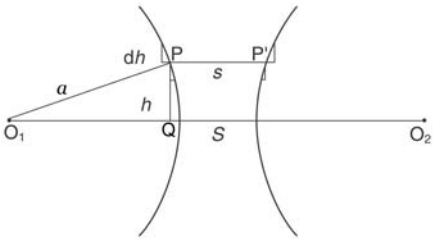

Fig. 2.3. Derjaguin's approximation for deriving the potential between two charged spheres. The surfaces of the spheres are divided symmetrically around the axis $\overline{O_1O_2}$ into sums with ring-like parallel layers of radius h and width dh. The potential between the spheres is obtained by summing up the potentials between the layers which are approximated by the potentials between parallel plates

For a large value of h, the line of force acting between the spheres deviates from the line of symmetry $\overline{O_1O_2}$. However, the axial symmetry around $\overline{O_1O_2}$ works in such a way that deviations cancel out with each other as a whole. The surfaces of the spheres are divided symmetrically around the axis $\overline{O_1O_2}$ into sums with ring-like parallel layers of radius h and width dh. The potential between the spheres is obtained by summing up the potentials between the layers which are approximated by the potentials between parallel plates. Namely, substituting $l = s/2$ in $U_{\mathrm{R}}(l)$ in (2.90) and adding contributions from all layers, we obtain the potential

$$U_{\mathrm{R}} = \int_0^\infty U_{\mathrm{R}}\Big(\frac{s}{2}\Big)\, 2\pi h \mathrm{d}h = \frac{2n_0 k_{\mathrm{B}} T}{\kappa} \Phi(0)^2 \int_S^\infty \Big(1 - \tanh\frac{\kappa s}{2}\Big)\, \pi a \mathrm{d}s \qquad (2.94)$$

for two charged spheres. As an upper limit ∞ is chosen, because the range of the repulsive force is much smaller than the dimensions of the spheres. In this calculation, we have used the estimation $2h\mathrm{d}h = \sqrt{a^2 - h^2}\mathrm{d}s \approx a\mathrm{d}s$ derived from the relation $a - \sqrt{a^2 - h^2} = (s - S)/2$ which is proved by Pythagoras' theorem. From straightforward integration, the repulsive potential for two approaching spheres is obtained in the form

$$U_{\mathrm{R}}(S) = \frac{1}{2}\epsilon a \psi_0^2 \ln[1 + \exp(-\kappa S)]\ . \qquad (2.95)$$

This Derjaguin potential is useful for describing the interaction of large spheres with thin electric double layers ($\kappa a \gg 1$).

Weak Repulsive Potential for Spherical Colloids

It is difficult to make general investigations of interactions between spherical macroions even in the mean field description with the linearized PB equation. Here, we derive the fundamental repulsive potential of the DLVO theory intuitively in the case of a weak field and explain its physical implications. A general derivation will be left to Chap. 6.

Verwey and Overbeek [6] obtained an osmotic repulsive potential between spherical colloidal particles with radius a and surface electric potential ψ_a as follows:

$$U_{\mathrm{R}}(R) = \epsilon a^2 \psi_a^2 \frac{1}{R} \exp[-\kappa(R-2a)]\vartheta \tag{2.96}$$

where R is the center-to-center distance of the particles. In this general expression, the factor ϑ is a function of R which takes different forms depending on the conditions of whether the surface potential ψ_a is constant or the surface charge number Z is constant. Recently, the simplified form with $\vartheta = 1$

$$U_{\mathrm{R}}(R) = \epsilon a^2 \psi_a^2 \frac{1}{R} \exp[-\kappa(R-2a)] \tag{2.97}$$

is used in many articles and books under the name of the *DLVO repulsive potential*.

Let us outline the route leading to the result in (2.97). When the charged particles come close to each other, the electric potentials around the particles overlap, resulting in an increase in the potential. This mechanism differs depending on the situations of whether the surface electric potential ψ_a or the surface charge number Z remains constant. Suppose here that the surface charge number Z of two spherical particles is constant. One particle remains stationary with its center at the origin. When the other particle approaches from infinity to a point with distance $R\,(R \geq 2a)$ from the origin, the stationary particle "feels" the energy difference

$$U_{\mathrm{R}}(R) = Ze[\psi(R) - \psi(\infty)] \,. \tag{2.98}$$

In this intuitive estimation, the potential $U_{\mathrm{R}}(R)$ is assumed to have its origin essentially in the electric interaction. Namely, the potential $U_{\mathrm{R}}(R)$ is equated with the energy difference originating from the electric potential difference between two particles at finite and infinite distances.

To make a further estimation of (2.98), we use the solution for the mean electric potential obtained in the DH theory for spherical ions with radius a for $\psi(R)$ in (2.98). From (2.56) $\psi(R)$ is estimated to be

$$\psi(R) = \psi_a \left(\frac{a}{R}\right) \mathrm{e}^{-\kappa(R-a)}, \tag{2.99}$$

and from (2.57) ψ_a and Z are related by

$$\psi_a = \frac{Ze}{\epsilon a(1+\kappa a)} \,. \tag{2.100}$$

Substituting these results into (2.98), we obtain the repulsive potential as

$$U_{\mathrm{R}}(R) = \frac{Z^2 e^2}{\epsilon} \frac{\mathrm{e}^{\kappa a}}{1+\kappa a} \frac{\mathrm{e}^{-\kappa R}}{R} \tag{2.101}$$

for two spherical particles with surface charge number Z and radius a.

Recent improvements in experimental techniques have stimulated rapid progress in studies of the colloidal dispersions with low ionic strength and small κa. For the analysis of such experiments, the potential in (2.101), called the *Debye-Hückel potential*, is often used. For the studies of dispersions where $\kappa a \ll 1$, the simplified potential without the geometrical factor $e^{\kappa a}/(1+\kappa a)$, i.e.,

$$U_{\mathrm{R}}^{\mathrm{Y}}(R) = \frac{Z^2 e^2}{\epsilon} \frac{\mathrm{e}^{-\kappa R}}{R} \tag{2.102}$$

is also used. This is called the *Yukawa potential*.

To find the repulsive potential with a constant surface electric potential, we make use of (2.100) again. As a result, we obtain from (2.101) the repulsive potential

$$U_{\mathrm{R}}(R) = \epsilon a^2 \psi_a^2 \frac{1}{R} \exp[-\kappa(R-a)](1+\kappa a) \tag{2.103}$$

for two spherical particle with constant ψ_a. This coincides with the general form of the DLVO potential in (2.96) with the factor $\vartheta = (1+\kappa a)\exp(-\kappa a)$.

2.4.2 London's Derivation of the van der Waals Attraction

As emphasized in Sect. 1.3, the van der Waals force plays a major role in solid state physics. This short-range strong attraction is also necessary in macroionic dispersions to explain instabilities such as coagulation.

London showed [17] that this attraction arises from the (electric dipole)-(electric dipole) interactions which are induced in neutral atoms (molecules) by quantum fluctuations. Here, describing first the electric dipoles in atoms as a system of harmonic oscillators with electric charges, we calculate the energy eigenvalue of the ground state of the system. The London attraction inversely proportional to the sixth power of the distance between two oscillators is derived from the energy eigenvalue [18]. This result is applied to obtain the intermolecular force between two spheres. Namely, summing up the London attraction between all pairs of atoms in the spherical macromolecules, we derive the van der Waals attraction between two spherical macromolecules.

London's Attraction between Harmonic Oscillators

The polarization of an atom is described by a 3-dimensional harmonic oscillator with mass m and angular frequency ω. The momentum operators conjugate to the displacement operators $\boldsymbol{r}_a$ and $\boldsymbol{r}_b$ of two atoms a and b are expressed, respectively, by $\boldsymbol{p}_a$ and $\boldsymbol{p}_b$. The Hamiltonian H_0 of the two free oscillators is given by

$$H_0 = \frac{1}{2m}\boldsymbol{p}_a^2 + \frac{1}{2}m\omega^2 \boldsymbol{r}_a^2 + \frac{1}{2m}\boldsymbol{p}_b^2 + \frac{1}{2}m\omega^2 \boldsymbol{r}_b^2 \tag{2.104}$$

and the energy eigenvalue of its ground state is $E_0 = 2\times 3\times \frac{1}{2}\hbar\omega = 3\hbar\omega$ where $\hbar = h/2\pi$ ($= 1.05459\times 10^{-34}$ J s) is the Planck constant divided by 2π.

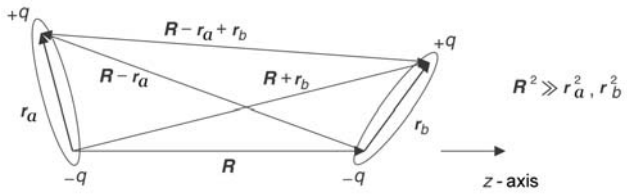

Fig. 2.4. Interaction between two electric dipoles. Two dipoles a and b with electric charges $\pm q$ are separated by $\boldsymbol{R}$. The dipoles with displacement vectors $\boldsymbol{r}_a$ and $\boldsymbol{r}_b$ ($\boldsymbol{R}^2 \gg \boldsymbol{r}_a^2, \boldsymbol{r}_b^2$) are drawn so large as to be easily seen

As shown in Fig. 2.4, the dipole-dipole interaction is calculated by the sum of the Coulomb interactions between the component charges $\pm q$ induced on the atoms by polarization as follows:

$$U = q^2 \left(\frac{1}{R} - \frac{1}{|\boldsymbol{R} - \boldsymbol{r}_a|} - \frac{1}{|\boldsymbol{R} + \boldsymbol{r}_b|} + \frac{1}{|\boldsymbol{R} - \boldsymbol{r}_a + \boldsymbol{r}_b|} \right)$$

$$\simeq q^2 \, \frac{\boldsymbol{r}_a \cdot \boldsymbol{r}_b - 3(\hat{\boldsymbol{R}} \cdot \boldsymbol{r}_a)(\hat{\boldsymbol{R}} \cdot \boldsymbol{r}_a)}{R^3} \tag{2.105}$$

where $\boldsymbol{R} = R\hat{\boldsymbol{R}}$ is the relative displacement between the atoms and $\hat{\boldsymbol{R}}$ is the unit vector. The relative distance of atoms $R = |\boldsymbol{R}|$ is assumed to be so large that $\boldsymbol{R}^2 \gg \boldsymbol{r}_a^2, \boldsymbol{r}_b^2$. Consequently, the Hamiltonian of the system of interacting harmonic oscillators is given by

$$H = H_0 + U \; . \tag{2.106}$$

Let us fix the z-axis in the direction of $\hat{\boldsymbol{R}}$ and express the Hamiltonian in terms of Cartesian coordinates as

$$H = H_x + H_y + H_z \tag{2.107}$$

where

$$H_x = \frac{1}{2m}(p_{ax}^2 + p_{bx}^2) + \frac{1}{2}m\omega(x_a^2 + x_b^2) + \frac{q^2}{R^3}x_a x_b, \tag{2.108}$$

$$H_y = \frac{1}{2m}(p_{ay}^2 + p_{by}^2) + \frac{1}{2}m\omega^2(y_a^2 + y_b^2) + \frac{q^2}{R^3}y_a y_b \tag{2.109}$$

and

$$H_z = \frac{1}{2m}(p_{az}^2 + p_{bz}^2) + \frac{1}{2}m\omega^2(z_a^2 + z_b^2) - \frac{2q^2}{R^3}z_a z_b \; . \tag{2.110}$$

It is readily proved that the orthogonal transformations

$$x_\pm = \frac{1}{\sqrt{2}}(x_a \pm x_b), \quad y_\pm = \frac{1}{\sqrt{2}}(y_a \pm y_b), \quad z_\pm = \frac{1}{\sqrt{2}}(z_a \pm z_b) \tag{2.111}$$

diagonalize the component Hamiltonians H_x, H_y and H_z as follows:

$$H_x = \left(\frac{1}{2m}p_{x+}^2 + \frac{1}{2}m\omega_{x+}^2 x_+^2\right) + \left(\frac{1}{2m}p_{x-}^2 + \frac{1}{2}m\omega_{x-}^2 x_-^2\right), \tag{2.112}$$

$$H_y = \left(\frac{1}{2m}p_{y+}^2 + \frac{1}{2}m\omega_{y+}^2 y_+^2\right) + \left(\frac{1}{2m}p_{y-}^2 + \frac{1}{2}m\omega_{y-}^2 y_-^2\right) \tag{2.113}$$

and

$$H_z = \left(\frac{1}{2m}p_{z+}^2 + \frac{1}{2}m\omega_{z+}^2 z_+^2\right) + \left(\frac{1}{2m}p_{z-}^2 + \frac{1}{2}m\omega_{z-}^2 z_-^2\right) \tag{2.114}$$

where $p_{x\pm}$, $p_{y\pm}$ and $p_{z\pm}$ are the momentum operators conjugate to $x_\pm$, $y_\pm$ and $z_\pm$, respectively. Here the angular frequencies in the transformed modes are given by

$$\omega_{x\pm} = \omega_{y\pm} = \sqrt{\omega^2 \pm \frac{q^2}{mR^3}}, \quad \omega_{z\pm} = \sqrt{\omega^2 \mp \frac{2q^2}{mR^3}}\ . \tag{2.115}$$

The ground state eigenvalue of the total Hamiltonian H is given by the sum of the energies of the zero-point oscillations in the diagonalized modes as

$$E(R) = \frac{1}{2}\hbar(\omega_{x+} + \omega_{x-} + \omega_{y+} + \omega_{y-} + \omega_{z+} + \omega_{z-}) \tag{2.116}$$

which depends on the distance between two atoms R. Here, let us extract the effect of the dipole-dipole interaction by taking the difference between the eigenvalues $E(R)$ of H and E_0 of H_0, i.e.,

$$U(R) = E(R) - E_0\ . \tag{2.117}$$

It is reasonable to interpret $U(R)$ as representing an effective interaction induced by quantum fluctuation on the atoms. Expanding $U(R)$ with respect to $1/R^3$ up to the second order, we find a potential of attractive force inversely proportional to the sixth power of distance as

$$U(R) = -\frac{3}{4}\hbar\omega\left(\frac{q^2}{m\omega^2}\right)^2 \frac{1}{R^6}\ . \tag{2.118}$$

This is the van der Waals attraction between neutral atoms derived by London. As the Planck constant indicates, this force arises as a purely quantum mechanical effect.

In this derivation in elementary quantum mechanics [18], the retardation effect of the electric interaction is not taken into account. The retardation effect calculated in quantum field theory [19,20] changes the power dependence of the attraction on the distance from $1/R^6$ to $1/R^7$. However, it is customary to ignore this modification in studies of colloidal dispersions. Henceforth, we

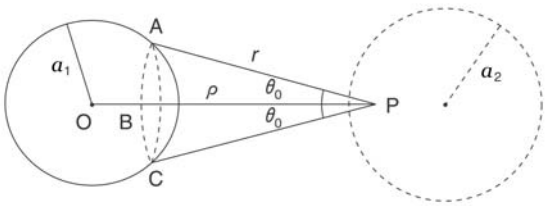

Fig. 2.5. Derivation of the van der Waals attractive potential for two spheres. Calculating first the potentials between the atom at P inside the sphere 2 and all atoms inside the sphere 1, the resultant potentials are summed up over all atoms inside the sphere 2

also assume that the van der Waals attraction is inversely proportional to the sixth power of the distance.

van der Waals Interaction between Spherical Particles

The van der Waals attractive potential between neutral macromolecules is considered to be derivable by summing those between constituent atoms of the molecules. Accordingly, the potential energy for the van der Waals attraction between two spherical molecules which have n atoms in a unit volume is estimated by the integral

$$U_{\mathrm{BB}} = -\int \mathrm{d}V_1 \int \mathrm{d}V_2\, n^2 \frac{\Lambda}{r^6} \tag{2.119}$$

where R in (2.118) is replaced by r and $\Lambda = \frac{3}{4}\hbar\omega\alpha^2$. The quantity $\hbar\omega$ is related to the excitation energies of atoms and $\alpha = q^2/m\omega^2$ is the polarizability. The integrations in (2.119) are taken over the whole volumes of the two spheres 1 and 2 by assuming that atoms are distributed continuously inside the spheres.

Consider two spheres with radius a_i $(i = 1, 2)$. Fixing the center-to-center distance R $(R \geq a_1 + a_2)$, we carry out the integrations in (2.119). As shown in Fig. 2.5, an atom is chosen at the point P inside the sphere 2 with distance ρ from the center of the sphere 1 $(\rho \geq a_1)$. Draw a spherical surface with radius r with its center at P and notice a circular cone APC restricted by the sphere 1. Using the relation $a_1^2 = \rho^2 + r^2 - 2r\rho\cos\theta_0$ with an aperture angle $\mathrm{APC} = 2\theta_0$, the solid angle extended by the circular cone is obtained by

$$\Omega_{a_1}(r) = 2\pi \int_0^{\theta_0} \sin\theta \mathrm{d}\theta = \frac{\pi}{\rho r}\left[a_1^2 - (\rho - r)^2\right] \tag{2.120}$$

by which the volume element of the sphere 1 is expressed as $dV_1 = \Omega_{a_1}(r)r^2\mathrm{d}r$. Accordingly, the van der Waals potential of the atom at P with all atoms of the sphere 1 is found to be

$$U_{\mathrm{BP}}(\rho) = -\int_{\rho - a_1}^{\rho + a_1} \frac{n\Lambda}{r^6}\frac{\pi r}{\rho}\left[a_1^2 - (\rho - r)^2\right]\mathrm{d}r\ . \tag{2.121}$$

Then, by expressing the volume element of the sphere 2 by $\mathrm{d}V_2 = \Omega_{a_2}(\rho)\rho^2\mathrm{d}\rho$, we integrate the potential U_{BP} over all atoms inside the sphere 2, viz,

$$U_{\mathrm{BB}}(R) = \int_{R-a_2}^{R+a_2} U_{\mathrm{BP}}(\rho) n \frac{\pi\rho}{R}\left[a_2^2 - (R-\rho)^2\right]\mathrm{d}\rho \,. \tag{2.122}$$

Finally, elementary integrations result in the potential of the van der Waals attraction for two spheres as follows:

$$\begin{aligned} U_{\mathrm{BB}}(R) &= -\frac{\pi^2}{6} n^2 \Lambda \\ &\times \left[\frac{2a_1a_2}{R^2-(a_1+a_2)^2} + \frac{2a_1a_2}{R^2-(a_1-a_2)^2} + \ln\frac{R^2-(a_1+a_2)^2}{R^2-(a_1-a_2)^2}\right] . \end{aligned} \tag{2.123}$$

In a monodisperse dispersion of spherical macromolecules with radius a, the potential of the van der Waals attraction takes the form [18]

$$U_{\mathrm{A}}(R) = -\frac{1}{6} A \left[\frac{2a^2}{R^2-4a^2} + \frac{2a^2}{R^2} + \ln\left(1 - \frac{4a^2}{R^2}\right)\right] \tag{2.124}$$

where A is a physical quantity called the *Hamaker constant* in vacuum [21]. In the present simplified derivation, this is estimated to be $A = \pi^2 n^2 \Lambda \simeq \frac{3}{4}\pi^2\hbar\omega\alpha^2 n^2$. In general, the Hamaker constant depends on details of excitation energies and polarizabilities of atoms which constitute the macromolecules.

Suppose that the two spherical macromolecules have a nearest surface-to-surface distance $S = R - 2a$. The potential U_{A} takes the forms

$$U_{\mathrm{A}}(S) = -\frac{1}{12} A \frac{a}{S} \tag{2.125}$$

for a sufficiently small S, and

$$U_{\mathrm{A}}(S) = -\frac{16}{9} A \frac{a^6}{S^6} \tag{2.126}$$

for a sufficiently large S.

Dependence of the Hamaker Constant on Dielectric Constants

Effects of the dielectric medium which have been ignored so far can be neatly taken into account in the following way. As shown in Fig. 2.6, the close and distant configurations of the molecules B and B′ are equivalent to replacing B′ by a region of medium S′ having the same volume as B′. This reasoning enables us to estimate the Hamaker constant A in a medium as follows:

$$A = A_{\mathrm{BB'}} + A_{\mathrm{SS'}} - A_{\mathrm{BS'}} - A_{\mathrm{SB'}} \tag{2.127}$$

where $A_{\mathrm{BB'}}$, $A_{\mathrm{SS'}}$, $A_{\mathrm{BS'}}$ and $A_{\mathrm{SB'}}$ are the Hamaker constants in vacuum which are calculated, respectively, for pairs (B and B′), (S and S′), (B and S′) and (S and B′). In colloid chemistry, there was a time when the formula

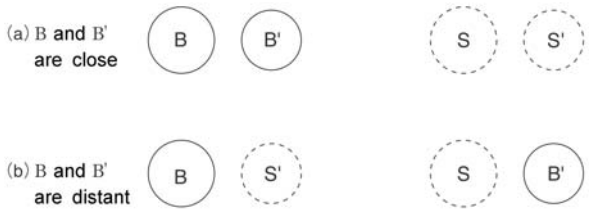

Fig. 2.6. Dielectric effects on the van der Waals attraction. B and B′ are spherical molecules. S and S′ represent spherical regions of a medium having the same volumes as B and B′. B and B′ are close in (a) and distant in (b). The difference in (a) and (b) results in the replacement of B′ and S′

$$A = (\sqrt{A_{\mathrm{BB}}} - \sqrt{A_{\mathrm{SS}}})^2 \tag{2.128}$$

was used for monodisperse dispersions by assuming the relation $A_{\mathrm{BS}} = \sqrt{A_{\mathrm{BB}} A_{\mathrm{SS}}}$. However, this relation can hold only in the case where the excitation energies and polarizabilities are the same for atoms in the solute and solvent molecules.

In fact, it is not so simple to determine the Hamaker constant in condensed matter as in the formula (2.128). Applying the Lifshitz theory on dielectric constants, Parsegian and Ninham [22] showed that the Hamaker constant is a function which can depend on the distance between molecules. However, traditionally in colloid chemistry, the Hamaker constants are dealt with as adjustable parameters to explain the observed data.

2.4.3 DLVO Potential and Schulze-Hardy Rule

In the DLVO theory, the potential for spherical macroions is constructed by adding the screened repulsive potential U_{R} and the van der Waals attractive potential U_{A} as follows:

$$U = U_{\mathrm{R}} + U_{\mathrm{A}} \,. \tag{2.129}$$

This is the standard DLVO potential. However, it is necessary to include a very short-range strong repulsion to describe phenomena of macromolecules whose surface-to-surface distance becomes tens of nanometers. In the DLVO theory, it is usual to use an effective potential of Lennard-Jones type (cf. Sect. 1.3) with a very deep minimum called the primary minimum.

In the DLVO theory, it is postulated that the small ions take a distribution of thermal equilibrium in a stationary configuration of macroions. However, as the Earnshaw theorem insists, such a stationary configuration is unstable. For the dispersion to be stable, the macroions must necessarily show dynamical behavior, viz, the *Brownian motion*. Interactions are not explicitly taken into consideration in the ordinary theory of the Brownian motion. In macroionic dispersions, however, an effective interaction such as U in (2.129) rules the

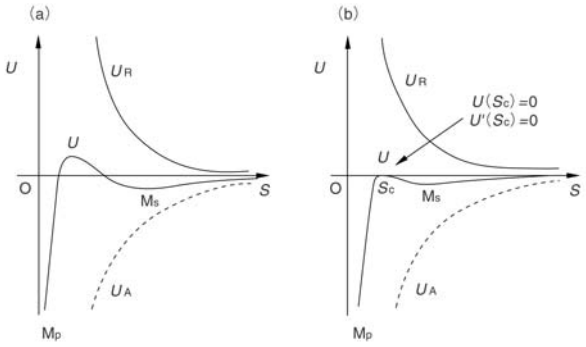

Fig. 2.7. DLVO potential $U = U_R + U_A$. (a) Crystallization takes place if the potential depth at the secondary minimum M_S is deeper than the thermal energy of order k_BT and the crystal melts if it is shallower than the thermal energy. U takes a maximum in between the primary and secondary minima, M_P and M_S. (b) The critical position S_c is determined by the conditions that both U and its derivative vanish at S_c

dynamical behavior of the macroions. That is why macroionic dispersions manifest phenomena with remarkable variety.

While the screened repulsive part U_R depends sensitively on the concentrations of salts and particles through κ, the attractive part U_A is almost insensitive to the salt concentrations. Therefore, by adjusting those concentrations properly, we are able to observe and control a variety of phenomena in macroionic dispersions.

Primary and Secondary Minima of DLVO Potential

In dispersions where the concentration of small ions is not very high, the repulsive force works strongly between the colloid particles because the screening effect is small. The approaching particles repel each other and continue Brownian motion. As a result, the dispersions are stabilized.

The repulsive potential U_R is weakened in dispersions with high salt concentration. When the barrier of the repulsive potential becomes lower than the thermal energy of order k_BT, the particles, attracting each other by the van der Waals force, fall into the primary minimum of a potential of Lennard-Jones type. In Fig. 2.7, the position of the primary minimum is denoted by M_P. Since the depth of the potential at the primary minimum is far deeper than the thermal energy, the particles are strongly bound. This is an irreversible process called *coagulation*. Consequently, increasing the salt concentration makes the dispersion unstable.

Superposition of the attractive potential U_A and the screened repulsive potential U_R may produce a relatively shallow minimum called the *secondary minimum*. The depth of the secondary minimum is very sensitive to the salt concentration. In Fig. 2.7, the position of the secondary minimum is at M_S.

It was predicted by the DLVO theory that, if the depth of the secondary minimum is larger than the thermal energy of order $k_{\mathrm{B}}T$, the colloidal particles tend to flocculate and form colloidal crystallites. This *flocculation* is a reversible process.

Derivation of the Schulze-Hardy Rule in the DLVO Theory [6]

To make muddy water clear, it is more effective to add bivalent ions such as Ca^{2+} than univalent ions such as Na^{+} and K^{+}, and far more effective to use trivalent ions such as Al^{3+} and Fe^{3+}. Empirically, it is known that the efficiency of coagulation of colloidal particles is proportional to the sixth power of the valency of the counterion in the added salt. This is the Schulze-Hardy rule. This empirical law is explained by a mechanism in which particles crossing over a Coulomb barrier lowered by added salt fall down irreversibly into the primary minimum. In this subsection we derive the Schulze-Hardy rule by using the DLVO potential in (2.129). The same argument is applicable to the new potential obtained in Chap. 6.

To examine the coagulation of spherical particles, it is necessary to consider the situation where the surface-to-surface distance $S = R - 2a$ is very small. In terms of the variable S, the DLVO potential (2.129) is written as

$$U(S) = U_{\mathrm{R}}(S) + U_{\mathrm{A}}(S) \tag{2.130}$$

with the approximated form

$$U_{\mathrm{R}}(S) = \frac{1}{2}\epsilon a \psi_a^2 \exp(-\kappa S) \tag{2.131}$$

which is derived by putting $R = 2a$ in the denominator of (2.97). This $U_{\mathrm{R}}(S)$ is identical with the leading term in the expansion of the logarithmic part of the Derjaguin potential (2.95) with $\psi_0 = \psi_a$. As for the attractive potential $U_{\mathrm{A}}(S)$, we use the approximate form

$$U_{\mathrm{A}}(S) = -\frac{1}{12} A \frac{a}{S} \tag{2.132}$$

in (2.125).

Suppose that the potential $U(S)$ takes a maximum at $S = S_{\mathrm{c}}$ outside of the primary minimum. It is reasonable to interpret that the coagulation starts when the maximum $U(S_{\mathrm{c}})$ vanishes as shown in Fig. 2.7 (b). Namely, the critical distance S_{c} at which the coagulation takes place must satisfy the relations

$$U_{\mathrm{R}}(S_{\mathrm{c}}) + U_{\mathrm{A}}(S_{\mathrm{c}}) = \frac{1}{2}\epsilon a \psi_a^2 \exp(-\kappa S_{\mathrm{c}}) - \frac{1}{12} A \frac{a}{S_{\mathrm{c}}} = 0 \tag{2.133}$$

and

$$\frac{\mathrm{d}\, U_{\mathrm{R}}}{\mathrm{d}\, S}\Big|_{S_{\mathrm{c}}} + \frac{\mathrm{d}\, U_{\mathrm{A}}}{\mathrm{d}\, S}\Big|_{S_{\mathrm{c}}} = -\kappa U_{\mathrm{R}}(S_{\mathrm{c}}) - \frac{1}{S_{\mathrm{c}}} U_{\mathrm{A}}(S_{\mathrm{c}}) = 0 \tag{2.134}$$

which are easily solved leading to the following two conditions as

$$S_{\rm c} = \frac{1}{\kappa} \tag{2.135}$$

and

$$\frac{1}{2}\epsilon a \psi_a^2 \exp(-1) = \frac{1}{12} A \kappa a \ . \tag{2.136}$$

Note that the surfaces of spherical particles can be approximated well by plate surfaces when the particles come closer to each other. Accordingly, we obtain the estimation $\gamma = ze\psi_a/(4k_{\rm B}T)$ by replacing the surface potential of the plate ψ_0 with that of the sphere ψ_a in the Gouy-Chapman relation (2.78). From these relations and the definition of κ, we obtain

$$n_0 = \frac{1152}{\pi \exp(2)} \frac{\epsilon^3 (k_{\rm B}T)^5 \gamma^4}{A^2 (ze)^6} \propto \frac{1}{z^6} \tag{2.137}$$

for the salt concentration. This is the proof of the Schulze-Hardy rule in the DLVO theory.

2.4.4 Shortcomings of the DLVO Theory

The DLVO theory is a successful framework in colloid chemistry which first elucidated the nature of a variety of phenomena in the mesoscopic regime from fundamental principles of physics. In particular, the proof of the Schulze-Hardy rule was a remarkable establishment in colloid chemistry, which had long been resorting to empirical laws and rules.

The DLVO theory is suitable for investigating the properties of concentrated dispersions with high salt concentrations. However, as will be clarified in Chaps. 4 and 5, the theory is not effective in describing ordering processes such as the evolution of colloidal crystals in dilute dispersions with low salt concentrations. In dilute dispersions of polystyrene latexes and silica colloids, crystals with lattice constants which are $2 \sim 10$ times larger than particle's diameter are observed. It is almost impossible to explain such long-range ordering by the DLVO mechanism of the secondary minimum.

A far more difficult and essential issue is the relation between the formation of colloidal crystals and salt concentrations. The formation of colloidal crystals requires a low salt concentration. However, the DLVO theory cannot make a quantitative explanation of this well known experimental fact. For some range of salt concentration, an increase in salt concentration is known to enhance crystallization by making the so-called secondary minimum deeper in the DLVO description.

To examine the physical conditions for crystal formation, it is useful to investigate the relation of *salt concentration and melting of crystals*. Hachisu et al. [23] made careful observations of iridescence in dispersions of polystyrene latexes by changing the volume fraction of particles and the concentration of

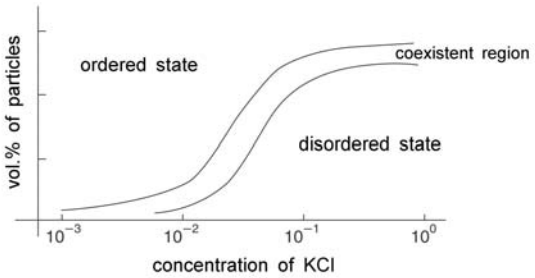

Fig. 2.8. Hachisu phase diagram. Hachisu et al. made careful observations of iridescence in dispersions of polystyrene latexes by changing the volume fraction of particles and concentration of added salts. An increase in salt concentration results in the disappearance of iridescence, showing the melting of colloidal crystals

added salts. The results were shown as a phase diagram, as in Fig. 2.8. In the region with a large volume fraction of particles and low KCl concentration, they observed iridescence and confirmed the formation of colloidal crystals. Even in dispersions with a relatively small volume fraction of particles, the iridescence can be seen when the KCl concentration is sufficiently low. They gradually increased the KCl concentration in such dispersions and confirmed that the iridescence evidencing the existence of crystalline ordering disappears in proportion to the KCl concentration. Namely, as shown in the phase diagram, an increase in the KCl concentration causes ordered states to melt into disordered states via a coexistence region. This phenomenon of the *salt-induced-melting of colloidal crystals* has been confirmed by many experiments, as described in Chap. 4.

Figure 2.9 is taken from the book written by Verwey and Overbeek [6] which is authoritative in lyophobic colloid chemistry. In the figure, the behavior of the DLVO potential around the secondary minimum versus $s = R/a$ is drawn for a large particle with radius $a = 1000\,\mathrm{nm}$ and Hamaker constant $A = 5 \times 10^{-13}\,\mathrm{J}$ in solutions of a symmetric electrolyte of valency $v = v_{\pm}$ at $T = 298\,\mathrm{K}$. Comparison of the potential curves is made against the screening factor $\kappa{=}(3 \times 10^5 \sim 3 \times 10^6)\,\mathrm{m}^{-1}$ and the dimensionless quantity $z = ve\psi_a/k_\mathrm{B}T = (1 \sim 8)$. The horizontal line for $6k_\mathrm{B}T$ is an indicator for flocculation into the secondary minimum. When κ increases from 3×10^5 to 10^6, the potential becomes deeper than the indicator line around the secondary minimum. This behavior is enhanced further when κ increases from 10^6 to 3×10^6. Therefore, the DLVO theory predicts that an increase in salt concentration necessarily stabilizes colloidal crystals. This prediction evidently contradicts the *salt-induced-melting of colloidal crystals* discovered by the Hachisu group.

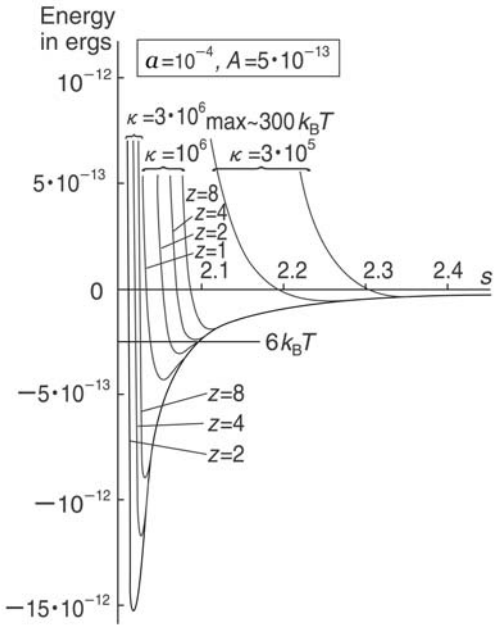

Fig. 2.9. Behavior of the DLVO potential around the secondary minimum versus $s = R/a$ for a coarse particle with radius $a = 1000\,\mathrm{nm}$ in solutions of a symmetric electrolyte of valency $v = v_{\pm}$. Hamaker constant $A = 5 \times 10^{-13}\,\mathrm{J}$ at $T = 298\,\mathrm{K}$ and $z = ve\psi_a/k_\mathrm{B}T$ is a dimensionless quantity

2.5 Summary

The DH theory established studies of strong electrolytes as an active field of chemical physics. The concepts of *ionic atmosphere* and *screening factor* developed in this theory are now indispensable in research on ionic solutions and dispersions. In this classical theory, the difference between the electric parts of the Helmholtz and Gibbs free energies F and G was clearly recognized. It is a historical irony that the DLVO theory which is a successor to the DH theory in the realm of macroionic dispersions disregarded this important difference.

The success of the DH theory depends largely on an approximate symmetry and impartiality between anions and cations in strong electrolytes. In contrast, such symmetry and impartiality are almost perfectly lost in macroionic dispersions. Namely, the masses, radii and charge numbers of the macroions are incomparably larger than those of the small ions. The time scales of motion of the macroions are also very large compared with those of the small ions. Therefore, it turns out to be necessary to take the viewpoint that the macroions are stationary and that a gas of small ions reaches thermal equilib-

rium in the environment of the macroions. Studies of macroionic dispersions have developed in the direction in which the asymmetry between the small ions and macroions is explicitly combined into the DH theory. The DLVO theory is a paragon of such an approach.

However, the DLVO theory fails to explain characteristics of the crystals in colloidal dispersions. The cause of this failure seems to exist in the design of the DLVO theory which ascribes both the strong irreversible process of coagulation and the weak reversible process of flocculation to a mechanism of overlapping of a screened Coulomb repulsion and a potential of Lennard-Jones type. It is natural to interpret the coagulation process as the irreversible trapping of particles by the so-called primary minimum. However, it is unreasonable to use the short-range van der Waals attraction to describe the formation and melting processes of colloidal crystals, since such processes are medium- and long-range reversible phenomena sensitive to the concentration of the small ions.

Does there exist a mechanism for flocculation which explains soft binding of the macroions without resort to the van der Waals attraction? With an awareness of this issue, let us notice the difference between the Helmholtz and Gibbs free energies F and G which was explicitly recognized in the DH theory and ignored in the DLVO theory. The decrease of the osmotic pressure derived from $G - F \neq 0$ shown in (2.43) and (2.68) suggests that the electric interaction can induce attractive effects among ionic species regardless of their size. Observing this point, Langmuir [13] inferred that similar phenomena should arise in colloidal dispersions and that an equation of osmotic pressure resembling a van der Waals isotherm leads to a phase transition in the dispersions. However, the Langmuir theory was incomplete, since by utilizing the DH theory as it stands he did not take the asymmetry between macroions and small ions into account.

To develop a new theory for macroionic dispersions, we should reexamine carefully the concepts of thermodynamics. A new theory which enables us to deal with the macroions and the small ions in an asymmetric manner and calculate not only F but also G must be able to explain both of the coagulation and flocculation phenomena.

References

1. Debye P, Hückel E (1923) Z Physik 24:185, 305; Debye P (1924) Z Physik 25:97
2. The Collected Papers of Peter J. W. Debye (1954) Interscience, New York
3. Levine S (1939) Proc Roy Soc London A170:145, 165; (1938) J Chem Phys 7:831
4. Levine S, Dube GP (1939) Trans Faraday Soc 35:1125, 1141; (1940) Phil Mag (7) 29:105; (1942) J Phys Chem 46:239
5. Derjaguin BV, Landau L (1941) Acta Physicochimica URSS 14:633; (1941) J Exptl Theoret Phys URSS 11:802
6. Verwey EJW, Overbeek JThG (1948) Theory of the stability of lyophobic colloids. Elsevier, Amsterdam
7. van der Waals JD (1873) Dissertation, Univ Leiden; English transl. van der Waals JD (1890) Physical Memoirs, Phys Soci London. Taylor and Francis, Milton Road, vol 1, Part 3
8. Landau LD, Lifshitz EM (1993), Statistical physics. Pergamon Press, London, Chap. 9
9. Fowler RH, Guggenheim EA (1956) Statistical thermodynamics. Cambridge Univ Press, New York, Chap. 9
10. McQuarrie DA (1973) Statistical mechanics. Harper Collins Publishers, New York, Chap. 15
11. Overbeek JThG (1987) J Chem Phys 87:4406
12. Hill TL (1964) Thermodynamics of small systems. W A Benjamin, New York
13. Langmuir I (1938) J Chem Phys 6:873
14. Gouy G (1910) J Physique 9:457; (1917) Ann Phys 7:129
15. Chapman DL (1913) Phil Mag 25:475
16. Derjaguin BV (1934) Kolloid Z 69:155; (1939) Acta Physicochimica URSS 10:333
17. London F (1930) Z Physik 63:245; (1937) Trans Faraday Soc 33:8; (1930) Z Phys Chem B11:222
18. Chu B (1969) Molecular forces (Based on the Baker Lectures of Peter J. W. Debye). John Wiley & Sons, New York
19. Feinberg G, Sucher J (1970) Phys Rev A 2:2395
20. Itzykson C, Zuber JB (1980) Quantum field theory, McGraw-Hill, New York, p.365.
21. Hamaker HC (1936) Rec Trav Chim 55:1015; (1937) 56:3, 727; (1937) Physica 4:1058

22. Parsegian VA, Ninham BW (1969) J Coll Interface Sci 37:332
23. Hachisu S, Kobayashi Y (1974) J Coll Interface Sci 46:470

3

Dilute Solutions of Flexible and Spherical Ionic Polymers

3.1 Introductory Remarks

We now take up the discussion of dilute solutions of ionic polymers, particularly their structure formation. As stated above, macroions have many electric charges, so that their solution behavior is unique in various ways [1], which is largely different from non-ionic polymers and low-molecular-weight ionic systems [2].

Synthetic ionic polymers have simple structures and can be regarded as models of much more complicated, naturally occurring ionic biopolymers. The polymers, whose main chains are composed of carbon-carbon single bonds, for example PAA, PSS and PAAM, may assume a variety of conformations in solutions, as a result of free rotation around the bonds. Therefore they are called flexible ionic polymers. The molecular weight of synthetic ionic polymers is not uniquely defined but show a distribution, however, this is no longer serious as before for some cases (such as PSS) thanks to the recent development of the living polymerization technique.

The principal interaction in electrolyte solutions is that of a long-range electrostatic origin. Its influence persists even at low concentrations. In low-molecular-weight electrolytes such as NaCl, the interionic interaction disappears at infinite dilution, at which the interionic distance is infinitely long. For ionic polymers, on the other hand, the intra-macroionic interaction does not disappear even at an infinite dilution, because ionizable groups (COOH for PAA) are connected to each other by covalent bonds. In vinyl polymers, the distance between two groups is fixed to about 0.25 nm. Even when the number concentration of macroions is decreased to zero, this distance is kept unchanged, so that the interaction does not cease to exist. In other words, the macroion solutions can never be ideal.

As depicted in Fig. 3.1, the electrostatic interaction in the macroionic solutions is in action between the following ionic species: inside a macroion domain, (1) ionized groups (COO^- for PAA), (2) ionized group and nearby counterions, and (3) counterions, and, outside of macroion domain, (4) macroions,

(5) macroion and counterion, and (6) counterions. It is formidably difficult to properly take into consideration all these interactions in theoretical treatments and interpretations. In most cases, discussions were simplified by choosing some interactions only and ignoring others. One example is the conclusion that flexible ionic polymer chains are stretched out to rods. As will be discussed in Chap. 7, the ionized groups should simply repel each other, because they are similarly charged, if there exist exclusively these groups in the macroion domain, in other words, if only the interaction (1) between the groups is considered. Then the polymer chain would be stretched out. However, a large number of counterions are experimentally demonstrated to be condensed in the macroion domain (See Sect. 3.1.1). These counterions must affect the ionized groups by the interaction (2), which would cause formation of triple ions or higher ionic aggregates inside the domain. This factor counteracts the forces to stretch the chains. A small number of such aggregates is enough to drastically influence the conformation of the flexible chains. Thus, whether this interaction can be ignored as widely assumed, and hence whether the rod-model is realistic, needs to be examined. It is true that this model has been taken for granted for flexible ionic polymers and has been used to construct various theories. However, in this monograph, we will not discuss these matters in detail.

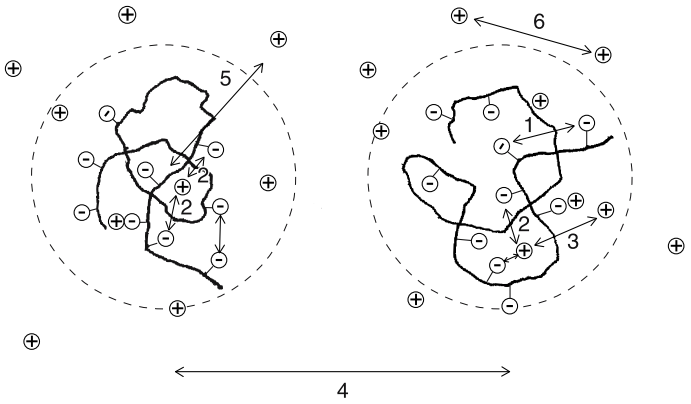

Fig. 3.1. Electrostatic interaction in macroionic solutions. In the macroion domain, electrostatic interaction is in operation (1) between (anionic) ionized groups, (2) between the group and nearby counterions, and (3) between counterions. Outside the macroion domain, it works (4) between macroions, (5) between the macroion and free counterions, and (6) between free counterions. ——: polymer chain, ⊖: ionized group, ⊕: counterion, broken circle: macroion domain

The intermacroion interaction (4) is often assumed to be negligible, or is not even considered, for example, as in some cell models mentioned in the Preface. This assumption would be correct only for extreme dilutions

or when the macroions have a very small number of charges. However, the experimental results shown in this monograph indicate the substantial role of this interaction.

Addition of simple salts lowers the electrostatic interaction by a shielding effect. Therefore, ionic polymers behave like non-ionic polymers in the presence of a large amount of salts. An example is the reduced viscosity-concentration curve. A concave curve is observed at low salt conditions for ionic polymer solutions whereas a straight line with a positive slope as usually found for non-ionic polymers is reported at high salt concentrations (See Chap. 7). In this monograph, except for a few cases, we do not deal with experimental observation under such a high salt condition, because only high molecular features of the dual characters of ionic polymers then stand out and the ionic features are suppressed.

3.1.1 Dissociation State of Ionic Polymers (Charge Number)

When NaCl is dissolved into water, it produces univalent cations and anions. At low concentrations, where the Debye-Hückel theory holds (below 10^{-3} mol L^{-1} for 1-1 electrolytes), the dissociation may be assumed to be complete. At higher concentrations or in solvents with lower dielectric constants, the interionic interaction is intensified, so that the dissociation becomes incomplete. As a consequence, ions coexist with ionic aggregates [3–5]. Ionic polymers generally have a large number of ionizable groups, so that their analytical valency (charge number) is high and hence a large portion of counterions are associated by the macroions. In other words, complete ionization as in the Debye-Hückel case does not take place. Let us take polyacrylic acid (PAA) as an example. As discussed in the Preface, one PAA molecule produces m univalent (cationic) counterions and one m-valent (anionic) PAA ion having an *analytical* charge number Z_{a}. However, a large number of m counterions are confined to the macroion domain, and some of them neutralize the ionized group charges. The rest contributes to the electric conductance. For convenience, let us assume that the fraction f of the total counterions is free and contributes to the conductance while $(1 - f)$ are bound by the macroions. The *net* charge number of the macroions Z_{n} [1] in solution is therefore smaller than Z_{a} with $f = Z_{\mathrm{n}}/Z_{\mathrm{a}}$. The reduction of the charge number was inferred from the outstanding non-ideality of the osmotic pressure of ionic polymer solutions [6]. The strong coupling between the counterions and macroions was called "counterion association" by Wall [7], "counterion fixation" by Osawa, Imai, and Kagawa [8], or "counterion condensation" by Imai and Osawa [9] and has been a topic of intensive theoretical and experimental investigation [10].

Wall et al. experimentally determined Z_{n} for a polyacrylate [7] by using Hittorf's technique to determine the transport number [11]. They measured

[1] The net charge number Z_{n} should be distinguished from the charge number of the n-th particle Z_n discussed in Chaps. 2 and 6.

the changes in the concentrations of PAA ions and Na^+ in the anode by passing electricity through aqueous solutions of sodium salts, the quantity of free counterions, and the transport number of macroions t_{2p}, which is the ratio of the amount of the electricity transported by PAA ions to the total amount. To get a higher precision, Na^{22} was used. Some results are listed in Table 3.1, which clearly shows that a large portion of the counterions $(1-f)$ migrated toward the anode together with PAA ions. The portions are 0.27 and 0.66 at degrees of neutralization α_d of 25% and 100%, respectively. At a fixed PAA concentration, the f decreases monotonously with increasing α_d. At a given α_d, six-fold increase in the polymer concentration increases f only slightly. The t_{2p} is almost constant $(0.4 \sim 0.5)$ in the α_d range between 25% and 100%. The Z_n of PAA ions and the net charge number per repeating unit (Z_n/m) become larger with increasing α_d.

Table 3.1. Transport number of PAA ions, degree of counterion-association $(1-f)$, equivalent conductivity Λ_{2p}, and fraction of net charge number Z_n/m at various degrees of neutralization [a]

α_d(%)	(1 - f)	t_{2p}	Λ_{2p} (S cm^2 equiv^{-1})	Z_n/m
0		0.047		
9.6	0.102	0.358	30.2	0.092
24.0	0.267	0.459	41.1	0.176
41.4	0.421	0.500	47.9	0.239
61.7	0.547	0.518	51.2	0.280
81.6	0.619	0.513	49.9	0.311
97.9	0.623	0.503	48.2	0.369

[a] Aqueous solutions of Na^{22}PAA ($m = 250$) at a polymer concentration of 0.0151 N and at rt.

According to these results, the PAA ions behave not as Z_a (250)-valent anions, but as 92 (250×0.369)-valent anions at an α_d of 97.9% [2]. When the polymer concentration is increased, f becomes larger and t_{2p} decreases, though data is not shown here. No substantial temperature dependence is seen between 0 and 42°C. As far as the properties in question are concerned, Na- and K-salts show no difference [12]. f increases more drastically by the addition of a neutral strontium salt than by that of a sodium salt [13]. A larger molecular weight PAA has a slightly smaller f.

Quaternary ammonium salts of PAA have larger f values than a Na-salt, for example 0.4 and $0.6 \sim 0.8$ for tetramethylammonium salts and tetrabutylammonium salts, respectively. This would be due to the exclusion volume effect of the counterions [14]. Sodium poly(styrene sulfonate)s (NaPSS) have

[2] When one ionizable group is contained in one repeating unit of polymer chain, like PAA, Z_a is equal to the degree of polymerization m. This is however not the case for copolymers containing more than two kinds of monomers.

f values of $0.45 \sim 0.55$ [14–16], whereas the f values of the acid form [17], tetramethylammonium salts, and tetrabutylammonium salts [17] are 0.38, 0.5, and 0.3, respectively. The contribution of hydrophobic interaction seems to play a role for these organic salts.

Recently Ohshima et al. studied the dissociation state of ionic dendrimers, a spherical polyelectrolyte [18]. By the electric neutrality condition we have

$$Z_{\mathrm{nd}} = \frac{Z_{\mathrm{c}} C_{\mathrm{c}}}{C_{\mathrm{d}}}, \tag{3.1}$$

where Z_{nd} is the net charge number of a dendrimer ion, Z_{c} and C_{c} are the valency and molarity of counterions, and C_{d} is the molarity of dendrimers. The specific conductivity $\kappa(\mathrm{S\ cm^{-1}})$ is given by

$$\kappa = \frac{1}{10^3} \left[\lambda_{\mathrm{c}} C_{\mathrm{c}} + \lambda_{\mathrm{d}} C_{\mathrm{d}}\right] + \kappa_{\mathrm{b}}, \tag{3.2}$$

where λ is the molar conductivity ($\mathrm{S\ cm^2\ mol^{-1}}$) and κ_{b} the specific conductivity of solvent, the subscripts c and d denote counterions and dendrimers, respectively. The diffusion constant D of ions of valency Z is given by the following equation

$$D = \left(\frac{RT}{F^2}\right)\left(\frac{\lambda}{Z^2}\right), \tag{3.3}$$

where F is the Faraday constant, R the gas constant, and T the temperature. Therefore we have

$$C_{\mathrm{c}} = \left(\frac{1}{2A}\right)\{-\lambda_{\mathrm{c}} + [\lambda_{\mathrm{c}}^2 + 4 \times 10^3 A(\kappa - \kappa_{\mathrm{b}})]^{1/2}\}, \tag{3.4}$$

where $A = D_{\mathrm{d}} F^2 Z_{\mathrm{c}}^2 / RTC_{\mathrm{d}}$. Using D_{d} observed by dynamic light scattering or calculated from the dendrimer radius, C_{c} can be estimated by (3.3) and (3.4) and Z_{nd} by (3.1) and hence the net charge density σ_{n} of the dendrimer ions is determined.

In this way the Z_{nd} and σ_{n} are obtained. Table 3.2 and Fig. 3.2 show the values for various salts of poly(amido amine) dendrimers of the 4^{th}, 7^{th}, and 10^{th} generations (G4, G7, and G10). As far as univalent counterions are concerned, σ_{n} is hardly counterion-dependent and is insensitive toward α_{d} when α_{d} is around 0.4. The bivalent sulfate ions interact more strongly with the dendrimer ions, so that they have a high degree of association, resulting in a *lower* σ_{n} than univalent ions.

Yamanaka et al. pointed out that, for colloidal particles and dendrimers, σ_{n} becomes larger with decreasing particle radius at a given σ_{a} [19] (See Chap. 4, Fig. 4.5). For a very small radius, $\sigma_{\mathrm{n}} = \sigma_{\mathrm{a}}$ holds, which corresponds to the complete dissociation assumed in the Debye-Hückel theory [2]. This tendency is clear in Table 3.2. As seen from the 9^{th} and 10^{th} rows, $\sigma_{\mathrm{n}}/\sigma_{\mathrm{a}}$ decreases with increasing radius. This is reasonable, since increase in radius results in a

Table 3.2. Charge number of a cationic dendrimer at a degree of neutralization of 0.6

	a (nm) [a]		Z_{nd} [d]		$\sigma_n(\mu C\ cm^{-2})$ [e]		$\sigma_a(\mu C\ cm^{-2})$ [f]	σ_n/σ_a	
	Water [b]	Acids [c]	Cl^-	SO_4^{2-}	Cl^-	SO_4^{2-}		Cl^-	SO_4^{2-}
G4	2.1	2.3	18	5	4.4	1.1	9.5	0.46	0.12
G7	4.3	4.5	44	11	2.7	0.6_6	19	0.14	0.04_4
G10	7.0	7.1	134	31	3.4	0.7_9	62	0.05_4	0.01_2

[a] radius, [b] $\alpha_d = 0$, [c] $\alpha_d = 1.0$, [d] net charge number, [e] net charge density, [f] analytical charge density.

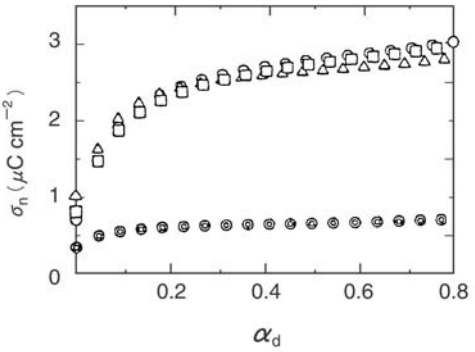

Fig. 3.2. The dependence of net charge density σ_n on the degree of neutralization α_d. Dendrimer weight fraction = 0.0012. Counterions: Cl^-(○), Br^-(□), IO_3^-(△), SO_4^{2-}(◎). Taken from [18] with the permission of the American Physical Society

larger charge number, therefore intensifying the interaction between particles and counterions, and causing stronger association of counterions (smaller σ_n).

The counterion association by macroions is outstanding in contrast with simple electrolyte systems. The electrostatic interaction is proportional to the squared charge number, so that the charge number of solute species is one of the most important parameters in determining properties of macroionic solutions. It is reminded that, not the analytical charge number Z_a (or analytical charge density σ_a), but the net charge number Z_n (net charge density σ_n) plays a decisive and direct role [3].

[3] The counterion association, and hence the net charge density, is discussed here in terms of transport number or electric conductivity. Although other quantities may be employed, the present approach would be more practical in light of its simplicity and the small number of assumptions involved.

3.1.2 Conformation and Extension of Flexible Ionic Polymers

So-called vinyl polymers have a main chain that contains C-C bonds, around which free rotations are possible. As a consequence, the polymer chains may assume various conformations in solution. Determination of their conformation has been one of the central topics in polymer science. When the polymers have ionic groups like PAA and PSS, the problem becomes highly complex because of the inter- and intra-macroion interactions. In the previous argument, the intermacroion interaction was assumed to be negligible "at infinite dilution" and only the intra-macroion contribution, particularly the interaction between ionized groups (the interaction 1 in Fig. 3.1), was taken into account. Because these groups are similarly charged, it was claimed that ionic polymer chains were more stretched out to a rod-like conformation than corresponding non-ionic counterparts. As will be described in Chap. 7, the intrinsic viscosity-molecular weight relationship was experimentally reported to be consistent with the rod-like model, so that this model gained popularity to some extent. However, there is another interaction which cannot be ignored, i.e., the interaction 2 in Fig. 3.1 between the ionized groups and nearby counterions. As Wall's experiments show, a large number of counterions are actually associated with the macroions. Thus it is not conceivable that the overall intra-macroion interaction is purely repulsive as inferred previously. In a polymer chain, monomer molecules are connected to each other by covalent bonds, so that the local monomer concentration in the macroion domains is extremely high, though its exact estimation is formidable. In the case of PAA, the distance between two neighboring COO^- groups is roughly of the order of 0.25 nm. In the case of 1-1 salt like NaCl, on the other hand, the Cl^--Cl^- distance is 0.62 nm at 10 mol L^{-1} if we assume an fcc-type distribution. Therefore the local concentration of the carboxylate groups would be in the order of $10 \times (0.62/0.25)^3 (= 152)$ mol L^{-1}. Though this is literally unrealistic, it can be understood that we are dealing with much higher ionic concentrations in ionic polymer solutions than the Debye-Hückel regime (lower than 10^{-3} mol L^{-1}).

In such concentrated solutions, simple ions are known to associate into ion pair, triple ions, quadrupoles and higher ionic aggregates [4,5]. Here we employ the term "aggregates" following Harned and Owen [4]. If a very small number of ionic aggregates is formed between the ionized groups and nearby counterions, they would act in a direction to make the polymer chains compact. Recent computer simulation work seems to substantiate this expectation [20].

Though the formation of such ionic aggregates in the macroion domain is yet to be experimentally confirmed, it is expected that the extension of macroion chains be determined by the balance of the widely accepted repulsive interaction between the ionized groups and of the ionic aggregate-mediated attraction between them. It would not be surprising that ionic polymer chains shrink up more strongly than corresponding non-ionic chains, if many ionic aggregates are formed to overwhelm the repulsion between the ionized groups.

The contribution of these two counteracting factors is not yet understood. However, if the degree of polymerization is not very low, the force to expand or contract polymer chains would be roughly isotropic. We infer that ionic polymer chains are not stretched out like rods but assume rather spherical geometry.

In the following, we avoid rod-model-dependent argument because we believe that the model is not justified, as will be considered in Chap. 7. We furthermore avert from discussion of the shape and extension of flexible ionic polymer chains, because experimental information has not been adequately accumulated. In the analysis of scattering data, we calculate the distance between neighboring macroions. By this distance we mean the spacing between the centers of gravity of spherical macroion domains. Though detailed discussion will be given in the following sections, experimental facts supporting ordered arrangement of macroions in solutions have commonly been found not only for flexible ionic polymers but also for globular proteins, ionic latex particles, ionic dendrimers, and spherical microgels. We believe that assuming spherical shapes for flexible polymers in solutions would not be highly unreasonable.

3.2 Scattering Study of Dilute Solutions of Ionic Polymers

The scattering technique using X-rays, light, and neutron beams is a powerful and standard method in the structural study of ionic polymer solutions. Historically famous are the X-ray scattering experiments by Bernal and Funkuchen [21] on gels and concentrated solutions of tobacco mosaic virus (TMV). They found clear Bragg diffraction peaks and concluded that TMV particles formed a more or less ordered distribution. The subsequent technical development made it possible to carry out the scattering measurements at lower angles and at low concentrations. By using the small-angle X-ray scattering (SAXS) method, a single broad peak has been found for solutions of a variety of synthetic ionic polymers and of ionic biopolymers. We take this peak as an indication of the ordered structures of these macroions in solutions.

In the 1940's, the intensity of light scattered from polymer solutions was reported to decrease drastically as the polymer was ionized. It was pointed out that the interaction between macroions led to some sort of "orderliness" [22]. The very low intensity from the two-component (salt-free) solutions and the difficulty of removing dust particles made it difficult to pursue further quantitative study of the problem. Furthermore, the long-range interaction under low salt conditions makes the theoretical interpretation of the scattered light intensity difficult. The static light scattering study of ionic polymer solutions is thus limited to three-component systems containing solvent, polymer, and a large amount of salt ($> 10^{-3}$ mol L^{-1}). Under such conditions, ionic polymer

solutions behave apparently like non-ionic polymer solutions because the electrostatic interaction is shielded, so that ionic characters cannot be a topical feature. The dynamic light scattering (DLS) technique later introduced [23,24] has been found to be quite versatile and provided reliable information of the ionic polymer solutions, particularly of their structure formation.

The small-angle neutron-scattering (SANS) technique was applied by many investigators for two- and three-component ionic polymer solutions since the latter half of the 70's. A single broad peak was found and first attributed to the ordering of macroions [25]. Later, an isotropic model was proposed to interpret the scattering peak.

3.2.1 Static Light Scattering

Theoretical Background

The detailed theoretical analysis of static light scattering (SLS) from polymer solutions is given by various authors such as Flory [26]. In this section, we briefly consider some features relevant to ionic polymer solutions. When the excess scattered intensity is denoted by $I_s(0)$ at a scattering angle $\theta = 0$ and at a distance r from the scatterer, $I(0)$ is defined by

$$I(0) = \frac{r^2 I_s(0)}{I_0}, \tag{3.5}$$

where I_0 is the incident light intensity. Considering the polarizability change and the dielectric constant change due to concentration fluctuation and the relationship between the free energy of the system with the osmotic pressure P, we have at $\theta = 0$

$$\frac{K'c}{I(0)} = \left(\frac{1}{RT}\right)\left(\frac{\partial P}{\partial c}\right), \tag{3.6}$$

where

$$K' = \frac{2\pi^2 n_0^2}{\lambda_0^4 N_A}\left(\frac{dn}{dc}\right)^2. \tag{3.7}$$

n_0 and n are the refractive indices of solvent and solution, respectively, and λ_0 is the wavelength of incident light in vacuum, c the solute concentration in g L^{-1}, and N_A the Avogadro constant.

It is assumed that, when the scatterer volume V_s is divided into small volume elements ΔV, (1) ΔV is small enough in comparison with the wavelength of the light so that the phase differences between the light rays from different places of the element can be ignored and (2) ΔV is large enough to make concentration fluctuations in nearby volume elements independent. When the scattering volume is divided into slices of thickness d, the first condition is satisfied if $2d \sin(\theta/2)/\lambda \ll 1$. Furthermore, when the range of intermolecular forces r is much smaller than d, the second condition is fulfilled. Thus, the above argument holds when $r \ll d \ll \lambda/2 \sin(\theta/2)$.

At $\theta \neq 0$ and $c \neq 0$, the intra- and inter-particle interference reduces the scattered intensity by $1/p\,(\theta, c)$ and we have

$$\frac{K'c}{I(\theta)} = \left(\frac{1}{RT}\right)\left(\frac{1}{p\,(\theta, c)}\right)\left(\frac{\partial P}{\partial c}\right). \tag{3.8}$$

At $c = 0$,

$$p\,(\theta, c) = p\,(\theta) = \frac{I\,(\theta)}{I\,(0)} \leq 1. \tag{3.9}$$

The $p(\theta)$ of homogeneous spheres is given by the form factor $f_M(\theta)$ and the structure factor $F(\theta)$ as follows

$$p(\theta) = f_M(\theta)F(\theta). \tag{3.10}$$

By virial expansion of the osmotic pressure, we have

$$\frac{K'c}{I(\theta)} = \left(\frac{1}{f_M\,(\theta)}\right)\left(\frac{1}{M_{\mathrm{W}}} + 2A_2c + \cdots\right), \tag{3.11}$$

where A_2 is the second virial coefficient.

The above discussion is for two-component systems, which are composed of a single solvent and a polyelectrolyte. Since the macroions and counterions can be scatterers and fluctuations of these species are not strongly correlated, (in other words, the fluctuation does not strictly satisfy the electric neutrality condition,) however, (3.5) through (3.11) cannot be applied to such systems. The interionic forces are of a long-range interaction, so that, without addition of salt, $r \ll \lambda/2\sin(\theta/2)$ is not satisfied and the fluctuation theory itself cannot be used, except at $\theta = 0$. The neutrality condition is believed to be valid in volume elements of a dimension of κ^{-1} (the Debye length). Then $\lambda\kappa \gg 2\sin(\theta/2)$, or $\kappa^{-1} \ll K^{-1}$, where K is the scattering vector. In the case of 1-1 type salts, this condition is judged to be satisfied above 10^{-3} mol L^{-1} [27]. In such three-component systems, the excess light scattering of a polyelectrolyte solution over the scattering of a salt solution, which is in a Donnan equilibrium with the polyelectrolyte solution, is given by concentration fluctuations of macroions and their surrounding ionic atmosphere [28]. Then we have

$$\frac{K^*c}{I(0)} = \left(\frac{1}{RT}\right)\left(\frac{\partial P}{\partial c}\right)_{\mu_{\mathrm{s}}}, \tag{3.12}$$

where the subscript μ_{s} implies that the chemical potentials of all solutes are constant except that used in differentiation, and K^* is expressed by

$$K^* = \frac{2\pi^2 n_0^2}{\lambda_0^4 N_{\mathrm{A}}}\left[\sum\left(\frac{\partial n}{\partial c_i}\right)_{P_i c_j}\left(\frac{\partial c_i}{\partial c}\right)_{\mu_{\mathrm{s}}}\right]^2, \tag{3.13}$$

with the subscript i implying solvent (0), macroion (1), and added salt (2). The term in [ ] on the right-hand side of (3.13) may be taken to be approximately equal to $(dn/dc)_{\mu_{\mathrm{s}}}$ [29]. Thus we have

$$K^* = \frac{2\pi^2 n^2}{\lambda_0^4 N_\mathrm{A}} \left(\frac{dn}{dc}\right)^2_{\mu_\mathrm{s}}. \tag{3.14}$$

This relation, which holds not at a constant concentration but at a constant chemical potential, is formally equivalent to (3.7) for the two-component systems. By virial expansion, we have

$$\frac{K^* c}{I(0)} = \frac{1}{M_\mathrm{W}} + 2A_2^* c + \cdots \tag{3.15}$$

When $C_\mathrm{s} > 10^{-3}$ mol L^{-1} and $c = 0$, $p(\theta)$ is equal to $f_M(\theta)$. At small K's, $f_M(\theta)$ is related to the z-average of the square of radius of gyration of scatterers $\langle R_\mathrm{g}^2 \rangle_\mathrm{z}$ by

$$f_M(\theta)^{-1} = 1 + \frac{\langle R_\mathrm{g}^2 \rangle_\mathrm{z} K^2}{3} + \cdots. \tag{3.16}$$

For binary polyelectrolyte-solvent systems ($C_\mathrm{s} = 0$), the above treatment is not valid. Even at $\theta = 0$, we have to be satisfied with qualitative argument. For example, the osmotic pressure of solution P is given by (3.17) using the osmotic pressure in the ideal state P_id and the osmotic coefficient g

$$P = gP_\mathrm{id} = \frac{gRTc\,(1 + \alpha_\mathrm{d} m)}{M}. \tag{3.17}$$

By combining (3.12) and (3.17), we have

$$\frac{K^* c}{I(0)} = \frac{(1 + \alpha_\mathrm{d} m)g}{mM_\mathrm{m}} + \frac{c}{M_\mathrm{m}} \left(\frac{dg}{dc}\right) \tag{3.18}$$

where M_m is the molecular weight of the monomer and $M = mM_\mathrm{m}$. When dg/dc is small and $\alpha_\mathrm{d}\, m \gg 1$, we have $K^* c/I(0) = \alpha_\mathrm{d} g/M_m$. This implies that the light scattering experiments of the binary polyelectrolyte solutions provide M_m, not M. For non-ionic polymer solutions, this is not the case. Equation (3.18) also implies that the scattered intensity is lowered with increasing α_d, or charge number. The scattered intensity of ionic polymers is lower than that of corresponding non-ionic polymers.

At $\theta \neq 0$, the scattered intensity for $C_\mathrm{s} = 0$ and its concentration dependence are difficult to discuss, but its angular dependence, namely $p(\theta, c) = I(\theta, c)/I(0, c)$, contains valuable information, since it is related to the form factor $f_M(\theta)$ and structure factor $F(\theta)$ by (3.10). From the latter, the radial distribution function $g(r)$ can be derived by the following equation

$$F(\theta) = 1 + 4\pi\rho \int_0^\infty [g(r) - 1][\frac{\sin(Kr)}{Kr}]r^2 dr, \tag{3.19}$$

where ρ is the number density of solutes.

When C_s is large, the light scattering behavior of flexible ionic polymers becomes formally the same as that of non-ionic polymers. By adopting the Zimm plot, the molecular weight, the second virial coefficient, and the radius of gyration can be determined.

Light Scattering of Salt-Free Systems

In the low C_s region, various unique properties are found for ionic polymers. However, since a rigorous theoretical background has not yet been established [30], we limit this section to experimental facts and their qualitative interpretation. By "salt-free" we mean that salts are not added. In water as a solvent, its dissociation produces 10^{-7} mol L^{-1} of H^+ and OH^-, which cannot be removed from the systems.

It is possible now to carry out light scattering experiments at polymer concentrations as low as 10^{-4} g L^{-1}. In Fig. 3.3 is shown the excess scattered intensity of aqueous solutions of sodium poly(styrene sulfonate)s (NaPSS) at such low concentrations, where the intensity no longer depends on the scattering vector K [31]. Under this condition, the intensity is determined solely by the form factor $f_M(K)$. The observed values are compared with theoretical intensities for rigid rods ($f_M(K) \propto K^{-1}$) and for Gaussian chains ($f_M(K) \propto K^{-2}$). A discrepancy is clear from the rod model. Krause et al. concluded that PSS ions are random-coils, not rigid rods [4].

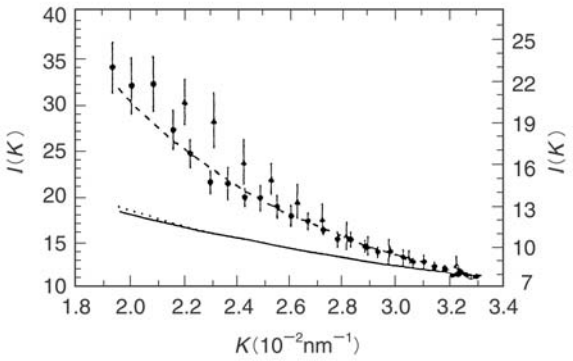

Fig. 3.3. Angular dependence of the excess scattered intensity of dilute solutions of NaPSS. •: $M_{W1} = 3.5 \times 10^5$, $c = 2.7 \times 10^{-4}$ g L^{-1}, ▲: $M_{W2} = 1.06 \times 10^6$, $c = 3.46 \times 10^{-4}$ g L^{-1}. The left coordinate is for M_{W1} while the right one is for M_{W2}. The real and dotted curves are the form factors of 429.6 and 128.6 nm long rods, respectively. The dashed one is for a random coil. Taken from [31] with the permission of Elsevier Science

When the polymer concentration is higher than 10^{-3} g L^{-1}, a single broad peak is observed in the scattered intensity $I(K)$ vs scattering vector K curve. Figure 3.4 is an example for NaPSS [32].

[4] Recently, Amis et al. reported by SANS experiments that the radius of gyration of PSS ions is in between random coils and rods. For details see Sect. 3.3

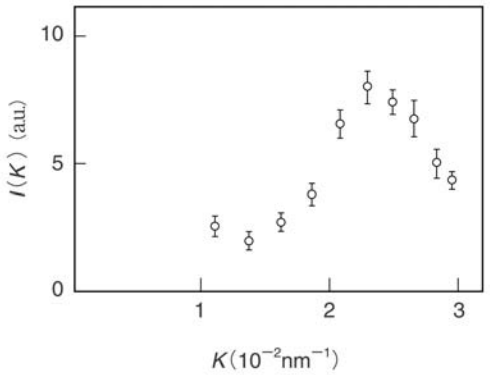

Fig. 3.4. Angular dependence of the scattered intensity of a NaPSS solution. $M_W = 7.8 \times 10^5$, $M_W/M_N < 1.1$, $c = 2.5 \times 10^{-2}$ g L^{-1}. Taken from [32] with the permission of the American Chemical Society

Before discussing the interpretation of the single broad peak, we note that a similar peak has also been found for semi-flexible ionic polysaccharides and for rod-like TMV. Furthermore, the peak has likewise been found in the SAXS curves and SANS curves of a variety of synthetic ionic polymers, globular proteins, nucleic acids, spherical polyelectrolyte gels, and ionic dendrimers. Thus it is reasonable to conclude that the peak has nothing to do with the shape of ionic polymers.

In the early 80's, it was proposed that the scattering peak of flexible ionic polymers could be accounted for in terms of an "isotropic model" [33–35]. According to this interpretation, the ionic polymers are stretched out as the result of the repulsion between ionized groups inside a macroion domain and distributed almost homogeneously in the solution to form "holes" around polymer chains by mutual repulsion. Based on this model it was argued that the $I(K)$ has a maximum because $F(K)$ is a monotonously increasing function with K and $f_M(K)$ is a decreasing function. Krause et al. estimated $F(K)$ by combining the observed $I(K)$ for NaPSS solutions with the theoretical values of $f_M(K)$ for rigid rod and Gaussian chain and found that $F(K)$ itself has a peak. This is not in accord with the isotropic model. Furthermore, since fully stretched polymer chains underlie this model, it cannot explain the presence of the scattering peak observed also for spherical polyelectrolytes, dendrimers, and globular proteins.

On the other hand, it was independently claimed that the scattering peak was due to more or less regular distribution (or structure formation) of macroions in solutions. The single broad peak was observed not only in the static light scattering experiments, but also in the SAXS and SANS experiments. Further, the peak was found for ionic colloidal particles as well as for flexible ionic polymers. It is tempting to suggest that the peak is a uni-

versal phenomenon for charged particles or solutes in general. In this regard, colloidal systems are advantageous in that the particles can be seen by using visible light and the structure formation can be directly confirmed. We will discuss the colloidal systems in detail in Chap. 4.

Figure 3.5 gives the angular dependence of the inverse excess scattered intensity for NaPSS salt-free solutions [36]. The $I(0)/I(\theta)$ changes linearly with $\sin^2(\theta/2)$ with a positive slope at higher concentrations and with a negative slope at lower concentrations. Sedlák and Amis claim that the positive slope is related to the size $R_{\mathrm{G,app}}$ of loose aggregates of polymer chains (or multi-chain domain according to their terminology) [37, 38]. Though detailed discussion will be given in Sect. 3.2.2, at least two diffusion modes (with diffusion coefficients D_{f} and D_{s}) are found by dynamic light scattering (DLS) for various ionic polymers under low salt conditions [39–41]. Sedlák and Amis estimated apparent diffusion coefficient D_{app} from K dependence, where the sizes of the multi-chain domains $R_{\mathrm{G,app}}$ were determined by using Burchard's relation as will be mentioned later. Their results are shown in Table 3.3. The $R_{\mathrm{G,app}}$ values obtained from the static and dynamic light scattering techniques appear to agree with each other and are not highly sensitive toward the molecular weight.

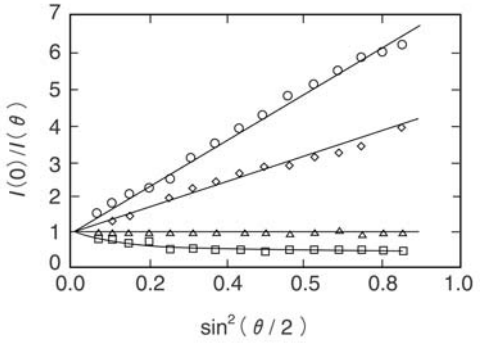

Fig. 3.5. Angular dependence of the reciprocal excess scattered intensity of NaPSS salt-free solutions. $C_s = 0$ mol L^{-1}, $M_{\mathrm{W}} = 1.2 \times 10^6$. c (g L^{-1}) = 45.6 (○), 11.6 (◊), 0.4 (△), 0.01 (□). Taken from [36] with the permission of the American Institute of Physics

We believe that the formation of loose aggregates of macroions, or the localized ordered structure, is due to electrostatic interaction between macroions. When the charge number of the macroions is lowered, the single broad peak in the scattering curve disappears [37]. When the concentration of added salt is raised, the peak disappears, suggesting the melting of the structure. The contribution of hydrophobic interaction to the structure formation is ruled

out [42]. We will come back to the structure formation in the discussion of colloidal dispersions (Chap. 4).

The concentration dependence of the scattered intensity for NaPSS solutions is shown in Fig. 3.6. The concentration dependences of the total scattered intensity $I_t(0)$, the excess intensity $I(0)$, and the reduced scattered intensity $I(0)/c$ change at $c = 0.5$ g L^{-1}. Similar changes are noticed in the molecular weight range between 5,000 and 1.2×10^6. It is not clear now, however, whether this can also be observed for other polyelectrolytes and why it happens.

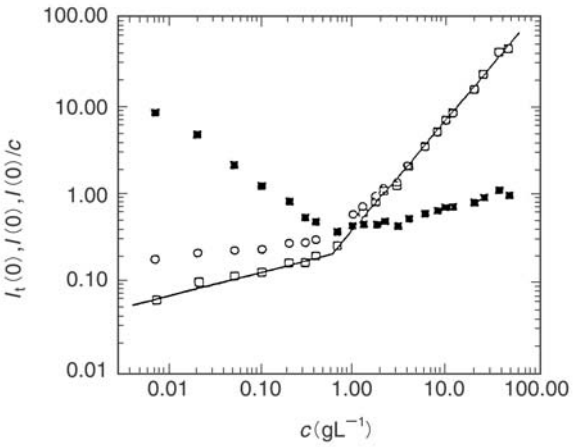

Fig. 3.6. Concentration dependence of the scattered intensity for NaPSS salt-free solutions. Total intensity $I_t(0)$ (○), excess scattered intensity $I(0)$ (□), reduced scattered intensity $I(0)/c$ (■). $M_W = 1.2\times10^6$. The intensity is normalized by a benzene standard. Taken from [36] with the permission of the American Institute of Physics

The $I(0)$ and the ratio of the scattering amplitudes of the slow and fast processes A_s/A_f are given as a function of the molecular weight in Fig. 3.7. The insensitivity of $I(0)$ toward M_W is related to the fact that the molecular weight cannot be determined for salt-free ionic polymer solutions by static light scattering (See (3.17)). Sedlák notes the correlation between $I(0)$ and A_s/A_f [30].

Light Scattering of Salt-Containing Systems

When salt concentration C_s is increased, the scattering peak tends to disappear. The position and height of the peak vary with (1) the size of the localized ordered structure, (2) the distortion of the structure, and (3) the thermal motion of macroions at lattice points (Debye-Waller effect). The salt concentration dependence of the scattering peak depends on how these factors are affected by salt addition. For flexible ionic polymers, the change of the

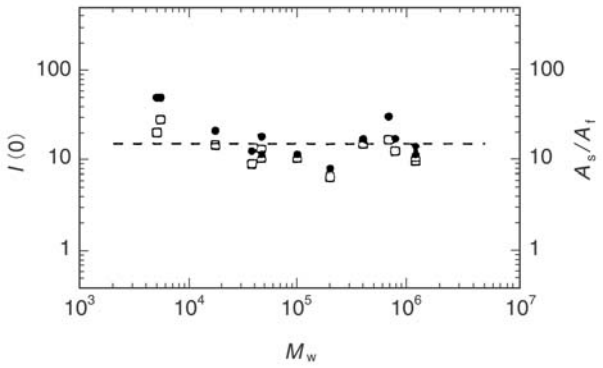

Fig. 3.7. Molecular weight dependence of the excess scattered intensity and the slow- and fast-mode scattered intensity amplitude ratio for a NaPSS solution. $I(0)$: □, A_s/A_f: ●. $c = 45.6$ g L^{-1}. Taken from [30] with the permission of Clarendon Press

polymer chain extension by addition of salts seems to make our understanding difficult. On the other hand, for rigid particles such as TMV, the peak position shifts toward higher K with increasing C_s, as was predicted by the theories by DLVO and Sogami (See Chap. 2, Fig. 2.9 and Chap. 6, Fig. 6.3).

When C_s is decreased at $c = 10^2 \sim 10^{-2}$ g L^{-1}, the so-called ordinary-extraordinary phase transition is observed. (See Sect. 3.2.2) As seen from Fig. 3.8, the slope of the angular dependence of the scattered intensity becomes less steep with increasing C_s, indicating that the localized ordered structures become smaller according to (3.16). Correspondingly the amplitude of the slow mode in DLS decreases. We will discuss this problem later.

The aqueous solutions of much higher C_s's become a poor solvent for ionic polymers. For example, a NaCl solution of 4.17 mol L^{-1} is apparently a θ solvent for NaPSS at 25°C [5]. As mentioned above, ionic polymers under such high salt concentrations formally behave like non-ionic polymers, but we will not go into detail here.

3.2.2 Dynamic Light Scattering

In SLS we considered the time average of the scattered intensity. In the dynamic light scattering, DLS, by which the information of the motion of solute particles, or diffusion coefficients, is obtained, we consider the time fluctuation of the scattered intensity. In the following we discuss some points directly relevant to our consideration of ionic polymers, though the readers are referred to other textbooks of the topic for detail [23, 24, 44, 45].

[5] In θ solvents, the second virial coefficient ((3.15)) is zero and the intermolecular interaction disappears. See a textbook of polymer chemistry such as [26].

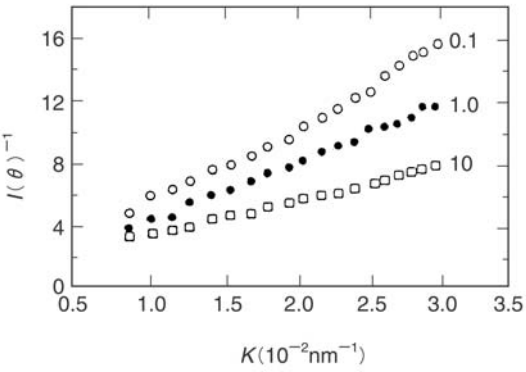

Fig. 3.8. Angular dependence of the inverse total scattered intensity from polynucleosome solutions. C_s = 10 m mol L^{-1}(□), 1.0 (•), 0.1 (○). Taken from [43] with the permission of the American Institute of Physics

When a scattering volume containing N macromolecules is irradiated with light at a frequency of ω_0 , the scattered electric field $E_s(K,t)$ is given at time t by

$$E_s(K,t) = \sum_{j=1}^{N} A_j(t) \exp\{i[\omega_0 t - K \cdot r_j(t)]\}, \tag{3.20}$$

where $r_j(t)$ is the position of particle j and $A_j(t)$ is the scattering amplitude. The average intensity of the scattered light $\bar{I}$ is given by $\bar{I} = \overline{|E_s|}^2$. The field correlation function $g^{(1)}(K,\tau)$ is given by

$$g^{(1)}(K,\tau) = \frac{\overline{E_s^*(t)E_s(t+\tau)}}{\bar{I}}, \tag{3.21}$$

According to Pusey and Tough [24], the initial decay rate of $g^{(1)}(K,\tau)$ is

$$\frac{dg^1(K,\tau)}{dt} = -D_{\mathrm{eff}}K^2 \tag{3.22}$$

with $D_{\mathrm{eff}} = D_0/F(K)$, where D_0 is the diffusion coefficient in non-interacting systems.

Ordinary-Extraordinary (O-E) Phase Transition

Lee and Schurr found by DLS that, when C_s was decreased, the diffusion coefficient of poly-L-lysine (PLL) sharply dropped at a critical concentration [46]. By subsequent intensive study, two relaxation modes with diffusion coefficients

D_f and D_s were found under low salt conditions from macroscopically homogeneous solutions [39]. In the case of a PLL of a degree of polymerization of 2500 (abbreviated PLL_{2500}), D_f was about 10^{-6} cm^2 s^{-1} at $C_s = 10^{-3}$ mol L^{-1} (KCl) and was interpreted as the diffusion coefficient of macroions coupled to counterions and coions with larger diffusion coefficient. For example, Na^+ has a diffusion coefficient of 2×10^{-5} cm^2 s^{-1}. The coupling causes the above reported D_f value, which is larger than the diffusion constant of poly(methyl methacrylate) in acetone, about 10^{-7} cm^2 s^{-1}. On the other hand, the D_s value was 4×10^{-8} cm^2 s^{-1}. The difference between D_f and D_s is very clear. The observed diffusion coefficient of various polyelectrolytes as a function of C_s is shown in Fig. 3.9. The O-E transition is seen to take place both for anionic and cationic polymers. The two relaxation modes were observed not only for synthetic ionic polymers but also for biopolymers such as t-RNA, DNA and bovine serum albumin (BSA). It seems that the two modes are characteristics of ionic polymers in general.

The O-E transition is reversible. It is reported that the drop of the diffusion coefficient at the transition is accompanied with a clear decrease in the scattered intensity. The change in other physical quantities, if any, is not outstanding.

Drifford and Dalbiez found the following relationship for the polymer concentration C_m^{OE} (in monomer unit) and the salt concentration C_s at the transition point [40],

$$\rho = \frac{C_m^{OE}\langle b\rangle}{2C_sQ}, \tag{3.23}$$

where Q is the Bjerrum length [6] and $\langle b\rangle$ is the distance between ionizable groups. The transition takes place at $\rho = 1$. The ordinary and extraordinary phases are observed for $\rho < 1$ and $\rho > 1$, respectively. This relationship was observed for PSS-salt solutions and found to be approximately valid for other flexible polymers. However, the transition for NaDNA and CaDNA was found at much lower DNA concentrations than (3.23) [49].

The coil-to-rod transition of flexible ionic polymers was first suspected to be responsible for the O-E transition. The diffusion coefficient expected for a cylinder (300×1.2 nm), a fully extended conformation of PLL_{955}, was 9×10^{-8} cm^2 s^{-1}, being much larger than the smallest experimental value of 4×10^{-9} cm^2 s^{-1}. Furthermore the slow mode was also found for non-flexible, globular BSA. Thus the conformation factor was excluded. The currently accepted idea is structure formation of macroions. The terminology varies from

[6] The Bjerrum length is defined by $Q = e^2/2\varepsilon k_BT$ for 1-1 type salts, where e is the elementary charge, ε the dielectric constant, and k_BT the kinetic energy. In order to modify the Debye-Hückel theory of strong electrolytes, Bjerrum assumed incomplete dissociation and regarded a pair of cation and anion within the distance Q as an ion-pair (Kgl.DanskeVid.Seisk.Math-fys. Medd., (1926) 7:No.9). At this distance, the electrostatic energy $e\psi$ is equal to the kinetic energy k_BT. The Debye approximation ($e\psi/k_BT \ll 1$) is no longer valid within Q.

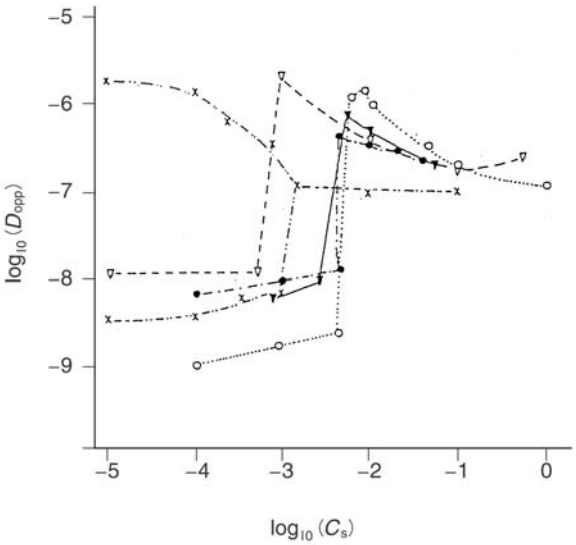

Fig. 3.9. Salt concentration dependence of diffusion coefficient of various ionic polymers in aqueous solutions. ×: Poly (2-vinyl pyridine) quaternized with benzyl bromide [41], ○: NaPSS [40], ▼: PLL_{955} [46], 3 g L^{-1}, ●: PLL_{946} [47], 2∼3 g L^{-1}, ▽: PLL_{3800} [48], 1 g L^{-1}. Taken from [45] with the permission of VCH Publishers, New York

author to author. We proposed the term "localized ordered structure" [50], Schmitz used "temporal aggregates" [45], and Sedlák and Amis "multi-chain domain" [38]. It is essentially a loose aggregate of a number of macroions. The mobility of macroions is considered to be lowered by being confined into the structures than in the free state. In other words, in the macroscopically homogeneous solutions, free macroions coexist with the structures, which we call a two-state structure [50], so that at least two diffusion modes are observable.

The above discussion would not be conclusive. However, in the case of colloidal dispersions, we can "see" directly such two-state structures. We will consider the colloidal systems in Chap. 4.

Various interpretations have been proposed for the structure formation. We claim that counterions in between macroions generate an attraction between similarly charged macroions. It is called the *counterion-mediated attraction*. This is a result of counterions simultaneously shared by a number of macroions. In other words, the pure repulsion between macroions is overwhelmed by the attraction between counterions and macroions. The mechanism is essentially the same as that in the case of formations of triple ions, quadrupole, and higher aggregates in simple salt solutions [4, 5]. Schmitz claims that an intermacroion attraction is generated by fluctuation of counterions [45]. According to Förster et al. [41], "temporal domain" is formed by

entanglement of polymer chains. This possibility cannot be ruled out since they used a concentration as high as 100 g L^{-1}, but it is not generally cogent since the extraordinary phase is also observed for samples, whose degree of polymerization is so low that entanglement is statistically infeasible.

Apart from their interpretation, the salt concentration dependence of the diffusion coefficient of quaternized poly (2-vinyl pyridine) in aqueous solutions is interesting. In Fig. 3.10 the D_f and D_s are plotted against c/C_s. At low c/C_s's only one diffusion coefficient is observed (the ordinary phase). When the concentration ratio is unity, two diffusion modes (D_f and D_s) are observed (the extraordinary phase). The D_f is almost constant in a high c/C_s region. This trend is observed also for other ionic polymers.

The polymer concentration dependence of D_s follows the power relation $D_s \sim c^{-0.1\sim-1}$. Förster et al. believed that the reptation model [51] was not valid since it should provide $D_s \sim c^{-3}$. They pointed out further that the $\langle R_g^2 \rangle$ values determined from the $I(0)/I(\theta) - K^2$ plots for a sample of a small molecular weight were much larger than the expected value for an extended conformation and concluded that $\langle R_g^2 \rangle$ was not a measure of a single chain, but corresponded to the size of loose aggregates of macroions, whose mobility was given by D_s.

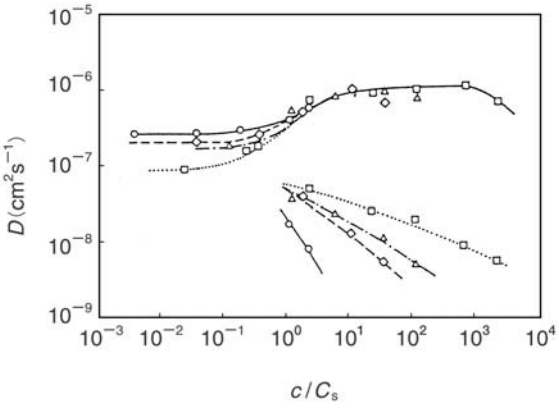

Fig. 3.10. Diffusion coefficient of poly(2-vinylpyridine) quaternized with benzyl bromide in salt-containing aqueous solutions. $M_W = 2 \times 10^5$, $M_W/M_N = 1.10$, degree of quaternization = 98 mol%, contour length of the polymer chain = 180 nm, $\langle b \rangle = 0.26$ nm, $C_s = 0$ (□), 0.001 (△), 0.01(◇), 0.1 (○). Taken from [41] with the permission of Elsevier Science

Using PSS samples with various molecular weights ($5 \times 10^3 \sim 1.2 \times 10^6$) Sedlák and Amis carried out SLS and DLS experiments in a wide range of polymer concentration ($0.01 \sim 45.6$ g L^{-1}) [36,38]. They studied the molecular weight dependence of the two diffusion coefficients (D_f and D_s). The relax-

ation rate Γ_f was found to satisfy the relationship $\Gamma_f = K^2 D_f$ and, as shown in Fig. 3.11, D_f stayed almost constant in the wide range of M_W . Since the polymer chains of the sample having the smallest M_W would not be involved in entanglement even at 45.6 g L^{-1}, its D_f is expected to correspond to a single chain motion. On the other hand, they claimed that, for high-molecular-weight samples, D_f corresponded to counterion-coupled motion of segments of chains in an entangled network. As for the slow process, D_s increased linearly with K^2, when calculated on the assumption of $\Gamma_s = K^2 D_s$ with Γ_s being the relaxation rate of the slow process. D_s decreased with increasing M_W.

As mentioned already, Sedlák and Amis attributed the slow mode to the motion of the loose aggregates of macroions and estimated their sizes $R_{G,app}$ by Burchard's relation [52], which reads

$$D_{app} = D_0(1 + C^* R_{G,app} K^2), \tag{3.24}$$

where D_{app} is the apparent diffusion coefficient of the aggregates, D_0 the diffusion coefficient at $K \to 0$, and C^* a constant depending on the scatterer's structure. In Table 3.3 are given the results obtained for two extreme cases, namely polydisperse chains with a most probable length distribution ($C^* = 0.200$) and monodisperse infinite arm star molecules ($C^* = 0.098$). For comparison, $R_{G,app}$ obtained using (3.16) by SLS is given. It is seen that the two $R_{G,app}$ values from SLS and DLS are in good agreement. However, these should be taken as approximate values because (3.16) is valid in the non-interacting systems.

Table 3.3. Apparent size of localized ordered structure for different molecular weight poly(styrene sulfonate)s at $c = 45$ g L^{-1}

$M_W \times 10^3$	$R_{G,app}$ (nm) from SLS	$R_{G,app}$ (nm) from DLS	
		$C^* = 0.200$	$C^* = 0.098$
5	62	35	57
8	57	39	65
38.2	56	37	61
100	85	40	67
400	70	46	77
780	91	54	90
1200	135	65	109

The sample with the lowest M_W has a contour length of about 6 nm, being much smaller than its $R_{G,app}$ (about 50 nm). This supports Sedlák-Amis' interpretation that $R_{G,app}$ corresponds to the size of multi-chain domains. The fact, that D_s is M_W-dependent while $R_{G,app}$ is not, seems to suggest that the slow diffusive mode is not Brownian motion of aggregates, in which polymer chains are tightly held.

The concentration dependence of the diffusion coefficients is shown in Figs. 3.12 $\sim$ 3.14. Only D_s is shown for the sample of the lowest molecular weight, because D_f cannot be accurately determined. The two coefficients agree with each other at $c = 0.01$ g L^{-1} and D_s decreases with increasing c, while D_f increases and levels off in the range between 0.5 and 45 g L^{-1}. Sedlák and Amis attributed D_f to the counterion-coupled motion of segments of entangled polymer chains at high concentrations. They also pointed out disagreement of the D_f results with the isotropic model by Odijk [53], which predicted a scaling relation $D \sim c^{1/2}$.

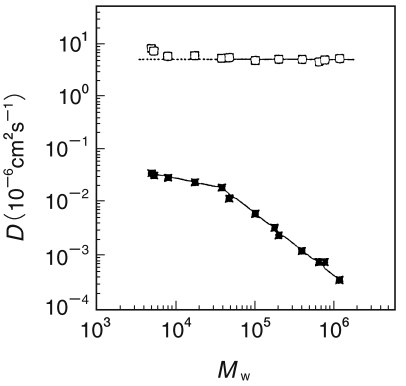

Fig. 3.11. Molecular weight dependence of diffusion coefficients. D_f (□), D_s (■), $c = 45.6$ g L^{-1}, $\theta = 90°$. Taken from [54] with the permission of the American Chemical Society

The so-called overlap concentration c^* is not a well-defined quantity for polyelectrolytes. The reason is that we need to know the radius of gyration of polymer chain $\langle R_g^2 \rangle^{1/2}$ in order to calculate c^* by

$$c^* = \frac{M_W}{\frac{4}{3}\pi N_A \langle R_g^2 \rangle^{3/2}}. \tag{3.25}$$

However, it is difficult to evaluate $\langle R_g^2 \rangle^{1/2}$ in salt-free solutions since (3.16) is valid only when $C_s > 10^{-3}$ mol L^{-1} and since the formation of non-space-filling ordered structure under low salt conditions affects the scattered intensity. Furthermore, since we cannot be sure about the conformation of ionic flexible polymers in solutions, discussion in terms of c^* does not seem worthy. The phase diagram of polyelectrolyte solutions has been constructed on the basis of c^* using a rod-like model for macroions [45]. Its physical significance is thus questionable.

According to Sedlák and Amis, for $c > 10$ g L^{-1}, the decreasing tendency of D_s with increasing concentration can be empirically represented by

$$\ln D_s = -0.0061 M_W^{0.35} \ln c. \tag{3.26}$$

If the isotropic model [33,53] is correct, D_s is independent of M_W. This is not experimentally the case. In this regard, we note that the small-angle X-ray scattering profiles to be discussed in Sect. 3.2.3 show a M_W dependence for NaPSS. At a high M_W (Fig. 3.14), discontinuous changes of D_s are seen at $c = 0.5$ and 10 g L^{-1}. The change at 0.5 g L^{-1} corresponds to the scattered intensity changes shown in Figs. 3.5 and 3.6. Above this concentration the $I(0)/I(\theta) - \sin^2(\theta/2)$ plots show positive slopes, from which the size of the localized ordered structure $R_{G,app}$ can be discussed. This is the two-state structure region, where a single broad scattering peak was observed by SAXS study of NaPSS solutions.

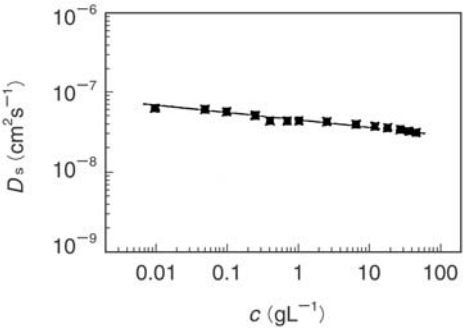

Fig. 3.12. Polymer concentration dependence of D_s. Sample: NaPSS, $M_W = 5\times10^3$, $\theta = 90°$. Taken from [54] with the permission of the American Chemical Society

3.2.3 Small-Angle X-ray Scattering

The structural study of solutions by Thomson scattering of X-ray can be carried out regardless of the salt concentration and is advantageous over light scattering as far as the difference in the electron densities of solute and solvent is large enough. Turbid systems, which cannot be investigated by light scattering, can be studied by X-ray because of its high transmission. The short wavelength of X-ray has restricted in use to smaller objects than by light scattering but this problem was recently solved by development of the ultra-small-angle X-ray scattering (USAXS) technique.

In the present section, we discuss the SAXS study of the structure formation in ionic polymer solutions. The first study in this field was performed by Bernal and Funkuchen on concentrated solutions and gels of tobacco mosaic virus (TMV) [21]. Because of its historical importance, we briefly discuss

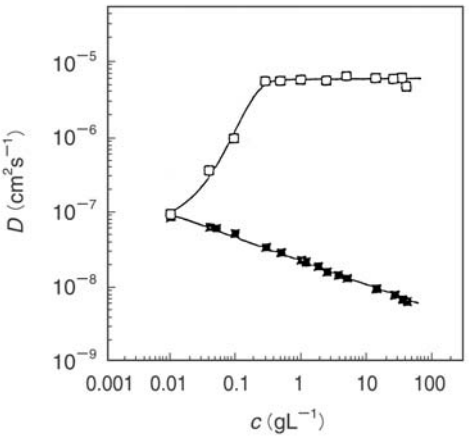

Fig. 3.13. Polymer concentration dependence of D_f and D_s. Sample: NaPSS, $M_W = 10^5$, $\theta = 90°$. D_s (■), D_f (□). Taken from [54] with the permission of the American Chemical Society

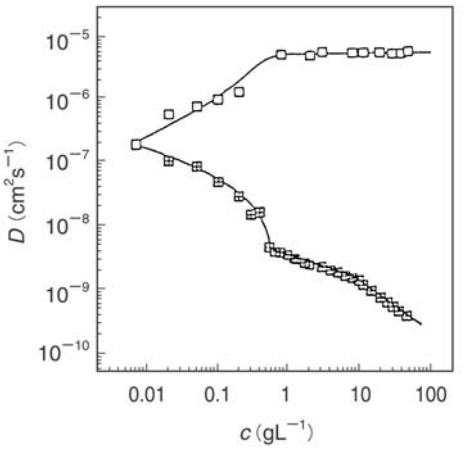

Fig. 3.14. Polymer concentration dependence of D_f and D_s. Sample: NaPSS, $M_W = 1.2\times10^6$, $\theta = 90°$, D_s (■), D_f (⊞). Taken from [54] with the permission of the American Chemical Society

their results here though TMV is not a flexible polymer. Figure 3.15 shows the scattering profile, from which the ordered distribution of the TMV particles shown in Fig. 3.16 was concluded. Bernal and Funkuchen state that the interparticle distance R (Å) is given by $R = 1650/N^{1/2}$, where $N(g)$ is dry weight in 100 cm^3, and that "the immediate consequence of the existence of this relation is that the particles distribute themselves in a hexagonal array so as to fill the available space as uniformly as possible". This is what we call the one-state structure. The existence of such a structure is acceptable at the high concentrations they used. Interestingly they discussed "positive tactoids", in which TMV rods are ordered in parallel as shown in Fig. 3.17 (a). At the same time they noticed "negative tactoids", around which the rods distributed in a more or less regular manner as shown in Fig. 3.17 (b) [7]. They stated that "such equidistance and parallelism can only be maintained by definite forces acting between the particles", and that, at higher concentrations, "these forces have a net repulsive character, but (at lower concentration) attractive forces must balance them". Furthermore, they pointed out that London-van der Waals forces were ineffective at such distances. It is highly interesting that essentially the same conclusion as that reached by Bernal and Funkuchen is derived from a recent study of dilute solutions.

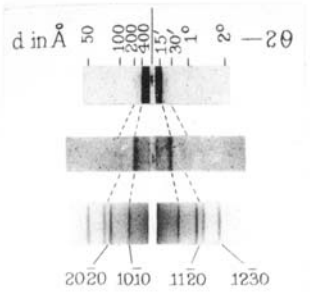

Fig. 3.15. X-ray scattering profiles of 13% TMV solution (uppermost), wet gel (middle), and dry gel (lowest). Taken from [21] with the permission of Rockefeller University Press

Following the Bernal-Funkuchen investigation, concentrated solutions of bovine serum albumin (BSA), hemoglobin, and other proteins and nucleic

[7] It was claimed that less concentrated TMV solutions coexist with concentrated solutions in the negative tactoid systems. However, the concentration inside the negative tactoids was not determined. The case in which the inside concentration is zero corresponds to void in our terminology. This possibility was not denied in the TMV solutions. As will be discussed in Chap. 4, voids can be confirmed by microscopic observation for charged colloidal systems.

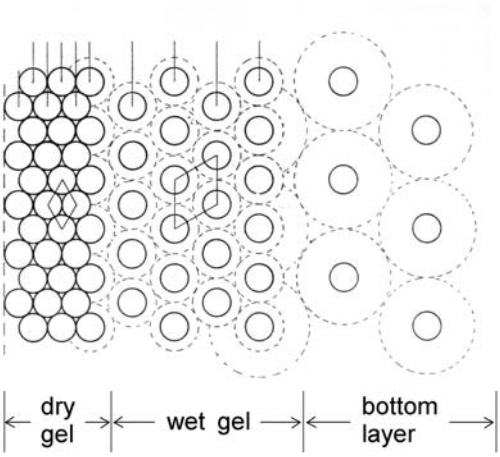

Fig. 3.16. Section across particles in successive layers of drying films illustrating orientation of single crystals in a dry gel. Taken from [21] with the permission of Rockefeller University Press

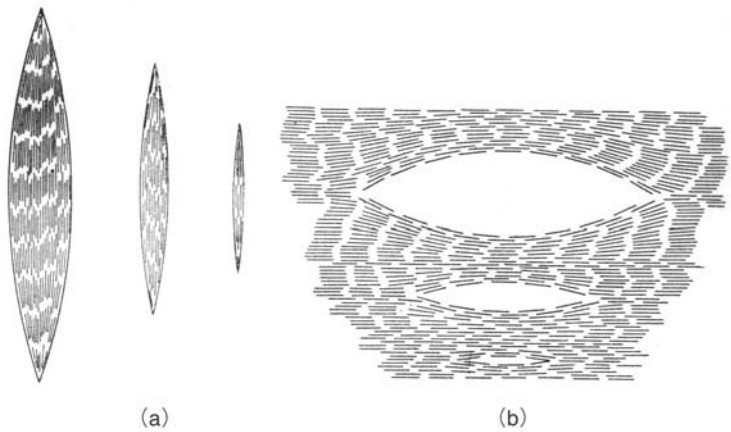

Fig. 3.17. (a) Orientation of particles in positive tactoids of various sizes. (b) Orientation of particles around negative tactoids. Taken from [21] with the permission of Rockefeller University Press

acids as well were studied by X-ray scattering [55]. It was pointed out that the Bragg spacing between the macroions obeyed the scaling laws $c^{-1/2}$ for BSA and $c^{-1/3}$ for hemoglobin.

SAXS Study of Flexible Ionic Polymer Solutions

The recent development in synthetic chemistry has made it possible to prepare compounds with simple chemical structures and to evade complicated functions of biopolymers. At the same time, it is now possible to carry out X-ray scattering at low angles with high precision. The SAXS technique is an important tool for the structural study of polymer solids and solutions. In this section, we briefly discuss the SAXS study of dilute solutions of flexible ionic polymers. See the review [56] for detail.

Dusek et al. [57] and Ise et al. [58] investigated independently and almost at the same time dilute aqueous solutions of neutralized polymethacrylic acid (PMA) and polyacrylic acid (PAA) by SAXS. A single broad peak was found when the polymers were neutralized. In the case of PMA, the peak appeared when the degree of neutralization α_{d} was 0.05, reflecting the strong influence of the electrostatic interaction. Ise et al. took the peak as due to more or less regular distribution of the macroions in solutions and the peak position K_{m} was interpreted to correspond to the distance between lattice planes.

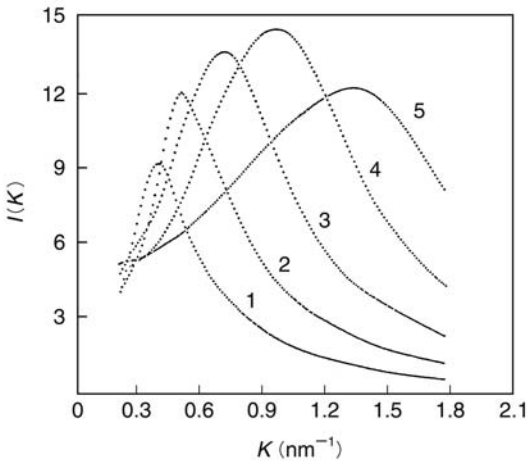

Fig. 3.18. SAXS profiles of aqueous solutions of sodium poly(styrene sulfonate)s. $M_{\mathrm{W}} = 7.4{\times}10^4$, $M_{\mathrm{W}}/M_{\mathrm{N}} = 1.17$. [NaPSS] = 10.0 g L^{-1} (curve 1), 20.0 (curve 2), 40.0 (curve 3), 80.0 (curve 4), and 160.0 (curve 5). Taken from [59] with the permission of the American Institute of Physics

Figure 3.18 shows typical scattering curves obtained for NaPSS solutions [59]. At all polymer concentrations employed, a single broad peak was observed. The peak position K_m shifted toward a larger scattering vector K (i.e., shorter spacing) with increasing polymer concentration. When neutral salts were added, K_m shifted toward a lower K, and the peak disappeared when the salt concentration C_s was high. The same C_s dependence of K_m was observed for other ionic polymers such as poly-L-lysine (PLL), polyallylamine hydrochloride (PAAm-HCl), chondroitin sulfate A and C (ChS-A and ChS-C) [60], bovine serum albumin (BSA) [60], lysozyme [60] and tRNA [60, 61]. Figure 3.19 shows the scattering curves for NaPSS solutions at $C_s = 0.1$ mol L^{-1} with varying cation valency of added salts. The higher the valency, the more effectively the scattering peak was suppressed. This fact also suggests that the peak is due to electrostatic interaction in solutions.

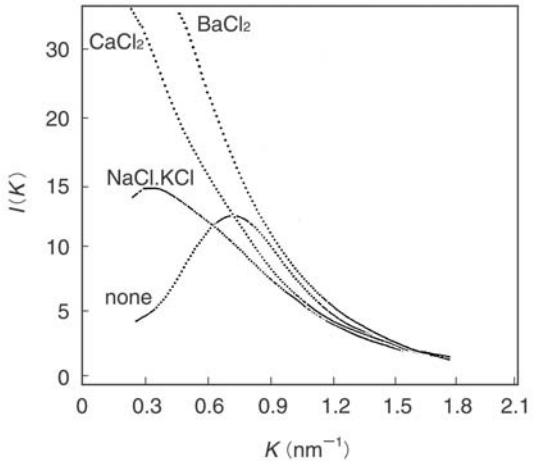

Fig. 3.19. SAXS profiles of NaPSS solutions at various salt concentrations. $M_W = 7.4\times10^4$, $M_W/M_N = 1.17$, [NaPSS] = 40 g L^{-1}, $C_s = 0.1$ mol L^{-1}. Taken from [59] with the permission of the American Institute of Physics

Figure 3.20 shows the scattering profiles for two NaPSS samples of different molecular weights and for their mixture [59]. The K_m clearly depends on the molecular weight. The K_m of the 1:1 mixture (in weight) of two samples is 0.83 nm^{-1} (curve 3) and differs from those of the single components (0.52 and 0.74 nm^{-1}). If the scattering peak reflects the physical properties of each single chain of the samples, we might expect curve 4 after mixing. Instead curve 3 was observed. This observation is not contradictory to our interpretation that the scattering peak was due to ordered arrangements of a large number of polymer chains. Furthermore, if each sample forms an ordered arrangement separately,

we would expect two peaks after mixing. This was not the case experimentally. Therefore, curve 3 observed after mixing was inferred to correspond to an ordered structure jointly formed by two samples. The lack of higher order peaks makes further detailed argument difficult.

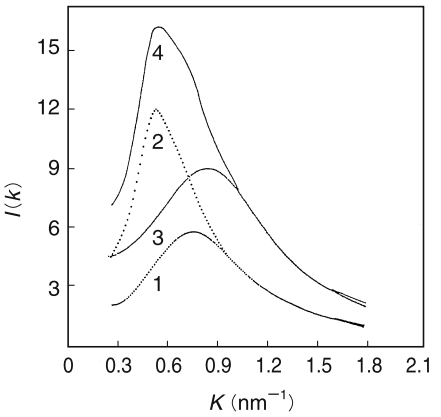

Fig. 3.20. Molecular weight dependence of SAXS profiles of NaPSS solutions and the mixing experiment. Curve 1: $M_W = 4600$, $c = 20$ g L^{-1}, curve 2: $M_W = 7.4 \times 10^4$, $c = 20$ g L^{-1}, curve 3: (20 + 20 g L^{-1}), curve 4: composite curve of 1 and 2. Taken from [59] with the permission of the American Institute of Physics

We mention that the molecular weight dependence of the SAXS profiles is incompatible with the isotropic model [33–35].

Figure 3.21 gives SAXS curves of polyvinylpyrolidone (PVP), a non-ionic water soluble polymer. The scattered intensity monotonously decreased with increasing K, showing no peak. Similarly, protein solutions did not show a scattering peak at the isoelectric point [60]. The origin of the peak, namely the structure formation, is thus suggested to be due to the intermacroion electrostatic interaction. When PVP was mixed with PSS, the NaPSS peak position was unaffected [59]. This fact implies that, at least under the present condition, *the structure formation is not due to the depletion forces* [10].

The scattered intensity was somewhat lowered and the K_m shifted toward larger K, though slightly, when the solution temperature was raised from 13 to 40°C (See Fig. 13 of [59]). This dependence is due to counteracting effects of thermal expansion and of the temperature dependence of the dielectric constant ε of water. The lowering of ε with increasing temperature should affect the electrostatic interaction. To explain the observed shift of K_m and hence the decrease in the spacing between lattice planes, the electrostatic *attraction* between macroions is concluded to play an overwhelming role over electrostatic repulsion. In this respect we note the consistency of our observation with Bernal-Funkuchen's results mentioned above. This consideration was on

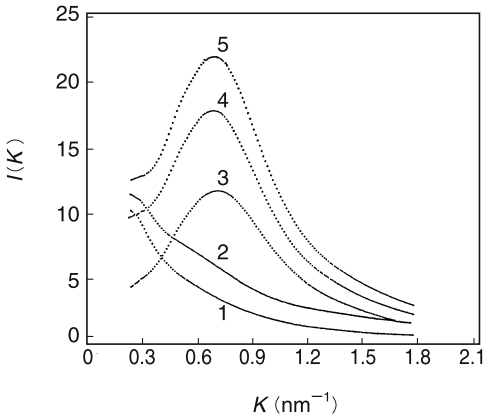

Fig. 3.21. SAXS profiles of polyvinylpyrolidone solutions and the mixture with NaPSS. Curve 1: PVP ($M_W = 4\times10^4$), $c = 40$ g L^{-1}, curve 2: PVP, $c = 80$ g L^{-1}, curve 3: NaPSS ($M_W = 7.4\times10^4$), $c = 40$ g L^{-1}, curve 4: NaPSS (40 g L^{-1}) + PVP (20 g L^{-1}), curve 5: NaPSS (40 g L^{-1}) + PVP (40 g L^{-1}). Taken from [59] with the permission of the American Institute of Physics

intermacroion interaction. On the *intra*macroion interaction, also, a similar trend was recently reported by Lindman et al. who observed that the end-to-end distance of a DNA single chain (contour length of 57 μm) was about 3 μm in water and 1 μm in a butanol-water (40:1) mixture [62]. The electrostatic attraction is important in this case, too, though the argument cannot be conclusive because the solvent power was not kept constant for solvents used.

Chu and his associates were the first to report the single broad peak for dilute solutions of tRNA [61]. Matsuoka et al. took up dilute solutions of various biopolymers such as BSA, lysozyme, chondroitin sulfate, and tRNA [60]. The dependences of the SAXS profiles of these biopolymers on polymer concentration, salt concentration, charge number, and temperature were qualitatively the same as those of the flexible ionic polymers. This fact tells us that the shape or dimension of solute molecules and the property of the polymer chain are not decisive factors for the single broad peak. What is common to all these solutes is the electrostatic interaction in the systems, which we believe is the most important factor producing the scattering profile.

Interpretation of the Single Broad Peak: The Bragg Distance between Macroions, the Average Distance, and Localized Ordered Structure

The single broad peak was experimentally confirmed for various macroionic solutions. As will be discussed later, a similar peak was found also in the small-angle neutron scattering (SANS) experiments. It is most tempting to suggest

that the peak originates from three-dimensional ordered array of macroions. However, the structure is maintained in solutions and is not rigid as we might imagine for atomic crystals. As a matter of fact, only the first order peak has been observed [8]. It seems that we need to accept fairly distorted structures. The crystal symmetry has not been identified yet. The most important difference is that the lattice constant of the localized ordered structure varies with the experimental conditions such as ionic strength, whereas this is not the case for solid crystals.

Taking these ambiguities into account, we proceed to the analysis of the solution structure of ionic polymers. Particularly interesting is the distance of lattice planes, or the distance between nearest neighboring macroions $2D_{\mathrm{exp}}$, which can be estimated from K_{m}. The results are shown for NaPSS in Table 3.4. This quantity is compared with the average distance $2D_0$, which is obtained from the solute concentration c by assuming a simple cubic (sc) symmetry covering the entire solution. Except for the samples with a low M_{W} and in salt-containing solutions, $2D_{\mathrm{exp}}$ is found to be smaller than $2D_0$. *For a high* M_{W} *sample (*Expt. 11*), the ratio* $2D_{\mathrm{exp}}/2D_0$ is 1/3.6. At a given *number* concentration, $2D_{\mathrm{exp}}$ becomes smaller with increasing degree of polymerization, and hence the number of charges of a macroion. (Compare Expts. 16 and 17, and Expts. 2 and 8.) These results indicate that *a simple electrostatic repulsion is not the only interaction between macroions.*

The relation $2D_{\mathrm{exp}} < 2D_0$ and the charge number dependence of $2D_{\mathrm{exp}}$ were also confirmed for other polyelectrolytes. The inequality relationship tells us that the ordered structure is non-space-filling and coexists with free macroions and counterions. We call such a situation the "two-state structure" [64]. The schematic view is shown in Fig. 3.22. Though unexpected in macroscopically homogeneous systems, the two-state structure can be confirmed with eyes for colloidal dispersions. It is most interesting that the macroscopically homogeneous solutions are microscopically inhomogeneous.

We propose that macroions attract each other, though similarly charged, through the intermediary of their counterions. We will discuss this topic in detail later.

SAXS Study of Dilute Solutions of Colloidal Silica Particles, Ionic Dendrimers, and Ionic Micelles

Since the conformation of flexible ionic polymers is not yet clear, it is difficult to give quantitative argument on the shape factor $f_M(K)$ and the struc-

[8] As will be discussed in Sect. 4.3.4, 22 scattering spots (third orders of diffraction) were observed by ultra-small-angle X-ray scattering for a single crystal of colloidal silica particles (particle radius a = about 55 nm). Antonietti et al. found three scattering peaks by light scattering for spherical microgels (a = 48 nm) [63]. The fact that only a single peak could be observed for macroions with a smaller a than these particles indicates that Brownian motion of solutes is an important factor controlling the number of the peak.

Table 3.4. SAXS data of NaPSS in aqueous solutions

Expt	M_W	c g L^{-1}	[NaCl] mol L^{-1}	K_m [a] nm^{-1}	$2D_{exp}$ [b] nm	$2D_0$ [c] nm	Temperature °C
1	1.8×10^4	10	0	0.46	13.6	14.4	25
2	1.8×10^4	20	0	0.53	11.9	11.4	25
3	1.8×10^4	40	0	0.78	8.1	9.1	25
4	1.8×10^4	80	0	1.04	6.0	7.2	25
5	7.4×10^4	10	0	0.40	15.7	23.1	25
6	7.4×10^4	20	0	0.52	12.2	18.3	25
7	7.4×10^4	40	0	0.73	8.7	14.5	25
8	7.4×10^4	80	0	0.96	6.5	11.5	25
9	7.4×10^4	160	0	1.34	4.7	9.2	25
10	4.6×10^3	40	0	0.91	6.9	5.8	25
11	7.8×10^5	40	0	0.73	8.7	31.9	25
12	1.8×10^4	40	0.05	0.67	9.4	9.1	25
13	1.8×10^4	40	0.10	0.51	(12.3) [d]	9.1	25
14	7.4×10^4	40	0	0.71	8.8	14.5	13
15	7.4×10^4	40	0	0.77	8.2	14.5	40
16	4.6×10^3	20	0	0.74	8.5	7.3	25
17	1.8×10^4	78	0	1.02	6.2	7.3	25
18	4.6×10^3 & 7.4×10^4	40	0	0.83	7.6	7.1	25

[a] scattering vector at the scattering maximum.
[b] nearest neighbor distance between macroions in the ordered structure.
[c] average distance calculated from the concentration by assuming a simple cubic distribution.
[d] a large error might be associated with the K_m value because of the high salt concentration.

ture factor $F(K)$. For spherical samples, on the other hand, we can estimate $F(K)$ from SAXS measurements. The results for monodisperse colloidal silica particles are shown in Fig. 3.23 [65]. $F(K)$ shows a single broad peak and suggests the presence of ordered structures. For this system, the peak positions of $F(K)$ and $I(K)$ agreed and the dependences of $F(K)$ on polymer and salt concentrations were the same as those found for flexible ionic polymers. $2D_{exp}$ was calculated from $F(K)$ by assuming sc, face-centered cubic (fcc) and body-centered cubic (bcc) to be 25.5, 27.5, and 27.5 nm at a concentration of 3.93 vol%, respectively. $2D_0$'s were 28.8, 32.4, and 31.5 nm, respectively. Clearly $2D_{exp} < 2D_0$, though the difference was not so large as for NaPSS, probably because of the low charge density of the silica particles. In Fig. 3.23 is also shown the theoretical structure factor $Z(K)$ for comparison, which was

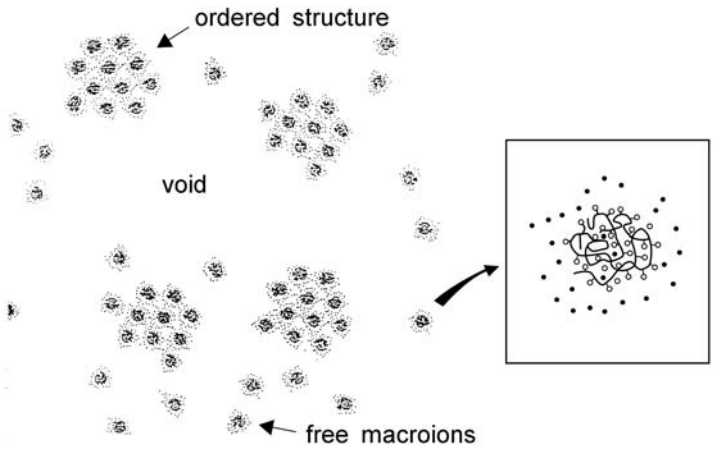

Fig. 3.22. The two-state structure in macroionic systems. The schematic view is depicted with the presumption that flexible macroions assume not an extended rod conformation but rather a randomly-coiled conformation. When the macroion concentration is increased, the ordered structures become space-filling, covering the entire volume of the system

obtained using a paracrystal theory by Matsuoka [66]. It is evident that the sc symmetry does not fit the observed $F(K)$. Whether fcc or bcc is more realistic cannot be judged since only the first peak was observed.

By using the SAXS technique, Ohshima et al. investigated the structures in dilute aqueous solutions of polyamido amine dendrimers of the 4^{th}, 7^{th}, and 10^{th} generations (G4, G7, and G10) with univalent and bivalent counterions [18]. The scattered intensity $I(K)$ of G7 is given in Fig. 3.24 at fixed weight fraction w and degree of neutralization α_{d}. By the degree of neutralization we imply the ratio of the amount of acid added to that of the end groups. Obviously a single broad peak was observed on top of the shape factor. Two points are noteworthy. First, for univalent counterions, the peak position did not depend on the counterion species. This corresponds to the insensitivity of the charge number toward the counterion species shown in Fig. 3.2. Secondly, $I(K)$ of the (bivalent) sulfate salt was indistinguishable from that of water, implying that no ordered structures were formed. This may be taken as implying that the charge number of the dendrimer with the bivalent counterions was smaller than that for the univalent ones, as experimentally observed (Table 3.2 and Fig. 3.2). Therefore the interaction between dendrimers with the bivalent counterions could not be strong enough to maintain the structure. Similar results were confirmed for G4 and G10. Though we omit graphical presentation, the peak position was not dependent on α_{d} in the α_{d} range be-

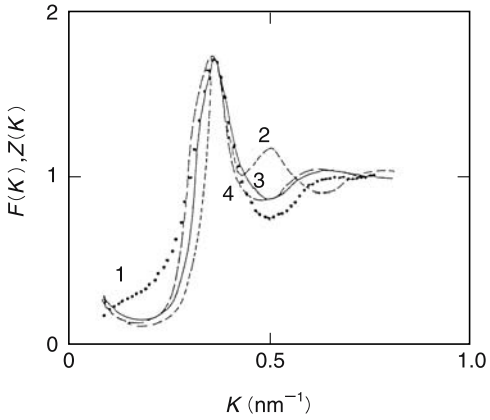

Fig. 3.23. Structure factor $F(K)$ of an aqueous dispersion of colloidal silica particles. Particle radius = 3.1 nm, concentration = 8.57 vol%. Curve 1 ($\cdots$): observed $F(K)$. curve 2: theoretical structure factor $Z(K)$ obtained for a sc crystal of the lattice constant a_0 of 18.0 nm with a paracrystalline distortion factor g of 0.163, curve 3: $Z(K)$ for an fcc crystal of $a_0 = 31.0$ nm with $g = 0.161$, curve 4: $Z(K)$ for a bcc crystal of $a_0 = 26.0$ nm with $g = 0.160$. Taken from [65] with the permission of the American Physical Society

tween 0.5 and 1.9 for the univalent counterions. This is due to the insensitivity of the charge number toward $\alpha_{\rm d}$ for $\alpha_{\rm d} > 0.5$ (Fig. 3.2).

Using the theoretical $f_M(K)$ for homogeneous spheres, $F(K)$ was derived from $I(K)$ as shown in Fig. 3.25. The peak position $K_{\rm m}$ of the single broad peak shifts toward larger K as the concentration is increased, suggesting that $2D_{\rm exp}$ decreases. This trend is the same as observed for $I(K)$ of flexible ionic polymer solutions (Fig. 3.18) and for colloidal dispersions as studied by microscopy (Table 4.3) and ultra-small-angle X-ray scattering (Table 4.6).

The peak of $F(K)$ becomes higher as $\alpha_{\rm d}$ increases. The same tendency is also noted for ammonia core G8 [67] and G5 [68] using SANS, indicating the important role of the electrostatic interaction in structure formation. When $1.5 < \alpha_{\rm d} < 1.9$, the peak is lowered by the shielding effect of excess acid.

Ohshima et al. calculated $2D_{\rm exp}$ from the peak position assuming an fcc structure and compared it with $2D_0$. The results are shown in Fig. 3.26 on a double logarithmic scale, from which $2D_{\rm exp}$ is seen to decrease with a slope of -0.34 with increasing dendrimer concentration. This slope is in rough agreement with the previous SANS measurement [67, 68]. We have $2D_{\rm exp} < 2D_0$ for G10 and $2D_{\rm exp} \approx 2D_0$ for G4. This indicates that the counterion-mediated attraction is stronger for G10 than for G4. We note that the charge number of dendrimers $Z_{\rm nd}$ becomes larger as the generation becomes higher, as seen from Table 3.2.

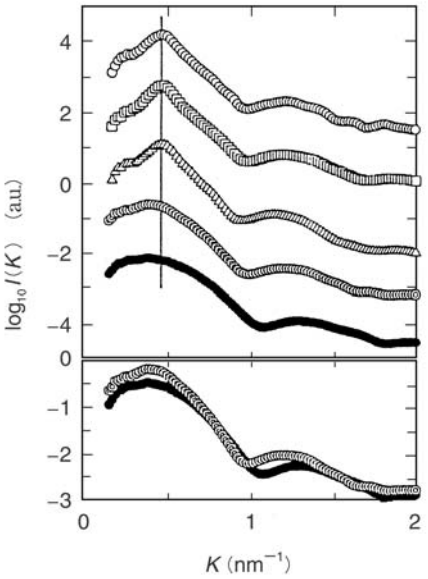

Fig. 3.24. SAXS profiles of aqueous solutions of a cationic dendrimer of the 7$^{\text{th}}$ generation. ○: hydrochloric acid, weight fraction $w = 0.050$, degree of neutralization $\alpha_{\text{d}} = 1.0$, □: hydrobromic acid ($w = 0.049$, $\alpha_{\text{d}} = 1.0$), △: iodic acid ($w = 0.050$, $\alpha_{\text{d}} = 1.1$), ◎: sulfuric acid ($w = 0.050$, $\alpha_{\text{d}} = 1.0$), •: water ($w = 0.050$, $\alpha_{\text{d}} = 0$). The vertical solid line: the first peak position. Each curve was shifted vertically. The inset (bottom) reproduces the scattering profiles of the sulfate salt and of the water-unneutralized dendrimer on the same scale. Taken from [18] with the permission of the American Physical Society

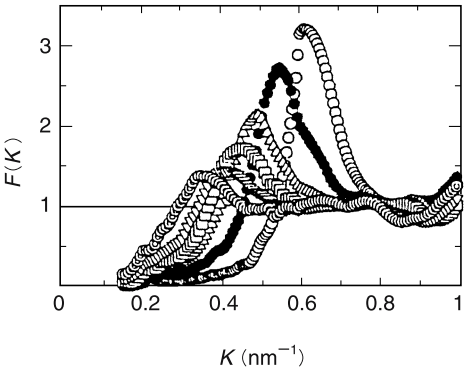

Fig. 3.25. Concentration dependence of the structure factor $F(K)$ of G7 dendrimer. $\alpha_{\text{d}} = 1.0$, ○: $w = 0.100$, •: 0.070, △: 0.050, □: 0.040, ▽: 0.030, ◎: 0.020. Taken from [18] with the permission of the American Physical Society

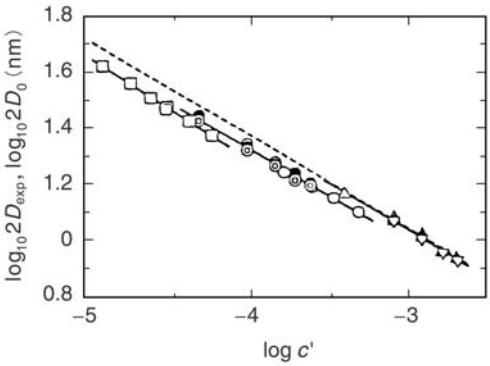

Fig. 3.26. Comparison of the closest interparticle distance $2D_{\rm exp}$ with the average interparticle spacing $2D_0$ for dendrimers. c': number concentration of dendrimers ($\rm nm^{-3}$). △: G4 (hydrochloride), ▲: G4 (perchlorate), ▽: G4 (iodate), ○: G7 (hydrochloride), ●: G7 (bromate), ◎: G7(iodate), □: G10 (hydrochloride), ——: $2D_0$ (fcc). Taken from [18] with the permission of the American Physical Society

However, not all experimental facts can be accounted for in terms of $Z_{\rm nd}$ alone. The G10 sulfate has a larger $Z_{\rm nd}$ than the G4 chloride. The former does not show the structure formation. In this case, the charge density $\sigma_{\rm n}$ plays an important role. In this respect, colloidal systems to be discussed in Chap. 4 are interesting. As clear from Table 4.3, the interaction between colloidal particles is determined by the charge density. On the other hand, $\sigma_{\rm n}$ of dendrimers stays almost constant over the three generations. Evidently colloidal particles and dendrimers behave differently. In the case of simple electrolytes, important is the charge number Z, not the charge density σ. The seeming difference among colloidal particles, dendrimers, and simple ions arises from their dimensions. At a given number density, the ratio of particle radius a and interparticle distance R for colloidal particles is large compared to those for the other two, so that the interparticle interaction is determined by the charges on the confronting surfaces of the two particles; the charges on the remote surfaces are not relevant. Thus, the surface charge density on the surfaces facing each other is decisive. On the other hand, the size of a simple ion is ignorable over R, so that the total number of charges on the ions is influential. The dendrimers sit in between the two extreme cases and both the charge density and charge number are determining factors of the interaction.

A single broad SAXS peak is also observed for solute ions such as ionic micelles, which are smaller than the dendrimers [69]. Dodecyltrimethyammonium chloride (DTAC) forms spherical micelles, whose association number (and hence analytical charge number) is about 50 and has a radius of 1.6 nm. $2D_{\rm exp}$ at 100 g $\rm L^{-1}$ was found from the scattering peak to be about 7 nm, while $2D_0$ was 6.5 nm. Because of its rather high polydispersity, $2D_{\rm exp}$ can be

regarded as almost equal to $2D_0$. We take the SAXS peak as indicating the ordered distribution of the spherical micelles in the solutions, in conformity with other macroions discussed in the above sections. Because of its relatively low charge numbers of the micelles, the structure happens to be space-filling.

3.2.4 Small-Angle Neutron Scattering

The neutron beam is scattered by interaction with the atomic nucleus. The scattering power of the nucleus at the state i is given by the neutron scattering length b_i, which corresponds to the atomic form factor of X-ray. The local scattering length density $\rho(r)$ of a molecule (radius a) in a homogeneous medium is given by the integration of b_i over the local volume v

$$\rho(r) = \left(\frac{3}{4\pi a^3}\right) \int_v b_i(r) dv. \tag{3.27}$$

The scattered intensity $I(K)$ is then given by

$$I(K) = \langle \left| \int_v (\rho(r) - \rho_s) \exp(iK \cdot r) dv \right|^2 \rangle, \tag{3.28}$$

where ρ_s is the scattering length density. From the measurements of $I(K)$ we can deduce the structural information much as we can by light scattering and X-ray scattering.

The SANS technique was employed intensively for ionic polymer solutions by French groups in the 1970's. A single broad peak was detected in the scattering profile. Cotton and Moan noticed for neutralized polymethacrylates (PMA) that the peak position K_m varied with concentrations of polymers and salt in the same manner as was discussed on SAXS measurements (Figs. 3.18 and 3.19) [25]. In Table 3.5 is presented the closest interparticle distance $2D_{exp}$ obtained from their data with the average spacing $2D_0$ from their concentrations. Interestingly $2D_{exp} < 2D_0$ holds, suggesting the two-state structure for PMMA, although the original authors did not mention this finding.

Table 3.5. SANS data of polymethacrylate-D_2O solutions at a degree of neutralization of 0.6

c (g L^{-1})	K_m (nm^{-1})	$2D_{exp}$ (nm)	$2D_0$ (nm) [a]
36.5	1.12	5.6	8.4
24.5	1.02	6.2	10.0
15.5	0.84	7.5	11.7
8.13	0.55	11.4	14.5

[a] Derived with the assumption that the sample was neutralized by NaOH.

SANS measurements were further carried out on NaPSS, α-L-glutamate, and so on. Though we cannot go into detail, the experimental results are

basically the same as those obtained by SAXS and indicate that $2D_{\rm exp} < 2D_0$ is valid. Table 3.6 gives $2D_{\rm exp}$ and $2D_0$ derived from the data by Nierlich et al. [70].

Table 3.6. Comparison of the Bragg spacing with the average spacing between macroions for SANS data of NaPSS-D_2O solutions [a]

c (g L^{-1})	$K_{\rm m}$ (nm^{-1})	$2D_{\rm exp}$ (nm)	$2D_0$ (nm)
5	0.33	19.0	28.8
10	0.45	13.9	22.8
29.1	0.68	9.2	16.0
47.6	0.97	6.5	13.6
90.9	1.26	5.0	10.9

[a] Nierlich et al. [70] on an NaPSS sample of $M_{\rm W} = 7.2{\times}10^4$.

Cotton and Moan found that $I(K)$ was increased with decreasing K at $K = 10^{-1}$ nm^{-1}. Nierlich et al. rejected this "upturn" phenomenon for $10^{-1} < K < 4 \times 10^{-1}$ nm^{-1}, because they could not observe the phenomenon for deuterated poly(styrene sulfonate)s in "ultra pure" H_2O while they observed the upturn for D_2O solutions of NaPSS. In short, the upturn was attributed to the "impurities" in D_2O. Such reasoning is not acceptable since purity check was not independently carried out. The upturn is real when structural inhomogeneities are in the solutions such as a two-state structure. As a matter of fact, the reciprocal excess scattered intensity decreases with decreasing K, as shown in Fig. 3.5.

Matsuoka et al. performed SANS measurements at smaller K regions ($3 \times 10^{-2} \sim 2 \times 10^{-1}$ nm^{-1}) on NaPSS-D_2O solutions, observed the scattering peak, and confirmed the upturn for $K < 10^{-1}$ nm^{-1} [71]. The peak position $K_{\rm m}$ observed agreed with that found in H_2O, indicating the universal nature of the scattering peak independent of the technique and solvent. Matsuoka et al. estimated the radius of gyration $R_{\rm G,app}$ of the localized structure by Guinier's law, which reads

$$I(K) = I(0) \exp\left[-\frac{R_{\rm G,app}^2 K^2}{3}\right], \tag{3.29}$$

and obtained thereby the radius $a_{\rm app}$ of a spherical structure. The results are shown in Table 3.7. The closest interparticle distance $2D_{\rm exp}$ was estimated from the scattering peak position and the number of macroions n contained in a structure was derived. Giunier's law is valid for homogeneous entities. Since the structure in question is composed of macroions and solvent, it is questionable to apply the law for such a case. Furthermore, it is not clear that K values are small enough for the Guinier law to be applied. As shown by Konishi et al. [72], the electrostatic interaction is unexpectedly intense.

Even at $\phi = 1.37 \times 10^{-2}$ and $C_s = 5 \times 10^{-4}$ mol L^{-1}, the scattered intensity observed at the finite particle concentration does not give a correct value for the particle radius. Thus the $R_{G,app}$ values obtained should be taken as approximate ones. It is hoped that the approximation can be improved. We note however that, at a given molecular weight and polymer concentration, the $R_{G,app}$ values obtained by SLS (Table 3.3) are of the same order of magnitude as those obtained by SANS (Table 3.7). There are no other data to compare the n values with, but the tendency to increase with increasing concentration seems reasonable. The n value was found to decrease with C_s [73], which is also acceptable.

Table 3.7. Apparent size of localized ordered structure for poly(styrene sulfonate) of $M_W = 10^5$ obtained by SANS

c	$R_{G,app}$	a_{app}	$2D_{exp}$	$2D_0$	n
g L^{-1}	nm	nm	nm	nm	
10	40.7	52.5	16.6	25.5	130
20	51.6	66.6	10.3	20.2	1100
30	68.6	88.6	8.5	16.0	4700

According to the Babinet principle, the positive difference in the scattering length densities or in the electron densities of an object and its surrounding cannot be distinguished from the negative one. In the foregoing discussion, the upturn observed was taken as due to localized ordered structures floating in the sea of solvent, but the possibility that it was caused by voids cannot be ruled out. As will be mentioned in Chap. 4, void structures can be confirmed by microscopic observation. This possibility is not nil even in flexible ionic polymer solutions whenever $2D_{exp} < 2D_0$ is observed. Matsuoka et al. examined a void-in-ordered structure model [73] and found that the number of voids decreased with increasing polymer concentration but was hardly affected by the salt concentration. Further quantitative investigation is necessary.

The upturn phenomenon was once attributed to dust or polymer aggregates, which is incorrect [70, 73]. If dust were responsible, it must be demonstrated that no upturn could be observed after having removed the dust from the solution. The "dust" theory seems to have been withdrawn in the subsequent work [74]. Nierlich et al. did not observe the upturn for deuterated poly(styrene sulfonate)-H_2O solutions because they did not extend their measurements to the scattering vector small enough to correspond to the size of the localized ordered domains, not because of the absence of dust.

Brief comments are necessary about SANS study of ionic micellar solutions [75]. A single broad peak was also observed in the SANS profiles of this group of materials [76]. From theoretical analysis based on a one-component Ornstein-Zernike equation, Hayter et al. concluded that the effective potential between ionic micelles was a DLVO-type repulsion [77]. Blum [78], Klein [79]

and Chen [80] discussed the SANS profiles using the mean-spherical approximation (MSA) or the rescaled MSA (RMSA) by assuming the DLVO potential. From its satisfactory agreement with the experimental finding, Chen concluded that a DLVO-type repulsion was in action between micelles [81]. Matsuoka et al. took the peak as due to the ordered arrangement of micelles and pointed out that the intermicellar Bragg distance $2D_{\rm exp}$ was almost equal to the average distance $2D_0$ [60]. For Li salts of dodecyl sulfate, the two distances were found to be 5.5 and 6.6 nm. This is reasonable since the ionic micelles have small numbers of charges so that the counterion-mediated attraction happens to be weak and hence the micelles are distributed uniformly in the solutions (one-state structure). Under such a special circumstance, the repulsive DLVO-type interaction certainly provides agreement with observation. This agreement however cannot be a reason to exclude the existence of the counterion-mediated attraction in general cases. Similar cases will be discussed in Chap. 9 in detail.

3.3 Recent Progress and Summary

After the above sections were completed, some important papers on related topics were published, which will briefly be discussed here. Cooper et al. carried out viscosity, SLS, and DLS measurements on non-aqueous solutions of ionomers [82, 83] [9], which have relatively small numbers of ionic groups on polymer chains. For N-methylformamide ($\varepsilon = 182$) and dimethylacetamide ($\varepsilon = 37$) solutions of a polyurethane-based ionomer (Fig. 3.27), the reduced viscosity was found to sharply increase with decreasing polymer concentration, as is observed for aqueous solutions of flexible ionic polymers (See Chap. 7, Fig. 7.1 curve 1). Two diffusion coefficients were observed by DLS from the ionomer solutions. Cooper et al. claimed that many polymer chains formed loose aggregates. This is the two-state structure discussed in Sect. 3.2.3. Because the solvent-polymer interaction changes from solvent to solvent, the solution properties of the ionomers would not be as simple as for polyelectrolyte-water systems. Furthermore, the ionic conductivity data in organic solvents is still not adequate, which makes the determination of the net charge number of the ionomers and hence the evaluation of the electrostatic interaction difficult. The experimental data implies that this interaction is qualitatively important for ionomer solutions.

Zhang et al. thoroughly studied aqueous solutions of PSS with univalent and bivalent counterions by SLS and SANS [84]. Although it was not mentioned, the $2D_{\rm exp}$ from the scattering peak position was 8 nm at a concentration of 40 g $\rm L^{-1}$ for sodium salt, while the $2D_0$ from concentration was 17 nm. The ratio $2D_{\rm exp}/2D_0$ is 0.47. This result is consistent with the SAXS data

[9] For a recent review on the ionomer solutions, see Hara M (1993) (ed) Polyelectrolytes: Science and Technology. Marcel Dekker, New York

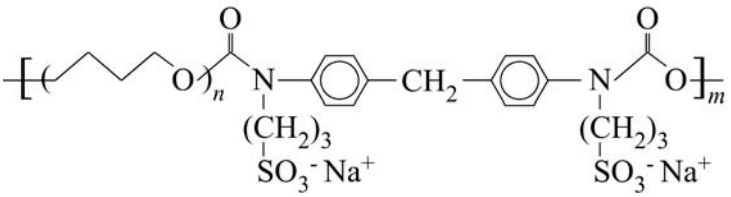

Fig. 3.27. Structure of polyurethane-based ionomers

(Table 3.4) for NaPSS, which showed that the larger the molecular weight the smaller the ratio. In fact, their molecular weight was 1.24×10^5, being larger than those of samples used in the SAXS study. The peak position of the SANS profiles was hardly dependent on the counterions (H^+, Na^+, and K^+ for univalent cases and Mg^{2+}, Ca^{2+}, and Cu^{2+} for bivalent ions). A similar trend was noticed for univalent counterion-dendrimer solutions (Fig. 3.24) and indicates that the electrostatic interaction, not the size of counterion, is predominant in determining the solution properties. Zhang et al. furthermore demonstrated that the peak position was not affected by addition of cyclic crown ether to KPSS solutions to allow K^+ to form stoichiometric coordination compounds. When the counterion valency was increased from one to two, the peak position of SANS profiles shifted to lower angles. Correspondingly, $2D_{\rm exp}$ increased from 8 nm to 16 nm. In other words, $2D_{\rm exp} \approx 2D_0$. The same tendency was observed for the dendrimers. As shown in Fig. 3.2 and Table 3.2, the net charge number $Z_{\rm n}$ of dendrimer is lower for bivalent counterions than for univalent ones, because the bivalent ions are more strongly bound than the univalent ions. As a result, the attraction between macroions is weaker for the bivalent ions. The change of $Z_{\rm n}$ with the counterion valency was observed for polyacrylates by Wall et al. [7,13,85] though Zhang et al. did not measure $Z_{\rm n}$ of PSS.

The radius of gyration $R_{\rm g}$ of the localized ordered structure (multi-chain domain) was determined from the angular dependence of scattered intensity using (3.16). NaPSS and MgPSS ($M_{\rm N} = 6.06 \times 10^4$) had $R_{\rm g}$ values of 48 and 21 nm at 40 g L^{-1}, respectively. This is acceptable because the net charge number of Mg-salt is lower than that of Na-salt. It is not certain that (3.16) can be applied for a no-salt condition or at 40 g L^{-1}. It is the second best choice due to the lack of the first best and the $R_{\rm g}$ values mentioned above should be taken as approximate.

Furthermore Zhang et al. carried out SANS measurements on the 1:1 mixture of deuterated and non-deuterated poly(styrene sulfonate)s at a mixing ratio of light and heavy waters, where their scattering length densities canceled out. They pointed out that the inter-polymer chain interactions then apparently vanished and the scattering from a single chain could be observed. The radius of gyration of polymer chain $R_{\rm g,c}$ estimated under such a condition decreased as Na^+ was replaced by Mg^{2+}. This seems reasonable, although it

is not clear whether the decrease in the net charge number caused a weaker repulsion between ionized groups or whether the ionized group-counterion interaction in the macroion domain was enhanced by the replacement. The $R_{g,c}$ values were mentioned to be smaller than the theoretical value for an extended rod model. This point was already made by Krause et al. [31] (Fig. 3.3). A quantitative comparison of the data of the two groups is difficult since Zhang et al carried out the measurements at $10 \sim 60$ g L^{-1}, while Krause et al. at 10^{-4} g L^{-1}.

The fast and slow diffusive modes (D_f and D_s) were also observed by Zhang et al. By the transfer from Na^+ to Mg^{2+} the D_f value decreased while the D_s value increased. The D_f decrease is reasonable because Mg^{2+} diffuses more slowly than Na^+. The increase of D_s was attributed to smaller $R_{g,c}$ of the magnesium salt and to lower solution viscosity.

Sedlák carried out detailed investigation of the nature of the localized ordered structure (or multi-chain domain) by SLS and DLS [86]. He concluded that the structures were not due to concentration fluctuation, which seems to be reasonable on the basis of the video observation of colloidal dispersions. He concluded furthermore that this structure was formed, not as the result of filtration treatment, but spontaneously from homogeneously dispersed macroions. This observation is the first for flexible macroions. On the other hand, the same has been observed for colloidal systems. For example, the colloidal dispersion to be shown in Fig. 4.6 of Chap. 4 is turbid at the beginning of the dialysis, indicating random distribution of particles. As the dialysis progresses, we notice that iridescent grains are spontaneously formed. This coloring is due to Bragg diffraction of visible light by localized ordered structures of colloidal particles.

Sedlák observed two diffusive modes even when the pore size D_{pore} of the filter, the number of filtrations, and the standing time of the solutions were varied. When D_{pore} became smaller, the D_s value became larger, suggesting that the ordered regions became smaller. This fact indicates that the ordered regions were destroyed when the solutions passed through the filter pores smaller than the ordered regions. This fact was also noted by SAXS measurements of flexible ionic polymer solutions and microscopic observation of colloidal dispersions before and after the filtration. The important point of Sedlák's observation is that *the ordered structures are so fragile that they are easily broken by filtration and are regenerated after the filtration and nevertheless are long-lived.* (The experiments were carried out over a 37 month period.) The fragility of colloidal crystals has been confirmed by microscopic observation and the ultra-small-angle X-ray scattering studies, as will be discussed in Sect. 4.3.2. The spontaneous formation of the local structures can be easily accepted by invoking an attraction between macroions or particles. Such fragility can be taken as implying that the potential well is very shallow.

It is noteworthy that the local structures cannot be filtered off through filtration operations and that they are long-lived in spite of being fragile.

Such a microscopic inhomogeneity has *not* been considered in the traditional theory of polymer solutions and colloidal dispersions.

Poly(alkyl-*p*-phenylene) sulfonates (PPPS) has been reported to form micelles in water media. The hydrophobic moiety, *n*-dodecyl group, attached to a phenylene chain, causes rod-like hollow cylinder-type micelles with the aliphatic chains in the center [87–89], as shown in Fig. 3.28. The diameter (d) and length (L) of the micelle and its molecular weight (M_{W}) have been characterized by static and dynamic light scattering techniques and small-angle X-ray scattering, from which the PPPS molecules were concluded to align in a direction parallel to the cylinder axis and the number of PPPS molecules in the cross-sectional area of the cylinder (N_{rad}) and the number in the cylinder direction (N_{ax}) were determined. It was pointed out that N_{ax} PPPS molecules were likely to be connected by "pairing". According to our terminology, this is a triple ion formation between sulfonic acid groups at the chain ends and counterions (H^+ or Na^+). For a *n*-dodecyl-PPPS24 sodium salt of a molecular weight of 24,000, M_{W} was 2.1×10^6, L 0.26 μm, d 3.1 nm, N_{ax} 17, and N_{rad} 6. A noteworthy result is that N_{ax} stays constant irrespective of the molecular weight of PPPS molecules for a given counterion. In other words, the micelles contain the same number of macromolecules. It appears that the number of chain-end pairing is an important factor.

Another interesting feature is the hierarchical structure formation, which is shown in Fig. 3.28 [90]. Even at very low PPPS27 concentrations below 10^{-2} g L^{-1}, no individual polymer chains were found, implying that the critical micelle concentration was unobservably small. At such low concentrations, the solutions contained only freely diffusing micelles. However, in the concentration range between 10^{-2} and 1 g L^{-1} there were observed ellipsoidal clusters with internal lyotropic ordering. The long and short axes (a and b) of the prolate ellipsoidal cluster were determined to be 300 and 120 nm at 0.09 g L^{-1}, which increased with increasing concentration. Above 10 g L^{-1}(D), a columnar phase of cylindrical micelles with an interplanar (Bragg) distance of about 15 nm was concluded.

The PPPS27 aqueous solution showed a negative second virial coefficient A_2 of -1.84×10^5 L mol g^{-2}, while a low-molecular-weight sample PPPS12 (molecular weight: 12,000) had a positive A_2 of 7.7×10^5. Wegner et al. argued that the overall interaction between similarly charged rod-like micelles might be attractive for univalent counterions and even more so for longer micelles.

It was pointed out in Sect. 3.2.3 that the attraction became stronger with increasing molecular weight of flexible ionic polymers, and hence macroionic charge number (See Table 3.4). We will demonstrate in Chap. 4 that the attraction is intensified with increasing charge number for colloidal particles. Therefore, the above-mentioned observation for the rod-like micelles suggests that the attraction in question does exist universally between charged entities, irrespective of the geometrical shapes.

Liu et al. studied supramolecular structure formation of highly soluble, fully hydrophilic giant polyoxomolybdate (POM) molecules and POM-

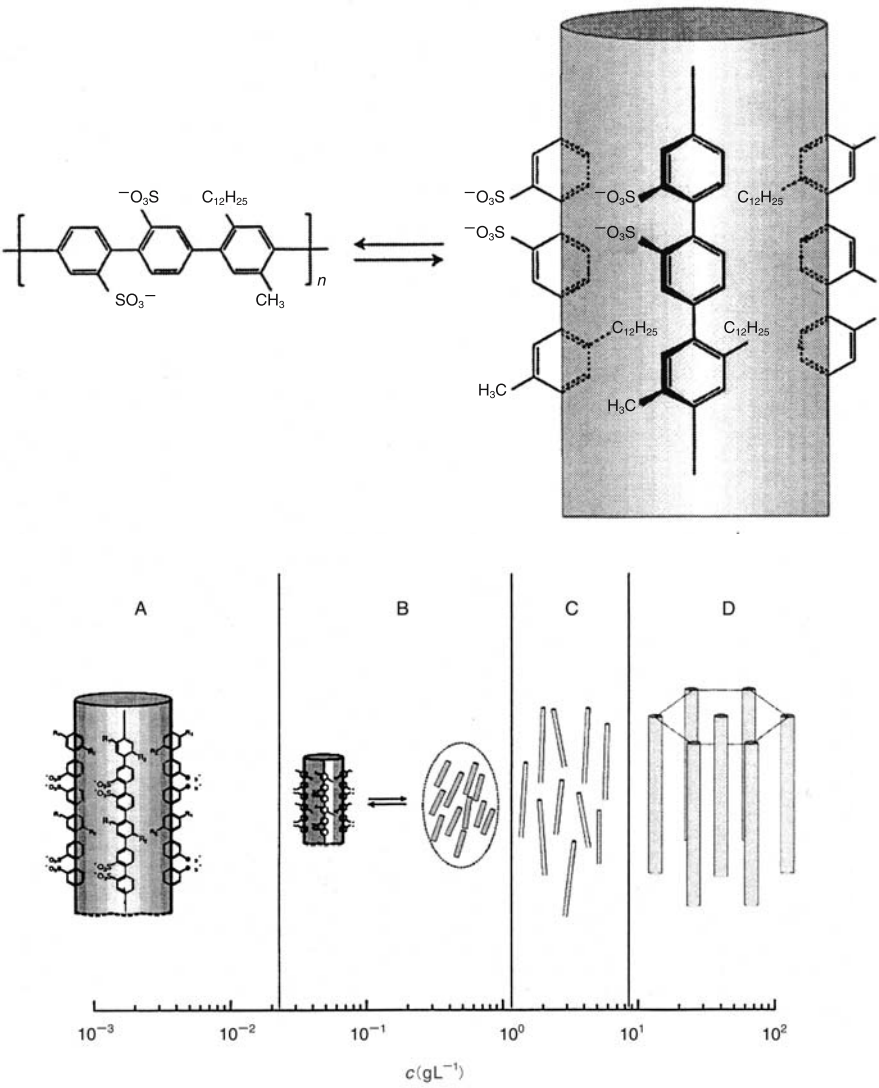

Fig. 3.28. Schematic representation of the hierarchical structure formation of PPPS27 (molecular weight: 27,000) in water. The PPPS molecules form cylindrical micelles in the concentration range A. At higher concentrations B, the micelles form ellipsoidal clusters with internal lyotropic order. In the concentration range C, a nematic phase is formed. At a higher concentration (D), a columnar phase of cylindrical micelles appears. Taken from [90] with the permission of the American Chemical Society

based molecules in aqueous solutions, in the cases of weak electrolytes [91, 92] and strong electrolytes, respectively [93]. The wheel-shaped molecules $Na_{15}[Mo(VI)_{126}Mo(V)_{28}O_{462}H_{14}(H_2O)_{70}] \cdot \sim 400H_2O$, $\{Mo_{154}\}$, existing as giant anions in solution, tend to associate into hollow, single-layer spherical vesicles, as shown in Fig. 3.29 (a) and (b). For a convenient review see [94]. It is novel in that, unlike conventional micelle-forming surfactant molecules, the POM molecules have no hydrophobic moiety so that the contribution of hydrophobic interaction in the vesicle formation does not come into question. For $\{Mo_{154}\}$, the dynamic and static light scattering experiments gave a molecular weight M_W of the vesicle of 2.54×10^7, (corresponding to 1,165 nanowheels) and an average hydrodynamic radius R_H of 45 nm. According to the Zimm plot, the radius of gyration R_G was 45.2 nm, which agreed with R_H. This implies that the vesicle is not a solid spherical particle, for which $R_G = 0.77$ R_H should hold. Furthermore, the number of the nanowheel molecules (1,165) in a vesicle was much smaller than that expected for a solid sphere (14,000), supporting the hollow structure. It was concluded that these 1,165 nanowheel molecules were distributed homogeneously on the surface of a vesicle with the interior filled with water molecules. Assuming a hexagonal packing, the center-to-center distance between two adjacent nanowheels was estimated to be about 5 nm. Transmission electron microscopy measurements confirmed these results. At a POM concentration of 0.01 mg mL^{-1}, the average distance between the nanowheel clusters was 150 nm, if they are freely dispersed in solution. The comparison of these distances implies that the POM ions are "concentrated" to form the hollow vesicles. Since the nanowheel diameter is 3.6 nm, the nanowheels are not in contact. In the complete absence of hydrophobic interaction, such an arrangement is explainable if we assume that a long-range electrostatic attraction and short-range repulsion are in operation between similarly charged POM ions.

Although further study is needed using various samples, the counterion-mediated attraction appears to play an important role for not only spherical but also non-spherical ionic systems. This is reasonable since this attraction has its origin in the electric neutrality of the ionic systems.

In the present chapter on flexible ionic polymers, we first considered the question of the reliability of the widely accepted "rod-model" of polyelectrolyte conformation. In this model the polymer chains were assumed to be stretched to a rod as the result of electrostatic repulsive interaction between ionized groups. In this consideration, a large number of counterions in macroion domains were ignored. Since the region inside the macroion domain has very high ionic concentrations, the complete dissociation is most unfeasible. In other words, ionic association phenomena such as the formation of ion pair, triple ions, and even higher aggregates can be anticipated. The *intra-macroion* association is believed to occur between ionized groups and near-by counterions with a greater ease than in simple ionic solutions. If one triple ion

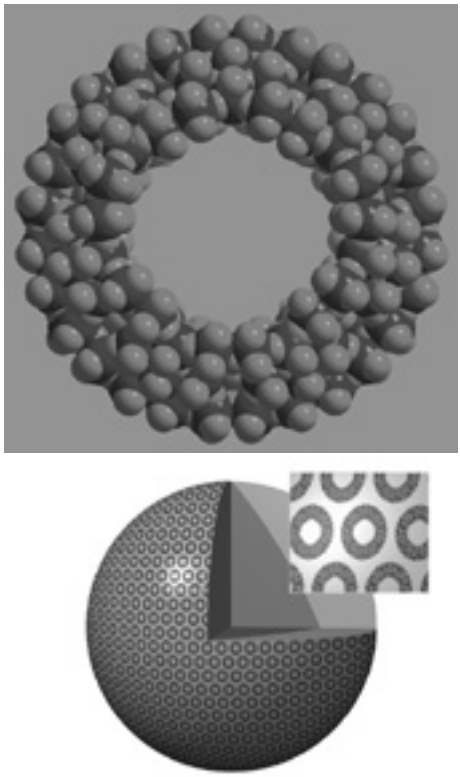

Fig. 3.29. Structure of the $\{Mo_{154}\}$-type nanowheel. top: single molecule. bottom: schematic illustration of the hollow vesicle formed from nanowheels in aqueous solutions, with inset showing enlarged nanowheels. Taken from [93] with the permission of the authors

is formed between a counterion and two ionized groups near both ends of a polymer chain, the macroion cannot be rod-like but would form a ring. The rod-model was initially inferred from the proportionality of the intrinsic viscosity to the squared molecular weight. This relation was derived for non-ionic polymer chains by taking into consideration hydrodynamic interactions only. The electrostatic interaction was completely out of consideration. Even if we set aside the technical difficulties in determining the intrinsic viscosity, it is highly questionable to apply the proportionality for ionic polymer solutions. The conformation of flexible macroions in low salt solutions needs a more careful approach from both experimental and theoretical points of view.

The angular dependence of the scattered intensity of very dilute solutions of flexible macroions does not agree with the rod-model. A single broad peak appears in the intensity-scattering vector curve. The angular dependence of

the inverse excess scattered intensity shows positive and negative slopes at high and low concentrations, respectively. From the positive slope the size of the local ordered structures connected with slow diffusive modes can be estimated. By dynamic light scattering measurements two diffusive modes (D_f and D_s) are found at low salt concentrations in macroscopically homogeneous solutions. The larger diffusion coefficient D_f does not depend on the molecular weight and can be observed for very low-molecular-weight samples, suggesting that this mode is related to a motion of a single polymer chain. The sizes of the local ordered structure estimated from D_s are in good agreement with those obtained by static light scattering measurements.

The single broad peak in the SAXS profile is observed not only for flexible ionic polymer solutions but also for solutions of globular proteins, ionic micelles and ionic dendrimers. The peak does not appear at high salt concentrations or at zero charge number, i.e., for non-ionic polymers. Thus, the peak is characteristic of macroionic systems and should be attributed to a property these macroionic solutes commonly possess. We believe that the peak reflects more or less ordered distribution of the solutes. Then, the peak position corresponds to the (Bragg) distance between the solutes in the ordered structure. This spacing is found to be smaller than the average distance which can be calculated from the solute concentration. The ratio of the two distances is small for high-molecular-weight samples. The smallest value observed is 0.27 for high-molecular-weight poly(styrene sulfonate). The fact that the ratio is smaller than unity indicates that the ordered structure is not space-filling but is localized and coexists with free solute species, maintaining a two-state structure.

A similar peak is observed also in the neutron scattering profiles. The dependence of the Bragg distance on various experimental parameters is qualitatively the same as that for the X-ray and neutron scattering. At small scattering vectors, the scattered intensity shows an upturn, suggesting the existence of large-scale density change in solutions.

The traditional understanding of condensed systems is based on the premise that the systems are structurally homogeneous. This premise can easily be accepted as realistic for concentrated solutions and has been taken for granted also for low concentrations. Given the two-state structure, i.e., microscopic inhomogeneity, experimentally, our understanding needs to be at least partially modified. To further confirm the rather unexpected result, we discuss colloidal dispersions in the next chapter. The colloidal particles are much larger than the macroions considered here, so that the particle distribution can be "seen". In other words, the observation made in the Fourier space by a scattering technique can be confirmed by real space experiments.

In the above, we discussed the properties directly related to the structure formation. Though not comparable with a systematic investigation of simple ionic solutions, intensive study has been carried out on the mean activity

(coefficient), heat of dilution, and molar volume of polyelectrolyte solutions corresponding to the derivatives of the chemical potential of the macroions with respect to the concentration, temperature, and pressure, for limited materials. The interested readers are referred to a review article for details [95].

References

1. Trommsdorf E, Thesis (1931). In: Staudinger H (1960) Die Hochmolekularen Organische Verbindungen-Kautschuk und Cellulose. Springer, Berlin, Heidelberg, New York, pp.333-377
2. Debye PJW, Hückel E (1923) Physik Z 24:185
3. Fowler RH, Guggenheim EA (1939) Statistical thermodynamics. Cambridge University Press, London, Chap. 9
4. Harned HS, Owen BB (1958) The physical chemistry of electrolytic solutions. Reinhold Publishing Co. New York,
5. Robinson RA, Stokes RH (1959) Electrolyte solutions. Butterworths Publications, London
6. Kern W, (1938) Z phys Chem A181:249; (1939) A184:197
7. Huizenga JR, Grieger PF, Wall FT (1950) J Am Chem Soc 72:2636
8. Oosawa F, Imai N, Kagawa I (1954) J Polymer Sci 13:93
9. (a) Imai N, Onishi T (1959) J Chem Phys 30:1115. (b) Onishi T, Imai N, Oosawa F (1960) J Phys Soc Jpn 15:896
10. Oosawa F (1971) Polyelectrolytes. Marcel Dekker, New York
11. See p.220 of [4]
12. Wall FT, Doremus RH (1954) J Am Chem Soc 76:1557
13. Wall FT, Eitel MJ (1957) J Am Chem Soc 79:1556
14. Mita K, Okubo T, Ise N (1976) Faraday Trans I 72:504, 1627
15. Skerjanc J, Dolar D, Leskovsek D (1967) Z phys Chem (Frankfurt) 56:207, 218; (1970) Z phys Chem (Frankfurt) 70:31
16. Baumgartner E, Lieberman S, Lagos A (1968) Z phys Chem (Frankfurt) 61:211
17. Dolar D, Span J, Pretner A (1968) J Polymer Sci Polymer Symposia 16:3557
18. Ohshima A, Konishi T, Yamanaka J, Ise N (2001) Phys Rev E64:051808
19. Yamanaka J, Hibi S, Ikeda S, Yonese M, in preparation
20. Stevens MJ, Kremer K (1995) J Chem Phys 103:1669
21. Bernal JD, Funkuchen I (1941) J Gen Physiol 25:111
22. (a) Guinand S, Boyer-Kawenoki F, Dobry A, Tonnelat J (1949) Compt rend 229:143. (b)Doty P, Steiner RF (1949) J Chem Phys 17:743
23. Berne BJ, Pecora R (1976) Dynamic light scattering. John Wiley, New York
24. Pusey, PN, Tough RJA (1985). In: Pecora R (ed) Dynamic light scattering. Plenum, New York
25. Cotton JP, Moan M (1976) J Phys Lett (Paris) 37:L-75

26. Flory PJ (1953) Principles of polymer chemistry. Cornell University Press, Ithaca, NY
27. Hermans JJ (1949) Rec Trav Chim 68:859
28. Vrij A, Overbeek JThG (1962) J Coll Sci 17:570
29. Casassa EF, Eisenberg H (1960) J Phys Chem 64:753
30. Sedlák M (1996) In:Brown W (ed) Light scattering. Principles and development. Clarendon Press, Oxford, Chap. 4
31. Krause R, Maier EE, Deggelmann M, Hagenbüchle, Schulze SF, Weber R (1989) Physica A160:135
32. Drifford M, Dalbiez JP (1984) J Phys Chem 88:5368
33. de Gennes PG, Pincus P, Velasco RM, Brochard F (1976) J Phys (Paris) 37:1461
34. Hayter J, Jannink G, Brochard WF, de Gennes PG (1980) J Phys Lett (Paris) 41:L-451
35. Benmouna M, Weill G, Benoit H, Akcasu Z (1982) J Phys (Paris) 43:1679
36. SedláK M, Amis EJ (1992) J Chem Phys 96:826
37. SedláK M, Konak C, Stepanek P, Jakes J (1987) Polymer 28:873
38. SedláK M, Amis EJ (1992) J Chem Phys 96:817
39. Schmitz KS, Lu M, Singh N, Ramsay DJ (1984) Biopolymers 23:1637
40. Drifford M, Dalbiez JP (1985) Biopolymers 24:1501
41. Förster S, Schmidt M, Antonietti M (1990) Polymer 31:781
42. Ermi BD, Amis EJ (1998) Macromolecules 31:7378
43. Schmitz, KS, Lu M, and Gauntt J (1983) J Chem Phys 78:5059
44. Schmitz K (1990) An introduction to dynamic light scattering by macromolecules. Academic Press, Boston
45. Schmitz KS (1993) Macroions in solution and colloidal suspension. VCH Publishers, New York
46. Lee WI, Schurr JM (1974) Biopolymers 13:903
47. Wilcoxon JP, Schurr JM (1983) J Chem Phys 78:3354
48. Ramsay DJ, Schmitz KS (1985) Macromolecules 18:2422
49. Ferrari ME, Bloomfield VA (1992) Macromolecules 25:5266
50. Ise N, Okubo T (1980) Acc Chem Res 13:303
51. Koene RS, Mandel M (1983) Macromolecules 16:973
52. Burchard W (1983) Adv Polym Sci 48:1
53. Odijk T (1979) Macromolecules 12:688
54. Amis EJ, Valachovic DE, Sedlák M (1994). In: Schmitz KS (ed) Macro-ion characterization from dilute solutions to complex fluids. American Chemical Society Series No. 548, Chap. 25
55. Riley DP, Oster G (1951) Discuss Faraday Soc 11:107
56. Matsuoka H, Ise N (1994) Adv Polym Sci 114:187
57. Plestil J, Mikes J, Dusek K (1979) Acta Polym 30:29
58. Ise N, Okuobo T, Hiragi Y, Kawai H, Hashimoto T, Fujimura M, Nakajima A, Hayashi H (1979) J Am Chem Soc 101:5836
59. Ise N, Okubo T, Kunugi S, Matsuoka H, Yamamoto K, Ishii Y (1984) J Chem Phys 81:3294
60. Matsuoka H, Ise N, Okubo T, Kunugi S, Tomiyama H, Yoshikawa Y (1985) J Chem Phys 83:378
61. Patkowski A, Gulari E, Chu B (1980) J Chem Phys 73:4187
62. Mel'nikov S, Khan M, Lindman B, Jönsson B (1999) J Am Chem Soc 121:1130
63. Gröhn F, Antonietti M (2000) Macromolecules 33:5938

64. Ise N, Okubo T, Yamamoto K, Kawai H, Hashimoto T, Fujimura M, Hiragi Y (1980) J Am Chem Soc 102:7901
65. Matsuoka H, Murai H, Ise N (1988) Phys Rev B37:1368
66. Matsuoka H, Tanaka H, Hashimoto T, Ise N (1987) Phys Rev B36:1754; Matsuoka H, Tanaka H, Iizuka N, Hashimoto T (1990) Phys. Rev B41:3854
67. Valachovic DE (1997) PhD thesis, University of Southern California
68. Nisato G, Ivkov R, Amis EJ (1999) Macromolecules 32:5895
69. Ishii Y, Matsuoka H, Ise N (1986) Ber Bunsenges Phys Chem 90:50
70. Nierlich M, Williams CE, Boue F, Cotton JP, Daoud M, Farnoux B, Jannink G, Picot C, Moan M, Wolff C, Rinaudo M, deGennes PG (1979) J Phys (Paris) 40:701
71. Matsuoka H, Schwahn D, Ise N (1991) Macromolecules 24:4227
72. Konishi T, Yamahara E, Ise N (1996) Langmuir 12:2608
73. Matsuoka H, Schwahn D, Ise N (1994) In: Schmitz K (ed) Macro-ion characterization for dilute solutions to complex fluids. American Chemical Society Series No.548. Chap. 27
74. van der Maarel JRC, Groot LCA, Hollander JG, Jesse W, Kuil ME, Leyte JC, Leyte-Zuiderweg LH, Mandel M, Cotton JP, Jannink G, Lapp A, Farago B (1993) Macromolecules 26:7295
75. For this topic, see Chen SH (1986) Ann Rev Phys Chem 37:351
76. Magid LJ (1986) Colloid Surface 19:129
77. Hayter JB, Penfold J (1981) Mol Phys 42:109; Hansen JP, Hayter JB (1982) Mol Phys 46:651
78. Senatore G, Blum L (1985) J Phys Chem 89:2676
79. Nagele G, Klein R, Medina-Nayola M (1985) J Chem Phys 83:2560
80. Sheu EY, Wu CF, Chen SH (1986) J Phys Chem 90:4179
81. Bendedouch D, Chen SH, Koehler WC (1983) J Phys Chem 87:2621
82. Nomula S, Cooper SL (2000) J Phys Chem B104:6963
83. Nomula S, Cooper SL (2001) Macromolecules 34:925
84. Zhang YB, Douglas JF, Ermi BD, Amis EJ (2001) J Chem Phys 114:3299
85. Wall FT, Eitel MJ (1957) J Am Chem Soc 79:1550
86. Sedlák M (2002) J Chem Phys 116:5236, 5246, 5256
87. Liu T, Rulken R, Wegner G, Chu B (1998) Macromolecules 31: 6119
88. Rulken R, Wegner G, Thurn-Albrecht T (1999) Langmuir 15:4022
89. Zaroslov YD, Gordeliy VI, Kuklin AI, Islamov AH, Philippova OE, Khokhlov AR, Wegner G (2002) Macromolecules 35:4466
90. Bockstaller M, Köhler W, Wegner G, Vlassopoulos D, Fytas G (2001) Macromolecules 34:6359
91. Liu T (2002) J Am Chem Soc 124:10942
92. Liu T (2003) J Am Chem Soc 125:312
93. Liu T, Diemann E, Li H, Dress AWM, Müller A (2003) Nature 426:59
94. Liu G, Chai Y, Liu T (2004) J Am Chem Soc 126:16690
95. Ise N (1970) Adv Polym Sci 7:536

4

Colloidal Dispersions

4.1 Introductory Remarks

Colloidal dispersions, in which particles of 1 nm to 10^3 nm diameter are suspended in liquids, were too complicated to investigate experimentally and theoretically in the past. Recently, it became possible to control particle diameter, its distribution, and electric charge numbers of the particles, mainly for polymer latexes or silica particles. Furthermore, the purification technique of the dispersions has been largely improved. Consequently, various interesting phenomena were found and have attracted keen attention of investigators in various fields. It is noteworthy that colloidal particles form in dispersions ordered structures similar to those found in atomic and molecular systems. The elastic constant of colloidal crystals of a particle density of $\sim 10^{13}$ cm^{-3} is about 10 dyne cm^{-2} whereas that of atomic crystals of a density of 10^{22} cm^{-3} is 10^{10} dyne cm^{-2}. There is found a good scaling relationship between the two crystals. From such a fact, colloidal systems are regarded as models of condensed systems, by which directly unobservable phenomena in atomic systems are simulated, albeit with different time scales.

Attention is drawn to the basic difference between atomic systems and colloidal dispersions. The combination of atomic nucleus and electrons corresponds to that of colloidal particles and counterions, but the behavior of the electrons is quantum-mechanical, whereas the motion of the counterions is of thermal origin. The motion of colloidal particles and counterions furthermore is governed by the temperature and viscosity of liquid. Such a basic difference between the two systems is reflected for example in that the lattice constant of atomic crystals is fixed, irrespectively of the concentration, whereas that of colloidal crystals varies with particle concentration, salt concentration, charge density of particles, and so on. We will come back to this topic later.

The investigation of colloidal systems is characterized by the fact that individual particles can be seen by microscope. The pioneering contribution in this respect was done by Zsigmondy. He invented the ultra-microscopic method in 1903 by which particles could be visualized as shining spots in dark

field by utilizing the Tyndall effect [1]. When the refractive index of particles differs largely from that of liquid medium, particles as small as 10 nm, much smaller than the wavelength of visible light, can be seen [2]. No information can be obtained on the shape and surface state of the particles but their location can be known as a function of time by this technique.

Perrin fractionated carefully gamboge particles and determined the Avogadro constant N_A by observing the sedimentation equilibrium, the rotational diffusion, and the Brownian motion of the particles in their aqueous dispersions [3]. By assuming the Einstein theory, the measurements of the rotational diffusion and Brownian motion led him to N_A values of 6.88×10^{23} and 6.50×10^{23}. We won't go into the details of these studies, but we shall discuss here only the sedimentation equilibrium experiments.

When (non-interacting) particles (density:ρ, radius:a) are at the sedimentation equilibrium in a liquid (density:ρ_0), the number of particles at a horizontal plane at a distance H from a reference plane (N_H) is given by

$$N_H = N_0 \exp\left[\frac{-4\pi N_A g a^3(\rho-\rho_0)H}{3RT}\right], \tag{4.1}$$

where N_0 is the number of the particle at the reference plane, g the gravitational acceleration, R the gas constant, and T the temperature. Knowing a, N_A can be determined by measuring N_H and N_0. N_A was 6.82×10^{23}, according to Perrin. It differs from the currently accepted value (6.02×10^{23}) but, considering the distribution of the particle diameter and the purification technique at that time and the neglect of the interparticle interaction in (4.1), the difference is acceptable.

In this chapter, we discuss recent study of several properties of colloidal dispersions. The particles would be electrically charged and spherical. Unless otherwise specified, the medium is light water, heavy water, or their mixtures. Figure 4.1 is an electronmicrograph of colloidal silica particles to be frequently discussed below. The synthetic method of such particles and non-spherical particles has developed remarkably. For details, we refer the readers to a monograph by Fitch [4].

Most frequently employed are polystyrene (PS)-based latex particles. They are synthesized by emulsion-polymerization of styrene (S) dispersed in water with potassium persulfate as initiator. The number of electric charges on the particles can be increased by addition of styrene sulfonate (SS-H). The advantage of PS-based latexes is that the particle radius a and the net charge number (Z_n) can be relatively easily controlled and the product particles have a narrow size distribution (monodisperse). In the case of copolymers of S and SS-H, it is believed that the affinity toward water favors SS-H gathering on the surface of the particles. Thus, one can assume the particle surface to be covered by sulfonate groups. When dispersed in dissociating solvent, ionic dissociation takes place as shown in Fig. 4.2. The short-range repulsion due to the particle charges can keep gigantic particles without aggregation in dispersions.

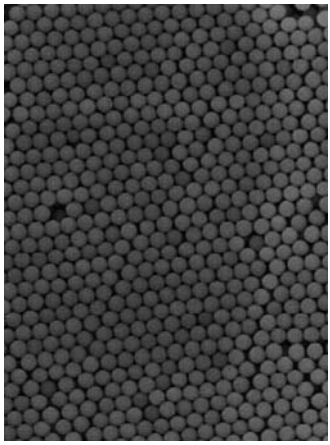

Fig. 4.1. Electron micrograph of monodisperse colloidal silica particles. 15 kV × 3,000X, Producer: PCR Co. Ltd, USA. $a = 0.5$mm. The powder sample was dispersed in water and purified. Then the particles were cast on a glass plate, kept at 60°C for 1 h, and photographed. This picture provides information of the shape, size and its distribution. At the same time, it shows how homogeneously and regularly the monodisperse particles are distributed at large volume fractions. The picture corresponds to high volume fractions ϕ such as 0.74 for fcc and 0.68 for bcc. Under these concentrated conditions, the interparticle distance $2D_{\rm exp}$ is very close to the average interparticle distance $2D_0$ that can be calculated from concentration by assuming a uniform distribution, and the structure formed can be accounted in terms of the interparticle repulsion exclusively. The concentration range to be considered in this chapter is $\phi < 0.1$, so that the particle distribution is far from the closest packing. At such low concentrations, the structure is non-space-filling as shown in Figs. 3.22 and 4.12, and $2D_{\rm exp} < 2D_0$. It is difficult to account for the non-space-filling systems in terms of the interparticle repulsion only; A long-range attraction between particles is one of the simplest interpretations. Photographed by Messrs. H. Nishino and F. Uchida, Fuji Chemical Co. Ltd.

4.1.1 Charge Number of Colloidal Particles

As was the case with flexible ionic polymers, the association of counterions with the colloidal particles results in the situation that the analytical charge number $Z_{\rm a}$ giving the total number of ionizable groups (and hence the corresponding surface charge density $\sigma_{\rm a}$) is largely different from the net charge number $Z_{\rm n}$ (and $\sigma_{\rm n}$). Ito et al. determined $Z_{\rm a}$ by conductivity measurement for polystyrene-based latex particles with protons as counterions and estimated the fraction of unbound (free) counterions f and $Z_{\rm n}$ by using the method of Wall discussed in Chap. 3, Sect. 3.1.1 [5] [1]. The results are shown in Table 4.1.

[1] The following assumptions were made to estimate f and the transference number $t_{2\rm p}$. The velocity of solvent is zero, and the difference in the specific conductivi-

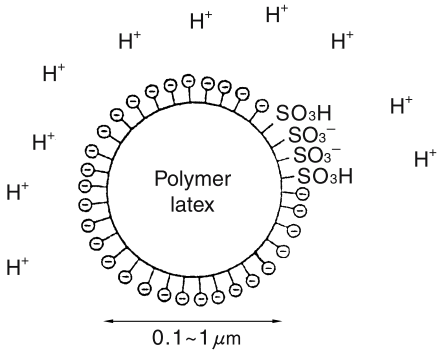

Fig. 4.2. Dissociation of charged latex particles of styrene-styrene sulfonate copolymers. The styrene component is in the interior of the sphere and styrene sulfonate component is on the surface. In a dissociating liquid, the sulfonate groups dissociate into macroions and their counterions.

The f value for latexes (0.1∼0.03) is much smaller than those for flexible ionic polymers (compare with Table 3.1) and tends to decrease with increasing σ_a. The transference number t_{2p} is smaller than 0.1, being smaller than that for flexible ionic polymers (∼0.5), showing the large hydrodynamic resistance of the particles.

Table 4.1 shows also theoretical f values obtained by Alexander et al [6]. According to this theory, the Z_n value is given by $15a/Q$ (a:particle radius, Q:Bejerrum length, See Chap. 3, footnote 5). The agreement with observation is satisfactory for a low-charge sample such as SS-36 but not so for high-charge ones (SS-39 and #1).

Very often the charged state of colloidal particles is discussed by ζ potentials of the particles. As shown in Fig. 4.3, this potential is defined as that on the slipping plane of the liquid medium on the particle surface. In Table 4.1, observed ζ potential is given. The correlation between Z_n and ζ is not clear from this table. For example, the magnitude of Z_n of SS-39 is about ten times larger than that of SS-36, whereas the ζ value of the former is slightly higher than that of the latter. Ito et al. were the first to evaluate Z_n by measuring f and t_{2p} and compare with ζ potential. Though we need more systematic comparison, it is rather difficult to admit the quantitative significance of the ζ potential, and to directly correlate ζ potential and Z_n because the distance

ties of dispersions and medium is attributed to the contribution of particles and free counterions. The specific conductivity is assumed to the equivalent ionic conductivity at infinite dilution, which is permissible at low concentrations usually employed. These assumptions are for protons as counterions and the t_{2p} values obtained is due to the Grotthus mechanism of the protons. For other counterions such as Na^+, t_{2p} is usually around 0.5.

Table 4.1. Dissociation state of polystyrene-based latex particles [a]

ϕ	f [b]	t_{2p}	Z_n	σ_n / μC cm^{-2}
(A) SS-36 (a=65 nm, Z_a=1.5×10^4 , σ_a=4.6 μC cm^{-2}, ζ [c]: −72∼ − 137 mV)				
0.012	0.13 [0.09]	0.09	1.95×10^3	0.58
0.028	0.12	0.10	1.80×10^3	0.54
0.055	0.14	0.13	2.10×10^3	0.64
(B) SS-39 (a=175 nm, Z_a=2.6 × 10^5 , σ_a=10.6 μC cm^{-2}, ζ [c]: −43∼ − 49 mV)				
0.015	0.08[0.01]	0.05	2.08×10^4	0.85
0.049	0.07	0.07	1.82×10^4	0.74
0.075	0.08	0.06	2.08×10^4	0.85
(C) #1 (a =38 nm, Z_a= 7.2×10^5 , σ_a=650 μC cm^{-2}, ζ [c]: −55∼ − 83 mV)				
0.0011	0.04[0.001]	0.05	2.9×10^4	26
0.0018	0.04	0.07	2.9×10^4	26
0.0023	0.04	0.10	2.9×10^4	26
0.0041	0.03	0.09	2.2×10^4	20

[a] The samples (A) and (B) are copolymers of styrene and styrene sulfonate and are believed to have the charges on the particle surface. (C) is prepared by sulfonation of polystyrene spheres with SO_3, and the charges are inside of the sphere and on the surface. Thus the surface charge density per unit surface is not important.
[b] The value in [ ] is due to Alexander et al.'s theory [6].
[c] Obtained by using a theory of Wiersema et al. [7] from the mobility found by electrophoresis at $\phi = 10^{-5}$.

between the slipping plane and particle surface cannot experimentally be determined, as Fitch pointed out [8].

The results above are for protons as counterions. No information is available for other counterions except Na^+. Ito et al. [5] measured f values for Na^+ salts of Latex #1 in the ϕ range between 3.3×10^{-3} and 9×10^{-4}. The f values observed are 0.06∼0.04, being about the same as for protons. However, the t_{2p} is 0.70∼0.60, larger than that for protons, reflecting the difference in the conduction mechanism.

The charges of colloidal silica particles come from the dissociation of weakly acidic silanol groups on the surface. Availing of this fact, Yamanaka et al. controlled the surface charge by adjusting pH [9]. This enables one to vary the charge number without greatly changing the particle size. They discussed about a simple method to determine Z_a and Z_n (and hence σ_a and σ_n) by using conductometric titration and conductivity measurements as follows.

When a sodium hydroxide solution is added to a dispersion of silica particles (a = 60 nm, σ_n = 0.08 μC cm^{-2}) in the acid form ($\phi < 2.6 \times 10^{-3}$), the analytical charge density σ_a increases with increasing [NaOH] ($< 2.5 \times 10^{-4}$ mol L^{-1}) according to the following relation

$$\sigma_a = \frac{10^{-3}}{3\phi} N_A e a [\mathrm{NaOH}] \tag{4.2}$$

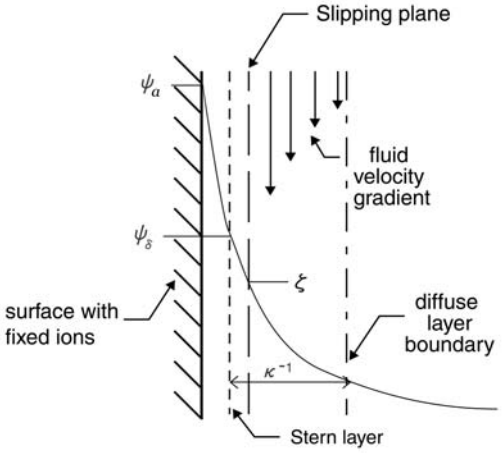

Fig. 4.3. Electric double layer around a charged particle in flowing medium. The particle should have a surface potential ψ_a due to its charges. The counterions are concentrated in the vicinity of the particle surface, some of them neutralize the particle charges, reducing the surface potential to ψ_a and others lower the potential near the surface. Reproduced with permission of Academic Press from [4]

where e is the elementary charge in coulomb (C), and a is the radius in cm. The total electric conductivity of the dispersion κ is composed of the contributions of (univalent) counterions, particles, and solvent (excess ions), so that

$$\kappa = 10^{-3} \left(\lambda_{\mathrm{c}} C_{\mathrm{c}} + \lambda_{\mathrm{p}} C_{\mathrm{p}}\right) + \kappa_{\mathrm{b}} \tag{4.3}$$

where λ is the equivalent conductivity, the suffixes c and p are counterions and particles, respectively, C_{c} and C_{p} are the concentrations of counterions and particles (mol L^{-1}), and κ_{b} is the solvent conductivity. The difference between the conductivities of Na^+ and K^+ salts gives C_{c} because the degree of association can be assumed to be the same for the two counterions as follows

$$\kappa_{\mathrm{Na}^+} - \kappa_{\mathrm{K}^+} = 10^{-3} \left(\lambda_{\mathrm{Na}^+} - \lambda_{\mathrm{K}^+}\right) C_{\mathrm{c}} \tag{4.4}$$

where λ_{Na^+} and λ_{K^+} are the equivalent conductance of the respective ions (50.1 and 73.5 S cm mol^{-1} for water at 25°C). The σ_{n} is given by

$$\sigma_{\mathrm{n}} = \frac{10^{-3}}{3\phi} N_{\mathrm{A}} e a C_{\mathrm{c}} \tag{4.5}$$

and the transference number $t_{2\mathrm{p}} (= \lambda_{\mathrm{p}} C_{\mathrm{p}} / (\lambda_{\mathrm{c}} C_{\mathrm{c}} + \lambda_{\mathrm{p}} C_{\mathrm{p}}))$ can be calculated, which is found to be ϕ-independent in the ϕ range between 0.01 and 0.03 and about 0.50 for Na-form silica particles.

The observed σ_{n} is plotted against σ_{a} in Fig. 4.4 [10]. Figure 4.4 (a) tells that the linear relation $\sigma_{\mathrm{n}} = \sigma_{\mathrm{a}}$ deviates largely from the observation, reflecting the striking counterion association. The renormalized charge number σ^*

obtained by Alexander et al.'s theory agrees with experimental values only at low charge condition but the deviation for high charge samples is clear. The straight line in Fig. 4.4 (b) is the following relation with C_1 and C_2 being 0.51 and -1.0,

$$\ln \sigma_{\rm n} = C_1 \ln \sigma_{\rm a} + C_2 \tag{4.6}$$

The $\sigma_{\rm n}/\sigma_{\rm a}$ values ($= f$) at $\sigma_{\rm a} = 0.3$ and 8 μC cm^{-2} are 0.63 and 0.13, respectively. The f is 0.16 for $\sigma_{\rm a} = 4.6$ μC cm^{-2} and is in agreement with that (0.12∼0.14) for SS-36 ($\sigma_{\rm a} = 4.6$ μC cm^{-2}) in Table 4.1. In light of the simplicity of this method, it is hoped that systematic study is carried out for other samples of various sizes and charge densities.

The $\sigma_{\rm n}$ is found insensitive toward the volume fraction ϕ and salt concentration $C_{\rm s}$ for a latex particle ($a = 60$ nm, $\sigma_{\rm a} = 5.64$ μC cm^{-2}), for $\phi < 3 \times 10^{-2}$ and $C_{\rm s} < 8 \times 10^{-5}$ mol L^{-1}) [10].

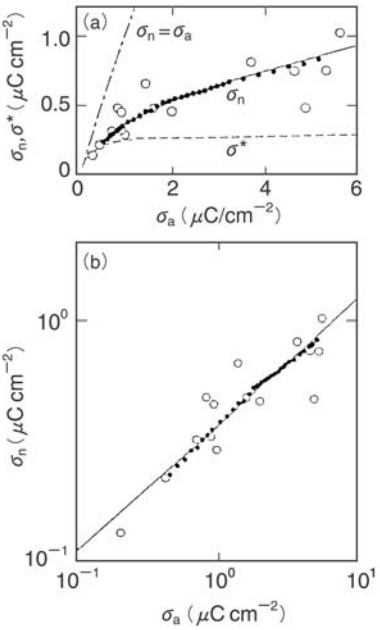

Fig. 4.4. The analytical and net charge densities ($\sigma_{\rm a}$ and $\sigma_{\rm n}$) in salt-free dispersions. •: silica particle ($a = 60$ nm) at $\phi = 0.02$. ∘: latex particles ($a = 40 \sim 300$ nm). (a) and (b): linear and double logarithmic plots, respectively. The dashed curve in (a) denotes the renormalized charge σ^* by Alexander et al.'s theory. The line $\sigma_{\rm a} = \sigma_{\rm n}$ is given for reference but clearly deviates from observation. Taken from [10] with the permission of the American Chemical Society

The main interaction in ionic systems, not only colloidal dispersions but also simple and polymeric solutions, is of electrostatic origin. It is proportional

to the product of the charge numbers and is of long-range nature. Therefore, to correctly evaluate the charge number of solute species is indispensable. On the other hand, there appear to exist three different perspectives regarding to the colloidal charge number. First colloidal phenomena are discussed in terms of Z_a (or σ_a), which arises from chemistry of the particle synthesis, secondly they are discussed in terms of a theoretical framework using Z_a and then, if disagreement with the theory is found, an net charge number Z_n is introduced to rescale Z_a in such a way that reasonable agreement with observation is reached. Third, the Z_n is determined by independent measurements such as conductivity and transference measurements. The first is not realistic in that strong counterion association due to quite high electric charges of the particles is ignored. The second view is often found in computer simulation work and the concept of renormalized charge is its example. This approach may be rationalized if the underlying theory is correct. Usually, in the colloid field, arguments are developed on the premise that the Derjaguin-Landau-Verwey-Overbeek (DLVO) theory [11, 12] is correct. Whether this premise is definitely correct cannot be judged unless the renormalized charge number is justified by comparing it with independent measurements. In most cases, the comparison with experiments is not done. The third perspective is seen in the determination of Z_n by transference and conductivity measurements. Although not many reports have been documented, the rather simple measurements are based on a minimum number of reasonable assumptions and can provide reliable data.

Yamanaka et al. adopted this method to determine σ_a and σ_n for particles of various diameters [13]. It is found that, at a given σ_a, σ_n increases with decreasing radius and approaches to the relation $\sigma_a = \sigma_n$, which is valid for simple electrolytes. The results are shown in Fig. 4.5. The observed size dependence of σ_n is due to weaker counterion association resulting from smaller Z_a with decreasing size at a given σ_a.

4.1.2 Purification of Colloidal Dispersions

The interaction between colloidal particles is highly sensitive toward coexisting salt level in the dispersions, as will be shown in subsequent sections. For example, the particles show Brownian diffusion when the ionic concentration is above 10^{-4} mol L^{-1} (for 1-1 salts). Below this concentration, the particles form ordered structures. Therefore, it is indispensable to remove the ionic impurities as much as possible, if reliable results are to be sought. Microscopic investigation of colloidal dispersions have revealed various phenomena, which have not been anticipated for condensed matter. In order to claim the reliability of these unusual observations, we see it fit to discuss the purification method here in detail.

The purification is done essentially by dialysis, and ion-exchange, and more recently ultra-filtration. It varies from particle to particle and with particle size, and a better method has always been sought by trial and error so that

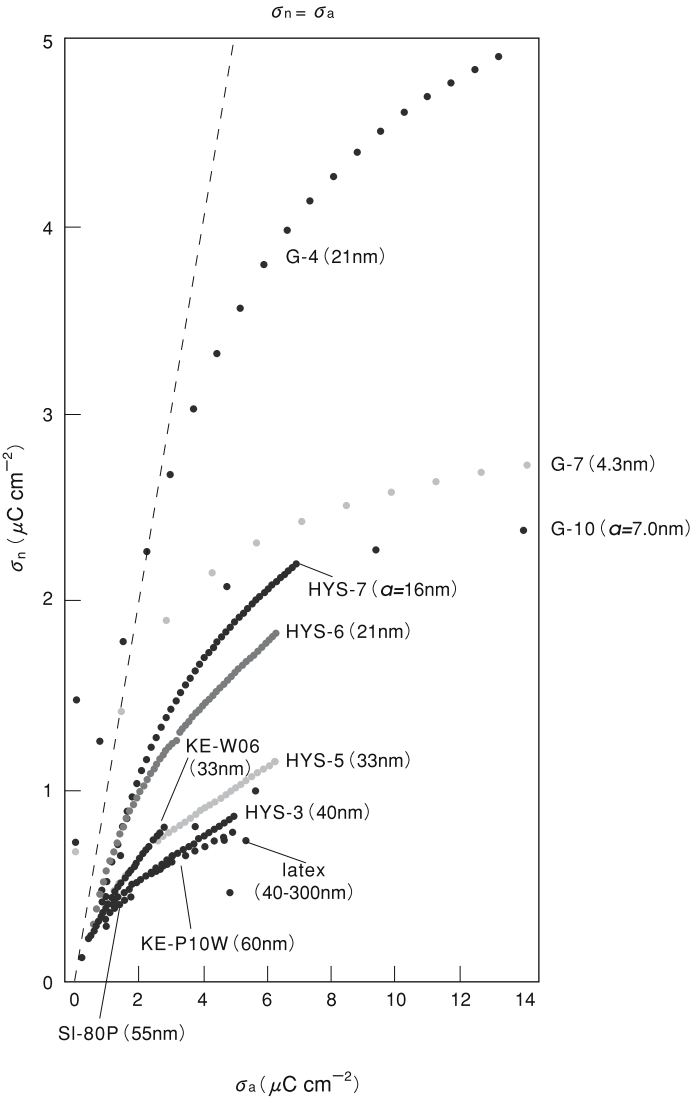

Fig. 4.5. The net charge density σ_n of various ionic species as a function of particle radius. KE: silica particle (Nippon Shokubai), HYS: prepared by Yamanaka et al. by the Stöber method, G: ionic dendrimers. Taken from an unpublished work by Yamanaka et al. [13]

detailed procedures adopted changes with time. We discuss first the method for latex particles [14–18]. Latex dispersions are washed by ultra-filtration with Milli-Q water using an Amicon Model 202 and DiafloXM300. When necessary, the Milli-Q water is irradiated by ultra-violet rays for disinfection [19]. Its electric conductivity is 0.4∼0.6 μS cm^{-1}. The washing is repeated until the filtrate stops showing ultraviolet adsorption at 220∼420 nm (due to styrene monomer) and its electric conductivity becomes time-independent. Then carefully purified ion-exchange resin particles are put into the dispersions for further purification. When the ordered structure is formed, the ion-exchange resin particles (density $\rho = 1.2 \sim 1.4$ g cm^{-3}) do not sediment down to the container bottom of the dispersion ($\rho \simeq 1.0$ g cm^{-3}) but are kept floating in dispersions after shaking. This is due to trapping of the large ion-exchange resin particles by the 3D-structure of colloidal crystal (lattice constant $\ll$ resin particle diameter) [20].

Colloidal silica dispersions are dialyzed against pure water. The extent of purification is judged by conductivity measurement of the dialysate. Then ion-exchange resin particles are introduced into the dispersion.

To avoid ionic impurities from glass walls, when necessary, polyethylene and polypropylene apparatus are used in sample preparation.

Besides the ionic impurities, possible contamination of polymeric substances should be avoided, in order to prevent the so-called depletion effect discussed in Chap. 3. If homopolymerizations have taken place, for example, in the case of the latexes of styrene-styrene sulfonate copolymers, the homopolymers produced are polystyrene and poly(styrene sulfonate). The former is water-insoluble and cannot stay in water media. The latter is water-soluble and can be detected by ultraviolet absorption in the purification process. As for silica particles, the monomer is tetra-functional silicate or alkoxide of silicic acid. It is difficult for them to grow into a linear polymer. Thus as far as these particles are concerned, we can state that contamination by these homopolymers and the depletion effect thereby is highly implausible [2].

[2] Recently, Belloni et al. adopted latex particles of copolymers of styrene (S)-butyl acrylate (BA) covered with acrylic acid (AA) sequences linked to the core polymers, and reported that their water dispersions showed higher osmotic pressures than a theoretical prediction. This result was attributed to polymeric substances leaching out from the particles. (Bonnet-Gonnet C, Belloni L, Cabane B (1994) Langmuir 10:4012) Based on this result, they argued that an attraction between particles appeared due to depletion effect and our claim of the existence of an interparticle electrostatic attraction was in error. (Belloni L, (2000) J. Phys. Condens. Matter 12:R549)) Since a very high AA content was used in their work, it might be true that homo- or copolymers of AA were produced in the preparation of their particles. Thus, as far as such a latex is used, as Belloni stated, there is definitely a possibility that the homopolymers can contribute largely to the osmotic pressure though they cannot optically be detected, do not contribute to any scattered intensity and are not small enough to across a dialysis membrane. Belloni et al.'s concern is reasonable to their own dispersions. Anticipating this

The dispersions thus purified are introduced into containers (quartz cuvette, capillary, etc.). It is advisable to introduce ion-exchange resin particles in such a way as not to interfere with measurements, to continuously remove ionic impurities during measurements.

4.2 Investigation by Optical Methods

4.2.1 Sedimentation Equilibrium of Free Particles

As stated above, Perrin determined the Avogadro constant by sedimentation equilibrium experiments. His work is of historical importance but its significance has not been fully appreciated in colloid field. This point is closely related to the problem of interparticle interaction, so that we discuss here sedimentation equilibrium experiment, though it is a rather classical topic.

Colloidal phenomena have been customarily interpreted in terms of the DLVO theory [11, 12]. As discussed in Chap. 2, this theoretical framework shows that electrically charged particles repel each other by the electrostatic interaction and attract each other by van der Waals interaction introduced in an ad hoc manner. Since the interparticle distance is of the order of μm, the van der Waals interaction may be ignored so that only the repulsion remains. This argument appears to be acceptable at high concentrations, but it is not so in dilute regions according to our observation. A rationale of this repulsion-only assumption is Alder's simulation [21], by which the equation of state for many-particle systems was derived by assuming purely repulsive hard-sphere potential. The following phases were found [22]:

$\phi < 0.5$: liquid
$0.5 < \phi < 0.55$: coexistence of liquid and crystal
$\phi > 0.55$: crystal

It is interesting that the hard-sphere potential led to the phase transition. However, experimental observation for latex dispersions show that the phase transition is highly sensitive toward coexisting salt concentration C_s and the liquid-crystal transition point is at $\phi \sim 0.05$ for $C_s = 10^{-5}$ mol L^{-1} [23], which

danger in advance, we avoided such an unreliable latex system and employed colloidal systems, namely, styrene-styrene sulfonate (SS) copolymer latexes in most cases, in which released homopolymers, if any, can be detected by adsorption and conductivity measurements. Belloni's criticism against our attraction is thus totally ungrounded. Most ironically, moreover, their measurements of a SS latex showed osmotic pressure in good agreement with the prediction. This indicates that the SS latex was not contaminated by water-soluble polymers according to their way of reasoning. However, we don't claim the legitimacy of our measurements and of the counterion-mediated attraction using the results of Belloni's SS latex.

is one order of magnitude lower than Alder's prediction. Taking the repulsion-only assumption for granted, Wadati and Toda introduced the concept of an effective hard-sphere of a radius a_{D}, which is

$$a_{\mathrm{D}} = a + \kappa^{-1} \tag{4.7}$$

where a is the hard-sphere radius and κ^{-1} is the Debye length [24] [3]. Since κ^{-1} increases with decreasing C_{s}, the ϕ - dependence of the transition point can qualitatively be accounted for by invoking a_{D}. Thus, it was claimed that the phase transition in colloidal systems was not due to attraction but an Alder transition of "effective hard-sphere" interacting each other by purely repulsive forces.

If this idea is generally correct, however, it should hold also for phenomena other than the phase transition in question. On the other hand, Perrin obtained a reasonable value for the Avogadro constant by using the particle radius estimated by microscope. If a_{D} were instead introduced, physically unacceptable results must have been obtained. The κ^{-1} concept was proposed by Debye and Hückel in 1923 [25] so that no information was provided to estimate κ^{-1} in Perrin's paper. Thus the sedimentation equilibrium was restudied with well-characterized latex particle dispersions [26]. The results are shown in Table 4.2. The a^* value obtained by (4.1) from the observed number of particles N_{H} in the plane at a height H by using $N_{\mathrm{A}} = 6.02 \times 10^{23}$ is slightly smaller than the a value obtained by electron microscopy and stays constant in the C_{s} range covered, as it should. The effective radius $(a + \kappa^{-1})$ decreases with increasing C_{s} and correspondingly the apparent Avogadro constant ${N_{\mathrm{A}}}^*$ increases to N_{A}. Needless to say, this C_{s} dependence of the Avogadro constant cannot be accepted. Likewise the concept of the effective hard-sphere radius cannot be admitted.

It has been often claimed that, besides the sedimentation equilibrium, various colloidal phenomena can satisfactorily be accounted for by introducing the effective radius or Debye length. In light of the physical absurdity of the argument, no further discussion is given on this effective sphere concept in this monograph.

As carefully noted by Alder and Wainwright [22], the purely repulsive potential was assumed so as to make no approximations in the calculation, not because it is realistic. They stated that realistic potentials would entail a considerable slowing down of the calculation. Recent technical developments made it possible to carry out simulation work with realistic potentials [27,28], which will be considered in Chap. 8 [4].

[3] In [24], a constant α was introduced as a coefficient of κ^{-1}.

[4] Recently, Suzuki pointed out the possibility that, in the Alder simulation, the boundary happened to act as the source of an attraction, causing apparently the transition, as the result of the high number densities. [Suzuki M (2000) Statistical mechanics, Iwanami Shoten, Tokyo, p 161. The English version will be published by Springer, Berlin Heidelberg New York.]

Table 4.2. Sedimentation equilibrium experiments for polymer latex particles [a] in NaCl-H_2O solutions at 25°C and the Avogadro constant

[NaCl] mol L^{-1}	a^* [b] nm	κ^{-1} nm	$(a+\kappa^{-1})$ [c] nm	$N_A^* \times 10^{-23}$ [d]
0	430	170	650	1.9
10^{-6}	430	130	610	2.3
10^{-5}	420	80	560	2.9
10^{-4}	430	30	510	3.9
10^{-3}	440	10	490	4.4

[a] $\sigma_a = 6.4$ μC cm^{-2}, $\phi = 10^{-4}$.
[b] a^*: particle radius obtained from the experiments by (4.1) with $N_A = 6.02 \times 10^{23}$.
[c] a: particle radius determined by electron micrograph (480 nm).
[d] $N_A{}^*$: apparent Avogadro constant obtained by (4.1) with the effective particle radius $(a + \kappa^{-1})$.

4.2.2 Brownian Motion of Free Particles

This theme was studied by Perrin. It was demonstrated that the particle motion could be described by Einstein's theory of Brownian motion [29] by using a determined by micrograph, not by a_D (4.7).

In recent studies, Ito et al. video-recorded the particle motion at $\phi < 0.01$ and at C_s of $10^{-2} \sim 10^{-4}$ mol L^{-1} and determined the root-mean-square-displacement $\langle x^2 \rangle^{1/2}$ by image data analyzer [17, 30]. When $\phi < 10^{-4}$, the Einstein theory was valid in this C_s range and the dependencies of $\langle x^2 \rangle^{1/2}$ on temperature and solvent viscosity (studied by addition of sucrose) were in quantitative agreement with the theory. When $\phi > 10^{-4}$, particularly at low C_s's, however, the deviation from the theory was obvious due to the particle charges.

4.2.3 Colloidal Crystals

When ionic impurity level is lowered, in other words at low C_s, monodisperse colloidal particles form crystal-like structure, which was carefully studied by diffraction of light by Luck [31]. For dried polymer latex samples [32] and later for dispersions of low ϕ's, iridescence was reported (For iridescence, see Fig. 4.6). This color was found to be due to the Bragg diffraction of visible light. Though the structure formation was believed to be true, it was Hachisu et al. who made doubly sure of it by visualization using ultra-microscope technique [33]. Figure 4.7 is a micrograph (confocal laser scanning microscope) of ordered structure obtained at a relatively low particle concentration.

Figure 4.7 shows the particle distribution in the horizontal focal plane. It is possible to observe particles in the vertical plane by adjusting the microscope configuration [16]. Important is that, both in the horizontal and vertical planes, the closest-packed plane, namely (110) plane and (111) plane for bcc

and fcc, was observed, ruling out the possibility that the plane was formed as a result of gravitational sedimentation.

Lattice Vibration, Lattice Plane Vibration, Lattice Defects

The lattice vibration in colloidal crystals was studied by Ito et al. using video-recording and an image data analyzer [17]. The positions of particles in 8.3 s are shown in Fig. 4.8. The corresponding trajectory of the particle centers is reproduced in Fig. 4.9. Clearly, the interparticle distance and the amplitude become larger with decreasing ϕ, in contrast with atomic crystals. The vibration is isotropic.

The trajectories of six neighboring particles on a lattice plane are displayed in Fig. 4.10 (a). By decomposing the trajectory into x and y directions, the displacement-time curve is obtained (Fig. 4.10 (b)). This curve is seen to have analogous shape and phase for the particles 1, 2, and 3, indicating that the motion of the lattice planes is somehow correlated to each other up to about 3 μm [34].

The above statements are for almost perfect crystals. In reality, particularly at low ϕ regions, such a perfect crystal cannot be expected. For example, lattice defects such as Schottky defects and edge-dislocations are frequently observed. Figure 4.11 shows the vibration of particles next to a point defect. The distribution of particle centers is not homogeneous, unlike that in the perfect crystal (Fig. 4.9). Because of the absence of a particle in the defect, the restoring forces in the direction to the defect are weaker than in other directions, as was assumed in Einstein's model for the calculation of the entropy change due to lattice defect [35].

Two-State Structure: Interparticle Attraction

It is easily accepted that the whole volume of dispersions will be covered by ordered structure when ϕ is very large. One of the extreme cases was shown in Fig. 4.1. Obviously, such a *space-filling* structure is caused by the exclusion volume of particles, namely repulsion. However, when ϕ is decreased to about 0.02, *non-space-filling* ordered structures (solid or crystal) are seen to coexist with free particles (liquid), which is called "two-state structure". Such a microscopic inhomogeneity was first confirmed in latex dispersions under the metallurgical microscope [36], and later the trajectory analysis of the particles [17] revealed the essential aspect of the two-state structure. Figure 4.12 shows the result. The distinction between particles in liquid and crystal states is very clear from the differences in their thermal motion. The motion of the free particles is enhanced to such an extent that the lattice vibration shown in Fig. 4.9 is almost indiscernible in comparison to the free particle motion. Another important point is the difference in the number densities of particles in the two states. Obviously from the figure, the density in the crystal domain is higher than that in liquid. This implies that the nearest interparticle

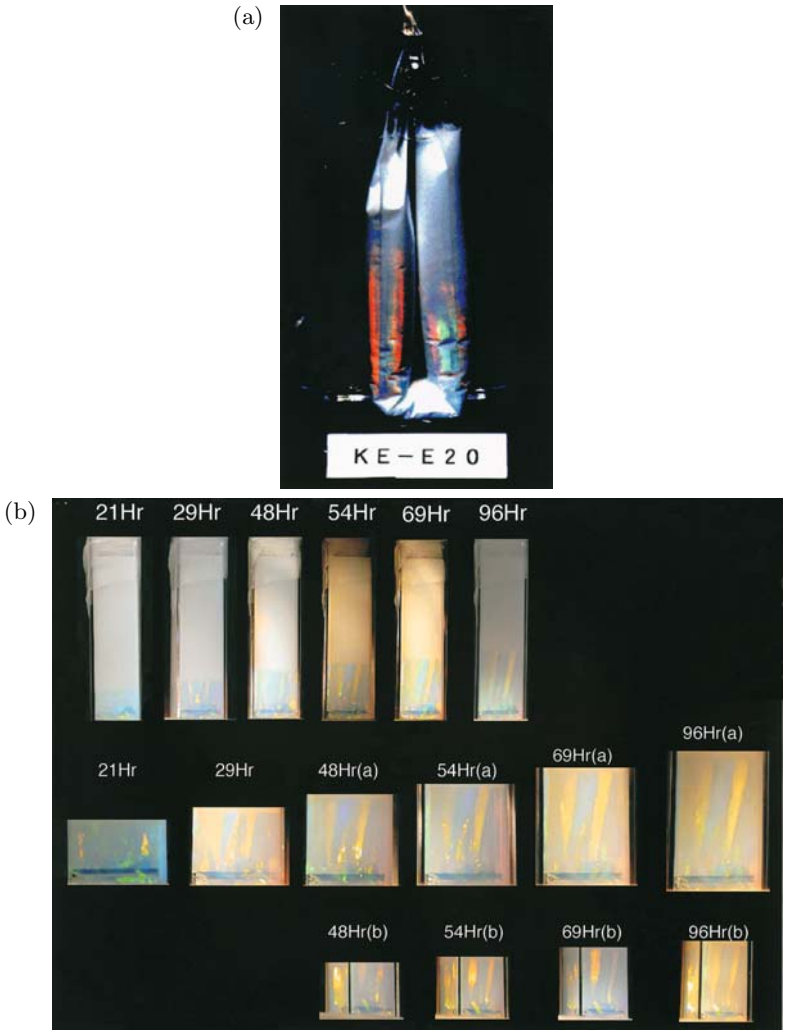

Fig. 4.6. (a) Iridescence of a colloidal silica dispersion during purification by dialysis. Sample: KE-E20 ($a = 100$ nm), Nihon Shokubai Co. Ltd. At the early stage of purification the dispersion is white and turbid, in which silica particles show Brownian motion. When impurity ions are removed by dialysis, the particles spontaneously form ordered structures in dispersion, which diffract visible light by Bragg law to show iridescence. (By courtesy of Professor J. Yamanaka, Nagoya City University). (b) Pillar-type colloidal crystals of silica particles. Sample: KE-P10W ($a = 60$ nm, $\phi = 0.03$), Nihon Shokubai Co. Ltd. The time change of the appearance of a dispersion container ($10 \times 10 \times 40$ mm) is photographed from three directions. The weakly iridescent pillar is seen to be 2 cm high after 96 h. (Yamanaka J, Murai M, Iwayama Y, Yonese M, Ito K, Sawada T (2004) J Am Chem Soc 126:7156) Similar crystals are also reported for different sillica samples (Shinohara T, Yamada H, Sogami IS, Ise N, Yoshiyama T (2004) Langmuir 20:5141)

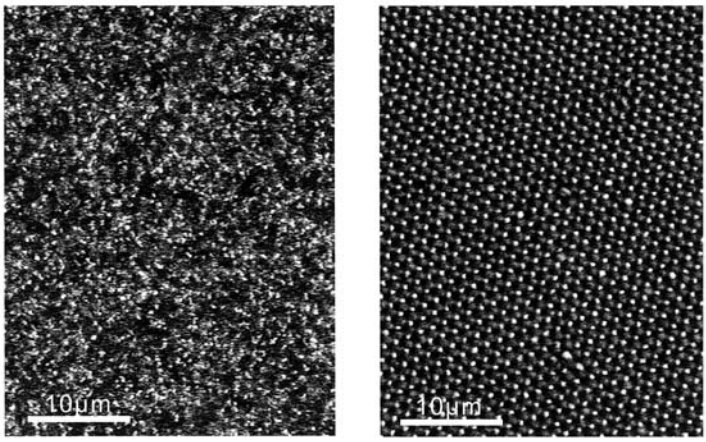

Fig. 4.7. A micrograph showing the ordered structure of polystyrene latex particles, $a = 150$ nm, $\sigma_a = 1.3$ μC cm^{-2}, $\phi = 5 \times 10^{-3}$, $C_s = 0$, taken by a confocal laser scanning microscope (LSM410, Carl-Zeiss). The picture (a) shows particles in motion just after violently shaking, whereas (b) shows the ordered arrangement. An edge dislocation is seen. At such a low concentration, the ordered structure does not necessarily cover the entire volume of dispersion. By courtesy of Dr. Hiroshi Yoshida (Hitachi Laboratory)

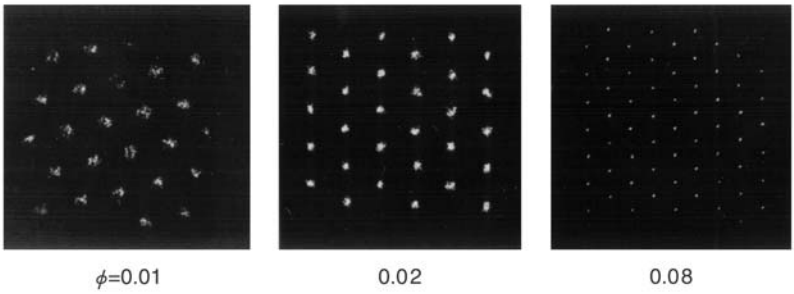

Fig. 4.8. Lattice vibration of latex particles in colloidal crystal. Sample: polystyrene-based latex ($a = 200$ nm, $\sigma_a = 6.9$ μC cm^{-2}), at rt. The particle motion over a period of 8.3 s was video-taped and the particle centers at every 1/30 s were reproduced on one frame. The interparticle distances $2D_{exp}$ are 730, 1070, and 1080 nm at $\phi = 0.08$, 0.02, and 0.01, respectively, and the lattice vibration is seen to be greater with decreasing ϕ. Taken from [17] with the permission of the American Chemical Society

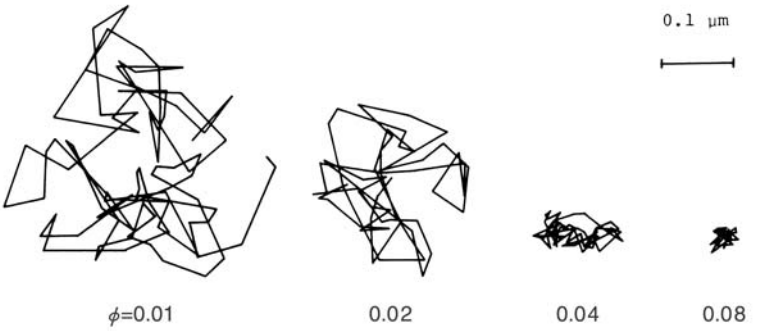

Fig. 4.9. Trajectory of particles in the lattice vibration. The experimental conditions are the same as in Fig. 4.8. For 0.01 and 0.02, 90 centers in 3 s are connected with staight lines whereas 60 centers in 2 s are shown for the higher concentrations. Taken from [17] with the permission of the American Chemical Society

distance $2D_{\text{exp}}$ in the crystal regions is smaller than the average spacing $2D_0$ calculated from the particle concentration assuming a uniform distribution. The inequality relation $2D_{\text{exp}} < 2D_0$ has been found also for dilute solutions of flexible and globular polyelectrolytes (See Chap. 3, Sect. 3.2). Furthermore, it is to be noted that there is no stable, fixed boundary between the two states. Though not clear in Fig. 4.12, we can observe that particles in the boundary region "evaporate" from and "condense" into crystal regions. The fact that a higher number density of particles can locally be maintained without a fixed interface indicates the existence of interparticle attraction, according to our interpretation.

The inhomogeneity shown in Fig. 4.12 implies that at least two diffusion constants may be observed from macroscopically homogeneous dispersions (See Chap. 3, Sect. 3.2.2).

Apart from the cause, the finding of such a microscopic inhomogeneity in macroscopically isotropic dispersions had not been accepted easily. Thus it had been regarded as "experimental artifact" but, 14 years after the first report [36] Larsen and Grier published a similar micrograph and trajectories [37].

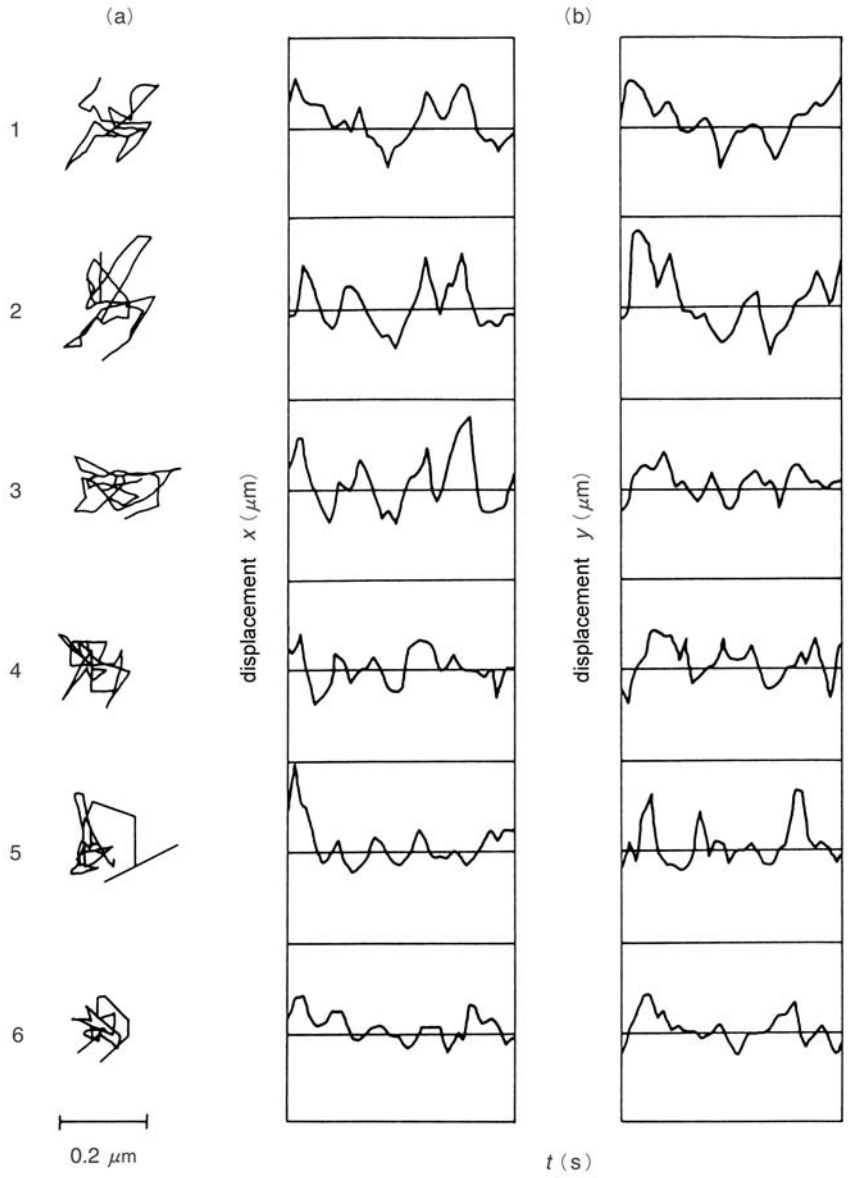

Fig. 4.10. Interparticle correlation in the lattice vibration. Sample:polystyrene-based latex particle (a = 200 nm, σ_a = 6.9 μC cm^{-2}), $\phi = 5 \times 10^{-3}$, at rt, interparticle distance: about 1 μm. (a) trajectory in 1 s. (b) displacement-time curve in x and y directions. The scale bar is for trajectory (a) and for displacements (b). Taken from [34] with the permission of the Royal Society of Chemistry

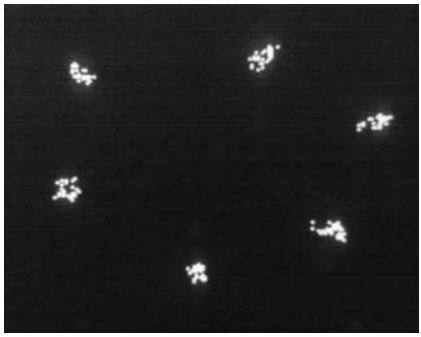

Fig. 4.11. Lattice vibration of particles neighboring a Schottky defect. Sample: polystyrene-based latex particle ($a = 250$ nm, $\sigma_a = 13.3$ μC cm^{-2}), $\phi = 10^{-2}$, at rt, time: 1 s, interparticle distance: about 1 μm. Taken from [34] with the permission of the Royal Society of Chemistry

Fig. 4.12. Trajectory of particles in the two-state structure. Sample: polystyrene-based latex particle ($a = 150$ nm, $\sigma_a = 1.3$ μC cm^{-2}), $\phi = 2 \times 10^{-2}$, at rt. The particle centers in about 20 consecutive frames in 11/15 s are reproduced in a new frame and connected by straight lines. The particle positions at the starting time colored green and those after 11/15 s yellow. The upper half shows free particles whereas the lower half the ordered particles with the interparticle distance of about 1 μm. The white lines without either green or yellow ends or both indicate the out-of-plane movement of the particles. Taken from [17] with the permission of the American Chemical Society

The Closest Interparticle Distance $2D_{exp}$: Dependences on the Particle Concentration, Charge Density, Salt Concentration, Dielectric Constant, and Temperature. Comparison with the Average Distance $2D_0$

A value of $2D_{exp}$ was determined from a single broad scattering peak by assuming the Bragg equation for flexible ionic polymers as mentioned in Chap. 3. On the other hand, this quantity for colloidal systems can be determined directly from micrographs. Thus studying $2D_{exp}$ in comparison with $2D_0$ for colloidal dispersions is meaningful in evaluating the reliability of the information on flexible polymers.

It was 1983 when the relation $2D_{exp} < 2D_0$ was found by microscopy [36] [5]. At that time, the spacing was estimated "manually" for a few pairs of particles and therefore the information was not as reliable as that derived for a large population by image-data-analyzer. However, the earlier results suggest important points and thus are shown in Table 4.3. Clearly, the $2D_{exp}$ decreases with increasing ϕ. Further, the sample (B) having a larger σ_a than (A) shows smaller $2D_{exp}/2D_0$. This trend indicates that the interparticle attraction becomes stronger with increasing σ_a, suggesting that it is the counterion-mediated attraction as discussed in Chap. 3.

Table 4.3. The closest interparticle distance $2D_{exp}$ at various particle volume fractions and the average distance $2D_0$

ϕ	$2D_{exp}$ (nm)	$2D_0$ (nm)	$2D_{exp}/2D_0$
(A) latex [a] ($a = 170$ nm, $\sigma_a = 0.04$ μC cm^{-2})			
0.004	1800	1900	0.93
0.0055	1500	1750	0.86
0.015	1000	1250	0.80
0.04	800	900	0.89
(B) latex [b] ($a = 419$ nm, $\sigma_a = 7.2$ μC cm^{-2})			
0.0075	1260	1940	0.65
0.014	1070	1570	0.68
0.0372	890	1140	0.78
0.559	820	990	0.83
0.112	710	790	0.90

[a] Measured from micrograph reported in [33]
[b] at rt, $C_s = 0$ mol L^{-1} [36]

[5] Krieger and Hiltner carried out light diffraction experiments on relatively concentrated latex dispersions ($\phi = 0.01 \sim 0.50$) and found a single broad peak, from which they noticed the relation $2D_{exp} < 2D_0$ [38]. Probably because the charge density was low and particle concentration was high, the ratio $2D_{exp}/2D_0$ was close to unity (∼0.96).

As shown in Table 4.4, $2D_{\rm exp}$ decreases with increasing $C_{\rm s}$, and cannot be determined at $\sim 10^{-4}$ mol $\rm L^{-1}$ because the ordered structure melts. According to the DLVO theory [11, 12], as $C_{\rm s}$ increases, the potential minimum simply deepens and the minimum position shifts toward shorter distances (Fig. 2.9). Thus $2D_{\rm exp}$ is to decrease. The observed decreasing tendency is in accord with the theory but the melting (or destabilization) of the structure cannot be accounted for by this theory. We discuss this property of the theory in Chap. 6 in detail.

Table 4.4. Dependence of $2D_{\rm exp}$ on salt concentration [a]

[NaCl] (mol $\rm L^{-1}$)	$2D_{\rm exp}$ (nm)	$2D_{\rm exp}/2D_0$
0	1270	0.94
1.71×10^{-5}	1130	0.84
6.84×10^{-5}	800	0.60
1.37×10^{-4}	No structure	

[a] Sample: latex particle ($a = 227$ nm, $\sigma_{\rm a} = 4.4$ μC $\rm cm^{-2}$), $\phi = 0.02$, at rt

Figure 4.13 indicates that $2D_{\rm exp}$ decreases with decreasing ε. If the structure is maintained by the electrostatic repulsion as widely claimed, the repulsion must be enhanced with decreasing ε, so that $2D_{\rm exp}$ becomes larger or stays unchanged. This is not the case experimentally. On the other hand, if the electrostatic attraction is predominant as we claim, it would be enhanced, causing $2D_{\rm exp}$ to decrease. This is found out experimentally.

The observed $2D_{\rm exp}$ decreases with rising temperature. The reason for such a physically unacceptable result derives from the temperature dependence of the dielectric constant of water. By considering this dependence, $2D_{\rm exp}$ increases as shown by the straight line in Fig. 4.14.

Two-dimensional Fourier Transform of Micrographs

The density function $\rho(\boldsymbol{r})$ in real space is related to the amplitude of the scattering wave $A(\boldsymbol{b})$ by

$$A(\boldsymbol{b}) = \int \rho\,(\boldsymbol{r}) \exp\left[-2\pi \mathrm{i}(\boldsymbol{b}\cdot\boldsymbol{r})\right] d\boldsymbol{r} \tag{4.8}$$

where $\boldsymbol{r}$ and $\boldsymbol{b}$ are the real space and reciprocal space vectors, respectively. In the case of colloidal systems, $\rho(\boldsymbol{r})$ can be obtained in the form of micrographs, which can be 2D-Fourier transformed (2D-FT) into the scattering profiles.

Figure 4.15 (a) is the binary image of the micrograph of almost perfect ordered structure and (b) is its 2D-Fourier pattern [39]. Figure 4.16 is for a disordered state and a two-state structure. When particles are highly ordered,

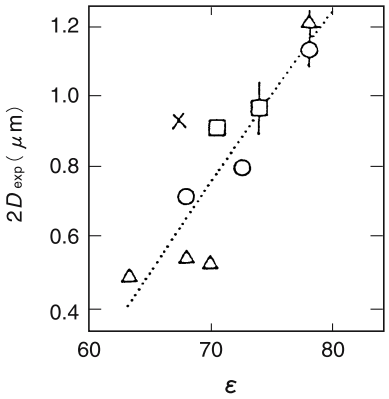

Fig. 4.13. Dependence of $2D_{\rm exp}$ on the dielectric constant ε. Sample: latex particle (a = 185 nm, $\sigma_{\rm a}$ = 7.2 μC cm^{-2}), ϕ = 0.013, at rt. Binary solvents: (light) water-ethyleneglycol (○), water-methanol (×), water-DMF (□), water-DMSO (□). The dotted line is a linear approximation of the $2D_{\rm exp}$-ε relationship, which will be employed in Fig. 4.14. Taken from [30] with the permission of the American Chemical Society

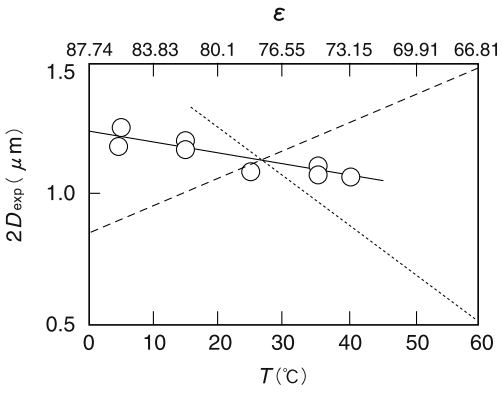

Fig. 4.14. Temperature dependence of $2D_{\rm exp}$. Sample: the same as in Fig. 4.13. ϕ: 0.02, medium: water. The dotted line corresponds to the line in Fig. 4.13. By this line the temperature correction of ε was made to obtain correct $2D_{\rm exp}$, which is shown by the dashed line. Taken from [30] with the permission of the American Chemical Society

its 2D-FT pattern gives discrete scattering spots, whereas no spots are found from the disordered state. Intermediate between the two extreme cases is the two-state structure. As the local structure becomes smaller and more distorted, the scattering profile changes from (d) to (b). Though there is a chasm between the 2D-FT image and reality, Figs. 4.15 and 4.16 provide strong support to our interpretation that the single broad scattering peak observed for flexible ionic polymer solutions is due to a two-state structure.

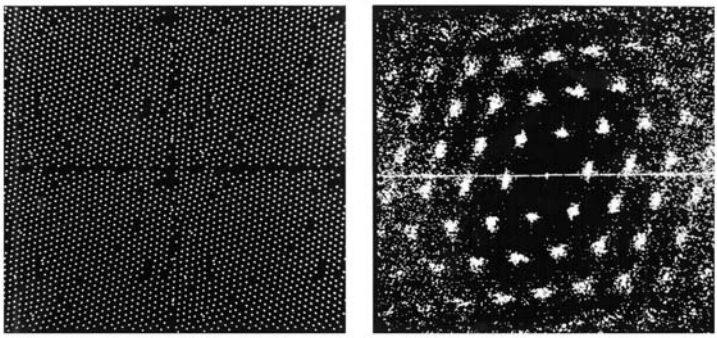

Fig. 4.15. Ordered structure and its Fourier pattern. Sample: latex ($a = 123$ nm, $\sigma_a = 1.9\,\mu C\,cm^{-2}$), $\phi = 5\times10^{-3}$, at rt. (a) is a micrograph of particles (reduced to a point with one pixel) forming (111) of fcc. (b) is the Fourier image of (a). Because of the crystal imperfections (Schottky defect, edge-dislocation, and so on), the Fourier image is not spot. Taken from [39] with the permission of the American Institute of Physics

For the real atomic and molecular systems, the $\rho(\boldsymbol{r})$ is inferred from the scattering profile. Hosemann designed patterns of atomic and molecular distributions, from which he experimentally obtained diffraction profiles of light [40]. This profile was compared with actually observed X-ray scattering images to discuss the pros and cons of inferred density function. The above-mentioned analysis is unique in that the scattering profile was examined on the basis of the experimentally observed density function.

Colloidal Crystal Growth

By using phase contrast microscopy, Luck demonstrated that the crystal growth in latex dispersions followed the Ostwald ripening rule [41, 42]. The larger crystals grow at the expense of smaller crystals, since the free energy of systems is decreased by transfer from a large number of small crystals to a small number of large crystals. The formation of free interface is due to at-

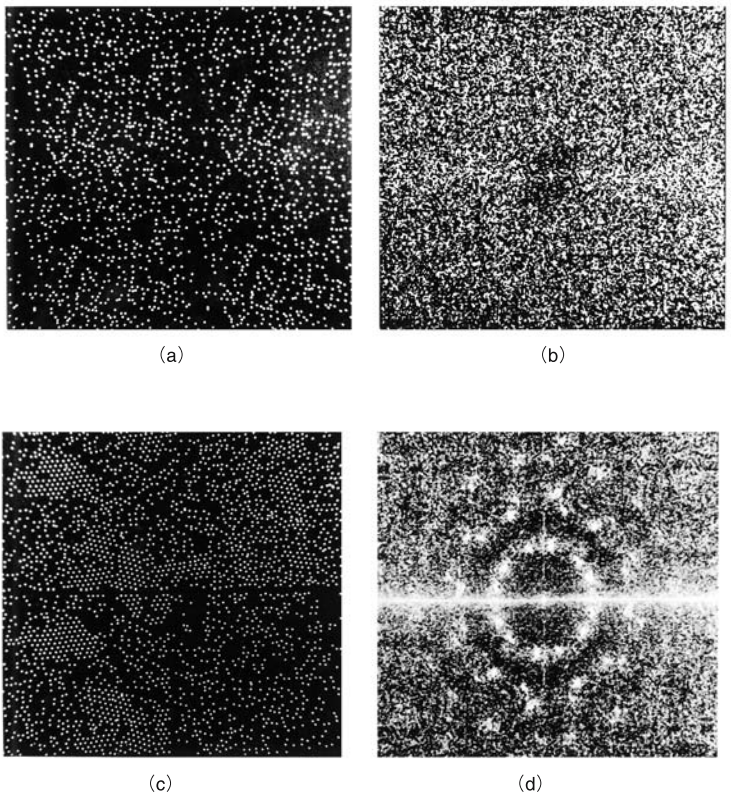

Fig. 4.16. The Fourier images of disordered state and the two-state structures. Sample: latex ($a = 123$ nm, $\sigma_a = 1.9$ μC cm^{-2}), $\phi = 0.01$, at rt. (a) is taken for disordered state at $C_s = 10^{-3}$ mol L^{-1} and (b) is its Fourier image. (c) shows the two-state structure and (d) is its Fourier image. Taken from [39] with the permission of the American Institute of Physics

traction between particles, so that Luck's observation supports the existence of the interparticle attraction.

Let us discuss recent results obtained by video imagery for about 20,000 particles [43, 44]. First the coordinates of the particle centers are determined by digital image processor and the 2D-FT is carried out to obtain the scattering profile. As is often the case at high ϕ's, it is assumed that (111) of fcc is observed. The coordinate information is fed to a work station to perform elementary unit analysis, radial distribution function $g(r)$ analysis, and trajectory analysis. The $2D_{exp}$ is determined by 2D-FT and three particles forming a triangle with a side of $2D_{exp}$ (1 ± 0.15) are searched by the computer using the algorithm shown in Fig. 4.17. This regular triangle is defined as the elementary unit and its number is given by N_u. A local structure con-

sisting of the elementary units with common sides is defined as a cluster with its number being N_c. By measuring all the distances between particles, the two-dimensional (2D) $g(r)$ is determined directly. The number of the nearest-neighbor particles N_n is calculated by

$$N_n = 2\pi N_p \int_{r_1}^{r_2} g(r) r dr \tag{4.9}$$

where N_p is the number density of particles, and the first peak of $g(r)$ is unity at r_1 and r_2.

Figure 4.18 shows the time evolution of particle distribution, elementary units, and clusters. As the colloidal systems evolve from disordered state to crystalline state [(a)→(b)→(c)→(d)], the N_u and N_c become larger and the entire space is finally covered by the ordered structure. The time changes of N_p, N_u, and N_c are shown in Fig. 4.19. The N_p increases with time because particles out of focus plane are brought into the crystal plane as crystallization proceeds. The N_u also shows a similar trend while the N_c displays a maximum.

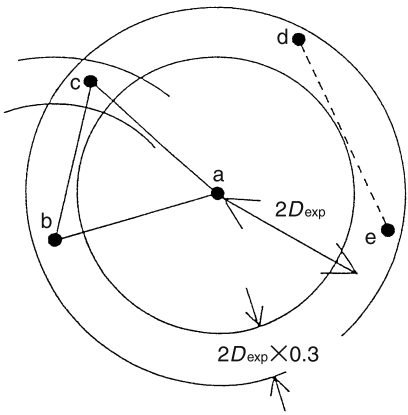

Fig. 4.17. Computer determination of the elementary unit of the ordered structure. Particles (b, c, d, and e), which are located at a distance $2D_{exp}$ (1 ± 0.15) from the central particle (a), are searched. Then the interparticle distance is determined between these particles; the particle pair having a distance of $2D_{exp}$ (1 ± 0.15) is picked up (b and c) while the pair which does not fulfill the above condition is abandoned. Taken from [43] with the permission of the American Physical Society

Figure 4.20 gives the radial distribution function $g(r)$ obtained directly by measuring the interparticle distance on a micrograph. The $g(r)$ shown in (a) is the same as observed for non-interacting systems. As time passes, the $g(r)$ starts to show peaks. The number of the nearest-neighbor particles N_n increases with time first rapidly and then up to about 4, where N_n is

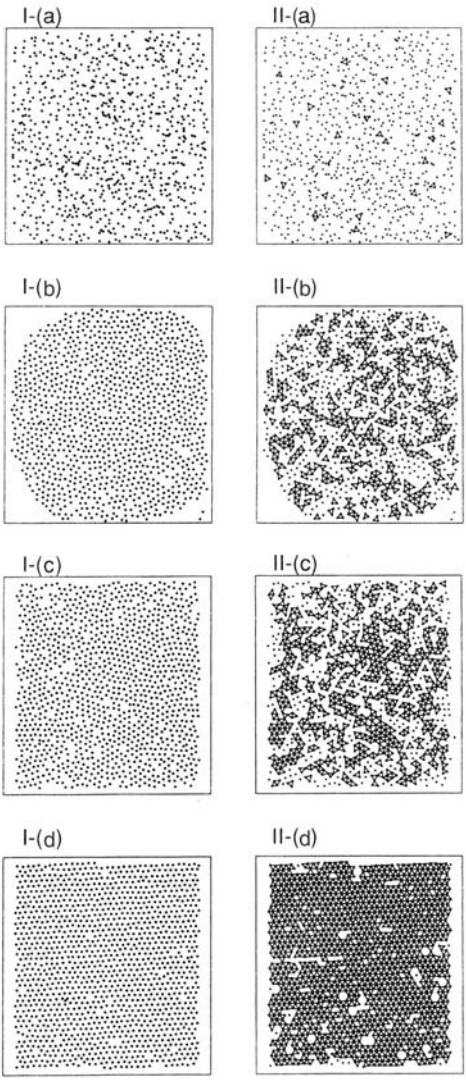

Fig. 4.18. Time evolution of particle distribution (I) and clusters (II) during crystal growth. Sample: latex (a = 120 nm, σ_a = 1.3 μC cm^{-2}), ϕ: 0.01, 25°C. Time after onset of crystallization: (a), 20 min, (b), 130 min, (c), 160 min, (d), 180 min. To purified latex dispersions, NaCl is added to the concentration of 10^{-4} mol L^{-1} to destroy ordered structure and to allow particles to do Brownian motion. Then purified ion-exchange resin particles are added to the dispersions ($t = 0$). The conductivity of the dispersion starts to decrease by ion-exchange. After 10 min, the conductivity is lowered to the level, which was observed before the addition of the ion-exchange resin particles, and stays constant. Taken from [43] with the permission of the American Physical Society

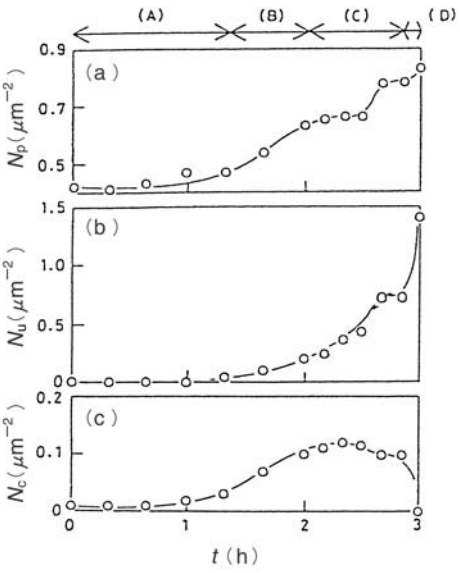

Fig. 4.19. Time evolution of the number density of particles N_p, the number of elementary units N_u, and the number of clusters N_c during crystallization. The experimental condition is the same as in Fig. 4.18. Taken from [44] with the permission of the Royal Society of Chemistry

temporarily saturated, as shown in Fig. 4.21. Then it quickly increases to 5.5, not to 6 because of lattice defects. Figure 4.22 shows the evolution of the fractions of clusters of various sizes. While the fraction of three-particle clusters increases with time and, passing a maximum, decreases, that of the 21 and more particle clusters simply increases. This is the Ostwald ripening process, in which larger clusters grow at the expense of smaller ones.

The above experiments are carried out for H_2O-latex particle (density $=1.05$ g cm^{-3}) systems by using a reversed type microscope, which enables to observe particle distribution near the bottom of the dispersion cell. Qualitatively the same results are obtained using a density-matched D_2O-H_2O mixture, ruling out the possibility that the observation in the H_2O systems is an artifact due to gravitational sedimentation of particles.

Structural Fragility of Colloidal Crystals

It is now clear that, at low salt concentrations, colloidal particles form ordered (crystalline) structures though in liquid media. Noteworthy is the difference from real atomic and molecular crystals. As stated in the Introductory Remarks, the lattice constant of colloidal crystals depends on the particle concen-

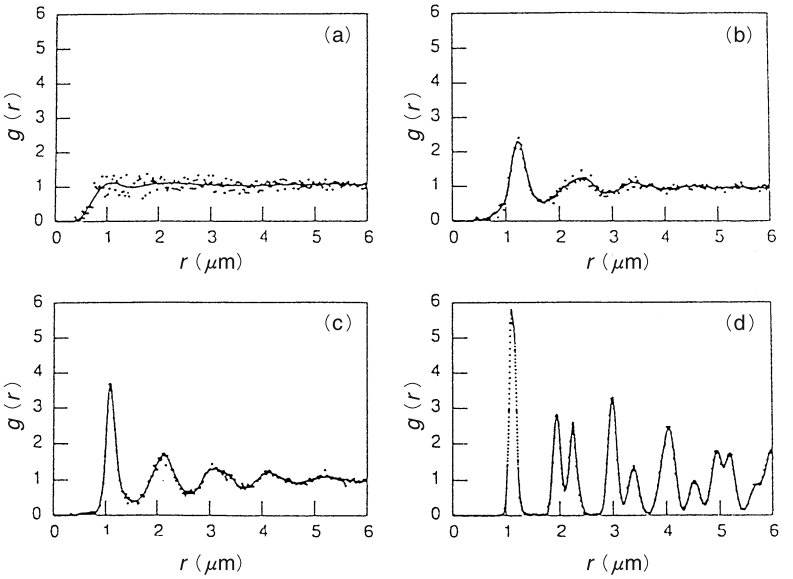

Fig. 4.20. Time evolution of radial distribution function determined by micrographs. Time after the onset of crystallization:the same as in Fig. 4.18. Taken from [44] with the permission of the Royal Society of Chemistry

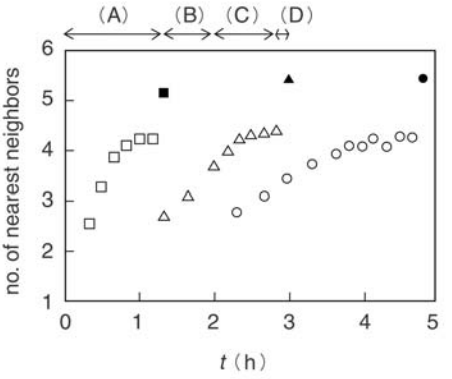

Fig. 4.21. Time evolution of the number of nearest neighbor particles during crystallization. The experimental condition is the same as in Fig. 4.18 except that the volume fraction; $\phi = 5 \times 10^{-3}$ (□), 10^{-2}(△), $2{\times}10^{-2}$ (○). The division into four stages refers to $\phi = 10^{-2}$. Taken from [44] with the permission of the Royal Society of Chemistry

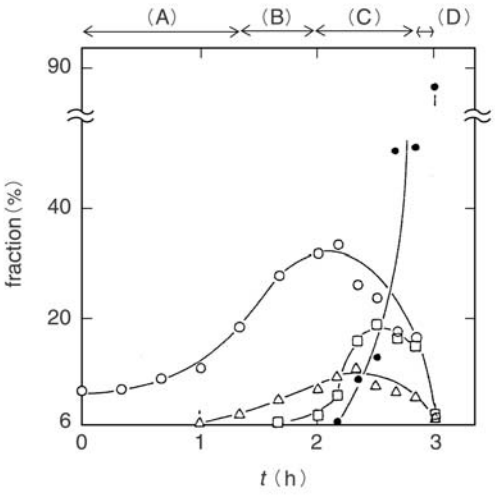

Fig. 4.22. Time change of the fractions of the particles forming the clusters of three (○), five (△), and 10-20 (□) and more than 21 particles (●). The experimental condition is the same as that in Fig. 4.18. Taken from [44] with the permission of the Royal Society of Chemistry

tration, salt concentration, charge density, the dielectric constant of medium, and so on. These dependences are not observed for atomic/molecular crystals. The difference comes from the interparticle interaction being essentially different from that in the atomic/molecular systems. Another characteristic of colloidal crystals is their fragility. When dispersion vessels are shaken violently, the colloidal crystals inside are easily destroyed and particles show Brownian motion (shear-melting). When strong light is irradiated on colloidal crystals for a prolonged period, the colloidal crystals are broken. When these external factors are removed, colloidal crystals are re-formed sooner or later. These facts indicate that the minimum of the interparticle potential is very shallow. The fact that the lattice constant varies with the experimental conditions indicates that the attractive component responsible for the potential minimum is sensitive toward the conditions. We have been proposing the existence of a counterion-mediated attraction between particles, and we believe that its physical basis is given, at least qualitatively, by the theory of Sogami (Chap. 6).

4.2.4 Inner Structure of Colloidal Dispersions and Crystals by Confocal Laser Scanning Microscopy

The observation mentioned in the preceding sections was made using a reversed-type metallurgical microscope. When the refractive indexes of particles and medium are sufficiently different, the dispersions become turbid, so

that particles far inside cannot be seen. It is not easy to observe polystyrene-based particles in water more than 10 μm distant from the coverslip (bottom of container vessel) by this technique, except at very high dilutions. Thus, it cannot definitely be ruled out that observation is distorted or affected by the presence of the glass/interface interface. It is indispensable to remove or minimize this effect by studying particles far inside the dispersions in order to obtain reliable information. For this purpose, the confocal laser scanning microscope (LSM) is useful, in which only light from the focus plane is allowed to form images by cutting off light from out-of-focus planes. By LSM, particles 200 μm distant from the coverslip can be observed. Most of the results obtained by LSM are consistent with those found by the reversed-type metallurgical microscope, indicating that the physical properties under consideration are not substantially, at least qualitatively, vitiated by the wall effect. However, some unanticipated results are obtained and worth discussing here.

Void Formation and Gas-Liquid Phase Transition

The inequality relationship $2D_{\exp} < 2D_0$ led us to the two-state structure and its existence was confirmed by microscope for colloidal dispersions. However it is not the sole result of the relationship. When the interparticle attraction is so strong that particle concentrations are raised locally, there would be formed spaces without particles filled with liquid medium only, namely voids. The inequality relation should hold also in such a case. The presence of voids was first mentioned by Hachisu et al., though briefly in their article [33], and later Ito [45] and Kesavamoorthy [46] took pictures of voids in dispersions by using a metallurgical microscope. A more systematic study became possible by using LSM [47–49].

The LSM images in Fig. 4.23 show the time evolution of voids. Clearly giant voids are formed slowly. Sometimes void can be as large as $50 \times 50 \times 150\ \mu m^3$ [50]. In the early stages, voids can be observed more easily deep inside of the dispersion than near the surface of the coverslip [48], which indicates that the void formation is not an artifact due to the interface effect [6].

Hachisu et al. mentioned void formation in his article [33] but did not present micrographs. In our study in an early stage as well as in their investigation, polystyrene-based latex particles were observed in H_2O. In this system, it was observed occasionally that a large number of particles in the microscope view violently moved as if the dispersion was stirred. Hachisu's description of such a movement was "Worms moved". We ourselves experienced this phenomenon. Our understanding now is that, when voids grew inside of the dispersion and reached a critical size, they could not resist the

[6] As will be discussed below, it was experimentally found that the concentrations of charged particles near a similarly charged glass surface are higher than in the bulk, in contrast with the widely accepted view. This concentration effect might prevent formation of voids near the glass surface.

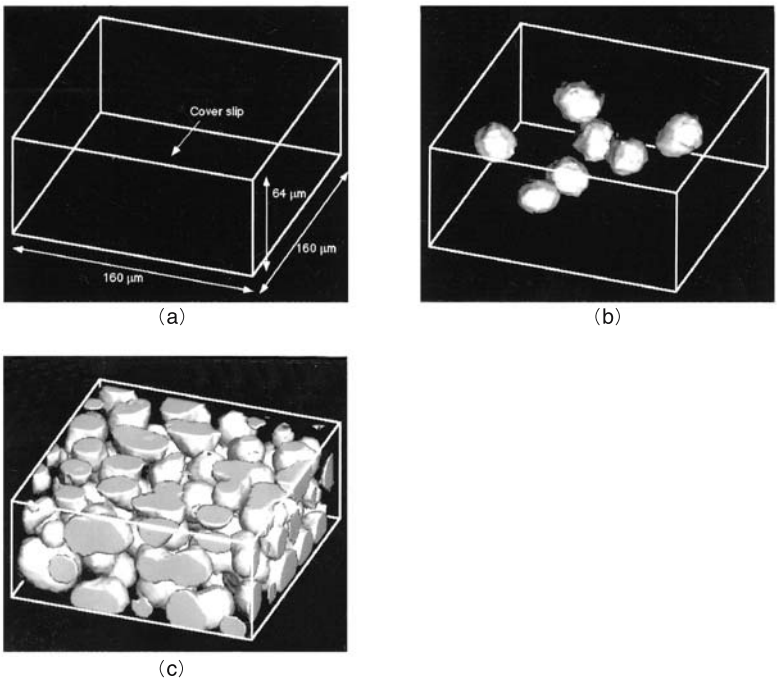

Fig. 4.23. Time evolution of voids. Sample: latex ($a = 60$ nm, $\sigma_a = 4.8$ μC cm^{-2}, $\sigma_n = 0.48$ μC cm^{-2}), $\phi = 10^{-3}$, medium: H_2O-D_2O (density = 1.047 g cm^{-3}). The black background is the liquidlike region while the white objects are voids. The 3D images are reconstructed from 40 LSM images, each 1.6 μm apart, observed by shifting the focus plane continuously from 3 to 67 μm. The purified dispersion and ion-exchange resin are introduced into the observation quartz cell and are kept standing in a constant temperature chamber at 23°C for two weeks. After confirming the formation of voids, the dispersion is homogenized by violent shaking, which corresponds to (a), and then kept standing in the constant temperature chamber until LSM observation on the 15th day (b) and 60th day (c). Taken from [49] with the permission of the American Institute of Physics

buoyancy due to the density difference between particles (∼1.05 g cm^{-3}) and medium (∼1 g cm^{-3}) to suddenly move up toward the air-dispersion interface. Thus, the dispersion and particles were "stirred". In our recent study shown in Fig. 4.23, the density difference was nil because a mixture of H_2O and D_2O with a density equal to that of the particles was used, so that the voids could stay inside of the dispersion. Thus no "worms" moved and we could carry out observation for a prolonged period.

The void formation is extraordinarily unexpected for condensed systems. Partly because of Hachisu's description, we occasionally came across the claim that some microorganisms are generated in dispersions and their aggregates

could give an erroneous impression of voids. However, in light of the stringency in purification of particles and medium, and also of the air-tightness of the dispersion vessel, this claim is not acceptable. Voids can be observed even after sterilization of the dispersion [19]. Furthermore, computer simulation work, in which there is no room for microorganisms, can reproduce voids when an attractive potential is assumed (Chap. 8). From these considerations, we claim that the voids are formed by an attractive interaction between particles, not by other factors such as the fortuitous growth of microorganisms.

Tata et al. found a gas-liquid phase transition for polystyrene-based latex particles in H_2O [51]. To examine whether the void formation is a thermodynamic phase transition, comparison was made between H_2O and a density-matched mixture of H_2O and D_2O for a latex. Table 4.5 shows that there is a critical concentration between $\phi = 10^{-3}$ and 1.5×10^{-3}, below which voids are generated in the density-matched system whereas the macroscopic phase separation takes place into particle-rich and particle-poor phases. From this observation it is concluded that the void formation is essentially a gas-liquid transition of latex particles under no-gravity conditions.

The critical concentration is believed to sensitively depend on the particle size, charge density, and salt concentration. Though further study is necessary, void formation cannot be excluded from consideration at low concentrations also for other particles and solute species, whenever $2D_{\mathrm{exp}} < 2D_0$ is observed. It is an important factor in elucidating the physical properties of ionic, condensed systems at high dilutions.

The void formation needs further comment. Various information on the state of solute species in solution is inferred from scaling of physico-chemical properties with regard to concentration. For example, Bernal and Funkuchen demonstrated that the position of the scattering maximum followed the square-root dependence on concentration for tobacco mosaic virus (TMV), from which they concluded that the rod-like particles formed ordered arrangements. The concentrations were very high so that the solution or gel may have been homogeneous. Under such conditions, scaling is reasonable. However, at low concentrations below the critical one, the systems are no longer microscopically homogeneous, so that the scaling with respect to the average concentration is not physically meaningful.

Table 4.5. Void formation and gas-liquid phase transition [a]

ϕ	H_2O-D_2O	H_2O
5×10^{-4}	voids	gas-liquid
10^{-3}	voids	gas-liquid
1.5×10^{-3}	homogeneous	homogeneous
2.0×10^{-3}	homogeneous	homogeneous
2.5×10^{-3}	homogeneous	homogeneous

[a] sample: latex ($a = 60$ nm, $\sigma_{\mathrm{a}} = 4.8$ μC cm^{-2}), $C_{\mathrm{s}} = 0$ mol L^{-1} , at 23°C.

Three-dimensional Phase Diagram: Re-entrant (Liquid-Solid-Liquid) Phase Transition

A 3D-phase diagram is shown in Fig. 4.24 as a function of σ_n, ϕ, and C_s for colloidal silica particles in water [52]. The σ_n is determined by the method discussed in Sect. 4.1.1. The distinction of solid state from liquid state is judged by iridescence and ultra-small-angle X-ray scattering (USAXS) profile. Figure 4.25 is USAXS curves, which have third-order diffraction peaks of (110) of bcc (curve b) on the top of the form factor of an isolated sphere and no peaks for liquid state (curves a and c). Interesting is the fact that powder patterns shown in Fig. 4.26 are observed in the solid phase far from the liquid-solid boundary in Fig. 4.25 [18]. When ϕ and C_s are fixed, the re-entrant phase transition, liquid→solid→liquid, takes place as σ_n increases. It is highly important that the liquid phase appears for low and high σ_n. If only the repulsive forces were in operation between colloidal particles, such a re-entrant behavior cannot be accounted for [7].

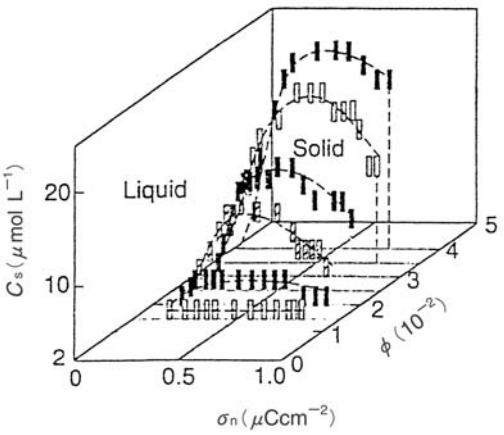

Fig. 4.24. Phase diagram for liquid-solid transition of an aqueous dispersion of silica particles as a function of net charge density σ_n, salt concentration C_s, and particle volume fraction ϕ. Sample: KE-P10W ($a = 60$ nm). The solid-liquid phase boundary is shown by rectangles. Dashed lines are eye-guides. Taken from [52] with the permission of the American Physical Society

[7] The re-entrant phase separation was recently observed for a more monodisperse polystyrene-latex particle than the silica particle (Toyotama et al. (2003) Langmuir 19:3236). The peak position of the liquid-solid boundary is at a net charge density of 0.5 μC cm^{-2} as was the case for the silica dispersions. This agreement indicates that the re-entrant behavior is not due to the polydispersity of the silica particle.

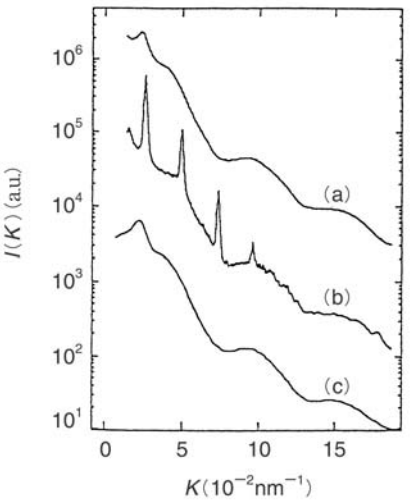

Fig. 4.25. USAXS profiles showing the re-entrant phase transition. Sample: KE-P10W (a = 60 nm). Curves (a) and (c) are in liquid phases (σ_n = 0.07 and 0.72 μC cm^{-2}), while curve (b) is observed in solid phase (σ_n = 0.36 μC cm^{-2}). C_s = 10 μmol L^{-1} , $\phi = 3 \times 10^{-2}$. Taken from [52] with the permission of the American Physical Society

Time Evolution of the Structure

When samples of relatively low charge densities are used, the counterion-mediated attraction is weak so that the rate of crystal growth is slow enough to be studied by LSM [18]. Figure 4.27 shows LSM images of particle distribution at $t = 1$ day after the onset of crystallization. The two-state structure is evident. Figure 4.28 shows the time evolution of the structure. When the dispersion is at rest after violent shaking, in other words at $t = 0$ s, crystallization starts. At $t = 10$ s, ordered grains appear in the disordered state. At $t = 40$ s, the whole system is covered by space-filling structure (one-state structure). At $t = 8$ min, disordered regions develop inside the space-filling crystalline grains, resulting in a Swiss cheese-like structure. The disordered regions grow and their number is diminished. The disordered regions at positions close to the grain-grain interfaces are extruded from the grains and form the interstitial disordered phase.

The Swiss-cheese structure cannot be accounted for in terms of the conventional nucleation and growth process. Corresponding to the formation of the Swiss-cheese structure, $2D_{exp}$ determined by USAXS decreases from 0.35 μm to 0.33 μm, suggesting the contraction of the structure. The whole process can be explained as follows by assuming an interparticle attraction. Judging from the fragility of colloidal crystals, the attraction is weak and the poten-

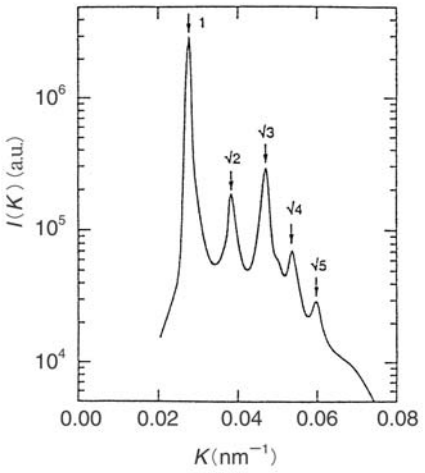

Fig. 4.26. USAXS profiles showing a powder pattern for the ordered silica dispersion. Sample: KE-P10W (a = 60 nm, σ_n = 0.23 umuC cm^{-2}). $C_\mathrm{s} \approx 3$ μmol L^{-1}. The profile is corrected for smearing effects due to the X-ray beam shape and the USAXS optics. The relative positions of the diffraction peaks with respect to the first peak position are indicated by the arrows. Taken from [18] with the permission of the American Chemical Society

tial minimum is very shallow. Thus just after shaking, the particles have high kinetic energy so that the particles overcome the shallow potential minimum and behave as if only repulsion is operative. This would be the situation at $t = 40$ s, at which the whole volume is covered by space-filling ordered structure, that is $2D_\mathrm{exp} \approx 2D_0$. As time passes, the particles cool off and some become trapped into the potential minimum. When the minimum position is located at shorter distances than $2D_0$ as is the case under the conditions employed, the crystal contracts, or the $2D_\mathrm{exp}$ becomes smaller, resulting in the Swiss-cheese structure.

Dependence of the Internal Structure on Charge Number and Particle Concentration

The re-entrant phase transition with respect to the charge number is also confirmed by LSM observation [18]. Figure 4.29 is LSM images with increasing net charge number Z_n. At low Z_n, particles could not be observed due to Brownian motion (liquid phase in Fig. 4.24). When Z_n is 720 and 1100, the dispersion is in the coexistence region of liquid and solid and the alignment of particles is seen as shown in the zoomed-in micrograph (inset). At $Z_\mathrm{n} = 1300$, the system re-enters into liquid region. The ordered structure is bcc according to USAXS study. When particle concentration (n_p: the number of particles in

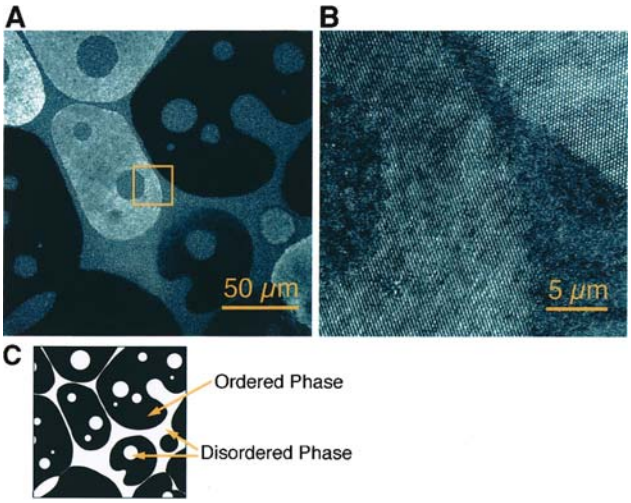

Fig. 4.27. LSM images of the two-state-structure in a silica dispersion. Sample: colloidal silica (a = 53 nm, σ_n = 0.23 μC cm^{-2}). ϕ = 0.0183. Distance from the coverslip z = 200 μm. The picture was taken by using Carl-Zeiss LSM 410 at t = 1 day after the onset of crystallization. The region indicated by the square in A is magnified in B. The thickness of the focus planes are 0.50 and 0.35 μm for A and B, respectively. C is a schematic illustration distinguishing the ordered and disordered phases in A. In the ordered region, particles (white dots) are arranged regularly (See B). In the disordered region, particles cannot be observed because of Brownian motion. The different brightness of the ordered regions indicates that the direction varies from region to region. On the other hand, the disordered regions have constant brightness. Taken from [18] with the permission of the American Chemical Society

1 μm^3) is increased from 2 to 80 μm^{-3} (as shown in Fig. 4.30) at a fixed Z_n (510) and C_s ($\sim$ 2 μmol L^{-1}), the dispersion changes from liquid (a), via the coexistence region of liquid and solid (b,c), to solid comprising of microcrystals (d). In this case, also, the crystals are bcc.

Interaction between Particle and Interface: Concentration of Charged Particles onto a Like-Charged Interface

According to the electric double layer theory [12], the potential ψ of a positively charged interface simply decreases with increasing distance r as shown in Fig. 4.3. The distribution of microions (point charges) in solution is assumed to be governed by the Poisson-Boltzmann equation,

$$\Delta\psi = \frac{-4\pi\rho}{\varepsilon} \tag{4.10}$$

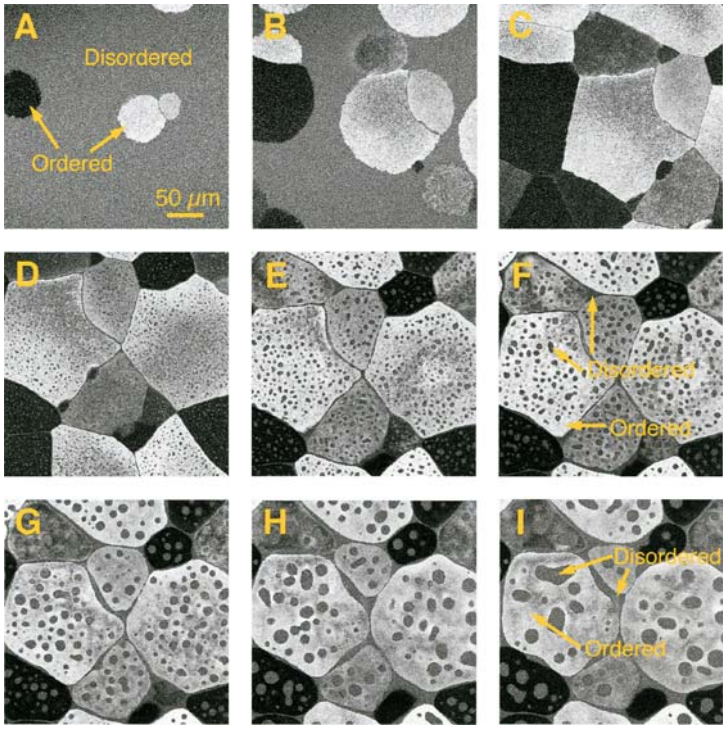

Fig. 4.28. Time evolution of the dispersion structure during crystallization. Sample: colloidal silica ($a = 53$ nm, $\sigma_n = 0.23$ μC cm^{-2}). $\phi = 0.0183$. $z = 200$ μm. The elapsed times t after homogenizing the dispersion are (A) 10 s, (B) 20 s, (C) 40 s, (D) 8 min, (E) 30 min, (F) 1 h, (G) 3 h, (H) 6 h, and (I) 9 h. At 10 and 20 s, the ordered regions are seen to coexist with the disordered region (the two-state structure) and at 40 s a space-filling ordered structure appears (one-state) and at 8 min disordered regions are formed in the ordered phase (two-state), forming the Swiss-cheese structure. The disordered regions grow with time and their number decreases. The space-filling structure at 40 s can be concluded from the observation that only 2% of 14000 lattice points are defects. Taking into consideration these defects, $2D_{exp}$ is calculated to be 0.35 μm, whereas the average spacing from concentration $2D_0$ is 0.36 μm. The agreement between $2D_{exp}$ and $2D_0$ supports the space-filling nature of the ordered structure (one-state). $2D_{exp}$ is found at 8 min to be 0.33 μm by USAXS measurements, which is consistent with the Swiss-cheese structure. Taken from [18] with the permission of the American Chemical Society

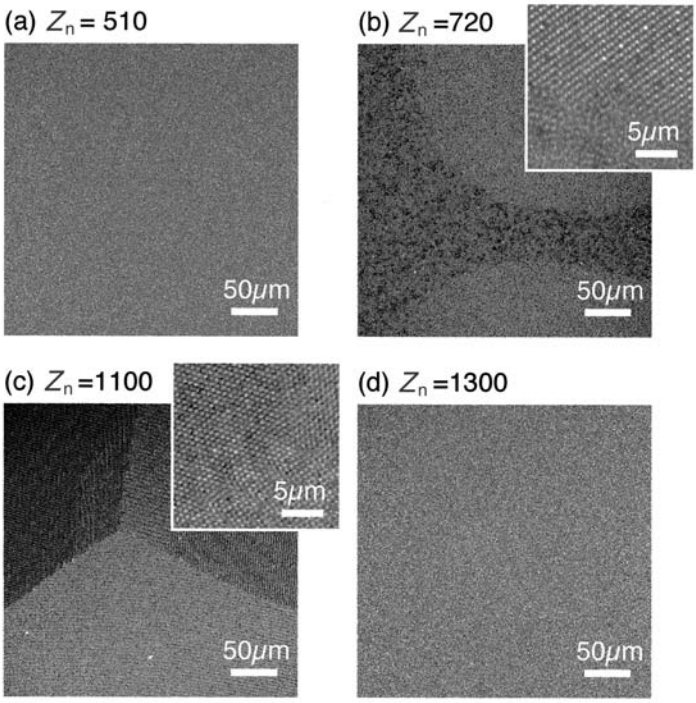

Fig. 4.29. Change of internal structures of colloidal dispersions with net charge number. LSM: Carl-Zeiss 410, z = 200 μm, n_p = 2 μm^{-3}, $C_s \approx$ 2 μmol L^{-1}. (a) silica particle ([NaOH] = 0 mol L^{-1}), (b)-(d) latex particles. The four kinds of particles have a of 0.11∼0.12 μm. Taken from [18] with the permission of the American Chemical Society

$$n_i = n \exp\left(\frac{-e\psi}{k_B T}\right) \tag{4.11}$$

where n is the average concentration of the 1-1 type microions (at $\psi = 0$) and n_i is the concentration of the ion i and ρ is the charge density. Furthermore the surface charge of the interface σ is assumed to be related to ρ by

$$\sigma = -\int_0^\infty \rho dr \tag{4.12}$$

These treatments have been regarded as reasonable. Thus it has been taken for granted that the concentration of the ions of the same sign charge as that at the interface increases with increasing distance from the interface whereas that of the oppositely charged ions decreases.

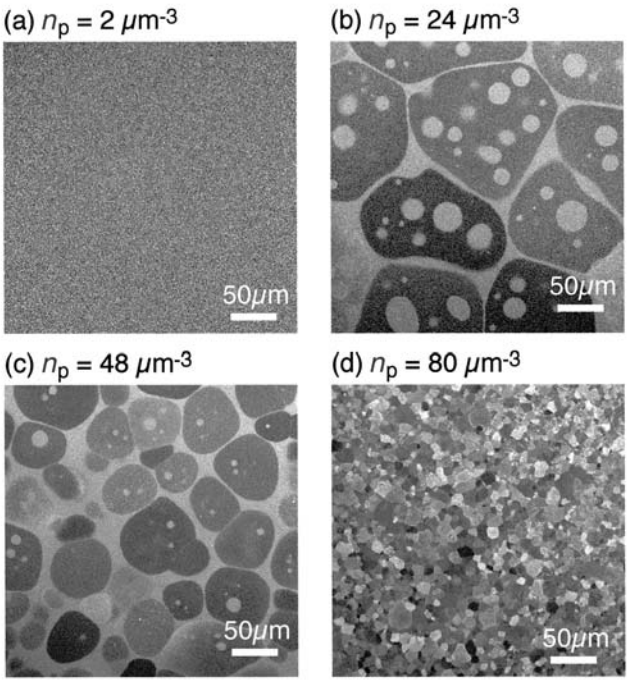

Fig. 4.30. LSM images of the internal structure in colloidal dispersions at four particle concentrations. Sample: silica particle ($a = 55$ nm), $z = 200$ μm, $Z_n = 510$, $C_s = \sim 2$ μmol L^{-1}. n_p = (a) 2, (b) 24, (c) 48, (d) 80 μm^{-3}. Taken from [18] with the permission of the American Chemical Society

Quite recently experimental facts have been found that are in conflict with the above basic relationships. We discuss here an LSM study on the latex particle/glass surface [53–56] and on a neutron scattering study on surfactant micelles/air-liquid interface [57].

Generally, a glass surface in contact with water is negatively charged because of the dissociation of silanol groups (-SiOH). When a dispersion of negatively charged latex particles is introduced into a glass vessel, the number of particles $N(z)$ in the dispersion is expected to increase with increasing distance from the glass surface z according to (4.11). However, the $N(z)$ actually observed by LSM *decreases* in the range of z between 10 and 60 μm as shown in Fig. 4.31. In other words, though the particles and the glass surface are similarly charged, the particles are positively *concentrated* in the vicinity of the surface. Only at long distances such as 100 μm, $N(z)$ becomes equal to the bulk value N_b expected from the average concentration. Addition of salt decreases the slope of the $N(z)$-z plot and the concentration does not occur at

10^{-4} mol L^{-1}. The salt concentration dependence indicates that the concentration effect is mainly due to electrostatic interaction. The above results are found also under the density-matched condition, showing that gravitational sedimentation is not responsible for the observation.

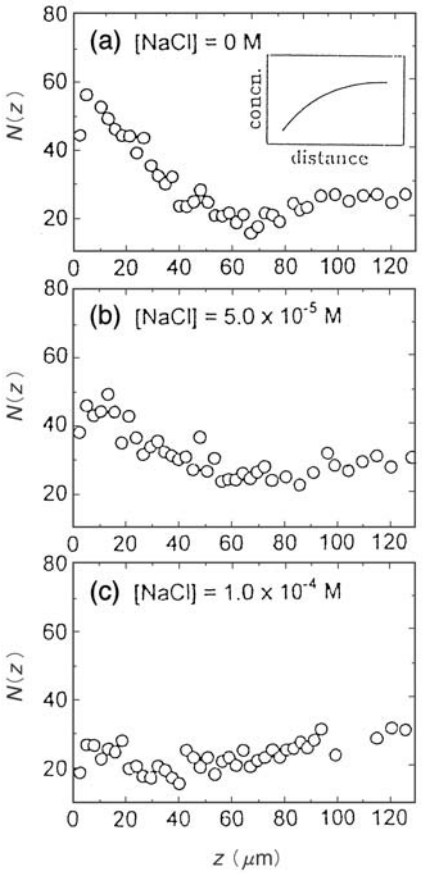

Fig. 4.31. Particle numbers $N(z)$ as a function of the distance from the surface of the glass coverslip z. Sample: latex (a = 280 nm, $\sigma_a = -5.5$ μC cm^{-2}), $\phi = 6.5 \times 10^{-4}$, ζ potential of the coverslip (base of the dispersion vessel) = $-70 \sim -90$ mV (in $10^{-4} \sim 10^{-6}$ mol L^{-1} NaCl solution). Microscope: LSM410 (Carl-Zeiss). Ordinate: particle number $N(z)$ in a horizontal plane of 37×31 μm^2. Depth of focus = $2 \sim 3$ μm. Average number of particles N_b calculated from ϕ: 20∼30. [NaCl]: a; 0, b; 1.0×10^{-5}, c; 10^{-4} mol L^{-1}. Taken from [53] with the permission of the American Chemical Society

Increase in the charge number on particles while keeping their radius constant makes the concentration effect more outstanding (Fig. 4.32). When the charge number on the glass interface is varied by modifying -SiOH groups chemically, *more negatively charged surfaces show stronger concentration of latex particles than the less charged one* for both poly (styrene sulfonate)- and polyacrylamide-modified cases, as shown in Fig. 4.33. It is often claimed that the widely accepted repulsion between particles pushes particles to the vicinity of the container wall, causing apparently the concentration effect. If this interpretation is correct, the more highly charged the interface is, the less number of particles are accumulated, the weaker the concentration effect. This is in contradiction with the observed fact in Fig. 4.33. This figure indicates that there is generated an electrostatic counterion-mediated *attraction* between the charged interface and particles. This attraction becomes more intense when both interface and particles are more highly charged. One may be reminded that the counterion-mediated attraction between interface and particles is essentially the same as that between particles, as discussed in the preceding sections.

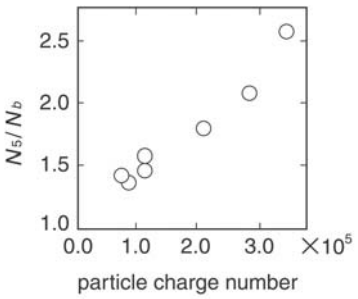

Fig. 4.32. Dependence of the concentration effect on the analytical charge number of particles. Sample: latex ($a = 110 \sim 300$ nm). The concentration effect is given by the ratio of the particle numbers at $z = 5\,\mu$m (N_5) and the bulk value N_b. Taken from [55] with the permission of the American Chemical Society

It is well-known that surfactant ions often form spherical micelles in solution at high concentrations and monolayers at the air-solution interface. For example, cationic surfactant molecules form positively charged micelles and positively charged interfaces as shown in Fig. 4.34 above the critical micelle concentration. Thomas et al. carried out neutron reflection studies at the interface and determined the volume fraction of the surfactant as a function of the distance z from the interface [57]. They found that ϕ is 0.6, 0.1, and 0.07 at $z = 0$, 10, and 20 nm, respectively. These values are larger than the ϕ value corresponding to the average concentration, showing that the concentration effect takes place.

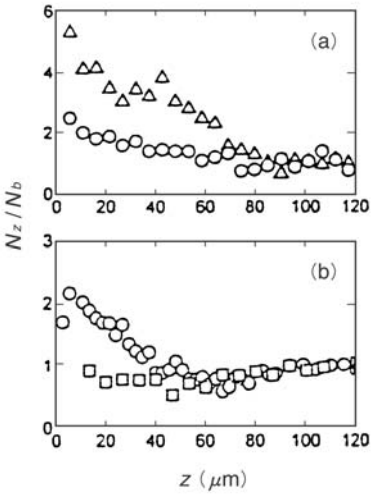

Fig. 4.33. Dependence of the concentration effect on the surface charge number of the glass surface. (a) Glass surface is modified by coupling poly(styrene sulfonate) chain with silanol groups to increase the negative charges. △: modified glass, ζ potential= -94 mV in 10^{-4} mol L^{-1} NaCl solution. ○: untreated glass, ζ potential= -70 mV in 10^{-4} mol L^{-1} NaCl solution. Sample: latex ($a = 300$ nm, $\sigma_a = -6.5$ μC cm^{-2}). $\phi = 8 \times 10^{-4}$. (b) Glass surface is modified with polyacrylamide to lower the charge number. □: modified surface, ζ potential=-4 mV in 10^{-2} mol L^{-1} NaCl solution. ○: untreated, ζ potential = -24 mV in 10^{-2} mol L^{-1} NaCl solution. Sample: latex ($a = 270$ nm, $\sigma_a = -5.9$ μC cm^{-2}), $\phi = 7 \times 10^{-4}$. Taken from [55] with the permission of the American Chemical Society

These results indicate that there exists an electrostatic, long-range attraction between a charged interface and similarly charged particles, whether they are latex particles or micelles, and whether they are cationic or anionic. The distance range of the concentration effect is 5∼80 μm for latex particles. The measurements at much shorter distances is difficult due to the unsatisfactory resolving power of the microscope. While (4.11) may be valid at short distances, the observation shows that it is no longer correct at longer distances. Furthermore, in light of the experimental results, the integration of (4.12) to estimate the charge number of the interface and therefore the interaction energy cannot be carried out from a to infinity. Thus, *the charge number of the interface, which has been obtained on the basis of the electric double layer theory, must be viewed with great caution.*

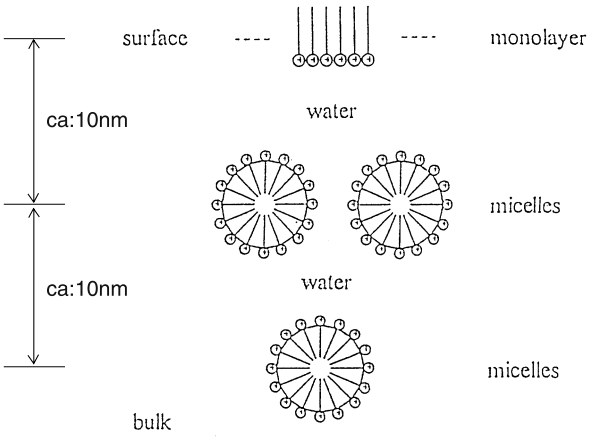

Fig. 4.34. A schematic view of the concentration effect of a cationic surfactant. The air-solution interface is positively charged. The counterions are not shown.

4.3 Investigation by Ultra-Small-Angle X-Ray Scattering (USAXS)

The small-angle X-ray scattering (SAXS) technique has its upper limit corresponding to around 50 nm in real space and cannot be applied to the structural study of colloidal materials, except particles of small radius (for example, Fig. 3.23). In order to make it possible to study colloidal dimensions by X-ray scattering, it is necessary to expand the measurements to much lower angles than SAXS. Bonse and Hart made it possible to measure X-rays in the so-called ultra-low angle region by highly collimating the incident X-ray beam as shown in Fig. 4.35 [58]. This is called the ultra-small-angle X-ray scattering (USAXS) technique and is used for colloidal systems [59–62]. When the collimation is done in one plane (for example, in the horizontal plane) and in two perpendicular planes (horizontal and vertical planes), we call it 1D-USAXS and 2D-USAXS, respectively.

4.3.1 Determination of Lattice Structure, Lattice Constant, and Direction of Colloidal Crystals

The 1D-USAXS optical system shown in Fig. 4.35 was used in combination with a rotating-anode X-ray generator [59] and the full width at the half maximum (FWHM) of the intensity-angle curve of the incident X-ray was about 4 s of arc, corresponding to 8 μm in real space. Figure 4.36 shows the USAXS curves for latex powder (curve 1) and for an ethanol dispersion (curve 2). The peak of the curve 1 is located at the same position as the peak B of curve 2. The peak positions of these curves agree with that of

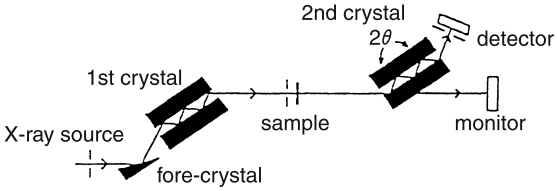

Fig. 4.35. The optical system of 1D-USAXS apparatus (overhead view). The incident X-ray hits the fore-crystal for monochromatization. Then the beam goes into the groove of the first crystal, which is cut for the direction parallel to the (220) plane of a Si single crystal. In the groove the beam is diffracted five times. The thus highly collimated beam hits the sample. The scattered X-ray goes into the second Si crystal. Only the scattered beam, which strictly satisfies the Bragg condition for the second crystal, can pass through the crystal after five Bragg diffractions and can be detected. Hence, by rotation of the second crystal (the minimum step is 0.02 sec), the scattered X-rays in a very small-angle region can be measured without being influenced by the incident beam. Taken from [59] with the permission of the National Academy of Sciences, USA

the curve 3, which is a theoretical scattering curve for an isolated sphere (radius $a = 150$ nm). By such fitting procedures, it is possible to estimate the radius of particles in dispersions and the particle size distribution. At low particle concentrations, powder patterns of fcc structures were observed for polystyrene latex (in H_2O-C_2H_5OH) and poly(methyl methacrylate) latex (in H_2O) [63] suggesting that microcrystals are randomly distributed in the dispersions.

Konishi et al. successfully prepared large single crystals of colloidal silica particles in water media and observed several orders of diffraction peaks [64]. In Fig. 4.37 typical USAXS curves are shown. The curve (a) was observed at the rotation angles of vertically held capillary (dispersion container) $\omega = 0°$ and $(60 \times \mathrm{m})°$ with m being an integer, when the capillary was rotated around its axis. The curve (b) was obtained at $\omega = 30°$ and $(30 + 60 \times \mathrm{m})°$. These results indicate that a bcc lattice is maintained in the capillary, with the $[1\bar{1}1]$ direction of the single crystal being vertical and parallel to the capillary axis, and the curve (a) gives the diffraction from the (110) planes. Because the incident X-ray is not point-like but linear (15 mm long and 1 mm wide) [8], diffraction can be observed also from the (020) planes, which gives the second peak of the curve (b). When the $[1\bar{1}1]$ direction is vertical, the (110) diffraction takes place in the horizontal plane, so that $\tilde{\theta} = \theta$. Then the distance between

[8] In this optical system, there remains a smearing effect in the vertical direction. Thus the true scattering angle θ (the angle made by the incident X-ray in the horizontal plane with the scattered X-ray) does not coincide with the apparent scattering angle $\tilde{\theta}$ which is determined experimentally in the horizontal plane. When the angle between the plane made by the incident and scattered X-rays and the horizontal plane is denoted by ϕ', $\tilde{\theta} = \theta \cos \phi'$.

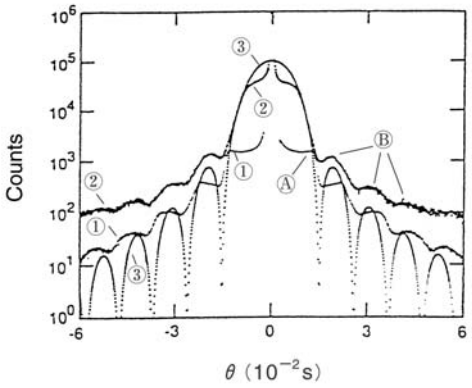

Fig. 4.36. 1D-USAXS curves for latex powder and dispersion. Sample: latex particle of styrene-styrene sulfonate copolymer (a = 145 nm). Curve 1: powder. Curve 2: ethanol dispersion ($\phi = 0.12$). Curve 3: theoretical scattering curve for an isolated sphere of radius 150 nm. The peak A of curve 2 is due to interference by close-packed particles. Taken from [59] with the permission of National Academy of Sciences, USA

(110) planes d_{110} is determined to be 210 nm by Bragg equation

$$\sin\frac{\theta}{2} = \frac{n\lambda}{2d} \tag{4.13}$$

where n is an integer, λ the wavelength of the X-ray, and d the distance between diffraction planes. The lattice constant a_0 is 300 nm by

$$d_{110} = \frac{a_0}{(h^2 + k^2 + l^2)^{1/2}} \tag{4.14}$$

where h, k, and l are the Miller indices. This a_0 value is in a good agreement with that (314 nm) obtained by the Kossel diffraction analysis for the same sample. The closest interparticle spacing $2D_{\exp}$ is found to be 260 nm from $2D_{\exp} = (3^{1/2}/2) \times a_0$, and the average spacing $2D_0[= (3^{1/2}/2) \times (8\pi/3\phi)^{1/3} \times a]$ is 290 nm for $\phi = 0.0376$ and $a = 56$ nm. Obviously, $2D_{\exp} < 2D_0$ and the single crystal occupies $0.72[= (260/290)^3]$ of the total dispersion volume. The rest (0.28) must be for voids or free Brownian particles. This suggests that the crystal contracted during the crystallization process.

It is to be noted that the single crystal was so large that the Hosemann plot [65] and Scherrer' equation [66] for size determination cannot be applied.

From the same silica dispersion as discussed above, which showed scattering profiles of a six-fold symmetry, another scattering pattern of a four-fold symmetry could be observed [67]. While the lattice structure and lattice constant remained unchanged, the [001] direction was found to be parallel to the capillary axis. Whether the profiles are six- or four-fold, the (110) planes were

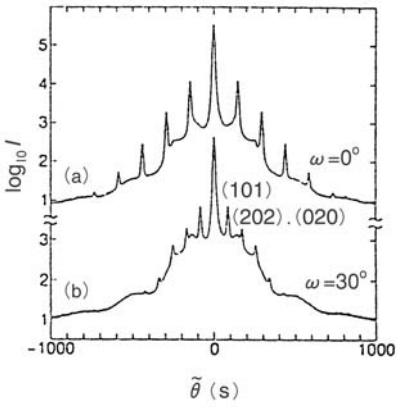

Fig. 4.37. The logarithm to base 10 of the USAXS intensity $I(\tilde{\theta})$ in counts per s versus the apparent scattering angle $\tilde{\theta}$. Sample: colloidal silica particles (a = 56 nm, σ_a = 0.24 μC cm^{-2}, σ_n = 0.06 μC cm^{-2}, ϕ = 0.0376). 25±1°C. The purified silica dispersion was introduced into a capillary with an inner diameter of 2 mm and length of 70 mm and ion-exchange resin particles were put in the lower part of the capillary and in the upper portion, held in place by nylon mesh. The measurements were carried out on the 84th days after the dispersion was introduced into the capillary. The capillary was held vertically during the measurements. The curve (a) was observed at a rotation angle ω of the capillary around its axis of 0° whereas the curve (b) was obtained at ω = 30°. Taken from [64] with the permission of the American Physical Society

found to be in parallel to the capillary wall. As seen from Figs. 4.38 and 4.39, three sets of the (110) planes are "parallel" to the capillary wall for the case of the six-fold symmetry, while two sets are for the four-fold case. We will demonstrate in the next section that colloidal crystals can be easily destroyed by shaking the capillary, a large number of microcrystals of the same structure and lattice constant as before the shaking can be re-formed, and the regenerated microcrystals show always a six-fold symmetry pattern from whichever of the two symmetry cases the microcrystals were allowed to be regenerated. This fact implies that the six-fold symmetry is more stable than the four-fold case. As discussed in Sect. 4.2.4, anionic particles are concentrated in the vicinity of an anionic glass interface. This concentration effect would facilitate the formation of the closest packed structure near the glass surface. The orientation of the crystal showing a six-fold symmetry pattern would be more strongly stabilized than that of a four-fold symmetry case because a larger number of particles can be under the influence of the surface for the former than for the latter.

The next question is how one orientation showing a six- or four-fold symmetry pattern can be selected. In the initial stage of crystallization, it is

plausible that nascent crystals orient randomly and show rotational diffusion. They all grow to certain sizes, and then the Ostwald ripening mechanism steps in, and only one or the other of the two orientations is allowed to grow to the single crystal. That either of $[1\bar{1}1]$ or [001] can be parallel to the capillary surface would be due to the curvature of the surface, which does not allow the crystal growth along other directions. In fact, only these two directions were experimentally found.

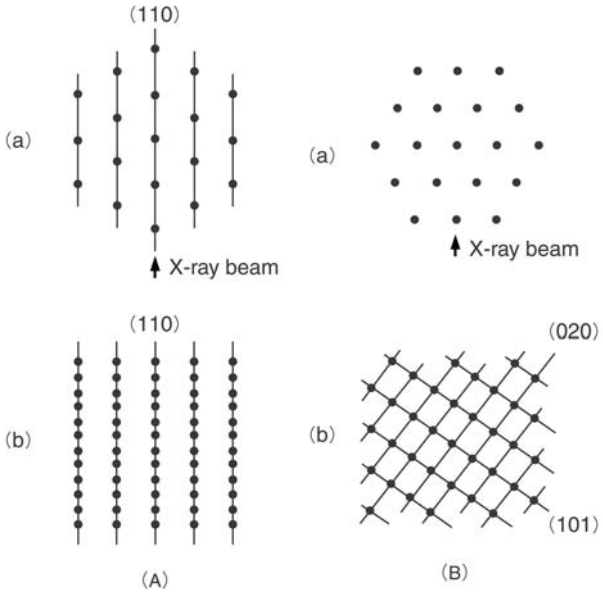

Fig. 4.38. bcc structure showing the six-fold symmetry profile. •: lattice point, —: lattice plane. (a) overview, (b) side view. (A) $\omega = 0$, (B) $\omega = 30°$. Taken from [64] with the permission of the American Physical Society

4.3.2 Rupture and Regeneration of Colloidal Crystals

Colloidal crystals are fragile and easily broken by shaking or by irradiation of strong light. We have discussed the breaking and regeneration of colloidal crystals of silica particles by shaking in [68].

Figure 4.40 is the scattering profile with a four-fold symmetry for a single crystal prior to shaking, from which a bcc structure with a lattice constant of 440 nm was concluded. Figure 4.41 shows the USAXS profiles measured over the period 1- 4 days after the dispersion was shaken and then kept standing. When the angle of rotation of the sample capillary in a plane perpendicular

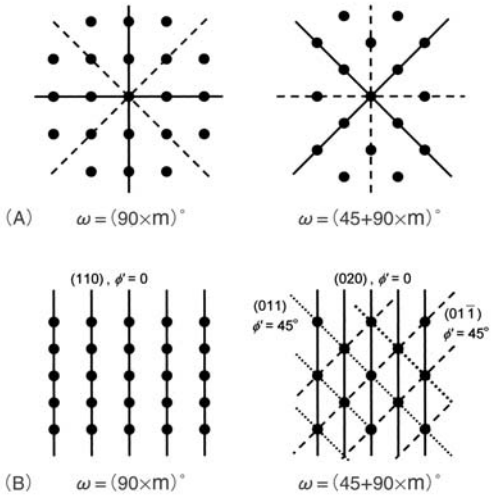

Fig. 4.39. bcc structure showing the four-fold symmetry profile. (A) overview with the [001] direction being parallel to the capillary axis. Solid line and dashed lines: incident X-ray for $\omega = (90 \times \mathrm{m})^\circ$ and $(45 + 90 \times \mathrm{m})^\circ$, respectively. (B) side view. Solid, broken, and dashed lines: lattice planes of the corresponding Miller indices. Taken from [67] with the permission of the American Chemical Society

to the incident X-ray is denoted by $\tilde{\phi}(= 0$ when the capillary is vertically held) [9] and the rotational angle of the capillary around its axis is given by ω the scattering profile is seen to be independent of ω and changes with $\tilde{\phi}$. This fact suggests that crystals regenerated after rupture are neither a single crystal nor powder-like.

Such a structure can be accounted for as follows if a large number of microcrystals (bcc) with a lattice constant of 430 nm are oriented in the capillary with the $[1\bar{1}1]$ direction in parallel with the capillary axis. If the angle between the diffraction plane and the capillary axis is denoted by ϕ_0, ϕ' is defined by the relation

$$\phi' = \phi_0 + \tilde{\phi} \tag{4.15}$$

Then when the lattice structure and its direction are determined, ϕ_0 is fixed. It is 0 and $\pm 54.7^\circ$for (110) of bcc, 35.3° for (200), and 0, $\pm 28.1^\circ$, and $\pm 70.5^\circ$ for (211). When these data are coupled with (4.13) and (4.14), the relationship between $\tilde{\theta}$ and $\tilde{\phi}$ is obtained. The results are shown in Fig. 4.42 by solid curves and are seen to be in good agreement with the observed values shown by the circles. From this comparison, we conclude that the bcc microcrystals are oriented with the $[1\bar{1}1]$ direction kept parallel to the capillary axis.

[9] In the caption of Fig. 3 of [68], $\tilde{\phi}$ was incorrectly defined. The correct definition is given in the text above and also in the Experimental Section of [68].

Note that *the size of the crystals changes by shaking but the lattice symmetry and the lattice constant are maintained unchanged*. By rupturing, the crystal direction changes by 54.7° (the angle between [001] and [1$\bar{1}$1]), resulting in a more stable six-fold symmetry profile. This fact, together with the independence of the profiles of ω suggests that, after shaking, a number of microcrystals are oriented along the capillary axis and distributed randomly around the [1$\bar{1}$1] direction. In Fig. 4.43, such a distribution is schematically shown.

Under the present condition, $2D_{\mathrm{exp}}$ and $2D_0$ were 370 and 390 nm, respectively. The difference is beyond the experimental error limit of the USAXS technique. It is tempting to suggest that the free energy of the total dispersion is lowered by keeping the (110) planes, closest packing plane of bcc, parallel to the capillary surface, which is made possible by the electrostatic attraction between particles and surface (Sect. 4.2.4) and this influence propagates to the interior of the dispersion.

The experimental results and interpretation discussed above are consistent with other experimental findings and seem to be reasonable now, although further systematic study is expected. For example, the influences of a planar glass interface (not capillary surface), the sign and number of interfacial charges, charge density and radius of particles, temperature, dielectric constant of solvent, and viscosity on colloidal crystals have to be examined in detail.

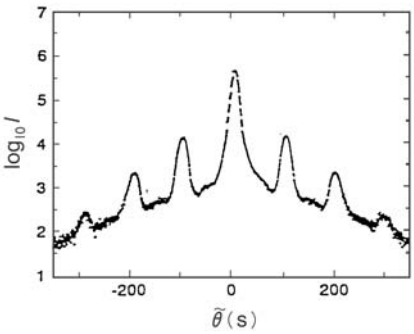

Fig. 4.40. The logarithm of the USAXS intensity $I(\tilde{\theta})$ before shaking in counts per s plotted against the apparent diffraction angle $\tilde{\theta}$. Sample: colloidal silica ($a = 56$ nm, $\sigma_{\mathrm{n}} = 0.06$ μC cm^{-2}). $\phi = 0.0153$. $\omega = 0$. $\tilde{\phi} = 0$. Taken from [68] with the permission of the American Chemical Society

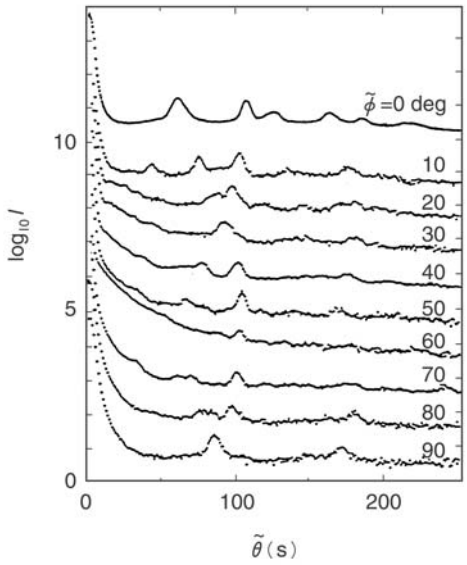

Fig. 4.41. USAXS profiles after shaking. Sample:the same as in Fig. 4.40. The $\tilde{\theta}$ scanning was carried out continuously with consecutive values of $\tilde{\phi}$ after shaking. The curves were independent of the rotational angle of the capillary ω with respect to its axis. The curves were shifted vertically by an order of 10. Taken from [68] with the permission of the American Chemical Society

4.3.3 Determination of Particle Radius and its Distribution

The radius of colloidal particles can be conveniently measured by the USAXS technique in dispersion (not in dried state) and without being bothered by turbidity. This can be achieved by curve fitting as shown in Fig. 4.36. However, at high volume fractions ϕ, the interparticle interference cannot be avoided at low scattering vectors K. To evade this difficulty, Konishi et al. extrapolated the scattered intensity $I(K)$ of colloidal silica dispersions to zero ϕ [69] and compared it with the theoretical value given for a randomly oriented ellipsoid having axes $2R$, $2R$, and $2\nu R$ by the following equation,

$$I\,(K) = C \int_0^\infty p\,(R)\,\nu^2 R^6 \Phi_{\mathrm{e}}^2\,(KR, \nu)\,dR \tag{4.16}$$

where C is a constant relating to the apparatus and the electron density difference, $p(R)$ equals $(1/2\pi\sigma^2)^{1/2} \exp[-(R - R_{\mathrm{n}})^2/2\sigma^2]$ where R_{n} and σ are the number average radius of the particles and the standard deviation, respectively, and Φ_{e}^2 is the particle scattering function of the ellipsoid. Good agreement was obtained with $\nu = 0.9 \sim 1.2$, which indicates that the silica particles (in Fig. 4.37) are either spheres or ellipsoids close to spheres. For

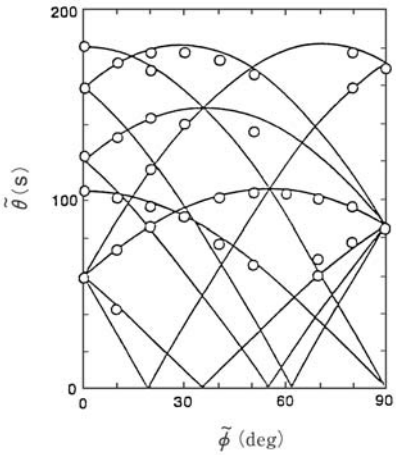

Fig. 4.42. Dependence of the apparent scattering angle $\tilde{\theta}$ on the rotational angle of the capillary in the plane perpendicular to the incident X-ray $\tilde{\phi}$. ○: observed. Solid curves: calculated. Taken from [68] with the permission of the American Chemical Society

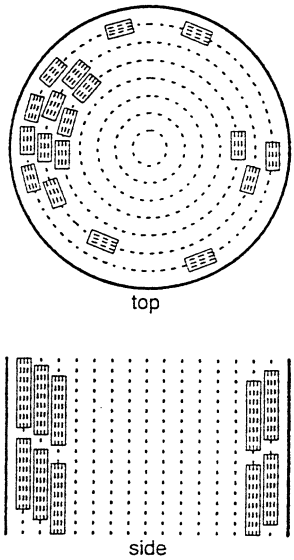

Fig. 4.43. Schematic view of the distribution and orientation of microcrystals (rectangles) in a capillary after shaking. The (110) planes are denoted by dashed lines. Taken from [68] with the permission of the American Chemical Society

$\nu = 1$, the z-average square radius R_z was found to be 56 nm, which is defined by the equation

$$R_z = \left[\frac{\int_0^\infty p(R) R^8 dR}{\int_0^\infty p(R) R^6 dR} \right]^{1/2} \tag{4.17}$$

and σ was 8%.

When the interparticle interaction can be ignored, the following Guinier law holds,

$$I(K) = I(K=0) \exp\left(-\frac{R_g^2 K^2}{3} \right) \tag{4.18}$$

where R_g is the root of the z-average square radius of gyration of the particle. It is required to have $I(K)$ values at low K and c, particularly for charged colloids. A good linear relationship is seen in Fig. 4.44 (a), which is the Guinier plot of the scattering data extrapolated to zero c, and from the initial slope R_g is found to be 47 nm. For spherical particles, we have

$$R_z^2 = \left(\frac{5}{3} \right) R_g^2, \tag{4.19}$$

from which R_z is found to be 60 nm, in agreement with the radius obtained by the curve-fitting with (4.16) within 8%.

Figure 4.44 (b) shows the Guinier plot of the observed intensity without extrapolation. A large deviation from the linearity is clear. Likewise, the form factor derived by using the $F(K)$ of Vrij et al. [70] is non-linear. This can be due to the remaining interference, even though the net charge density and volume fraction are not high (0.06 μC cm^{-2} and 0.0137, respectively). The extrapolation to zero concentration is necessary to correctly estimate the size of charged particles by the Guinier plot.

4.3.4 Structural Analysis of Colloidal Crystals by 2D-USAXS

Since the incident X-ray in the 1D-USAXS apparatus is collimated only in one plane, there remains a smearing effect. As a consequence, it is not easy, though not impossible, to study oriented samples. To overcome this difficulty, 2D-USAXS apparatus is being used, in which the X-ray is collimated in two perpendicular planes according to the principle of Bonse and Hart [58, 71, 72]. The scattered intensity $I(K)$ can be directly measured as a function of scattering vector K. Its optical system is shown in Fig. 4.45. By the collimation in the two planes, the cross section of the incident X-ray of a 2D-USAXS apparatus constructed by Konishi is 1×1 mm^2, and its intensity distribution is almost of point-symmetry. The smearing effect can be ignored. The FWHM of the intensity profile of the direct X-ray beam is about 17 s of arc, corresponding to a density fluctuation of 2 μm in real space.

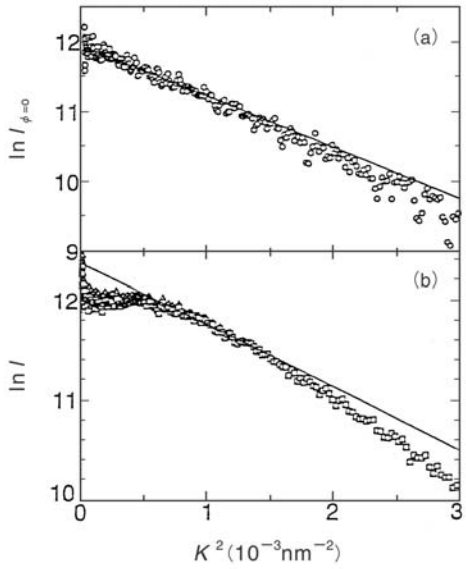

Fig. 4.44. Guinier plots for charged particles. Sample: colloidal silica particles in water. (a) plot of extrapolated ($\phi \to 0$) USAXS data. ○: experimental, solid line: Guinier slope obtained by the least squares method from the data at $K^2 = 4.93 \times 10^{-5} \sim 8.86 \times 10^{-4}$ nm^{-2}. (b) plots of observed USAXS data and the form factor. □: observed intensity, △: observed intensity corrected using the calculated structure factor (See text), solid line: Guinier slope for an isolated sphere ($a = 56$ nm). Taken from [69] with the permission of the American Chemical Society

Figure 4.46 is 2D-USAXS profiles for a silica dispersion. About 30 scattering spots are observed for $118 < \theta < 203$ s. From the values of θ, ϕ_s, and χ, the scattering vector $\boldsymbol{K}$ is determined by the following equation

$$\boldsymbol{K} = (K\cos\chi\cos\phi_s, K\cos\chi\sin\phi_s, K\sin\chi) \tag{4.20}$$

By the method of Busing and Levy [73], the Miller indices can be determined using 3×3 matrices (**UB**)

$$\begin{pmatrix} K_x \\ K_y \\ K_z \end{pmatrix} = \mathbf{UB} \begin{pmatrix} h \\ k \\ l \end{pmatrix}. \tag{4.21}$$

From experimental data we obtain

$$\mathbf{UB} = \begin{pmatrix} 1.21 & 1.11 & -0.07 \\ -0.59 & 0.73 & 1.35 \\ 0.93 & -0.98 & -0.93 \end{pmatrix} \times 10^{-2}\text{nm}^{-1}. \tag{4.22}$$

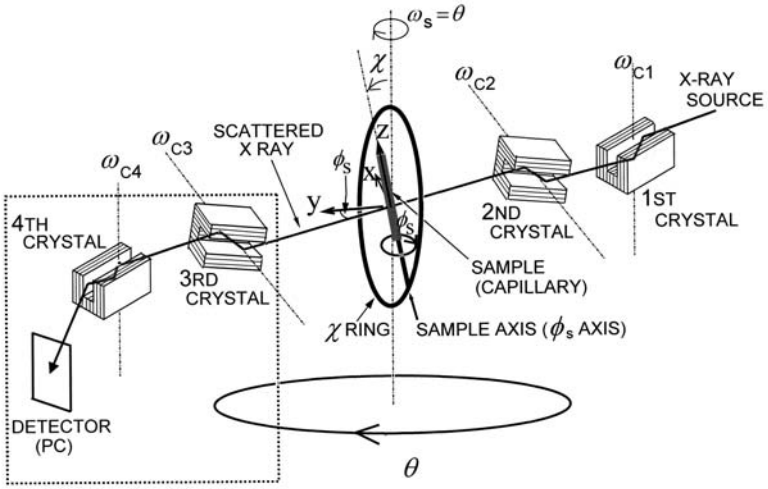

Fig. 4.45. Optical system of 2D-USAXS apparatus. The Ge single crystals were cut parallel to the (111) planes. The X-ray is collimated in the horizontal and vertical planes. The sample capillary is fixed on the χ ring, which can be rotated by ω_s about the vertical axis. $\omega_s = 0$ when the axis of the χ ring is parallel to the X-ray beam. By rotating the capillary in the ring by χ and about the capillary axis by ϕ_s the direction of the scattering vector can be changed. $\chi = 0$ when the capillary is kept vertically and $\phi_s = 0$ when the x axis of the coordinate system associated with the sample is in the plane of the χ ring. To change the magnitude of the scattering vector, we keep $\omega_{C3} = \omega_{C4} = 0$ and rotate the third and fourth crystals together with the detector, which are surrounded by the dashed line in the figure, by θ about the vertical axis at the sample, keeping the rotation angle ω_s being equal to $\theta/2$. By removing the second and third crystals, this converts to the 1D-USAXS apparatus. Taken from [72] with the permission of the American Physical Society

This result indicates that a bcc single crystal is formed in the dispersion, the lattice constant is 380 nm, and the $[1\bar{1}1]$ direction is kept parallel to the capillary axis.

Starting from these conclusions, we conversely calculated the positions of the scattering spots using (4.21) and (4.22). The results are shown by circles in Fig. 4.46. Excellent agreements with the observation are obtained for 22 spots. Other spots, which could not be reproduced by the above calculation, indicate that there are formed microcrystals in the dispersion, in addition to the single crystal. As a matter of fact, the capillary surface has a curvature while the surface of bcc crystal is planar. Thus there can be small space between the two surfaces, where tiny crystals can grow.

Strong X-ray source such as synchrotron is now available and makes it possible to study colloidal systems having small density differences between

particle and medium. Sirota et al. studied polystyrene-based latex particles in mixtures of H_2O and ethanol ($\phi = 0.06 \sim 0.30$) [74]. They found correlated liquid and bcc and fcc structures at small ϕ. The occurrence of a glass phase was concluded at large ϕ from the high and narrow structure factor. The phase diagram was found to quantitatively disagree with a computer simulation by Robbins et al. [75] using the purely repulsive Yukawa potential (See Chap. 2), though the general features were qualitatively reproduced.

Vos et al. investigated colloidal crystals in concentrated H_2O dispersions of polystyrene-based latex particles [76]. Figure 4.47 is the scattering profile at $\phi = 0.56$. It was concluded that an fcc single crystal with a lattice constant of 370 nm was maintained with the (111) plane kept parallel to the container surface. These findings are in agreement with microscopic observation (Sect. 4.2.3) and with Kossel line analysis (Chap. 5). From a large number of very sharp scattering spots, the root-mean-square displacement by the Debye-Waller effect was claimed to be 3.5% of the interparticle distance at such high ϕ's. The small displacement at high ϕ's is in qualitative agreement with the microscopic observation shown in Fig. 4.8.

Furthermore Vos et al. studied polystyrene latex particles in methanol and silica particles in dimethylformamide and in water ($\phi < 0.001$) [77] to determine the K dependence of the maximum and obtained the distribution of a from the K^2 dependence of the peak height.

4.3.5 Interparticle Distance as Determined by the USAXS Technique

The SAXS measurements of flexible ionic polymer solutions provided only a single broad scattering peak as discussed in Chap. 3. However, we can observe several orders of scattering peaks and spots by the USAXS methods, so that the lattice constant and interparticle distance $2D_{\mathrm{exp}}$ can be obtained more precisely. In Table 4.6, $2D_{\mathrm{exp}}$ is compared with the average spacing $2D_0$ estimated from concentration. The ratio, $2D_{\mathrm{exp}}/2D_0$, is equal to unity in concentrated dispersions and is smaller than unity at low concentrations. The ratio for silica particles in this table is $0.88 \sim 0.92$, while that for latex particles in Table 4.3 was $0.65 \sim 0.90$. This difference may be due to the lower charge density of silica particles.

Matsuoka et al. studied the salt concentration dependence of $2D_{\mathrm{exp}}$ by the 1D-USAXS technique for water dispersions of poly(methyl methacrylate) (MMA) particles [78]. Powder patterns of fcc were observed at $\phi \approx 0.04$ and in a C_{s} range between 0 and 10^{-5} mol L^{-1}. It was noticed that $2D_{\mathrm{exp}}$ from peak position increased with increasing C_{s} and decreased after passing through a maximum ($\approx 2D_0$). The maximum was located at $\kappa a = 1.3$. The decreasing tendency of $2D_{\mathrm{exp}}$ has been widely observed (Table 4.4) and is in accord with the DLVO theory and with Sogami theory to be discussed in Chap. 6. However, the increasing trend below $\kappa a = 1.3$ was observed for the first time. Yamanaka et al. carried out a USAXS study for water dispersion of silica

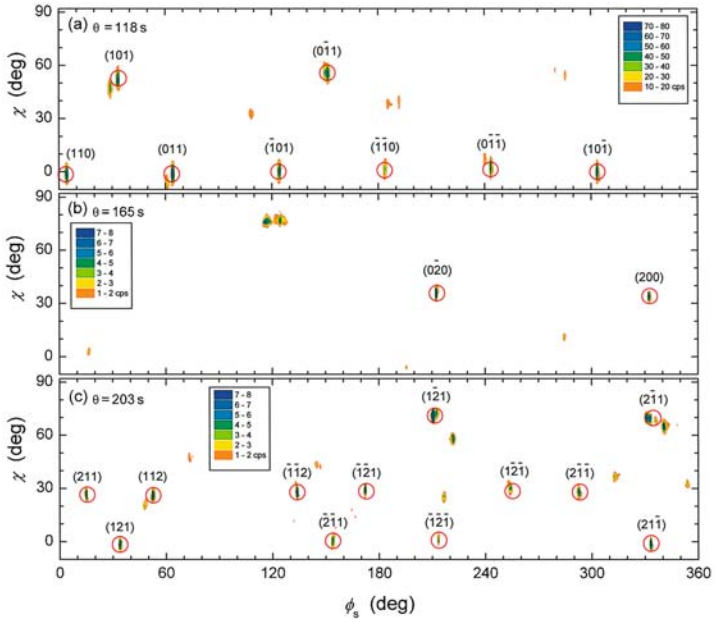

Fig. 4.46. 2D-USAXS profiles of a dilute water dispersion of silica particles. Sample: silica particles (the same as in Fig. 4.37). $\phi \approx 0.025$. (a) $\theta = 118$ s, (b) 165 s, (c) 203 s. The Miller indices are given by the corresponding spots. ◯: theoretical scattering spot positions computed for a bcc single crystal of a lattice constant 380 nm with the $[1\bar{1}1]$ direction parallel to the capillary axis. Taken from [72] with the permission of the American Physical Society

Table 4.6. The interparticle distance as determined by the USAXS method

ϕ	$2D_{\mathrm{exp}}$ nm	$2D_0$ nm	$2D_{\mathrm{exp}}/2D_0$
Silica particles [a] (a =55 nm, σ_{a}= 0.24 μC cm^{-2}, σ_{n} =0.07 μC cm^{-2})			
0.0096	390	450	0.88
0.0301	280	310	0.91
0.0753	200	230	0.92
Polystyrene latex particles [b] (a =120 nm, σ_{a} :not reported)			
0.56	257	265	0.97

[a] T. Konishi, N.Ise, unpublished.
[b] Calculated from the data in W.L.Vos et al. *Langmuir* **13**, 6004 (1997).

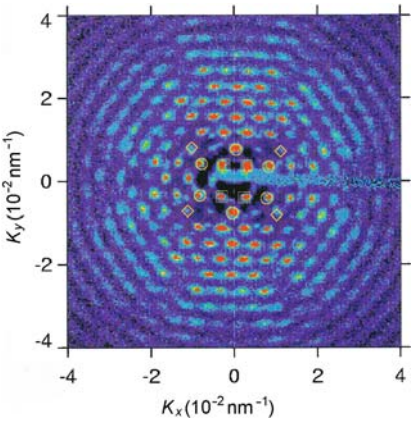

Fig. 4.47. USAXS profiles of a concentrated water dispersion of polystyrene-based latex particles. $a = 120.8$ nm, X-ray: European Synchrotron Radiation Facility, wavelength = 0.09880 nm, cross-section = 0.2×0.5 mm^2, $\phi = 0.56$. Taken from [76] with the permission of the American Chemical Society

particles at C_s lower than 10^{-5}mol L^{-1} and found that $2D_{exp}$ was smaller than $2D_0$ and was insensitive toward C_s. The difference between MMA latex and silica particle might be due to the smaller charge number of the latter. Further systematic study seems necessary on the C_s dependence of $2D_{exp}$.

4.4 Static and Dynamic Light Scattering, Neutron Scattering, and Dynamic X-Ray Scattering

Since colloidal particles are large, the point-scatterer assumption is no longer valid. Furthermore, multiple scattering becomes important when the refractive index difference between particle and solvent is large. Thus it is not easy to obtain correct interpretation of light scattering data for water dispersions of polystyrene-based latex particles and silica particles. It is required to avoid such technical difficulties by careful selection of the experimental condition or by devising experimental setups to measure only single scattering. In the following section, we consider recent light scattering study for particles or solutes of relatively small diameters at low concentrations [51, 79]. See the review article [80] for papers that are not discussed here.

4.4.1 Static Light Scattering

According to the Rayleigh-Gans approximation [81], the scattered intensity $I(K)$ from a volume V_s containing N particles is given by the following equation

$$I(K) = A_{\mathrm{RG}} f_M(K) F(K) \tag{4.23}$$

where $K = 4\pi n_{\mathrm{m}} \sin\theta/\lambda$ with n_{m} being the refractive index of the medium or solvent and $f_M(K)$ and $F(K)$ are the form factor and the structure factor, respectively. They are given by the following equations,

$$F(K) = 1 + \left(\frac{1}{N}\right) \sum_{i>j=1} \exp\left[\mathrm{i}\boldsymbol{K} \cdot (\boldsymbol{r}_i - \boldsymbol{r}_j)\right] \tag{4.24}$$

and

$$f_M(K) = \left(\frac{1}{Ka}\right)^6 \left[3\left\{\sin(Ka) - (Ka)\cos(Ka)\right\}\right]^2 \tag{4.25}$$

with a being the particle radius and $\boldsymbol{r}_i$ the center of the gravity of the sphere i, and A_{RG} is given by for vertically polarized scattered light

$$A_{\mathrm{RG}} = \frac{9\pi^2 n_{\mathrm{m}} (m_{\mathrm{r}} - 1)^2}{\lambda^4 (m_{\mathrm{r}} + 2)^2} \left(\frac{4\pi a^3}{3}\right)^2 n_{\mathrm{p}}^* V_{\mathrm{s}} \left(\frac{I_0}{r_{\mathrm{d}}^2}\right) \tag{4.26}$$

where m_{r} is $n_{\mathrm{p}}/n_{\mathrm{m}}$ and n_{p} the refractive index of the particle, n_{p}^* the number of the particles per unit volume (cm^{-3}), I_0 the intensity of incident light, and r_{d} the distance between the scattering volume and detector.

As mentioned in Sect. 4.2.4, there can be observed voids or macroscopic gas-liquid phase separation at low ϕ's of colloidal particles. Above a critical ϕ, a phase separation into dense and dilute phases takes place. The particle distribution in each phase was studied by light scattering [79]. The level of C_{s} in water dispersions of polystyrene latex particles (a =55 nm, $n_{\mathrm{p}}^* < 5 \times 10^{12}$ cm^{-3}) was lowered by addition of mixed ion-exchange resins. Before the addition, the $F(K)$ was hardly K-dependent, indicating the absence of spatial correlation. Figure 4.48 shows the appearance of dispersions of various latex concentrations several days after the deionization was attained. At $n_{\mathrm{p}}^* = 4.11 \times 10^{12}$ (a) and 3.26×10^{12} (b), the dispersions looked homogeneously turbid, while phase separation into transparent top layer and turbid layer took place at $n_{\mathrm{p}}^* = 1.61 \times 10^{12}$ (c) and 1.58×10^{12} cm^{-3} (d). The $F(K)$ for (b) and (d) is demonstrated in Fig. 4.49 (a) and (b). As seen from (a), the $F(K)$ at different heights in the homogeneous phase indicates liquid-like structure and is height-independent, indicating that the particle distribution is homogeneous. On the other hand, (b) shows liquid-like $F(K)$ at the lower part of the dispersions and gas-like structure factor at the top, implying that gas-liquid equilibrium is maintained.

It is worth mentioning that a re-entrant phase transition was observed in light water when C_{s} was decreased by the deionization process. At high, intermediate, and low C_{s}, respectively, the dispersion was homogeneously liquid-like, it displayed a gas-liquid phase separation, and it again became homogeneous. The re-entrant transition is unique for colloidal systems, and is not observed in real atomic and molecular systems. The reason for this is that

particles interact with other macroions and counterions, not in vacuum but in liquid medium. One should remember that this "gas-liquid phase" equilibrium is observed in light water. When the density difference between particles and medium is eliminated by using a mixture of D_2O and H_2O, the phase separation occurs in the form of voids. This latter interesting phenomenon will be discussed in Chap. 8.

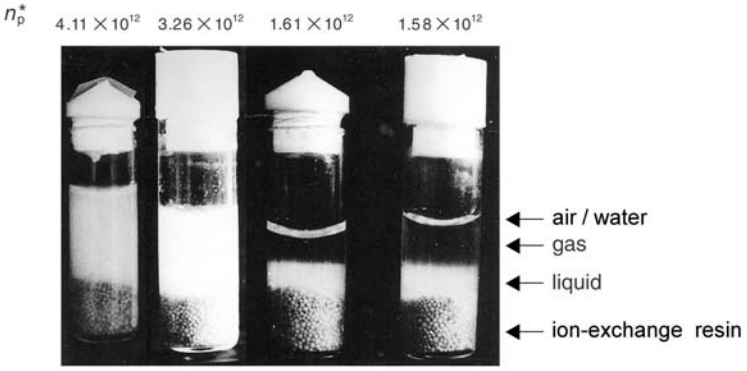

Fig. 4.48. Photograph of sample cells of polystyrene latex-light water dispersions several days after the deionization equilibrium was attained. The ion-exchange resin particles are seen at the bottom of the cells. $n_p^* \times 10^{-12}$: (a) 4.11, (b) 3.26, (c) 1.61, and (d) 1.58. For small particle concentrations [(c) and (d)], a turbid liquid phase is on the top of the resin particles and in equilibrium with transparent gas phases. On the other hand, when particle concentration is high, the dispersion phase-separates at the early stage of deionization (namely at high C_s) and becomes homogeneous with the progress of deionization as shown in (a) and (b). Taken from [79] with the permission of VCH Publishers

It is well known that bcc and fcc structures are formed at low and high particle concentrations, respectively. Assuming bcc under the condition of Fig. 4.48, the Bragg spacing between particles $2D_{exp}$ is estimated from the peak position of $F(K)$ and shown in Fig. 4.50, which is compared with the average interparticle distance $2D_0$. Clearly, $2D_{exp} < 2D_0$ at low concentrations. This observation is consistent with those for flexible ionic polymers (Chap. 3) and ionic colloids (Chap. 4). Theoretical interparticle distance estimated by Sogami's theory (Chap. 6) is shown by the broken curve in Fig. 4.50. A good agreement is seen.

Antonietti et al. prepared polystyrene microgels by polymerization of styrene in microemulsion with cross-linking, and subsequently sulfonated (about 70%) the gels to obtain spherical, anionic polyelectrolytes ($a = 7 \sim 50$ nm) [82]. This is an interesting material having intermediate sizes between colloidal particles and flexible polymers. Gröhn and Antonietti investigated

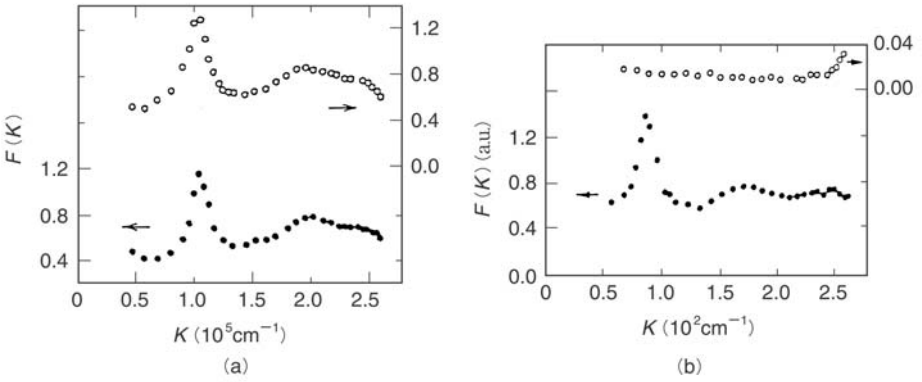

Fig. 4.49. Structure factor at different heights of dispersions. (a) top (○) and lower regions (●) of Fig. 4.48 (b). (b) transparent top (○) and lower regions(●) of Fig. 4.48 (d). Taken from [79] with the permission of VCH Publishers

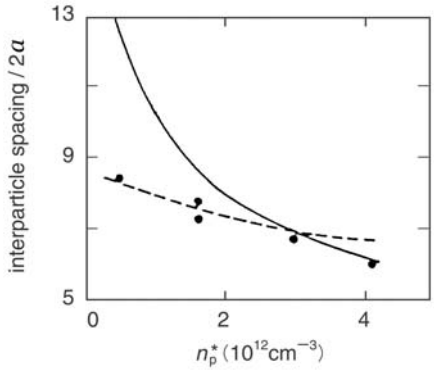

Fig. 4.50. Interparticle (Bragg) distance from the structure factor and average distance $2D_0$. Particle distribution: bcc. Salt concentration= 3×10^{15} cm^{-3}. •: observed, full curve: $2D_0$, broken curve: interparticle distance calculated by Sogami theory (See Chap. 6). Taken from [79] with the permission of VCH Publishers

their solution structure in detail by using static light scattering [83]. Table 4.7 gives some physical properties. The structure factor $F(K)$ obtained from the observed scattered intensity has at least two peaks with the height of the first peak being $1.5 \sim 3.0$. This suggests that the microgels also form ordered structures under salt-free condition. The interparticle (Bragg) distance $2D_{\mathrm{exp}}$ was smaller than the average distance $2D_0$ at low concentrations, while $2D_{\mathrm{exp}} \approx 2D_0$ at high concentrations, as shown in Fig. 4.51. Macroscopic phase separation into dense and rarified phases was observed except a sample of small radius (K411b) at low concentrations, where $2D_{\mathrm{exp}} < 2D_0$. The solution stayed homogeneous at high concentrations, where $2D_{\mathrm{exp}} \approx 2D_0$. The $2D_{\mathrm{exp}}$ in the dense phase at the bottom of solution container was height-independent, showing that the phase separation observed was not due to gravitational sedimentation. In the case of K411b, no separation was observed; the solution looked homogeneous but small regions having strong scattering power were floating within it. This would be the same as the two-state structure discussed in Chap. 3. The inequality relation $2D_{\mathrm{exp}} < 2D_0$ was observed at low concentrations of flexible ionic polymers, proteins, and ionic colloid particles but the gas-liquid phase separation was reported only for the colloidal systems. These experiences are in line with the fact that no separation took place for the small-size microgel. This can be attributed to the vigorous Brownian motion of the small entities.

When C_{s} was decreased, the peak position for K24 shifted toward larger angles and the peak height was lowered. At a NaCl concentration of 5×10^{-6}mol L^{-1}, the peak disappeared. In other words, the $2D_{\mathrm{exp}}$ was decreased with increasing C_{s}. This trend is the same as for colloidal particles (Sect. 4.2.3, in particular Table 4.4), but is opposite to the observation for flexible polymers.

When the cross-linking density was lowered from 1/20 to 1/40 and 1/80, no phase separation was observed, the scattering peak disappeared, and an upturn was observed at lower scattering angles.

Table 4.7. Properties of polyelectrolyte microgels [a]

	Cross-linking density	Hydrodynamic radius (nm)	Polydispersity[a]	$M_{\mathrm{W}} \times 10^6$
K8		48.0	0.17	69.4
K24		43.5	0.05	46.8
K28		31.5	0.12	15.0
L33	1/20	23.7	0.12	8.30
L35b		19.8	0.14	5.40
K411b		6.7	0.11	
K64	1/40	40	0.20	16.0
K2	1/80	38	0.24	13.8

[a] Determined by dynamic light scattering at a NaCl concentration of 0.5 mol L^{-1}.

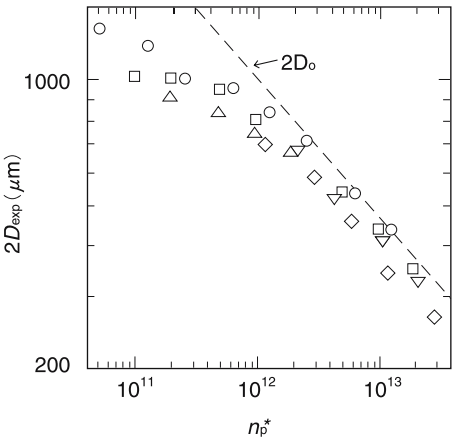

Fig. 4.51. Comparison of interparticle distance $2D_{\rm exp}$ with average interparticle distance $2D_0$ for polyelectrolyte microgels of various sizes. Abscissa: number density of microgels ($\rm cm^{-3}$), broken line: $2D_0$, gel radius; ○: 48 nm, □: 44 nm, △: 32 nm, ▽: 24 nm, ◇: 19 nm. Taken from [83] with the permission of the American Chemical Society

4.4.2 Dynamic Light Scattering

In the dynamic light scattering of colloidal systems, we have to try to avoid the influence of multiple scattering or, otherwise, we have to be satisfied with approximate evaluation of the experimental data. A new experimental technique, two-color dynamic light scattering (TCDLS), is being developed to measure separately single scattering only [84–86]. However, no measurements have been reported on water dispersions of ionic colloidal particles.

We discuss here the study by Härtl et al. by the refractive index-matching technique using mixed solvents [87] . The samples were carboxylated silica particles ($a = 45$ nm) in water-glycerin ($\phi = 7.36 \times 10^{-4} \sim 4.58 \times 10^{-3}$). By static light scattering (SLS) the scattered intensity $I(K)$ was determined at $C_{\rm s} = 0$ and > 0, $f_M(K)$ was estimated at high $C_{\rm s}$, (where $F(K) = 1$), and $F(K)$ at $C_{\rm s} = 0$ was determined. The results are shown in Fig. 4.52 (a), in which theoretical $F(K)$ derived by rescaled mean spherical approximation (RMSA) of Hansen and Hayter [88] is shown for comparison. The field autocorrelation function $g^{(1)}(K, \tau)$ is given by

$$g^{(1)}(K, \tau) = \exp\left(-K^2 D_0 \tau\right) \tag{4.27}$$

from which the diffusion coefficient of free particles D_0 can be determined. When τ is small, we have

$$D_{\rm eff}(K) = D_0 \left(\frac{H(K)}{F(K)}\right) \tag{4.28}$$

where D_{eff} is the effective diffusion coefficient and $H(K)$ is the hydrodynamic factor [89,90]. Härtl et al. carried out DLS measurements to determine D_{eff}, from which $H(K)$ was estimated using $F(K)$ from SLS. The results are shown in Fig. 4.52 (b). It is seen that $F(K)$ and $H(K)$ have a peak at the same aK [10]. This implies that previous interpretation of DLS data based on the assumption of $H(K) = 1$ is permissible as far as the peak position, and hence the information of the interparticle distance, is concerned.

We turn to the simultaneous investigation of particle distribution in dispersions by microscope in real space and by DLS in Fourier space [91]. By using fluorescent poly(methyl methacrylate) (PMMA) latex particles and fluorescence microscopy, much smaller particles can be studied than by ordinary optical microscopy. The binary images of micrographs showing particle distribution are shown in Fig. 4.53 (a) and (b). In (a) an ordered region is seen to coexist with free particles (two-state structure). Its 2D-Fourier pattern (c) shows a first-order peak and the second halo, though not clear.

The radial distribution function $g(r)$ was determined by measuring the interparticle distance for 35,000 particles (Sect. 4.2.3). The $g(r)$ was Fourier-transformed to the structure factor $F(K)$ and is shown in Fig. 4.54.

As seen from Fig. 4.54, the D_0/D_{eff} determined by DLS and the $F(K)$ derived from $g(r)$ agreed with each other as far as the peak position is concerned. The interparticle distance $2D_{\text{exp}}$ can be estimated by three different techniques, and is shown in Table 4.8. The three methods provide consistent values for $2D_{\text{exp}}$. Furthermore, the $2D_{\text{exp}}$ found is smaller than the average distance $2D_0$. The $2D_{\text{exp}}$ is practically temperature-indenpendent, indicating that thermal expansion of crystals is counterbalanced by shrinking caused by intensification of the particle-particle attraction due to decrease in the dielectric constant (Sect. 4.2.3).

The DLS technique provides information of particles inside the dispersions, whereas particles in the vicinity of the container wall can be observed by the ordinary microscope. The fact that these two techniques consistently showed the inequality relation $2D_{\text{exp}} < 2D_0$ can be taken as implying the negligibly

[10] The good agreements of RMSA results with observation in Fig. 4.52 were obtained assuming that the net charge number of particles (Z_{n}) was 550. On the other hand, the ζ potential was measured on the sample, from which about 10^4 was estimated for Z_{n} . The discrepancy between the two Z_{n} values is too large. It was not made clear how the RMSA results were influenced by Z_{n} so that it is not obvious that the agreement of the RMSA results with experiments proves the elimination of the multiple scattering. The ambiguity associated with the ζ potential was mentioned in Sect. 4.1.1. The RMSA calculation with a Z_{n} value measured by an independent technique has to be performed. It is desirable that the problem of the multiple scattering be systematically investigated by a technique such as dynamic X-ray scattering.

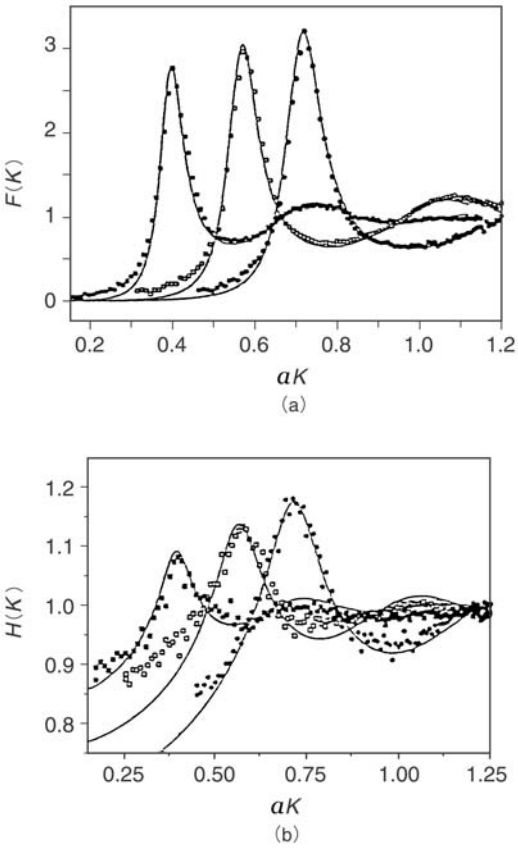

Fig. 4.52. (a) Structure factor and hydrodynamic factor of carboxylated silica particle dispersions. Medium: water-glycerin. ϕ, ■: 7.63×10^{-4}, □: 2.29×10^{-3}, •: 4.58×10^{-3}. —: Structure factor obtained by the RMSA. (b) Hydrodynamic factor calculated by Nägele-Baur's theory [90]. Taken from [87] with the permission of the American Institute of Physics

small influence of the wall on the particle distribution, at least within the experimental precision [11].

[11] This statement must be taken cautiously. As a matter of fact, we know for colloidal crystals that the closest packed planes of bcc or fcc are maintained in parallel to the surface of container wall, according to microscopic observation (Sect. 4.2.3), USAXS measurement (Sect. 4.3.2) and Kossel diffraction technique (Chap. 5). This fact indicates the presence of a weak electrostatic attraction between the container wall and the particles (Sect. 4.2.4).

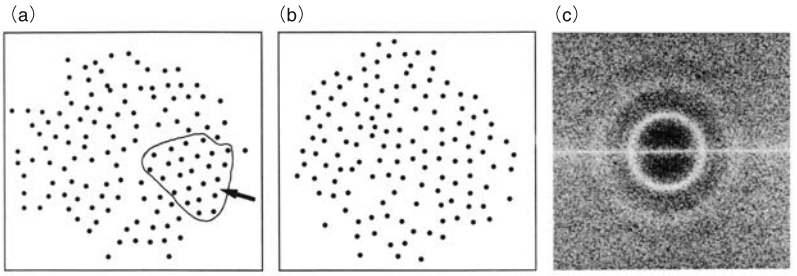

Fig. 4.53. Computer-treated binary images of the two-state structure and the 2D-Fourier pattern. Sample: PMMA particle containing coumarin 6 ($a = 70$ nm). Medium: water. $\phi = 1.5 \times 10^{-3}$. (a) and (b) show particle distributions at different locations in a dispersion. In (a), the ordered region is pointed to by an arrow. The Fourier transform was carried out by using 48 distribution images as shown in (a) and (b). Taken from [91] with the permission of the American Chemical Society

Table 4.8. Interparticle distance estimated from radial distribution function, 2D-Fourier pattern, and dynamic light scattering [a]

ϕ	Temperature (°C)	$2D_{\mathrm{exp}}$ (μm)			$2D_0$ (μm)
		$g(r)$	2D-Fourier	DLS	
0.0015	20	0.91	0.95	0.97	1.11
	25	0.89	0.95	0.95	
	30	0.89	0.92	0.90	
	50	0.88	0.95	0.98	
0.001	20	0.98	1.02	1.05	1.27

[a] Sample: fluorescent poly(methyl methacrylate) particles $a = 70$ nm, $\sigma_{\mathrm{a}} = 0.75$ μC cm^{-2}.

4.4.3 Neutron Scattering

Taking advantage of the strong penetration of neutrons due to their weak interaction with matter, a number of papers have been published on structural studies of concentrated colloidal dispersions by small-angle neutron scattering. However, not so many studies have been carried out on dilute dispersions of ionic colloidal particles. In the present section, we discuss the work on polystyrene latex particles by Ottewill and his associates [92]. The scattered intensity $I(K)$ from interacting systems is given by

$$I(K) = An_{\mathrm{p}}^{*} \left(\frac{4\pi a^3}{3} \right)^2 (\rho_{\mathrm{p}} - \rho_{\mathrm{s}})^2 f_M(K) F(K) \tag{4.29}$$

where A is a constant containing instrumental factors, ρ_{p} and ρ_{s} are the coherent neutron-scattering length density of the particle and the medium, respectively, n_{p}^{*} is the number of particles per cm^3. For monodisperse spheres,

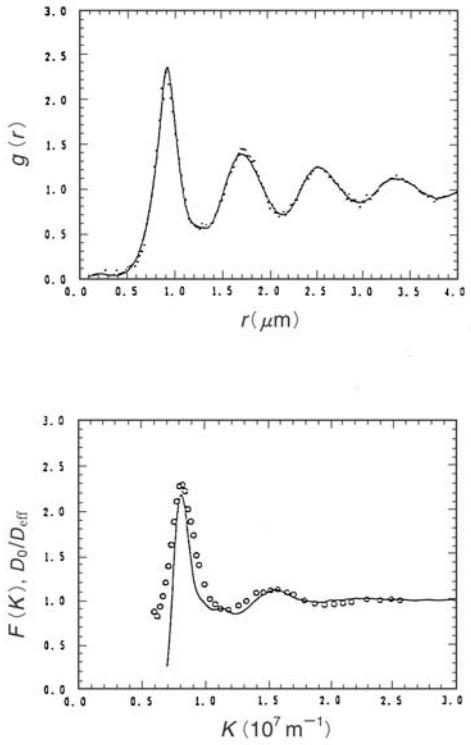

Fig. 4.54. Radial distribution function and structure factor as determined by fluorescence microscopy and by dynamic light scattering. Sample: fluorescent PMMA latex ($a = 70$ nm). $\phi = 1.5 \times 10^{-3}$. ○: D_0/D_{eff} determined by DLS. Solid curve: $F(K)$ obtained from $g(r)$ determined by the positions of 35,000 particles by microscopy. Taken from [91] with the permission of the American Chemical Society

$f_M(K)$ is given by (4.25), so that $F(K)$ can be estimated from $I(K)$ and can be converted to $g(r)$. The values of $F(K)$ obtained have one or two peaks as shown in Fig. 4.55, suggesting the existence of spatial correlation of the particles. The peak position shifts toward higher angles with increasing particle volume fraction and salt concentration, in accordance with microscopic observation (Tables 4.3 and 4.4).

The $g(r)$ obtained at $C_s = 10^{-4}$ mol L^{-1} and $\phi = 0.01$ shows a form close to that expected for a liquid-like system. This is reasonable under the condition. When ϕ is increased, the first and second peaks are found, suggesting the structural correlation. This trend is in qualitative agreement with the microscopic investigation discussed in Sect. 4.2.3.

Cebula et al. further estimated the potential of mean force between particles $\Phi(r)$ by the following equation

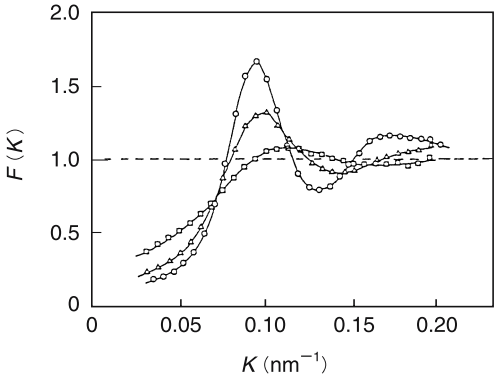

Fig. 4.55. Structure factor of colloidal dispersions. Sample: polystyrene latex ($a = 15.7$ nm, $\sigma_a = 4.2$ μC cm^{-2}). $\phi = 0.04$, C_s (NaCl); ○: no salt, △: 10^{-3} mol L^{-1}, □: 5×10^{-3} mol L^{-1}. Taken from [92] with the permission of the Chemical Society

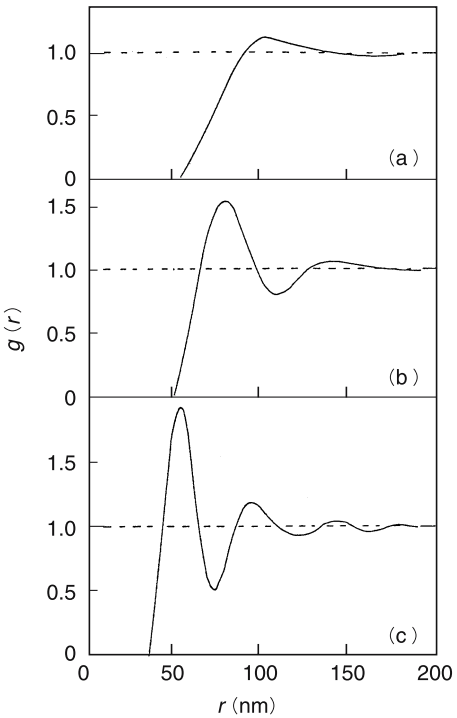

Fig. 4.56. Radial distribution function of latex dispersions as studied by SANS. Sample: polystyrene latex ($a = 15.7$ nm), $C_s = 10^{-4}$ mol L^{-1}, ϕ: (a) 0.01, (b) 0.04, (c) 0.13. Taken from [92] with the permission of the Chemical Society

$$g(r) = \exp\left(\frac{-\Phi(r)}{k_{\mathrm{B}}T}\right) \tag{4.30}$$

and noticed the presence of potential minima at $C_{\mathrm{s}} = 10^{-4}$ mol L^{-1}, as seen from Fig. 4.56. The depth of the potential well was reported to be 0.1 $k_{\mathrm{B}}T$ at $\phi = 0.01$(a) and 0.6 $k_{\mathrm{B}}T$ at $\phi = 0.13$(c). Since this technique to evaluate the potential is relevant to recent direct measurements of the pair potential at very low particle concentrations, it will be again discussed in Chap. 9. Cebula et al. estimated the effective radius of particles (a_{eff}) by fitting the observed $F(K)$ with a hard-sphere model, which was found to be larger than the real radius by a factor of 1.6∼3.0. As discussed in Sect. 4.2.1, this discrepancy may be ascribed to the deficiency of the model. Furthermore, the $F(K)$ was estimated by using the repulsive potential U_{R} of the DLVO theory and a theory of Ashcroft and Lekner [93],

$$U_{\mathrm{R}} = \frac{\varepsilon a^2 \psi_a^2}{R} \exp(2\kappa a) \exp(-\kappa R) \tag{4.31}$$

where ψ_a is the surface potential and R is the interparticle distance. It was reported that the best fit with observation was reached using a_{eff} of 43.5 and 25.1 nm and $\psi_a = -20$ and -11 mV at $\phi = 0.01$ and 0.11, respectively. On the other hand, the ζ potential was observed to be-58 mV, considerably different from ψ_a. The a_{eff} is much larger than a (15.7 nm). Thus, the authors pointed out that "there are a number of problems attached to (4.31) for interacting systems". The $g(r)$ was calculated by Brownian dynamics simulation assuming (4.31) and compared with the observed values. The best fit was obtained when $\sigma_{\mathrm{n}} = 0.21$ μC cm^{-2}. The σ_{a} was measured to be 4.2 μC cm^{-2}. According to the experimentally found relation, (4.6), σ_{n} corresponding to this σ_{a} value is 0.72 μC cm^{-2}, three times larger than that from fitting the equation. It is desirable to check the validity of the DLVO theory by determining directly the σ_{n} value, rather than by the measurements of ζ which is ambiguous as mentioned in Sect. 4.1.1.

The influence of shear stress on ionic colloidal crystals has been investigated by light scattering [94] and by neutron scattering [95]. The former has been used at low concentrations to avoid multiple scattering, where the viscosity is low and the shear stress effect is not large. Neutron scattering is more appropriate under conditions where the effect is pronounced. Ackerson et al. studied the influence of the shear rate ($\dot{\gamma} = 0 \sim 10^3$ s^{-1}) for polystyrene-based latex ($a = 50$ nm)-$\mathrm{D_2O}$ dispersions at $\phi = 0.14$ by using a Couette viscometer. It was concluded that, at $\dot{\gamma} = 0$, the [111] of hcp was maintained parallel to the direction of the shear stress, or the (111) plane was kept parallel to the vertical wall of container. At $\dot{\gamma} = 30$ s^{-1} the (111) planes slipped past one another, resulting in a strained close packed structure. When $\dot{\gamma}$ was increased to 160 s^{-1}, the crystal structure was further distorted, resulting in weaker iridescence. The scattering profile showed an amorphous structure with some tendency for particles to align parallel to the direction of the shear.

Ackerson et al. noted that the iridescence was interestingly intensified at this shear rate. The fact that the close packed planes were kept parallel to the container wall was also observed by microscope (Sect. 4.2.3), USAXS technique (Sect. 4.3.2) and Kossel diffraction (Chap. 5). The fact that such an orientation was maintained at $\dot{\gamma} = 0$ seems to suggest that it was not caused by the flow of the dispersion, but by the attraction between the interface and particles (Sect. 4.2.4).

4.4.4 Dynamic X-Ray Scattering

Using a synchrotron as a source of strong X-rays, Vos et al. performed simultaneously dynamic X-ray scattering (DXS) experiments and DLS measurements for dispersions of silica particles (a =56 nm, n =1.465) in a refractive index-matched mixture of ethanol (n =1.36) and benzyl alcohol (n =1.54). The correlation functions of the scattered intensity $g^{(2)}$ obtained from the two techniques agreed satisfactorily. The ratio of D_0 and D_{eff} (from the relaxation rate $\Gamma = K^2 D_{\text{eff}}$) is shown in Fig. 4.57. The data from DXS and DLS are seen in good agreement in the K region where the two methods were accessible. Also in Fig. 4.57 are shown the structure factor $F(K)$ values obtained from the scattered intensity of the independent static light scattering and the form factor $f_M(K)$. The $F(K)$ is found to be in satisfactory agreement with the D_0/D_{eff} with respect to the peak position. For comparative purposes, the structure factor calculated with a theory of Percus and Yevick [97] for hard spheres is given by the dotted curve. Except at low K's, its agreement with the observation is not satisfactory.

Although Vos et al. did not mention it, the interparticle (Bragg) distance ($2D_{\text{exp}}$) is estimated to be 0.13 μm from the peak position of the $F(K)$. On the other hand, the average distance $2D_0$ from the concentration given is 0.16 for simple cubic (sc) and 0.18 μm for fcc. Clearly $2D_{\text{exp}} < 2D_0$, suggesting the formation of the two-state structure. As seen from Table 4.3, it was at low volume fractions ϕ below 0.06 for a high charge density particle that this inequality relation was distinctly found in aqueous media and it was believed less plausible at higher concentrations. Remarkably, Vos et al.'s data shows that the relation is valid at $\phi = 0.164$ in non-aqueous media. This result is acceptable in light of the microscopic observation (Fig. 4.13), which indicated that $2D_{\text{exp}}$ became smaller with decreasing dielectric constant ε of the medium. These outcomes imply that the interparticle interaction is of an electrostatic origin and attractive and therefore the attraction is intensified, causing contraction of the crystals. If the electrostatic interaction *were* repulsive as the DLVO theory claims, the interaction must be intensified so that the interparticle distance should become larger or stay unchanged. This is contrary to the experimental observation.

We turn to the case, in which the refractive index matching was not effected. Figure 4.58 shows the results of DXS and DLS on a dispersion of silica particles in ethanol. The DXS data gives a straight line passing through the

origin, whose slope corresponds to D_0. On the other hand, such a linear relation is not found for DLS, though the concentration was low and the refractive index difference was not so large. Vos et al. suggested that this was due to multiple scattering in DLS.

In Sect. 4.4.2, we discussed the analysis by Härtl et al. of the hydrodynamic factor $H(K)$ (See footnote 10). They fitted the observed $H(K)$ to that calculated by RMSA assuming a net charge number and claimed that multiple scattering would not be influential. This argument seems to be misleading. Using the charge number determined by an independent measurement, and the D_{eff} evaluated by DXS, the pros and cons of the RMSA theory and the potential used have to be examined.

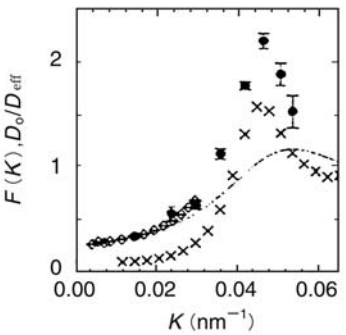

Fig. 4.57. The K dependence of the diffusion coefficient determined by dynamic X-ray scattering and dynamic light scattering. •: DXS, ◊: DLS, ×: static structure factor, broken curve: structure factor determined by a hard sphere model, $\phi = 0.164$. Taken from [96] with the permission of the American Physical Society

4.5 Summary

In this chapter we have discussed dispersions of colloidal particles, which are so large that their distribution in dispersions can be studied by optical microscopy. It is shown that the analytical charge number Z_{a} and the net charge number Z_{n} can be determined by conductometric titration and conductance measurements, and an empirical relation between Z_{a} and Z_{n} (4.6) is proposed. Because the interactions between charged particles and their counterions are strong, Z_{n} is much smaller than Z_{a}. The dispersion state of colloidal particles depends on the concentration of ionic impurity. Above 10^{-4} mol L^{-1} of coexisting salt, the particles display Brownian motion, while they form an ordered structure at lower salt concentrations. It is indispensable to remove the

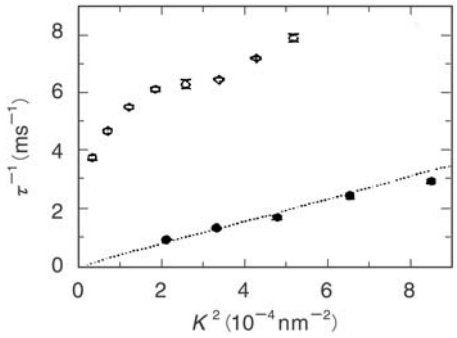

Fig. 4.58. The K^2 dependence of the relaxation rate in an ethanol dispersion of silica particles. •: DXS, ◊: DLS, $\phi = 0.078$, dotted line: diffusion constant calculated by Einstein-Stokes theory. Taken from [96] with the permission of the American Physical Society

impurity as much as possible, if particle distribution, and hence interparticle interaction, are to be investigated. The purification procedures are discussed in detail. The sedimentation equilibrium experiments, from which the Avogadro constant was determined, are re-studied and the concept of effective hard sphere is shown to be physically unacceptable.

By combining the microscopic technique with video imagery, the trajectory of free particles is demonstrated to be quite different from that of particles in the coexisting ordered region, proving the existence of the two-state structure. By using this technique the lattice vibration, lattice defects and so on are visualized. The particles interact with each other in liquids, so that the lattice constant of colloidal crystals varies with experimental parameters. For example, the lattice constant decreases with increasing particle concentration. The interparticle distance in the ordered regions is smaller than the average distance calculable from the concentrations. This fact is consistent with the two-state structure, namely coexistence of free particles (of low number density) and ordered regions (of higher density). At the interface of the ordered regions, particles are seen to "evaporate" into free particle (gas-like) regions and to condense onto ordered (crystal-like) regions. Such a structure suggests the presence of an attraction between particles. The closest interparticle distance becomes smaller with increasing charge density of particles and with increasing salt concentration. In water as a medium, the closest distance apparently decreases with rising temperature as a result of the decrease in the dielectric constant. The observed Bragg distance decreases with decreasing dielectric constant. This fact suggests that the electrostatic attraction between particles overwhelms the DLVO repulsion. The scattering profiles can be derived by Fourier-transformation of the micrographs of particle distributions.

From micrographs showing regular crystal-like arrangement of particles, scattering spots are obtained, while a few scattering peaks are found from the two-state structure. This result substantiates the interpretation of a single broad peak observed for ionic polymer solutions (Chap. 3) in terms of the two-state structure. The radial distribution function $g(r)$ of particles can be determined from the microscopic measurements combined with video-imagery. The time evolution of the $g(r)$ shows that larger crystals grow at the expense of smaller ones. This is nothing other than Ostwald ripening.

By using a confocal laser scanning microscope (LSM), observation of particles deep inside dispersions (200 μm from the container wall) is possible. This technique enables us to observe large and stable voids inside polystyrene latex particle dispersions of a density-matched H_2O-D_2O mixture. Under the same conditions except in H_2O, on the other hand, the same particles show a gas-liquid phase transition. Thus the void formation is a gas-liquid phase separation under zero-gravity condition. The charged state of silica particles can be controlled by changing pH of their dispersions. The dispersion state is found to depend on the charge density. When the charge density is increased, the particles show a transition from liquid-like to crystal-like distribution. By further increase in the charge density, liquid-like distribution is revived. This is called the re-entrant transition. Colloidal crystals are discovered to evolve by the following steps; crystal nuclei are formed and grow to transient large crystals covering the whole volume of dispersions (one-state structure). Then liquid-like regions are created in the crystals, which shrink to result in Swiss-cheese-like structures.

The above observations can easily be accounted for if a (counterion-mediated) attraction is in operation. A similar attraction is noticed between particles and similarly charged interface, in contradiction to the double layer interaction theory. Neutron reflectivity measurements show that the concentration of cationic micelles near a positively charged air-water interface is higher than the average concentration. Microscopic investigation also tells that anionic particles are concentrated in the vicinity of an anionic glass interface (5 μm $\sim$ 50 μm). Such a concentration gradient becomes more pronounced when the charge numbers of the interface and particles increase. This observation implies that the double layer interaction theory is not valid in the distance range mentioned above.

The colloidal dimension corresponds to diffraction angles lower than those accessible by SAXS. Ultra-small angle X-ray scattering (USAXS) apparatus is constructed by the Bonse-Hart optical systems. The electron density fluctuation as large as 8 μm can be studied by the 1D-USAXS apparatus, in which the incident X-ray is collimated in one plane. Colloidal silica dispersions show several orders of diffraction, suggesting the formation of a single crystal. The crystal symmetry, lattice constant, and crystal orientation can be determined accurately. The closest interparticle (Bragg) distance $2D_{\mathrm{exp}}$ is found to be smaller than the average distance $2D_0$, substantiating the formation of the two-state structure. The closest packed plane of single crystals is

maintained parallel to the container wall, in agreement with the observation by microscopy and Kossel diffraction analysis. The incident X-ray of the 2D-USAXS apparatus, in which collimation in two vertical planes is effected, has a point symmetry, so that smearing effects can be ignored. This enables one to carry out structural analysis of oriented samples more easily. Fluctuation of 2 μm can be studied. A single crystal of colloidal silica particles gives a large number of diffraction spots, from which the crystal symmetry, lattice constant, and orientation can be accurately and uniquely determined. At low volume fractions of particles, $2D_{\mathrm{exp}}$ is smaller than $2D_0$ whereas they are equal at high volume fractions.

Multiple scattering restricts the application of static light scattering to dilute dispersions of colloidal particles. Solutions of polyelectrolyte microgels give scattering profiles of at least two peaks. The inequality relation $2D_{\mathrm{exp}} < 2D_0$ is confirmed also for this system at low concentrations while the two distances are equal at higher concentrations, as found for conventional colloidal systems.

Dynamic light scattering is used for colloidal particles under the condition that the multiple scattering is not important and provides the diffusion coefficient and the structure factor. Neutron scattering also gives information on structure formation. The results obtained by these techniques are consistent with those by other techniques such as microscopy and USAXS. When the refractive indices of particle and medium are matched, the dynamic X-ray scattering gives the structure factor, in good agreement with dynamic light scattering.

From the above discussion, it is seen that the information obtained for colloidal particle dispersions, particularly the real-space information by microscopy, is consistent with that obtained for flexible ionic polymers in Fourier space.

Before leaving this chapter, it seems necessary to comment on papers posing questions on the experimental observation of the microscopic inhomogeneities such as void formation, gas-liquid phase transitions, etc. By using osmotic pressure, light scattering, and USAXS, Reus et al. examined colloidal crystals of latex particles of copolymers of bromostyrene and styrene sulfonate [98] and claimed that their "samples are always monophasic and the possibility of holes as often reported (for example by Dosho et al. [50]) is undoubtly excluded by their experiments". It is briefly reminded that dispersions, in which voids (or holes according to Reus et al.'s terminology) could be observed by microscopy, were macroscopically homogeneous [48–50]. As repeatedly emphasized in the above sections, the voids are so fragile that they can be destroyed easily by stirring the dispersions. The colloidal crystals are likewise fragile. As discussed in Sect. 4.3.2, the crystals can be destroyed by stirring. When the dispersions are thereafter kept standing, microcrystals of the same symmetry and lattice constant as those obtained prior to stirring can be reproduced. Sedlák also demonstrated for flexible polymers that the multi-chain domains, or the localized ordered structures according to our ter-

minology, are not filterable entities and can be broken by filtration process, but are regenerated after filtration [99]. Obviously, such an intrinsic nature of the microscopic inhomogeneity in macroscopically homogeneous systems undoubtedly has been misapprehended by Reus et al. They stirred their dispersions for $1 \sim 2$ min, waited for a few min to reach "equilibrium", and measured the osmotic pressure. Such a procedure would be acceptable only when the inhomogeneity is not fragile but filterable. It is highly plausible that these authors ruptured what they wanted to disprove. Their negative opinion on the structural inhomogeneity [100] has to be discarded.

References

1. Siedentopf H, Zsigmondy R (1903) Ann Phys 10:1
2. Zsigmondy R (1966) Nobel lectures. Elsevier, Amsterdam, p.45
3. Perrin J (1913) Les Atomes. Libraire Felix, Alcan
4. Fitch RM (1997) Polymer colloids: A comprehensive introduction. Academic Press, New York
5. Ito K, Ise N, Okubo T (1985) J Chem Phys 82:5732
6. Alexander S, Chaikin PM, Grant P, Morales GJ, Pincus P, Hone D (1984) J Chem Phys 80:5776
7. Wiersema PH, Loeb AL, Overbeek JThG (1966) J Coll Interface Sci 22:78
8. See [4], Chap. 8
9. Yamanaka J, Hayashi Y, Ise N, Yamaguchi T (1997) Phys Rev E55:3028
10. Yamanaka J, Yoshida H, Koga T, Ise N, Hashimoto T (1999) Langmuir 15:4198
11. Derjaguin BV, Landau L (1941) Acta Physicochem 14:633
12. Verwey EJW, Overbeek JThG (1948) Theory of the stability of lyophobic colloids, Elsevier, Amsterdam
13. Yamanaka J, Hibi S, Ikeda S, Yonese M, publication in preparation
14. Kamel, AA, El-Aassar MS, Vanderhoff JW (1981) J Dispersion Sci Tech 2:183
15. See [4], Chap. 5
16. Ito K, Nakamura H, Ise N (1986) J Chem Phys 85:6136
17. Ito K, Nakamura H, Yoshida H, Ise N (1988) J Am Chem Soc 110:6955
18. Yoshida H, Yamanaka J, Koga T, Koga T. Ise N, Hashimoto T (1999) Langmuir 15:2684
19. Yoshida H, Yamanaka J, private communication
20. Ise N, Okubo T, Kitano H, Sugimura M, Date S (1982) Naturwissenschaften 69:544
21. Alder BJ, Hoover WG, Young DA (1968) J Chem Phys 49:3688
22. Alder BJ, Wainwright TE (1959) J Chem Phys 31:459
23. Hachisu S, Kobayashi Y, Kose A (1973) J Coll Interface Sci 42:342
24. Wadati M, Toda M (1972) J Phys Soc Jpn 32:1147
25. Debye PJW, Hükel E (1923) Phys Z 24:185
26. Ito K, Ieki T, Ise N (1992) Langmuir 8:2952
27. Matsumoto M, Kataoka Y (1988) In: Ise N, Sogami I (eds) Ordering and organization in ionic solutions.World Scientific, Singapore, p.574
28. Tata BVR, Arora AK, Valsakumar MC (1993) Phys Rev E47:3404

29. Einstein A (1905) Ann Phys (Leipzig) 17:549
30. Ise N, Ito K, Okubo T, Dosho S, Sogami I (1985) J Am Chem Soc 107:8074
31. Luck W, Klier M, Wesslau H (1963) Ber Bunsenges 67:75 and 84
32. Alfrey T, Bradford EB, Vanderhoff JF, Oster G (1954) J Opt Soc Am 44:603
33. Kose A, Ozaki M, Takano K, Kobayashi Y, Hachisu S (1973) J Coll Interface Sci 44:330
34. Ise N, Matsuoka H, Ito K, Yoshida H (1990) Faraday Discuss Chem Soc 90:153
35. See for example Henderson B (1972) Defects in crystalline solids. Edward Arnold, London
36. Ise N, Okubo T, Sugimura M, Ito K, Nolte H (1983) J Chem Phys 78:536
37. Larsen AE, Grier DG (1997) Nature 385:230
38. Krieger IM, Hiltner PA (1971) In: Fitch RM (ed) Polymer colloids. Plenum, New York, p.63
39. Ito K, Ise N (1987) J Chem Phys 86:6502
40. Hosemann R (1962) Polymer 3:349
41. Ostwald W (1900) Z physk Chem (1900) 34:495
42. Luck WAP (1967) Phys Bl 23:304
43. Ito K, Okumura H, Yoshida H, Ise N (1990) Phys Rev B41:5403
44. Yoshida H, Ito K, Ise N (1991) J Chem Soc Faraday Trans 87:371
45. Ise N, Matsuoka H, Ito K (1988) In: Ise N, Sogami I (eds) Ordering and organization in ionic solutions. World Scientific, Singapore, p.397
46. Kesavamoorthy R, Rajalakshmi M, Rao CB (1989) J Phys: Condens Matter 1:7149
47. Ito K, Yoshida H, Ise N (1992) Chem Lett 1992:2081
48. Ito K, Yoshida H, Ise N (1994) Science 263:66
49. Yoshida H, Ise N, Hashimoto T (1995) J Chem Phys 103:10146
50. Dosho S, Ise N, Ito K, Iwai S, Kitano H. Matsuoka H, Nakamura H, Okumura H, Ono T, Sogami I, Ueno Y, Yoshida H, Yoshiyama T (1993) Langmuir 9:394
51. Tata BVR, Rajalakshmi M, Arora AK (1992) Phys Rev Lett 69:3778
52. Yamanaka J,Yoshida H,Koga T, Ise N, Hashimoto T (1998) Phys Rev Lett 80:5806
53. Ito K, Muramoto T,Kitano H (1995) J Am Chem Soc 117:5005
54. Ito K, Muramoto T, Kitano H (1996) Proc Japan Acad 72B:62
55. Muramoto T, Ito K, Kitano H (1997) J Am Chem Soc 119:3592
56. Ito K, Muramoto T, Kitano H (1994) Hyoumen 32:553 (in Japanese)
57. Lu JR, Simister EA, Thomas RK, Penfold J (1993) J Phys Chem 97:13907
58. Bonse U, Hart M (1966) Z Phys 189:151
59. Matsuoka H, Kakigami K, Ise N, Kobayashi Y, Machitani Y, Kikuchi T, Kato T (1991) Proc Natl Acad Sci USA 88:6618
60. North AN, Rigden JS, Mackie AR (1992) Rev Sci Instrum 63:1741
61. Chu B, Li Y, Gao T (1992) Rev Sci Instrum 63:4128
62. Lambard J, Lesieur P, Zemb T (1992) J Phys I (Paris) 2:1191
63. Matsuoka H, Kakigami K Ise N (1991) Proc Japan Acad B67:170
64. Konishi T, Ise N, Matsuoka H, Yamaoka H, Sogami IS, Yoshiyama T (1995) Phys Rev B51:3914
65. Hindeleh AM, Hosemann R (1982) Polymer 23:1101
66. Cullity BD (1956) Elements of x-ray diffraction. Addison-Wesley, Reading, MA, Chap. 3
67. Konishi T, Ise N (1995) J Am Chem Soc 117:8422

68. Konishi T, Ise N (1997) Langmuir 13:5007
69. Konishi T, Yamahara E, Ise N (1996) Langmuir 12:2608
70. Vrij A, Jansen JW, Dhont JKG, Pathmamanoharan C, Kops-Werkhoven MM, Fijnaut HM (1983) Faraday Discuss Chem Soc 76:19
71. Pahl R, Bonse U, Pekala RW, Kinney JH (1991) J Appl Crystallogr 24:771
72. Konishi T, Ise N (1998) Phys Rev B57:2655
73. Busing WR, Levy HA (1967) Acta Crystallogr 22:457
74. Sirota EB, Ou-Yang HD, Sinha SK, Chaikin PM, Axe JD, Fujii Y (1989) Phys Rev Lett 62:1524
75. Robbins MO, Kremer K, Grest GS (1988) J Chem Phys 88:3286
76. Vos WL, Megens M, van Kats CM, Bösecke P (1997) Langmuir 13:6004
77. Megens M, van Kats CM, Bösecke P, Vos WL (1997) Langmuir 13:6120
78. Matsuoka H, Harada T, Kago K,Yamaoka H (1996) Langmuir 12:5588
79. Tata BVR, Arora AK (1996) In: Tata BVR, Arora AK (eds) Ordering and phase transitions in charged colloids. VCH, New York, Chap. 6
80. Arora AK, Tata BVR (1998) Adv Coll Interface Sci 78:49
81. Kerker M (1969) The scattering of light and other electromagnetic radiation. Academic Press, New York
82. Antonietti M, Briel A, Förster S (1996) J Chem Phys 105:7795
83. Gröhn F, Antonietti M (2000) Macromolecules 33:5938
84. Phillies GDJ (1981) J Chem Phys 74:260; Phys Rev A24:1939
85. Schätzel K, Drewel M, Ahrens J (1990) J Phys: Condens Matter 2:SA393; Segrè PN, van Megen W, Pusey PN, Schätzel K, Peters W (1995) J Mod Opt 42:1929
86. Pusey PN, Segrè PN, Poon WCK, Meeker SP, Behrend OP, Moussaïd A (1998) In: Ottewil RH, Rennie AR (eds) Modern aspects of colloidal dispersions. Kluwer, Dordrecht, The Netherland, p.77
87. Härtl W, Beck C, Hempelmann R (1999) J Chem Phys 110:7070
88. Hansen JP, Hayter JB (1982) Mol Phys 46:651
89. Pusey PN, Tough RJA (1985) In: Pecora R (ed) Dynamic light scattering. Plenum, New York, Chap. 4
90. Nägele G, Baur P (1997) Europhys Lett 38:557
91. Yoshida H, Ito K, Ise N (1990) J Am Chem Soc 112:592
92. Cebula DJ, Goodwin JW, Jeffrey GC, Ottewill RH (1983) Faraday Discuss Chem Soc 76:37
93. Ashcroft NW, Lekner J (1966) Phys Rev 145:83
94. Ackerson BJ, Clark NA (1983) Physica 118A:221
95. Ackerson BJ, Hayter JB, Clark NA, Cotter L (1986) J Chem Phys 84:2344
96. Riese DO, Vos WL, Wegdam GH, Poelwijk FJ, Abernathy DL, Grübel G (2000) Phys Rev E61:1676
97. Percus JK, Yevick GJ (1958) Phys Rev 110:1
98. Reus V, Belloni L, Zemb T, Lutterbach N, Versmold H (1997) J Phys II France 7:603
99. Sedlák M (2002) J Chem Phys 116:5236, 5246, 5256
100. Belloni L (2000) J Phys:Condens Matter 12:R549

5

Kikuchi–Kossel Line Analysis on Colloidal Crystals

5.1 Introductory Remarks

Colloidal dispersions of spherical macroions with radius $0.1 \sim 1.0$ μm are interesting thermodynamic systems being full of a variety of phenomena. As shown in the previous chapter, we are able to observe and examine thermal agitation and local crystalline ordering of particles [1, 2] by using an optical microscope. It is also possible to record processes of ordering formation advancing gradually in colloidal dispersions in real time by laser diffraction methods. The main purpose of this chapter is to report the results of analyses on crystallization in dilute colloidal dispersions by the *Kikuchi–Kossel method of laser diffraction* [3–5]. As will be recognized below, this method is especially suitable for examining the development of colloidal crystals.

Colloidal particles of dispersions which are easy to deal with and most widely used in the world are polystyrene latexes and silica colloids. Data used in this chapter are taken from the experiments with sulfonate-modified polystyrene latexes. As shown in Table 5.1, the latexes used in the experiments have large *analytical charges* and are approximately monodisperse. The diam-

Table 5.1. Properties of latexes

Latex	Diameter (nm)	Number of SO_3H groups per particle	Charge density $[-e/(nm)^2]$
SSH − 6	120	1.2×10^4	2.7×10^{-1}
N − 100	120	1.8×10^4	4.0×10^{-1}
N − 150	150	1.7×10^4	2.4×10^{-1}
SS − 32	156	3.0×10^4	3.9×10^{-1}
N − 400	400	3.2×10^5	6.4×10^{-1}
N − 601	600	4.9×10^5	4.3×10^{-1}

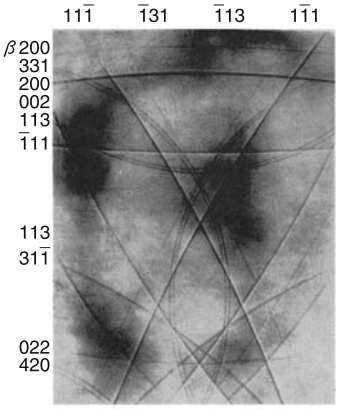

Fig. 5.1. Kossel image of a Cu single crystal observed by Kossel et al. with electron excitation. The Miller indices are attached to the Kossel lines

eter and charge density of the latex particle were determined, respectively, by electron micrography and conductometric titration.

Sample latexes are dialyzed (or ultra-filtrated) with pure water and purified by anion-cation exchange resins. Dispersions of well-deionized latexes which begin to show iridescence are introduced into rectangular quartz cuvettes of dimensions (45 mm height)×(10 mm width)×(1 mm inner thickness). It takes several hours (minutes) for dilute (concentrated) dispersions to be in iridescent states again after being introduced into the cuvettes. We use such dispersions as specimens for laser diffraction analyses on crystallization when they begin to show iridescence in the cuvette.

It is possible to regard such well-deionized specimens as systems consisting of latex particles, counterions, H^+, and solvent, water. We examine experimental results of optical laser diffraction on salt-free monodisperse dispersions of latex particles with particle volume fractions of $0.01 \sim 0.10$.

5.2 Kikuchi–Kossel Diffraction Images

Stimulated by the Davisson-Germer work in 1927 which demonstrated the wave nature of the electron, Kikuchi started immediately to do challenging electron diffraction experiments. He used mica plates of varying thickness as specimens and discovered various peculiar diffraction patterns of single crystals in 1928 [6–8]. While mesh-like diffraction patterns consisting of regular triangles were found for thin mica specimens (100∼200 nm), repetitions of white and black diffraction lines were observed for thick mica specimen (several hundred nm). Kikuchi named these diffraction lines of a bright and dark pair the P-lines. He interpreted the P-lines correctly as the diffraction

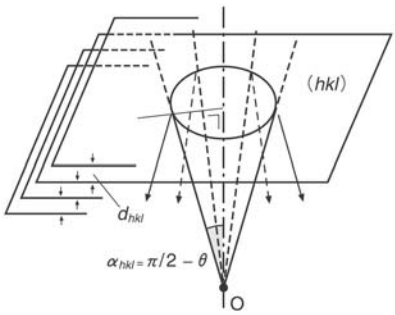

Fig. 5.2. Kossel cone of the monochromatic spherical waves diverging from a point source O which are diffracted by lattice planes with index (hkl) and spacing d_{hkl}. Waves diffracted by the lattice planes remain in dark and bright conical sections on photo films placed in front of and behind the crystal

patterns, by crystal lattice planes, of the secondary monochromatic electron beams produced in open angles by inelastic scattering [1].

Independently of the Kikuchi experiments, Kossel et al. [10, 11] succeeded in 1934 in observing the characteristic diffraction patterns of fluorescent X-rays which were produced by Cu atoms excited by electron beams incident on a Cu single crystal. Figure 5.1 is an example of a *Kossel diffraction image* by a single crystal of Cu. Kossel showed clearly that such characteristic images are nothing but the diffraction patterns of monochromatic X-rays diverging from a point source inside a single crystal.

The interpretation of the Kossel lines by Kossel is very simple and clear. As shown in Fig. 5.2, when monochromatic X-rays with wavelength λ diverging from a point source illuminate the family of lattice planes with Miller indices (hkl), the components satisfying the Bragg condition

$$2d_{hkl} \sin\theta = n\lambda, \tag{5.1}$$

where n is an integer are reflected and the components with other angles pass through the lattice planes. Accordingly, if a photosensitive film is placed behind the crystal, X-rays do not reach such regions of the film that cross a circular cone with the semi-vertical angle $\alpha_{hkl} = \pi/2 - \theta$ which is complementary to the Bragg angle. Consequently, families of white conic sections are recorded on the negative film.

Such a circular cone is called a *Kossel cone*. The central line of the Kossel cone is identical with the normal of the lattice planes. Diffraction by different

[1] It was difficult to elucidate theoretically all such diffraction images which were later called generically Kikuchi lines [9], since electron beams interacting strongly with matter produce complicated diffraction images. Kikuchi also found peculiar diffraction images called Kikuchi bands.

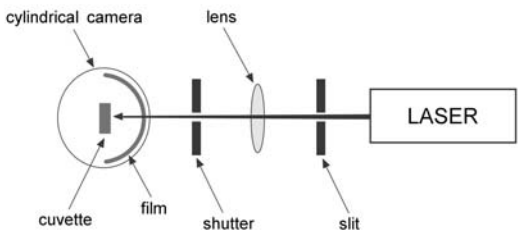

Fig. 5.3. Apparatus for photography of Kossel images of colloidal crystals. Incident laser beams collimated by a slit and focused by a lens pass through a hole punched in a film (Fuji FG) and illuminate the colloidal crystals. The specimen cuvette is placed on the head of a goniometer at the center of a cylindrical camera

families of lattice planes produces respective diffraction patterns of conic sections which are recorded on the photo film. We call these diffraction lines the *Kossel lines* and the geometrical pattern made by them the *Kossel diffraction image* (*pattern*). The semi-vertical angle of the Kossel cone is decided by the distance between the crystal and the photo film, and the spacing of the lattice planes d_{hkl} is determined from the wavelength of the laser beam.

Lattice spacings of colloidal crystals are several thousand times larger than those of atomic crystals and comparable with the wavelength of visible light. Therefore, it is suitable to use optical lasers with high coherence to investigate ordering formation in colloidal dispersions.

Clark et al. [12] photographed the *pseudo-Kossel images* of colloidal crystals by using divergent laser beams produced from a thin sheet with point-like scatterers placed outside of the container. In their experiments, the point-like sources of diverging beams were placed outside of the crystals. Yoshiyama and Sogami [3–5] observed the *intrinsic Kossel images* produced by spherical secondary waves diverging from point-like sources which exist inside the dispersions in the process of examining diffraction spots with incident parallel laser beams.

Figure 5.3 shows schematically the apparatus for Kossel line analysis of colloidal crystals. The cuvette with specimen is fixed vertically on a goniometer head. Covering the cuvette with a cylindrical camera and adjusting the incident laser beams so as to be normal to a wide surface of the cuvette, we set a film so as to be exposed with beams of backward reflection.

Large single crystals can grow in sufficiently dilute dispersions in the last stages of crystallization. For such a dispersion, which has high transparency for the laser, it is possible to take a photograph of a transmitted *forward Kossel diffraction image* by setting a film behind the cuvette. Since the dispersions have low transparency in most cases, we punch a hole in a film, set it in front of the cuvette as in Fig. 5.3 and take a photograph of a reflected *backward Kossel diffraction image*.

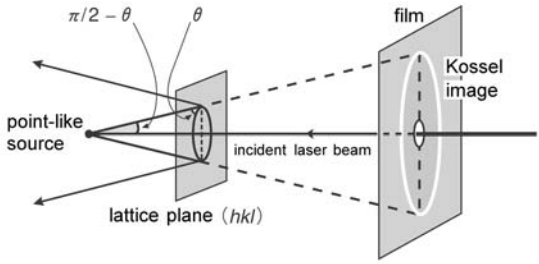

Fig. 5.4. Mechanism for generation of a Kossel diffraction image. Secondary waves diverging from a point-like source in the colloidal crystal are incident onto the (hkl) lattice planes. The component waves satisfying the Bragg condition are reflected and other components pass through the lattice planes. As a result, the cross-sections of the Kossel diffraction cones with the film surface are recorded as conical sections

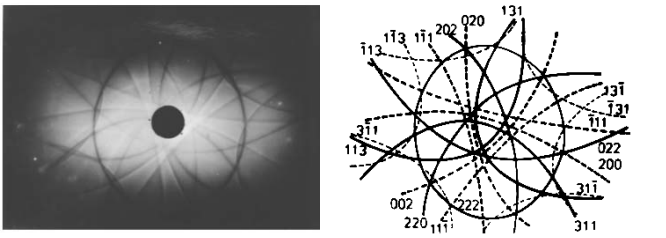

Fig. 5.5. Backward Kossel diffraction lines and their indices, from a colloidal crystal illuminated by He-Ne laser beams. The specimen was the 1.0 vol% dispersion of the SSH-6 latex. The colloidal crystal has an fcc structure with lattice constant $a_0 = 893$ nm

Figure 5.4, which corresponds to the camera part in Fig. 5.3, shows schematically the mechanism for generation of a Kossel diffraction image. The parallel laser waves which are incident from the right and scattered at a point-like defect inside the colloidal crystal generate secondary diverging spherical waves. The secondary spherical waves diffracted by the (hkl) lattice planes generate unique patterns of Kossel lines. Namely the component waves satisfying the Bragg condition are reflected and other components pass through the lattice planes. The cross-sections between the Kossel diffraction cones and the film surface are recorded as conical sections on the film.

Note that families of the Kossel lines diffracted from many families of lattice planes are recorded on a film. There is a one-to-one correspondence between a Kossel line and a family of lattice planes with a definite Miller index. Figure 5.5 shows an example of Kossel lines and their associated Miller indices. The Kossel line enables us to determine accurately the lattice spacing and the

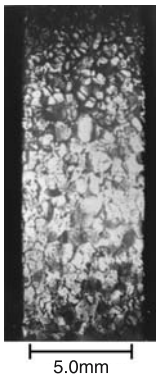

Fig. 5.6. Traverse Lang photograph using Ar laser beams recording ordered and disordered distributions of the SS-32 latex particles in a dispersion with a 5.0 vol% particle concentration. Bright and dark parts represent, respectively, ordered crystalline regions and disordered regions

diffraction pattern allows us to decide uniquely the crystal symmetry. The Kossel diffraction pattern records *exact information on the three-dimensional structure of the colloidal crystal*.

A He-Ne laser with wavelength $\lambda = 632.8$ nm and an Ar laser with wavelength $\lambda = 488.0$ nm were most frequently used. The time for exposure was 30∼60 s for the He-Ne laser (5∼20 mW) and approximately 1 s for the Ar laser (5 mW). A He-Cd ultra-violet laser with $\lambda = 325.0$ nm was also used.

The elastic constants of matter are approximately proportional to its density (or concentration) [13]. Since lattice constants of colloidal crystals are about 10^3 times larger than those of ordinary atomic crystals, the concentrations of colloidal crystals are about $(10^3)^3$ times smaller than the density of atomic crystals. Accordingly, colloidal crystals are approximately 10^9 times softer than atomic crystals. In fact, measurements of compressibility effects due to gravity [14–16] have confirmed that the *bulk modulus* of colloidal crystals lies in the range $1 \sim 10^3$ Pa, while that of metals is known to lie in the range $10^{10} \sim 10^{12}$ Pa. Such extreme softness causes the colloidal crystals to have defects which scatter the incident laser waves and generate secondary expanding waves.

Figure 5.6 shows a traverse photograph [17] taken by the Lang method [18] using Ar laser beams for a specimen with a 5.0 vol% particle concentration. Bright patchy patterns in this picture prove that the dispersion is filled with a large number of crystal grains with a size distribution ranging up to a few millimeters. Dark hazy regions and cracks represent disordered regions where particles are in either liquid-like or glassy states.

Measurements of the coordinates of three points on a Kossel line [19] enable us to determine the direction of the axis and the semi-vertical angle of the Kossel diffraction cone. The photographed Kossel lines were distorted owing

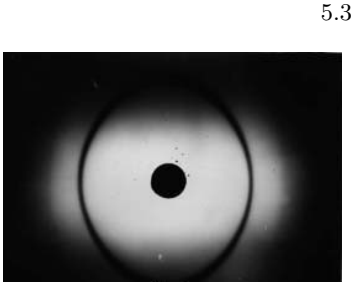

Fig. 5.7. Backward Kossel image using Ar beams showing a *random layer structure*. At $t = 20$ h after preparation, only a single Kossel ring with fcc index 111 was observed for the specimen of SS-32 latex with a concentration of 6.0 vol%

to the curvature of the cylindrical film holder and by the effects of refraction at the air-quartz and quartz-dispersion interfaces. The deformation due to the geometry of camera was properly corrected using the diameter of the film holder, which is given with high accuracy. The refractive effect of the quartz cuvette plate is merely a parallel displacement of beams by the thickness of the plate. To correct the refractive effect by using Snell's law, we estimate the refractive index of colloidal dispersion n_{C} by the formula

$$n_{\mathrm{C}} = n_{\mathrm{W}}(1 - \phi) + n_{\mathrm{PS}}\phi \tag{5.2}$$

proposed by Hiltner-Krieger [20], where ϕ is the volume fraction of the latex particles, and n_{W} and n_{PS} are the indices for water and polystyrene ($n_{\mathrm{W}} = 1.33$ and $n_{\mathrm{PS}} = 1.6$ for visible light).

5.3 Crystal Growth

In the initial stage of the ordering formation, the wall effect plays an important role. Three-dimensional isotropic symmetry degrades to two-dimensional symmetry in the region close to the cuvette surface where the crystallization starts to take place. Direct observation by optical microscope confirms that the particles, executing Brownian motion, come close together and begin to form a two-dimensional hexagonal arrangement in a plane parallel to the cuvette surface. Such hexagonal close-packed (hcp) planes increase sheet by sheet until the dispersion begins to exhibit a faint pink (blue) iridescence for a dilute (concentrated) specimen to which the laser diffraction experiment becomes applicable.

Starting from the two dimensional hcp structure, further processes of crystallization advance in the colloidal dispersions. Using data of the Kossel diffraction experiments [3–5], we examine the crystallization processes in this section by dividing the processes into three stages: an early era of layer structures, a transitive stage and a later era of cubic structures.

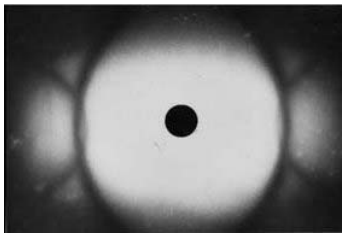

Fig. 5.8. Backward Kossel image using Ar beams showing a *stacking structure with one sliding degree of freedom.* At $t = 24$ h after preparation, the 111 Kossel ring associated with the 002 and $\underline{002}$ Kossel rings was observed for the specimen of SS-32 latex with a concentration of 9.78 vol%

5.3.1 Era of Layer Structures

At this stage, the wall effect is influential on the ordering formation. Figure 5.7 shows a backward Kossel diffraction image consisting of only a single broad ring, observed at the earliest stage. This ring is the cross-section between the film surface and the Kossel cone originating from equally spaced two-dimensional hcp layers parallel to the cuvette wall and normal to the incident beam direction. Since these layers are confirmed to develop to the (111) plane of the fcc structure in the later stage of crystallization, the fcc index 111 is given to this Kossel ring. The fact that no Kossel line appears other than the 111 ring proves that no higher relative symmetry exists between the planes of adjacent (111) layers. Therefore, it is reasonable to identify this earliest three-dimensional ordering in the colloidal dispersion with the *random layer structure* discovered for amorphous graphite by Warren [21] and Franklin [22].

In Fig. 5.8, two new Kossel rings appear and cut across the 111 Kossel ring. The interplanar distance d_{111} corresponding to the 111 Kossel ring is 220 nm so that the lattice constant is estimated to be $a_0 = \sqrt{3}\, d_{111} = 380$ nm. The new rings can have this value for the lattice constant only if they acquire the indices 002 and $\underline{002}$. Here, the underlined index shows the twin ring with respect to the (111) lattice plane. This kind of diffraction pattern can be explained by a model in which the (002) and ($\underline{002}$) lattice planes are formed by sliding the two-dimensional hcp layers freely along one direction ($[1\bar{1}0]$ and $[11\bar{2}]$, respectively) keeping the interplanar distance d_{111} constant. Ackerson and Clark [23] have proposed a similar model for describing the change of symmetry in the packing of layers of bcc structure.

Figure 5.9 shows six Kossel rings crossing symmetrically over the 111 Kossel ring. By assigning the indices 200, $0\bar{2}0$, 002, $\bar{2}00$, 020, and $00\bar{2}$ to these rings, we get a lattice constant $a_0 = 430$ nm which is approximately identical to the value $a_0 = 420$ nm estimated from the 111 Kossel ring. This diffraction pattern is explained by a *stacking disorder structure* [24] in which

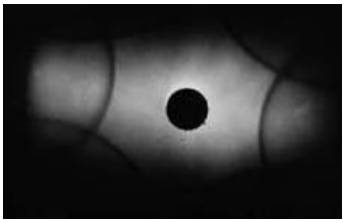

Fig. 5.9. Backward Kossel image using Ar beams showing a *stacking disorder structure*. The 111 Kossel ring and six Kossel rings with {200} and {$\underline{200}$} were observed at $t = 720$ h after preparation for the specimen of SS-32 latex with a concentration of 6.0 vol%

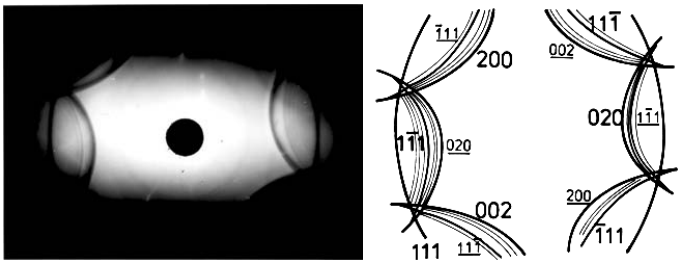

Fig. 5.10. Backward Kossel diffraction pattern taken using He-Ne beams at $t = 3120$ h for the specimen of latex N-100 with a concentration of 2.1 vol%. New families of the Kossel lines indexed as {$\bar{1}11$} and {$\underline{\bar{1}11}$} turned up with sheaves of fine diffraction lines, which proved the appearance of a *stacking structure with multi-variant periodicity*

two-dimensional hcp layers conventionally called A, B, and C stack together in a statistically random manner.

5.3.2 Transitive Stage from Layer Structures to Cubic Structures

In the transitive stage from the era of layer structures to the era of cubic structures, there appears a crystallographically interesting state. Figure 5.10 provides a picture of such a transitive state. In addition to the 111 ring and {200} and {$\underline{200}$} families of Kossel lines, there appear weak but definite signals of new {$\bar{1}11$} and {$\underline{\bar{1}11}$} families accompanying sheaves of fine and faint diffraction lines. The appearance of the new families {$\bar{1}11$} and {$\underline{\bar{1}11}$} indicates that the correlation among the layers has increased beyond the stacking disorder structure. Namely, the hcp layers A, B and C have begun to arrange in a somewhat regular order. The bunches of fine diffraction lines imply that the layers are arranged in many ordered units with different periods. This peculiar stage of the ordering formation may be named a *stacking structure with multi-variant periodicity*.

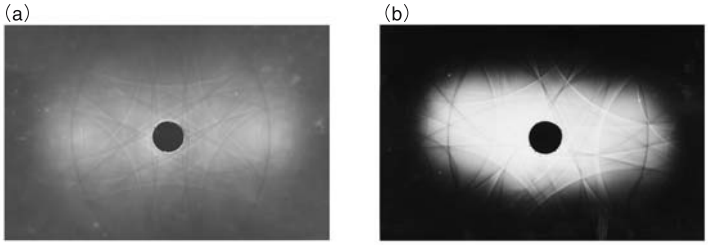

Fig. 5.11. Backward Kossel images observed using Ar beams in the early stages of cubic structures for the specimen of latex N-100 with a concentration of 0.58 vol%. (a) The Kossel pattern with six-fold symmetry observed at $t = 1344$ h proves the appearance of an fcc twin structure with twin plane (111). (b) The Kossel pattern with three-fold symmetry photographed at $t = 1896$ h leads to the normal fcc structure

5.3.3 Era of Cubic Structures

With the advance of the ordering formation, Kossel images with new richer structures appeared, as shown in Figs. 5.11–5.13. The crystal system of all the diffraction patterns in these figures was proved to be cubic, because a third predicted line is readily confirmed to pass through the intersection point of two Kossel lines independently of the value of the lattice constant. For example, the 220 (200) line passes through the point of intersection of the 200 and 020 (101 and $10\bar{1}$) lines in the case of the fcc (bcc) structure.

The Kossel pattern with six-fold symmetry in Fig. 5.11 (a) shows that the first stage of this era set in with an fcc twin structure with a (111) twin plane. In spite of crystallographic equality, the only twin plane observed, without exception, was the (111) plane parallel to the widest cuvette surface to which the incident beams entered normally.

The Kossel image with three-fold symmetry in Fig. 5.11 (b) proves that the ordering process in the concentrated dispersions (≥ 3 vol%) terminated at this stage. In the dilute dispersions (≤ 2 vol%), the ordering formation proceeds further.

The Kossel pattern recorded in Fig. 5.12 exhibits a very interesting phenomenon, i.e., coexistence of the fcc structure and a bcc twin structure in the same colloidal crystal grain. The solid lines indexed by uppercase letters and the broken lines indexed by lowercase letters represent, respectively, the fcc structure and the bcc twin structure with a $(1\bar{1}2)$ twin plane. The Kossel lines thus indexed lead to the lattice constants $a_0(\mathrm{fcc}) = 967$ nm for the fcc structure and $a_0(\mathrm{bcc}) = 770$ nm for the bcc twin structure. From these lattice constants we obtain values for the interparticle distance as follows:

$$R(\mathrm{fcc}) = \frac{1}{\sqrt{2}}\, a_0(\mathrm{fcc}) \ = 680\,\mathrm{nm},$$

$$R(\mathrm{bcc}) = \frac{\sqrt{3}}{2}\, a_0(\mathrm{bcc}) = 670\,\mathrm{nm},$$

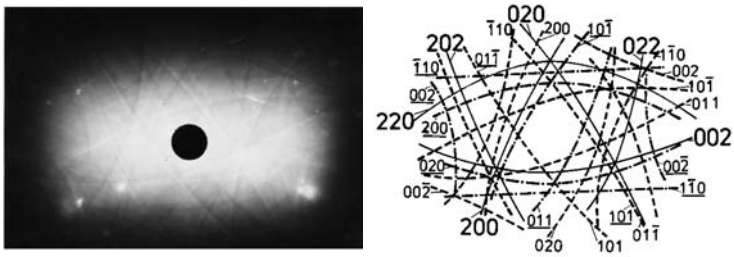

Fig. 5.12. Coexistence of the normal fcc structure and the bcc twin structure. The Kossel image was recorded at $t = 888$ h using Ar beams for the specimen of latex N-150 with a concentration of 0.30 vol%. The solid (dashed) lines indexed with uppercase (lowercase) letters represent the fcc (bcc twin) structure

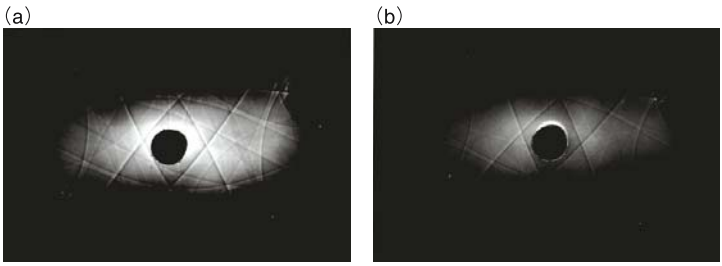

Fig. 5.13. Backward Kossel images observed using Ar beams in the last stages of ordering formation for the specimen of latex SS-32 with a concentration of 0.49 vol%. (a) The Kossel pattern photographed at $t = 1848$ h proves the appearance of a bcc twin with twin plane $(1\bar{1}2)$. (b) The Kossel pattern with two-fold symmetry photographed at $t = 2496$ h demonstrates the formation of the normal bcc structure

which are roughly the same. Two types of structure coexist, with the fcc (111) plane parallel to the bcc (110) plane and with the fcc $[1\bar{2}1]$ axis parallel to the bcc $[\bar{1}10]$ axis. Figure 5.12 recorded the fcc to bcc twin phase transition at the very instant of the transition.

In the dilute dispersions, the bcc structure turns up in the last stages of the ordering formation. Figure 5.13 (a) shows the bcc twin structure with $(1\bar{1}2)$ twin plane. In contrast to the fcc twin structure which has the (111) twin plane parallel to the cuvette surface, the twin plane of all the bcc twin structures observed so far is limited, without exception, to either $(1\bar{1}2)$ or $(\bar{1}12)$, both of which are normal to the cuvette surface. The Kossel pattern with two-fold symmetry in Fig. 5.13 (b) exhibits the normal bcc structure [2].

The results of our analysis show that the ordering formation in salt-free monodisperse dispersions of latex particles develops through multi-stage phase

[2] In the colloidal silica dispersions, crystallization proceeds so rapidly that it is hard to observe the era of layer structure and the fcc structure.

transitions as follows:

two-dimensional hcp structure
→ random layer structure
→ layer structure with one sliding degree of freedom
→ stacking disorder structure
→ stacking structure with multi-variant periodicity
→ fcc twin structure with twin plane (111)
→ normal fcc structure
→ bcc twin structure with twin plane $(1\bar{1}2)$ or $(\bar{1}12)$
→ normal bcc structure .

It is remarkable that the colloidal crystals develop through such a route of *multi-stage phase transitions* in the dispersions. It is also worthwhile to recognize that the three-dimensional hcp structure does not appear on the route of the ordering formation.

The three early stages of three-dimensional ordering, which we called the era of layer structures, are characterized by strong anisotropy originating in the wall effect which initiated the formation of a two-dimensional hcp arrangement of the colloidal particles. After the intermediate stage of stacking structures with multi-variant periodicity, the ordering formation proceeds further to the era of cubic structures. Thermal agitation and interaction among particles gradually rectify the anisotropy, and complete the formation of crystals with cubic symmetry. While the crystallization terminates with the fcc structure in concentrated dispersions, it develops further to the bcc structure in dilute dispersions. Therefore, the fcc (bcc) structure is more favored thermodynamically than the bcc (fcc) structure in concentrated (dilute) dispersions.

Note that the influence of the wall effect persists through all stages of crystal growth. It imposes a severe restriction on the formation of the twin plane. The fcc (bcc) crystallite keeps its most dense plane (111) ((110)) parallel to the cuvette surface. No twin plane other than (111) ($(1\bar{1}2)$ or $(\bar{1}12)$) is confirmed to appear in the fcc (bcc) structure. In this way, the mark of the wall effect remains in the orientation of the crystallite even in the terminating stages of crystallization.

5.4 Colloidal Alloy Crystals

Figure 5.14 shows the Kossel diffraction image of a *colloidal alloy crystal* which grew in a salt-free dispersion with a volume fraction of 0.04 consisting of a one-to-one mixture of latex particles with different radii 220 nm and 77 nm. In this image, we recognize some of the Kossel lines characteristic of the fcc structure of a single crystal ($h + k + l = 3\times$ integers) and very dense families of thin Kossel lines. By comparison with computer simulations, the colloidal

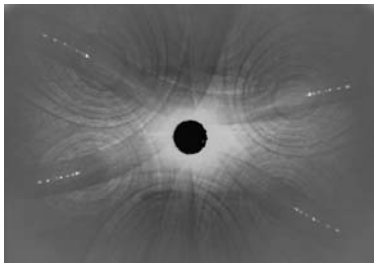

Fig. 5.14. Backward Kossel diffraction image of a colloidal alloy crystal. The colloidal alloy crystal grew in a dispersion of a one-to-one mixture of latex particles with radius 220 nm and radius 77 nm. The photograph was taken using He-Ne beams at $t = 240$ h after preparation

alloy crystal was proved to have a stacking super-lattice structure of two-dimensional stacking planes consisting of an hcp array of large latex particles with inter-particle distance $a = 522$ nm, with small latex particles distributed in vacant parts. The lattice constant of the super-lattice in the hexagonal system is $a = 522$ nm and $c = 76700$ nm and the super-lattice has a stacking period of 180 layers.

5.5 Fine Structure of Kossel Lines

Laue allotted the last chapter of his book 'Röntgenstrahl-Interferenzen' [25] to investigation of the Kossel lines in X-ray experiments. He seemed to expect that the structure of the Kossel lines would play an important role in elucidating the structure of the dispersion surface of electromagnetic waves in crystals. His expectation was realized in the peculiar structure of the Kikuchi lines of electron beams for atomic crystals [26,27] and in the Kossel diffraction of colloidal crystals [28]. This is because the electron beams and optical laser beams interact with matter much more strongly than X-rays. The diffraction lines of laser beams become broad and have a variety of *fine structures*.

An example is shown in Fig. 5.15. This is a photograph with indices of the Kossel diffraction image taken using Ar laser beams for a 3.4 vol% dispersion of latex N-400, which has a large surface charge density. Fine structures with line uncrossings and splittings are observed at otherwise intersecting points of Kossel rings. In particular, the separations are prominent at the intersections of the $h = \{022\}$ and $h' = \{113\}$ Kossel rings. It is possible to interpret this kind of *anomaly of diffraction lines* as interference effects of light waves reflected by different lattice planes inside a colloidal crystal. Namely, the anomalies at the intersection point of two Kossel lines with indices h and h' result from the simultaneous reflections of light waves by two lattice planes. Interference occurs between the reflected partial waves having wave vector $\boldsymbol{K}_h$ which arise

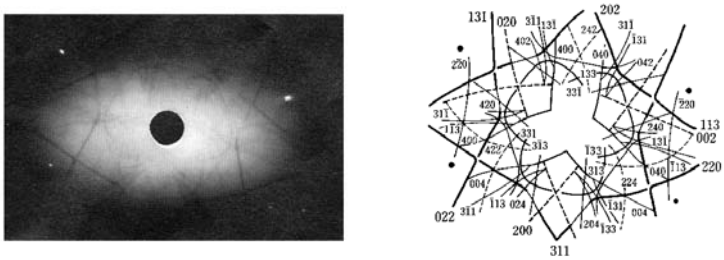

Fig. 5.15. Anomalies of diffraction lines in a backward Kossel image. The picture was photographed using Ar laser beams for the dispersion of latex N-400 with a volume fraction of 0.034. Gaps are observed at the crossings of the Kossel rings {220} and {131}

partly through direct reflection of the primary wave with wave vector $\boldsymbol{K}_0$ by the lattice plane h and partly through successive reflections, first by the lattice plane h' (or $h - h' = (1\bar{1}\bar{1})$) and then by the lattice plane $h - h'$ (h').

For the structure analyses of colloidal crystals, it is sufficient to use the geometrical interpretation given by Kossel. To investigate the anomaly of Kossel diffraction lines quantitatively, however, it is necessary to use the dynamical theory of diffraction [3] developed by Laue and Ewald [29]. We were able to explain the anomalies at intersecting points of the Kossel rings with indices $h = \{220\}$ and $h' = \{131\}$ by using the three wave approximation [28, 30, 31] in the dynamical theory of diffraction.

5.6 Summary

The Kikuchi-Kossel diffraction of laser beams provides a unique and definite method of structure analysis of colloidal crystals, since its geometrical pattern corresponds one-to-one with the symmetry of the crystal structure. Real time observation with the Kikuchi-Kossel method confirmed that the ordering formation in salt-free colloidal dispersions proceeds by way of *multi-stage phase transitions*. This discovery of multi-stage phase transitions in colloidal dispersions has important physical implications. Even though its experimental verification is difficult, it is not unnatural to speculate that the crystallization in ordinary atomic and molecular systems also proceeds through *multi-stage phase transitions*.

Is it possible to explain such a variety of phenomena in ordering processes in colloidal dispersions by the classical DLVO theory? As shown in Chap. 2,

[3] In the dynamical theory, each Kossel ring should be interpreted as the direct manifestation of the locus of the gap in the dispersion surface at the Brillouin-zone boundary [28].

the classical DLVO theory ascribed the formation of colloidal crystals to the secondary minimum of the combined potential of the van der Waals attraction and the screened Coulomb repulsion. However, the discovery of the salt-induced-melting of the colloidal crystals [1] excluded this scheme based on the secondary minimum. To improve this deficiency of the classical DLVO theory, Wadati and Toda [32] proposed discarding the contribution of the van der Waals attraction and resorting to the Alder-Wainwright mechanism [33] to describe the ordering formation in colloidal dispersions. However, it seems almost impossible to explain the occurrence of the many-faceted sequence of phase transitions from a viewpoint based on the repulsion-only theory.

Recently, an effective theory based on the so-called *volume term*, which is independent of the particle configuration and depends on the state of dispersion, has been studied extensively to explain the coexistence of phases with different particle densities. However, it seems inevitable to assume the existence of medium-range strong repulsion and long-range weak attraction in order to explain the stable evolution of crystallites through multi-stage phase transitions in colloidal dispersions.

Finally, it is worthwhile to note the fact that the precision of the Kikuchi–Kossel diffraction method is very high. It is now possible to determine the lattice constant to within an error of 0.2% [16, 34]. Therefore, the Kikuchi-Kossel diffraction method provides a powerful tool for the investigation of colloidal dispersions, and at the same time *the colloidal crystals provides a very suitable system for light diffraction* to investigate experimentally the dynamical theory of light. In addition, the Kikuchi-Kossel diffraction method is applicable to study photonic band structures [35] of colloidal crystals which can be used as three-dimensional photonic crystals.

References

1. Hachisu S, Kobayashi Y, Kose A (1973) J Coll Interface Sci 42:342
2. Kose A, Ozaki M, Takano K, Kobayashi K, Hachisu S (1973) J Coll lnterface Sci 44:330
3. Yoshiyama T, Sogami I, Ise N (1984) Phys Rev Lett 53:2153
4. Yoshiyama T (1986) Polymer 27:827
5. Sogami IS, Yoshiyama T (1990) Phase Transition 21:171
6. Kikuchi S (1928-29) Jpn J Phys 5:83; Nishikawa S, Kikuchi S (1928) Proc Imp Acad Japan 4:475
7. Shinohara K (1934) Phys Rev 47:740
8. Sur B, Rogge RB, Hammond RP, Anghel VNP, Katsaras J (2002) Phys Rev Lett 88:065505
9. Peng LM, Dudarev SL, Whelan MJ (2004) High-energy electron diffraction and microscopy, Oxford University Press, Oxford, p.282
10. Kossel W, Loeck V, Voges H (1935) Z Physik 94:139
11. Kossel W, Voges H (1937) Ann Phys 23:677
12. Clark NA, Hurd AJ, Ackerson BJ (1979) Nature 281:57
13. Sood AK (1991) Solid State Physics 45:1
14. Crandall RS, Williams R (1977) Science 198:293
15. Kesavamoorthy R, Arora AK (1985) J Phys A18:3389; (1986) J Phys C19:2833
16. Shinohara T, Yoshiyama T, Sogami IS, Konishi T, Ise N (2001) Langmuir 17:8010
17. Yoshiyama T, Sogami IS (1987) Langmuir 3:851
18. Lang AR (1959) J Appl Phys 30:1748
19. Yoshiyama T, Sogami IS (1996) Crystal growth in colloidal suspensions: Kossel line analysis. In: Arora AK, Tata BVR (eds) Ordering and phase transitions in charged colloids. VCH, New York, Chap. 3
20. Hiltner PA, Krieger IM (1969) J Phys Chem 73:2386
21. Warren BE (1941) Phys Rev 59:693
22. Franklin RE (1959) Acta Crystal 3:107
23. Ackerson BJ, Clark NA (1981) Phys Rev Lett 46:123
24. Wilson AJC (1942) Proc Roy Soc London A180:277
25. Laue M (1960) Röntgenstrahl-Interferenzen, 3rd edn. Akademische Verlagsgesellschaft, Frankfurt
26. Doyle PA (1968) Acta Crystallogr A24:81

27. Kambe K (1957) J Phys Soc Jpn 12:13
28. Yoshiyama T, Sogami IS (1986) Phys Rev Lett 56:1609
29. James RW (1967) The optical principles of the diffraction of x-Rays. Bell, London
30. Ewald PP (1937) Z Kristallogr A97:1
31. Chang SL (1984) Multiple diffraction of x-rays in crystals. Springer, Berlin Heidelberg New York
32. Wadati M, Toda M (1972) J Phys Soc Jpn 32:1147
33. Alder BJ, Wainwright TE (1957) J Chem Phys 27:1208; (1959) J Chem Phys 31:459
34. Shinohara T, Yamada H, Sogami IS, Ise N, Yoshiyama T (2004) Langmuir 20:5141
35. Tarhan İİ, Watson GH (1996) Phys Rev Lett 76:315

6

Effective Interactions between Macroions 2

6.1 Introductory Remarks

The ionic atmosphere, which arises as a result of mutual screening of unlike charges, is one of the key concepts in the theory of ionic solutions. Such screening between unlike charges occurs much more strongly in macroionic dispersions. If a macroion has a large analytic surface charge, the strength of the electric field becomes large near the surface of the macroion. Consequently, counterions attracted strongly by the surface charges accumulate on the surface and bring about the so-called *counterion condensation*.

Yamanaka et al. [1] made intensive studies on the screening effects of analytical charges of spherical macroions. The results of their measurements, in Fig. 4.4, show that an increase in *analytical surface charge* leads to a tendency of saturation of the *net surface charge*. This effect was confirmed to be enhanced for macroions with larger diameter. Therefore, dispersions of spherical macroions with large analytical surface charges and large diameter should be described as a system of particles with reduced net surface charges [2–4]. In such a description, it is relevant to regard the counterions which are condensed and frozen near the surface as belonging to the macroion.

Henceforth, we call a macroion with net surface charges an *effective particle* and a macroion with its large analytical surface charge a *naked macroion*. The word *macroion* is used generically for both of them, when no distinction is necessary. Let us name the region surrounding a naked macroion where counterions are condensed a *layer of condensation*. It is natural to consider that the whole volume inside the layer of condensation belongs to the effective particle. The volume of such an effective particle is called an *effective volume of the particle*.

Let us consider a region outside of the layer of condensation. Counterions in this outside region form the so-called *diffuse layer* by surrounding diffusely the effective particle. It is important to note that the counterion condensation is a thermodynamic phenomenon. Namely, the counterions are condensed on

average. Therefore, it is a natural picture to regard the counterions as statistically exchanged between the layer of condensation and the diffuse layer and, as a result, the *net charge number* of the effective particle fluctuates around its mean value. In particular, the counterions tend to spread into the diffuse layer in dilute dispersion with low salt concentrations. Therefore, the layer of condensation of the effective particle has the role of a *source of counterions* into the diffuse layer.

Following the mean field theory in Chap. 2, it is postulated that the effective particles form a stationary configuration in which the gas of small ions takes rapidly chemical and thermal equilibrium. In a thermodynamic description of macroionic dispersions where macroions and small ions interact strongly, the concept of the volume of the system must be carefully dealt with. First of all, we call the region occupied by the whole dispersion in a container the region Ω and represent its volume by the same symbol Ω. Next, the region inside Ω and outside the region occupied by all of the naked macroions is called the region V_0 and its volume is represented by the same symbol V_0. Similarly, the region inside Ω and outside the region occupied by all of the effective particles is called the *effective region of the system* V and its volume, called the *effective volume of the system*, is represented by the same symbol V. While the region Ω is simply-connected, the regions V_0 and V are multiply-connected.

As shown in Chaps. 4 and 5, investigations of ordering formations in monodisperse colloidal dispersions have clarified the limit of application of the DLVO theory. In particular, the salt-induced-melting of colloidal crystals discovered by Hachisu's group [5] required a reexamination of the theoretical basis of the DLVO theory. The fact that the colloidal crystals can have large lattice spacings of the order of 10^3 nm also suggests that the cohesive force for the crystals could not be of short-range, like the van der Waals attraction, but should be of long-range, like the electric interaction. This idea of Coulombic attraction between like-charges was proposed first by Langmuir [6]. In this chapter, we develop a new mean field theory for macroionic dispersions [7, 8] which corrects the defect of the DLVO theory and supports the Coulombic attraction hypothesis.

To formulate a *thermodynamic theory of macroionic dispersions*, which are inhomogeneous and non-additive, it is natural and relevant to take the ordinary thermodynamics for homogeneous systems as a conceptual and theoretical framework. Provided that the degrees of inhomogeneousness and non-additivity are small, we consider that variables and relations in the ordinary thermodynamics maintain their ordinary physical meanings to a good approximation and use them under certain restrictions. Although the electric energy E and the Helmholtz and Gibbs free energies F and G are no longer the extensive variables in the exact sense, they play central roles as quasi-extensive variables in the thermodynamic theory of macroionic dispersions. Note that, as a natural consequence, the Gibbs-Duhem relation which is a criterion of

additivity does not hold in any form of the thermodynamic theory of the macroionic dispersions.

To clarify characteristic features of macroionic systems consisting of the small ion gas and its fixed environment of macromolecules, it is necessary to examine first the difference in the degrees of inhomogeneousness of the systems with respect to the temperature T and an effective volume V. Although the kinetic energies of the small ions may increase instantaneously and local heating-up may occur near the surfaces of the macroions, those small fluctuations are immediately averaged away by the thermal motion of solvent molecules. Therefore, we are allowed to assume that the macroionic systems are almost homogeneous with respect to temperature T and that the thermodynamic relation

$$\frac{\partial}{\partial T}\left(\frac{F}{T}\right) = -\frac{U}{T^2} \tag{6.1}$$

holds for the internal energy U and the Helmholtz free energy F. By contrast, the macromolecules are postulated to take a stationary configuration in the macroionic dispersion. It is impossible to average away such an inhomogeneousness with respect to the macromolecule distribution. If we *preaverage* the system with respect to the configuration of the macromolecules, the notions of the positions and the pair potentials of the molecules lose their physical meanings. Therefore, it is relevant to consider that the macroionic systems are intrinsically inhomogeneous and that, in contrast to (6.1), the thermodynamic relation

$$\frac{\partial}{\partial V}\left(\frac{F}{V}\right) = -\frac{G}{V^2} \tag{6.2}$$

which includes the derivative with respect to the effective volume V, does not hold for the Helmholtz free energy F and the Gibbs free energy G. The effective volume V must be treated differently from the temperature T for the macroionic systems.

While (6.1) holds, (6.2) does not hold for the macroionic dispersions. We regard these features to be essential in characterizing the macroionic dispersions as an inhomogeneous system. Accordingly, in a *thermodynamic theory of macroionic dispersions*, it must not be allowed to take derivative of thermodynamic functions with respect to the volume V.

In ordinary thermodynamic theory, there are two different routes to derive the Gibbs free energy from the Helmholtz free energy. So we introduce here, tentatively, two kinds of Gibbs free energies G' and G'' which are calculated, respectively, by using the relation in (6.2) and by taking the sum of chemical potentials of constituents. The equality $G' = G''$ holds only for a homogeneous system and the Gibbs free energy has a unique and strict physical meaning only for such a system. As shown in Sect. 2.3, the equality surely holds in the DH theory of strong electrolyte. However, (6.2) does not hold for the macroionic dispersions and it is forbidden to use the "Gibbs free energy" G' to describe the systems. Therefore, it is permitted only to follow the route leading

to the "Gibbs free energy" G''. In the present formalism, we postulate that the degree of inhomogeneousness of the macroionic systems considered here is not too large, such that the difference $|G' - G''|$ is sizably smaller than G''. Accordingly, using the concepts and variables of the ordinary thermodynamics for homogeneous systems as the standard, we calculate the free energy G'' which works to include effects of inhomogeneousness of the macroionic system. Henceforth, we call the calculable G'' simply the Gibbs free energy G of the system.

In Sect. 6.2, noting the experimental fact [1] that the observed net charges of macroions are much reduced from their analytical charges, we reformulate a new linearized theory for effective macroions with net charges. To avoid confusion, we specify first the characteristics of a system of macroions with net charges and then calculate the Helmholtz and Gibbs free energies F and G of the small ion gas in an environment of stationary macroions. From the Gibbs free energy G, which is a function of the configuration of the macroions, adiabatic pair potentials for macroions that have a medium-range strong repulsive part and a long-range weak attractive tail are obtained.

In Sect. 6.3, a general mean field theory for describing macroionic dispersions is developed without resort to the linear approximation. Using the method of analytical mechanics [9], we derive a generating functional which produces the PB equation and associated boundary conditions. The generating functional enables us to represent these two free energies F and G of the system in terms of the mean electric potential. By taking the difference between G and F, an equation of state for the osmotic pressure is derived.

As an application of the results in Sect. 6.3, we investigate a system of parallel charged plates immersed in an electrolyte in a finite container in Sect. 6.4. In such a one-dimensional system, it is possible to solve the PB equation exactly and to obtain the free energies of the system analytically. With numerical analyses, we find that both of the Helmholtz and Gibbs free energies provide medium-range strong repulsion and long-range weak attraction working between the charged plates.

6.2 Reconstruction of a Linearized Mean Field Theory

In this section, the effective volume of the system is assumed to be sufficiently large. We describe the gas of small ions in the effective region V thermodynamically by using the linearized PB equation. Namely, the thermodynamic properties of the macroionic dispersion are assumed to be governed by the gas of small ions with large degrees of freedom in the effective region of the system V. Therefore, the effective volume V of the small ion gas must be chosen as the relevant thermodynamic variable. In the linearized theory used in this section, Ω and V_0 are auxiliary parameters. It is important to discriminate the three regions V, V_0 and Ω ($V \subset V_0 \subset \Omega$) in the following formulation of the linearized theory.

6.2.1 Gibbs (Macroionic) System

In this way, a dilute dispersion of macroions with large surface charges is regarded as a system consisting of a group of effective particles with reduced net surface charges and a gas of small ions in a stationary environment of effective particles. The gas of small ions is in chemical and thermal equilibrium, exchanging counterions with the layers of condensation near the surfaces of the effective particles. It is relevant to describe the thermodynamic states of such a system in terms of the Gibbs free energy. Therefore, we call such a system the *Gibbs macroionic system* or simply the *Gibbs system* and develop a new mean field theory to describe the Gibbs system.

In the Gibbs macroionic system, we apply the linear approximation to the PB equation for the mean electric potential in the effective region V of the system. Namely, provided that the deviation of the average electric energy from a certain value of standard is smaller than the thermal energy in the diffuse layer, the Boltzmann distribution function is approximated by the linear term with respect to the deviation of the electric potential. In this formalism, the properties of the layer of condensation are ruled by nonlinear effects of the PB equation and the thermodynamic states in the region of the diffuse layer are described by its linear effects.

The procedures for deriving the thermodynamic quantities of the Gibbs macroionic system are almost the same as those of the DH theory in Chap. 2. First, the electric energy of the system E is calculated by using the solution of the linearized PB equation. Next, the Helmholtz free energy F is obtained by using Debye's charging-up formula proved in Sect. 6.3. Then, calculating the chemical potentials from F and summing them all up, we obtain the Gibbs free energy G. Depending on whether this procedure is stopped at F or continued to derive G, we are confronted with completely different results. While the Helmholtz free energy F reproduces the purely repulsive screened Coulomb potential of the DLVO theory, the Gibbs free energy G gives rise to a potential with a medium-range strong repulsive part and a long-range weak attractive tail.

In the DLVO theory explained in Chap. 2, there is no difference between analytical charges and net charges, and the concept of net charges is not introduced. Here we regard the dispersions of macroions with small analytical surface charges also as Gibbs systems. In such cases, since the effect of counterion condensation is small, the fluctuation of the surface charges of the effective particles is also small.

6.2.2 Model of the Gibbs (Macroionic) System

To formulate a mean field theory for the Gibbs system, we model it as a system which satisfies the following conditions.

Properties of the Gibbs (Macroionic) System

1. M effective particles are assumed to take a stationary configuration $\{\boldsymbol{R}\} \equiv \{\boldsymbol{R}_n : n = 1, 2, \cdots, M\}$ where $\boldsymbol{R}_n$ is the displacement vector for the center of mass of the n-th effective particle. Small ions are assumed to reach rapidly chemical and thermal equilibrium [1] in the environment of effective particles. The distribution function for the surface charges $Z_n e$ of the n-th effective particle is given by [2]

$$\rho_n(\boldsymbol{r}) = \frac{1}{(2\pi)^3} \int \tilde{\rho}_n(\boldsymbol{k}) \mathrm{e}^{\mathrm{i}\boldsymbol{k}\cdot\boldsymbol{r}} \mathrm{d}\boldsymbol{k} \tag{6.3}$$

with the Fourier component

$$\tilde{\rho}_n(\boldsymbol{k}) = \int \rho_n(\boldsymbol{r}) \mathrm{e}^{-\mathrm{i}\boldsymbol{k}\cdot\boldsymbol{r}} \mathrm{d}\boldsymbol{r} = \mathrm{e}^{-\mathrm{i}\boldsymbol{k}\cdot\boldsymbol{R}_n} f_n(\boldsymbol{k}) \tag{6.4}$$

which is a function of $\boldsymbol{R}_n$ and a form factor $f_n(\boldsymbol{k})$. The distribution function $\rho_n(\boldsymbol{r})$ is normalized as

$$\tilde{\rho}_n(0) = \int \rho_n(\boldsymbol{r}) \mathrm{d}\boldsymbol{r} = 1 \,. \tag{6.5}$$

2. Small ions with valency z_i in chemical and thermal equilibrium in the dispersion take the Boltzmann distribution. In the effective region V where the deviation of the electric potential $z_i e[\psi(\boldsymbol{r}) - \breve{\psi}]$ from a standard value $\breve{\psi}$ is smaller than the thermal energy $k_{\mathrm{B}}T$, the linear approximation

$$n_i(\boldsymbol{r}) = n_{i0}^* \left\{ 1 - \frac{z_i e}{k_{\mathrm{B}}T} [\psi(\boldsymbol{r}) - \breve{\psi}] \right\} \tag{6.6}$$

is assumed to hold, where n_{i0}^* is defined by

$$n_{i0}^* = n_{i0} \exp\left\{ -\frac{z_i e}{k_{\mathrm{B}}T} \breve{\psi} \right\} \tag{6.7}$$

and the standard value $\breve{\psi}$ is chosen so as to optimize the linear approximation.

[1] The Earnshaw theorem stated in Sect. 1.3 insists that a configuration of a group of "stationary particles" is unstable. For the group of effective particles to be stable, the particles must execute Brownian motion. Just as in the DLVO theory, the time scale for the small ions to reach equilibrium is considered to be far shorter than that of the Brownian motion.

[2] The net charge number Z_n and its distribution depend, in principle, on the physical state of the system: Z_n can change its value depending on a configuration of effective particles. In the present formalism, however, this dependence is considered to be negligibly small.

3. The solvent is dealt first with as a continuous medium with a dielectric constant ϵ. The particle nature of the solvent is explicitly taken into account in the theory at the stage of derivation of the Gibbs free energy.

Electric Energy and Free Energies

The derivation of thermodynamic quantities of the dispersion requires a compact analytic expression for the electric energy E of the system. As will be shown in the next section, E is expressible either by the electric field variable or by quantities associated with the charged particles [10].

From (2.20), the electric field energy E is given by the integral of the electric field density over the effective volume of the system V as follows:

$$E = E^{\mathrm{el}}(V : \psi, \epsilon) = \frac{\epsilon}{8\pi} \int_V [\nabla\psi(\boldsymbol{r})]^2 \, \mathrm{d}\boldsymbol{r} \tag{6.8}$$

in terms of the mean electric potential ψ. Although this integral representation is compact, it is impossible to obtain a concise analytical result by carrying out the integration, because the region V is not simply-connected.

Here we notice that the whole region of the dispersion Ω is the sum of the effective region and the regions occupied by the effective particles as

$$\Omega = V + \sum_n \omega_n, \tag{6.9}$$

where ω_n is the effective volume of the n-th particle. Evidently the integral in (6.8) is rewritten by the difference of the contributions from the volume Ω of the whole dispersion and the volume $\sum_n \omega_n$ as

$$E = E^{\mathrm{el}}(\Omega : \psi, \epsilon) - \sum_n E^{\mathrm{el}}(\omega_n : \psi, \epsilon) \tag{6.10}$$

where

$$E^{\mathrm{el}}(\omega_n : \psi, \epsilon) = \frac{\epsilon}{8\pi} \int_{\omega_n} [\nabla\psi(\boldsymbol{r})]^2 \, \mathrm{d}\boldsymbol{r} \, . \tag{6.11}$$

The electric field energy E is now expressed in terms of the quantities $E^{\mathrm{el}}(\Omega : \psi, \epsilon)$ and $E^{\mathrm{el}}(\omega_n : \psi, \epsilon)$ which are obtained by the integrals over the simply-connected regions.

One of the salient points of the new linearized theory developed in this section is to neglect totally the contributions $\sum_n E^{\mathrm{el}}(\omega_n : \psi, \epsilon)$ in (6.10) which arise from the integrals over the region occupied by the effective particles. In Sect. 6.5, physical meanings of this approximation will be investigated in detail. Knott and Ford [11] calculated the quantities in (6.11) for a dilute dispersion of monodisperse particles with the mean electric potential that is obtained in the linear approximation in the present scheme. They found additional complicated correction terms to the Helmholtz free energy F in (6.33)-(6.35). With their result for F which includes numerical integrations,

however, it is impossible to reproduce the DLVO repulsive potential from F and to obtain an analytical expression for the Gibbs free energy G, whose derivation is the overriding necessity in the present formalism.

As one of the basic assumptions of our mean field theory, we postulate that the electric energy of the dilute dispersion is well approximated by the integral over the simply-connected region Ω as [3]

$$E \simeq E^{\mathrm{el}}(\Omega : \psi, \epsilon) = \frac{\epsilon}{8\pi} \int_{\Omega} [\nabla\psi(\boldsymbol{r})]^2 \, \mathrm{d}\boldsymbol{r} \tag{6.12}$$

in the new linearized theory, which enables us to calculate analytically both of the free energies of the system F and G.

In this linearized theory, the mean electric potential $\psi(\boldsymbol{r})$ is given by a superposition of contributions from effective particles which have the stationary configuration $\{\boldsymbol{R}\}$. Therefore, after the integration in (6.12), the total electric energy E takes the form

$$E = \frac{1}{2} \sum_{m \neq n} U^{\mathrm{E}}_{mn} + \sum_{n} V^{\mathrm{E}}_{n} \tag{6.13}$$

where U^{E}_{mn} is an *electric pair potential* depending on the relative configuration and orientation of the m-th and n-th effective particles and V^{E}_{n} is the single electric potential (i.e., one-body potential) of the n-th effective particle due to its ionic atmosphere. In the DH theory of electrolytes, the pair potential U^{E}_{mn} does not exist and the single potential corresponds to the energy of the ionic atmosphere. There is no term which depends on the positions of more than three particles in this approximation, since the electric-field energy density depends quadratically on $\psi(\boldsymbol{r})$. From E, we are able to derive the free energies F and G as the sums of pair potentials and single potentials.

6.2.3 Mean Electric Potential in the Effective Region V

In the environment of the stationary distribution of the effective particles, the PB equation for the mean electric potential $\psi(\boldsymbol{r})$ takes the form

$$\epsilon\nabla^2\psi(\boldsymbol{r}) = -4\pi \sum_{i=1}^{\mu} z_i e n_i(\boldsymbol{r}) - 4\pi \sum_{n=1}^{M} Z_n e \rho_n(\boldsymbol{r}) \tag{6.14}$$

where M is the number of particles and μ is the number of small ion species. The second term on the right-hand side of this equation represents the surface charge distributions, which depend on the configuration of the particles.

[3] Owing to this approximation, this theory is often regarded as permitting small ions to penetrate the interiors of macroions [11, 12]. This is not correct. The relevant thermodynamic variable of this theory is not Ω but V. The contributions $E^{\mathrm{el}}(\omega_n : \psi, \epsilon)$ are assumed numerically small and neglected as a mathematical approximation.

Shifted Linearized PB Equation

To solve (6.14) in the effective region V, we apply the linear approximation in (6.6) to obtain

$$\epsilon(\nabla^2 - \kappa^2)[\psi(\boldsymbol{r}) - \breve{\psi}] = -4\pi \sum_{i=1}^{\mu} z_i e n_{i0}^* - 4\pi \sum_{n=1}^{M} Z_n e \rho_n(\boldsymbol{r}) \tag{6.15}$$

where the Debye screening factor is defined by

$$\kappa^2 = \frac{4\pi e^2}{\epsilon k_{\mathrm{B}} T} \sum_{i=1}^{\mu} z_i^2 n_{i0}^* \,. \tag{6.16}$$

To eliminate the constant term in the linearized differential equation (6.15), the mean electric potential is transformed as

$$\psi(\boldsymbol{r}) = \varphi(\boldsymbol{r}) + \breve{\psi} + \frac{4\pi e}{\epsilon \kappa^2} \sum_{i=1}^{\mu} z_i n_{i0}^* \tag{6.17}$$

where $\breve{\psi}$ is the value of the mean electric potential chosen to optimize the linear approximation. Henceforth, the new potential $\varphi(\boldsymbol{r})$ is called the *shifted mean electric potential*. It is not necessary to specify the value $\breve{\psi}$ at this stage, since the electric energy E in (6.12) depends only on the gradient of the mean electric potential as $\nabla\psi = \nabla\varphi$ and all thermodynamic quantities are derivable from E.

The shifted potential $\varphi(\boldsymbol{r})$ satisfies the linear differential equation

$$\epsilon(\nabla^2 - \kappa^2)\varphi(\boldsymbol{r}) = -4\pi \sum_{n} Z_n e \rho_n(\boldsymbol{r}) \tag{6.18}$$

which is readily solved by Fourier transformation as follows:

$$\varphi(\boldsymbol{r}) = \frac{e}{2\pi^2 \epsilon} \sum_{n=1}^{M} Z_n \int \frac{1}{k^2 + \kappa^2} \tilde{\rho}_n(\boldsymbol{k}) \mathrm{e}^{\mathrm{i}\boldsymbol{k}\cdot\boldsymbol{r}} \mathrm{d}\boldsymbol{k} \,. \tag{6.19}$$

Performing the partial integration in (6.12) and using (6.18), the total electric energy of the system E is rewritten in the form

$$\begin{aligned} E &= \frac{\epsilon}{8\pi} \int [\nabla\varphi(\boldsymbol{r})]^2 \, \mathrm{d}\boldsymbol{r} \\ &= \frac{1}{2} \int \varphi(\boldsymbol{r}) \left[-\frac{\epsilon\kappa^2}{4\pi} \varphi(\boldsymbol{r}) \right] \mathrm{d}\boldsymbol{r} + \frac{1}{2} \sum_{n} Z_n e \int \varphi(\boldsymbol{r}) \rho_n(\boldsymbol{r}) \, \mathrm{d}\boldsymbol{r} \end{aligned} \tag{6.20}$$

where contributions from the container surface are neglected for simplicity. The first term represents the electric energy of all the small ions, which have

charge distribution $-(\epsilon\kappa^2/4\pi)\varphi(\boldsymbol{r})$ in the potential field $\varphi(\boldsymbol{r})$. The second term is apparently the electric energy of the particles in $\varphi(\boldsymbol{r})$. As will be clarified later, it is the first term which is responsible for an attractive force between effective particles through the intermediary of counterions at the level of electric energy.

Neutrality Condition for Electric Charges

Let us define the average value of a function $f(\boldsymbol{r})$ over an arbitrarily chosen test volume v in the effective region V by

$$\langle f\rangle = \frac{1}{v}\int f(\boldsymbol{r})\,\mathrm{d}\boldsymbol{r}\ . \tag{6.21}$$

Here, v is assumed to be so large that the relation

$$\int_v \mathrm{e}^{\mathrm{i}\boldsymbol{k}\cdot\boldsymbol{r}}\,\mathrm{d}\boldsymbol{r} \Rightarrow (2\pi)^3\delta(\boldsymbol{k}) \tag{6.22}$$

holds. Taking the average value of $\varphi(\boldsymbol{r})$ in (6.19) leads to

$$\langle\varphi\rangle = \frac{1}{v}\int_v \varphi(\boldsymbol{r})\,\mathrm{d}\boldsymbol{r} = \frac{1}{v}\frac{4\pi e}{\epsilon\kappa^2}\sum_n Z_n \tag{6.23}$$

which enables us to calculate the average value of $n_i(\boldsymbol{r})$ as

$$\begin{aligned}\langle n_i\rangle &= \frac{1}{v}\int_v n_{i0}^*\{1-\frac{z_i e}{k_{\mathrm{B}}T}[\psi(\boldsymbol{r})-\breve{\psi}]\}\,\mathrm{d}\boldsymbol{r}\\ &= n_{i0}^* - \left[\sum_i z_i n_{i0}^* + \frac{1}{v}\sum_n Z_n\right]\frac{z_i n_{i0}^*}{\sum_i z_i^2 n_{i0}^*}\ .\end{aligned} \tag{6.24}$$

Consequently, the *condition for electric neutrality* is found to be

$$\sum_{i\in v} z_i\langle n_i\rangle + \frac{1}{v}\sum_{n\in v} Z_n = 0 \tag{6.25}$$

where the sum is taken over all the small ions and effective particles in v. To examine the physical meaning of the parameter n_{i0}^* in the linearized distribution function (6.6), let us take the average value of the squared distribution function $n_i(\boldsymbol{r})^2$ as follows:

$$\begin{aligned}\langle n_i^2\rangle &= \frac{1}{v}\int_v n_{i0}^{*2}\left\{1-\frac{z_i e}{k_{\mathrm{B}}T}[\psi(\boldsymbol{r})-\breve{\psi}]\right\}^2\mathrm{d}\boldsymbol{r}\\ &= n_{i0}^{*2}\frac{1}{v}\left\{v - 2\frac{z_i e}{k_{\mathrm{B}}T}\int_v[\psi(\boldsymbol{r})-\breve{\psi}]\mathrm{d}\boldsymbol{r}\right\}\\ &= n_{i0}^{*2} - 2n_{i0}^*\left[\sum_i z_i n_{i0}^* + \frac{1}{v}\sum_n Z_n\right]\frac{z_i n_{i0}^*}{\sum_i z_i^2 n_{i0}^*}\\ &= -n_{i0}^{*2} + 2n_{i0}^*\langle n_i\rangle\ .\end{aligned} \tag{6.26}$$

In this estimation, terms proportional to $(\psi - \breve{\psi})^2$ have been neglected. Note that this result can be rewritten in the form

$$(n_{i0}^* - \langle n_i \rangle)^2 + \langle (n_i - \langle n_i \rangle)^2 \rangle = 0 \,. \tag{6.27}$$

Since the two terms in this equation cannot be negative, both of them must be zero. The parameter n_{i0}^* should be interpreted as the average number of small ions of i-th species $\langle n_i \rangle$. Therefore, applying this result to the effective region V, we obtain

$$n_{i0}^* = \langle n_i \rangle = \frac{N_i}{V} \tag{6.28}$$

where N_i is the total number of small ions of i-th species in V. The other relation $\langle (n_i - \langle n_i \rangle)^2 \rangle = 0$ states that the fluctuation of the linearized distribution of small ions vanishes when averaged over a large region.

6.2.4 Adiabatic Pair Potentials for Effective Particles

To obtain an analytical expression for E, the integration in (6.12) must be taken over a sufficiently large volume Ω. All the thermodynamic energies are proved to consist of adiabatic pair potentials that depend on the relative displacement between particles and adiabatic single potentials which arise from correlations of a particle with its surrounding cloud of small ions.

Electric Potential: E-Potential

Substituting (6.17) and (6.19) into (6.12) and noting $\nabla\psi(\boldsymbol{r}) = \nabla\varphi(\boldsymbol{r})$, we carry out the integration by using the relation (6.22). The total electric energy E is obtained in the form (6.13) with

$$\begin{aligned} U_{mn}^{\mathrm{E}} &= \frac{e^2}{2\pi^2\epsilon} Z_m Z_n \int \frac{k^2}{(k^2+\kappa^2)^2} \tilde{\rho}_m(\boldsymbol{k}) \tilde{\rho}_n(-\boldsymbol{k}) \, \mathrm{d}\boldsymbol{k} \\ &= \frac{e^2}{2\pi^2\epsilon} Z_m Z_n \int \left[-\frac{\kappa^2}{(k^2+\kappa^2)^2} + \frac{1}{k^2+\kappa^2} \right] \tilde{\rho}_m(\boldsymbol{k}) \tilde{\rho}_n(-\boldsymbol{k}) \, \mathrm{d}\boldsymbol{k} \end{aligned} \tag{6.29}$$

and

$$V_n^{\mathrm{E}} = \frac{e^2}{4\pi^2\epsilon} Z_n^2 \int \frac{k^2}{(k^2+\kappa^2)^2} \tilde{\rho}_n(\boldsymbol{k}) \tilde{\rho}_n(-\boldsymbol{k}) \, \mathrm{d}\boldsymbol{k} \,. \tag{6.30}$$

Hereafter, we call U_{mn}^{E} the *pair E-potential* and V_n^{E} the *single E-potential*.

The first and second terms in the integrand on the right-hand side of (6.29) which correspond, respectively, to the first and second terms on the right-hand side of (6.20), become origins of attractive and repulsive parts in the effective particle interaction. At this stage of calculation in the formulation of a classical field theory, the degrees of freedom of the electric field and the small ions are completely integrated out. As a result, the pair E-potentials become functions of the relative displacement of the effective particles through the Fourier transforms in (6.4).

Helmholtz Potential: F-Potential

In order to derive the Helmholtz free energy F from E, the Debye charging-up formula

$$F = F^0 + \int_0^{e^2} \frac{E}{e^2}\,\mathrm{d}e^2 \tag{6.31}$$

is used. Since (6.29) and (6.30) have a simple dependence on e^2, the relation

$$\int_0^{e^2} \frac{k^2}{(k^2+\kappa^2)^2}\,\mathrm{d}e^2 = \frac{e^2}{k^2+\kappa^2} \tag{6.32}$$

allows us to integrate F term by term, leading to

$$F = F^0 + \frac{1}{2}\sum_{m\neq n} U^{\mathrm{F}}_{mn} + \sum_n V^{\mathrm{F}}_n \tag{6.33}$$

where

$$U^{\mathrm{F}}_{mn} = \frac{e^2}{2\pi^2\epsilon} Z_m Z_n \int \frac{1}{k^2+\kappa^2}\tilde{\rho}_m(\boldsymbol{k})\tilde{\rho}_n(-\boldsymbol{k})\,\mathrm{d}\boldsymbol{k} \tag{6.34}$$

and

$$V^{\mathrm{F}}_n = \frac{e^2}{4\pi^2\epsilon} Z_n^2 \int \frac{1}{k^2+\kappa^2}\tilde{\rho}_n(\boldsymbol{k})\tilde{\rho}_n(-\boldsymbol{k})\,\mathrm{d}\boldsymbol{k}\,. \tag{6.35}$$

Henceforth, U^{F}_{mn} and V^{F}_m are simply called, respectively, the *pair F-potential* and the *single F-potential*. F^0 is the Helmholtz free energy in the limit $e = 0$.

Note that the pole of second order with a minus sign in the integral representation (6.29) for the pair E-potential U^{E}_{mn} disappears in the representation (6.34) owing to the parameter integral (6.32). This mechanism causes the attractive part in U^{E}_{mn} to disappear in U^{F}_{mn}.

All these results can also be reproduced by using the thermodynamic relation (6.1). Namely, applying the formula

$$\int_0^T \frac{k^2}{(k^2+\kappa^2)^2T^2}\,\mathrm{d}T = -\frac{1}{(k^2+\kappa^2)T} \tag{6.36}$$

to carry out termwise integrations and using (6.1), we obtain the expressions in (6.33)–(6.35). This method is applicable, since the macroionic dispersion is a uniform system with respect to temperature T and the factors $\tilde{\rho}_m(\pm\boldsymbol{k})$ are assumed to be independent of T.

Gibbs Potential: G-Potential

The integral representation in (6.34) shows that the pair F-potential U^{F}_{mn} depends on the configuration of the effective particles through the Fourier factors $\tilde{\rho}_n(\pm\boldsymbol{k})$. Accordingly, the Helmholtz free energy of the system is a function of the particle configurations. It is important to recognize that in general the effective volume V also depends on the configuration and that it is not possible to find their functional dependence a priori. Later, as will be

shown in (6.53) and (6.54), an implicit relation between the effective volume V of the small ion gas and the configuration of the effective particles is found as a result of the theory to be developed.

To derive the Gibbs free energy $G \equiv G''$ of the macroionic dispersion which is intrinsically inhomogeneous, we have to calculate chemical potentials of the small ions from the Helmholtz free energy. We examine first the monodisperse system.

– **Monodisperse System** –

Suppose that the effective particle has a net surface charge number Z and that the total number of small ions of i-th species is $N_i = \langle n_i \rangle V$. From (6.25) and (6.28), the neutrality condition in the region V is given by

$$\sum_i z_i N_i + ZM = 0 \,. \tag{6.37}$$

In the Gibbs macroionic system, while the number of effective particles M is fixed, the value of the net surface charge number Z is variable. The chemical potential of the small ions of i-th species is calculated by taking the derivative of the Helmholtz free energy $F(V, T, N_i, Z(N_i))$ with respect to N_i. In this calculation, it is necessary to notice that Z is not an independent variable but depends on N_i through the neutrality condition (6.37).

Following the method in the DH theory which was developed in Sect. 2.3, we derive the Gibbs free energy $G(P, T, N, N_i)$ by summing up all the chemical potentials of the small ions in the stationary configuration of the particles. Taking the neutrality condition into account, $G(P, T, N, N_i)$ is calculated to be

$$\begin{aligned} G &= \left\{ \left[\sum_i N_i \left(\frac{\partial F}{\partial N_i} \right)_{V,T} \right]_{\text{neutrality}} \right\}_{V=Nv} \\ &= \left[\sum_i N_i \left(\frac{\partial F}{\partial N_i} \right)_{V,T,Z} + \sum_i N_i \left(\frac{\partial Z}{\partial N_i} \right)_{V,T} \left(\frac{\partial F}{\partial Z} \right)_{V,T,N_i} \right]_{V=Nv} . \end{aligned} \tag{6.38}$$

In this calculation, V is first dealt with as an independent variable and then replaced by $V = Nv$ where v is the molecular volume of the solvent molecules. There is no contribution from the derivative of F with respect to N in (6.38). As pointed out in Sect. 2.3 [4], it is not permissible to take the derivative of F with respect to N.

[4] Overbeek [13] proposed including the contribution from the solvent molecules in this calculation. This is to interpret the Helmholtz free energy as $F(V = Nv, T, N_i)$ and disregard the neutrality condition. Then, the electric parts of F and G coincide with each other, since κ^2 is the homogeneous function of order 1 with respect to N_i and of order -1 with respect to N.

In (6.38), F depends, directly and indirectly through Z, on N_i. The neutrality condition (6.37) states that Z is a homogeneous function of order 1 with respect to N_i. Accordingly, by using the relation of homogeneity

$$\sum_i N_i \frac{\partial Z}{\partial N_i} = Z, \tag{6.39}$$

we can simplify (6.38) as

$$G = \left[\sum_i N_i \left(\frac{\partial F}{\partial N_i} \right)_{V,T,Z} + Z \left(\frac{\partial F}{\partial Z} \right)_{V,T,N_i} \right]_{V=Nv} \tag{6.40}$$

where the derivatives with respect to Z and N_i can be taken as if they were independent of each other. The first term is the contribution from the chemical potentials of the small ions calculated by fixing Z. The new quantity $\partial F/\partial Z$ in the second term should be interpreted as a *chemical potential of the net charge number* which measures the degree of fluctuation of the net surface charge of the particles. Namely, (6.40) shows that the free energy G of the Gibbs system consists of the chemical potentials of the small ions and the chemical potential of the net surface charge numbers. The new concept of the chemical potential of the fluctuating surface charge numbers of the effective particles plays an important role in the Gibbs system.

– **Polydisperse System** –

Next, we apply the concept found in the monodisperse system to the polydisperse system. In the monodisperse system, the surface charge number Z of the effective particles was assumed to fluctuate and $\partial F/\partial Z$ was interpreted as the chemical potential of the charge number. Then it is natural and relevant to interpret that the surface charge number Z_n of the n-th effective particle can fluctuate and $\partial F/\partial Z_n$ is the chemical potential of the net surface charge number Z_n in the polydisperse system.

Equation (6.25) leads to the neutrality condition in the polydisperse system as

$$\sum_i z_i N_i + \sum_n Z_n = 0 \tag{6.41}$$

which states that there is a relation among the $N_i\,(i = 1, \cdots, \mu)$ and $Z_n\,(n = 1, \cdots, M)$. So, one variable chosen arbitrarily is regarded as a function of the other variables. Here, let us choose Z_l as the dependent variable. Then, Z_l becomes a homogeneous function of order 1 and satisfies the relation

$$\sum_i N_i \frac{\partial Z_l}{\partial N_i} + \sum_{n \neq l} Z_n \frac{\partial Z_l}{\partial Z_n} = Z_l \ . \tag{6.42}$$

Accordingly, as a natural generalization of (6.40), the Gibbs free energy of the system is given by the sum of independent chemical potentials as follows:

$$
\begin{aligned}
G &= \left\{ \left[\sum_i N_i \left(\frac{\partial F}{\partial N_i} \right)_{V,T} + \sum_{n \neq l} Z_n \left(\frac{\partial F}{\partial Z_n} \right)_{V,T} \right]_{\text{neutrality}} \right\}_{V=Nv} \\
&= \left\{ \sum_i N_i \left(\frac{\partial F}{\partial N_i} \right)_{V,T,Z_n} + \sum_{n \neq l} Z_n \left(\frac{\partial F}{\partial Z_n} \right)_{V,T,Z_l} \right. \\
&\quad \left. + \left[\sum_i N_i \left(\frac{\partial Z_l}{\partial N_i} \right)_{V,T} + \sum_{n \neq l} Z_n \left(\frac{\partial Z_l}{\partial Z_n} \right)_{V,T} \right] \left(\frac{\partial F}{\partial Z_l} \right)_{V,T} \right\}_{V=Nv} .
\end{aligned} \tag{6.43}
$$

At the second stage in this calculation, the term including the derivative of F with respect to Z_l represents the effect that F depends on N_i and Z_n $(n \neq l)$ through Z_l. Applying the homogeneous relation (6.42), we obtain the Gibbs free energy of the polydisperse system as

$$
G = \left[\sum_i N_i \left(\frac{\partial F}{\partial N_i} \right)_{V,T,Z_n} + \sum_n Z_n \left(\frac{\partial F}{\partial Z_n} \right)_{V,T,N_i} \right]_{V=Nv} \tag{6.44}
$$

where the first term is the contribution from the chemical potentials of the small ions and the second term is that of the chemical potentials of the net surface charge numbers of the effective particles. In this way, the Gibbs free energy of the Gibbs system is given generally by the sum of the chemical potentials of the small ions and net surface charge numbers. Clearly, (6.44) reduces to (6.40) in the monodisperse limit.

Substituting (6.33)–(6.35) into (6.44), we can derive G from F by termwise differentiations. Namely, using the relations

$$
\sum_i N_i \left(\frac{\partial F}{\partial N_i} \right)_{V,T,Z} = \kappa^2 \frac{\partial F}{\partial \kappa^2} \tag{6.45}
$$

and

$$
\sum_n Z_n \frac{\partial F}{\partial Z_n} = 2(F - F^0), \tag{6.46}
$$

we readily obtain the Gibbs free energy as follows:

$$
G = G^0 + \frac{1}{2} \sum_{m \neq n} U^{\mathrm{G}}_{mn} + \sum_n V^{\mathrm{G}}_n \tag{6.47}
$$

where

$$
\begin{aligned}
U^{\mathrm{G}}_{mn} &= \frac{e^2}{2\pi^2 \epsilon} Z_m Z_n \int \left[\frac{1}{k^2 + \kappa^2} + \frac{k^2}{(k^2 + \kappa^2)^2} \right] \tilde{\rho}_m(\boldsymbol{k}) \tilde{\rho}_n(-\boldsymbol{k}) \, \mathrm{d}\boldsymbol{k} \\
&= U^{\mathrm{E}}_{mn} + U^{\mathrm{F}}_{mn}
\end{aligned} \tag{6.48}
$$

is called the *pair G-potential* (*pair Gibbs potential*) and

$$\begin{aligned} V_n^{\mathrm{G}} &= \frac{e^2}{4\pi^2\epsilon} Z_n^2 \int \left[\frac{1}{k^2+\kappa^2} + \frac{k^2}{(k^2+\kappa^2)^2} \right] \tilde{\rho}_n(\boldsymbol{k}) \tilde{\rho}_n(-\boldsymbol{k}) \, \mathrm{d}\boldsymbol{k} \\ &= V_n^{\mathrm{E}} + V_n^{\mathrm{F}} \end{aligned} \tag{6.49}$$

is called the *single G-potential* (*single Gibbs potential*). Here, G^0 is the Gibbs free energy in the limit $e^2 \to 0$. Evidently, there exists a relation among the three kinds of thermodynamic energies E, F and G as

$$G - G^0 = F - F^0 + E \, . \tag{6.50}$$

In the next section, this is proved to be a general relation which is derivable without recourse to the linear approximation in the mean field theory.

In the isothermal and isobaric processes of the small ion gas, the Gibbs free energy G decreases and takes its minimum value at chemical and thermal equilibrium. The pair G-potential U_{mn}^{G} depends on the relative displacement $\boldsymbol{R}_m - \boldsymbol{R}_n$ of the effective particles through the factor $\tilde{\rho}_m(\boldsymbol{k})\tilde{\rho}_n(-\boldsymbol{k})$ in the integral representation (6.48). Therefore, the configuration of the effective particles changes in the direction of minimizing G, i.e., the sum of U_{mn}^{G}. Therefore, U_{mn}^{G} must be interpreted as the adiabatic pair potential between the m-th and n-th effective particles.

Equation of State of Small Ion Gas

In the limit of vanishing electric charge, the Gibbs and Helmholtz free energies G^0 and F^0 satisfy the relation

$$G^0 - F^0 = k_{\mathrm{B}} T \sum_i N_i + P_0 V \tag{6.51}$$

where the first term represents the van't Hoff law and the second term expresses contributions from the solvent. For the charged system, the difference between the Gibbs and Helmholtz free energies G and F is written

$$G - F = (P_0 + P)V \tag{6.52}$$

where P is the osmotic pressure of the small ion gas.

From (6.50), we obtain the equation of state for small ion gas in the effective volume V as follows:

$$PV = k_{\mathrm{B}} T \sum_i N_i + E \, . \tag{6.53}$$

It is possible to interpret this as meaning that (6.53) allows us to express the effective volume V as a function of the osmotic pressure P and temperature T. However, it is highly difficult to find its analytical functional form, because E depends on V through the Debye screening factor.

The osmotic pressure P can be interpreted as acting against the surfaces of the region of condensation. Through such surfaces, the gas of small ions in the effective volume V and the small ions (mainly counterions) trapped in the region of condensation are in chemical and thermal equilibrium. Although difficult to formulate, conditions of such an equilibrium work to determine the effective volume and net surface charges of the particles. Equation (6.53) states that the PV term depends on the configuration of the effective particles through the electric energy E. This is a natural consequence of the fact that the gas of small ions is in the electric environment formed by the effective particles.

Let us consider quasi-static infinitesimal changes $\Delta \boldsymbol{R}_{mn} = \Delta(\boldsymbol{R}_m - \boldsymbol{R}_n)$ made on the electric environment of the effective particles and examine a change induced in the gas of small ions in an isothermal and isobaric state. From (6.53) and (6.13), we find

$$-P\Delta V = \frac{1}{2}\sum_{m\neq n}\left(-\frac{\partial U^{\mathrm{E}}_{mn}}{\partial \boldsymbol{R}_{mn}}\right)\cdot \Delta \boldsymbol{R}_{mn}\ . \tag{6.54}$$

This relation shows that the work done on the array of effective particles is equal to the work $-P\Delta V$ done on the gas of small ions [5]. The effective volume of the small ion gas V depends on the configuration $\{\boldsymbol{R}\}$. This result reconfirms that it is not possible to calculate the Gibbs free energy G through the relation (6.2). As shown in the arguments and results in Sect. 2.3 and the present section, *the Helmholtz and Gibbs free energies must be clearly distinguished in the description of ionic systems.*

6.2.5 Adiabatic Potential for Spherical Effective Particles

In this subsection, we consider the Gibbs system of spherical particles which is important for both theoretical and experimental studies. Calculation of the electric energy and free energy gives rise to three kinds of adiabatic potentials.

Shifted Mean Electric Potential

Suppose that the n-th spherical particle has a net charge number Z_n and an effective radius a_n. Since the form factor of a spherical particle satisfies $f_n(\boldsymbol{k}) = f_n(k)$, the angular integration in the representation (6.19) is easily

[5] Here it is instructive to notice the sign of both sides of (6.54). It is the pair G-potential that governs the thermodynamic behavior of the small ion gas in the environment of effective particles. As will be recognized in Fig. 6.2 for the monodisperse system, the pair E-potential U^{E} increases monotonically and rather gradually around the minimum position of the potential U^{G}. The left-hand side of (6.54) is positive for a compression ($\Delta V < 0$) against the osmotic pressure and its right-hand side also takes a positive value for a decrease of interparticle distance $|\Delta \boldsymbol{R}_{mn}|$ around the G-potential minimum.

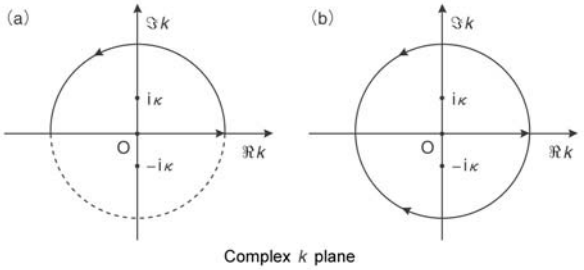

Fig. 6.1. Contours in the complex k plane. In integrations for the shifted mean electric potential and the pair F-potential, the contour is taken in the upper half plane as in (a) and the pole of first order at $k = i\kappa$ contributes to the residue. To calculate the single F-potential, it is necessary to divide the sine function of the form factor $f_n(k)$ into a sum of exponential functions and to calculate the residue of the pole at $\pm i\kappa$ by choosing the contours as in (b) in the complex k plane so that termwise contributions vanish at $|k| \to \infty$

carried out. Consequently, the integral representation of the shifted mean electric potential $\varphi(\boldsymbol{r})$ is simplified into the form

$$\varphi(\boldsymbol{r}) = \frac{e}{\pi i} \sum_n \frac{Z_n}{\epsilon|\boldsymbol{r} - \boldsymbol{R}_n|} \int_{-\infty}^{\infty} \frac{k}{k^2 + \kappa^2} f_n(k) \exp\{ik|\boldsymbol{r} - \boldsymbol{R}_n|\} \, dk \, . \tag{6.55}$$

By a residue calculation in the complex k plane along the contour in Fig. 6.1 (a), $\varphi(\boldsymbol{r})$ is expressed by the superposition of the screened Coulomb potentials around the effective particles as

$$\varphi(\boldsymbol{r}) = \sum_n \frac{Z_n^* e}{\epsilon|\boldsymbol{r} - \boldsymbol{R}_n|} \exp\{-\kappa|\boldsymbol{r} - \boldsymbol{R}_n|\} \tag{6.56}$$

where Z_n^* is the charge number including the effect of form factor defined by

$$Z_n^* = Z_n f_n(i\kappa) \, . \tag{6.57}$$

Adiabatic Pair Potentials

Thanks to the spherical symmetry of the form factor $f_n(\boldsymbol{k}) = f_n(k)$, the angular integrations in (6.34) and (6.35) are readily performed. Then, the adiabatic pair F-potential U_{mn}^{F} has the integral representation

$$U_{mn}^{\mathrm{F}} = \frac{Z_m Z_n e^2}{\pi \epsilon i} \frac{1}{R_{mn}} \int_{-\infty}^{\infty} \frac{k}{k^2 + \kappa^2} f_m(k) f_n(k) \, e^{ikR_{mn}} \, dk \tag{6.58}$$

where

$$R_{mn} = |\boldsymbol{R}_m - \boldsymbol{R}_n| \tag{6.59}$$

is the center-to-center distance between the m-th and n-th particles.

The charge distribution function of the n-th particle at the position $\boldsymbol{R}_n$ is given by

$$\rho_n(\boldsymbol{r}) = \frac{1}{4\pi a_n^2}\delta(|\boldsymbol{r} - \boldsymbol{R}_n| - a_n) \tag{6.60}$$

in terms of the Dirac δ-function. The inverse Fourier transform leads to the form factor

$$f_n(k) = \frac{\sin ka_n}{ka_n} \,. \tag{6.61}$$

Substituting this form factor into (6.58) and taking the inequality $R_{mn} = |\boldsymbol{R}_m - \boldsymbol{R}_n| \geq a_m + a_n$ into account, we carry out the residue calculation in the complex k plane obtaining

$$U_{mn}^{\mathrm{F}} = \frac{Z_m^* Z_m^* e^2}{\epsilon}\frac{1}{R_{mn}}\,\mathrm{e}^{-\kappa R_{mn}} \,. \tag{6.62}$$

This is a pure repulsive potential.

Comparison between (6.29), (6.34), and (6.48) provides the following simple relations among the three adiabatic pair potentials as

$$U_{mn}^{\mathrm{E}} = U_{mn}^{\mathrm{F}} + \frac{1}{2}\kappa\frac{\partial U_{mn}^{\mathrm{F}}}{\partial \kappa} \tag{6.63}$$

and

$$U_{mn}^{\mathrm{G}} = U_{mn}^{\mathrm{F}} + U_{mn}^{\mathrm{E}} = 2U_{mn}^{\mathrm{F}} + \frac{1}{2}\kappa\frac{\partial U_{mn}^{\mathrm{F}}}{\partial \kappa} \,. \tag{6.64}$$

With these relations, the other two adiabatic potentials U_{mn}^{E} and U_{mn}^{G} are determined in the forms

$$U_{mn}^{\mathrm{E}} = \frac{Z_m^* Z_n^* e^2}{2\epsilon}\left[\frac{\kappa a_m \coth(\kappa a_m) + \kappa a_n \coth(\kappa a_n)}{R_{mn}} - \kappa\right]\mathrm{e}^{-\kappa R_{mn}} \tag{6.65}$$

and

$$U_{mn}^{\mathrm{G}} = \frac{Z_m^* Z_n^* e^2}{2\epsilon}\left[\frac{2 + \kappa a_m \coth(\kappa a_m) + \kappa a_n \coth(\kappa a_n)}{R_{mn}} - \kappa\right]\mathrm{e}^{-\kappa R_{mn}}. \tag{6.66}$$

The adiabatic potential U_{mn}^{E} represents the electric energy of the effective particles with displacement R_{mn}. This potential shows that the electric energy becomes positive at medium-range and negative at long-range for the m-th and n-th effective particles with like charges ($Z_m Z_n > 0$). This pair E-potential U_{mn}^{E} is almost identical to the potential proposed first by Levine and Dube [14, 15]. In this potential, the entropy effect is not fully included.

The adiabatic potential U_{mn}^{F} describes the Helmholtz free energy of the particles with relative displacement R_{mn}. In contrast to the pair E-potential, this pair F-potential U_{mn}^{F} is repulsive for all relative displacements of particles. The entropy of the small ion gas works to cancel out the attractive part

Table 6.1. The three adiabatic pair potentials $U^{\mathrm{E}}(R)$, $U^{\mathrm{F}}(R)$, and $U^{\mathrm{G}}(R)$ for particles with net charge number Z and effective radius a. R is the center-to-center interparticle distance and Z^* is the net charge number including the form factor

Pair E-potential : $U^{\mathrm{E}}(R)$	$\dfrac{Z^{*2}e^2}{\epsilon}\left[\dfrac{\kappa a\coth(\kappa a)}{R}-\dfrac{1}{2}\kappa\right]\mathrm{e}^{-\kappa R}$
Pair F-potential : $U^{\mathrm{F}}(R)$	$\dfrac{Z^{*2}e^2}{\epsilon}\dfrac{1}{R}\mathrm{e}^{-\kappa R}$
Pair G-potential : $U^{\mathrm{G}}(R)$	$\dfrac{Z^{*2}e^2}{\epsilon}\left[\dfrac{1+\kappa a\coth(\kappa a)}{R}-\dfrac{1}{2}\kappa\right]\mathrm{e}^{-\kappa R}$

existing in the pair E-potential. This is the mechanism discovered in the DLVO theory [16]. As recognized later, the pair F-potential U^{F}_{mn} results in the DLVO repulsive potential described in Chap. 2.

The exponential function with a negative sign in (6.66) shows that an attractive force is revived in the pair potential U^{G}_{mn} which represents the Gibbs free energy of the m-th and n-th effective particles. This attraction arises through the PV term in the relation $G = F + (P_0 + P)V$. Namely, the PV term of the small ion gas which is related to the internal energy E via the equation of state (6.53) revives a weak attractive component in the pair G-potential U^{G}_{mn}.

Adiabatic Pair Potentials in Monodisperse Gibbs System

The three kinds of adiabatic pair potentials of a monodisperse system of effective particles with net charge number Z and effective radius a are listed in Table 6.1. The behavior of these potentials against the center-to-center interparticle distance is drawn in Fig. 6.2. Here we make a quantitative analysis of the monodisperse system.

In Fig. 6.2, the three adiabatic potentials are compared in the case of $\kappa a = 1$. The pair E-potential $U^{\mathrm{E}}(R)$ takes a fairly deep minimum at $R = 3.40a$. While the pair F-potential $U^{\mathrm{F}}(R)$ is purely repulsive for all interparticle distances, the pair G-potential $U^{\mathrm{G}}(R)$ has a weak attractive tail at long-range and takes a shallow minimum at $R = 5.47a$.

For all values of κa, the Gibbs pair potential $U^{\mathrm{G}}(R)$ is strongly repulsive at medium-range and weakly attractive at long-range and takes a minimum at the center-to-center distance

$$R_{\min} = \frac{\kappa a\coth(\kappa a) + 1 + \sqrt{[\kappa a\coth(\kappa a)+1][\kappa a\coth(\kappa a)+3]}}{\kappa}\,. \qquad (6.67)$$

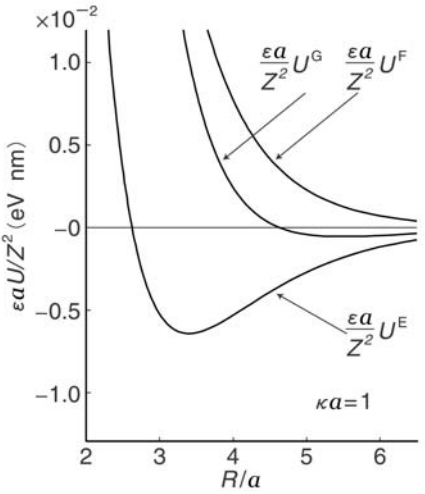

Fig. 6.2. Comparison of the three adiabatic pair potentials for particles with net charge number Z and effective radius a as functions of the center-to-center interparticle distance. Potential curves in the reduced forms $\epsilon a U^{\mathrm{E}}/Z^2$, $\epsilon a U^{\mathrm{F}}/Z^2$ and $\epsilon a U^{\mathrm{G}}/Z^2$ are drawn for the case $\kappa a = 1$

In Fig. 6.3, the behavior of the Gibbs pair potential $U^{\mathrm{G}}(R)$ is drawn on changing κa from 0.8 to 2.0. The depth of the potential minimum and the thickness of the repulsive wall depend sensitively on the value of κa.

Figure 6.4 shows the dependence on κa of the interparticle distance at the potential minimum $R_{\min}$ given in (6.67) and the depth $U^{\mathrm{G}}(R_{\min})$. The distance $R_{\min}$ decreases monotonically for increasing κa. The depth of the potential minimum $U^{\mathrm{G}}(R_{\min})$ becomes deeper for increasing κa, takes a maximal value at $\kappa a \simeq 1$ and then becomes shallower for larger values of κa.

Around $\kappa a \simeq 1$, the interparticle distance $R_{\min}$ where the binding energy between particles takes its maximum value behaves as

$$R_{\min} \simeq \frac{2(1+\sqrt{2})}{\kappa} \,. \tag{6.68}$$

When the depth of the potential minimum becomes deeper than the thermal energy $k_{\mathrm{B}}T$, the effective particles tend to form a crystalline structure in the dispersion. In the dilute limit where $\kappa a \ll 1$, the interparticle distance of the G-potential minimum varies as

$$R_{\min} \simeq \frac{1+\sqrt{3}}{\kappa} \,. \tag{6.69}$$

Let us compare Fig. 6.3 with Fig. 2.9. If we increase κa from $\kappa a \simeq 1$ by adding salt, the depth of the Gibbs potential becomes shallower in Fig. 6.3.

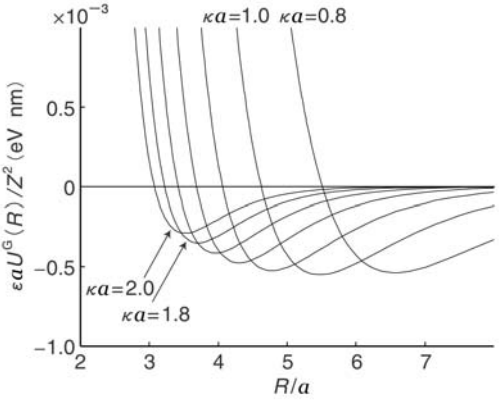

Fig. 6.3. The pair Gibbs potential $\epsilon a U^{\mathrm{G}}(R)/Z^2$ versus R/a. Seven curves are drawn for different values of κa. The potential minimum becomes deepest around $\kappa a \approx 1$. For larger values of κa, the potential minimum becomes shallower

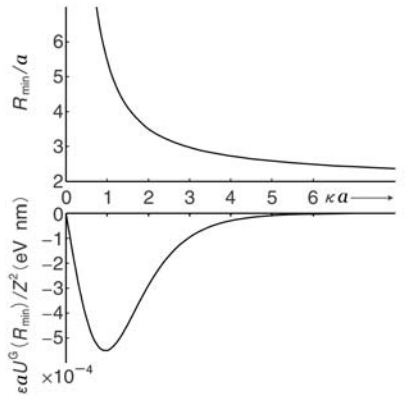

Fig. 6.4. Behavior of the interparticle distance $R_{\min}/a$ and the depth $\epsilon a U^{\mathrm{G}}(R_{\min})/Z^2$ versus κa

Therefore, increasing the salt concentration leads to melting of colloidal crystals [6]. This is consistent with the discovery by the Hachisu group [5]. By contrast, Fig. 2.9 shows that the depth of the secondary minimum of the DLVO potential become deeper when the salt concentration is increased. For large values of κa, the Gibbs potential and the DLVO potential have completely

[6] There is a linkage between the salt-induced-melting of colloidal crystals and the coexistence of ordered and disordered phases. A simple qualitative argument on this linkage is given when the equation of state (6.90) for osmotic pressure is investigated at the end of this section.

different behaviors. It is impossible to change the characteristics of the DLVO potential by adjusting the value of the Hamaker constant A. Therefore, while the Gibbs potential can describe the salt-induced-melting of colloidal crystals, the DLVO mechanism of the secondary minimum fails to explain it.

To examine crystallization by comparing the Gibbs free energy with the thermal energy $k_{\mathrm{B}}T$, it is necessary to take a so-called lattice sum. The Gibbs free energy per particle is given by

$$E_{\text{lattice sum}}(d;t) = \frac{1}{2}\sum_i n_i(t) U^{\mathrm{G}}[R_i(t)] \tag{6.70}$$

for a crystal of type t, where $R_i(t)$ is the distance from one lattice point to the i-th lattice point, $n_i(t)$ is the number of lattice points on the spherical surface with radius $R_i(t)$ and d is the spacing of the nearest lattice points. As examined in Chap. 5, only crystals which are destined to develop into a cubic system are observed in the dispersions of polystyrene latexes. So, the type of crystal t is fcc (face-centered cubic), bcc (body-centered cubic) or sc (simple cubic). For each type of crystal, only d is a variable parameter, since the $R_i(t)/d$ and $n_i(t)$ are fixed [17]. To investigate the stability of the crystals further, it is necessary to estimate the effects of lattice vibrations.

Adiabatic Single Potentials in Monodisperse Gibbs System

After the angular integrations, the integral representation (6.35) for the adiabatic single potential V_n^{F} takes the form

$$V_n^{\mathrm{F}} = \frac{Z_n^{*2}e^2}{2\pi\epsilon}\int_{-\infty}^{\infty} \frac{k^2}{k^2+\kappa^2}\, f_n^2(k)\,\mathrm{d}k \tag{6.71}$$

which, via a residue calculation along the contour in Fig. 6.1 (b), results in

$$V_n^{\mathrm{F}} = \frac{Z_n^{*2}e^2}{4\epsilon\kappa a_n}(1-\mathrm{e}^{-2\kappa a_n})\ . \tag{6.72}$$

This is the Helmholtz free energy of the n-th particle with net charge number Z_n and effective radius a_n in the dispersion. Comparison of the three integral representations (6.30), (6.35), and (6.49) gives rise to the relations

$$V_n^{\mathrm{E}} = V_n^{\mathrm{F}} + \frac{1}{2}\kappa\frac{\partial V_n^{\mathrm{F}}}{\partial\kappa} \tag{6.73}$$

and

$$V_n^{\mathrm{G}} = 2V_n^{\mathrm{F}} + \frac{1}{2}\kappa\frac{\partial V_n^{\mathrm{F}}}{\partial\kappa}\ . \tag{6.74}$$

Using these relations, we obtain

$$V_n^{\mathrm{E}} = \frac{Z_n^{*2}e^2}{4\epsilon a_n}\left[\frac{1}{2\kappa a_n}\left(1-\mathrm{e}^{-2\kappa a_n}\right)+\mathrm{e}^{-2\kappa a_n}\right] \tag{6.75}$$

for the single E-potential, and

$$V_n^{\mathrm{G}} = \frac{Z_n^{*2} e^2}{4\epsilon a_n} \left[\frac{3}{2\kappa a_n} \left(1 - \mathrm{e}^{-2\kappa a_n}\right) + \mathrm{e}^{-2\kappa a_n} \right] \tag{6.76}$$

for the single G-potential. For small κa, the single G-potential V_n^{G} can be expanded into the power series

$$V_n^{\mathrm{G}} = \frac{Z_n^{*2} e^2}{\epsilon a_n} - \frac{5}{4} \frac{(Z_n^* e)^2}{\epsilon} \kappa + \frac{(Z_n^* e)^2}{\epsilon} \kappa^2 a_n \cdots \tag{6.77}$$

where the first term is the self-energy and the remaining terms represent effects of the Gibbs free energy of the particle in the cloud of small ions.

Evidently the single G-potential V_n^{G} should be interpreted as the Gibbs free energy which is carried by the n-th particle in the cloud of small ions. Note that no direct correlation among the small ions is included in the single G-potential. This is a point which differs sharply from the symmetric description in the DH theory of electrolytes where anions and cations form mutual atmospheres with each other. In dispersions with large concentrations of small ions, it is necessary to include the effects of cluster formation among the small ions by using the DH method. Such dispersions with high salt concentrations, however, are special cases that lose the characteristics of stable macroionic systems.

6.2.6 Adiabatic Potentials for Non-Spherical Macroions

In general, it is not simple to obtain the pair potentials or single potentials for non-spherical macroion systems. Thus we have to limit ourselves to general remarks on this problem.

Is it possible to apply the basic concepts such as the Gibbs macroionic system, effective particles, net charges and effective volumes to systems containing non-spherical macroions? As discussed in Chap. 3, flexible ionic polymers might often assume rather *randomly coiled* conformations. The physical reasons for this are the "entropy effect" and the "interaction between counterions and ionized groups". First, the configuration number of a long polymer chain is huge, and the probability for the chain to assume a fully stretched linear conformation is very small. The second reason is *loose counterion associations*. As shown in Fig. 3.1 in Chap. 3, the interaction between ionized groups inside a macroion domain (interaction 1 in Fig. 3.1) is repulsive, as widely accepted. However, a large number of counterions are forced to be localized in the macroion domains by strong attractions from the macroions. Some of them neutralize the ionized group charges and others loosely interact with the ionized group charges (interaction 2 in Fig. 3.1). By the interaction 2, which has hitherto been completely ignored, the ionized group charges attract each other through the intermediary of nearby counterions to make it most unfeasible for the polymer chain to assume a fully stretched conformation.

In reality, the main chains of flexible ionic polymers would have a high degree of freedom because of free rotation around the chains. The chains are incessantly subject to micro-Brownian motion so that they change their shape continuously and at the same time show rotational and translational motion as a whole. These motions would have their own time constants, which have to be known accurately. One of the approximations we can apply is to *pre-average* the internal motions on the assumption that these are much faster than the translational motion. As the simplest picture, consequently, we treat the macroions as spherical particles with an average *radius of gyration*.

There exist macroions which should be described on average not as spherical particles but as ellipsoidal or rod-like particles. For such macroions, the degrees of rotation as well as translation have physical importance and their form factors $\rho(\boldsymbol{k})$ depend also on the Euler angles which describe their orientations. Accordingly, the pair potentials of ellipsoidal and rod-like particles are functions of the relative center-to-center coordinates and Euler angles.

Liquid crystals [18] are important examples of ordered systems of rod-like particles. On increasing temperature, the system shows several phase transitions, *solid phase* → *smectic phase* → *nematic phase* → *liquid phase*, by losing translational symmetries and then the orientational symmetry. In the smectic phase where the orientational order along the particle axis and a translational order along it are preserved, the centers of mass of the particles have a random distribution in the directions orthogonal to the axis. In the nematic phase which still has the orientational order, the centers of mass of particles are random in all directions.

It is relevant to regard the dispersions of non-spherical macroions also as a Gibbs system, if the difference between the analytical and net charges of the macroions is large. The pair G-potential for non-spherical macroions has naturally a weak attractive part for a distance which is larger than the average radius of the macroion. Although we do not consider non-spherical macroions here, there may be systems that are suited to experimental and theoretical investigations of effective interactions in macroionic dispersions.

One extreme example of non-spherical macroion, studied intensively in the DLVO theory, is that of highly charged parallel plates immersed in an electrolyte. The real shining example of such systems is the n-butylammonium vermiculite gels. The n-butylammonium vermiculite crystals soaked in dilute solutions of n-butylammonium chloride swell macroscopically up to, say, 4000%. The swelling is reversible and perfectly homogeneous, and the plates remain to a high degree parallel in the osmotically swollen gel phase. It is impossible to explain the stability of a system with such large lattice constants without a long-range attractive force [19]. Smalley [20] succeeded in describing the system of the n-butylammonium vermiculite gels by using the linearized mean field theory [7, 8] developed in this section. In Sect. 6.4, we investigate the n-butylammonium vermiculite gels in the mean field theory without recourse to the linear approximation.

6.2.7 New Effective Pair Potential

In this subsection, we compare the new pair potentials with the DLVO potential explained in Sect. 2.4.

The adiabatic pair potentials derived in this section were expressed in terms of surface charges. To make comparison with the DLVO potential, we express them in terms of the surface potential. For this purpose, let us examine the monodisperse Gibbs system. Choosing one effective particle arbitrarily, we name it the particle a. By taking the origin at its center, the shifted mean electric potential $\varphi(\boldsymbol{r})$ in (6.56) is written as

$$\varphi(\boldsymbol{r}) = \frac{Z^* e}{\epsilon r} \mathrm{e}^{-\kappa r} + \sum_n{}' \frac{Z^* e}{\epsilon |\boldsymbol{r} - \boldsymbol{R}_n|} \mathrm{e}^{-\kappa |\boldsymbol{r} - \boldsymbol{R}_n|} \tag{6.78}$$

where the first term is the screened electric potential of the particle a and the second term is the contribution from all particles other than a.

To obtain the relation between the surface charge and the surface potential, it is necessary to fix a value of the unknown potential $\breve{\psi}$ which relates the mean electric potential $\psi(\boldsymbol{r})$ to the shifted mean electric potential $\varphi(\boldsymbol{r})$ in (6.17). The value of $\breve{\psi}$ should be chosen so as to optimize the expansion of the Boltzmann distribution function with respect to the difference $e[\psi(\boldsymbol{r}) - \breve{\psi}]/k_{\mathrm{B}}T$. However, for the sake of brevity, we take here the choice

$$\breve{\psi} = -\frac{k_{\mathrm{B}}T}{e} \frac{\sum_i z_i N_i}{\sum_i N_i} \tag{6.79}$$

which makes the relation between $\psi(\boldsymbol{r})$ and $\varphi(\boldsymbol{r})$ to be the simplest possible as [7]

$$\psi(\boldsymbol{r}) = \varphi(\boldsymbol{r}) \; . \tag{6.80}$$

Putting $r = a$ in (6.78), the surface potential is related to the surface charge number by

$$\psi_a = \psi(\boldsymbol{r})\Big|_{r=a} = \frac{Z^* e}{\epsilon a} \mathrm{e}^{-\kappa a} \vartheta^{-\frac{1}{2}} \tag{6.81}$$

where $\vartheta^{-\frac{1}{2}}$ is the ratio of the surface potential originating from all particles except for the particle a and the surface potential $Z^* e/(\epsilon a) e^{-\kappa a}$ of the particle a, viz,

$$\vartheta^{-\frac{1}{2}} = 1 + \sum_n{}' \frac{a}{|\boldsymbol{r} - \boldsymbol{R}_n|} \exp[-\kappa(|\boldsymbol{r} - \boldsymbol{R}_n| - a)]\Big|_{r=a} \; . \tag{6.82}$$

Note that the factor ϑ is a function of the configuration of the particles.

[7] If this simplest choice is not adopted, the correction term $\delta\breve{\psi} \equiv \breve{\psi} + (K_{\mathrm{B}}T/e)(\sum_i z_i N_i / \sum_i N_i)$ must be included in the right-hand side of (6.80). Accordingly, we have to replace the surface potential ψ_a by a modified surface potential $\psi_a^* = \psi_a - \delta\breve{\psi}$ in the adiabatic pair potentials in terms of the surface electric potential, i.e., U_{E}, U_{F}, and U_{G}.

Table 6.2. The three adiabatic pair potentials $U_{\rm E}(R)$, $U_{\rm F}(R)$ and $U_{\rm G}(R)$ expressed in terms of the surface electric potential ψ_a. R is the center-to-center distance between effective particles with radius a

Pair E-potential : $U_{\rm E}(R)$	$\epsilon a^2\psi_a^2\vartheta\left[\dfrac{\kappa a\coth(\kappa a)}{R}-\dfrac{1}{2}\kappa\right]\mathrm{e}^{-\kappa(R-2a)}$
Pair F-potential : $U_{\rm F}(R)$	$\epsilon a^2\psi_a^2\vartheta\dfrac{1}{R}\mathrm{e}^{-\kappa(R-2a)}$
Pair G-potential : $U_{\rm G}(R)$	$\epsilon a^2\psi_a^2\vartheta\left[\dfrac{1+\kappa a\coth(\kappa a)}{R}-\dfrac{1}{2}\kappa\right]\mathrm{e}^{-\kappa(R-2a)}$

Adiabatic Pair Potentials in terms of Surface Electric Potential

The relation (6.81) allows us to express the surface charge number Z^* in terms of the surface electric potential ψ_a. Consequently, the adiabatic pair potentials in terms of net charge number $U^{\rm E}(R)$, $U^{\rm F}(R)$, and $U^{\rm G}(R)$ in Table 6.1 are transformed into the adiabatic pair potentials in terms of the surface potential $U_{\rm E}(R)$, $U_{\rm F}(R)$, and $U_{\rm G}(R)$ in Table 6.2. Note that the adiabatic pair F-potential

$$U_{\rm F}(R)=\epsilon a^2\psi_a^2\frac{1}{R}\mathrm{e}^{-\kappa(R-2a)}\vartheta \tag{6.83}$$

which is derived from the Helmholtz free energy F coincides with the DLVO repulsive potential $U_{\rm R}(R)$ in (2.96). Therefore, the original DLVO potential is reinterpreted to be given by the sum of the van der Waals attractive potential $U_{\rm A}(R)$ and the pair F-potential $U_{\rm F}(R)$ in the new mean field theory.

The free energy which describes the chemical and thermal evolution of dilute macroionic dispersions with low salt concentrations is not the Helmholtz free energy F but the Gibbs free energy G. It is necessary to select not the pair F-potential but the pair G-potential as the adiabatic potential for effective particles in the Gibbs system.

Accordingly, in place of the original DLVO potential, we must use the sum of the van der Waals potential $U_{\rm A}(R)$ and the pair G-potential as an effective total potential which explains both the phenomena of irreversible coagulation and reversible flocculation. Therefore, the total potential between effective particles in the Gibbs system is given by

$$\begin{aligned}U(R)&=U^{\rm G}(R)+U_{\rm A}(R)\\&=\frac{(Z^*e)^2}{\epsilon}\vartheta\left[\frac{1+\kappa a\coth(\kappa a)}{R}-\frac{1}{2}\kappa\right]\mathrm{e}^{-\kappa R}+U_{\rm A}(R)\end{aligned} \tag{6.84}$$

in the case of the particles with constant surface charge number, and

$$\begin{aligned} U(R) &= U_{\mathrm{G}}(R) + U_{\mathrm{A}}(R) \\ &= \epsilon a^2 \psi_a^2 \vartheta \left[\frac{1 + \kappa a \coth(\kappa a)}{R} - \frac{1}{2}\kappa \right] \mathrm{e}^{-\kappa(R-2a)} + U_{\mathrm{A}}(R) \end{aligned} \tag{6.85}$$

in the case of particles with constant surface potential. The phenomena of colloidal crystals examined in Chaps. 4 and 5 are medium- and long-range reversible processes in dilute dispersions with low salt concentrations. In the present scheme, it is considered to be the pair G-potential $U^{\mathrm{G}}(R)$ or $U_{\mathrm{G}}(R)$ that governs these reversible processes.

Derivation of the Schulze-Hardy Rule from the New Potential

One of reasons why the DLVO scheme was accepted as the standard theory of colloid chemistry lies in its successful derivation of the Schulze-Hardy rule. Therefore, for the new potential (6.85) to replace the original DLVO potential, it is necessary to derive the Schulze-Hardy rule from it.

As shown in Fig. 6.2, when the two particles come closer, the pair G-potential $U^{\mathrm{G}}(R)$ approaches to the pair F-potential $U^{\mathrm{F}}(R)$ up to a constant factor. Similarly the pair G-potential $U_{\mathrm{G}}(R)$ approaches to the pair F-potential U_{F}, which just coincides with the original repulsive potential of the DLVO theory. With these grounds it is natural to postulate that, just as with the DLVO potential, the new total adiabatic potential in (6.85) is applicable also to concentrated dispersions with high salt concentrations.

The G-potential U_{G} is attractive at large interparticle separation only. Its attractive part can safely be ignored in examining the behavior of particles at close approach. It is also possible to approximate $R \approx 2a$ and to put $\vartheta = 1$ in (6.85), viz,

$$U_{\mathrm{R}}(S) \simeq \frac{1}{2}\epsilon a \psi_a^2 \left[1 + \kappa a \coth(\kappa a) - \kappa a\right] \mathrm{e}^{-\kappa S} \tag{6.86}$$

where $S = R - 2a$ is the surface-to-surface distance. As for the van der Waals potential, (2.125) should be used as it stands. Using these potentials and applying the analysis made in Sect. 2.4 to $U(S) = U_{\mathrm{R}}(S) + U_{\mathrm{A}}(S)$, we obtain the condition

$$\frac{1}{2}\epsilon a \psi_a^2 \left(1 + \frac{2\kappa a \mathrm{e}^{-2\kappa a}}{1 - \mathrm{e}^{-2\kappa a}}\right) \exp(-1) = \frac{1}{12} A \kappa a \tag{6.87}$$

in place of (2.136). Under the natural assumption $1 \gg e^{-2\kappa a}$, this equation reduces exactly to (2.136). Therefore, following the argument given in Sect. 2.4, we can solve this equation with respect to the salt concentration n yielding

$$n = \frac{1152}{\pi \exp(2)} \frac{\epsilon^3 (k_{\mathrm{B}}T)^5 \gamma^4}{A^2 (ze)^6} \tag{6.88}$$

which coincides with (2.137). Therefore, it is confirmed that the Schulze-Hardy rule can be derived also from (6.85) to a good approximation.

6.2.8 Commentary on the New Linearized Mean Field Theory

The present scheme of the linearized mean field theory has the new total adiabatic potential in (6.84) or (6.85) for effective particles which have, respectively, a constant surface charge number and a constant surface electric potential. For the Gibbs system with constant temperature T, the thermodynamic behavior of the particles is described by the Boltzmann distribution function

$$\exp\left[-\frac{1}{k_{\mathrm{B}}T}\left(\frac{1}{2}\sum_{m\neq n}U(R_{mn})\right)\right]. \tag{6.89}$$

Using this distribution function, computer simulations are made to investigate general processes in macroionic dispersions in Chap. 8. The van der Waals potential $U_{\mathrm{A}}(R)$ can be ignored in (6.89) to describe medium- and long-range reversible processes in dilute dispersions.

Equation (6.53) shows that the gas of small ions in the environment of the stationary configuration of effective particles obeys the equation of state

$$PV = k_{\mathrm{B}}T\sum_{i}N_i + \frac{1}{2}\sum_{m\neq n}U^{\mathrm{E}}_{mn} + \sum_{n}V^{\mathrm{E}}_{n}\,. \tag{6.90}$$

The state of small ion gas depends not only on concentrations of small ions and particles but also on configurations of particles. For the ordered (disordered) state in which particles have a smaller (larger) average relative distance, the osmotic pressure P of small ion gas is low (high) since the sum of the electric pair potentials, i.e., $\sum U^{E}_{m,n}$, takes a relatively small (large) value.

Note that the pair E-potential U^{E} varies rather gradually in the region where the G-potential U^{G} takes small values as recognized in Fig. 6.2. Accordingly, for some range of concentrations of small ions and particles, variation of the osmotic pressure P in (6.90) becomes not to be too sensitive to realistic configurations of particles governed by the pair G-potential. This characteristic of (6.90) is consistent with the coexistence of ordered and disordered states in the Hachisu phase diagram for colloidal dispersion.

Dependence of the PV term in (6.90) on the states of particles is a natural consequence of the fact that the small ion gas is in the stationary environment of particles. The PV term requires inevitably to distinguish the Helmholtz and Gibbs free energies, F and G, of macroionic systems. Nevertheless, only the difference between the electric energy E and the Helmholtz free energy F was discussed and the relation between the two free energies F and G was completely ignored in the famous controversy in the early 1940's. Surprisingly this disregard remained until the middle of the 1980's notwithstanding that the existence of the electric part of the PV term and the inequality between F and G had already been established in the DH theory. The main reason for this disregard is deep-rooted in the *difficulty in formulating the thermodynamics of inhomogeneous systems* [8]. Another reason for this originates probably in

[8] This problem is not yet solved even now.

the impact provided by the successful proof of the Schulze-Hardy rule in the DLVO theory.

In 1938, before the advent of the DLVO theory, Langmuir [6] had pointed out the important role of the PV term for colloidal dispersions and clearly recognized the difference between F and G. However, since there was no theory other than the DH theory for ionic systems at that period, he had to apply it to describe the colloidal dispersions. In his formalism where both of the small ions and colloidal particles were described by the linearized Boltzmann distribution functions, definite positions were not attributed to particles and the concept of effective pair potentials could not be introduced for particles. Therefore, the equation of state for osmotic pressure played major roles to analyze the properties of colloidal dispersions in the Langmuir theory. It was also a failure of Langmuir to ignore totally the effect of the van der Waals attraction in his ingenious theory.

Homogeneousness is an indispensable prerequisite for ordinary thermodynamics. The internal energy and free energies are usually regarded as extensive variables which satisfy *additivity*. The existence of macroions with definite positions which exert long-range forces on the gas of small ions violate both of these prerequisites. Therefore, the *Gibbs-Duhem relation* which is the criterion of additivity can no longer hold exactly in macroionic dispersions. In general, the internal energy and free energies lose additivity in a system with the influence of long-range interactions [9]. Consequently, both the DLVO repulsive potential and the new repulsive potential derived in this section must be interpreted as manifestations of the violation of additivity in the system of the small ion gas in the stationary environment of effective particles.

Finally it should be pointed out that, compared to the DH theory, the DLVO theory and the present formalism are less complete with respect to estimations of correlations among small ions. While the formation of ionic atmospheres among small ions is the main effect in the DH theory, the interactions between the macroions and counterions are considered to be dominant in the macroionic dispersions. At the present, the correlations among small ions are assumed to be of only secondary importance in effective interactions between macroions. More detail and quantitative analysis of the small ion correlations remains for future investigations.

6.3 Integral Representations for Free Energies of Macroionic Dispersions

In the previous section, the free energies of macroionic dispersions of effective particles were calculated by solving the linearized PB equation. Applying the

[9] In a strong electrolyte, the long-range Coulomb interactions among anions and cations are metamorphosed into short-range interactions through mutual formation of ionic atmospheres.

method of analytical mechanics [9], we develop in this section a general mean field theory that allows us to investigate macroionic systems without recourse to a linear approximation.

We construct a generating functional which gives rise to the PB equation with Neumann's boundary conditions for an average electric potential in a macroionic dispersion through an extremal condition. In contrast to the linearized theory where the net charges of macroions are described in terms of distribution functions, the surface charges are introduced as the boundary conditions of the PB equation in this theory. This formalism enables us to deal naturally with excluded volume effects.

The extremum of the generating functional is proved to be identical with the Helmholtz free energy of the system F which has an integral representation in terms of the average electric potential satisfying the PB equation. From the Helmholtz free energy F, the chemical potentials of the small ions and *chemical potentials of the net charge numbers of the macroions* are calculated and, as their total sum, an integral representation of the Gibbs free energy G of the system is derived. The difference between the two free energies $G - F$ results in an equation of state for the osmotic pressure of a small ion gas in a stationary environment of the macroions in the dispersion.

As a byproduct of the general theory in this section, we examine what the electric energy of general systems of macroions is and give a proof of Debye's charging-up formula from a general definition of statistical mechanics.

6.3.1 Model of Macroionic Dispersions

We investigate a dispersion with number M of macroions in a container with a sufficiently large volume Ω. This volume Ω can be expressed in two ways as

$$\Omega = V + \sum_{n=1}^{M} \omega_n = V_0 + \sum_{n=1}^{M} \omega_{0n} \tag{6.91}$$

in terms of the volume ω_n (ω_{0n}) of the n-th effective particle (naked macroion). Namely, V (V_0) is the volume which is obtained by subtracting the volumes of the effective particles (those of the naked macroions) from Ω.

In this section, we investigate the PB equation for a macroionic dispersion without recourse to linear approximation. Therefore, it is possible to consider the system as consisting of either naked macroions or effective particles. In the case where our main concern is to find relations between analytical charges and net charges of macroions, we should deal with the naked macroions and investigate the PB equation in the regions $\Omega - V_0 = \sum_{n=1}^{M} \omega_{0n}$ or $V_0 - V = \sum_{n=1}^{M} (\omega_n - \omega_{0n})$. As in the previous section, however, our main concern in this book lies in the study of structure formation in macroionic systems. Therefore, we only consider the dispersion as consisting of effective particles with net surface charges in this section.

As a basic postulate of the present scheme, a thermodynamic function Q of the system such as the internal energy U, the Helmholtz free energy F or the Gibbs free energy G is generically postulated to consist of the sum of its electric part $Q^{\rm el}$ and non-electric part Q^0 as $Q = Q^{\rm el} + Q^0$.

Here, we use again the extended primitive model to describe the macroionic dispersion. Namely, the solvent of the system is postulated to form a uniform background medium with dielectric constant ϵ, and the particle nature of the solvent is implemented at the stage of description with the Gibbs free energy by postulating the relation $V = Nv$ where N is the total number of solvent molecules and v is the molecular volume of the solvent.

Effective particles with net surface charges $Z_n e$ [1] take a stationary configuration which is represented by the set $\{\boldsymbol{R}_n : n = 1, 2, \cdots, M\}$ of their center-of-mass coordinates. In a stationary environment of effective particles, the gas of small ions rapidly reaches thermal equilibrium, in which the gas of j-th species of small ions with valency z_j $(j = 1, \cdots, s)$ has a number density given by the Boltzmann distribution

$$n_j(\boldsymbol{r}) = n_{j_0} \mathrm{e}^{-z_j \phi(\boldsymbol{r})} \tag{6.92}$$

where $\phi(\boldsymbol{r})$ is the ratio of the ordinary average electric potential $\psi(\boldsymbol{r})$ to the thermal energy $k_{\rm B}T = 1/\beta$, i.e.,

$$\phi(\boldsymbol{r}) = \beta e \psi(\boldsymbol{r}) \, . \tag{6.93}$$

The coefficient n_{j_0} in (6.92) is a constant determined by the number N_j of small ions in the volume V as

$$N_j = n_{j_0} \int_V \mathrm{e}^{-z_j \phi(\boldsymbol{r})} \mathrm{d}\boldsymbol{r} \, . \tag{6.94}$$

The dimensionless potential $\phi(\boldsymbol{r})$ satisfies the PB equation

$$\nabla^2 \phi(\boldsymbol{r}) = -4\pi \lambda_{\rm B} \sum_{j=1}^{s} z_j n_j(\boldsymbol{r}) \tag{6.95}$$

with the Neumann boundary conditions

$$\boldsymbol{\nu}_n \cdot \nabla \phi(\boldsymbol{r}) = -4\pi \lambda_{\rm B} Z_n \sigma_n(\boldsymbol{r}) \tag{6.96}$$

on the particle surfaces $S_n (n = 1, \cdots, M)$ and the inner surface of the container S_0 with surface charge $Z_0 e$. Here $\lambda_{\rm B} = e^2\beta/\epsilon$ is the *Bjerrum length*, $\boldsymbol{\nu}_n$ is a unit vector normal to the surface of the n-th effective particles S_n and $\sigma_n(\boldsymbol{r})$ is its surface charge density normalized by the condition

$$\oint_{S_n} \sigma_n(\boldsymbol{r}) \mathrm{d}S_n = 1 \tag{6.97}$$

on the surface S_n.

6.3.2 Generating Functional of the PB Equation with Boundary Conditions

In analytical mechanics, the basic equations for various systems are described in a unified way by the Euler-Lagrange equation, which is derived from the principle of minimum action. Macroionic dispersions are quite different from mechanical systems. Nevertheless, it turns out to be possible to construct a generating functional from which the basic equation and its associated boundary conditions, i.e., (6.95) and (6.96), are deduced by imposing the extremal condition upon it. In fact, we can prove that the generating functional for the PB equation and its boundary conditions is given by

$$\beta\mathcal{F}[\chi] = -\frac{1}{8\pi\lambda_{\mathrm{B}}}\int_V \{\nabla\chi(\boldsymbol{r})\}^2 \mathrm{d}\boldsymbol{r} + \sum_{n=0}^{M} Z_n \oint_{S_n} \chi(\boldsymbol{r})\sigma_n(\boldsymbol{r})\mathrm{d}S_n$$
$$-\sum_{j=1}^{s} N_j \ln\left(\frac{1}{V}\int_V \mathrm{e}^{-z_j\chi(\boldsymbol{r})}\mathrm{d}\boldsymbol{r}\right) \tag{6.98}$$

where $\chi(\boldsymbol{r})$ is an unknown smooth function, the volume integral is taken over V and the surface integrals are done on the surfaces of the particles and the inner surface of the container.

To examine the extremal condition of the functional, let us calculate the difference between $\mathcal{F}[\chi+\delta\chi]$ and $\mathcal{F}[\chi]$. Noting the identical relation $\nabla\chi\cdot\nabla\delta\chi = \nabla\cdot(\delta\chi\nabla\chi) - (\nabla^2\chi)\delta\chi$ and applying the Gauss integral theorem, we obtain

$$\begin{aligned}\delta\beta\mathcal{F} &\equiv \beta\mathcal{F}[\chi+\delta\chi] - \beta\mathcal{F}[\chi] \\ &= \frac{1}{4\pi\lambda_{\mathrm{B}}}\int_V \left[\nabla^2\chi + 4\pi\lambda_{\mathrm{B}}\sum_{j=1}^{s} z_j \frac{N_j \mathrm{e}^{-z_j\chi}}{\displaystyle\int_V \mathrm{e}^{-z_j\chi}\mathrm{d}\boldsymbol{r}}\right]\delta\chi\mathrm{d}\boldsymbol{r} \\ &\quad + \frac{1}{4\pi\lambda_{\mathrm{B}}}\sum_{n=0}^{M}\oint_{S_n}\left(\boldsymbol{\nu}_n\cdot\nabla\chi + 4\pi\lambda_{\mathrm{B}}Z_n\sigma_n\right)\delta\chi\mathrm{d}S_n + \mathcal{O}\left((\delta\chi)^2\right). \end{aligned} \tag{6.99}$$

For the functional $\mathcal{F}[\chi]$ to take an extremum at $\chi(\boldsymbol{r}) = \phi(\boldsymbol{r})$, $\delta\beta\mathcal{F}$ must be an infinitesimal of the second order with respect to an arbitrary variation $\delta\chi$ as

$$\delta\beta\mathcal{F} = \beta\mathcal{F}[\phi+\delta\chi] - \beta\mathcal{F}[\phi] = \mathcal{O}\left((\delta\chi)^2\right). \tag{6.100}$$

This implies that the first and second terms on the right-hand side of (6.99) which consist of infinitesimals of the first order must vanish at $\chi(\boldsymbol{r}) = \phi(\boldsymbol{r})$. Therefore, the extremal condition of the functional $\mathcal{F}[\chi]$ gives rise simultaneously to the PB equation (6.95) and the boundary conditions (6.96). For later arguments, it is convenient to express the extremal condition of the generating functional at $\chi(\boldsymbol{r}) = \phi(\boldsymbol{r})$ in (6.100) as

$$\frac{\delta\beta\mathcal{F}[\phi]}{\delta\phi} = 0\,. \tag{6.101}$$

As shown below, the generating functional $\mathcal{F}$ is deeply related with the Helmholtz free energy of the system.

6.3.3 Integral Representation for the Helmholtz Free Energy

The electric field energy of the system E is calculated by an integral of the density $\epsilon(-\nabla\psi(\boldsymbol{r}))^2/8\pi$ over the volume V. Since the velocities of all the ionic species are small, the magnetic field makes almost no contribution to thermodynamic quantities. Therefore, it is relevant to postulate that the internal energy of the system U is the sum of the non-electric part U^0 and the electric part $U^{\rm el} = E$ which is given by

$$\beta U^{\rm el} \equiv \beta E = \frac{1}{8\pi\lambda_{\rm B}} \int_V (\nabla\phi)^2 {\rm d}\boldsymbol{r}\,. \tag{6.102}$$

Applying the Gauss integral theorem and using the PB equation with associated boundary conditions, we find a different expression for the right-hand side of (6.102) as

$$\frac{1}{8\pi\lambda_{\rm B}} \int_V (\nabla\phi)^2 {\rm d}\boldsymbol{r} = \frac{1}{2}\sum_{n=0}^{M} Z_n \oint_{S_n} \phi\sigma_n {\rm d}S_n + \frac{1}{2}\sum_{j=1}^{s} \int_V z_j n_j \phi\, {\rm d}\boldsymbol{r}\,. \tag{6.103}$$

While the quantity on the left-hand side of this equation is the energy of the electric field in the dispersion, the quantities on the right-hand side represent the energy arising from interactions of the electric field with the small ions and particles. This relation can be used to express free energies in different but equivalent forms suitable for various purposes.

As proved later in this section, the electric parts of the Helmholtz free energy and the internal energy, $F^{\rm el}$ and $U^{\rm el} = E$, are related by Debye's charging-up formula

$$e^2 \left(\frac{\partial\beta F^{\rm el}}{\partial e^2}\right) = \beta E \tag{6.104}$$

where the derivative with respect to the parameter e^2 is taken under the condition of fixed environment where the temperature, the volume, the numbers of small ions and particles, the charge numbers of particles, and also the configuration $\{\boldsymbol{R}\}$ of particles are all fixed. To solve this parametric differential equation, let us examine the extremum of the generating functional, viz, $\mathcal{F}[\phi]$. Noting that $\mathcal{F}[\phi]$ depends on e^2 through the Bjerrum length $\lambda_{\rm B}$ and the average electric potential ϕ, we prove readily that

$$e^2 \left(\frac{\partial\beta\mathcal{F}[\phi]}{\partial e^2}\right) = e^2 \frac{\partial\lambda_{\rm B}}{\partial e^2} \left(\frac{\partial\beta\mathcal{F}[\phi]}{\partial\lambda_{\rm B}}\right)_{\phi} + e^2 \frac{\partial\phi}{\partial e^2} \left(\frac{\delta\beta\mathcal{F}[\phi]}{\delta\phi}\right)_{\lambda_{\rm B}}$$

$$= \lambda_{\mathrm{B}} \frac{1}{8\pi\lambda_{\mathrm{B}}^2} \int_V [\nabla\phi(\boldsymbol{r})]^2 \, \mathrm{d}\boldsymbol{r}$$
$$= \beta E \tag{6.105}$$

where the parametric derivative is taken again under the condition of stationary environment and the condition of extremum in (6.101) is used. Comparison of (6.104) and (6.105) leads to $F^{\mathrm{el}} = \mathcal{F}[\phi]$. Namely, the electric part of the Helmholtz free energy of the system is the extremum of the generating functional.

This result enables us to express the Helmholtz free energy F of the macroionic dispersion in terms of the average electric potential ϕ satisfying the PB equation with the Neumann boundary conditions as follows:

$$\begin{aligned} F &= \mathcal{F}[\phi] + F^0 \\ &= -\frac{1}{2} k_{\mathrm{B}} T \sum_{j=1}^{s} z_j \int_V n_j \phi \mathrm{d}\boldsymbol{r} + \frac{1}{2} k_{\mathrm{B}} T \sum_{n=0}^{M} Z_n \oint_{S_n} \phi \sigma_n \mathrm{d}S_n \\ &\quad -k_{\mathrm{B}} T \sum_{j=1}^{s} N_j \ln \left(\frac{1}{V} \int_V \mathrm{e}^{-z_j \phi} \mathrm{d}\boldsymbol{r} \right) + F^0 \end{aligned} \tag{6.106}$$

where F^0 is the non-electric part of the Helmholtz free energy. This integral representation is exact in the mean field description. With the identity in (6.103) we may express the Helmholtz free energy F in different forms.

The Helmholtz free energy and the internal energy are subject to the thermodynamic equation in (6.1), which is rewritten as

$$\frac{\partial \beta F}{\partial \beta} = U \, . \tag{6.107}$$

It is also possible to obtain (6.106) by applying this relation to the electric parts of the Helmholtz free energy and the internal energy.

6.3.4 Integral Representation for the Gibbs Free Energy

Integrating the PB equation in (6.95) over the volume V and applying the Gauss integral theorem with the boundary conditions in (6.96), we obtain the condition of electric charge neutrality as

$$\sum_{j=1}^{s} z_j N_j + \sum_{n=0}^{M} Z_n = 0 \, . \tag{6.108}$$

This relation has another physical meaning. Note that the Boltzmann distribution in (6.92) with the coefficient defined by (6.94) is invariant under the transformation of the mean electric potential, $\phi(\boldsymbol{r}) \to \phi(\boldsymbol{r}) + c$, where c is an

arbitrary constant. The electric energy E from which the electric parts of free energies are deduced is also invariant under this constant shift of the potential which we call the *weak gauge transformation*, since E depends on the gradient of the mean electric potential. We call this invariance the *weak gauge invariance*. Requirement of the right-hand side of (6.103) being invariant under this transformation leads readily to the relation in (6.108). Therefore, the neutrality condition is a necessary constraint [22] for the weak gauge invariance of the theory.

In a macroionic dispersion where the number and configuration of the particles are fixed, this condition requires that the net charge number of the effective particles Z_n must change against a variation of the number of small ions N_i. Therefore the chemical potential of the small ions which is obtained by $\partial F/\partial N_j$ must necessarily be correlated to the derivative of F with respect to Z_n. Following the argument in Sect. 6.2, we interpret the derivative of the Helmholtz free energy with respect to the net charge number Z_n, $\partial F/\partial Z_n$, as the *chemical potential of the net charge number* of the n-th particle [7, 8] [10]. The Gibbs free energy G of the system is obtained by summing up the chemical potentials of the small ions of all kinds and the chemical potentials for the net charge numbers of all particles ($n = 0, 1, \cdots, M$).

To take derivatives of F with respect to N_j and Z_n and to sum up the component chemical potentials without contradiction to the constraint condition in (6.108), we introduce the following differential operator $D_{\rm c}$ as

$$D_{\rm c} = \sum_{j=1}^{s} N_j \frac{\partial}{\partial N_j} + \sum_{n=0}^{M} Z_n \frac{\partial}{\partial Z_n} \ . \tag{6.109}$$

It is readily confirmed that, when applied to the neutrality condition, this operator reproduces the condition itself without resulting in any additional constraint [22]. Therefore, this operator $D_{\rm c}$ can be interpreted as a kind of *covariant derivative* which generates the weak gauge transformation and preserving a *surface spanned by the constraint of the neutrality condition* in a fictitious space $(N_1, \cdots, N_s, Z_1, \cdots, Z_M)$ [9].

For application of the covariant derivative $D_{\rm c}$, it is convenient to use the Helmholtz free energy in the form

$$\begin{aligned} \beta F = &-\frac{1}{8\pi\lambda_{\rm B}} \int_V \{\nabla\phi(\boldsymbol{r})\}^2 {\rm d}\boldsymbol{r} + \sum_{n=0}^{M} Z_n \oint_{S_n} \phi(\boldsymbol{r})\sigma_n(\boldsymbol{r}){\rm d}S_n \\ &- \sum_{j=1}^{s} N_j \ln\left(\frac{1}{V}\int_V {\rm e}^{-z_j\phi(\boldsymbol{r})}{\rm d}\boldsymbol{r}\right) + \beta F^0 \ . \end{aligned} \tag{6.110}$$

This expression shows that F has an implicit dependence on the variables N_j and Z_n through the average potential ϕ satisfying the PB equation with

[10] Here the surface of the 0-th particle represents the inner surface of the container. Namely, the fluctuating net charges $Z_0 e$ on the inner surface have the chemical potential $\partial F/\partial Z_0$ and make contributions to G.

the Neumann boundary conditions as well as an explicit dependence on these variables. Taking these points into account, we apply the operator D_c to F finding

$$D_c(\beta F)_{T,V} = \sum_{j=1}^{s} N_j \left(\frac{\partial \beta F}{\partial N_j}\right)_{T,V,Z_n,\phi} + \sum_{n=0}^{M} Z_n \left(\frac{\partial \beta F}{\partial Z_n}\right)_{T,V,N_j,\phi} + D_c(\phi) \left(\frac{\delta \beta F}{\delta \phi}\right)_{T,V,N_j,Z_n} . \tag{6.111}$$

Here all derivatives are to be taken under the condition that T, V, and the configuration of the particles are fixed. Then, using the extremal condition in (6.101) and the definition $G = D_c(F)$, we obtain the following integral representation for the Gibbs free energy of a macroionic dispersion

$$\beta G = \left[\sum_{n=0}^{M} Z_n \oint_{S_n} \phi(\boldsymbol{r}) \sigma_n(\boldsymbol{r}) \mathrm{d}S_n - \sum_{j=1}^{s} N_j \ln \left(\frac{1}{V} \int_V \mathrm{e}^{-z_j \phi(\boldsymbol{r})} \mathrm{d}\boldsymbol{r} \right) + \beta G^0 \right]_{V=Nv} \tag{6.112}$$

where $G^0 = D_c(F^0)$ is the non-electric part of the Gibbs free energy.

In this result, it is essential to note that the Gibbs free energy G no longer depends on the volume variable V of the system. The particle nature of the solvent molecules is taken into account in the theory by the replacement $V = Nv$ in G. This replacement of the extended primitive model is allowed only at the final stage of this derivation. If the replacement is done in the Helmholtz free energy, there arise contradictions, as emphasized in Sect. 2.2, footnote 2 and Sect. 6.2, footnote 4.

In this way, we have derived integral representations of the thermodynamic energies E, F, and G of the system in the mean field description by eliminating the physical degrees of freedom of the electric field and the small ions. It is instructive to note that those integral representations are all invariant under the weak gauge transformation provided that the neutrality condition (6.108) holds.

The thermodynamic quantities E, F, and G are functions of the configuration of macroions $\{\boldsymbol{R}\}$. It is a matter of necessity to analyze the behavior of the Gibbs free energy $G(\{\boldsymbol{R}\})$, since it governs the thermodynamic stability of the system. Its $\{\boldsymbol{R}\}$-dependent part effectively gives rise to an adiabatic potential for macroions.

Among the integral representations of the three thermodynamic energies in (6.102), (6.110), and (6.112), there holds the relation

$$G - F = G^0 - F^0 + E . \tag{6.113}$$

The difference between G and F is related to the osmotic pressure of the dispersion P as

$$G - F = (P_0 + P)V \tag{6.114}$$

which reduces to

$$G^0 - F^0 = P_0 V + k_{\mathrm{B}} T \sum_{j=1}^{s} N_j \tag{6.115}$$

in the limit where all the solutes become neutral. Here, $P_0 V$ and $k_{\mathrm{B}} T \sum_j N_j$ are the contributions from the pressure term of the solvent and the van't Hoff term. Therefore, the gas of small ions in the environment of the particles is subject to the equation of state

$$PV = k_{\mathrm{B}} T \sum_{j=1}^{s} N_j + E \tag{6.116}$$

for the osmotic pressure. This relation agrees with the result in (6.53) obtained in the theory of the linearized PB equation [7,8] where the electric energy has contributions from the pair potentials U^{E}_{mn} and the single potentials V^{E}_n, as in (6.90). In general, the electric energy $E(\{\boldsymbol{R}\})$ depends on the configuration of the particles and the physicochemical state of the dispersion. As discussed at the end of Sect. 6.2, the equation of state for the osmotic pressure must be investigated in connection with the Gibbs free energy $G(\{\boldsymbol{R}\})$.

6.3.5 Debye's Charging-up Formula

Motion of the small ions in a stationary configuration of macroions $\{\boldsymbol{R}\}$ is described by the Hamiltonian function

$$H = T(\boldsymbol{p}_1, \boldsymbol{p}_2 \cdots) + e^2 V_{\mathrm{C}}(\boldsymbol{q}_1, \boldsymbol{q}_2 \cdots; \{\boldsymbol{R}\}) \tag{6.117}$$

where $\boldsymbol{q}_j$ and $\boldsymbol{p}_j$ are the coordinate and momentum of the j-th small ion, $T(\boldsymbol{p}_1, \boldsymbol{p}_2, \cdots)$ is the kinetic energy of the small ions and $e^2 V_{\mathrm{C}}(\boldsymbol{q}_1, \boldsymbol{q}_2, \cdots; \{\boldsymbol{R}\})$ is the sum of the Coulomb potentials of the small ions and the effective particles.

Statistical mechanics defines the Helmholtz free energy F by

$$F = -k_{\mathrm{B}} T \ln \int \int \mathrm{e}^{-\beta H} \prod \mathrm{d}\boldsymbol{q} \prod \mathrm{d}\boldsymbol{p} \tag{6.118}$$

where the multiple integrations are taken over the phase space for all of the small ions. This free energy F is decomposed into the sum

$$F = F^{\mathrm{el}} + F^0 \tag{6.119}$$

in terms of the electric part

$$F^{\mathrm{el}} = -k_{\mathrm{B}} T \ln \int_V \exp\{-\beta e^2 V_{\mathrm{C}}(\boldsymbol{q}_1, \boldsymbol{q}_2, \cdots; \{\boldsymbol{R}\})\} \prod \frac{1}{V} \mathrm{d}\boldsymbol{q} \tag{6.120}$$

and the non-electric part

$$F^0 = -k_{\mathrm{B}}T \ln \int \int \exp\{-\beta T(\boldsymbol{p}_1, \boldsymbol{p}_2, \cdots)\} \prod \mathrm{d}\boldsymbol{p} \prod \mathrm{d}\boldsymbol{q} \,. \tag{6.121}$$

The electric part F^{el} is normalized so as to satisfy the condition

$$\lim_{e \to 0} F^{\mathrm{el}} = 0 \,. \tag{6.122}$$

The non-electric part F^0 is given by the Helmholtz free energy of an ideal gas [21].

It is impossible to obtain an analytical form for F^{el} by carrying out the multiple integrations in (6.120). Let us derive Debye's charging-up formula which allows us to estimate F^{el} in the mean field description. The parametric derivative of (6.120) with respect to e^2 yields the following relation:

$$e^2 \left(\frac{\partial F^{\mathrm{el}}}{\partial e^2} \right)_{T,V,N,\{\boldsymbol{R}\}} = \langle V_{\mathrm{C}} \rangle \tag{6.123}$$

where

$$\langle V_{\mathrm{C}} \rangle = \frac{\displaystyle\int e^2 V_{\mathrm{C}} \mathrm{e}^{-\beta e^2 V_{\mathrm{C}}} \mathrm{d}\boldsymbol{q}}{\displaystyle\int \mathrm{e}^{-\beta e^2 V_{\mathrm{C}}} \mathrm{d}\boldsymbol{q}} \,. \tag{6.124}$$

Evidently, the physical quantity $\langle V_{\mathrm{C}} \rangle$ is the thermodynamic average of the electric energy of the system. The key ingredient of the present formalism is to identify this quantity $\langle V_{\mathrm{C}} \rangle$ with the average electric field energy E of the system estimated in mean field theory. Namely, we set

$$\langle V_{\mathrm{C}} \rangle = E = \frac{1}{8\pi\lambda_B} \int (\nabla\phi)^2 \mathrm{d}\boldsymbol{r} \tag{6.125}$$

in terms of the mean electric potential satisfying the PB equation. This estimation is exact in the mean field description. Accordingly, by solving the parametric differential equation (6.123) with the average energy E in (6.102) under the condition in (6.122), we are able to obtain the electric part of the Helmholtz free energy F^{el} in mean field theory.

6.4 Highly Charged Plates Immersed in an Electrolyte

As an application of the general formalism of mean field theory developed in the previous section, we investigate here the free energies of highly charged plates immersed in an electrolyte solution in a finite container. In the one-dimensional problem, the PB equation is solved exactly under either the

Dirichlet or Neumann boundary condition in terms of Jacobi's elliptic functions and the free energies which are determined by the mean electric potential are expressed analytically in terms of the Legendre elliptic integrals. From the Helmholtz and Gibbs free energies, which are exact in our formalism of the mean field theory, we obtain effective adiabatic potentials for the charged plates with long-range weak attractive parts as well as medium-range strong repulsive parts irrespective of the type of boundary conditions. Comparison of the Helmholtz and Gibbs adiabatic potentials proves that, while the two potentials show similar behaviors, the Gibbs adiabatic potential has the stronger attractive effect. The adiabatic potential explains qualitatively well the swelling phenomena of the n-butylammonium vermiculite gels [23–25].

6.4.1 Models of One-Dimensional Systems

Let us consider $N+1$ infinite plates with uniform surface charges and infinitesimal thickness immersed in a 1-1 electrolyte solution parallel to flat walls of a container with finite width. The solution is divided into regions R_i confined by the i-th and $(i+1)$-th plates with separation d_i $(i = 1, 2, \cdots, N)$, region $\mathrm{R}_{\mathrm{o}}^l$ with separation D_l between the left container wall and the 1st plate and region $\mathrm{R}_{\mathrm{o}}^r$ with separation D_r between the $(N+1)$-th plate and the right container wall. The distance D between the left and right container walls is given by

$$D = D_l + D_r + \sum_{i=1}^{N} d_i \ . \tag{6.126}$$

As a basic postulate, we assume that thermal equilibrium is achieved throughout all regions of the solution and accordingly the number density of the small ions with valency z_j $(z_\pm = \pm 1)$, which are described as point particles, is determined by the common Boltzmann distribution

$$n_j(x) = n_0 \mathrm{e}^{-z_j \phi(x)} \tag{6.127}$$

for all the regions R_i, $\mathrm{R}_{\mathrm{o}}^l$, and $\mathrm{R}_{\mathrm{o}}^r$. Here x is the space coordinate taken normally to the plate surfaces with its origin at the midpoint between the container walls and $\phi(x) = \beta e \psi(x)$ is the ratio of the mean electric potential $\psi(x)$ and the thermal energy $k_{\mathrm{B}}T = 1/\beta$. The normalization constant n_0 takes a common value throughout all regions. The solvent is treated as a continuous medium with uniform dielectric constant ε.

In the mean field description, the potential $\phi(x)$ obeys the PB equation

$$\frac{\mathrm{d}^2 \phi(x)}{\mathrm{d}x^2} = \kappa^2 \sinh \phi(x), \tag{6.128}$$

where κ is the parameter in defined by

$$\kappa = \sqrt{8\pi \lambda_{\mathrm{B}} n_0} \tag{6.129}$$

with the Bjerrum length λ_{B}.

The geometrical symmetry of the plate configuration requires the derivative of the potential to vanish at the midpoint $x = x_i^0$ of the region R_i [26,27], i.e.,

$$\left.\frac{\mathrm{d}\phi(x)}{\mathrm{d}x}\right|_{x=x_i^0} = 0\,. \tag{6.130}$$

The surfaces of all the plates are considered naturally to form equipotential surfaces as

$$\phi(x_i \pm 0) = \phi_{\mathrm{S}} \tag{6.131}$$

where x_i is the coordinate of the i-th plate. Note that the value of ϕ_{S} is not yet specified at this stage. The left and right outer surfaces of the plate system have the uniform surface charge densities Z_{o}^l and Z_{o}^r (nm^{-2}), i.e.,

$$-\left.\frac{\mathrm{d}\phi(x)}{\mathrm{d}x}\right|_{x=x_1-0} = -4\pi Z_{\mathrm{o}}^l\lambda_{\mathrm{B}}, \quad -\left.\frac{\mathrm{d}\phi(x)}{\mathrm{d}x}\right|_{x=x_{N+1}+0} = 4\pi Z_{\mathrm{o}}^r\lambda_{\mathrm{B}}\,. \tag{6.132}$$

All other inner surfaces have uniform surface charge densities Z_i as

$$-\left.\frac{\mathrm{d}\phi(x)}{\mathrm{d}x}\right|_{x=x_{i+1}-0} = -4\pi Z_i\lambda_{\mathrm{B}}, \quad -\left.\frac{\mathrm{d}\phi(x)}{\mathrm{d}x}\right|_{x=x_i+0} = 4\pi Z_i\lambda_{\mathrm{B}}\,. \tag{6.133}$$

In consideration of the fact that the surface charge of many stably dispersed macroions is negative, we assume $Z_i, Z_{\mathrm{o}}^l, Z_{\mathrm{o}}^r < 0$. In the present section we impose the Neumann-type boundary condition that the container surfaces have no charge [28,29]. This boundary condition is expressed by

$$\left.\frac{\mathrm{d}\phi(x)}{\mathrm{d}x}\right|_{x=x_{\mathrm{c}}^l+0} = \left.\frac{\mathrm{d}\phi(x)}{\mathrm{d}x}\right|_{x=x_{\mathrm{c}}^r-0} = 0, \tag{6.134}$$

where x_c^l and x_c^r are the coordinates of the left and right inner surfaces of the container. This condition (6.134) can be changed to take into account situations where the container surfaces are not neutral.

To derive the mean electric potential, one more boundary condition must be imposed in addition to the conditions (6.130)∼(6.134). There are two choices of the remaining boundary condition. One is a model with the Dirichlet boundary condition in which the value of the surface potential ϕ_{S} is specified (Dirichlet model). The other is a model with the Neumann boundary condition in which the values of the surface charge densities Z_{o}^l and Z_{o}^r are given (Neumann model).

6.4.2 Solutions of the PB Equation

We introduce the general region R to be later attributed to each region $\mathrm{R}_i, \mathrm{R}_{\mathrm{o}}^l, \mathrm{R}_{\mathrm{o}}^r$ by parameter replacement. It is sufficient to derive the free energy in the general region R by solving the PB equation under appropriate

boundary conditions and then to apply the result to all the regions to obtain the free energy of the system. The coordinate origin $x = 0$ is taken at the point where the ϕ has its extremum:

$$\left.\frac{\mathrm{d}\phi(x)}{\mathrm{d}x}\right|_{x=0} = 0, \tag{6.135}$$

i.e., x_i^0 in the inner region R_i and $x_c^l\,(x_c^r)$ in the outer region $\mathrm{R}_\mathrm{o}^l\,(\mathrm{R}_\mathrm{o}^r)$. The first integral of the PB equation in R is found to be

$$\left[\frac{\mathrm{d}\phi(x)}{\mathrm{d}x}\right]^2 - 2\kappa^2\cosh\phi(x) = -2\kappa^2\cosh\phi(0)\ . \tag{6.136}$$

It is convenient to introduce the auxiliary quantities

$$g(x) = k^{-\frac{1}{2}}\exp\left[\frac{1}{2}\phi(x)\right], \quad k = \exp\left[\phi(0)\right]\ . \tag{6.137}$$

For a system with negative surface charge, $\phi(x) \le \phi(0) < 0$. Therefore the values of k and $g(x)$ are restricted, respectively, to the intervals

$$0 < k < 1, \quad 0 < g(x) \le g(0) = 1\ . \tag{6.138}$$

Consequently, (6.136) is converted into the elliptic integral as

$$\begin{aligned} x &= \pm\frac{2\sqrt{k}}{\kappa}\int_1^{g(x)}\frac{\mathrm{d}t}{\sqrt{(1-t^2)(1-k^2t^2)}} \\ &\equiv \pm\frac{2\sqrt{k}}{\kappa}[F(\sin^{-1}g(x),k) - K], \end{aligned} \tag{6.139}$$

where the $-(+)$ sign on the right-hand side is for $x > 0$ ($x < 0$), F is the elliptic integral with modulus k of the first kind in Legendre's normal form [30, 31] defined by

$$F(\varphi,k) = \int_0^\varphi \frac{\mathrm{d}\psi}{\sqrt{1-k^2\sin^2\psi}} \tag{6.140}$$

and $K = F(\pi/2,k)$ is the perfect elliptic integral of the first kind. Hence the mean electric potential $\phi(x)$ is expressed in terms of Jacobi's elliptic function sn with modulus k [30, 31] as follows:

$$\phi(x) = 2\ln\left[\mathrm{sn}\left(-\frac{\kappa}{2\sqrt{k}}|x| + K(k),k\right)\right] + \phi(0)\ . \tag{6.141}$$

Consider that the region R is sandwiched by plates with the surface charge densities $Z_\mathrm{L} \le 0$ at the position $x = -l_\mathrm{L}$ and $Z_\mathrm{R} \le 0$ at $x = l_\mathrm{R}$. The boundary conditions are

$$-\left.\frac{\mathrm{d}\phi(x)}{\mathrm{d}x}\right|_{x=-l_\mathrm{L}+0} = 4\pi Z_\mathrm{L}\lambda_\mathrm{B},\ -\left.\frac{\mathrm{d}\phi(x)}{\mathrm{d}x}\right|_{x=l_\mathrm{R}-0} = -4\pi Z_\mathrm{R}\lambda_\mathrm{B} \tag{6.142}$$

and the interplate distance is $d = l_{\rm L} + l_{\rm R}$. Substituting (6.141) into (6.142), we obtain

$$4\pi|Z_{\rm L}|\lambda_{\rm B} = \frac{\kappa}{\sqrt{k}} \frac{\mathrm{cn}\left(-\frac{\kappa}{2\sqrt{k}} l_{\rm L} + K(k), k\right) \mathrm{dn}\left(-\frac{\kappa}{2\sqrt{k}} l_{\rm L} + K(k), k\right)}{\mathrm{sn}\left(-\frac{\kappa}{2\sqrt{k}} l_{\rm L} + K(k), k\right)} \tag{6.143}$$

and

$$4\pi|Z_{\rm R}|\lambda_{\rm B} = \frac{\kappa}{\sqrt{k}} \frac{\mathrm{cn}\left(-\frac{\kappa}{2\sqrt{k}} l_{\rm R} + K(k), k\right) \mathrm{dn}\left(-\frac{\kappa}{2\sqrt{k}} l_{\rm R} + K(k), k\right)}{\mathrm{sn}\left(-\frac{\kappa}{2\sqrt{k}} l_{\rm R} + K(k), k\right)} \,. \tag{6.144}$$

By giving the values of $Z_{\rm L}$ (or $\phi(-l_{\rm L})$), $Z_{\rm R}$ (or $\phi(l_{\rm R})$) and d, the values of k, $l_{\rm L}$ and $l_{\rm R}$ are determined.

Noting that the potential $\phi(x)$ is symmetric with respect to the origin, the Boltzmann distribution (6.127) is integrated to give the numbers of small ions in the region R as

$$\begin{aligned} N_+ &= \int_{-l_{\rm L}}^{l_{\rm R}} n_0 \mathrm{e}^{-\phi(x)} \mathrm{d}x \\ &= \left\{ |Z_{\rm L}| + \frac{n_0 l_{\rm L}}{k} + \frac{2n_0}{\kappa\sqrt{k}} \left[E(-\frac{\kappa}{2\sqrt{k}} l_{\rm L} + K(k)) - E(K(k)) \right] \right\} \\ &\quad + \{\mathrm{L} \to \mathrm{R}\} \end{aligned} \tag{6.145}$$

and

$$\begin{aligned} N_- &= \int_{-l_{\rm L}}^{l_{\rm R}} n_0 \mathrm{e}^{\phi(x)} \mathrm{d}x \\ &= \left\{ \frac{n_0 l_{\rm L}}{k} + \frac{2n_0}{\kappa\sqrt{k}} \left[E(-\frac{\kappa}{2\sqrt{k}} l_{\rm L} + K(k)) - E(K(k)) \right] \right\} \\ &\quad + \{\mathrm{L} \to \mathrm{R}\} \end{aligned} \tag{6.146}$$

where

$$E(K(k)) = E(\pi/2, k), \quad E(-\frac{\kappa}{2\sqrt{k}} l + K(k)) = E(\theta, k) \tag{6.147}$$

in which $E(\varphi, k)$ is the Legendre elliptic integral of the second kind [30, 31]

$$E(\varphi, k) = \int_0^{\varphi} \sqrt{1 - k^2 \sin^2 \psi} \, \mathrm{d}\psi \tag{6.148}$$

and the value of θ is fixed by

$$F(\theta, k) = -\frac{\kappa}{2\sqrt{k}} l + K(k) = -\frac{\kappa}{2\sqrt{k}} l + F(\pi/2, k) \tag{6.149}$$

and

$$E(u) = E(\theta, k), \quad u = \int_0^\theta \frac{\mathrm{d}\phi}{\sqrt{1 - k^2 \sin^2 \phi}} = F(\theta, k) \; . \tag{6.150}$$

The difference between (6.145) and (6.146) confirms the condition for charge neutrality in this region as

$$N_+ - N_- = |Z_\mathrm{L}| + |Z_\mathrm{R}| \; . \tag{6.151}$$

6.4.3 Thermodynamic Energies of the System

Using the first integral of the PB equation in (6.136), the definition of the modulus k in (6.137) and the expressions (6.145) and (6.146) for $N_\pm$, we obtain

$$\begin{aligned} \beta E &= \frac{1}{8\pi\lambda_\mathrm{B}} \int_{-l_\mathrm{L}}^{l_\mathrm{R}} \left[\frac{\mathrm{d}\phi(x)}{\mathrm{d}x}\right]^2 \mathrm{d}x \\ &= \frac{2\kappa^2}{8\pi\lambda_\mathrm{B}} \int_{-l_\mathrm{L}}^{l_\mathrm{R}} [\cosh\phi(x) - \cosh\phi(0)] \mathrm{d}x \\ &= N_+ + N_- - n_0 d \frac{1+k^2}{k} \end{aligned} \tag{6.152}$$

for the total electrostatic energy of the system. In this section, we use the expressions F^osm and G^osm for the non-electric parts of the Helmholtz and Gibbs free energies. This is to avoid confusion of these parts with contributions to the free energies from the outer regions.

The formula (6.110) in the previous section for the Helmholtz free energy, $F = F^\mathrm{el} + F^\mathrm{osm}$, is readily cast into one-dimensional form as follows:

$$\begin{aligned} \beta F = {} & Z_\mathrm{L}\phi(x)\Big|_{x=-l_\mathrm{L}+0} + Z_\mathrm{R}\phi(x)\Big|_{x=l_\mathrm{R}-0} - \frac{1}{8\pi\lambda_\mathrm{B}} \int_{-l_\mathrm{L}}^{l_\mathrm{R}} \left[\frac{\mathrm{d}\phi(x)}{\mathrm{d}x}\right]^2 \mathrm{d}x \\ & - N_+ \ln\left[\frac{1}{d}\int_{-l_\mathrm{L}}^{l_\mathrm{R}} \mathrm{e}^{-\phi(x)} \mathrm{d}x\right] - N_- \ln\left[\frac{1}{d}\int_{-l_\mathrm{L}}^{l_\mathrm{R}} \mathrm{e}^{\phi(x)} \mathrm{d}x\right] + \beta F^\mathrm{osm} \end{aligned} \tag{6.153}$$

Substitution of the $\phi(x)$ in (6.141) into this formula yields the electric part of the Helmholtz free energy of the region R as

$$\begin{aligned} \beta F^\mathrm{el} = {} & -\left\{2|Z_\mathrm{L}| \ln\left[\sqrt{k}\,\mathrm{sn}\left(-\frac{\kappa}{2\sqrt{k}} l_\mathrm{L} + K(k), k\right)\right]\right\} - \{\mathrm{L} \to \mathrm{R}\} \\ & - N_+ \left[1 + \ln\left(\frac{N_+}{n_0 d}\right)\right] - N_- \left[1 + \ln\left(\frac{N_-}{n_0 d}\right)\right] + n_0 d \frac{1+k^2}{k} \; . \end{aligned} \tag{6.154}$$

Using the formula for an ideal gas [21], the osmotic part F^osm of the Helmholtz free energy is found to be

$$\beta F^{\mathrm{osm}} = -N_+ \left\{ 1 + \ln \left[\frac{d}{N_+} \left(\frac{m_+}{m_{\mathrm{p}}} \right)^{\frac{3}{2}} {\lambda_{\mathrm{S}}}^{-3} \right] \right\} - N_- \left\{ 1 + \ln \left[\frac{d}{N_-} \left(\frac{m_-}{m_{\mathrm{p}}} \right)^{\frac{3}{2}} {\lambda_{\mathrm{S}}}^{-3} \right] \right\} . \tag{6.155}$$

Here, m_+ and m_- are the masses of the counterion and co-ion, m_{p} is the proton mass and

$$\lambda_{\mathrm{S}} \equiv \sqrt{2\pi\hbar^2 \beta m_{\mathrm{p}}^{-1}} \tag{6.156}$$

is the unit of length characterizing the size of *quantum cells in phase space* [21].

From the general formula (6.112) in the previous section, we obtain the following expression for the Gibbs free energy $G = G^{\mathrm{el}} + G^{\mathrm{osm}}$ of the one-dimensional system as

$$\beta G = Z_{\mathrm{L}} \phi(x) \Big|_{x=-l_{\mathrm{L}}+0} + Z_{\mathrm{R}} \phi(x) \Big|_{x=l_{\mathrm{R}}-0} - N_+ \ln \left[\frac{1}{d} \int_{-l_{\mathrm{L}}}^{l_{\mathrm{R}}} \mathrm{e}^{-\phi(x)} \mathrm{d}x \right] - N_- \ln \left[\frac{1}{d} \int_{-l_{\mathrm{L}}}^{l_{\mathrm{R}}} \mathrm{e}^{\phi(x)} \mathrm{d}x \right] + \beta G^{\mathrm{osm}} \tag{6.157}$$

The same procedure as that used to derive the relations (6.154) and (6.155) leads to the results

$$\beta G^{\mathrm{el}} = -\left\{ 2|Z_{\mathrm{L}}| \ln \left[\sqrt{k}\, \mathrm{sn} \left(-\frac{\kappa}{2\sqrt{k}} l_{\mathrm{L}} + K(k), k \right) \right] \right\} - \{\mathrm{L} \to \mathrm{R}\} - N_+ \ln \left(\frac{N_+}{n_0 d} \right) - N_- \ln \left(\frac{N_-}{n_0 d} \right) \tag{6.158}$$

for the electric part and

$$\beta G^{\mathrm{osm}} = -N_+ \ln \left[\frac{d}{N_+ \lambda_{\mathrm{S}}^3} \left(\frac{m_+}{m_{\mathrm{p}}} \right)^{\frac{3}{2}} \right] - N_- \ln \left[\frac{d}{N_- \lambda_{\mathrm{S}}^3} \left(\frac{m_-}{m_{\mathrm{p}}} \right)^{\frac{3}{2}} \right] \tag{6.159}$$

for the osmotic part of the Gibbs free energy. It is also straightforward to verify the following relations

$$\beta G - \beta G^{\mathrm{osm}} = \beta F - \beta F^{\mathrm{osm}} + \beta E \tag{6.160}$$

and

$$\beta G^{\mathrm{osm}} = \beta F^{\mathrm{osm}} + N_+ + N_- . \tag{6.161}$$

6.4.4 Adiabatic Potential

The Helmholtz and Gibbs free energies thus obtained for each region are functions of the width of that region. Summing up those functions of all regions, we can derive the Helmholtz and Gibbs adiabatic potentials.

• **Free Energies in Inner Region** R_i

Let us apply the result obtained above to the inner region R_i. So firstly, by performing the replacements $Z_\mathrm{L}, Z_\mathrm{R} \to Z_i$, $k \to k_i$, $N_\pm \to N_{i\pm}$ and $d \to d_i$ to (6.154), the electric part of the Helmholtz free energy in the region R_i sandwiched between two plates is obtained as

$$\begin{aligned}\beta F_i^{\mathrm{el}}(d_i) = &-4|Z_i| \ln\left[\sqrt{k_i}\,\mathrm{sn}\left(-\frac{\kappa}{4\sqrt{k_i}}d_i + K(k_i), k_i\right)\right] \\ &-N_{i+}\left[1 + \ln\left(\frac{N_{i+}}{n_0 d_i}\right)\right] - N_{i-}\left[1 + \ln\left(\frac{N_{i-}}{n_0 d_i}\right)\right] \\ &+n_0 d_i \frac{1+k_i^2}{k_i} \end{aligned} \tag{6.162}$$

where k_i is the modulus in the region R_i. From (6.155), the osmotic part is represented as

$$\begin{aligned}\beta F_i^{\mathrm{osm}}(d_i) = &-N_{i+}\left\{1 + \ln\left[\frac{d_i}{N_{i+}}\left(\frac{m_+}{m_\mathrm{p}}\right)^{\frac{3}{2}}{\lambda_\mathrm{S}}^{-3}\right]\right\} \\ &-N_{i-}\left\{1 + \ln\left[\frac{d_i}{N_{i-}}\left(\frac{m_-}{m_\mathrm{p}}\right)^{\frac{3}{2}}{\lambda_\mathrm{S}}^{-3}\right]\right\}. \end{aligned} \tag{6.163}$$

Similarly, from (6.158) and (6.159), the electric part and the osmotic part of the Gibbs free energy in the inner region R_i are determined, respectively, as

$$\begin{aligned}\beta G_i^{\mathrm{el}}(d_i) = &-4|Z_i| \ln\left[\sqrt{k_i}\,\mathrm{sn}\left(-\frac{\kappa}{4\sqrt{k_i}}d_i + K(k_i), k_i\right)\right] \\ &-N_{i+}\ln\left(\frac{N_{i+}}{n_0 d_i}\right) - N_{i-}\ln\left(\frac{N_{i-}}{n_0 d_i}\right) \end{aligned} \tag{6.164}$$

and

$$\begin{aligned}\beta G_i^{\mathrm{osm}}(d_i) = &-N_{i+}\ln\left[\frac{d_i}{N_{i+}\lambda_\mathrm{S}^3}\left(\frac{m_+}{m_\mathrm{p}}\right)^{\frac{3}{2}}\right] \\ &-N_{i-}\ln\left[\frac{d_i}{N_{i-}\lambda_\mathrm{S}^3}\left(\frac{m_-}{m_\mathrm{p}}\right)^{\frac{3}{2}}\right]. \end{aligned} \tag{6.165}$$

• **Free Energies in Outer Region** $\mathrm{R}_\mathrm{o}^l \cup \mathrm{R}_\mathrm{o}^r$

For the outer region $\mathrm{R}_\mathrm{o}^l \cup \mathrm{R}_\mathrm{o}^r$ outside the plates, by performing similar replacements to those carried out in (6.154) and (6.155), the electric part and the osmotic part of the Helmholtz free energy are obtained as

$$\beta F_{\rm o}^{\rm el}(D_l, D_r) = -\left\{ 2|Z_{\rm o}^l| \ln\left[\sqrt{k_{\rm o}^l}\, {\rm sn}\left(-\frac{\kappa}{2\sqrt{k_{\rm o}^l}} D_l + K(k_{\rm o}^l), k_{\rm o}^l \right) \right] \right.$$
$$+ N_{\rm o+}^l \left[1 + \ln\left(\frac{N_{\rm o+}^l}{n_0 D_l} \right) \right] + N_{\rm o-}^l \left[1 + \ln\left(\frac{N_{\rm o-}^l}{n_0 D_l} \right) \right]$$
$$\left. - n_0 D_l \frac{1 + {k_{\rm o}^l}^2}{k_{\rm o}^l} \right\} - \{l \to r\} \tag{6.166}$$

and

$$\beta F_{\rm o}^{\rm osm}(D_l, D_r) = -\left\{ N_{\rm o+}^l \left(1 + \ln\left[\frac{D_l}{N_{\rm o+}^l} \left(\frac{m_+}{m_{\rm p}} \right)^{\frac{3}{2}} {\lambda_{\rm S}}^{-3} \right] \right) \right.$$
$$\left. - N_{\rm o-}^l \left(1 + \ln\left[\frac{D_l}{N_{\rm o-}^l} \left(\frac{m_-}{m_{\rm p}} \right)^{\frac{3}{2}} {\lambda_{\rm S}}^{-3} \right] \right) \right\}$$
$$- \{l \to r\} \tag{6.167}$$

respectively. Here, $k_{\rm o}^l$ and $k_{\rm o}^r$ are the moduli, and $N_{\rm o\pm}^l$ and $N_{\rm o\pm}^r$ the numbers of small ions in the regions ${\rm R}_{\rm o}^l$ and ${\rm R}_{\rm o}^r$.

Similarly, from (6.158) and (6.159), the electric part and the osmotic part of the Gibbs free energy in the outer region ${\rm R}_{\rm o}^l \cup {\rm R}_{\rm o}^r$ are determined, respectively, by

$$\beta G_{\rm o}^{\rm el}(D_l, D_r) = -\left\{ 2|Z_{\rm o}^l| \ln\left[\sqrt{k_{\rm o}^l}\, {\rm sn}\left(-\frac{\kappa}{2\sqrt{k_{\rm o}^l}} D_l + K(k_{\rm o}^l), k_{\rm o}^l \right) \right] \right.$$
$$\left. + N_{\rm o-}^l \ln\left(\frac{N_{\rm o-}^l}{n_0 D_l} \right) + N_{\rm o+}^l \ln\left(\frac{N_{\rm o+}^l}{n_0 D_l} \right) \right\} - \{l \to r\} \tag{6.168}$$

and

$$\beta G_{\rm o}^{\rm osm}(D_l, D_r) = -\left\{ N_{\rm o+}^l \ln\left[\frac{D_l}{N_{\rm o+}^l \lambda_{\rm S}^3} \left(\frac{m_+}{m_{\rm p}} \right)^{\frac{3}{2}} \right] \right.$$
$$\left. - N_{\rm o-}^l \ln\left[\frac{D_l}{N_{\rm o-}^l \lambda_{\rm S}^3} \left(\frac{m_-}{m_{\rm p}} \right)^{\frac{3}{2}} \right] \right\} - \{l \to r\}\,. \tag{6.169}$$

• Helmholtz and Gibbs Adiabatic Potentials

In this way, the free energy of each region has been expressed as a function of the width of that region. Summing up these electric and osmotic parts of the free energies of all regions, we get the total free energy of the system. This total free energy is the arrangement function for $(N+1)$ plates laid in the container, and is interpreted as the adiabatic potential with regard to the interplate distances. Thus, the *Helmholtz adiabatic potential* and the *Gibbs adiabatic potential* of the $(N+1)$ plate system are obtained as

$$U^{\mathrm{F}}_{N+1}(d_1,\cdots,d_N;D_l,D_r)=\sum_{i=1}^{N}[F^{\mathrm{el}}_i(d_i)+F^{\mathrm{osm}}_i(d_i)] \\ +F^{\mathrm{el}}_{\mathrm{o}}(D_l,D_r)+F^{\mathrm{osm}}_{\mathrm{o}}(D_l,D_r) \quad (6.170)$$

and

$$U^{\mathrm{G}}_{N+1}(d_1,\cdots,d_M;D_l,D_r)=\sum_{i=1}^{N}\left[G^{\mathrm{el}}_i(d_i)+G^{\mathrm{osm}}_i(d_i)\right] \\ +G^{\mathrm{el}}_{\mathrm{o}}(D_l,D_r)+G^{\mathrm{osm}}_{\mathrm{o}}(D_l,D_r), \quad (6.171)$$

respectively.

The formulae (6.170) and (6.171) for the adiabatic potential are exact within the framework of the mean field description. However, the structures of the electric parts F^{el} and G^{el} are too complex to disclose their analytic properties. Here we examine the adiabatic potentials numerically [28, 29] following the *Carlson theory of elliptic integrals* [32–35] which is explained in the end of this section.

6.4.5 Numerical Results

To proceed with numerical computation, it is necessary to enter a set of parameters designed to describe an experimental situation. We use values of the chemical fixed parameters specified by the n-butylammonium vermiculite gels: $m_+ = 74\ m_{\mathrm{p}}$ and $m_- = 36\ m_{\mathrm{p}}$. The average density of small ions n_0 (nm^{-3}) is given by

$$n_0 = 6.02\times 10^{-1}\times C_{\mathrm{s}} \quad (6.172)$$

with C_{s} ($\mathrm{mol\ L}^{-1}$) the salt concentration. We take $k_{\mathrm{B}}T = 0.025$ eV $= 4.0\times 10^{-21}$ J, ${\lambda_{\mathrm{S}}}^{-2} = 96\ \mathrm{nm}^{-2}$, and $\lambda_{\mathrm{B}} = 0.72$ nm. It is natural to assume that the physicochemical state is the same in all of the inner regions R_i ($i = 1, 2, \cdots, N$). Therefore, we examine mainly the *two plate system* ($N = 1$) with a symmetric configuration ($D_l = D_r = (D-d)/2$), except for Figs. 6.13 and 6.14. To investigate the wall effect for such a system, the width D of the container is set to be 200 nm in this section.

Here, the value of the surface potential ϕ_{S} must be determined to make analysis in the Dirichlet model. Analysis of the effect of uniaxial stress on the swelling of n-butylammonium vermiculite results in the average value of the surface potential $\psi_{\mathrm{S}} \simeq -70$ mV being insensitive to electrolyte concentration [25]. The surface potential is also found to be independent of electrolyte concentration for the smectite minerals and has the value $\psi_{\mathrm{S}} \simeq -60$ mV [36]. Using these values and taking into account the fact that the surface potential ϕ_{S} is as hard to measure as the charge densities Z^l_{o} and Z^r_{o}, we make numerical calculations of the thermodynamic quantities for the range of values $\phi_{\mathrm{S}} = \beta e\psi_{\mathrm{S}} = -2.0 \sim -8.0$, corresponding to $\psi_{\mathrm{S}} = -50 \sim -200$ mV.

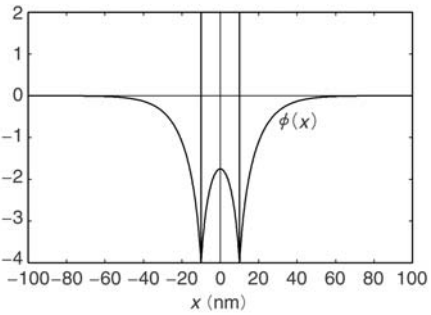

Fig. 6.5. Variation of the dimensionless electric potential $\phi(x)$ against the coordinate x whose origin is taken at the midpoint between two plates with separation $d = 20$ nm ($N = 1$). The concentration of the external soaking solution is $C_s = 0.001$ mol L^{-1} and the surface potential $\phi_S = -4.0$ in the Dirichlet model, which corresponds to the surface charge density $Z_o = -0.084$ nm^{-2} in the Neumann model. The two plates are located at $x_1 = -10$ nm and $x_2 = 10$ nm

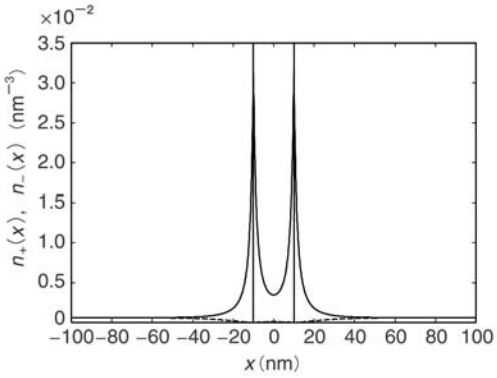

Fig. 6.6. Distributions of small ions (n_+: solid line; n_-: dashed line) for the interplate distance $d = 20$ nm, the electrolyte concentration $C_s = 0.001$ mol L^{-1} and the surface potential $\phi_S = -4.0$ in the Dirichlet model (the surface charge density $Z_o = -0.084$ nm^{-2} in the Neumann model)

Numerical results are obtained for the plate system satisfying the conditions $Z_o \equiv Z_o^l = Z_o^r$ (except for Figs. 6.13 and 6.14).

Figures 6.5 and 6.6 show the behavior of the mean electric potential $\phi(x)$ and the small ion distributions $n_\pm(x)$ for the distances $d = 20$ nm and $D_l = D_r = 90$ nm, the salt concentration $C_s = 0.001$ mol L^{-1}, and the surface potential $\phi_S = -4.0$ (the surface charge density $Z_o = -0.084$ nm^{-2} in the Neumann model). The origin of the coordinate x is taken at the midpoint of the container.

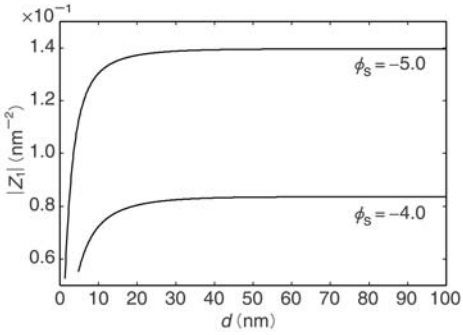

Fig. 6.7. Dependence of the magnitude of the inner surface charge density $|Z_1|$ on the interplate distance d for $\phi_S = -4.0$ and -5.0 in the Dirichlet model ($Z_o = -0.084$ and -0.140 nm^{-2} in the Neumann model) when $C_s = 0.001$ mol L^{-1}. $|Z_1|$ vanishes rapidly to zero as $d \to 0$, and it saturates quickly to the outer surface charge density $|Z_o|$ with increasing d

Figure 6.5 shows that the potential satisfies $\phi(x) = 0$ on the surfaces ($x_c^l = -100$ nm and $x_c^r = 100$ nm) of the container walls. The distribution functions of positive and negative ions approach a common value n_0 near the container walls. This indicates the solution to be locally neutral at points far from the plates, and the conditions of the infinite container

$$\phi(\pm\infty) = 0, \quad \left.\frac{\mathrm{d}\phi(x)}{\mathrm{d}x}\right|_{x=\pm\infty} = 0 \tag{6.173}$$

are also realized approximately for the finite container. Near the plates, the surface electric charges of the plate attract counterions, and exclude coions. Figure 6.6 shows that the distribution for counterions becomes dominant and coions are almost excluded in the region sandwiched by the plates and that a sizable amount of counterions exists around the midpoint of the region. This can be interpreted as meaning that *the excess counterions distributed over the central part of this region are shared by two plates.*

The charge density Z_1 of the inner surface of the plate varies subject to the relations (6.143) and (6.144). The behaviour of the charge density Z_1 of the inner surface of the plate as a function of the interplate distance d is drawn in Fig. 6.7 for $\phi_S = -4.0$ and -5.0 ($Z_o = -0.084$ and -0.140 nm^{-2} in the Neumann model) when $C_s = 0.001$ mol L^{-1}. Z_1 approaches rapidly to the charge density of the outer plate surface Z_o with increasing d, and it reduces rapidly to zero as $d \to 0$. This latter property of Z_1 is essential for the consistency of the theory. If Z_1 remained non-zero at $d = 0$, the charge balance condition (6.151) would break down because the numbers of small ions N_{1+} and N_{1-} in R_1 vanish in this limit. This reduction of the charge density Z_1 should be interpreted as occurring through the recombination of surface

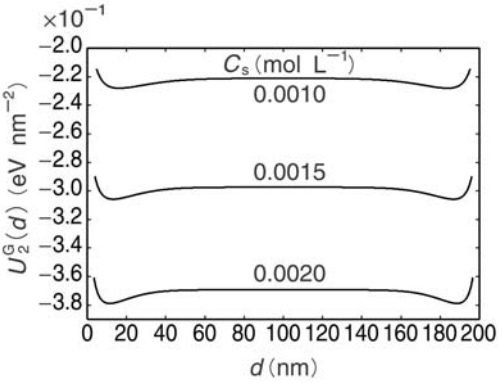

Fig. 6.8. The Gibbs adiabatic potentials $U_2^{\rm G}(d)$ for three values of the electrolyte concentration $C_{\rm s}$ in the Dirichlet model. The surface potential of all plates is taken to be $\phi_{\rm S} = -4.0$ ($Z_{\rm o} = -0.084$, -0.102, and -0.118 nm^{-2} for $C_{\rm s} = 0.0010$, 0.0015, and 0.0020 mol L^{-1} in the Neumann model). The potential $U_2^{\rm G}$ takes a minimum around $d = 15$ nm and 185 nm

charges with counterions. To describe such a phenomenon at the molecular level goes beyond the scope of mean field theory. Here, it is implicit that the plate changes its surface charge density to satisfy the condition of charge balance in each region.

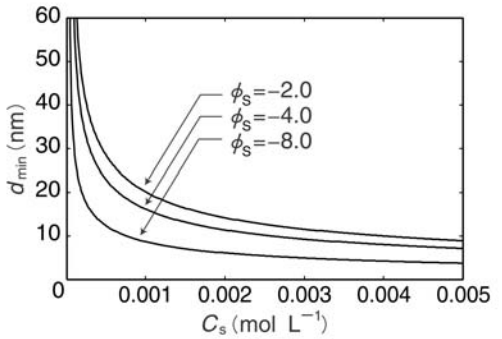

Fig. 6.9. The trajectories of the stable interplate distance $d_{\rm min}$ of the Gibbs adiabatic potential $U_2^{\rm G}$ plotted against the concentration $C_{\rm s}$ of the external soaking solution for three values of the surface potential $\phi_{\rm S}$ in the Dirichlet model. The width of the container is set to be 200 nm and $D_l = D_r$. The swelling is enhanced for small values of $|\phi_{\rm S}|$

The behaviour of the total adiabatic potential $U_2^{\rm G}(d)$ is shown in Fig. 6.8 for the concentrations $C_{\rm s} = 0.001 \sim 0.002$ mol L^{-1}. It is repulsive at medium-

range and attractive at long-range between two plates (and between plate and container surface). This characteristic of the potential does not depend on change of salt concentration ($C_s = 0.0010, 0.0015, 0.0020$ mol L^{-1}).

In Fig. 6.9 the trajectories of the interplate distance d_{min} (the smaller one) for the potential minimum are drawn for different values of ϕ_S, showing the increase of the plate separation against the dilution of the salt concentration C_s. d_{min} approaches $D/2$ as $C_s \to 0$. We note that the swelling is enhanced for small values of $|\phi_S|$.

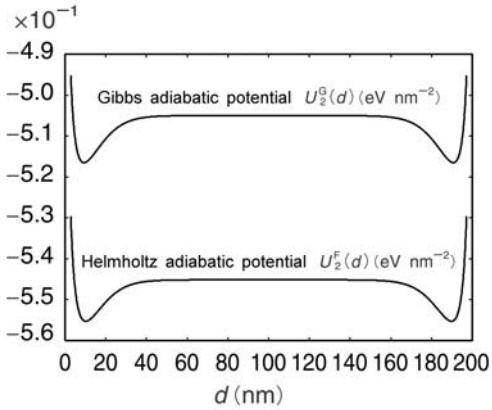

Fig. 6.10. Comparison between the Helmholtz adiabatic potential $U_2^F(d)$ and Gibbs adiabatic potential $U_2^G(d)$ for the salt concentration $C_s = 0.003$ mol L^{-1}, the container width $D = 200$ nm ($D_l = D_r$) and the surface potential $\phi_S = -4.0$ in the Dirichlet model

In Fig. 6.10, the adiabatic potentials $U_2^F(d)$ and $U_2^G(d)$ are drawn on the same energy scale for $C_s = 0.003$ mol L^{-1} and $\phi_S = -4.0$. Both adiabatic potentials take minima around $d = 15$nm (and $d = 185$nm) and a maximum at $d = 100$ nm. Evidently, the Gibbs potential $U_2^G(d)$ is larger than the Helmholtz potential $U_2^F(d)$ for all d by the van't Hoff term $(N^+ + N^-)k_BT$.

For both of the Helmholtz and Gibbs adiabatic potentials, the potential difference $U_2(100 \text{ nm}) - U_2(d_{min})$ which measures the strength of the plate binding is plotted against the salt concentration C_s for $\phi_S = -4.0$ in Fig. 6.11. Although the $U_2^G(d)$ is larger than the $U_2^F(d)$ for all d, the $U_2^G(d)$ turns out to exert a stronger binding force than the $U_2^F(d)$. In Fig. 6.12, the values of the interplate distance d_{min} for the two adiabatic potentials are compared by changing the salt concentration C_s for $\phi_S = -4.0$. The interplate distance d_{min} of $U_2^G(d)$ is smaller than that of $U_2^F(d)$ for all d.

Consequently, the two adiabatic potentials have qualitatively the same structure, with a repulsive component and an attractive component, but the Gibbs adiabatic potential shows the stronger attractive effect. Both adiabatic

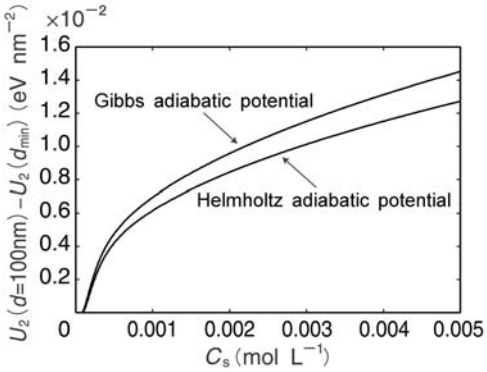

Fig. 6.11. The potential differences $U_2(100\ \mathrm{nm}) - U_2(d_{\min})$ for the Helmholtz and Gibbs adiabatic potentials plotted against the concentration C_s of the external soaking solution for the surface potential $\phi_\mathrm{S} = -4.0$ in the Dirichlet model. The width of the container is set to be 200 nm and $D_l = D_r$. The potential difference measures the strength of the binding between the plates

potentials have repulsive components for small d and weak attractive components for large d ($< D/2$).

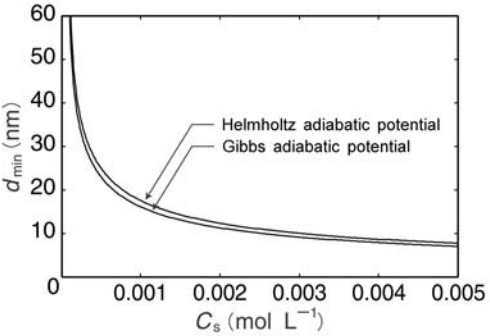

Fig. 6.12. The trajectories of the stable interplate distance $d_{\min}$ of the Helmholtz and Gibbs adiabatic potentials plotted against the concentration C_s of the external soaking solution for the surface potential $\phi_\mathrm{S} = -4.0$ in the Dirichlet model. The width of the container is set to be 200 nm and $D_l = D_r$

Next, let us change D_l, in fixing d_i to $d_{\min}$, the value at which the adiabatic potential takes its minimum in the case of $D_l = D_r$. Figure 6.13 shows the adiabatic potentials U_2^G for $D = 200$ nm, $C_\mathrm{s} = 0.001$ and 0.002 mol L^{-1} in the Dirichlet model as a function of the central position between the two plates. The potential U_2^G in Fig. 6.8 takes a minimum at $d = 16.2$ nm for $C_\mathrm{s} =$

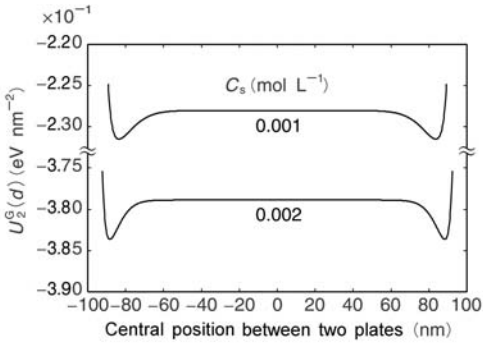

Fig. 6.13. The Gibbs adiabatic potentials U_2^{G} for $C_{\mathrm{s}} = 0.001$ and 0.002 mol L^{-1} in the Dirichlet model as a function of the central position between two the plates. The origin of the coordinate system is taken at the midpoint between the container surfaces. The surface potential of all plates is taken to be $\phi_{\mathrm{S}} = -4.0$. The interplate distances d are fixed to the values at which the Gibbs adiabatic potentials take a minimum

0.001 mol L^{-1} and $d = 11.4$ nm for $C_{\mathrm{s}} = 0.002$ mol L^{-1}. The surface potential of all plates is taken to be $\phi_{\mathrm{S}} = -4.0$. The potential U_2^{G} takes a minimum at the two symmetric positions $D_l = d_{\min}/2$ and $D_r = d_{\min}/2$ for the central position between the two plates in Fig. 6.13. When the container walls have a surface electric charge, this left-right symmetry exists so long as the size of the electric charge is equal on the left and right walls of the container. In an actual system, *this left-right symmetry breaks down spontaneously*, and a potential minimum is chosen on either the left-side or the right-side near a container surface.

In the case of the many plate system ($N \geq 2$), we can obtain the adiabatic potential $U_N^{\mathrm{G}}(d_1, \cdots, d_N; D_l, D_r)$ by summing up the contributions from all the regions. The potential takes a minimum at $d_1 = d_2 = \cdots = d_N$, if the plate system is symmetric with no defects. For example, Fig. 6.14 shows the adiabatic potential U_7^{G} and the electrostatic potential $\phi(x)$ for $N = 6$, $C_{\mathrm{s}} = 0.001$ mol L^{-1} and $d_i = 16.2$ nm ($i = 1, 2, \cdots, 6$) in the Dirichlet model. The potential U_7^{G} is shown as a function of the central position between the first plate and the seventh plate in the upper graph of Fig. 6.14. When the nearest neighbor plate to the container wall is at a distance of 8.1 nm from the container surface, the Gibbs adiabatic potential takes a minimum. The lower graph of Fig. 6.14 represents the behaviour of the mean electric potential $\phi(x)$ in the plate configuration at which the potential U_7^{G} takes its minimum ($2D_l = d_i = 16.2$ nm). The surface potential of all plates is taken to be $\phi_{\mathrm{S}} = -4.0$. The potential U_7^{G} takes a minimum at $d_i = 16.2$ nm, similar to the case of $D_l = D_r$. The value $d_i = 16.2$ nm is the same as $d_{\min}$ of Fig. 6.8.

As seen from Fig. 6.13 and the upper graph of Fig. 6.14, the minimum point of the adiabatic potential exists in two symmetrical positions. Actually, this

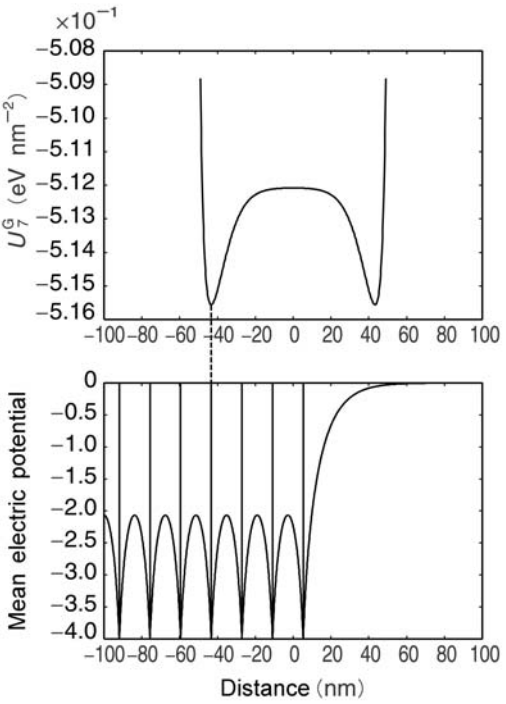

Fig. 6.14. The case of a seven plate system ($N = 6$). The Gibbs adiabatic potential U_7^{G} and the electrostatic potential $\phi(x)$ for $C_{\mathrm{s}} = 0.001$ mol L^{-1} and $d_i = 16.2$ nm ($i = 1, 2, \cdots, 6$) in the Dirichlet model. The origin of the coordinate x is taken at the midpoint between the container surfaces. The potential U_7^{G} is shown as a function of the central position between the first plate and the seventh plate in the upper graph. The surface potential of all plates is taken to be $\phi_{\mathrm{S}} = -4.0$. When the plate near the container wall is at a distance of 8.1 nm from the container surface, the Gibbs adiabatic potential takes a minimum. The lower graph represents the behaviour of $\phi(x)$ at the minimum point of U_7^{G} ($2D_l = d_i = 16.2$ nm). The potential U_7^{G} takes a minimum at $d_i = 16.2$ nm for $C_{\mathrm{s}} = 0.001$ mol L^{-1}, $\phi_{\mathrm{S}} = -4.0$ and $D_l = D_r$

left-right symmetry is "spontaneously" broken according to external initial conditions, and either one is realized. In Fig. 6.14, we have chosen the potential minimum near the left wall surface.

In this way we have calculated the Gibbs and Helmholtz free energies of highly charged plates in a container with finite width and have derived the adiabatic potentials for the plates in mean field theory. Comparing the two adiabatic potentials, the Gibbs potential U^{G} becomes larger than the Helmholtz potential U^{F}. This is mainly due to the osmotic term $(N_+ + N_-)k_{\mathrm{B}}T$. However, the potential minimum of U^{G} is deeper than that of U^{F} (see Fig. 6.11) and the interplate distance $d_{\min}$ of U^{G} is smaller than that of U^{F} (see Fig. 6.12). Consequently, it has been proved that the two adiabatic potentials have qual-

itatively the same structure, with a medium-range repulsive component and a long-range attractive component, but that the Gibbs adiabatic potential has the stronger attractive effect.

The adiabatic potential expressed in (6.170) and (6.171) as the sum of the contributions from pairs of surfaces consists of an osmotic part and an electric part. The osmotic pressures arise from the random motion of the small ions trapped in the regions $\mathrm{R}_i, \mathrm{R}_{\mathrm{o}}^l$ and $\mathrm{R}_{\mathrm{o}}^r$. On the other hand, the electric part of the adiabatic potential represents the interaction mediated, not by material entities, but by the electric field produced by the equilibrium distribution of the small ions and the plate charges. By attracting counterions and repelling coions, the fixed surface charges of the plates create asymmetric distributions of small ions both in number and in charge. From these asymmetries, the plates receive two kinds of reaction. First, the excess of small ions in number induces an osmotic repulsion between the plates. Second, the counterions which are shared by two plates give rise to an excess of charge opposite to that of the plates, and this induces an effective electric attraction between the plates. As is well known, the counterions distributed close to the plates work to shield their surface charges. Figure 6.6 shows, however, that there exist counterions at the middle of the inner region which do not belong to either of the plates. It is those counterions which result in an attraction, *a counterion mediated attraction*, between the plates of both sides. It is a delicate balance of these two diametrically opposed effects that leads to the osmotic and electric stability attained at the minimum of the adiabatic potential (6.171). The approximation used in the DLVO theory failed to compute these competing effects correctly, because it ignored the strong correlation between the plate charges and the counterions.

Here it is relevant to notice the difference between the parameter κ defined in (6.129) and Debye's screening parameter. The exact solution of the PB equation in (6.141) has an x dependence of the form $-\kappa|x|/(2\sqrt{k})$. In the weak field limit, the linearized PB equation has the solution of an exponential function with the $|x|$ dependence in the form (Debye's screening parameter)$\times|x|$. Therefore, it is possible to interpret this as meaning that Debye's screening parameter corresponds approximately to the factor $\kappa/(2\sqrt{k})$ in the present theory.

6.4.6 Carlson's Theory of Elliptic Integrals

Traditionally numerical computations of the elliptic integrals have been done by means of the Gauss and Landen transformations [30, 31] which reduce the value of modulus k to 1. However it is difficult to apply such schemes to calculation of the elliptic integrals with the modulus depending on many unknown parameters. Recently, discovery of new relations among the elliptic integrals by Carlson enables us to proceed effectively with numerical computation in a unified manner.

Carlson introduced new functions through the following symmetric integral representations with simple cut structure as [32–34]

$$R_{\mathrm{F}}(x,y,z)=\frac{1}{2}\int_0^\infty \frac{1}{\sqrt{(t+x)(t+y)(t+z)}}\mathrm{d}t \tag{6.174}$$

and

$$R_{\mathrm{J}}(x,y,z,\rho)=\frac{3}{2}\int_0^\infty \frac{1}{\sqrt{(t+x)(t+y)(t+z)}(t+\rho)}\mathrm{d}t\ . \tag{6.175}$$

With these functions, the Legendre elliptic integrals of the first and second kinds in (6.140) and (6.148) are expressed as [32]

$$F(\varphi,k)=R_{\mathrm{F}}(\cos^2\varphi,1-k^2\sin^2\varphi,1)\sin\varphi, \tag{6.176}$$

and

$$\begin{aligned}E(\varphi,k)=&R_{\mathrm{F}}(\cos^2\varphi,1-k^2\sin^2\varphi,1)\sin\varphi\\&-\frac{1}{3}k^2R_{\mathrm{J}}(\cos^2\varphi,1-k^2\sin^2\varphi,1)\sin^3\varphi\ ,\end{aligned} \tag{6.177}$$

respectively. The most important properties of the Carlson functions are the following relations called the *Carlson's duplication theorem* [33, 34]:

$$R_{\mathrm{F}}(x_0,y_0,z_0)=R_{\mathrm{F}}(x_n,y_n,z_n) \tag{6.178}$$

and

$$R_{\mathrm{J}}(x_0,y_0,z_0,\rho_0)=3\sum_{m=0}^{n-1}4^{-m}R_{\mathrm{F}}(\alpha_m,\beta_m)+4^{-n}R_{\mathrm{J}}(x_n,y_n,z_n,\rho_n) \tag{6.179}$$

where

$$\alpha_n=\{\rho_n(\sqrt{x_n}+\sqrt{y_n}+\sqrt{z_n})+\sqrt{x_ny_nz_n}\}^2,\quad \beta_n=\rho_n(\rho_n+\lambda_n)^2 \tag{6.180}$$

$$\lambda_n=\sqrt{x_ny_n}+\sqrt{y_nz_n}+\sqrt{z_nx_n}, \tag{6.181}$$

$$x_0=x,\quad y_0=y,\quad z_0=z,\quad \rho_0=\rho, \tag{6.182}$$

and

$$x_{n+1}=\frac{x_n+\lambda_n}{4},\quad y_{n+1}=\frac{y_n+\lambda_n}{4},\quad z_{n+1}=\frac{z_n+\lambda_n}{4},\quad \rho_{n+1}=\frac{\rho_n+\lambda_n}{4}\ . \tag{6.183}$$

Iterative application of this theorem to R_{F} and R_{J} makes their arguments nearly equal and brings them close to the elementary functions. Namely, at the limit of $x_n,y_n,z_n\to x=y=z$, the Carlson functions R_{F} and R_{J} are reduced to

$$R_{\mathrm{F}}(x,x,x)=\frac{1}{\sqrt{x}},\quad R_{\mathrm{J}}(x,x,x,x)=\frac{1}{\sqrt{x^3}}\ . \tag{6.184}$$

Then, with the Taylor expansion of R_{F} and R_{J} around (6.184), we are able to make good numerical estimates of the Legendre elliptic integrals. Compared with the method of Gauss and Landen transformations, Carlson algorithms provide a unified scheme for rapid numerical calculations. Computer programs for Carlson's algorithm have been given by Press and Teukolsky [35].

6.5 Summary and Discussion

The basic physical quantity used in this chapter to formulate the mean field theory for macroionic dispersions is the mean electric potential subject to the PB equation. The thermodynamic states of the small ions which have the largest thermodynamic degrees of freedom in our extended primitive model are described by Boltzmann distributions depending on the potential, and the electric parts of all thermodynamic quantities of the dispersions are described in terms of the potential.

In Sect. 6.1, the concept of effective particles with reduced net surface charges was introduced, and the linearized mean field theory for dispersions consisting of such effective particles was developed in Sect. 6.2. The mean electric potential was explicitly determined for a dispersion of spherical effective particles and this enabled us to obtain the Helmholtz and Gibbs free energies, F and G, as well as the electric field energy E, in compact analytical forms. These energies give rise to three kinds of adiabatic potentials, $U^a(\{\boldsymbol{R}\})$ $(a=\mathrm{E},\mathrm{F},\mathrm{G})$ in the case of constant surface charge and $U_a(\{\boldsymbol{R}\})$ $(a=\mathrm{E},\mathrm{F},\mathrm{G})$ in the case of constant surface potential. The adiabatic potential $U^{\mathrm{E}}(\{\boldsymbol{R}\})$, which has a medium-range strong repulsion and a long-range strong attraction, is approximately equal to that of the Levine-Dube theory [14, 15], and the adiabatic potential $U_{\mathrm{F}}(\{\boldsymbol{R}\})$, which is purely repulsive, has the same form as that of the DLVO theory. The Gibbs adiabatic potential $U^{\mathrm{G}}(\{\boldsymbol{R}\})$ $(U_{\mathrm{G}}(\{\boldsymbol{R}\}))$ has a medium-range strong repulsion and a long-range weak attraction. The thermodynamic states of a macroionic dispersion of effective particles are described by the Gibbs adiabatic potential.

In Sect. 6.3, we formulated a general theory of macroionic dispersions in which integral representations were derived for thermodynamic energies without resort to a linear approximation. Compared with the density functional theory [39, 40], our theory is compact and easy to handle. The theory was applied in Sect. 6.4 to the investigation of a system of highly-charged parallel plates immersed in an electrolyte. The PB equation for such a one-dimensional system can be solved exactly and all thermodynamic quantities were obtained in analytical forms with elliptic functions and integrals. Both the Helmholtz and Gibbs free energies, which were determined as functions of the interplate distance, were proved to have a medium-range strong repulsion and a long-range weak attraction.

The long-range behavior of the Helmholtz free energy F is diametrically different in the theories with the linearized and non-linearized PB equation. In the linearized theory, the strong correlation between the macroions and small ions can be incorporated, not in the Helmholtz free energy F, but only in the Gibbs free energy G, which describes the behavior of the macroionic dispersion in an osmotic equilibrium of a small ion gas. It is the electric pair potential U^{E} in the equation of state (6.90) for the osmotic pressure that revives the long-range weak attraction in the Gibbs free energy.

As clarified in Sect. 6.3, the mean field theory for ionic solutions and dispersions is invariant under a weak gauge transformation provided that the constraint of neutrality in (6.108) is satisfied. This general feature, however, is lost in the new linearized theory formulated in Sect. 6.2. The invariance of the theory under the weak gauge transformation

$$\begin{cases} \psi(\boldsymbol{r}) \to \psi(\boldsymbol{r}) - \breve{\psi} \\ n_{i0} \ \to n_{i0} \exp\left\{ -\dfrac{z_i e}{k_{\mathrm{B}} T} \breve{\psi} \right\} \end{cases} \tag{6.185}$$

was abandoned when the distribution function in (6.6) was expanded into a power series with respect to the deviation of the mean electric potential $\psi(\boldsymbol{r}) - \breve{\psi}$ from a constant potential $\breve{\psi}$ and its linear term only was retained. Namely, the linear approximation is done by fixing the weak gauge degree of freedom in the mean electric potential.

In the linearized theory developed in Sect. 6.2, we postulated in (6.8) that the electric energy E of a macroionic dispersion was given by the integral of the energy density of the electric field over the effective region V. Then, we made the decisive assumption in (6.12) that the electric energy E can be approximated by the integral of the energy density over the whole region Ω of the dispersion. In an attempt to improve this approximation, Knott and Ford [11] calculated the excluded volume effect at the level of the Helmholtz free energy F.

Note that the electric field produced by the macroions in a macroionic dispersion has influence, in general, both in the effective region V and the region $\Omega - V$ occupied by the macroions. It is usual, however, to define the electric energy E by (6.8) by ignoring the contribution from the region $\Omega - V$ in investigating physical states in the region V. For this ordinary definition to be valid, physical states in the two regions must be sufficiently decoupled. To clarify the physical meanings of various approximation schemes from a general viewpoint, we define here the electric field energy E of the dispersion as the sum of the contributions from both regions V and $\Omega - V$.

Let us take a region $\mathcal{V}$ arbitrarily in the dispersion in the container with volume Ω and express the background dielectric constant in $\mathcal{V}$ generically as $\epsilon_{\mathcal{V}}$. Provided that an exact electric potential $\psi_{\mathcal{V}}(\boldsymbol{r})$ is known, the electric field energy in $\mathcal{V}$ is given by the integral

$$E^{\mathrm{el}}(\mathcal{V} : \psi_{\mathcal{V}}, \epsilon_{\mathcal{V}}) = \frac{\epsilon_{\mathcal{V}}}{8\pi} \int_{\mathcal{V}} [\nabla \psi_{\mathcal{V}}(\boldsymbol{r})]^2 \, \mathrm{d}\boldsymbol{r} \, . \tag{6.186}$$

Then the *total electric energy* of the macroionic dispersion is expressed by the sum of contributions from the two regions V and $\Omega - V = \sum_n \omega_n$ as follows:

$$E = E^{\mathrm{el}}(V : \psi_V, \epsilon_V) + \sum_n E^{\mathrm{el}}(\omega_n : \psi_n, \epsilon_n) \tag{6.187}$$

where $\psi_n(\boldsymbol{r})$ and ϵ_n are, respectively, the mean electric potential and dielectric constant inside the n-th particle with effective volume ω_n.

For our analysis, it is relevant to express the electric energy of the system in (6.187) as

$$E = E^{\mathrm{el}}(\Omega : \psi_V, \epsilon_V) - \sum_n \Delta_n \tag{6.188}$$

in terms of the integral over the simply-connected region Ω and the correction terms

$$\Delta_n = E^{\mathrm{el}}(\omega_n : \psi_V, \epsilon_V) - E^{\mathrm{el}}(\omega_n : \psi_n, \epsilon_n) \, . \tag{6.189}$$

To estimate the correction term Δ_n, we have to calculate $E^{\mathrm{el}}(\omega_n : \psi_V, \epsilon_V)$ with the mean electric potential ψ_V derived from the PB equation in the external effective region V and $E^{\mathrm{el}}(\omega_n : \psi_n, \epsilon_n)$ with the electric potential ψ_n inside the n-th macroion.

From this general viewpoint, we find that the degree of cancellation in the correction term Δ_n just corresponds to different schemes of approximation. The maximum cancellation in the correction terms, i.e., $\Delta_n = 0$, realizes the approximations made in (6.12). Therefore, this approximation is applicable to the dispersions in which the internal and external states of the macroions are strongly correlated. Contrastingly, the minimum cancellation in the correction term, i.e., $\Delta_n = E^{\mathrm{el}}(\omega_n : \psi_V, \epsilon_V)$, is almost equivalent to the Knott-Ford approximation [11]. Hence this type of approximation should be applied to dispersions consisting of such macroions whose internal and external states are strongly decoupled.

The larger the surface charges of the effective particles, the better the shielding of the inner region ω_n occurs from the outer region V. Such shielding, however, does not necessarily work well for every kinds of effective macroions. In order to estimate the effect of the shielding, it is relevant to divide the second term on the right-hand side of (6.189) into contributions from the layer of condensation $\omega_n - \omega_{0n}$ and the naked macroion ω_{0n}.

In the case of dispersions consisting of colloidal particles with large analytical charges, it is reasonable to assume that the inner regions of the particles are isolated from the outer region, and that the layer of condensation and the outer diffuse layer are rather closely related with each other. Accordingly, the contributions from the layers of condensation, i.e., $\sum_n E^{\mathrm{el}}(\omega_n - \omega_{0\mathrm{n}} : \psi_n, \epsilon_n)$, work to sizably reduce the first term on the right-hand side of (6.189). This cancellation mechanism between the two terms in (6.189) is much more enhanced in dilute dispersions of effective particles with large analytical charges.

Therefore, it was permissible to postulate the approximation scheme in (6.12) for the dilute dispersions of effective colloidal particles treated in Sect. 6.2.

In comparison with colloidal particles, the flexible ionic polymers discussed in Chap. 3 are unlikely to have large surface charges. To regard such an entity as a spherical particle with an average radius of gyration, it is required to pre-average its internal degrees of freedom. Accordingly, we should consider that the internal and external states are related rather closely in such systems with pre-averaged effective particles. To describe dispersions of such quasi-open effective particles, there is one simple and plausible picture. It is to postulate that the internal electric state in such effective particles is approximately the same as that of the external region. With this picture, the scheme with the assumption $\Delta_n \approx 0$ turns out to be a better approximation for the dispersions of quasi-open effective particles.

In this book, we postulate *a posteriori* that the correction terms in (6.189) do not take large values, such that the condition

$$E^{\mathrm{el}}(\Omega : \psi_V, \epsilon_V) \gg \sum_n \Delta_n \tag{6.190}$$

holds. With this condition validating the approximation scheme in (6.12), we succeeded in obtaining the electric energy in such a compact form that it enabled us to derive the adiabatic pair potentials in concise expressions. As the results of the Knott-Ford calculation proved, the inclusion of the correction terms $\Delta_n = E^{\mathrm{el}}(\omega_n : \psi, \epsilon)$ into the theory completely deprived the pair potential U^{F} of its conciseness.

Apparently, these arguments on the correction term Δ_n still remain at a crude and primitive stage. Therefore, it is necessary to stimulate theoretical work on the excluded volume effects further. For this purpose, it is also necessary to carry out experimental studies of various macroionic dispersions consisting of effective particles with different types of excluded volume effects.

Here it seems appropriate to look over an approximate aspect of the concepts and relations of ordinary thermodynamics used in the present theory of macroionic dispersions. In the ordinary thermodynamics, the Gibbs free energy of dilute solutions is the sum of the chemical potentials of all solutes. Using this definition selectively, we calculated the "Gibbs free energy G'' of macroionic dispersions" by summing up the chemical potentials of the small ions and the surface charge numbers. Reflecting the properties of the system, the resultant quantity G'' naturally includes effects of inhomogeneousness and non-additivity of the system [11]. This is an essential feature of the present

[11] Woodward [37] made an analysis of the Gibbs free energy $G = G''$ derived in the present scheme and correctly found the effects of violation of the homogeneousness. Nevertheless, he misunderstood his result and insisted that *the inhomogeneity of the microions due to the presence of the charged colloids invalidates the key assumption of the theory that the Gibbs free energy is a first-order homogeneous function of the particle numbers* [38].

scheme of thermodynamics, irrespective of whether or not the theory is linearized, for macroionic dispersions. The search for a new theory of macroionic dispersions with a more careful use of the ordinary thermodynamics is a problem to be solved in future.

The present formalism of mean field theory will provide a new basis for investigating a variety of phenomena of macroionic dispersions. However, there still remain many challenging problems to be solved, such as a compact estimation of the excluded volume term, comparison with the local density functional formalism [39,40] and modifications of the PB equation [41–43]. In the late 1990's, some people claimed that gas/liquid-like separations can be described by a DLVO type repulsive potential with a state-dependent volume term [44–49] arising from the Helmholtz free energy in the linearization approximation to the PB equation. However, more recent papers [50, 51] have shown that predictions of gas/liquid-like separation in the *volume term theory* can be clearly traced back to artifacts due to the application of the linearization scheme beyond its range of validity. As shown by Tamashiro and Schiessel, the phase transitions predicted under linearized theories at the level of the Helmholtz free energy always point towards the state-dependent volume term which is also responsible for the spurious phase transition that they observed by linearization of the PB equation in a Wigner-Seitz cell model. Such observations emphasize the importance of looking for a more effective theory beyond linearized approximations and a mean field description.

References

1. Yamanaka J, Yoshida H, Koga T, Ise N, Hashimoto T (1999) Langmuir 15:4198
2. Schaefer DW (1977) J Chem Phys 66:3980
3. Alexander S, Chaikin PM, Grant P, Morales GJ, Pincus P (1984) 80:5776
4. Ito K, Ise N, Okubo T (1985) J Chem Phys 82:5732
5. Hachisu S, Kobayashi Y (1974) J Coll Interface Sci 46:470
6. Langmuir I (1938) J Chem Phys 6:873
7. Sogami I (1983) Phys Lett A 96:199
8. Sogami I, Ise N (1984) J Chem Phys 81:6320
9. Sogami IS (2003) e-print cond-mat/0305674; Sogami IS, Smalley MV, Shinohara T (2005) Prog Theor Phys 113:235
10. Schwinger J (1970) Particles, sources and fields. Addison-Wesley, New York, vol 1
11. Knott M, Ford IJ (2001) Phys Rev E 63:031403; (2002) ibid 65:061401
12. van Roij R, Dijkstra M, Hansen J-P (1999) Phys Rev E 59:2010
13. Overbeek JThG (1987) J Chem Phys 87:4406
14. Levine S (1939) Proc Roy Soc London A170:145, 165; (1938) J Chem Phys 7:831
15. Levine S, Dube GP (1939) Trans Faraday Soc 35:1125, 1141; (1940) Phil Mag (7) 29:105; (1942) J Phys Chem 46:239
16. Verwey EJW, Overbeek JThG (1948) Theory of the stability of lyophobic colloids. Elsevier, Amsterdam
17. Hirschfelder JO, Curtiss CF, Bird RB (1954) Molecular theory of gases and liquids. Wiley, New York. Table 13.9
18. Chistyakov IG (1967) Soviet Phys-Uspekhi 9:551
19. Smalley MV, Thomas RK, Braganza LF, Matsuo T (1989) Clays Clay Min 37:474; Braganza LF, Crawford RJ, Smalley MV, Thomas RK (1990) ibid 38:90
20. Smalley MV (1990) Mol Phys 71:1251
21. Landau LD, Lifshitz EM (1959) Statistical physics. Pergamon, New York, §42
22. Dirac PAM (1950) Can J Math 2:129; (1967) Lectures on quantum mechanics. Academic Press, New York
23. Walker GF (1960) Nature 187:312
24. Williams GD, Moody KR, Smalley MV, King SM (1994) Clays Clay Min 42:614; Hatharasinghe HLM, Smalley MV, Swenson J, Hannon AC, King SM (2000) Langmuir 16:5562
25. Crawford RJ, Smalley MV, Thomas RK (1991) Adv Colloid Interface Sci 34:537

26. Derjaguin BV (1934) Kolloid Z 69:155; Acta Physicochem URSS (1939) 10:333
27. Pieranski P (1983) Contemp Phys 24:25
28. Sogami IS, Shinohara T, Smalley MV (1992) Mol Phys 76:1
29. Sogami IS, Shinohara T (2001) Colloids Surfaces A 190:25; Shinohara T, Smalley MV, Sogami IS (2003) Mol Phys 101:1883
30. Erdélyi A, Magnus W, Oberhettinger F, Tricomi FG (1953) Higher transcendental functions. McGraw-Hill, New York, vol 2
31. Byrd PE, Friedman MD (1971) Handbook of elliptic integrals for engineers and scientists. 2nd edn, Springer, Berlin, Heidelberg, New York
32. Carlson BC (1977) Special functions of applied mathematics. Academic Press, New York, Chap. 9
33. Carlson BC (1977) SIAM J Math Anal 8:231; (1978) ibid 9:524; Zill DG, Carlson BC (1970) Math Comput 24:199
34. Carlson BC (1979) Numer Math 33:1
35. Press WH, Teukolsky SA (1990) Comput Phys 4:92; Press WH, Teukolsky SA, Vetterling WT, Flannery BP (1996) Numerical recipes in fortran 77, The art of scientific computing (Volume 1 of Fortran Numerical Recipes), 2nd edn. Cambridge University Press, Cambridge
36. Low PF (1987) Langmuir 3:18
37. Woodward CE (1988) J Chem Phys 89:5140
38. van Roij R, Evans R (1999) J Phys: Condens Matter 11:10047
39. Trizac E, Hansen J-P (1997) Phys Rev E 56:3137; Leote de Carvalho RJF, Trizac E, Hansen J-P (2000) Phys Rev E 61:1634; Hansen J-P, Löwen H (2000) Ann Rev Phys Chem 51:209
40. Trizac E (2001) Langmuir 17:4793
41. Borukhov I, Andelman D, Orland H (1997) Phys Rev Lett 79:435
42. Trizac E, Raimbault J-L (1999) Phys Rev E 60:6530
43. Neu JC (1999) Phys Rev Lett 82:1072
44. Beresford-Smith B, Chan DYC, Mitchell DJ (1985) J Coll Interface Sci 105:216
45. Chan DYC (2001) Phys Rev E 63:061806
46. Grimson MJ, Silbert M (1991) Mol Phys 74:397
47. van Roij R, Hansen J-P (1997) Phys Rev Lett 79:3082; van Roij R, Dijkstra M, Hansen J-P (1999) Phys Rev E 59:2010
48. Warren PB (2000) J Chem Phys 112:4683
49. Chan DYC, Linse P, Petris SN (2001) Langmuir 17:4202
50. von Grünberg HH, van Roij R, Klein G (2001) Europhys Lett 55:580
51. Tamashiro MN, Schiessel H (2003) J Chem Phys 119:1855

7

Viscometric Properties of Dilute Ionic Polymer Solutions and Colloidal Dispersions

7.1 Introductory Remarks

The viscosity of dilute solutions of polymers potentially provides information on the molecular weight, polymer conformation, and chain interaction. Early viscosity measurements of flexible ionic polymers were interpreted in terms of a "rod-model". In the present chapter, we discuss how this model was derived for ionic polymers and clarify problems associated with this model.

The viscosity coefficient η of a dilute solution of *non-ionic* polymer (polymer concentration c) is related to that of solvent η_0 by the relation

$$\frac{\eta - \eta_0}{\eta_0 c} \equiv \frac{\eta_{\rm sp}}{c} = [\eta] + k'[\eta]^2 c + \cdots, \tag{7.1}$$

where $[\eta]$ is the intrinsic viscosity, $\eta_{\rm sp}$ the specific viscosity, $\eta_{\rm sp}/c$ the reduced viscosity, and k' Huggin's coefficient. $[\eta]$ is related to the molecular weight M by

$$[\eta] = KM^{\alpha}, \tag{7.2}$$

where K and α are constants depending on polymer, solvent, and temperature. This relation, known as the Houwink-Mark-Sakurada (HMS) equation, has been important in characterizing polymers since the early days of polymer sciences and is discussed in [1]. For large M, the exponent α is known to take values of $2, 0.8 \sim 0.5$, and 0 for rod, random-coil, and compact particles, respectively.

7.2 Viscosity of Dilute Solutions of Flexible Ionic Polymers

The reduced viscosity $\eta_{\rm sp}/c$ of non-ionic polymers increases linearly with c at small values of c, as predicted by (7.1). On the other hand, the $\eta_{\rm sp}/c$-c plot of ionic polymers has a large negative slope when the concentration

of coexisting salt is low as shown in Fig. 7.1. Fuoss proposed the following empirical relationship [2]

$$\frac{\eta_{\mathrm{sp}}}{c} = \frac{A}{1 + Bc^{1/2}} + D, \tag{7.3}$$

where A, B, and D are constants, and $[\eta]$ is determined by $(A + D)$. When η_{sp}/c is extrapolated to $c = 0$, the HMS exponent α was found to be 0.82 and 1.87 for unneutralized and completely neutralized polymethacrylate (PMA), respectively. Fuoss concluded that the unneutralized PMA was random-coiled while the ionized sample assumed a rod-like conformation *at infinite dilution*. He further claimed that the dissociation of the ionizable groups was enhanced, with decreasing c, resulting in a stronger repulsion between ionized groups inside the macroion domain, chain swelling, and hence a higher η_{sp}/c. This interpretation was widely accepted at that time, though these findings have often been misconstrued. Later Fuoss' "infinite dilution" condition was ignored and the belief became established that "flexible ionic polymer chains" are generally stretched out into a rod-like configuration even at finite concentrations. Intensive theoretical studies have since been carried out on the rod-model for ionic polymers, despite the weak experimental foundation for this model. We would not discuss these in the present monograph.

Soon after the Fuoss extrapolation for $[\eta]$ was proposed, a small number of investigators performed very cautious experiments and claimed that the extrapolation was questionable. They found that the η_{sp}/c value did not monotonically increase with decreasing c, but it decreased after passing a *maximum* at a low c. It is true that quantitative comparison of the viscosity data was difficult because the results were sensitive to trace ionic impurities [3]. Figure 7.2 shows recent results with sodium poly(styrene sulfonate)s (Na-PSS) [4]. For a NaPSS with $M_{\mathrm{W}} = 1.7 \times 10^6$, the maximum is located at 6×10^{-3} g L^{-1}, above which η_{sp}/c decreased in agreement with curve 1 of Fig. 7.1. The maximum is an outstanding feature of high-molecular-weight samples, and is clearly incompatible with the Fuoss extrapolation. Taking the maximum as reliable, the observed η_{sp}/c was extrapolated to $c = 0$ to obtain $[\eta]$, which was plotted against M in Fig. 7.3 [1]. The line A gives $\alpha = 1.6$, while if we take the line B we obtain $\alpha = 1.2$. Notably, this range of values is

[1] Low-molecular-weight compounds and biopolymers have definite molecular weights. On the other hand, the molecular weights of polymers synthesized chemically have a distribution. Thus, their molecular weights are averaged quantities, depending on the methods used. The osmometry and light scattering give the number-average molecular weight M_{N} and weight-average molecular weight M_{W}, respectively, which are defined by

$$M_{\mathrm{N}} = \frac{\sum M_m N_m}{\sum N_m},$$

$$M_{\mathrm{W}} = \frac{\sum M_m^2 N_m}{\sum M_m N_m},$$

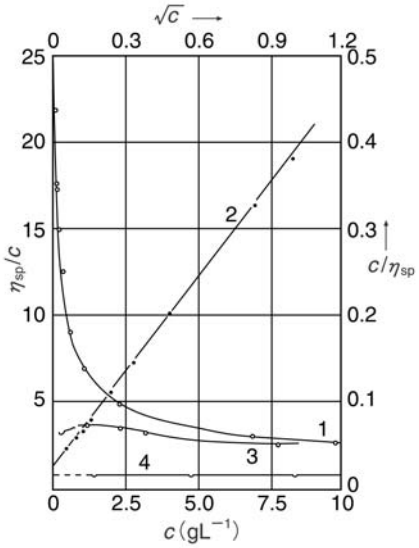

Fig. 7.1. Viscosity curve for flexible ionic polymer. Sample: poly(vinyl pyridine) quaternized with butyl bromide ($PVPBu^+ Br^-$). Solvent: H_2O (1), 10^{-3}mol L^{-1}KBr aqueous solution (3), 3.35×10^{-2} mol L^{-1} KBr aqueous solution (4). Curve 2: test of (7.3) with coordinates right and above. Taken from [2] with the permission of Springer Verlag

inconsistent with $\alpha = 2$. On the same line of reasoning, Vink reported $\alpha = 1.1$ for sodium salts of carboxymethyl cellulose (CMC), which is considered to be more rigid than NaPSS [6]. In our view, this makes the rod model suspect, even in the idealized infinite dilution limit.

While the $[\eta]$-M relation needs to be examined also for other polyelectrolytes, the presence of the maximum in the η_{sp}/c-c plots is not an artifact and the treatment given above for NaPSS is an improvement over the Fuoss extrapolation in that the maximum was taken into account to determine $[\eta]$. According to the conventional interpretation, the result $\alpha \neq 2$ implies that rod-model for macroions is *not* justified. It is of interest to point out that this conclusion is in accord with those by Butler [3], Krause [7], and Zhang [8]. Bultler et al. measured the sedimentation coefficient for NaPSS and pointed out that the end-to-end distance of PSS chain [2] was smaller than one half

where M_m and N_m are the molecular weight and number of polymer species of a degree of polymerization m, respectively. For details about these notational conventions and further discussion of these basic polymer properties, see standard textbooks on polymer chemistry such as [5].

[2] Flexible polymer chains may assume various conformations in solutions. Thus, the extension of the polymer chains is discussed in terms of the mean-square end-to-end distance, or the mean-square radius of gyration.

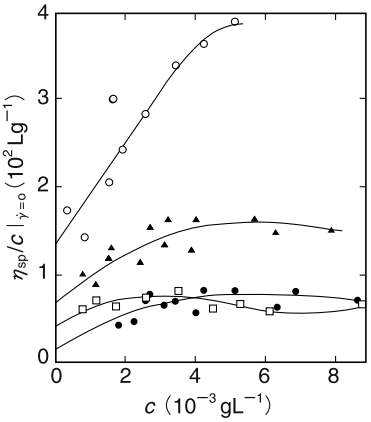

Fig. 7.2. The maximum in η_{sp}/c-c plots. Sample: sodium poly(styrene sulfonate)s. ○: weight-average molecular weight $M_W = 1.7 \times 10^6$, degree of P sulfonation $DS = 0.88$, ▲: $M_W = 1.1 \times 10^6$, $DS = 0.81$, □: $M_W = 6.7 \times 10^5$, $DS = 0.73$, ●: $M_W = 3.7 \times 10^5$, $DS = 0.85$. Solvent: H_2O, temperature: 25°C. The full lines are by the first-order least-squares method. Taken from [4] with the permission of the American Chemical Society

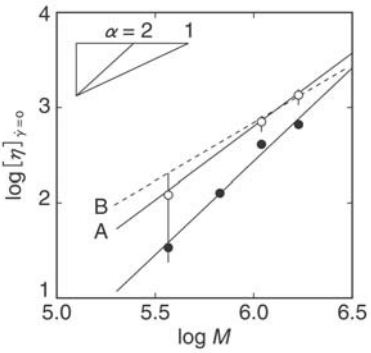

Fig. 7.3. The intrinsic viscosity and molecular weight for sodium poly(styrene sulfonate)s. Solvent: H_2O, temperature: 25°C. ○: observed. The lines A and B correspond to $\alpha = 1.6$ and 1.2 of the HMS equation, respectively. Filled circles: Kirkwood-Auer theory. Taken from [4] with the permission of the American Chemical Society

of the fully stretched length. Krause et al. demonstrated for NaPSS solutions (10^{-4} g L^{-1}) without salt that the scattered intensity of light showed an angular dependence, which was close to the theoretical value for Gaussian chains and quite different from the prediction of the rod-model. Though at a much higher concentration (40 g L^{-1}), Zhang et al. showed by the neutron scattering that the radius of gyration of PSS chains was smaller than the theoretical value for a rod, although a worm-like chain model description intermediate between a random coil and rod was claimed to be a reasonable description of the chain dimension in the low salt limit.

Since the experimental rationale for rod-model is not well founded, we must reconsider the interpretation of the steep increase of η_{sp}/c with decreasing c (Curve 1, Fig. 7.1). This tendency was interpreted as implying that the dissociation of the ionizable groups was enhanced (to the complete dissociation at the infinite dilution) with decreasing concentration, causing a stronger repulsion between ionized groups and chain stretching. It appears that recent experimental findings do not support the interpretation, either. Notably a similar dependence of the reduced viscosity on the concentration was found for colloidal particles and spherical polyelectrolyte gels [9, 10], which cannot exhibit any appreciable swelling because of cross-linking inside the particles. Moreover, η_{sp}/c has been observed to increase with decreasing c for polymers having only one ionizable group at one end of the polymer chain [11]. In solutions of such telechelic polymers, *intra*molecular (electrostatic) interaction is definitely absent. Thus, the accepted view that the change in η_{sp}/c was due to the variation in chain expansion must also be reconsidered.

It is noteworthy that the solution viscosity of polyelectrolytes is strongly influenced by interactions (1) between ionized groups, (2) between ionized groups and nearby counterions associated in the macroion domain, and (3) between macroions. The first factor was considered by Fuoss and acts in such a way to stretch the macroion chain. If we are interested in the intrinsic viscosity itself, not in the concentration dependence of reduced viscosity, the third factor may be put out of consideration.

This important second factor was not considered by Fuoss. As was discussed in Chaps. 3 through 6, cations attract cations through the intermediary of anions, as exemplified by formation of triple ion, quadrupole, and higher ionic aggregates at concentrations higher than the Debye-Hückel range. Similar association is anticipated to take place between counterions and the ionized groups inside the macroion domain, because the "ionic" concentration inside the domain is unexpectedly high (See Chap. 3, Sect. 3.1.2). The intramacroion association would cause folding-up of the polymer chain in counteraction to the repulsive interaction between the ionized groups. Unfortunately, experiment-based information on the dimensions of flexible macroions is very limited. A systematic study of this basic problem remains to be considered.

Electrostatic interactions play an important role in the viscometric properties of ionic polymer solutions and colloidal dispersions. We next consider these charged systems comparatively.

7.3 Viscosity of Dilute Dispersions of Ionic Colloidal Particles

Unlike flexible polymers, the colloidal particles are not highly deformable. Analysis is then simplified, particularly when spherical particles are chosen. The information obtained for the colloidal particles can then be useful in judging the pros and cons of the interpretation mentioned in the preceding sections on flexible ionic polymers.

7.3.1 The Einstein Law of Viscosity of Dispersions of Spherical Particles

On the purely hydrodynamic consideration, Einstein derived the following relation on the reduced viscosity of non-interacting rigid spheres [12] [3],

$$\frac{\eta_{sp}}{\phi} = 2.5, \tag{7.4}$$

where ϕ is the volume fraction of spheres. This equation tells us that the reduced viscosity does not depend on the particle size and concentration but is equal to 2.5. The theory corresponds to $\alpha = 0$ in (7.2) and is known to be valid for some solutions such as aqueous sucrose solution and rubber latex dispersions [13].

Later the Einstein theory was found not to be valid for starch, cellulose, and linear paraffins. The triggered theoretical consideration about molecular conformation in relation to viscosity are led early on to the HMS equation via Staudinger's relation. Staudinger had earlier postulated rod-like conformation of polymers, but later measurements showed that this interpretation was not generally true as in the case of Fuoss for polyelectrolytes. It is of interest to mention here a work by Onsager [14], in which he derived a viscosity relation for ellipsoids and suggested from comparison with the measured viscosity of paraffin solutions that such molecules do not retain a straight linear shape in solution.

7.3.2 Experimental Results of Dispersions of Latex Particles and Microgels

Now it is possible to prepare colloidal particles, whose radius a and size distribution are well characterized, and to purify them extensively. It is of particular interest to examine the Einstein law using such particles. In this section, we discuss recent experimental data reported for latex particles and ionic microgels [9, 10].

[3] The reduced viscosity here is given by ϕ , not by concentration c as was the case for flexible polymers.

Table 7.1 gives physical properties of the ionic latex particles employed. The a values are practically fixed (60 nm) and the analytical charge density σ_a is varied. According to dynamic light scattering, the dispersion of 1B76 showed *two peaks* in the structure factor-scattering vector profile at $\phi = 0.002$, and the Bragg distance from the peak position $2D_{exp}$ was 0.70 μm, while the average distance from concentration $2D_0$ was 0.79 μm, suggesting the existence of the two-state structure. For all samples, the η_{sp}/ϕ values decreased with increasing rate of shear $\dot{\gamma}$ (shear-thinning effect). When the coexisting NaCl concentration is lower than 10^{-4} mol L^{-1}, the η_{sp}/ϕ values were much higher than the Einstein prediction. Only at 10^{-3} mol L^{-1}, the theory agreed with the observation. In Fig. 7.4 is shown the viscosity data of dispersions of a latex having a relatively low charge density. The deviation from the theory and the shear-thinning effect are clear. In the ϕ range in Fig. 7.4, η_{sp}/ϕ increased with increasing ϕ. The deviation from the Einstein law and the shear rate dependence would be due to the electrostatic interaction between particles and the formation of localized ordered structure. As a matter of fact, this interaction and the local order are destroyed by the addition of a neutral salt. The dispersion of 1B76 showed a Newtonian flow at 5×10^{-5} mol L^{-1} and the viscosity approached the Einstein prediction, as shown in Fig. 7.5. The reduced viscosity extrapolated to $\dot{\gamma} = 0, \eta_{sp}/\phi\,|_{\dot{\gamma}=0}$, is shown at various NaCl concentrations and ϕ in Figs. 7.6 and 7.7.

Table 7.1. Radius of latex particles and analytical charge density

	a (nm)	Charge number Z_a (10^3/particle) [a]	Charge density σ_a (μC cm^{-2})
MS-1	65	12.1	3.65
MS-5	55 [b]	1.6	0.82
1B76	55 [b]	2.1	0.88
N-100	60 [c]	16.1	5.64

[a] by conductometric titration.
[b] by electron micrograph.
[c] from the brochure of the producer.

Figures 7.6 and 7.7 show that *the higher the charge density, the lower the reduced viscosity.* This variation disappears at high salt concentrations. Furthermore, a maximum exists in the $\eta_{sp}/\phi\,|_{\dot{\gamma}=0}$-$\phi$ curves for 1B76 and MS-5 (Fig. 7.7). This is qualitatively similar to the observations on flexible ionic polymers [4], suggesting that the sharp increase of the reduced viscosity with decreasing concentration of flexible polymers is *not* due to stretching-out of the polymer chains.

[4] The maximum was supposedly located at much lower concentrations for MS-1 and N-100. Though this seems to be due to higher charge densities of these samples, a systematic study is yet to be done using samples of various charge densities.

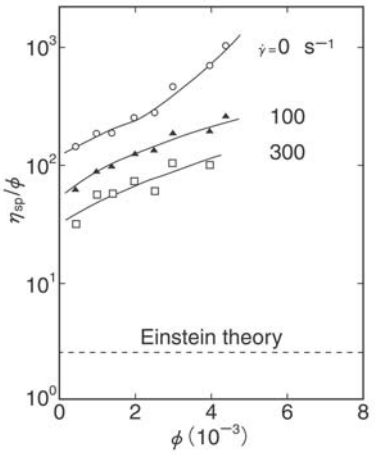

Fig. 7.4. Reduced viscosity as a function of the volume fraction of particles. Sample: MS-5, medium: H_2O, salt concentration $C_s = 0$, 25°C. The broken line represents the Einstein law. Taken from [9] with the permission of Academic Press

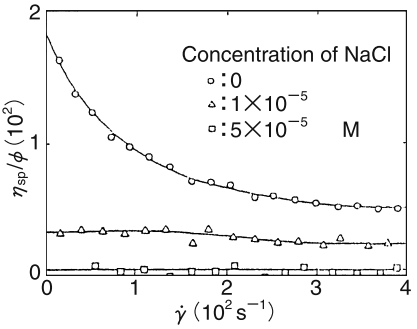

Fig. 7.5. Dependence of the reduced viscosity on the shear rate $\dot{\gamma}$. Sample: 1B76, $\phi = 4.1 \times 10^{-3}$, 25°C. Taken from [9] with the permission of Academic Press

The size of the microgels used by Antonietti et al. is believed to be constant with varying concentration. As shown in Fig. 7.8, the η_{sp}/c decreases with increasing c, in agreement with the observation on latex and flexible ionic polymers.

According to Fig. 7.8, *the larger the particles, the lower the viscosity.* While the degree of sulfonation is fixed at about 70%, η_{sp}/c decreases with increasing radius a. According to (7.2), the viscosity is expected to increase with increasing molecular weight, and hence hydrodynamic volume. The a dependence of the viscosity observed is therefore rather surprising and shows that

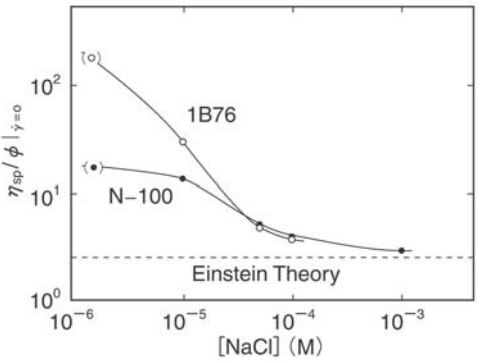

Fig. 7.6. Dependence of $\eta_{sp}/\phi|_{\dot{\gamma}=0}$ on NaCl concentration C_s. $\phi = 4.0 \times 10^{-3}$, 25°C. The data in ( ) is the viscosity in H_2O without NaCl ($[H^+] = 1.4 \times 10^{-6}$ mol L^{-1}). Taken from [9] with the permission of Academic Press

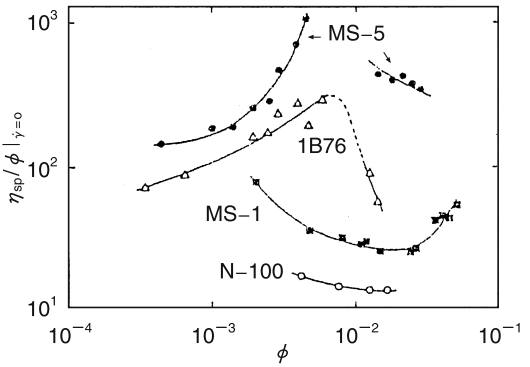

Fig. 7.7. Dependence of $\eta_{sp}/\phi|_{\dot{\gamma}=0}$ on ϕ. $C_s = 0, 25$°C. Taken from [9] with the permission of Academic Press

the viscosity of ionic polymer solutions is determined by special factors that do not come into question for non-ionic systems.

7.3.3 Ionic Atmosphere and Its Distortion (The Primary Electroviscous Effect)

As discussed in Chap. 2, a spherical ionic atmosphere is formed around a central ion in solvent at rest as a result of the balance of the kinetic factor and electrostatic interaction. Its radius κ^{-1} is given by (2.35). Though not at all mentioned in the original paper [15], the significance of the Debye approach based on the Poisson-Boltzmann equation has been demonstrated to be much deeper than originally considered. Detailed discussion of this fundamental

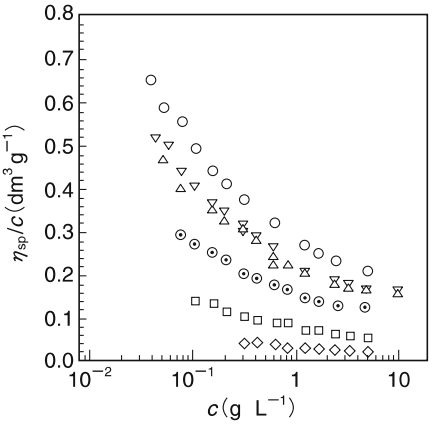

Fig. 7.8. Concentration dependence of the reduced viscosity of micro-gel particles of various radii a. ○: 11.9 nm, ▽: 25.1, △: 27.3, ⊙: 37.4, □: 52.5, ◇: 67.8. Taken from [10] with the permission of the American Institute of Physics

problem is given in the textbooks by Harned and Owen [16] and Fowler and Guggenheim [17]. The time-average ionic distribution is determined by the thermal motion of ions and ionic interaction. The quantity of ionic charges in the shell of a thickness dr of the ionic atmosphere is shown to be at the maximum at the distance κ^{-1}. The atmosphere does not represent a hard shell, which is impenetrable to ions, as imagined from the effective hard sphere discussed in Chap. 4, Sect. 4.2.1. When the solvent flows in a direction, the thermal motion of ions is affected so that the atmosphere is distorted. Though the distortion is small in the microscopic scale, it has a pronounced influence on macroscopic physical properties of the ionic solutions such as the viscosity.

Booth theoretically considered the effect of the distortion (the primary electroviscous effect) for a rigid sphere in dispersion on the basis of the equations of continuity and motion of solvent and the equation of motion of ions [18]. The assumptions made were that (1) the sphere was non-conducting, and the surface charges were fixed without surface conduction, (2) the supporting electrolyte was symmetric, (3) κ^{-1} was smaller than the average interparticle distance ($2D_0$), and (4) the solvent was incompressible. No interparticle interaction was taken into consideration according to the assumption (3). The final result is

$$\frac{\eta_{\mathrm{sp}}}{\phi} = 2.5\left[1 + C_1\left(\frac{e^2 Z_{\mathrm{n}}}{\varepsilon a k_{\mathrm{B}} T}\right)^2 Z(\kappa a)\right], \tag{7.5}$$

where

$$C_1 = \left(\frac{\varepsilon k_{\mathrm{B}} T}{\eta_0 e^2}\right)\frac{\sum n_i z_i^2 w_i^{-1}}{\sum n_i z_i^2} \tag{7.6}$$

and Z_n is the net charge number of the particles, n_i, z_i, and w_i are the concentration, valency, and mobility of the (micro)ion i, and $Z(\kappa a)$ is a monotonically decreasing function of κa, representing the deformability of the ionic atmosphere. $Z(\kappa a) \approx 3/2\pi\kappa^4 a^4$ for large κa, while $Z(\kappa a) \approx 1/200\pi\kappa a + 11\kappa a/3200\pi$ for small κa.

The first term on the right-hand side of (7.5) corresponds to the Einstein law and the second to the electroviscous effect. The latter becomes more pronounced at small κa, or when the radius of the atmosphere is large. This is understandable since the solvent velocity is zero at the particle surface and becomes larger with increasing distance.

We next compare this theory with experiments. Using colloidal particles shown in Table 7.2, Yamanaka et al. examined the κa dependence of the function $Z(\kappa a)$ with varying salt concentrations (κ) at a fixed a and with varying a at a constant κ [19]. Figure 7.9 shows the results for $\phi = 3.5 \times 10^{-3}$. The experimental points can be represented by a single curve, implying that the electroviscous effect depends on the product κa. The theoretical curve is seen to agree with experiments at large κa, which is reasonable in light of the assumptions involved in the derivation of (7.5).

Goring et al. [20] and Stone-Masui et al. [21] reported that the electroviscous effect became smaller with increasing ionic strength for polystyrene latex dispersions. Masui concluded that the agreement between the theory and experiments is satisfactory in the κa range between 0.7 and 10.

Table 7.2. Properties of colloidal particles

Sample	a (nm)	$Z_n(10^3$/particle)	$Z_a/a(\mathrm{nm}^{-1})$
KE-E10 [a]	40	0.12	3.0
KE-E20 [a]	90	0.81	9.0
KE-P30W [a]	140	0.98	7.2
N-1000 [b]	500	94	188

[a] colloidal silica particle.
[b] polystyrene-based latex.

The observed reduced viscosity of dispersions of three latexes at a constant radius is compared with the theoretical results in Table 7.3. The agreement is gratifying for the two samples having low charge numbers but substantial deviation arises for highly charged N-100.

Though systematic study is yet to be done on various solvents, we discuss here the recent results for ethylene glycol (EG)-H_2O systems [22]. The physical properties of the binary mixtures are given in Table 7.4. The net charge number Z_n is determined from the number of H^+, which contributes to conductance, the observed conductance and the w_{H^+} values. For 1P30, Z_n is $30 \sim 35$ at [EG] = 40 vol%, being lower than the value in H_2O. From the ε value in Table 7.4, it is shown that κ^{-1} is practically constant for [EG] <

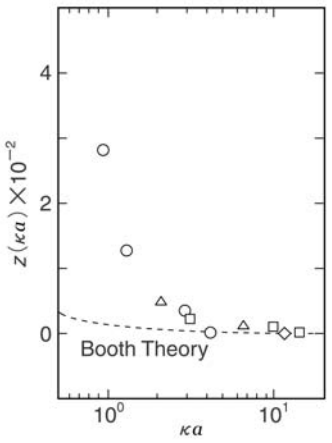

Fig. 7.9. Influence of the particle radius and salt concentration on the electroviscous effect. Samples: KE-E10 (○, $a = 40$ nm), KE-E20 (△, 90 nm), KE-P30W (□, 140 nm), N-1000 (◇, 500 nm). $\phi = 3.5 \times 10^{-3}$. Broken curve: Booth theory. Taken from [19] with the permission of the American Physical Society

Table 7.3. Net charge number and the electroviscous effect

Latex	$Z_n(10^3/\text{particle})$	$C_s(\text{mol L}^{-1})$	$(\eta_{sp}/\phi)_{expt}$ [a]	$(\eta_{sp}/\phi)_{theo}$
1P30 ($a = 55$ nm)	0.3	5×10^{-5}	3.1	2.6
		10^{-4}	3.0	2.6
1B76 (55 nm)	0.8	5×10^{-5}	2.9	3.4
		10^{-4}	2.9	3.0
N-100 (60 nm)	2.8	5×10^{-5}	3.6	11.0
		10^{-4}	3.1	7.2

[a] Extrapolated values to $\phi = 0$.

40%. As is shown in Table 7.5, the agreement between $(\eta_{sp}/\phi)_{theo}$ and the observed value is gratifying, though the theory gives systematically lower values. Further study is necessary to see whether the discrepancy is significant or not.

The influence of counterions on the viscosity of colloidal dispersions has not extensively been studied. We discuss briefly the preliminary results by Yamanaka et al. on H^+, Na^+, and $(CH_3CH_2)_4N^+$ (Et_4N^+) [23]. The degrees of association of these counterions are assumed to be the same, and thus Z_n does not depend on the counterions. The equivalent conductivities for Na^+ and Et_4N^+ are 50.10 and 32.66 S cm^2 mol^{-1}, respectively. That for H^+ is inferred to be about the same as that for Na^+ on the basis of the geometrical

Table 7.4. Physical properties of ethylene glycol-water mixtures at 25°C.

			w (S cm^2 equiv^{-1})			
[EG] vol%	ε	η_0 (cPs)	w_{H^+}	w_{K^+}	w_{Cl^-}	ρ(g cm^{-3})
0	78.5	0.89	349.8	72.4	69.3	0.997
20	72.2	1.51		47.1	46.4	1.026
40	65.6	2.60	153.0	28.0	28.0	1.055
60	57.7	4.59	68.4	16.7	16.7	1.079
80	48.5	8.52	28.5	8.7	8.7	1.100
100	37.7	16.74	24.1	4.8	4.8	1.117

Table 7.5. Electroviscous effect in ethylene glycol-water mixtures at 25°C and 10^{-5}mol L^{-1} KCl

[EG] vol%	$(\eta_{sp}/\phi)_{expt}$ [a]	$(\eta_{sp}/\phi)_{theo}$
0	3.6	2.9
20	4.0	
40	3.5	2.7

[a] Latex 1P30 ($a = 55$ nm), extrapolated to $\phi = 0$.

size [5]. The viscosity values calculated using these data and those observed are compared in Table 7.6. The agreement is qualitatively satisfactory.

Table 7.6. Electroviscous effect for three counterions

Counterions	$(\eta_{sp}/\phi)_{expt}$ [a]	$(\eta_{sp}/\phi)_{theo}$
H^+	3.7	
Na^+	4.1	6.0
Et_4N^+	5.2	7.1

[a] Latex N-100 ($a = 55$ nm), $C_s = 5 \times 10^{-5}$ mol L^{-1}, extrapolated to $\phi = 0$.

The above consideration shows that the Booth theory can account for the observed viscosity when κa is large and Z_n is small. The deviation from the Einstein law may be ascribed to the distortion of the ionic atmosphere.

Theoretical consideration for small κa is still lacking and is awaited for.

When the particle concentration is high, the interparticle interaction has to be considered (secondary electroviscous effect). Unfortunately, no satisfactory theory has been formulated. The viscosity increase due to deformation of particles is called the tertiary electroviscous effect, which should not be as important for colloidal particles as for flexible ionic polymers. It is inferred that the localized ordered structure becomes modified (deformed or rotated) under

[5] The apparent equivalent conductivity of H^+ is 349.81 S cm^2 mol^{-1}. The high conductivity is due to the proton-jump mechanism. The value mentioned in the text is for the mobility of H^+ when it migrates as a unit under electric field.

shear field, causing higher viscosity of macroionic systems. As schematically shown in Fig. 7.10, the solvent flow produces a torque to rotate the structure. Because the potential well is very shallow, particles near the surface of the structure can easily fall off under flow. In other words, the structure undergoes deformation. This factor seems to also contribute to viscosity and to play an important role in the shear-thinning effect demonstrated in Fig. 7.5. It would be highly plausible that this factor is also influential for flexible ionic polymers. Systematic study on the correlation between the localized structure and viscosity is needed.

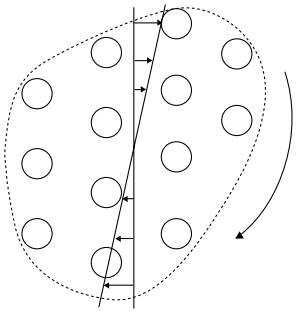

Fig. 7.10. Local structure under flow.

7.4 Summary

In this chapter, we reviewed experimental measurements and conceptual viewpoints previously considered to interpret and understand solution viscosity of flexible ionic polymers. We first discussed the origin of the widely accepted rod-model and pointed out several problems that require the model to be reconsidered. It was remarked that the electrostatic interaction between ionized groups and nearby counterions in the macroion domain had been overlooked. In light of the complete absence of theoretical and experimental elucidation of this interaction, it is not possible now to conclude about the shape and extension of flexible ionic polymer chains in solutions.

We note that the (intra-macroion) interaction between the ionized groups through the intermediary of the counterions is essentially the same as the counterion-mediated attraction between macroions discussed in the preceding chapters.

It was made clear that the viscosity behavior of dilute dispersions of colloidal particles was similar to that of flexible ionic polymers in various ways. For example, the reduced viscosity-concentration curve commonly has a maximum and shear-thinning effect is pronounced for these two systems. We often

came across the claim that the shear-thinning effect supported the rod-model for flexible polymers, but it seems unreasonable in light of the fact that spherical particles also display a similar effect. The observation that the reduced viscosity of ionic colloidal dispersions is not increased but lowered with increasing charge density at a given radius (Fig. 7.7) suggests a substantial influence of the electrostatic factor on the viscosity. This influence is also concluded to be outstanding from the experimental fact that the reduced viscosity decreases with increasing particle radius at a given degree of sulfonation (presumably at a given charge density) (Fig. 7.8). The reduced viscosity of non-ionic polymer solutions is governed largely by hydrodynamic interactions. Both hydrodynamic interaction and electrostatic interaction between ions seem to play important roles in ionic polymers. In other words, it is not reasonable to analyze the observed viscosity data of ionic polymers using theories derived for non-ionic polymers. The rod-model for ionic polymers, which was concluded by application of (7.2), is not justified to such an extent as widely accepted. This is however not to say that (7.2) is totally invalid for ionic polymers. If the contribution of the electrostatic factors in the reduced viscosity can duly be elucidated, though formidably difficult at present, and if this contribution is subtracted from the observed viscosity, the residual viscosity should be described by (7.2). In fact, when a large amount of salt is added, the electrostatic factor is suppressed, and the viscosity of dispersions of colloidal spheres then obeys the Einstein law, which is a special case of (7.2) at $\alpha = 0$.

The large deviation from the Einstein behavior under low- and no-salt conditions is due to electrostatic interaction. At least a part of the deviation originates from the distortion of the ionic atmosphere around colloidal particles (the primary electroviscous effect). The Booth theory is shown to agree with the observed viscosity at large κa and for low charge particles. It is true that the viscosity under low-salt conditions cannot be accounted for in terms of the Booth theory. Extension of the Booth theory to such conditions is important for further progress.

From the above argument, it is clear that our understanding of the shape and size of flexible ionic polymers in solutions is far from satisfactory. The prevailing interpretation favoring the rod-model does not seem to have a firm foundation. That the model was successful even qualitatively does not necessarily imply that other models may be excluded. Fact-based analyses rather than artificial models are required for progress.

References

1. Yamakawa H (1971) Modern theory of polymer solutions. Harper & Row, New York
2. Fuoss RM (1951) Discuss Faraday Soc 11:125
3. Butler JAV, Conway BE (1953) Nature 172:152; Fujita H, Homma T (1954) J Colloid Sci 9:591; Eisenberg H, Pouyet J (1954) J Polym Sci 13:85; Butler JAV, Robins AB, Shooter KV (1957) Proc R Soc London A241:299
4. Yamanaka J, Matsuoka H, Kitano H, Hasegawa M, Ise N (1990) J Am Chem Soc 112:587
5. Flory PJ (1953) Principles of polymer chemistry. Cornell University Press, Ithaca, NY
6. Vink H (1970) Makromol Chem 131:133
7. Krause R, Maier EE, Deggelmann M, Hagenbüchle H, Schulze SF, Weber R (1989) Physica A160:135
8. Zhang YB, Douglas JF, Ermi BD, Amis EJ (2001) J Chem Phys 114:3299
9. Yamanaka J, Matsuoka H, Kitano, H, Ise N (1990) J Coll Interface Sci 134:92
10. Antonietti M, Briel A, Förster S (1996) J Chem Phys 105:7795
11. Hara M, Wu J, Jerome RJ (1988) Macromolecules 21:3330
12. Einstein A (1906) Ann Phys 19:289
13. Staudinger H, Joseph I, Leupold EO (1931) Liebig Ann 488:127
14. Onsager L (1932) Phys Rev 40:1028
15. Debye PJW, Hückel E (1923) Physik Z 24:185
16. Harned HS, Owen BB (1958) The physical chemistry of electrolytic solutions, 3rd edn. Reinhold, New York
17. Fowler RH, Guggenheim EA (1939) Statistical thermodynamics. Cambridge, Chap. 9
18. Booth F (1950) Proc R Soc London A203:533
19. Yamanaka J, Ise N, Miyoshi H, Yamaguchi T (1995) Phys Rev E51:1276
20. Chan FS, Goring DAI (1966) J Coll Interface Sci 22:371
21. Stone-Masui J, Watillon A (1968) J Coll Interface Sci 28:187
22. Yamanaka J, Matsuoka H, Kitano H, Ise N, Yamaguchi T, Saeki S, Tsubokawa M (1991) Langmuir 7:1928
23. Yamanaka J, Hashimoto S, Matsuoka H, Kitano H, Ise N, Yamaguchi T, Saeki S, Tsubokawa M (1992) Langmuir 8:338

8

Phase Transitions by Computer Simulation

8.1 Introductory Remarks

Computer simulation is widely employed these days to obtain information on microscopic properties of a molecular assembly [1]. Colloidal systems are not an exception. The molecular dynamics (MD) simulation is to obtain the trajectories of the component particles by solving Newton's equations of motion successively. In the Monte Carlo (MC) simulation, the partition function is numerically calculated. These two methods have their own advantages and disadvantages. In this chapter, we discuss some simulation work carried out on colloidal systems.

At the beginning, the basic nature and limits of this technique are to be noted. In both MD and MC simulations, pair potential (two-body potential) is assumed between the particles. If it is correctly estimated and if a precise numerical solution can be obtained therefrom, the physical properties of the assembly to be deduced by the simulation are expected not to be far from those actually observed. In reality, the expectation would not necessarily be fulfilled because ad hoc assumptions such as the minimum image convention or non-realistic, simple potential need to be introduced depending on the performance of the computer. To be correct, there may be many cases in which we cannot be certain how far the expectation has been fulfilled.

There exists a trend to regard simulation work as almighty because "experimental condition" or "parameter" can be adjusted more easily in simulation than in actual experiments. This trend is not acceptable. It is also wrong to judge simulation as simple calculation. It is true that, by simulation, various microscopic information, which cannot be obtained by approximate theories, can be derived and physical properties under experimentally inaccessible conditions can be discussed. Therefore, simulation is a technique to help us reach the correct understanding of observation.

8.2 Phase Transition of Hard-Sphere Model (Alder Transition)

The first MD simulation was carried out by Alder and Wainwright [2,3]. They assumed the following pair potential

$$U^{\mathrm{Al}}(R) = 0 \qquad (R \geq 2a) \tag{8.1}$$
$$U^{\mathrm{Al}}(R) = \infty \qquad (R < 2a),$$

where a is the particle radius, and calculated the equation of state of the system containing N hard spheres,

$$\frac{PV}{N\,k_{\mathrm{B}}T} - 1 = \left(\frac{1}{N\langle\nu^2\rangle}\right)\left(\frac{\Delta\Sigma}{\Delta t}\right) \tag{8.2}$$

where $\langle\nu^2\rangle$ is the mean square velocity relative to the center of mass of the system, t the time, and Σ is defined by

$$\Sigma = \Sigma(r_{\mathrm{a}i} - r_{\mathrm{b}i}) \cdot \Delta\nu_{\mathrm{a}i}, \tag{8.3}$$

with $r_{\mathrm{a}i}$ and $r_{\mathrm{b}i}$ being the positions of spheres a and b involved in collision i, and $\Delta\nu_{\mathrm{a}i}$ being the velocity change of particle a in the collision. By plotting Σ against t, $\Delta\Sigma/\Delta t$ and hence $(PV/N\,k_{\mathrm{B}}T - 1)$ is determined [4]. When the MD simulation is carried out with face-centered cubic arrangement of particles as the initial configuration, the pressure P first remains at low values and then increases abruptly, indicating the onset of phase transition. The particle trajectories before and after the transition are shown in Fig. 8.1 (a) and (b) for $V/V_0 = 1.525$, when the specific volume for closest packed configuration is given by V_0. By assuming the single occupancy model, Hoover and Ree determined the density N/V at the freezing point to be $0.667\,N/V_0$ [5]. This corresponds to a volume fraction ϕ of 0.49.

The phase transition of the hard-sphere systems mentioned above is called the Alder transition, in which solid (crystalline) state and liquid state are stable above and below $\phi = 0.5$, respectively. Noteworthy is that the transition takes place in purely repulsive systems. It is interesting to examine whether this is the case in real systems. In this respect, simulation by Longuet-Higgins and Widom is suggestive [6]. They introduced an attractive component (the second term of the right-hand side of (8.4)) into the hard-sphere potential as follows

$$\frac{PV_0}{Nk_{\mathrm{B}}T} = \frac{P^0V_0}{Nk_{\mathrm{B}}T} - \lambda\left(\frac{V_0}{V}\right)^2 \tag{8.4}$$

where

$$\lambda = \frac{a_1N}{V_0k_{\mathrm{B}}T}, \tag{8.5}$$

P^0 is the pressure that would be exerted by the hard-sphere, and a_1 is a constant with the positive sign. The concentration range of the phase transition

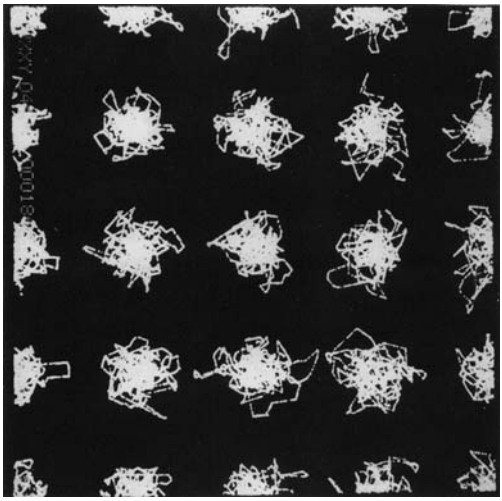

(a)

(b)

Fig. 8.1. Trajectory of hard-spheres as determined by the MD simulation. Particle number = 32, $V/V_0 = 1.525$. (a) solid state. (b) liquid state. Taken from [3] with the permission of Societa' Italiana de Fisica and Scientific American

was shown to become wider with increasing λ from 0 (the Alder transition). (For details, refer to the original paper.) It was claimed that λ was 14.7 at the triple point where solid, liquid, and gas coexist, and that good agreement between the computed results and observed values was noticed for the entropy of melting, specific heat at constant pressure, and compressibility of argon, when the contribution of the attraction was considered.

It has been proposed [7, 8] that the order-disorder transition of colloidal dispersions can be accounted for in terms of the Alder transition. However, as pointed out in Chap. 4, the phase transition of colloidal systems takes place at much lower ϕ's than the prediction by Alder. For example, Fig. 4.12 was obtained at $\phi = 0.02$, being one order of magnitude lower than the simulation results. We believe that this discrepancy is due to inadequacy of the hard-sphere model in charged systems as will be explained in Sect. 8.4 [1].

8.3 Phase Transition by Yukawa Potential and DLVO Potential

Computer simulation using the hard-sphere potential was improved by adopting the Yukawa potential energy $U_{\mathrm{R}}^{\mathrm{Y}}$ and DLVO potential energy U_{R} [10, 11]. When the volume fraction ϕ is increased in colloidal systems, the crystals show transition from body-centered cubic (bcc) to face-centered cubic (fcc) structure, as confirmed by light diffraction [12], pseudo-Kossel line [13], intrinsic Kossel line [14] and microscopy [15]. Robbins et al. examined the bcc-fcc transition by a constant volume simulation using $U_{\mathrm{R}}^{\mathrm{Y}}$. Let us denote the particle number by N, the particle number density by ${n_{\mathrm{p}}}^{*}$, the particle charge by $Z_{\mathrm{n}}e$, the potential energy per particle by $U_{\mathrm{R}}^{\mathrm{Y}}(R)$ [16]. $U_{\mathrm{R}}^{\mathrm{Y}}(R)$ is given by

$$U_{\mathrm{R}}^{\mathrm{Y}}(R) = \left(\frac{1}{2N}\right) U_0 \left(\frac{a_{\mathrm{s}}}{R_{ij}}\right) \sum_{\substack{i,j=1 \\ i \neq j}}^{N} \exp\left(-\lambda R_{ij}/a_{\mathrm{s}}\right) \tag{8.6}$$

where R_{ij} is the distance between particles i and j, $a_{\mathrm{s}} = {n_{\mathrm{p}}}^{*-1/3}$,

$$U_0 = \frac{(Z_{\mathrm{n}}e)^2}{\varepsilon a_{\mathrm{s}}} \equiv U_{\mathrm{a}} \exp(\lambda)\,, \tag{8.7}$$

$$\lambda = \kappa a_{\mathrm{s}}$$

and

$$\kappa^2 = \frac{4\pi n_{\mathrm{s}} e^2}{\varepsilon k_{\mathrm{B}} T} \tag{8.8}$$

with n_{s} being the number density of (univalent) small ions. Figure 8.2 shows the results of the simulation.

[1] As mentioned in Chap. 4, Sect. 4.2.1, the concept of an effective hard-sphere with a radius a_{D} (4.7) was invoked to explain this discrepancy. However, since this led to a physically absurd outcome that the Avogadro constant is not a universal constant, we will not follow this type of argument. Sood pointed out that some effective hard-sphere models provided rather poor agreement with observations [9].

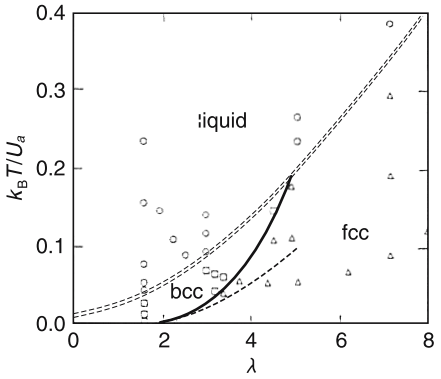

Fig. 8.2. Phase diagram of Yukawa systems. ○: liquid phase. △: fcc. □: bcc. = = =: borderline between liquid and solid where the root-mean-square displacement reaches 19% of a_s. ——: borderline between fcc and bcc by MD simulation. – – –: borderline by lattice dynamics calculation. Taken from [16] with the permission of American Institute of Physics

As correctly pointed out by Robbins et al. there is no distinction between gas and liquid phases in the phase diagram, because the interaction is assumed to be purely repulsive. The triangles and squares indicate points where fcc and bcc are stable, respectively. The curve (= = =) is a melting line inferred by the Lindemann condition, the real curve is the borderline of fcc and bcc obtained by MD simulation, and the dashed curve is that obtained by lattice dynamics calculation. The MD simulation indicates that bcc is not stable at larger λ and that the transition fcc $\rightarrow$ bcc $\rightarrow$ liquid takes place when $1.72 < \lambda < 4.9$ with increasing temperature. Alexander and McTague pointed out the appearance of bcc before melting [17], though this observation has been made for metals but not for colloidal crystals yet. The higher stability of bcc at elevated temperature implies its higher entropy than fcc, which is suggested to be due to the lower frequency mode of the bcc phase.

In the Yukawa systems, all ions are assumed to be point charges. This assumption is not appropriate for colloidal particles. In this sense, the following DLVO potential $U_{\mathrm{R}}(R)$ is more realistic than $U_{\mathrm{R}}^{\mathrm{Y}}$,

$$U_{\mathrm{R}}(R) = \frac{Z_{\mathrm{n}}^2 e^2 \exp(2\kappa a) \exp(-\kappa R)}{\varepsilon R (1+\kappa a)^2}. \tag{8.9}$$

$U_{\mathrm{R}}(R)$ differs from $U_{\mathrm{R}}^{\mathrm{Y}}$ by the geometrical factor, $\exp(2\kappa a)/(1+\kappa a)^2$. When $\kappa a < 1$, this factor is not important but generally speaking, the two potentials give different results. By a MD simulation using U_{R}, Thirumalai et al. found that the liquid phase spontaneously changes into a bcc phase [18]. Such a transition is not noticed in the MD simulation by Robbins et al. with $U_{\mathrm{R}}^{\mathrm{Y}}$. It is reminded that the compressibility of the systems calculated by U_{R} shows

a minimum at a small ϕ, while that from $U_{\mathrm{R}}^{\mathrm{Y}}$ decreases simply, implying the infinite compressibility, a physically unacceptable result. Shih and Stroud found a re-entrant phase transition (liquid → solid → liquid) with respect to ϕ when $U_{\mathrm{R}}^{\mathrm{Y}}$ was assumed [19]. They believed that the re-entrant behavior was an artifact of the point-charge approximation, since it disappeared when U_{R} was used [2].

Sirota et al. [23] obtained a phase diagram of ethanol-water dispersions of polystyrene latex particles by synchrotron X-ray and compared the results with the simulation by Robbins et al. As shown in Fig. 8.3, the observed boundary of the bcc-fcc transition is qualitatively reproduced by the simulation, though quantitative agreement is not satisfactory. Better agreement could not be yielded when different values of Z_{n} were invoked, according to Sirota et al. It is to be noted that, at large ϕ's, a glass phase was found for colloidal systems for the first time, which is distinguished from the liquid state by its larger and sharper peaks in the structure factor.

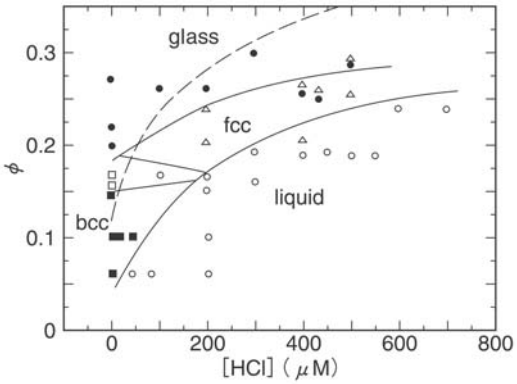

Fig. 8.3. Phase diagram of ethanol (0.9)-water (0.1) dispersions of polystyrene latex particles. $a = 45.5$ nm, $Z_{\mathrm{n}} = 135$ (500 in water). Added salt: HCl, dielectric constant of the medium $\varepsilon = 38$. ■: bcc, △: fcc, □: coexistence of bcc and fcc, •: glass state, ○: liquid state. Solid line: observed boundary (eye-guide), dashed curve: fcc-liquid boundary obtained by simulation with the Yukawa potential. Taken from [23] with the permission of the American Physical society

[2] It should be mentioned that Arora et al. have found a re-entrant phase transition with respect to C_{s} [20] and Tata et al. observed a re-entrant phase transition as a function of ϕ [21]. In these cases, homogeneous liquid phase changes first into inhomogeneous gas-liquid phases and then into a homogeneous liquid phase. On the other hand, Yamanaka et al. found the transition from homogeneous liquid phase, through liquid-crystal phases, to homogeneous liquid phase as a function of the charge density of particles [22].

Robbins et al. considered the exclusion volume effect by introducing the geometrical factor to U_{a} [(8.7)] instead of U_{R}. We denote the corrected U_{a} by U_{ag}. This is a convenient method but is adequate for qualitative argument. The elastic constant of colloidal crystal is calculated by this method. It is reported that a good agreement is obtained by invoking renormalized charge number, though this charge number is not confirmed by an independent method (for example, the conductivity measurement).

By using this technique, Yamanaka et al. determined phase diagrams of dispersions of particles of various sizes [24]. Figures 8.4 and 8.5 are their results for particles of $a = 78$ nm (used in Kossel line analysis [14]) and 123 nm (used in microscopic observation [15]), respectively. The bcc-fcc transition is observed between $\phi = 0.02$ and 0.03 by Kossel line analysis and between 0.005 and 0.01 by microscopy, while it is located in the fcc region in the simulation.

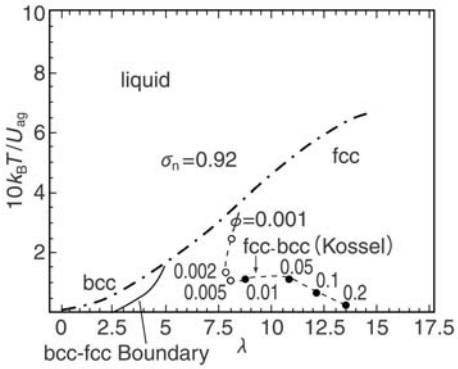

Fig. 8.4. The bcc-fcc transition observed by Kossel line analysis and simulation with a geometrical factor-corrected Yukawa potential U_{ag}. Sample: polystyrene latex ($a = 78$ nm, $\sigma_{\mathrm{a}} = 6.3$ μC cm^{-2}), medium: water, $C_{\mathrm{s}} = 2$ μM. (σ_{n} was estimated to be 0.92 μC cm^{-2} by an empirical relation of Yamanaka et al. [25]) Circles: observed by Kossel line [14]. ○: bcc, ●: fcc. —— and – · – · – · represent the bcc-fcc transition and the borderline between solid and liquid phases, respectively. - - - -: Equi-net charge number line ($\sigma_{\mathrm{n}} = 0.92$ μC cm^{-2}). The arrow shows the fcc-bcc transition point observed by Kossel line analysis. Taken from [24] with the permission of the authors.

Experimentally it has been confirmed that bcc is formed for colloidal silica dispersions at higher ϕ regions than in polystyrene latex cases [26–28]. It seems that this fact is not in accord with the U_{ag}-based simulation, either [3].

[3] Good agreement has been obtained between the simulation and observation by invoking the renormalized charge number σ^* [29]. This seems to be due to the fact that the particles used had a low charge density so that $\sigma_{\mathrm{n}} = \sigma^*$ held. See Fig. 4.4 in Chap. 4. Comparison for samples of higher charge densities is desirable.

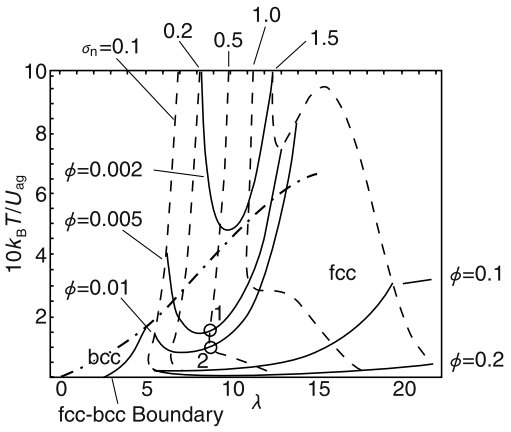

Fig. 8.5. The bcc-fcc transition observed by microscope and simulation with U_{ag}. Sample: polystyrene latex ($a = 123$ nm, $\sigma_{\mathrm{a}} = 1.9$ μC cm^{-2}). Medium: water. $C_{\mathrm{s}} = 2$ μM. σ_{n} was found to be 0.51 μC cm^{-2} by Yamanaka's equation [25]. – · –: liquid-solid borderline. —: fcc-bcc boundary. Equi-ϕ curves and equi-σ_{n} curves are shown for convenience. ∘1 and ∘2 indicate the microscopic observation at $\phi = 0.005$ and 0.01 by Ito et al. [15], who found only fcc at $\phi = 0.02$ and mixture of bcc and fcc at $\phi = 0.01$. Taken from [24] with the permission of the authors

It should be noted that Sood et al. examined various theories which were proposed for phase equilibria of colloidal systems. Agreement with experiments is not always satisfactory [9, 30].

8.4 Phase Transitions by Pair G-Potential

In the above sections, we considered simulations with purely repulsive potentials. Although quantitative agreement with experimental data is not satisfactory, the solid-liquid transitions and the solid-solid transition could be reproduced qualitatively. As pointed out by Robbins et al. the liquid-gas transition could not be found in Figs. 8.4 and 8.5. In reality, however, macroscopic liquid-gas phase separation [21, 31] and microscopic voids were observed in macroscopically homogeneous colloidal dispersions [32–34]. Thus we find it necessary to more or less modify the repulsion-only assumption and to accept the presence of interparticle attraction in addition to the repulsion. In this section, we discuss the MC and MD simulations carried out with the pair G-potential U^{G} [35] containing a short-range repulsion and long-range attraction, which was derived in Chap. 6. (See Tables 6.1 and 6.2.) It is noted that Overbeek claimed that this potential is incorrect [36] but this criticism is in error as mentioned in Chap. 2, footnote 1 and Chap. 6, footnote 1. If his argument *were* correct, the Debye-Hückel theory is also wrong.

8.4.1 bcc-fcc Transition, Solid-Liquid Equilibrium, Homogeneous-Inhomogeneous Transition, and Voids

Before entering into the details of the simulation, we summarize the main features of the work by Tata et al [37–39]. A MC simulation was carried out using the Metropolis algorithm with periodic boundary condition for a canonical ensemble (at constant number of particles N, volume V, and temperature T) [40–42]. The particles in aqueous dispersions of spherical particles (radius a, net charge number Z_{n}) are assumed to interact via U^{G} given by

$$U^{\mathrm{G}}(R) = \frac{Z_{\mathrm{n}}^2 e^2}{2\varepsilon}\left[\frac{\sinh(\kappa a)}{\kappa a}\right]^2\left[\frac{A}{R}-\kappa\right]\exp(-\kappa R) \tag{8.10}$$

where

$$A = 2 + 2\kappa a\coth(\kappa a) \tag{8.11}$$

and

$$\kappa^2 = \frac{4\pi e^2}{\varepsilon k_{\mathrm{B}} T}(n_{\mathrm{p}} Z_{\mathrm{n}} + C_{\mathrm{s}}) \tag{8.12}$$

with n_{p} and C_{s} being particle concentration and salt concentration, respectively, and with R being the center-to-center interparticle distance. Counterions and salt ions are assumed to be univalent.

The position of the potential minimum R_{m} is given by

$$R_{\mathrm{m}} = \frac{1}{2\kappa}\left\{A + [A(A+4)]^{1/2}\right\}. \tag{8.13}$$

The length of the MC cell l is

$$l^3 = \frac{N}{n_{\mathrm{p}}}. \tag{8.14}$$

The particles were assumed to take an initial configuration, liquid-like distribution, bcc, or fcc, and the total energy of the system and the height of the first peak of the structure factor $F(K)$ were monitored to check whether the system had reached thermal equilibrium. Simulation results were found to be the same within the statistical error for $N \geq 432$, and hence N was then fixed at 432. After the equilibrium was established, the radial distribution function $g(r)$ (r: distance), coordinate-averaged pair correlation function $g_{\mathrm{c}}(r)$, and mean square displacement $\langle r^2\rangle$ were calculated. The $g_{\mathrm{c}}(r)$ was obtained by averaging the particle coordinates over a sufficiently large number of configurations and is free from thermal broadening [43].

In the simulation a was fixed at 55 nm, and the parameters were the volume fraction ϕ, the surface charge density σ_{n} , and C_{s}. Figure 8.6 gives $g(r)$ and $g_{\mathrm{c}}(r)$ at relatively high ϕ's. The crystal symmetry can be inferred from the relative positions of the peaks. It is seen that the bcc-fcc transition took place at $\phi = 0.14 \sim 0.2$. Sirota et al. determined Z_{n} to be 65 from the elastic

constant of colloidal crystal ($a = 45.5$ nm, $\sigma_n = 0.16$ μC cm^{-2}) and reported that the bcc-fcc transition occurred at $\phi = 0.15 \sim 0.20$ (Fig. 8.3). Considering the difference in the particle diameter, this result might be claimed to be in a good agreement with Fig. 8.6. It is hoped that the Z_n derived indirectly from the elastic constant G is confirmed by a direct measurement [4].

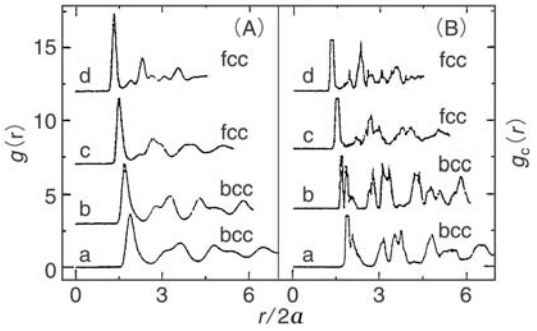

Fig. 8.6. MC simulation with U^G. (A) radial distribution function $g(r)$. $a = 55$ nm, $C_s = 0$. $\sigma_n = 0.15\,\mu$C cm^{-2}. Curves a, b, c, and d are shifted vertically. ϕ =0.1, 0.14, 0.2, and 0.3, respectively. (B) coordinate-averaged pair correlation function $g_c(r)$ with the same parameters as in (A). The heights of the first peak are 10.2, 11.8, 9.5 and 8.3, respectively. Taken from [42] with the permission of the American Physical Society

The charge density and salt concentration are important parameters affecting the dispersion state. Figure 8.7 shows how U^G varies with these parameters [31]. This potential contains a short-range repulsive branch and a long-range attractive branch. With increasing salt concentration n_i, the potential minimum shifts to shorter distances and the potential depth becomes first deeper and then shallower. When n_i is very large, the depth becomes negligible and the particles interact with each other with a repulsive interaction. The n_i dependence of the position of potential minimum is the same as that of the DLVO theory (See Fig. 2.9). However, it is noted that U^G *differs from* U_R i*n that the potential depth in the latter (the potential minimum) monotonously becomes deeper with increasing* n_i. If this dependence of U_R is correct, colloidal crystal would be more and more stabilized as salt

[4] The elastic constant G is defined by $G = (A_1/R)(\partial^2 U/\partial R^2)$ where $U(Z_n, R)$ is the interparticle potential and A_1 a constant depending on the crystal symmetry. Thus to obtain Z_n from G, it is necessary to assume U. As will be mentioned in Chap. 9, the observed value of G can be reproduced almost equally satisfactorily by both the DLVO and Sogami potentials. Therefore a method which does not depend on the potential form is necessary to determine Z_n uniquely.

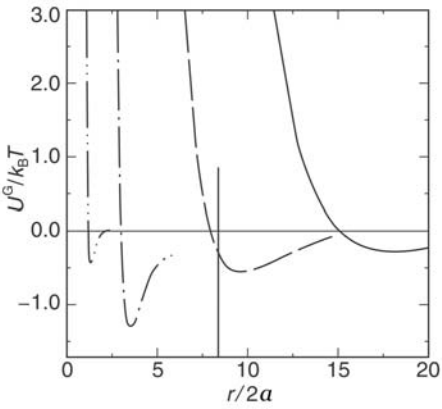

Fig. 8.7. Salt concentration dependence of U^{G}. ——: $n_i = 0$(ions cm^{-3}), – – –: 1.73×10^{15}, — · —: 1.99×10^{16}, — ·· —: 6.65×10^{17}. The vertical line indicates the average interparticle distance at a particle concentration of 1.33×10^{12} cm^{-3}. Taken from [31] with the permission of VCH Publishers, New York

concentration increases, which is experimentally not the case as discussed in Chap. 4.

When the position R_{m} of the potential minimum of U^{G} is located outside of the average interparticle distance $2D_0$, particles interact with each other with a purely repulsive potential, so that the systems become homogeneous. If $R_{\mathrm{m}} < 2D_0$, on the other hand, the systems separate into concentrated and dilute phases, resulting inhomegeneous dispersions. Though data are not shown, when $n_i/n_{\mathrm{p}}^* Z_{\mathrm{n}} > 100 (n_i > 6.65 \times 10^{16})$, the $g(r)$ has a single peak at R_{m} and decreases rapidly with increasing r. This implies that there is no structural correlation at short distances. The peak position is at a distance shorter than $2D_0$, but the correlation does not show up because of shallow potential depth. In Fig. 8.8 ($78 \geq n_i/n_{\mathrm{p}}^* Z_{\mathrm{n}} \geq 7$), $g(r)$ shows peaks, indicating a short-range correlation. The first peak is very high and at a distance shorter than $2D_0$ and near R_{m}, and slowly decays. This indicates that the system is inhomogeneous. Though not graphically shown, $g(r)$ has the shape for a liquid for $n_i/n_{\mathrm{p}}^* Z_{\mathrm{n}} = 5$ and shows a bcc structure at $n_i = 0$.

In the inhomogeneous systems, particularly when the first peak is located at a much shorter distance than $2D_0$, particles form clusters or condensed phases. When n_i is large, two-particle clusters are formed. As n_i is lowered, many-particle clusters are maintained [37]. When $n_i/n_{\mathrm{p}}^* Z_{\mathrm{n}}$ is smaller than 80 ($n_i < 5.18 \times 10^{16}$), almost 100% of particles are in clusters, whereas the fraction becomes smaller at large n_i.

The n_i dependence found by the MC simulation agrees fairly well with the observation [33]. It is noted that macroscopic phase separation was actually observed in polystyrene particles (density=1.05 g cm^{-3})-light water dis-

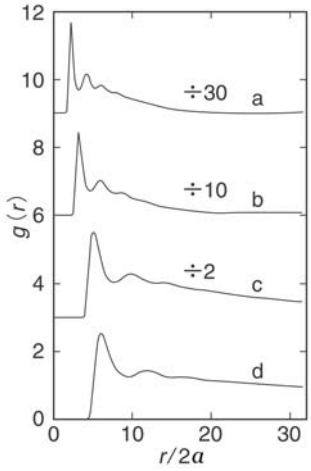

Fig. 8.8. MC simulation of salt concentration dependence with U^{G}. $a = 55$ nm, $n_{\mathrm{p}}^{*} = 1.33 \times 10^{12}$ particles cm^{-3}, $Z_{\mathrm{n}} = 500$. n_i, curve a: 5.18×10^{16} ($n_i/n_{\mathrm{p}}^{*} Z_{\mathrm{n}} = 78$), b: 1.99×10^{16}, c: 6.65×10^{15}, d: 4.66×10^{15} cm^{-3}. The heights of the curve a, b, and c are compressed by factors of 30, 10, and 2, respectively, and shifted vertically. Taken from [31] with the permission of VCH Publisher, New York

persions as the result of gravitational sedimentation, whereas clusters having high particle concentrations were floating in dilute phases in the simulation work, because the gravity was not taken into account. The difference between the simulation results and observation is apparent and therefore not essential.

The ϕ dependence of $g(r)$ is shown in Fig. 8.9. When ϕ is lowered, crystals melt into a liquid structure at $\phi = 0.0175$ (between curve b and c).

In Table 8.1 are listed relevant simulation parameters for relatively high volume fractions such as the position R_{m} of the potential minimum of U^{G}, its depth U_{m}, and the average interparticle distance $2D_0$ calculated for bcc or fcc. Except at very high C_{s}'s, R_{m} is larger than $2D_0$, indicating that repulsive interaction plays a major role and particles behave as if they interact with each other exclusively by repulsive forces. As a result, particles take their positions as far away as possible from each other. Correspondingly, the positions of the first peaks of $g(r)$ of Fig. 8.6 (A) are $1.4 \times (2a)$, $1.5 \times (2a)$, and $1.65 \times (2a)$ for $\phi = 0.3, 0.2$, and 0.14, respectively, in good agreement with $2D_0$ in Table 8.1. In other words, the particles are distributed almost homogeneously in the systems, forming a liquid state, fcc, or bcc structure. The one-state structure, not two-state structure, is maintained under the condition. It has been under such a condition (for example, at high ϕ's and low σ_{n}'s) that the DLVO theory is found to be valid. Table 8.1 shows that the Sogami theory also can account for the experimental results under the same conditions and indicates that *the DLVO theory is not the only theory that describes correctly colloidal*

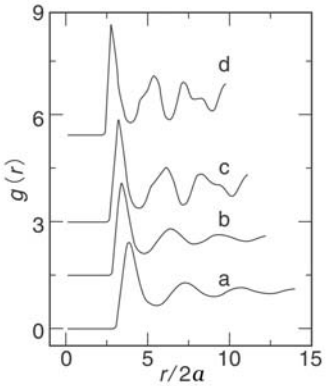

Fig. 8.9. MC simulation of particle volume fraction dependence with U^G. a = 55 nm. ϕ, curve a: 0.01, b: 0.015, c: 0.02, d: 0.03. $\sigma_n = 0.2$ μC cm^{-2}, $C_s = 4$ μM. Taken from [42] with the permission of the American Physical Society

interactions. Though the relevant logical problem will be dissected in Chap. 9, it is not possible to judge whether the DLVO theory or the Sogami theory is valid, as far as the one-state structure is concerned.

We turn to MC simulation in more dilute regions. Tata et al. found a gas-liquid phase transition below a critical particle concentration and under low salt conditions for polystyrene latex-light water dispersions [31]. Using the same latex particles, Yoshida et al. found void structures in the density-matched mixture of light water and heavy water and confirmed the gas-liquid phase separation in light water [44]. This result seems to imply that the void formation and gas-liquid phase transition is thermodynamically equivalent.

Later, Tata et al. concluded that the dense phase in equilibrium with voids was in a glassy state from simultaneous microscopic and ultra-small-angle X-ray scattering experiments on poly(chlorostyrene-styrene sulfonate) particles [41]. Mohanty and Tata demonstrated the presence of the glassy state by a recent MC simulation [45].

The Yukawa and DLVO potentials are purely repulsive so that they cannot explain the macroscopic phase separation observed by Tata et al., and the microscopic inhomogeneity found by Yoshida and Tata et al. at low ϕ's. Whether the dense phase coexisting with voids is glass-like or liquid-like cannot be discussed by those potentials. Therefore, it is of particular interest to carry out MC simulation using U^G. Table 8.2 shows the results and $g(r)$ obtained is displayed in Figs. 8.10 and 8.11. Two or three peaks are seen in the ϕ range between 0.25×10^{-3} and 1.12×10^{-3} (Fig. 8.10), suggesting a short-range order. The $g(r)$ slowly decreases with increasing r. The position of the first peak is at R_m, which is smaller than $2D_0$ (see Table 8.2). This means that the particle distribution is inhomegeneous. Figure 8.10 (B) gives the projection of particle coordinates in the MC cell, which indicates that "liquid-like droplets"

Table 8.1. Simulation parameters for the ϕ range between 0.3 and 0.03. κ: reciprocal Debye radius, R_m: the position of the minimum of U^G, U_m: depth of the potential minimum, $2D_0$: average interparticle distance.

ϕ	σ_n μC cm^{-2}	C_s μM	$2\kappa a$	$R_m/2a$	U_m/k_BT	$2D_0/2a$	state
0.30	0.15	0	4.092	1.737	0.591	1.352	fcc
-	-	50	4.830	1.614	0.495	-	fcc
-	-	65	5.030	1.587	0.471	-	fcc
-	-	160	6.149	1.476	0.356	-	fcc
-	-	350	7.926	1.369	0.237	-	L
0.25	0.15	0	3.736	1.737	0.639	1.437	fcc
-	-	250	6.846	1.427	0.302	-	L
0.20	0.15	0	3.341	1.931	0.689	1.547	fcc
-	-	30	3.888	1.781	0.619	-	fcc
-	-	200	6.123	1.478	0.358	-	L
0.14	0.15	0	2.795	2.152	0.742	1.742	bcc
-	-	10	3.022	2.049	0.723	-	bcc
-	-	140	5.123	1.576	0.460	-	L
0.03	0.2	0	1.494	3.478	1.177	2.83	bcc
-	-	4	1.661	3.179	1.240	-	bcc
-	-	6	1.739	3.061	1.263	-	bcc
-	-	6.5	1.757	3.034	1.269	-	L
-	-	7	1.776	3.008	1.274	-	L
-	-	8	1.813	2.958	1.283	-	L
-	-	10	1.884	2.867	1.299	-	L
-	-	15	2.051	2.683	1.328	-	L
0.03	0.085	0	0.974	5.121	0.159	2.83	bcc
-	-	0.1	0.981	5.088	0.160	-	bcc
-	-	0.4	1.001	4.994	0.163	-	bcc
-	-	1	1.039	4.820	0.167	-	L
-	-	2	1.101	4.570	0.175	-	L
0.03	0.05	0	0.747	6.590	0.0442	2.83	L
-	0.06	-	0.818	6.039	0.069	-	L
-	0.09	-	1.002	4.986	0.183	-	bcc
-	0.1	-	1.057	4.748	0.235	-	bcc
-	0.12	-	1.157	4.366	0.361	-	bcc
-	0.175	-	1.398	3.687	0.868	-	bcc

L: liquid state

of high particle density are formed and coexist with dilute gas phase. When ϕ is increased over 2.27×10^{-3} the system becomes homogeneously liquid-like, as is shown in Fig. 8.11. This is in accord with the observed fact that gas-liquid phase equilibrium is maintained for $\phi < 1.12 \times 10^{-3}$ and homogeneously liquid-like structure is formed for large ϕ's. According to Table 8.2, R_{m} is smaller than $2D_0$ for small ϕ's and $U_{\mathrm{m}} < k_{\mathrm{B}}T$. Thus particles attract each other by the attractive tail but the shallow minimum allows some particles to escape to gas phase, causing the gas-liquid coexistence. It is noted that the inhomogeneous structure, namely gas-liquid coexistence, is generated when the difference between R_{m} and $2D_0$ is large for small ϕ and the system is homogeneous when the difference is small.

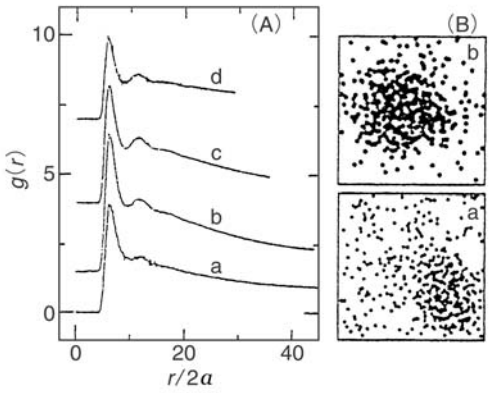

Fig. 8.10. MC simulation with U^{G}. (A) $g(r)$ at small volume fractions. $\sigma_{\mathrm{n}} = 0.21\ \mu\mathrm{C\ cm^{-2}}$, $C_{\mathrm{s}} = 4\ \mu\mathrm{M}$. ϕ, curve a: 0.25×10^{-3}, b: 0.32×10^{-3}, c: 0.60×10^{-3}, d: 1.12×10^{-3}. The curves b, c, and d are shifted vertically. (B) Projection of the particle coordinates in the MC cell with the same parameters as in (A). Taken from [42] with the permission of the American Physical Society

The systems become inhomogeneous when the potential depth U_{m} is large ($> 2k_{\mathrm{B}}T$) and $R_{\mathrm{m}} < 2D_0$. Since U_{m} depends on charge density σ_{n} and C_{s}, it is interesting to carry out MC simulation to understand how these parameters affect the systems. Figure 8.12 (A) gives the results for various σ_{n} with fixed ϕ and C_{s} and (B) those for various C_{s} with given ϕ and σ_{n}. From $g_{\mathrm{c}}(r)$ and the projection of the particle centers in (A), the system is seen to have a homogeneous crystal state for $\sigma_{\mathrm{n}} = 0.2\,\mu\mathrm{C\,cm^{-2}}$ and $C_{\mathrm{s}} = 0$. The position of the first peak of $g_{\mathrm{c}}(r)$ is $2D_0$. When $\sigma_{\mathrm{n}} > 0.4\ \mu\mathrm{C\ cm^{-2}}$, the first peak position is located at r smaller than $2D_0$ and $g_{\mathrm{c}}(r)$ has no clear peak at large r's. This implies that the space outside of the voids (the dense phase region) has only a short-range order similar to that in a liquid.

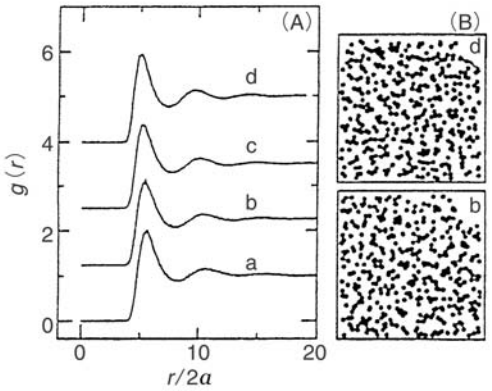

Fig. 8.11. MC simulation with U^{G}. (A) $g(r)$ at intermediate volume fractions. Other parameters are the same as Fig. 8.10. ϕ, curve a: 2.27×10^{-3}, b: 2.86×10^{-3}, c: 3.40×10^{-3}, d: 4.0×10^{-3}. The curves b, c, and d are shifted vertically. (B) Projection of the particle coordinates in the MC cell with the same parameters as in (A). Taken from [42] with the permission of the American Physical Society

Table 8.2. Simulation parameters for the ϕ range between 15×10^{-3} and 0.20×10^{-3}. $\sigma_{\mathrm{n}} = 0.21$ μC cm^{-2}, $C_{\mathrm{s}} = 4$ μM. κ: reciprocal Debye radius, R_{m}: minimum position of U^{G}, U_{m}: depth of U^{G}, $2D_0$: average interparticle distance

$\phi/10^{-3}$	$2\kappa a$	$R_{\mathrm{m}}/2a$	$U_{\mathrm{m}}/k_{\mathrm{B}}T$	$2D_0/2a$
Homogeneous liquid state				
15	1.303	3.922	1.198	3.57
10	1.143	4.414	1.097	4.08
9	1.109	4.540	1.073	4.22
4	0.916	5.426	0.926	5.53
3.4	0.890	5.575	0.772	5.85
2.86	0.866	5.720	0.884	6.19
2.27	0.839	5.896	0.861	6.69
Inhomogeneous gas-liquid coexistence				
1.6	0.807	6.118	0.833	7.52
1.12	0.784	6.290	0.810	8.46
0.60	0.757	6.504	0.790	10.43
0.32	0.743	6.630	0.780	12.85
0.25	0.739	6.659	0.772	13.96
0.20	0.736	6.682	0.770	15.03

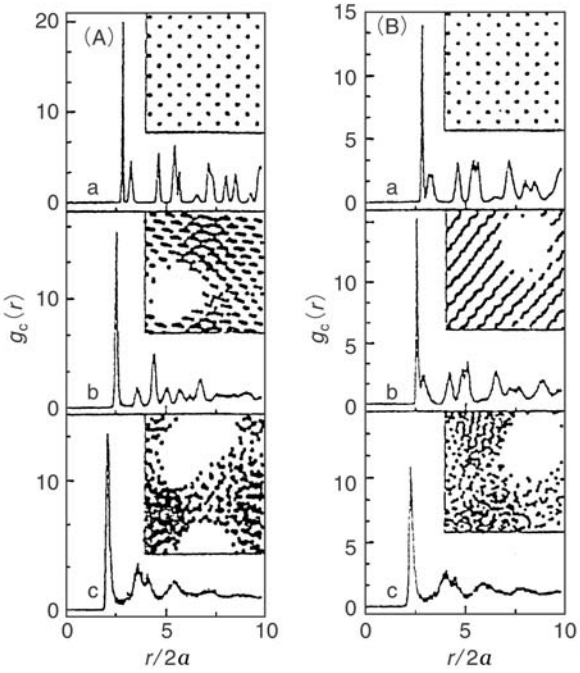

Fig. 8.12. MC simulation with U^{G}. (A): $g_{\mathrm{c}}(r)$ with various σ_{n}. $\phi = 0.03$, $C_{\mathrm{s}} = 0$. σ_{n}, curve a: 0.2, b: 0.4, c: 0.68 μC cm^{-2}. (B): $g_{\mathrm{c}}(r)$ with various C_{s}. $\phi = 0.03$, $\sigma_{\mathrm{n}} = 0.35$ μC cm^{-2}. C_{s}, curve a: 0, b: 2, c: 15 μM. The insets give the projection of the particle centers in the MC cell. Taken from [42] with the permission of the American Physical Society

The height of the first peak of structure factor $F(K)_{\max}$ in a wide range of σ_{n} values is shown in Fig. 8.13 [46]. The change of $F(K)_{\max}$ tells that the liquid-crystal-liquid transitions take place at $\sigma_{\mathrm{n}} = 0.1$ and 0.37 μC cm^{-2}. This is a re-entrant phase transition discussed in Chap. 4, Sect. 4.2.4. In other words, this transition can be accounted for at least qualitatively in term of U^{G} which contains a short-range repulsion and a long-range attraction.

The $g_{\mathrm{c}}(r)$-r diagram in Fig. 8.12 (B) is for $\sigma_{\mathrm{n}} = 0.35$ μC cm^{-2}, which is slightly lower than the upper limit of the re-entrant transition (0.37 μC cm^{-2}) shown in Fig. 8.13. It is seen that the system has a homogeneous crystal phase at $C_{\mathrm{s}} = 0$, as expected. As C_{s} increases, the system becomes inhomogeneous and void is generated. It is noted that such inhomogeneities are maintained when U_{m} is larger than $k_{\mathrm{B}}T$ and R_{m} is smaller than $2D_0$. Though it is practically impossible to correctly estimate the volume of each void, the fraction of the total sum of the volume of all voids f_v can be calculated by $f_v = [1 - (R_{\mathrm{m}}/2D_0)^3]$. Thus, under the condition where R_{m} and $2D_0$ are

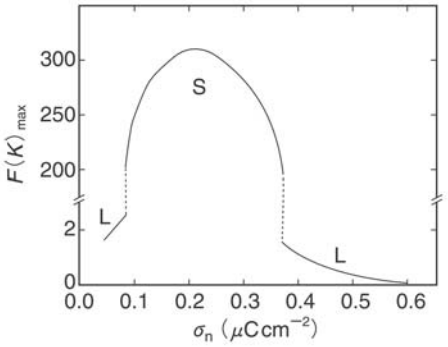

Fig. 8.13. Charge density dependence of the peak height of the structure factor calculated by MC simulation with U^{G}. $\phi = 0.03$, $C_{\mathrm{s}} = 0$. Taken from [46] with the permission of the American Chemical Society

largely different, voids can easily be observed. Since R_{m} is controlled by the experimental parameters such as $a, \phi, C_{\mathrm{s}}, \sigma_{\mathrm{n}}, \varepsilon$, and T [(8.13)], it monotonously decreases with increasing κa, as seen from Fig. 6.4, and U_{m} first decreases and increases after a minimum to zero. Thus the formation of voids and the homogeneous-inhomogeneous transition are sensitive toward the experimental conditions. In this respect, further systematic study, particularly of the influence of ε and T, must be carried out [5].

As mentioned in Sect. 8.3, the bcc-fcc transition could qualitatively be reproduced by the Yukawa potential. This does not imply, however, that only repulsion is in action between colloidal particles. As shown in Fig. 8.6, the transition can also be accounted for by using attraction-containing U^{G}. Thus it is not appropriate to discuss the pros and cons of these two potentials for one particular phenomenon such as the bcc-fcc transition. On the other hand, the microscopic inhomogeneity actually observed cannot be explained by a purely repulsive potential like Yukawa potential or DLVO potential but it can be reproduced by U^{G}. Clearly, the latter is more realistic than the former two potentials.

The U^{G} also has a repulsive tail at short distances as does the DLVO potential. It is of interest to compare these two potentials for relatively low charge samples at high volume fractions, where only short distances matter. We show the phase diagram constructed using the geometrical factor-corrected

[5] As mentioned in Chap. 4, Sect. 4.2.3, the closest interparticle distance $2D_{\mathrm{exp}}$ decreases with decreasing ε and rising T [47]. A similar T dependence was later observed by Asher and the associates [48]. Mel'nikov et al. observed a DNA chain to shrink with decreasing ε [49]. The decreasing tendency indicates that the distance is basically determined by electrostatic *attraction*. If the repulsion on the contrary plays the main role, the distance should increase or stay unchanged with decreasing ε.

Yukawa potential U_{ag} in Figs. 8.14 and 8.15. The arrows indicate the boundary points obtained by the above-discussed simulation with U^G for the bcc-fcc transition (Fig. 8.6), liquid-bcc transition (Fig. 8.13) and bcc-liquid transition (Fig. 8.13). Except the bcc-liquid transition in Fig. 8.15, the Yukawa potential is seen to provide roughly consistent results. It is therefore clear that *the contribution of the attractive interaction is not apparently important as far as low charge densities are concerned* (Fig. 8.14). The bcc-liquid transition in the U^G scheme, which takes place at a higher charge density (around at $\sigma_n = 0.37\ \mu C\ cm^{-2}$ according to Fig. 8.13), is found in the fcc region according to the Yukawa scheme. The difference between the two potentials manifests itself.

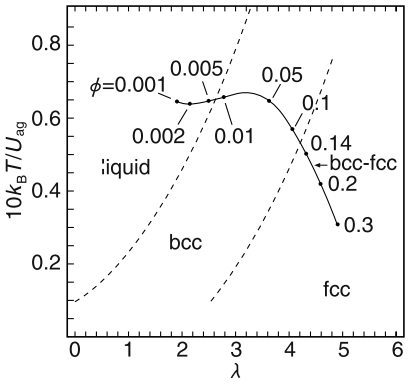

Fig. 8.14. Simulation using the geometrical factor-corrected Yukawa potential U_{ag} and MC simulation with U^G. $a = 55$ nm, $C_s = 0$, and $\sigma_n = 0.15\ \mu C\ cm^{-2}$D The arrow indicates the bcc-fcc transition point obtained by MC simulation with U^G. Taken from [24] with the permission of the authors

8.4.2 MC Simulation at Very Low Volume Fractions

We consider here the MC simulation at low ϕ values such as $10^{-5} \sim 10^{-4}$. The pair potential $U(r)$ is related to the radial distribution function $g(r)$ by the following equation [50]

$$g(r) = \exp\left(\frac{-U(r)}{k_B T}\right). \tag{8.15}$$

In Fig. 8.16, U^G is compared with the potential energy derived by (8.15) from $g(r)$, which was obtained by the MC simulation. We notice a very good agreement. This fact indicates that (8.15) is valid at very low ϕ values and the potential derived is a true pair potential. Table 8.3 gives the parameters in the

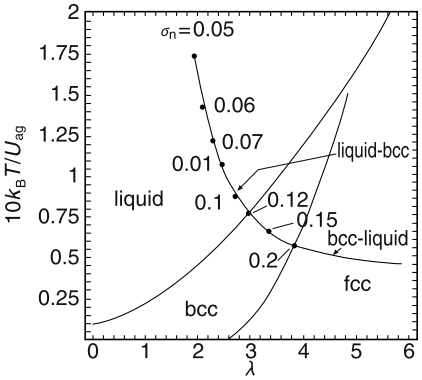

Fig. 8.15. Simulation using the geometrical factor-corrected Yukawa potential $U_{\rm ag}$ and MC simulation with $U^{\rm G}$. $a = 55$ nm, $C_{\rm s} = 0$, and $\phi = 0.03$. The arrows show the points of the liquid-bcc transition and the bcc-liquid transition obtained by the MC simulation. Taken from [24] with the permission of the authors

MC simulation. At such low ϕ's, $R_{\rm m}$ is much smaller than $2D_0$ but particles rove around freely because $U_{\rm m}$ is small. Thus the systems are homogeneously gas-like. Correspondingly the $g(r)$ in Fig. 8.17 has a peak only at $r = R_{\rm m}$. Interestingly, the peak position does not change with ϕ, indicating that the system can be regarded as noninteracting at such low ϕ's. The insensitivity of $g(r)$ toward ϕ was observed by Kepler and Fraden [51].

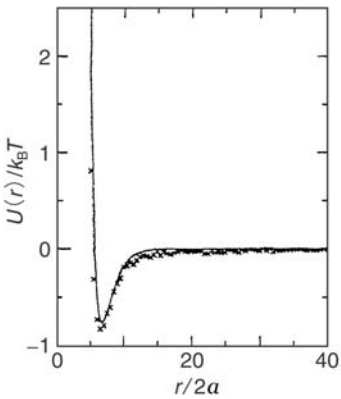

Fig. 8.16. Simulation with $U^{\rm G}$ at a very low volume fraction. $\phi = 10^{-5}$, $\sigma_{\rm n} = 0.21$ μC cm^{-2}, $C_{\rm s} = 4$ μM. —: $U^{\rm G}$, ×: potential energy derived from $g(r)$ computed by the simulation. Taken from [42] with the permission of the American Physical Society

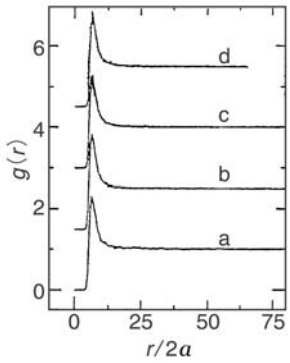

Fig. 8.17. Radial distribution function computed by simulation with U^{G} at very low volume fractions. $\sigma_{\mathrm{n}} = 0.21$ μC cm^{-2}, $C_{\mathrm{s}} = 4$ μM. ϕ, curve a: 10^{-5}, b: 3×10^{-5}, c: 6×10^{-5}, d: 10^{-4}. The curves b, c, and d are shifted vertically. Taken from [42] with the permission of the American Physical Society

Table 8.3. Simulation parameters at very low volume fractions. $\sigma_{\mathrm{n}} = 0.21$ μC cm^{-2}, $C_{\mathrm{s}} = 4$ μM, κ: reciprocal Debye radius, R_{m}: minimum position of U^{G}, U_{m}: depth of U^{G}, $2D_0$: average interparticle distance

$\phi/10^{-4}$	$2\kappa a$	$R_{\mathrm{m}}/2a$	$U_{\mathrm{m}}/k_{\mathrm{B}}T$	$2D_0/2a$	state
0.1	0.726	6.772	0.760	40.82	gas
0.3	0.727	6.762	0.761	28.30	gas
0.6	0.728	6.743	0.763	22.46	gas
1.0	0.732	6.729	0.765	18.95	gas

From the above argument on the MC simulation with U^{G}, which contains screened Coulomb repulsion *and* long-range attraction, we obtained the following:

1. The fcc structure at low C_{s} and high ϕ and the bcc symmetry are reproduced by U^{G} [6]. When C_{s} is increased, the colloidal crystals are destroyed. The bcc-fcc transition can be reproduced also by the purely repulsive Yukawa potential $U_{\mathrm{R}}^{\mathrm{Y}}$ and DLVO potential U_{R}. The fact that the transition can be at least qualitatively accounted for in terms of the three potentials, U^{G} , $U_{\mathrm{R}}^{\mathrm{Y}}$, and U_{R} indicates that the pure repulsion is not solely responsible for the transition.

[6] Orthorhombic crystals, in addition to bcc and fcc, were recently found for colloidal silica dispersions by Kossel line analysis. This is due to gravitational sedimentation of the particles and high sensitivity of the Kossel technique. [Shinohara T, Yamada H, Sogami IS, Ise N, Yoshiyama T (2004) Langmuir, 20:5141]

2. The systems are homogeneously liquid-like at low charge densities σ_{n}. When σ_{n} increases, the systems take crystal structure at a critical charge density σ_{n1} and again disordered state at σ_{n2}. The re-entrant phase transition is confirmed by experiment.
3. The U^{G} is also repulsive under the condition that its potential minimum position R_{m} is larger than the average interparticle distance $2D_0$. For example at large ϕ's corresponding to small $2D_0$, the system can be described by purely repulsive interaction. Under such conditions, the pros and cons of U^{G} and U_{R} cannot be argued.
4. When $R_{\mathrm{m}} < 2D_0$ and when σ_{n} is between the lower and upper critical concentrations σ_{n1} and σ_{n2}, the systems are inhomogeneous at low ϕ's, showing the coexistence of gas-liquid phases. When σ_{n} becomes larger, and when the potential depth U_{m} is large enough, voids are formed. At fixed σ_{n} and ϕ , increase in C_{s} causes the phase transition from homogeneous crystal, through coexistence of voids and crystal, to coexistence of voids and liquid.
5. At a very small ϕ, the exponential relation between $g(r)$ and the pair potential energy $U(r)$ is confirmed. The $g(r)$ derived by the simulation has a peak, independently of ϕ, as observed.

It is once again noted that the structural inhomogeneities such as voids and gas-liquid phase equilibrium cannot be reproduced by purely repulsive DLVO potential, whereas they are reproduced by an attraction-containing U^{G}. This clearly substantiates the important contribution of the attraction in real colloidal dispersions. Secondly, it is important to note that the parameters κ, R_{m}, U_{m}, and $2D_0$ are uniquely determined by (8.12), (8.13), and (8.10) using the experimental parameters $a, \phi, C_{\mathrm{s}}, \varepsilon$, and T. σ_{n} is determined directly by the conductivity measurements or the transference experiments (Sect. 4.1.1) without invoking any theoretical framework. Thirdly, the agreement of the MC simulation with U^{G} with experimental findings is true but still qualitative. One of the reasons is the stringent requirement to carry out experiments under low salt or no salt conditions. It must be understood that it is not easy to precisely reproduce the level of the ionic concentrations even in experiments performed with the utmost care. Furthermore, the dispersion states are highly sensitive toward the ionic concentrations. Therefore it is required to accumulate more reliable experimental data before U^{G} can be claimed to be quantitatively satisfactory, though it is definitely much more realistic than U_{R}. Recently Knott and Ford [52] reconsidered the assumptions in Sogami theory [35] and solved the Poisson-Boltzmann equation analytically by taking into account the exclusion volume effect of particles and counterions. They showed that the effective pair potential contained an attractive component even at the level of Hemholtz free energy. It would be interesting topics to compare the Knott-Ford potential with experiments and to carry out simulation using this potential.

Wang performed MD simulation using U^{G} [53], and noticed void formation, in agreement with the MC simulation. However, he could not reproduce the void formation when the potential containing attractive component derived by Tokuyama [54] was used.

8.5 Summary

In the present chapter, some computer simulation work has been discussed. Alder and Wainwright were the first to demonstrate the crystal-liquid (order-disorder) transition using a purely repulsive potential. The transition took place at a volume fraction of around 0.5. In colloidal dispersions, the transition actually occurred below 0.02, one order of magnitude lower than the simulation. The discrepancy is believed to be due to the repulsive potential invoked, namely the contribution of ignored attraction. This inference is supported by the success of the MC simulation with the pair G-potential U^{G}.

Using the purely repulsive Yukawa potential and DLVO potential, qualitative agreement was reached for the transition between bcc and fcc and that between liquid-bcc phases. The liquid-bcc-fcc phase diagram was constructed by introducing the geometrical factor, which agreed with observation only qualitatively.

It might be possible to obtain a better agreement with experiments by introducing ad hoc assumptions on the basis of a purely repulsive interaction. We do not follow this line of argument; instead we accept the presence of an attractive component on top of the widely recognized repulsion. Experiments show that there is an electrostatic attraction between similarly charged colloidal particles through the intermediary of the counterions. At present it seems to be only U^{G} that accounts for this observation. The criticism of this potential by Overbeek is in error. The MC simulation using this potential could explain the bcc-fcc transition and melting of colloidal crystal by addition of salt. At low volume fractions, the DLVO potential could not reproduce the gas-liquid equilibrium and void formation, whereas the pair G-potential could. The simulation study has clarified the important nature of the interparticle attraction.

References

1. Allen MP, Tildesley DJ (1987) Computer simulation of liquids. Oxford Science, Oxford
2. Alder BJ, Wainwright TE (1957) J Chem Phys 27:1208
3. Alder BJ (1959) Scientific American 201:113
4. Wainwright TE, Alder BJ (1958) Nuovo cimento 9 (Suppl Ser10):116
5. Hoover WG, Ree FH (1967) J Chem Phys 47:4873, (1968) J Chem Phys 49:3609
6. Longuet-Higgins HC, Widom B (1964) Mol Phys 8:549
7. Wadati M, Toda M (1972) J Phys Soc Jpn 32:1147
8. Takano K, Hachisu S (1977) J Chem Phys 67:2604
9. Sood AJ (1991) Solid State Physics 45:1
10. Derjaguin BV, Landau L (1941) Acta Physiochim 14:633
11. Verwey EJW, Overbeek JThG (1948) Theory of the stability of lyophobic colloids. Elsevier, New York
12. William R, Crandall RS (1974) Phys Lett 48A:225
13. Clark NA, Hurd A, Ackerson BJ (1979) Nature 281:57
14. Yoshiyama T, Sogami I, Ise N (1984) Phys Rev Lett 53:2153
15. Ito K, Nakamura H, Ise N (1986) J Chem Phys 85:6136
16. Robbins MO, Kremer K, Grest GS (1988) J Chem Phys 88:3286
17. Alexander S, McTague JP (1978) Phys Rev Lett 41:702
18. Rosenberg RO, Thirumalai D (1987) Phys Rev A 36:5690
19. Shih WH, Stroud D (1983) J Chem Phys 79:6254
20. Arora AK, Tata BVR (1988) Phys Rev Lett 60:2438
21. Tata BVR, Rajalakshmi M, Arora AK (1992) Phys Rev Lett 69:3778
22. Yamanaka J, Yoshida H, Koga T, Ise N, Hashimoto T (1998) Phys Rev Lett 80:5806
23. Sirota EB, Ou-Yang HD, Sinha SK, Chaikin PM, Axe JD, Fujii Y (1989) Phys Rev Lett 62:1524
24. Yamanaka J, Yonese M, publication in preparation
25. Yamanaka J, Hayashi Y, Ise N, Yamaguchi T (1997) Phys Rev E 55:3028
26. Konishi T, Ise N, Matsuoka H, Yamaoka H, Sogami I,Yoshiyama T (1995) Phys Rev B 51:3914
27. Konishi T, Ise N (1995) J Am Chem Soc 117:8422
28. Yamanaka J, Koga T, Ise N, Hashimoto T (1996) Phys Rev E 53:R4314
29. Monovoukas Y, Gast A (1989) J Coll Interface Sci 128:533

30. Chakrabarti J, Krishnamurthy HR, Sengupta S, Sood AK (1996) In: Arora AK, Tata BVR (eds) Ordering and phase transitions in charged colloids. VCH, New York, Chap. 9
31. Tata BVR, Arora AK (1996) In: Arrora AK, Tata BVR (eds) Ordering and phase transitions in charged colloids. VCH, New York, Chap. 6
32. Ise N (1988) In: Ise N, Sogami I (eds) Ordering and organization in ionic solutions. World Scientific, Singapore, p.624
33. Kesavamoorthy R, Rajalakshimi M, Rao CB (1989) J Phys Condens Matter 1:7149
34. Ito K, Yoshida H, Ise N (1994) Science 263:66
35. Sogami I, Ise N (1984) J Chem Phys 81:6320
36. Overbeek JThG (1987) J Chem Phys 87:4406
37. Tata BVR, Arora AK, Valsakumar MC (1993) Phys Rev E 47:3404
38. Tata BVR, Arora AK (1991) J Phys Condens Matter 3:7983; (1992) 4:7699; (1995) 7:3817
39. Arora AK ,Tata BVR (1996) In: Arrora AK, Tata BVR (eds) Ordering and phase transitions in charged colloids. VCH, New York, Chap. 7
40. Tata BVR, Ise N (1998) Phys Rev B 54:6050
41. Tata BVR, Yamahara E, Rajamani PV, Ise N (1997) Phys Rev Lett 78:2660
42. Tata BVR, Ise N (1998) Phys Rev E 58:2237
43. Nose S, Yonezawa F (1986) J Chem Phys 84:1803
44. Yoshida H, Ise N, Hashimoto T (1995) J Chem Phys 103:10146
45. Mohanty PS, Tata BVR (2003) J Coll Interface Sci 264:101
46. Ise N, Konishi T, Tata BVR (1999) Langmuir 15:4176
47. Ise N, Ito K, Okubo T, Dosho S, Sogami I (1985) J Am Chem Soc 107:8074
48. Rundquist PA, Jagannathan S, Kesavamoorthy R, Branardic C, Xu S, Asher SA (1991) J Chem Phys 94:711
49. Mel'nikov SM, Khan MO, Lindman B, Jönsson B (1999) J Am Chem Soc 121:1130
50. McQuarrie DA (1976) Statistical mechanics. Harper Collins Publishers, New York, Chap. 15
51. Kepler GM, Fraden S (1994) Phys Rev Lett 73:356
52. Knott M, Ford IJ (2001) Phys Rev E 63:031403
53. Wang KG (2000) Phys Rev E 62:6937
54. Tokuyama M (1999) Phys Rev E 59:R2550

9

Further Problems of Interparticle Interaction

9.1 Introductory Remarks

In this monograph, we discussed some properties of dilute solutions or dispersions of macroions with reference to the intermacroion interaction for flexible ionic polymers and ionic colloidal particles. In short, for highly charged macroions, we tried to present the experimental and theoretical verification of the existence of an electrostatic, intermacroion attraction through the intermediary of counterions in addition to the widely recognized, short-range repulsive interaction. As discussed in detail in Chap. 2, the electrostatic interaction between macroions is purely repulsive in the conventional theoretical framework based on the DLVO theory and the long-range attraction does not come into question. However, one of the simple explanations of the observed microscopic inhomogeneity is an attraction. As far as the conventional framework is concerned, this observed fact cannot be accounted for unless ad hoc assumptions are introduced. Thus, the growing body of experimental evidence for the presence of long-range attraction has led to a controversy over the nature of interparticle interaction for some time. In this chapter, we re-examine the controversy from both logical and experimental standpoints [1].

It is noted that McBride and Baveye reviewed the development of the Coulombic attraction concept with reference to clay colloids [1]. They pointed

[1] In some papers, which claimed that the repulsion-only assumption, or the DLVO theory, was correct and the attraction-repulsion assumption was wrong, attraction was mixed up with repulsion [Bloomfield VA, et al. (1991) Macromolecules 24:5791; (1992) 25:5266], or arguments equivalent to saying that the gravitational acceleration was $980 \times 10\,\mathrm{cm\,s^{-2}}$ and that the Avogadro constant was not an universal constant were presented [Okubo T. (1987) J Chem Phys 87:6733; (1988) Acc Chem Res 21:281]. Interested readers are referred to the following references for details regarding these serious difficulties [Ise N, Matsuoka H (1994) Macromolecules 27:5218, Yamanaka J et al. (1990) J Coll Interface Sci 134:92, Results and Discussion Section H and Ise N, Yoshida, H (1996) Acc Chem Res 29:3].

out that the DLVO theory adequately described the repulsive interaction between *isolated* like-charged particles, whereas a long-range attraction was necessary to explain *multi-particle* interaction at low salt concentrations and for highly charged particles.

9.2 Charge Density of Colloidal Particles and the DLVO Theory

As discussed in Chap. 2, the DLVO theory was originally constructed to elucidate the forces between two charged, infinite interfaces accompanying the electric double layers when they come close to each other [2]. On the basis of this theory, the interaction between two charged spheres (radius:a, charge:$Z_{\mathrm{n}}\, e$) is discussed. Therefore,when this theory is compared with observed results of colloidal particles, experimental data obtained at finite concentrations have to be extrapolated to infinite dilution. Strictly speaking, the DLVO theory cannot be applied for many-particle problems such as crystallization/melting of colloidal crystals. Thus, the theory is restricted to low charge particles, for which the interparticle interaction is weak.

This limitation of the DLVO theory is clearly recognized if experimental results of highly charged particles are closely considered. In Chap. 4, we discussed the transition from homogeneous to inhomogeneous states with increasing charge density. It was demonstrated by a Monte Carlo simulation in Chap. 8 that this transition could be accounted for by the Sogami potential, or pair G-potential, $U^{\mathrm{G}}(R)$, but not by the DLVO potential. It seems that particles of relatively low charge densities had been chosen in the past. In Table 9.1 are shown some samples employed in representative cases, their net charge density σ_{n}, and the technique applied for the σ_{n} determination.

9.3 DLVO Potential or Pair G-Potential?

Detailed discussion was given on the DLVO theory in Chap. 2 and on the Sogami theory in Chap. 6. The latter deals with many-particle problems and led to the pair G-potential which has a short-range repulsion and a long-range attraction. On the other hand, the DLVO theory gave a purely repulsive potential. As was demonstrated in Chap. 8, the structural inhomogeneities observed for colloidal dispersions could be qualitatively reproduced by the pair G-potential but they could not even qualitatively be described by the DLVO potential. However, various properties were claimed to be accountable by the DLVO potential. In this section, we demonstrate that this claimed success does not have so firm foundation as widely believed.

Table 9.1. Net charge density σ_n of macroions [a]

Author	σ_n μC cm^{-2}	Radius nm	Reference	Note
Category A (Repulsion was detected or claimed.)				
Ackerson	0.038	100	3	b
Versmold	0.001	385	4	c
Grier	0.02 (3.8)	320	5	d
Grier	(2)	325	6	e
Grier	0.07	425	7	f
Category B (Attraction was detected.)				
Ito	1.33	250	8	g
Fraden	0.16	635	9	h
Carbajal-Tinoco	0.37	250	10	i
Yoshida	0.23	53	11	j
Yamanaka	0.5	60	12	k
Tata	0.21	55	13	l
Tata	0.25	90	14	m
Antonietti	5	48	15	n
Ohshima	4.3	7.0	16	o
Category C (Attraction was detected but the data were treated with repulsion.)				
William-Crandall	0.37	50	17	p
Asher	0.45	42	18	q

[a] Polystyrene latex unless otherwise stated.
[b] Curve-fitting with a space-filling model.
[c] Curve-fitting of the directly measured potential with the DLVO potential.
[d,e,f] Curve-fitting of the observed potential with the DLVO potential. The value in the parentheses is the analytical charge density σ_a obtained from the titratable charge number given by the authors, namely 3.2×10^5 per particle or $1e$ per 10 nm^2. The reported values change from sample to sample, though a latex of the same lot number was used.
[g] Conductometric titration, from which σ_n was estimated assuming $\sigma_n/\sigma_a(=f) = 0.1$ [19].
[h] The authors reported a charge density of $1e/10$ nm^2. It is not clear from the paper whether it denotes σ_a or σ_n. If it is σ_a, σ_n is 0.16 μC cm^{-2}.
[i] From the reported values of analytical charge number (5×10^4 per particle) and particle radius (250 nm) the σ_a was determined and the σ_n was estimated by (4.6) [20].
[j] Silica particle. Conductivity measurements.
[k] Silica particle. Conductivity measurements.
[l] Curve-fitting with Sogami potential.
[m] Conductivity measurements.
[n] Sulfonated polystyrene-microgel. Assuming $f = 0.04$, σ_n was obtained from σ_a [19], which was calculated using the molecular weight and the degree of sulfonation (70%) reported.
[o] Dendrimer of the 10th generation. Conductivity measurements.
[p] From the charge number reported by the original authors [(1977) Science 198:393].
[q] From the reported analytical charge number. See [21] for comparison with the rescaled charge number.

9.3.1 Structure Factor

Tata et al. carried out a computer simulation to obtain the structure factor $F(K)$ assuming the DLVO potential U_{R} (8.9) and the pair G-potential U^{G} (8.10) and compared the results with the observed $F(K)$ [22]. In Fig. 9.1 the results of a Monte Carlo (MC) simulation are shown. The DLVO potential is seen to give good agreement with the observed $F(K)$. However, the pair G-potential shows a likewise satisfactory agreement with the observation, so that $F(K)$ is in fact insensitive to the potential form. Thus, $F(K)$ *is not an appropriate physical quantity to judge the pros and cons of these potentials*. Furthermore, *the DLVO potential cannot be claimed to be the only correct potential*. Further study is necessary to understand why the two different potentials agree satisfactorily with observation. The commentary on this problem by Rajagopalan [23] is interesting. Tata et al. also showed by a molecular dynamics simulation that both U_{R} and U^{G} agreed satisfactorily with observation, providing further evidence for the insensitivity just mentioned.

Sood discussed the analysis of colloidal phenomena in terms of theoretical approaches for liquids [24]. Particularly, hypernetted chain approximation (HNC), mean spherical approximation (MSA), and rescaled mean spherical approximation (RMSA) were considered. It was noted that the HNC and RMSA methods could satisfactorily reproduce observed $F(K)$, when combined with U_{R}. U^{G} was not examined because analytical solutions in a closed form could not be obtained. It is difficult to compare these two potentials in such a theoretical framework.

9.3.2 Shear Modulus of Colloidal Crystals

The shear modulus of crystals G is given by

$$G = \left(\frac{A}{R}\right)\left(\frac{\partial^2 U}{\partial R^2}\right), \tag{9.1}$$

where A is a constant and 0.833 for fcc and 0.510 for bcc [25] [2], U the interparticle potential and R the interparticle distance. By introducing the DLVO potential or the pair G-potential into U the G values for the respective potentials can be calculated [27]. The results are shown with the observed values [28]

[2] According to van de Ven [26], the constant A in (9.1) is 0.283, not 0.833, for fcc. If the former is adopted, a much larger value has to be assumed for Z_{n} to obtain agreement with the observed shear modulus. The discrepancy from the value adopted by Chaikin et al. would then become smaller. This type of argument is not constructive, however. The Z_{n} value has to be checked by independent measurements. According to a theory of Alexander et al. [29], the largest net charge number is given by $(15a/Q)$, where Q is the Bjerrum radius and 0.357 nm for 1-1 electrolytes in water at 25°C, and is about 2000, which differs largely from Chaikin et al.'s value.

in Fig. 9.2. The theoretical values calculated with $Z_n = 180$ or 170 are seen to be in agreement with the experiments. It can be understood that the shear modulus is not a property to judge the pros and cons of the interparticle interaction, either. Another factor to be considered is the low charge density of the particles employed. $Z_n = 180$ corresponds to $\sigma_n = 0.09\ \mu C\ cm^{-2}$. The charge number reported by Lindsay and Chaikin (305) gives $\sigma_n = 0.16\ \mu C\ cm^{-2}$. According to these σ_n values, the sample belongs to Category A in Table 9.1. In other words, attraction is not expected to appear. Thus it is true that the DLVO potential can reproduce the experimental values. However, the observation can also be accounted for by the pair G-potential as seen from Fig. 9.2. Experimental study on particles having much larger charge numbers is necessary to unanimously judge which of the DLVO potential or the pair G-potential is more appropriate for the shear modulus.

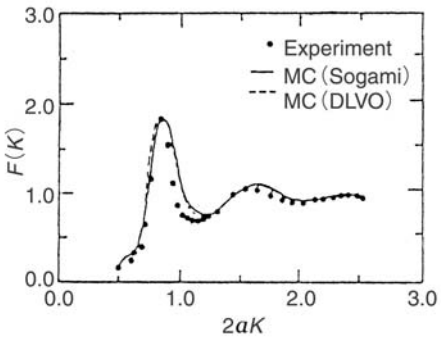

Fig. 9.1. Comparison of structure factors $F(K)$ observed and computed by a Monte-Carlo simulation. $\phi = 9 \times 10^{-4}$, $a = 54.5$ nm, $\sigma_n = 0.21\,\mu C\ cm^{-2}$, $C_s \approx$ about 3 μmol L^{-1}. •: observed, - - - - -: DLVO potential, ——: pair G-potential. Taken from [22] with the permission of the Indian Academy of Sciences

9.3.3 Thermal Contraction of Colloidal Crystals

As mentioned in Chap. 4, Ito et al. found that colloidal crystals *contract* with rising temperature [30]. This fact shows the unique property of colloidal crystals, which is not found in atomic crystals. The reason is that particles interact with each other through liquid medium (not a vacuum). Later, this trend was also observed by Asher's group [18]. While the two groups observed the same dependence, their interpretation is contradictory. Asher et al. explained their observations in terms of the DLVO potential, while Ito et al. ascribed the contraction to enhanced counterion-mediated attraction between particles caused by a decrease in the dielectric constant ε of medium (water) with rising temperature. Actually, when the temperature dependence of

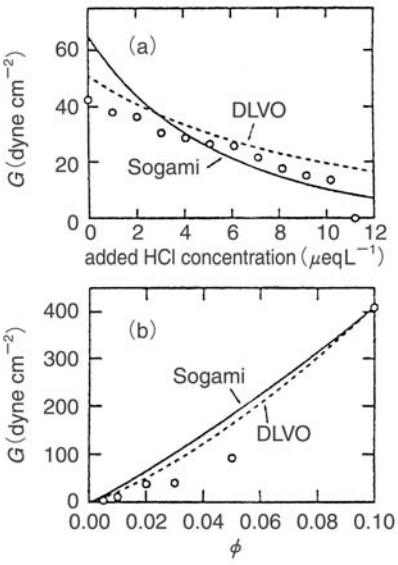

Fig. 9.2. Comparison of observed and theoretical shear moduli G. ○: observed by Lindsay and Chaikin, - - - - -: DLVO potential ($Z_n = 180$), ——: pair G-potential ($Z_n = 170$), $a = 54.5$ nm. (a) salt concentration dependence at $\phi = 0.02$. (b) particle concentration dependence at $C_s = 0$. Taken from [27] with the permission of the American Physical Society

ε is taken into account, the colloidal crystals are shown to monotonously expand. This is physically acceptable. (Compare the solid and broken lines in Fig. 4.14.) On the other hand, Asher et al.'s experimental data themselves are shown here to be inconsistent with the DLVO potential and with their interpretation.

In experiments of Asher et al., a water dispersion ($\phi = 0.02$) of dyed sulfonated polystyrene latex ($a = 41.5$ nm, $Z_a = 2370$) was locally heated and the variation of the lattice constant a_0 was observed by the Kossel line analysis. The crystal symmetry was bcc prior to the heating and a_0 was 245 nm. The volume fraction of particles ϕ in the crystal was calculated to be 0.0264 [21]. This value is 30% higher than the overall volume fraction (0.02). This fact implies that the bcc structure ($\phi = 0.0264$) must coexist with regions of ϕ lower than 0.02. In other words, the two-state structure is maintained. (See Chap. 4, Sect. 4.2.3) This is inconsistent with a purely repulsive DLVO potential.

Let's pass this inconsistency over for a while and consider how the DLVO potential U_R changes with temperature (See (8.9)). The Debye parameter κ changes with ε with varying temperature. For water, ε decreases from 87.90 to 69.88 and εT decreases from 2.40×10^4 to 2.26×10^4 when temperature rises from 0 to 50°C. Accordingly κ/κ_{298} increases from 0.988 to 1.118, where

κ_{298} refers to the parameter at 298 K. This implies that the DLVO potential is weakened with rising temperature. The heating caused locally the temperature rise while the rest of the dispersion was unaffected. It was claimed that, by the temperature dependence of κ, the heated region contracted as a result of repulsion in the surrounding, unheated region. Obviously, there are two regions of different temperatures, or the whole system is not in thermal equilibrium. Whether the DLVO theory may be applied to such a non-equilibrium system is a serious question.

Another problem is the charge number. From the reported values of a and Z_{a}, σ_{a} is calculated to be 1.75 μC cm^{-2}, from which σ_{n} is 0.45 μC cm^{-2} by Yamanaka's relation [20]. A value twice as large as this was given as the rescaled charge number by the original authors (1150 and charge density = 0.88 μC cm^{-2}). It is necessary to determine the charge number independently and thereby discuss the pros and cons of the theoretical framework adopted.

On the other hand, Ito et al. changed the temperature of the whole dispersion, so that the dispersion is believed to be in thermal equilibrium. If the particles are assumed to behave following the DLVO theory, the temperature rise weakens the interparticle repulsion, causing contraction of the crystals. The contraction of the lattice constant is estimated to be 1.3% by a temperature rise of 50°C [21].

The temperature dependence of the lattice constant in the Sogami theory can be estimated by (8.13). The results are shown in Fig. 9.3. The 50° temperature rise gives 2.4% contraction of the lattice constant.

Thus, both theories predict contraction of colloidal crystals with rising temperature. If we take one single fact of thermal contraction in isolation, we cannot distinguish between the two potentials. Again, it is not legitimate to claim that the DLVO theory is "correct" based on this observation.

9.3.4 Schulze-Hardy Rule

According to Schulze-Hardy rule, the coagulation power of colloidal particles is related to the sixth power of the valency of added simple ions z. It was widely known that this empirical rule could be accounted for in terms of the DLVO theory, in which it was understood the coagulation was caused by the van der Waals forces. The derivation of the rule from the DLVO theory was given in Chap. 2. In Chap. 6, however, when coupled with the van der Waals attraction, pair G-potential was demonstrated to lead a main term proportional to $1/z^6$ and an additional term containing $1/z^8$. Since the G-pair potential, like the DLVO potential, also shows a repulsion at short distances (Fig. 6.2), it would be no wonder if the two potentials support the empirical rule. It is concluded from this fact that which of the two potentials is more appropriate for the coagulation phenomenon cannot be judged. The frequent

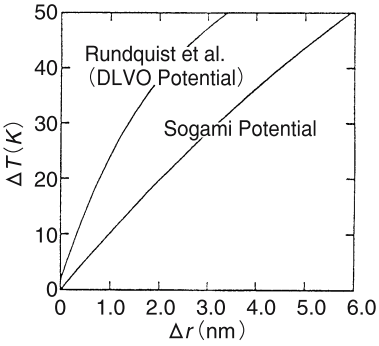

Fig. 9.3. Comparison of the Sogami prediction for the thermal contraction of colloidal crystals with the DLVO prediction. $\kappa = 2.19 \times 10^{-2}$ nm^{-1}. $a = 41$ nm. The κ value was obtained from (8.12) using the reported a and $R_{\rm m}$ (= 245 nm) and corresponds to 4.5×10^{-5} mol L^{-1} of 1-1 electrolytes. Taken from [21] with the permission of the American Physical Society

claim, that the DLVO theory excels others because it provides a theoretical proof to the empirical rule, is also unwarranted.

The discussion above for four physical quantities indicates that the DLVO theory is consistent with observation, but other models are also consistent, so that the theory cannot be considered established.

We restricted our discussion above to only four properties. The reason for this choice is that they are all relatively simple physical observations that don't involve ambiguous adjustable parameters. We know of many other properties or interpretations which have been believed to substantiate the DLVO theory. In most cases, unknown parameters are involved so that the true nature of the interparticle interaction cannot really be judged, leading only to circular arguments.

That the two potentials provided agreement with experiments may suggest that the quantity in question is not sensitive toward the interaction potential or it is substantially determined by a potential tail common to the two potentials, namely the short-range repulsion. In order to understand the colloidal interaction correctly, we need further systematic study using samples having much higher charge densities at low volume fractions.

9.4 Direct Measurements of Interparticle Potential

9.4.1 Measurements by Grier, Fraden, Tinoco, and Versmold

The arguments on the colloidal interaction so far presented have all been indirect in the sense that the potential was inferred from measured quantities. This way of approach has been adopted for atomic and molecular systems and is unavoidable and conventional. However, we can see large colloidal particles optically so that the following direct method is possible in principle. At low volume fractions the radial distribution function $g(r)$ is given by the pair potential energy $U(r)$ as follows,

$$g\left(r\right) = \exp\left[\frac{-U\left(r\right)}{k_{\mathrm{B}}T}\right]. \tag{9.2}$$

If the particle positions are determined as a function of time by a video imagery technique, the $g(r)$ can be determined, from which $U(r)$ is estimated by (9.2) [4, 5, 9, 10]. Even at lowest concentrations experimentally accessible, the measured potential may not correspond exactly to the pair potential. To circumvent this difficulty, an optical tweezers technique [5] or a simulation method [9] was devised.

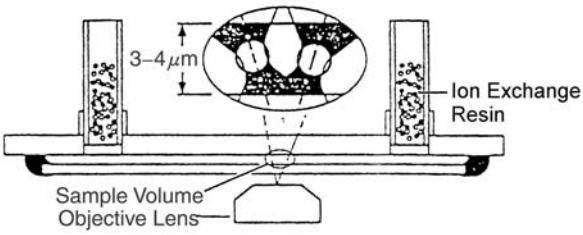

Fig. 9.4. Dispersion cell for the direct measurement of the interaction potential. The dispersion is put in a space between two glass plates (gap: $3 \sim 4$ μm). A pair of particles are held at a fixed separation with dual optical tweezers (See the inset) and released. The subsequent motion of the particles is recorded by a video camera. Taken from [5] with the permission of the American Physical Society

Figure 9.4 shows the experimental setup by Grier et al [5]. Colloidal dispersions were introduced into a space between two glass plates $3 \sim 4\,\mu$m apart. The dispersions were in contact with ion-exchange resin particles to remove continuously ionic impurities. Two particles were fixed by a tweezers at a distance of $1.5 \sim 1.7\,\mu$m. Their positions were recorded by a video imagery after the laser beams were cut off. The experimental error in the interparticle

distance is reported to be 50 nm. The information obtained for 796 pairs of particles was used.

Grier et al. pointed out that the observed potential curve agreed with the DLVO prediction when Z_n and κ^{-1}in (8.9) were adjusted as independent parameters. The best fit was obtained for $Z_n = 1991 \pm 150$ and $\kappa^{-1} = 161 \pm 10$ nm. The κ^{-1} value corresponds to 3.6 μmol L^{-1} for 1-1 salts and seems not to be unreasonable in the presence of ion-exchange resins. Certainly the agreement between theory and experiments is satisfactory. However, the Z_n value was not checked by an independent measurement. The analytical charge number Z_a was reported to be 3.2×10^5 per particle. Then Z_n/Z_a is 0.006. According to the empirical relation by Yamanaka [20], Z_n is 1.1×10^4 for $Z_a = 3.2 \times 10^5$, and Z_n/Z_a is 0.03, being one order of magnitude larger than Grier's value. Thus, it is difficult to conclude from their measurements that the DLVO theory gives a correct potential [3].

In their subsequent paper [7], Grier et al. carried out the measurements on latex spheres in a space made by two parallel glass plates and reported that a DLVO-type repulsion was detected when the distance h between the glass plate and sphere was 9.5 μm whereas an attraction appeared when h was 2.5 μm, as shown in Fig. 9.5. It was pointed out that the larger the particle, the deeper the potential minimum. Grier et al. invoked the interaction between the glass wall and ionic atmosphere around a particle as a cause of the attraction. On the other hand, Squires and Brenner suggested that a hydrodynamic effect was responsible for the "attraction" as follows [31]. The anionic particles are repelled by negative charges on the glass interface and forced to move up from the interface. The liquid medium following the repelled particles drags in other nearby particles, diminishing an apparent horizontal distance between two particles. This effect seems to result in an attraction. The idea is interesting but questions are raised by this argument. For example, when a particle is at the mid point between the two plates, the particle would not move. Then the attraction would not appear. Experimental check must be done on this point. Squires and Brenner considered that interparticle interaction was intrinsically repulsive. If so, no attraction, but repulsion should be observed if particle is at the mid point. As discussed in Chap. 4, Sect. 4.2.4, however, experiments show that attraction is in action between particles far from the interface. Furthermore, the concentration effect of particles is outstanding at a distance of 5 μm from a similarly charge interface [32–34]. This effect was not taken

[3] A polystyrene latex sample (Duke Scientific, No. 5065A) has been used in a series of experiments by Grier's group [5–7]. Its titratable charge number was reported to be 3.2×10^5 per particle or $1e/10\text{nm}^2$, presumably based on the information from the producer. It is not clear whether the difference of a factor about 2 in the two values is due to the time change of the charge number. In [5] the net charge number Z_n was determined to be 1991 by fitting with the DLVO potential, whereas a value of 5964 was reported in [7]. The two values differ by a factor of three. Before agreement is claimed, the Z_n must be checked by independent measurements.

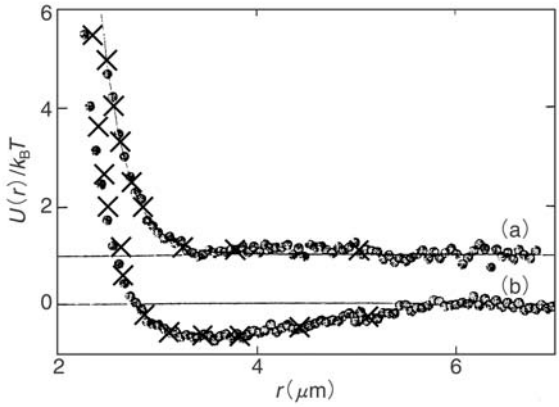

Fig. 9.5. Interparticle interaction potential near a glass surface as a function of the interparticle distance. Sample: polystyrene latex particles ($a = 0.33$ μm). The curve (a) is obtained at a distance h of 9.5 μm from the glass surface, is purely repulsive, and agrees with the DLVO potential (broken curve). The curve (b) is the potential at $h = 2.5$ μm and has a potential minimum of $\sim 0.7\ k_BT$. The crosses denote some results of the simulation by Squires and Brenner. The two curves are shifted vertically by 1 k_BT. Taken from [31] with the permission of the American Physical Society

into account in Squires-Brenner's argument. Since this effect counteracts the repulsive action on a particle from the charged wall, the hydrodynamic factor discussed by them might not be so large as they suggest. To evaluate the hydrodynamic effect quantitatively, it is required to know the charge numbers of the particles and the interface exactly. The former can be measured fairly precisely. On the other hand, it is necessary to measure ζ potential of the glass surface to know the plate charge. Because of the ambiguity of the ζ potential [35], it would not be simple to quantitatively verify the hydrodynamic effect.

Whether Squires-Brenner's argument is quantitatively correct or not, the region near the interface is very different from the inside of dispersion. According to Prieve et al.'s results [36], who measured directly the motion of large latex particles, their diffusion coefficient in the vicinity of interface is only 2% of that in the bulk. According to video-recording by Yoshino [37], the displacement of particles in a narrow space between two glass plates is much larger than the prediction of the Einstein theory of Brownian motion. This is understandable since the theory is derived for unconfined particles which are free in all directions whereas the particle motion under the confined condition is free in the direction parallel to the two glass plates but restricted in the vertical direction. Since the influence of these factors on the particle motion and hence on the $g(r)$ is not easily evaluated, *it is appropriate to avoid measurements in the vicinity of the glass wall, if correct interparticle interaction*

potential is sought. Squires and Brenner's suggestion calls attention to the danger of the interface effect.

Crocker and Grier fitted the observed potential with the DLVO potential and with pair G-potential to obtain Z_n and κ^{-1}. Their results are shown in Table 9.2. The parameters obtained from the pair G-potential are shown with the suffix s. Crocker et al. claimed that the pair G-potential is not a correct pair potential for the isolated pair of particles on the basis of the systematic change of κ_s^{-1} with the particle radius a. On the contrary, κ^{-1} from the DLVO theory was a-independent. It was further noted that, in mixtures of two particles of different sizes, the observed potential could be reproduced when the geometrical average of the two charge numbers (Table 9.2) was used and no attractive tail could be observed. From these observations the DLVO theory was claimed to be quantitatively satisfactory.

The above argument cannot be accepted for the following reasons [38]. First, unlike the DLVO theory, the Sogami theory was developed for multiparticle systems. The experimental data obtained for a pair of particles by Crocker et al. cannot be compared with the Sogami theory. As seen from (8.12), κ^{-1} and Z_n cannot necessarily be independent parameters. Furthermore, the salt concentration C_s of the medium is determined by microions generated from a large number of particles not chosen for the direct measurements. Therefore the κ^{-1} values must first be compared with the ionic strength of the medium. Unfortunately this quantity was not measured.

Secondly, both Z_n and Z_{ns} have also to be examined by independent measurements of the conductivity of the dispersions. Yamanaka et al. tried to determine Z_n and Z_a of the latex samples of the same catalog number of the same producer as studied by Grier et al. by the conductance measurements and the conductometric titration [39]. The presence of strongly acidic groups alleged by Crocker et al. could not be confirmed and the charge numbers of the samples were too low to be determined. The sample 5153A of the largest radius among others was particularly not stable and considerable amounts of aggregates were found. Obviously it is one of the minimum requirements to select stable, homogeneous dispersions for the measurements of physico-chemical properties such as interparticle interaction. Furthermore, as discussed in the preceding chapters, the attraction in question is undetectably weak for samples of such low charge numbers. It is hoped that the direct measurements are carried out using well-defined, highly charged and stable particles.

Table 9.2. Interaction parameters of the DLVO potential and the pair G-potential determined by Crocker-Grier's measurements

$2a$ (μm)	Z_n	κ^{-1} (nm)	ζ_0 (mV)	Z_{ns}	κ_s^{-1} (nm)
1.53	22793	289	−167	1767	960
0.97	13796	268	−165	1525	730
0.65	5964	272	−145	777	670

The confined geometry was also adopted by Kepler and Fraden [9]. The gap between two glass plates was $2 \sim 6$ μm and the gravitational sedimentation was avoided by using a mixture of H_2O and D_2O. The position of particles was determined by a video imagery technique of particles on the mid plane between the two glass plates. The distance between two particles was claimed to be determined with an experimental error of 20 nm. The $g(r)$ was obtained from $500 \sim 5000$ video images (90×70 μm), which contained $30 \sim 300$ particles per image. The $g(r)$ thus obtained could be converted to a trial potential by using (9.2), from which the pair potential was extracted with the help of the Brownian dynamics simulation as follows. The trial potential was compared with a Lennard-Jones (LJ) potential to determine the parameters, from which a new LJ potential was determined and incorporated into (9.2) to obtain a modified $g(r)$. The process was iterated until the modified $g(r)$ agreed with the observed one.

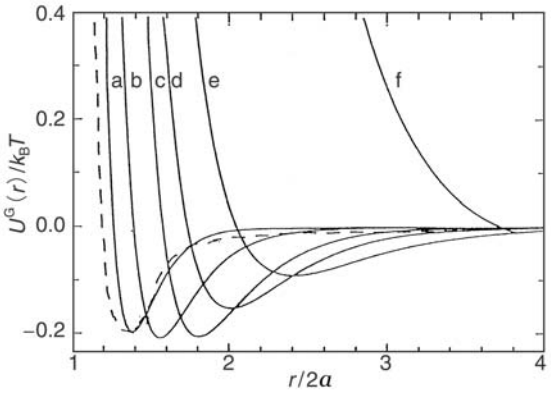

Fig. 9.6. The interparticle pair potential measured by Kepler and Fraden (solid curve) and the pair G-potential (broken curve). Sample: polystyrene-based latex particle (reported surface charge density: $0.1e$ nm^{-2}, $a = 640$ nm), solvent: H_2O-D_2O (1:1) mixture. The number density of particles on the focal plane: 12×10^{-3} μm^{-2}. The salt concentration, though not measured, decreases from a to f. The pair G-potential is calculated by Tata and Arora [40].

The pair potential thus determined is shown in Fig. 9.6. The following three points are noteworthy. First, except at the lowest salt concentration (curve f), the pair potential shows an outstanding minimum (attraction). This attraction is fairly strong. According to Kepler and Fraden, the Hamaker constant A must be $10^{-19} \sim 3.3 \times 10^{-18}$J, if we try to account for it with the DLVO theory (2.128). These values are much larger than the usually accepted ones $10^{-21} \sim 10^{-20}$. The result by Kepler and Fraden was obtained with the surface potential ψ_a of 25 mV, which is given by the Debye-Hückel theory as

follows

$$\psi_a = \frac{Z_n e}{\varepsilon a}(1 + \kappa a). \tag{9.3}$$

The result did not change when 100 mV was chosen for ψ_a. Conversely, if the observed potential curve was fitted assuming $A = 10^{-20}$ J, ψ_a was found to be 5 mV. Thus, Kepler and Fraden concluded that the DLVO theory, which was derived for unconfined particles, could not be applied for particles confined in a small space.

Secondly, the C_s dependence of the position of the potential minimum and the depth is interesting. As the original authors pointed out, the minimum position shifts toward to shorter distances and the minimum becomes first deeper and then shallower when C_s is increased. These trends observed are the same as those of the pair G-potential shown in Fig. 6.4. Unfortunately, C_s was not measured by the original authors, so that quantitative comparison is difficult.

Thirdly, the observed potential can be reproduced by the pair G-potential calculated (the broken curve in Fig. 9.6) assuming $C_s = 2.9$ μmol L^{-1}, as pointed out by Tata and Arora [40]. The C_s value seems reasonable in the presence of ion-exchange resin. From the agreement of the minimum position and depth, Tata and Arora argued that the results by Kepler-Fraden supported the counterion-mediated attraction discussed by Sogami.

Using a confined geometry, Carbajole-Tinoco [10] also detected a strong attraction at much higher particle concentrations. They also noticed that the attraction could not be accounted for in terms of the DLVO theory, unless a Hamaker constant larger by one order of magnitude than that usually accepted was assumed. Interestingly, from the reported charge number, the net charge density σ_n is estimated to be 0.37 μC cm^{-2}, which is much larger than that of Grier's sample (0.02). It is noted that, unlike Grier et al.. Tinoco et al. carried out the measurements under the condition that the attraction can be strong enough to be detected.

Rajagopalan found an inversion procedure to evaluate $U(r)$ from the observed $g(r)$ by using a Monte Carlo simulation with the predictor-corrector method [23, 41]. In an exploratory study they started from a LJ potential, from which $g(r)$ was obtained by simulation. The potential was then estimated by the inversion procedure from the $g(r)$ and found to be in an excellent agreement with the original LJ potential. Rao and Rajagopalan applied this procedure for the $g(r)$ observed by Kepler and Fraden to obtain the potential curve [41]. As is clear from Fig. 9.7, the inversion procedure gave a satisfactory agreement with the curve by Kepler and Fraden. With respect to the pair G-potential, agreement is satisfactory as far as the minimum position and depth are concerned. Most interesting is that, in the case of the lowest C_s in Fig. 9.6 (curve f), only repulsion was obtained by Kepler and Fraden whereas an attractive tail was found in the potential by the inversion procedure and a shallow potential minimum was seen in the Tata-Arora analysis using the pair G-potential, as shown in Fig. 9.8.

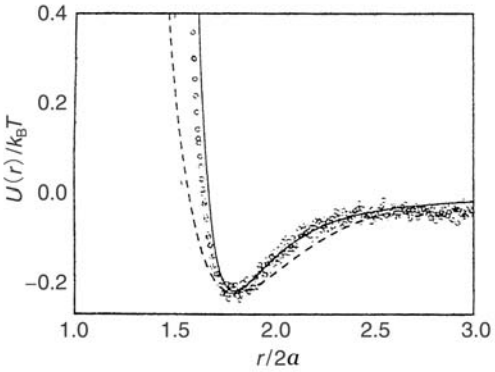

Fig. 9.7. Comparison of the interparticle potentials observed and calculated by the inversion procedure. The salt concentration corresponds to the curve c in Fig. 9.6. ○: pair potential obtained by the inversion procedure from $g(r)$ observed by Kepler and Fraden. Solid curve: potential reported by Kepler and Fraden. Broken curve: pair G-potential calculated by Tata and Arora [40]. Taken from [41] with the permission of the American Physical Society

Tinoco et al. adopted the hypernetted-chain (HNC) approximation in computing $U(r)$ from the observed $g(r)$ [10]. Rao and Rajagopalan pointed out that this approximation is not quantitatively satisfactory [23].

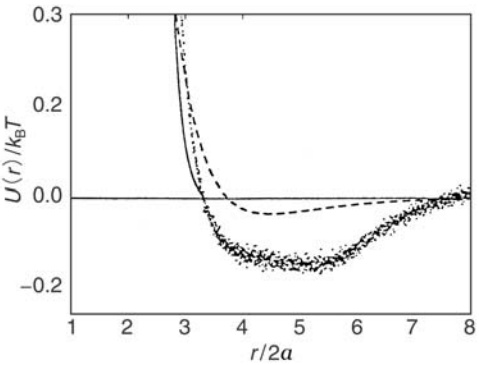

Fig. 9.8. Comparison of the interparticle potentials observed and calculated by the inversion procedure. The salt concentration corresponds to the curve f in Fig. 9.6. •: inverted potential. Solid curve: observed by Kepler and Fraden. Broken curve: pair G-potential [40]. Taken from [41] with the permission of the American Physical Society

Versmold et al. microscopically determined the particle distribution and hence $g(r)$ for polystyrene latex particles ($a = 385\,\mathrm{nm}$) [4]. The measurements were carried out at low volume fractions ϕ, where the $g(r)$ obtained from 20,000 video frames showed no ϕ dependence. It was claimed that the focal planes were maintained at distances of $2 \sim 6$ μm from the glass surface so that the results were not affected by the glass interface. The $g(r)$ obtained monotonously increased with the interparticle distance r, conversing to unity. The original authors emphasized the good agreement with the DLVO potential and remarked that no sign of attraction was found. In their experiments, C_s was controlled by addition of NaCl and the κ^{-1} values determined by fitting with the DLVO theory was claimed to correspond to C_s. The net charge number Z_n was found to be 190 per particle by the fitting. This value was not confirmed by independent measurements, however. Even if it is correct, the charge number is too small. As was already emphasized, attraction does not appear for such low charge particles. As a matter of fact, Tata calculated the pair G-potential under the conditions of Versmold et al. and found that the depth of the potential minimum is only $0.02\ k_\mathrm{B}T$, which is experimentally undetectable [40]. This implies that the results of Versmold et al. can be equally satisfactorily reproduced by the DLVO theory and the Sogami theory. The situation is exactly the same as for the structure factor, elastic properties, thermal contraction, and the Schulze-Hardy rule discussed in Sect. 9.3. In other words, Versmold et al.'s experiment cannot justify the advantage of the DLVO theory and the absence of the attraction, contrary to their claim.

In these measurements, the particle positions need to be determined precisely and with high reproducibility to obtain the correct interaction potential. This is not so easy to achieve, as inferred from the following recent development. Durand and Franck devised techniques to address the basic difficulty associated with the confined geometry [42], by which they found that the potential was much shorter ranged than would be expected based on the DLVO theory. This result is at variance with those discussed in this section.

9.4.2 Measurement by Sugimoto et al.

In this approach, the forces between particles are measured by detecting the critical laser beam power at the moment of the displacement of particle trapped by an attenuating beam while the other particle of the pair is held by another beam at the full power [43]. The gravitational sedimentation for large particle was avoided by using a H_2O-D_2O mixture and the focal plane of microscope was set at 10 μm away from glass surface to circumvent the wall effect. In order to minimize the influence of airborne CO_2 the measurement was performed in a nitrogen atmosphere. The results are shown in Fig. 9.9. It was claimed that, in agreement with the DLVO theory, purely repulsive forces only were observed between two polystyrene latex particles ($a = 2.13$ μm).

Comments seem to be necessary regarding this claim. First, all measurements were done at $C_\mathrm{s} > 10^{-4}$ mol L^{-1}. At such salt concentrations, as

mentioned in Chap. 4 and other places, the counterion-mediated attraction disappears for conventional colloid particles, and the depth of the potential minimum of the pair G-potential is zero (Fig. 6.4); no attraction can be detected. Therefore, it is a matter of course that Sugimoto et al. could not find the attraction. Secondly, the surface-to-surface distances are 200 nm at most for particles of a radius of 2.13 μm. At such a short distance, even the pair G-potential has a repulsive tail. The attraction between colloidal particles appeared at distances of $\sim$ μm for particles of radii of 0.5 μm. Unless Sugimoto's technique can be extended to such larger distances, it cannot be used for judging the nature of the interparticle interaction [4].

9.4.3 Surface Force Measurements and Atomic Force Microscopy

The recent technical development made it possible to measure the forces between two surfaces. Pashley and Israelachvilli reported by surface force measurements that repulsive forces were in action between two mica surfaces in salt solutions [44]. Pashley et al. observed a repulsion between silica particle and silica flat surface at $C_s > 10^{-4}$ mol L^{-1} [45]. By the scanning force microscope (SFM) Lindsay et al. observed a repulsion between latex particles and between latex particle and mica surface at a separation shorter than 10^2 nm from the surface and at C_s of 10^{-2} mol $L^{-1}$and noticed a good agreement with the DLVO theory [46]. At lower C_s's, agreement with the theory was less satisfactory. The atomic force microscopy was employed for titanium oxide particles [47]. In the charged state, a repulsion was observed while a van der Waals attraction was reportedly in action within 10 nm at a separation of 50 nm and at C_s's higher than 10^{-4} mol L^{-1}. This repulsion did not agree with the DLVO prediction, which the authors pointed out was due to the "surface roughness".

To repeat, the counterion-mediated attraction does not show up at such salt concentrations and at short separations and therefore it is no wonder only repulsion was observed. These results cannot prove the absence of the attraction.

[4] Using the ζ value reported by Sugimoto, and assuming $\zeta = \psi_a$, the net charge number Z_n can be estimated from (9.3). It increases with C_s within the C_s range employed. This trend is not consistent with the information from direct conductivity measurements. The assumption might be the source of the C_s dependence. However, Fitch pointed out [35] that "because there is no direct measure of the distance of the slipping plane from the surface, it is impossible to relate ζ directly to the surface potential". It is necessary to analyze experimental results with reliable parameters such as the independently measurable net charge number. Otherwise it cannot finally be judged whether the observation is correct or not and/or whether the theory is justified or not. As mentioned above, furthermore, even the pair G-potential is repulsive at such short distances. It would be logically wrong to conclude that Sugimoto et al.'s measurements ruled out the contribution of the long-range attraction in colloidal interaction.

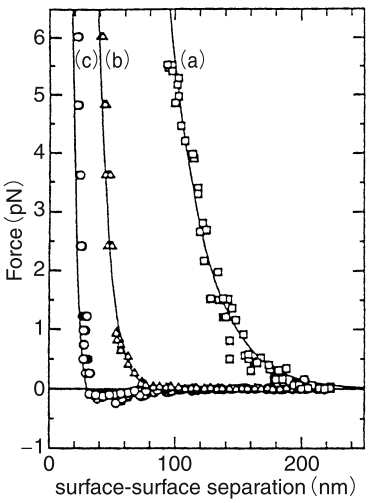

Fig. 9.9. Interparticle forces as a function of the surface-to-surface separation between two latex particles as measured by Sugimoto et al.'s technique. Curve (a) C_s ($NaClO_4$) = 1.15×10^{-4}, (b) 1.00×10^{-3}, (c) 5.00×10^{-3} mol L^{-1}. The solid curves are the DLVO potential with a Hamaker constant of 5.0×10^{-21} J. Taken from [43] with the permission of the American Chemical Society

Vinogradova et al. measured the forces between polystyrene surfaces by an atomic force microscope-related apparatus and found that a long-range attractive force was in action rather than a potential of the DLVO type [48]. They attributed the attractive force to submicroscopic "gas bubbles" attached to the polystyrene surface and anchored by or trapped between surface asperities. Although it is presently difficult to judge whether this interpretation is correct, it is to be noted that their experimental conditions (pH6, KCl concentrations of $10^{-4} \sim 10^{-2}$ mol L^{-1}, and range of measurements (100 nm) for particles of radii between $1.8 \sim 4.4$ μm) are very different from those discussed in Chap. 4. The counterion-mediated attraction can hardly exist for colloidal particles at such high salt concentrations with a potential minimum at distances of $\sim$ μm for much smaller particles, and most experiments were carried out at much lower pH's.

When mica surfaces are modified with surface active agents having long-chain alkyl groups, hydrophobic surfaces are prepared. Attraction was detected between the two surfaces at separations of 15 nm [49] and 300 nm [50]. This is clearly due to the hydrophobic interaction between the surfaces and is not the electrostatic attraction discussed in the present monograph.

Although there is a clear philosophical preference for the "direct methods" of measuring colloidal interactions discussed above, these measurements were done in the vicinity of glass surfaces so that the results might have been influenced by the wall effect. It is true that the samples used were not adequately characterized. Under the experimental condition employed such as salt concentration and particle separation, the attraction happens to be weak and the repulsion is overwhelmingly strong. Therefore, the role of the attraction cannot be assessed by these experiments. Except the cases of Fraden and Tinoco, particles of low charge densities were chosen, for which the attraction is not strong. It is not logical to negate the attraction by experiments under the conditions where the attraction is not detectable.

In order to obtain the correct information of the interparticle interaction, measurements have to be performed with *free* particles without being interfered by the wall effect. Furthermore, highly charged particles need to be used, if the attraction is to be verified.

9.5 Comparison of Recent Computer Simulation with Experiments

Structure formation was experimentally confirmed for solutions of ionic dendrimers with univalent counterions (Fig. 3.25) and the inequality relation $2D_{\rm exp} < 2D_0$ was observed for higher generations (Fig. 3.26). This indicates that the counterion-mediated attraction is in action even when univalent ions are counterions. When *bivalent* counterion is used, the scattering peak is *not* observed (Fig. 3.24). This is because the net charge density of the dendrimers is lower with bivalent counterions than with univalent ones (Table 3.2), so that the attraction is weaker. As discussed in Chap. 3, Sect. 3.3, a similar influence of the counterion valency on intermacroion interaction was noticed by Zhang et al. on sodium poly(styrene sulfonate)s [51]. This dependence on the valency of the counterions is in clear contradiction with recent computer simulations [52, 53], which showed that only repulsion was generated between macroions with univalent counterions and an attraction appeared when the valency of the counterions became larger. The attraction in the simulations appeared at very short distances, at variance with the experimental observation on macroionic systems [5]. The potential minimum was found at

[5] Low charge particles with small radius which were considered in the simulation by Linse et al. [53] correspond to ionic micelles or ionic dendrimers. As discussed in Sects. 3.2.3 and 3.2.4, dodecyltrimethyammonium hydrochloride forms spherical micelles of $Z_{\rm n}$ smaller than 50 and of $a = 1.6$ nm. The SAXS profile indicated that the micelles formed homogeneously ordered structure throughout the solution with a Bragg spacing $2D_{\rm exp}$ of 7 nm. The $2D_{\rm exp}$ value was found to be nearly equal to the average spacing $2D_0$. There is no need to invoke the attraction that was concluded by the simulation. Ionic dendrimers of the $7^{\rm th}$ and $10^{\rm th}$ generations

interparticle distances shorter than 5 nm according to the simulation on 60-valent macroions with bivalent counterions [51]. Experiments show that the minimum is located at several ten nm for the dendrimers and at $\sim$ μm for colloidal particles. Obviously, the computer simulations do not correctly describe macroionic interaction. One reason would be the "bare" electrostatic interaction energy $U_{ij}(r)$ assumed in the simulations, which reads

$$U_{ij}(r) = \frac{Z_i Z_j e^2}{4\pi\varepsilon r}, \qquad r \geq (a_i + a_j)/2 \tag{9.4}$$

where Z is the charge number of the species i or j, ε the dielectric constant, a the radius of particle or counterions. This assumption is correct for an isolated pair of ions, but is not so when a large number of ions are present in reality. This point would be understood if the Debye-Hückel theory is closely examined.

Recently Terao and Nakayama carried out a simulation using (9.4) for interaction between charged interface and particles [54]. They found a concentration effect of charged particles near a similarly charged interface. The largest effect was found at a distance of 10 nm from the interface. This result seems to correspond to the experimental data for spherical micelles by Thomas et al. [32], while the simulation result was considerably smaller than that observed for latex particles (5 μm $\sim$ 60 μm) [33, 34].

A simulation by Wu et al. [55] showed that only repulsion was present in 0.5 mol L^{-1} with univalent counterions between macroions in conformity with the DLVO theory, whereas attraction appeared at short distances for bivalent counterions. It is noted that attraction has not been experimentally found at such high salt concentrations for ionic colloidal particles.

9.6 Other Related Problems

In the present monograph, the mean-field Poisson-Boltzmann (PB) equation provides a basis of our theoretical discussion of the properties of charged colloidal solutions. While various issues can be raised with this approximation, the Debye-Hükel theory is an often analytically tractable theory that clearly succeeds in describing many of the essential properties (dynamic and thermodynamic) of ionic solutions at 'low' concentrations, the theory becoming exact in the 'infinite dilution' limit where fluctuation effects vanish. Moreover, the formal generalization of the PB description of charged colloidal solutions by Sogami predicts the emergence of non-trivial phenomena at finite particle concentrations that have experimentally testable ramifications. Specifically, the

with univalent counterions form ordered structures with $2D_{\text{exp}}$ of 12 $\sim$ 40 nm. This spacing was smaller than $2D_0$ (Fig. 3.25), indicating the presence of an attraction. In the simulation, however, no attraction was concluded for univalent counterions (Fig. 1 in [53]).

Sogami model indicates the existence of an effective long-range electrostatic attraction between similarly charged macroions that is mediated by correlations created by the attractive interactions with counterions of opposite charge [6]. This many-body effect, which does not exist in the limit of infinite dilution and which is not confinement-induced, derives from the global condition of thermodynamic equilibrium and overall charge neutrality. These theoretical predictions are contrasted with those of the popular DLVO theory (also based on the PB model), that indicate that like-charged particles universally exhibit repulsive interparticle interactions. Notably, the DLVO theory is an infinite dilution theory relevant to describing the interactions of two *isolated* charged particles and does not address itself to the complex many-body effects that the Sogami model indicates are essential for understanding finite concentration colloidal dispersions in the thermodynamic limit. Since the arguments favoring one model over the other are apparently too subtle to be answered any time soon by theoretical concerns alone (the validity of mean field theory itself being just one of the fundamental unanswered questions), we take the pragmatic approach of assessing which model of ionic interaction best describes *real* colloidal solutions from an experimental standpoint.

Quite independently of the Sogami theory, a phenomenological "volume term" model has been introduced to describe the effective attraction observed in measurements [56–58]. It was claimed that, without invoking an attraction, the phase-separation phenomena experimentally found could be accounted for in terms of this theory. Recently, however, von Grünberg et al. [59] demonstrated that the prediction of a gas-liquid phase coexistence by the volume term theory was spurious. Independently, Tamashiro and Shiessel also pointed out [60] that the thermodynamic instability predicted by the volume term theory was a mathematical artifact and did not correspond to the experimentally observed microscopic inhomogeneity discussed in Chap. 4.

We have often come across the assertion that the formation of colloidal crystals can be accounted for by increase in entropy (S). Since $\Delta G = \Delta H - T\Delta S$, there can be two possibilities in the crystallization process:(1) the enthalpy decreases irrespectively of the entropy change ($\Delta H < 0$) and (2) the entropy largely increases, irrespectively of the enthalpy change ($\Delta S > 0$). Thus the concept of the entropy-driven crystallization (the 2^{nd} case) cannot readily be negated. We have been guided by an idea that crystallization proceeds with enthalpy decrease (the 1^{st} case). When particles form crystals from disordered states, the entropy change is unfavorable. As far as the configurational entropy is concerned, therefore, the account in terms of the enthalpy decrease (stabilization by an attraction) seems reasonable.

[6] Bowen and Shariff claimed on the basis of nonlinear Poisson-Boltzmann equation that an attraction can exist between confined colloidal particles (Bowen WR, Sharif AO (1998) Nature 393:663) and that a new type of interaction described by the Sogami theory was not necessary. However, this calculation turned out to be in error [Neu, JC (1999) Phys. Rev. Lett. 82:1072] and critical comment on the Sogami theory should be disregarded.

In previous arguments favoring the entropy-driven crystallization, it appears, particles are assumed, though implicitly, to interact with purely repulsive DLVO potential. Since the coexistence of crystalline regions and disordered regions (self-sustaining crystals) cannot be accounted for by this potential, the entropy change was invoked. In order for this reasoning to be correct, there must be additional entropy increases counteracting to the negative contribution of the configurational entropy. From the standpoint admitting the presence of attraction, this reasoning confuses the assumption and conclusion. This is not logically acceptable2, and does not prove the DLVO theory, nor disproves the attraction. The final judgment can be made only when the entropy increase of the total system by crystallization can be measured by independent experiments without assuming the interparticle potential.

References

1. McBride RV, Baveye P (2002) Soil Sci Soc Am J 66:1207
2. Verwey EJW, Overbeek JThG (1948) Theory of the stability of lyophobic colloids. Elsevier, Amsterdam
3. Ackerson BJ, Clark NA (1984) Phys Rev A 30:906
4. Vondermassen K, Bongers J, Mueller A, Versmold H (1994) Langmuir 10:1351
5. Crocker JC, Grier DG (1994) Phys Rev Lett 73:352
6. Larsen AE, Grier DG (1996) Phys Rev Lett 76:3862
7. Crocker JC, Grier DG (1996) Phys Rev Lett 77:1897
8. Ito K, Nakamura H, Ise N (1986) J Chem Phys 85:6136
9. Kepler GM, Fraden S (1994) Phys Rev Lett 73:356
10. Carbajal-Tinoco MD, Castro-Roman F, Arauz-Lara JL (1996) Phys Rev E 53:3745
11. Yoshida H, Yamanaka J, Koga T, Ise N, Hashimoto T (1998) Langmuir 14:569
12. Yamanaka J, Yoshida H, Koga T, Ise N, Hashimoto T (1998) Phys Rev Lett 80:5806
13. Tata BVR, Rajalskshmi M, Arora AK (1992) Phys Rev Lett 69:3778
14. Tata BVR, Yamahara E, Rajamani PV, Ise N (1997) Phys Rev Lett 78:2660
15. Gröhn F, Antonietti M (2000) Macromolecules 33:5938
16. Ohshima A, Konishi T, Yamanaka J, Ise N (2001) Phys Rev E 64:051808
17. Williams R, Crandall RS (1974) Phys Lett 48A:225
18. Rundquist PA, Jagannathan S, Kesavamoorthy R, Branardic C, Xu S, Asher SA (1991) J Chem Phys 94:711
19. Ito K, Ise N, Okubo T (1985) J Chem Phys 82:5732
20. Yamanaka J, Hayashi Y, Ise N, Yamaguchi T (1997) Phys Rev E 55:3028
21. Ise N, Smalley MV (1994) Phys Rev B 50:16722
22. Tata BVR, Sood AK, Kesavamoorthy R (1990) Pramana J Phys 34:23
23. Rajagopalan R (1996) In:Arora AK, Tata BVR (eds) Ordering and phase transitions in charged colloids. VCH, New York, Chap. 13
24. Sood AK (1991) Solid State Phys 45:1
25. Buscall R, Goodwin JW, Hawkins MW, Ottewill RH (1982) J Chem Soc Faraday Trans I 78:2889
26. van de Ven TGM (1989) Colloidal hydrodynamics. Academic Press, San Diego, Chap. 8, p.544
27. Ito K, Sumaru K, Ise N (1992) Phys Rev B 46:3105

28. Lindsay HM, Chaikin PM (1982) J Chem Phys 76:3774
29. Alexander S, Chaikin PM, Grant P, Morales GJ, Pincus P, Horn D (1984) J Chem Phys 80:5776
30. Ise N, Ito K, Okubo T, Dosho S, Sogami I (1985) J Am Chem Soc 107:8074
31. Squires TM, Brenner MP (2000) Phys Rev Lett 85:4976
32. Lu JR, Simister EA, Thomas RK, Penhold J (1993) J Phys Chem 97:13907
33. Ito K, Muramoto T, Kitano H (1995) J Am Chem Soc 117:5005
34. Muramoto T, Ito K, Kitano H (1997) J Am Chem Soc 119:3592
35. Fitch RM (1997) Polymer colloids: A comprehensive introduction. Academic Press, San Diego
36. Prieve DC, Bike SG, Frej NA (1990) Faraday Discuss Chem Soc 90:209
37. Yoshino S (1984) Presented at Rheology Group Meeting, High Polymer Society of Japan, Nagoya, June
38. Tata BVR, Ise N (2000) Phys Rev E 61:983
39. Yamanaka J (2000) private communication
40. Tata BVR, Arora AK (1995) Phys Rev Lett 75:3200
41. Rao KS, Rajagopalan R (1998) Phys Rev E 57:3227
42. Durand RV, Franck C (2000) Phys Rev E 61:6922
43. Sugimoto T, Takahashi T, Itoh H, Sato S, Muramatsu A (1997) Langmuir 13:5528
44. Pashley RM, Israelachvilli JN (1984) J Coll Interface Sci 101:511
45. Ducker WA, Senden TJ, Pashley RM (1992) Langmuir 8:1831
46. Li YQ, Tao NJ, Pan J, Garcia AA, Lindsay SM (1993) Langmuir 9:637
47. Larson I, Drummond CJ, Chan DYC, Grieser F (1993) J Am Chem Soc 115:11885
48. Vinogradova OI, Yakubov GE, Butt H-J (2001) J Chem Phys 114:8124
49. Pashley RM, McGuiggan PM, Ninham BW, Evans DF (1985) Science 229:1088
50. Kurihara K, Kunitake T (1992) J Am Chem Soc 114:10927
51. Zhang YB, Douglas JF, Ermi BD, Amis EJ (2001) J Chem Phys 114:3299
52. Hribar B, Vlachy V (2000) Biophys J 78:694
53. Lobaskin V, Lyubartsev A, Linse P (2001) Phys Rev E 63:020401(R)
54. Terao T, Nakayama T (2002) Phys Rev E 65:021405
55. Wu JZ, Bratko D, Prausnitz JM (1998) Proc Natl Acad Sci USA 95:15169
56. van Roij R, Dijkstra M, Hansen JP (1999) Phys Rev E 59:2010
57. Denton AR (1999) J Phys:Condens Matter 11:10061
58. Warren PB (2000) J Chem Phys 112:4683
59. von Grünberg HH, van Roij R, Klein G (2001) Europhys Lett 55:580
60. Tamashiro MN, Shiessel H (2003) J Chem Phys 119:1855

Index